MCEER
EARTHQUAKE ENGINEERING TO EXTREME EVENTS

ISSN 1520-295X

Characterizing the Rotational Components of Earthquake Ground Motion

by
Dhiman Basu, Andrew S. Whittaker
and Michael C. Constantinou

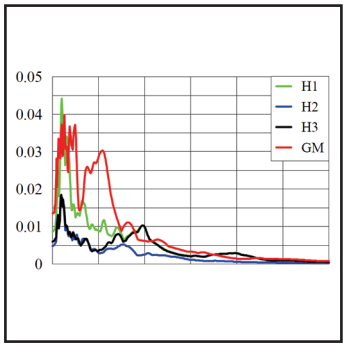

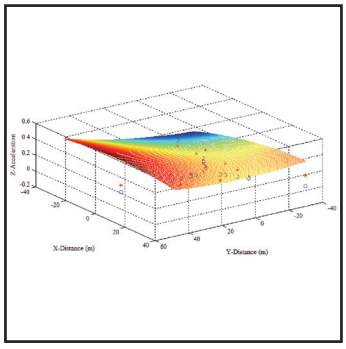

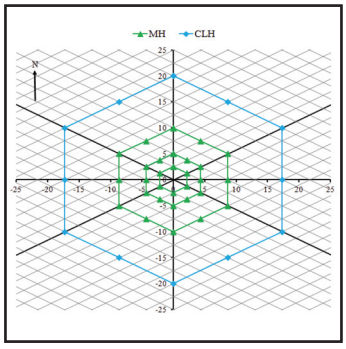

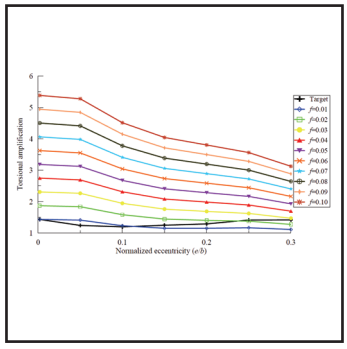

Technical Report MCEER-12-0005

June 15, 2012

This research was conducted at the University at Buffalo, State University of New York and was supported by MCEER Thrust Area 3, Innovative Technologies.

NOTICE

This report was prepared by the University at Buffalo, State University of New York as a result of research sponsored by MCEER. Neither MCEER, associates of MCEER, its sponsors, the University at Buffalo, State University of New York, nor any person acting on their behalf:

a. makes any warranty, express or implied, with respect to the use of any information, apparatus, method, or process disclosed in this report or that such use may not infringe upon privately owned rights; or

b. assumes any liabilities of whatsoever kind with respect to the use of, or the damage resulting from the use of, any information, apparatus, method, or process disclosed in this report.

Any opinions, findings, and conclusions or recommendations expressed in this publication are those of the author(s) and do not necessarily reflect the views of MCEER, the National Science Foundation, or other sponsors.

Characterizing the Rotational Components of Earthquake Ground Motion

by

Dhiman Basu,[1] Andrew S. Whittaker[2] and Michael C. Constantinou[3]

Publication Date: June 15, 2012
Submittal Date: May 1, 2012

Technical Report MCEER-12-0005

MCEER Thrust Area 3, Innovative Technologies

1 Post-Doctoral Scholar, Department of Civil, Structural and Environmental Engineering, University at Buffalo, State University of New York
2 Professor and Chair, Department of Civil, Structural and Environmental Engineering, University at Buffalo, State University of New York
3 Professor, Department of Civil, Structural and Environmental Engineering, University at Buffalo, State University of New York

MCEER
University at Buffalo, State University of New York
133A Ketter Hall, Buffalo, NY 14260
Phone: (716) 645-3391; Fax (716) 645-3399
E-mail: *mceer@buffalo.edu*; WWW Site: *http://mceer.buffalo.edu*

Preface

MCEER is a national center of excellence dedicated to the discovery and development of new knowledge, tools and technologies that equip communities to become more disaster resilient in the face of earthquakes and other extreme events. MCEER accomplishes this through a system of multidisciplinary, multi-hazard research, in tandem with complimentary education and outreach initiatives.

Headquartered at the University at Buffalo, The State University of New York, MCEER was originally established by the National Science Foundation in 1986, as the first National Center for Earthquake Engineering Research (NCEER). In 1998, it became known as the Multidisciplinary Center for Earthquake Engineering Research (MCEER), from which the current name, MCEER, evolved.

Comprising a consortium of researchers and industry partners from numerous disciplines and institutions throughout the United States, MCEER's mission has expanded from its original focus on earthquake engineering to one which addresses the technical and socio-economic impacts of a variety of hazards, both natural and man-made, on critical infrastructure, facilities, and society.

The Center derives support from several Federal agencies, including the National Science Foundation, Federal Highway Administration, National Institute of Standards and Technology, Department of Homeland Security / Federal Emergency Management Agency, and the State of New York, other state governments, academic institutions, foreign governments and private industry.

In this project, procedures are derived to extract rotational components of ground motion from recorded translational data. Two categories of procedures are developed: Single Station Procedure (SSP) and Multiple Station Procedure (MSP). One of the newly developed MSPs, the Surface Distribution Method (SDM), enabled the development of a design procedure for dense seismic arrays, whose primary purpose is to extract rotational ground motions. Design criteria are proposed to determine the length of the array, the number of recording stations and their spatial distribution. An improved definition of accidental eccentricity is proposed for building design and studied for a wide range of one-story elastic systems, and nonlinear isolation systems. A preliminary investigation of the effect of rotational ground motions on the response of several types of structures is performed, and it is found that rotational components of ground motion significantly affect structural response.

ABSTRACT

Rotational components of ground motion, torsion about the vertical axis and rocking about orthogonal horizontal axes are not routinely considered in seismic design because such components have not been recorded and their effects on the response of structures are unknown. Rotational recordings are unavailable because instruments are by-and-large unavailable. Thus, the characterization of rotational components of ground motion is a focus of this report. Two categories of procedures are derived to extract rotational components of ground motion from recorded translational data: Single Station Procedure (SSP) and Multiple Station Procedure (MSP). Single station procedures employ translational data recorded at a single station. Multiple station procedures employ three-component translational acceleration time series recorded in an array of closely spaced but spatially distributed accelerographs.

One of the newly developed MSPs, the Surface Distribution Method (SDM), enables the development of a design procedure for dense seismic arrays, whose primary purpose is to extract rotational ground motions. Design criteria are proposed to determine the length of the array, the number of recording stations and their spatial distribution.

Seismic codes and standards currently recommend the shifting of the center of mass to account for the effect of accidental torsion. This method does not produce the desired result, which is an increase in torsional response with an increase in accidental eccentricity. An improved definition of accidental eccentricity is proposed and studied for a wide range of one-story elastic systems, and nonlinear isolation systems. A preliminary investigation of the effect of rotational ground motions on the response of structures is performed. The rotational excitations are calculated using the SDM. The sample structures are a chimney subjected to horizontal and rocking ground motions, and four-story, base-isolated and fixed-based buildings subjected to horizontal, torsional and rocking ground motions. Rotational components of ground motion significantly affect the response of these structures.

ACKNOWLEDGEMENTS

Financial support for the research described in this report was provided by MCEER Thrust Area 3, Innovative Technologies. This support is gratefully acknowledged. Any opinions, findings, conclusions or recommendations expressed in this report are those of the authors and do not necessarily reflect those of MCEER, the State of New York, or other sponsors.

The authors thank Dr. Apostolos Papageorgiou of the University of Patras, Greece, for his constructive suggestions in the initial stages of this study, as well as the *Institute of Earth Science, Academia, Sinica*, *Taiwan* for sharing strong motion data and Dr. George Mavroeidis for his assistance in this effort.

TABLE OF CONTENTS

Section	Title	Page
1	**INTRODUCTION**	**1**
1.1	Introduction	1
1.2	Rotational Components of Ground Motion—Analytical Studies	1
1.3	Extracting Rotational Excitations—Experimental Studies	8
1.4	Effect of Rotational Excitations on Structural Response	11
1.5	Building Code Treatment of Torsional Response	12
1.6	Objectives of the Report	14
1.7	Report Organization	14
2	**DENSE SEISMIC ARRAY AND EARTHQUAKE GROUND MOTION**	**17**
2.1	Introduction	17
2.2	Instrumentation	18
2.3	Geological Characteristics of the Site	21
2.4	Data Processing	29
2.5	Translational Components of Ground Motion	29
2.6	Rotational Components of Ground Motion	29
2.6.1	Geodetic Method	29
2.6.2	Extracted Rotational Components	32
3	**ESTIMATING ROTATIONAL COMPONENTS OF GROUND MOTION USING A SINGLE STATION APPROACH**	**37**
3.1	Introduction	37
3.2	Deconstructing Translational Time Series and Reconstructing Rotational Time Series	37
3.3	Propagation of Harmonic Plane Waves	38
3.4	Reflection of SV Wave: Incidence Angle Less than or Equal to Critical Angle	40
3.4.1	Incident Wave (n=0)	41
3.4.2	Reflected P Wave (n=1)	41
3.4.3	Reflected SV Wave (n=2)	42
3.4.4	Zero Traction at the Free Surface and Amplification Factors	42
3.4.5	Resultant Displacement Field	44
3.4.6	Plane Stress Condition and Estimation of Rocking	44
3.4.7	Rocking at Surface Incident Point	45
3.4.8	Relationship between Rocking and Vertical Accelerations at the Surface Incident Point	45
3.4.9	Relationship between Rocking and Horizontal Accelerations at the Surface Incident Point	46
3.4.10	Translational Accelerations at the Surface Incident Point	46
3.5	Reflection of SV Wave: Incidence Angle Exceeds Critical Angle	47
3.5.1	Reflected P Wave (n=1)	47
3.5.2	Zero Traction at the Free Surface and Amplification Factors	48
3.5.3	Resultant Displacement Field	49

TABLE OF CONTENTS (CONT'D)

Section	Title	Page
3.5.4	Plane Stress Condition and Estimation of Rocking	50
3.5.5	Rocking at the Surface Incident Point	50
3.5.6	Relationship between Rocking and Vertical Accelerations at the Surface Incident Point	50
3.5.7	Relationship between Rocking and Horizontal Accelerations at the Surface Incident Point	51
3.5.8	Translational Accelerations at the Surface Incident Point	51
3.5.9	Change of Variables	52
3.6	Reflection of a Homogeneous P Wave	52
3.6.1	Incident Wave (n=0)	52
3.6.2	Zero Traction at the Free Surface and Amplification Factors	53
3.6.3	Resultant Displacement Field	54
3.6.4	Plane Stress Condition and Estimation of Rocking	55
3.6.5	Rocking at Surface the Incident Point	55
3.6.6	Relationship between Rocking and Vertical Accelerations at the Surface Incident Point	56
3.6.7	Relationship between Rocking and Horizontal Accelerations at the Surface Incident Point	56
3.6.8	Translational Accelerations at the Surface Incident Point	57
3.7	Reflection of an Inhomogeneous P Wave	57
3.7.1	Incident Wave (n=0)	58
3.7.2	Zero Traction at the Free Surface and Amplification Factors	59
3.7.3	Resultant Displacement Field	60
3.7.4	Plane Stress Condition and Estimation of Rocking	61
3.7.5	Rocking at the Surface Incident Point	61
3.7.6	Relationship between Rocking and Vertical Accelerations at the Surface Incident Point	62
3.7.7	Relationship between Rocking and Horizontal Accelerations at the Surface Incident Point	62
3.7.8	Translational Accelerations at the Surface Incident Point	63
3.7.9	Change of Variables	64
3.8	Reflection of an SH Wave	64
3.9	Compatibility/Consistency Condition	65
3.9.1	SV Wave Incidence Angle Not Exceeding the Critical Angle	65
3.9.2	SV Wave Incidence Angle Exceeding the Critical Angle	67
3.10	Special Cases	68
3.10.1	Case 1: Incident SV (also SH) Wave has the Same Phase	68
3.10.2	Case 2: Incident SV (also SH) Wave has a Different Phase	70
3.11	General Case	73
3.11.1	Hypothesis H1: Equal Angle of Incidence of the P and SV Waves	73
3.11.1.1	SV Wave Incidence Angle Not Exceeding the Critical Angle	73
3.11.1.2	SV Wave Incidence Angle Exceeding the Critical Angle	74

TABLE OF CONTENTS (CONT'D)

Section	Title	Page
3.11.1.3	SV Wave Incidence at Critical Angle (SVcrP)	77
3.11.2	Hypothesis H2: Power Compatibility	78
3.11.2.1	SV Wave Incidence Angle Not Exceeding the Critical Angle	78
3.11.2.2	SV Wave Incidence Angle Exceeding the Critical Angle	79
3.12	Deriving Rotational Components of Ground Motion from a Point Source	80
3.13	A Composite Method (H3)	82
3.14	Comparison of Composite Method (H3) and Hypothesis 1 and 2	93
3.15	Finite Rupture Length	93
3.15.1	Symmetric Bi-lateral Fault Rupture	93
3.15.2	Asymmetrical Bi-lateral Fault Rupture	97
3.15.3	Results and Discussions on Effect of Fault Rupture	98
3.16	A Comparison of the Single Station Procedure and the Geodetic Method	99
4	**ESTIMATING ROTATIONAL COMPONENTS OF GROUND MOTION USING DATA FROM MULTIPLE RECORDING STATIONS**	**115**
4.1	Introduction	115
4.2	Formulation of the Uncoupled Geodetic Method	115
4.3	Acceleration Gradient Method (AGM)	117
4.3.1	First-Order Method	117
4.3.2	Second-Order Method	120
4.3.3	Uncoupled Second-Order AGM (AGM2)	123
4.3.4	Uncoupled AGM of Order n	125
4.4	Physical Interpretation of the AGM with Different Orders	127
4.5	Numerical Error in Higher Order AGMs and Recommendations	131
4.6	Computations using Recordings from the Lotung Array	136
5	**ESTIMATING ROTATIONAL COMPONENTS OF GROUND MOTION USING A SURFACE DISTRIBUTION METHOD**	**161**
5.1	Introduction	161
5.2	Formulation of the SDM	163
5.2.1	Computation of Rotational Acceleration History	168
5.2.2	Minimum Seismic Array Dimension	168
5.3	Application of the Surface Distribution Method	169
5.3.1	Estimation of Torsional Motion	170
5.3.2	Estimation of Rocking Motion	171
5.4	Computations using Recordings from a Strong Motion Array	172
5.4.1	Apparent Wave Velocity	173
5.4.2	Relative Contributions of the P and SV Waves to the Vertical Motion	175
5.4.3	Maximum Frequency Content of the SV Wave	175
5.5	Comparison of Rotational Spectra using SDM, AGM, GM and SSP	180
5.5.1	Torsional Spectra	182
5.5.2	Rocking Spectra	182

TABLE OF CONTENTS (CONT'D)

Section	Title	Page
6	**DIMENSIONS OF A DENSE ARRAY TO EXTRACT ROTATIONAL COMPONENTS OF EARTHQUAKE GROUND MOTION**	**197**
6.1	Introduction	197
6.2	Sensitivity of the SDM to Station Spatial Distribution	198
6.3	Sensitivity of the AGM and GM to Station Spatial Distribution	201
6.4	Design Objectives for a Dense Array	201
6.5	Conceptual Design of a Dense Array	208
6.5.1	Case 1: FFT with Respect to Time	209
6.5.2	Case 2: FFT with Respect to Spatial Coordinates	210
6.5.3	Comparison of Case 1 and Case 2	211
6.5.4	Wave Propagation Assumption Not Satisfied	213
6.5.5	Design Criteria	213
6.6	Design of a General Two-Dimensional Dense Array	214
6.7	Design of a Specific Two-Dimensional Dense Array	216
6.8	Array Design using Bounded Site Characteristics	220
6.9	Length of the Array using Circular and Rectangular Approximations	224
7	**QUANTIFICATION OF ACCIDENTAL ECCENTRICITY DUE TO TORSIONAL GROUND MOTION**	**225**
7.1	Introduction	225
7.2	Mathematical Model for Dynamic Analysis	230
7.3	Conventional Calculation of Accidental Eccentricity	231
7.3.1	Ground Motion Considered	232
7.3.2	Procedure	233
7.3.3	Results and Discussions	234
7.4	Alternate Definition of Accidental Eccentricity	238
7.4.1	Evaluation Procedure	249
7.4.2	Scaling of Accidental Eccentricity	249
7.4.3	Results and Discussions	249
7.5	Accidental Eccentricity in Nonlinear Isolation Systems	250
7.5.1	Results and Discussions	254
7.5.2	Properties of the Associated Elastic Systems	255
7.5.3	Isolator Modeling With Orthogonal Coupling	258
7.5.4	Effect of Yield Displacement of Isolators on Accidental Eccentricity	259
7.6	Analysis and Validation of Results with SAP2000	260
7.7	Discussion on the Proposed Definition of Accidental Eccentricity	262
8	**EFFECT OF ROTATIONAL GROUND MOTIONS ON STRUCTURAL RESPONSE**	**275**
8.1	Introduction	275
8.2	Description of Ground Motions	275
8.3	Seismic Response of a Chimney	276

TABLE OF CONTENTS (CONT'D)

Section	Title	Page
8.3.1	Continuum Model	276
8.3.2	Ground Motions Used for Analysis	280
8.3.3	Solution of the Differential Equation using Explicit Finite Difference Method	280
8.3.4	Mathematical Models	280
8.3.5	Analysis, Results and Discussion	281
8.4	Response of a Four-Story, Base-Isolated Building	287
8.4.1	System Descriptions	287
8.4.2	Ground Motion Considered	288
8.4.3	Combination of Input Ground Motions	288
8.4.4	Analysis, Results and Discussions	289
8.4.5	Torsional Response of the Building at the Stiffening Regime	295
8.5	Response of Four Story Fixed-Base Building	296
9	**SUMMARY, CONCLUSIONS AND RECOMMENDATIONS**	**309**
9.1	Summary	309
9.2	Conclusions	311
9.3	Recommendations	314
10	**REFERENCES**	**317**

APPENDICES (Provided on attached CD)

A	AGM2 AND HIGH FREQUENCY ERRORS	357
B	UTILITY OF THE ACCELERATION GRADIENT METHOD	371
C	DYNAMIC ANALYSIS OF A ONE-STORY TORSIONALLY COUPLED BUILDING	397
D	SEISMIC ANALYSIS OF A CHIMNEY SUBJECTED TO TRANSLATIONAL AND ROCKING GROUND MOTIONS	403
E	MATLAB CODES FOR AGM, SDM, AND SSP	Electronic Content

LIST OF FIGURES

FIGURE	TITLE	PAGE
2-1	Location of the LSST array in Lotung, Taiwan	19
2-2	Location of the free surface stations	19
2-3	Location of the bore-hole stations	20
2-4	Placement of accelerometers on the containment structure	20
2-5	Lotung model containment structure	21
2-6	Seismic refraction cross-sections (adapted from Wen and Yeh, 1984)	23
2-7	Velocity profile near the LSST array (Wen and Yeh, 1984)	24
2-8	Location of boreholes and the containment structure models (Chen et al. 1990)	25
2-9	Sample borehole data (locations S-4, E-2 and S-1; Moh, 1986)	25
2-10	Distribution of the shear wave velocity at locations L2, L6 and L7 (Chen et al., 1990)	26
2-11	Shear modulus ratio and damping ratio test for soil (Chen et al., 1990)	27
2-12	Translational acceleration records at all 15 surface stations	33
2-13	Coordinate system	35
2-14	Rotational accelerations using GM and FFT of horizontal accelerations at station FA1_1	36
3-1	Waves propagating from the source (hypocenter) to the recording station through principal plane and reflection of the incident wave from the free surface	39
3-2	Torsional spectra computed using three different hypotheses and geodetic method	83
3-3	Rocking (*xz* plane) spectra computed using three different hypotheses and geodetic method	86
3-4	Rocking (*yz* plane) spectra computed using three different hypotheses and geodetic method	89
3-5	Calculation of transition period at station FA1_1	92
3-6	Evolution of principal planes with the propagation of fault rupture	94
3-7	Effect of rupture on torsional spectra	101
3-8	Effect of rupture on rocking (*xz* plane) spectra	104
3-9	Effect of rupture on rocking (*yz* plane) spectra	107
3-10	Torsional histories computed using SSP (H3) and GM	110
3-11	Rocking histories on the *xz* plane computed using SSP (H3) and GM	111
3-12	Rocking histories on the *yz* plane computed using SSP (H3) and GM	112
3-13	Averaged rotational histories computed using SSP (H3) and GM	113
3-14	Recorded translational acceleration at Station FA1_1	114
4-1	Schematic comparison of GM and AGM2	118
4-2	Snapshots of acceleration along each arm and FFT of acceleration at one station on each arm	119
4-3	Best-fit surface for the distribution of the vertical acceleration (m/sec^2) at time instant 5.995 sec using AGM2	130

LIST OF FIGURES (CONT'D)

FIGURE	TITLE	PAGE
4-4	Best-fit surface for the distribution of the vertical acceleration (m/sec^2) at time instant 5.995 sec using AGM3	130
4-5	Best-fit surface for the distribution of the vertical acceleration (m/sec^2) at time instant 5.995 sec using AGM4	131
4-6	Spectra computed using AGM1 and GM	141
4-7	Torsional spectra computed using three different methods	142
4-8	Rocking (*xz* plane) spectra computed using three different methods	149
4-9	Rocking (*yz* plane) spectra computed using three different methods	152
4-10	Rocking (SRSS) spectra computed using three different methods	155
4-11	Rocking (Geomean) spectra computed using three different methods	158
5-1	Wave propagation on a horizontal (*xy*) plane	165
5-2	Comparison of torsional acceleration and derivative of SH wave component of horizontal acceleration scaled by the apparent SH wave velocity	176
5-3	Comparison of SV wave contribution to rocking acceleration and derivative of SV wave contribution to the vertical acceleration scaled by the apparent SV wave velocity	177
5-4	Comparison of P wave contribution to rocking acceleration and derivative of P wave contribution to the vertical acceleration scaled by the apparent P wave velocity	178
5-5	Comparison of rocking acceleration and derivative of vertical acceleration scaled by the apparent wave velocity	179
5-6	Contributions of P and SV wave to the vertical acceleration at Station FA1_1	180
5-7	Spectra of rocking acceleration and derivative of vertical acceleration scaled by the apparent P wave velocity	181
5-8	Torsional spectra computed using four different methods	184
5-9	Fourier amplitude spectra of the SH wave contribution to the horizontal motion (normal to the principal plane)	187
5-10	Rocking (*xz* plane) spectra computed using three different methods	188
5-11	Rocking (*yz* plane) spectra computed using three different methods	191
5-12	Rocking (SRSS) spectra computed using four different methods	194
6-1	The dimensions of the Lotung LSST array	199
6-2	Torsional spectra computed using different sets of recorded motions, SDM	202
6-3	Rocking (*xz* plane) spectra computed using different sets of recorded motions, SDM	202
6-4	Rocking (*yz* plane) spectra computed using different sets of recorded motions, SDM	203
6-5	Rocking (SRSS) spectra computed using different sets of recorded motions, SDM	203
6-6	Torsional spectra computed using different sets of recorded motions, AGM	204

LIST OF FIGURES (CONT'D)

FIGURE	TITLE	PAGE
6-7	Rocking (*xz* plane) spectra computed using different sets of recorded motions, AGM	204
6-8	Rocking (*yz* plane) spectra computed using different sets of recorded motions, AGM	205
6-9	Rocking (SRSS) spectra computed using different sets of recorded motions, AGM	205
6-10	Torsional spectra computed using different sets of recorded motions, GM	206
6-11	Rocking (*xz* plane) spectra computed using different sets of recorded motions, GM	206
6-12	Rocking (*yz* plane) spectra computed using different sets of recorded motions, GM	207
6-13	Rocking (SRSS) spectra computed using different sets of recorded motions, GM	207
6-14	Arrangement of stations in the design of a dense array	215
6-15	Fourier amplitude spectra for January 16, 1986 event recorded at station FA1_1 of LSST array, Lotung (Taiwan)	218
6-16	Identifying MH and CLH for the horizontal motion using response spectra	219
6-17	Identifying MH and CLH for the vertical motion using response spectra	219
6-18	Location of the surface-stations when designed using the MH and the CLH of the January 16, 1986 event recorded at LSST, Lotung (Taiwan); all dimensions are in meters	221
6-19	Level 1 simplification of the station layout presented in Figure 6-18; all dimensions are in meters	222
6-20	Level 2 simplification of the station layout presented in Figure 6-18; all dimensions are in meters	223
7-1	Calculation of torsional amplification factor	229
7-2	Analytical model	229
7-3	Input ground acceleration data	233
7-4	Torsional amplification for System 1, Shift 1, conventional approach	236
7-5	Variation of torsional amplification for System 1, Shift 1, conventional approach	238
7-6	Torsional amplification for System 1, Shift 2, conventional approach	239
7-7	Variation of torsional amplification in System 1, Shift 2, conventional approach	241
7-8	Torsional amplification for System 2, Shift 1, conventional approach	242
7-9	Variation of torsional amplification in System 2, Shift 1, conventional approach	244
7-10	Torsional amplification for System 2, Shift 2, conventional approach	245
7-11	Variation of torsional amplification in System 2, Shift 2, conventional approach	247
7-12	Schematic representation of the alternative definition of accidental eccentricity	248
7-13	Variation of torsional amplification in System 1 as a function of normalized eccentricity, proposed approach, $f = \bar{e}_a / b$	251

LIST OF FIGURES (CONT'D)

FIGURE	TITLE	PAGE
7-14	Variation of torsional amplification in System 1 as a function of accidental eccentricity, proposed approach, $f = \overline{e}_a / b$	252
7-15	Variation of torsional amplification in System 2 as a function of normalized eccentricity, proposed approach, $f = \overline{e}_a / b$	252
7-16	Variation of torsional amplification in System 2 as a function of accidental eccentricity, proposed approach, $f = \overline{e}_a / b$	253
7-17	Force-displacement relationship for a typical isolator	253
7-18	Variation of torsional amplification in nonlinear isolation system, $T_d = 4$ sec, $\Omega = 1.25$, $Q/W = 0.05$, $Y = 5$ mm, orthogonally uncoupled, $f = \overline{e}_a / b$	255
7-19	Variation of torsional amplification in nonlinear isolation system, $T_d = 4$ sec, $\Omega = 1.25$, $Q/W = 0.05$, $Y = 5$ mm, orthogonally coupled, $f = \overline{e}_a / b$	259
7-20	Analysis of conventional approach for System 1	270
7-21	Analysis of conventional approach for System 2	271
7-22	Proposed approach for 5% damped elastic systems, $f = \overline{e}_a / b$	272
7-23	Proposed approach for nonlinear isolation system, $f = \overline{e}_a / b$	272
7-24	Hysteresis for element 1, $T_d = 4$ sec, $\Omega = 1.25$, $Q/W = 0.05$, $Y = 5$ mm orthogonally coupled	273
7-25	Y-displacement history at the midpoint (edge) of side A, $T_d = 4$ sec, $\Omega = 1.25$, $Q/W = 0.05$, $Y = 5$ mm, orthogonally coupled	273
8-1	Translational ground motions recorded at station FA1_1 and associated 5% damped spectra	277
8-2	Rotational ground motions at station FA1_1 and associated 5% damped spectra	278
8-3	Continuum model of a chimney on a flexible foundation	279
8-4	Effect of rocking excitation on tip displacement, $\eta = 14$	282
8-5	Effect of rocking excitation on base shear, $\eta = 14$	283
8-6	Effect of rocking excitation on base moment, $\eta = 14$	284
8-7	Four story, isolated building, all dimensions are in mm (adapted from Sarlis and Constantinou, 2010)	289
8-8	Schematic sketch of a Triple Friction Pendulum (TFP) isolator (Sarlis and Constantinou, 2010)	290
8-9	Force-displacement loops for a TFP isolator (Sarlis and Constantinou, 2010)	290
8-10	Hysteresis along the x direction of the isolator at Corner A of the base-isolated building, input scale factor = 4.5	297
8-11	Hysteresis along the y direction of the isolator at Corner A of the base-isolated building, input scale factor = 4.5	300
8-12	Floor acceleration spectra along the x direction at roof level, Corner A of the base-isolated building, input scale factor = 4.5	303

LIST OF FIGURES (CONT'D)

FIGURE	TITLE	PAGE
8-13	Floor acceleration spectra along the *y* direction at roof level, Corner A of the base-isolated building, input scale factor = 4.5	303
8-14	Response histories of the base-isolated building, input scale factor = 12	304
8-15	Hysteresis of the isolator at Corner A, input scale factor = 12	305
8-16	Floor acceleration spectra along the *x* direction at roof level, Corner A of the fixed-base building, input scale factor = 1.0	307
8-17	Floor acceleration spectra along the *y* direction at roof level, Corner A of the fixed-base building, input scale factor = 1.0	307

LIST OF TABLES

TABLE	TITLE	PAGE
2-1	Description of stations	22
2-2	Peak translational accelerations and velocities at the surface stations for the January 16, 1986 earthquake recorded in the LSST array, Lotung	32
3-1	Critical Time Period (CTP) associated with different stations	92
4-1	AGM1 using normalized data kernel	137
4-2	AGM2 using normalized data kernel	137
4-3	AGM3 using normalized data kernel	137
4-4	AGM4 using normalized data kernel	138
4-5	AGM1 using original data kernel	138
4-6	AGM2 using original data kernel	138
4-7	AGM3 using original data kernel	139
4-8	AGM4 using original data kernel	139
4-9	Apparent wave velocity	146
5-1	Apparent wave velocities	173
6-1	Sets of motions considered in the sensitivity analysis	199
6-2	Array dimensions associated with the inclusion of different tiers	200
7-1	Accidental eccentricity $\bar{e}_a/b$ for an elastic system	250
7-2	Accidental eccentricity (%) for an uncoupled isolation system, $Y = 5$ mm	255
7-3	Accidental eccentricity $\bar{e}_a/b$ in nonlinear isolation system, $Y = 5$ mm	259
7-4	Accidental eccentricity $\bar{e}_a/b$ in nonlinear isolation system, $Y = 1$ mm	260
7-5	Accidental eccentricity $\bar{e}_a/b$ in nonlinear isolation system, $Y = 10$ mm	260
7-6	Peak displacements for the conventional approach for 5% damped System 1 (all displacements in mm)	263
7-7	Peak displacements for the conventional approach for 0.1% damped System 1 (all displacements in mm)	264
7-8	Peak displacements for the conventional approach for 5% damped System 2 (all displacements in mm)	265
7-9	Peak displacements for the conventional approach for 0.1% damped System 2 (all displacements in mm)	266
7-10	Peak displacements for the proposed approach for 5% damped elastic System 1 (all displacements in mm)	267
7-11	Peak displacements for the proposed approach for 5% damped elastic System 2 (all displacements in mm)	267
7-12	Element properties used in SAP analysis for nonlinear isolation system	268
7-13	Peak displacements for the proposed approach for nonlinear isolation system—orthogonally uncoupled (all displacements in mm)	268

LIST OF TABLES (CONT'D)

TABLE	TITLE	PAGE
7-14	Peak displacements for the proposed approach for nonlinear isolation system--orthogonally coupled (all displacements in mm)	269
8-1	Response of linearly tapering chimneys to lateral and/or rocking excitation	285
8-2	Contributions from the rocking excitation - linearly tapered chimneys	285
8-3	Response of straight chimneys to lateral and/or rocking excitation	286
8-4	Contributions from the rocking excitation to the response of straight chimneys	286
8-5	Properties of TFP isolator (Sarlis and Constantinou, 2010)	288
8-6	Load combinations	291
8-7	Maximum resultant isolator displacement (base-isolated building)	292
8-8	Maximum displacement at the ground floor level (base-isolated building)	293
8-9	Maximum displacement at the roof level (base-isolated building)	294
8-10	Maximum displacement at the roof level (fixed-base building)	306

CHAPTER 1

INTRODUCTION

1.1. Introduction

Seismic analysis, design and performance assessment of buildings, bridges and safety-related nuclear structures is based on two or three translational components of earthquake ground motion. Although the rotational components (rocking and torsional) may contribute significantly to the response and damage of these structures, their effect is unknown because their intensity and frequency content are not measured by accelerographs deployed in the free field. Until rotational components are measured directly or robust procedures are available to extract rotational time series from translational time series, routine seismic design and performance assessment cannot consider rotational motions. If rotational time series can be extracted for each recording station and earthquake, it will be possible to generate ground motion attenuation functions and uniform hazard and risk spectra for these components of earthquake ground motion.

This report addresses the rotational components of ground motion and their effect on the response of structures. New procedures are presented to extract rotational components of ground motion from recorded translational acceleration time series. Some of the seminal studies on rotational components of ground motion and the torsional and rocking response of structures are described in the following sections of this chapter. The specific objectives of the report are presented in Section 1.6 and its organization is presented in Section 1.7.

1.2. Rotational Components of Ground Motion—Analytical Studies

Penzien and Watabe (1975) showed most of the energy released by an earthquake travels to a recording station on a *principal plane* and that the three components of ground motion along and normal

to the principal plane are uncorrelated. They defined the vertical plane comprising the recording station and the epicenter as the principal plane, and its projection on the horizontal plane as the principal axis. In the absence of surface waves, this idealization allows the contribution of the SH wave to be computed as the resultant of the components of the recorded horizontal ground motions normal to the principal plane. P and SV waves contribute to the ground motion along the principal axis and in the vertical direction. Bolt (1988) provides information on these body waves.

Trifunac (1982) derived the Fourier amplitude spectra of rotational components of ground motion from the translational components assuming the incidence of a single type of body wave (P, SH or SV). Surface waves, which can contribute to the rotational component of ground motion, were not considered. For the SV wave, the rocking component was not derived from the horizontal translational records because the relationship is indeterminate at an angle of incidence of 45 degrees and the result is very sensitive for angles of incidence close to 45 degrees. Wong and Trifunac (1979) developed a procedure to generate strong-motion translational accelerograms from a given Fourier amplitude spectra. The procedure was later extended to torsional accelerograms and considered wave dispersion and wave passage effects (Lee and Trifunac, 1985). A similar study was performed for rocking accelerograms (Lee and Trifunac, 1987).

Bouchon and Aki (1982) studied the characteristics of the propagation of earthquake-induced dynamic strain and rotational fields for two types of faults: strike-slip and dip-slip. The displacement field associated with each source mechanism was computed using a discrete wave-number method. Bouchon and Aki (1977) first proposed this method in two spatial dimensions. Bouchon (1979) extended the method to three spatial dimensions and then applied it to strike-slip and reverse fault sources (Bouchon 1980a, b). The numerical data chosen for the strike-slip fault simulated the displacement field associated with the Parkfield earthquake of 1966; the data for dip-slip faulting simulated the San Fernando earthquake of 1971. For strike-slip faulting, these authors reported: a) the longitudinal strain field was the largest in the vicinity of the fault and rapidly decreased with the distance away from the fault zone, b) if

this strain was extensional along any direction (say, along the fault), then it was compressional along the orthogonal direction (normal to the fault), c) shear strain dominated over the longitudinal strain at any site and efficiently radiated away from the source along an azimuth close to the direction of propagation of rupture, d) radiation was in the form of SH and Love waves, e) rocking rotation decayed very rapidly away from the source, f) torsional rotation at any site was triggered only after the arrival of an SH wave, and g) large torsional components were restricted to a zone around the strike of the fault and decayed rapidly along the transverse direction. Further, the time series of the spatial and temporal derivatives of the displacement at all the stations in the faulting zone along the direction of rupture propagation were very similar. They compared the ratio of the amplitudes of the spatial and temporal derivatives at each of these stations and concluded for strike-slip faulting: a) the velocity of rupture is a better measure of the apparent wave velocity than the shear wave velocity, b) the bedrock shear wave velocity is a better measure of the apparent wave velocity at stations located near the fault but in the opposite direction to the rupture, and c) there is no best measure of the apparent wave velocity at distant stations and at stations located normal to the direction of rupture. For dip-slip faulting: a) the longitudinal strain field dominated over the shear strain field, b) rocking motion was efficiently radiated in the form of P, SV and Rayleigh waves, and c) the value of the apparent wave velocity varies as a function of the location of the site with respect to the fault and frequency range.

Castellani and Boffi (1986, 1989) performed one of the few studies that addressed the simultaneous presence of body and surface waves. They first decomposed the contributions from the surface and body waves using a technique described by Sugito et al. (1984). The decomposition was based on a series of assumptions: i) the surface wave arrives after the body wave, ii) the very high and very low frequency contents of the recordings are due solely to contributions from the body and surface waves, respectively, and iii) initial and final phases of the signals are contributed solely by body and surface waves, respectively. The time- and frequency-separation parameters required for this decomposition were computed from the evolutionary spectra discussed in Kameda (1975), which was originally proposed by

Corotis et al. (1972). The body wave contributions were then decomposed into P and S waves using a theory developed by Haskell (1953). The contributions of the individual types of waves to the rotational components were computed using classical relationships and then superposed. The frequency dependency of the incident angle was neglected and an apparent (horizontal) wave velocity assumed. Knowledge of the local geology of the site is required. The application of the procedure to records from the Imperial Valley, California earthquake of October 15, 1979, at source-to-site distances ranging between 18 and 22 km, showed the contribution of surface waves to be negligible for frequencies greater than 1 Hz.

Gomberg and Bodin (1994) used data recorded at station TPNV from the Little Skull Mountain (LSM), and Landers earthquakes of June 1992 to estimate dynamic strains and rotational components. The station was 26 and 280 km from the epicenters of the LSM and Landers earthquakes, respectively.

Gomberg (1997) estimated the rotational components (and dynamic strains) induced in the Northridge, California earthquake using classical relationships and translational records. Relationships were derived by only considering S waves and estimating the apparent wave velocity. The apparent wave velocity was calculated using the arrival of the S wave and was used to scale the velocity seismogram.

Zembaty (2009a) derived the spectral densities of rotational components from the translational components. For torsional components, horizontal motion normal to the principal plane was considered; rocking was related to both the horizontal and vertical motions on the principal plane. Simultaneous incidence of the P and S waves was assumed. The angles of incidence for the P and S waves were assumed to be both equal and frequency independent. This angle of incidence was an input to the analysis.

Most of the studies performed to date have either neglected the effect of dispersion on surface waves and the frequency-dependent angle of incidence for body waves or use site-specific geologic knowledge to account for them. Li et al. (2002) estimated the frequency-dependent velocities of the surface waves, which can improve the estimation of rotational components from far-field recordings where the

contributions of the body waves are very small. Assuming a single body wave, Li et al. (2004) estimated the frequency-dependent angle of incidence and approximately accounted for the effect of dispersion without knowledge of site-specific local geology. However, the Li et al. (2004) procedure cannot be extended to general cases where more than one type of wave contributes to the translational time series.

Rotational motion is computed in most of the above studies using data recorded at a single station and is based on the assumption of a principal plane that was first proposed by Penzien and Watabe (1975). These studies are identified as a Single Station Procedures (SSP) in this report. The assumption of a principal plane is reasonable when the site is distant from the source. Identification of different types of waves in the recorded data is then possible because of their temporal separation. However, for near-field recordings, spatial variation can also be attributed (Castellani and Zembaty, 1996) to: i) source-to-site propagation effects, ii) wave scattering due to soil inhomogeneity, and iii) impulsive stresses within and around the source (Aki and Tsujiura, 1959). Accordingly, the existence of a principal plane and the use of solutions based on classical plane wave propagation are of questionable value for extracting rotational components of ground motion from near-fault recordings.

The use of translational strong-motion records to estimate rotational components of ground motion dates back to the mid 1980s. All of these studies have used data recorded at multiple stations and are identified in this report as Multistation Procedures (MSPs). Niazi (1986) estimated rotational motions induced in a long, narrow *rigid* foundation from data recorded in the El Centro Differential Array (ECDA) in Southern California. Five stations in the ECDA are approximately aligned and spaced between 18 and 213 m apart. The recorded acceleration data were first integrated to obtain velocity and displacement histories. Next, at every instant of recording, a best-fit straight line was fitted (using the weighted least-squares method) through the computed displacement and the velocity distribution across the array. The slope of the displacement straight line was taken as an estimate of the rotation and that of the velocity straight line enabled an estimate of the rotational velocity. The effect of foundation length

was studied by varying the selected set of stations. The weights selected in the least-squares method reduced the influence of the end stations.

The Geodetic Method (GM) (Spudich et al., 1995) can be considered as an extension of the work of Niazi. Stations were distributed in a three-dimensional space and the relative displacement between any station pair (with a common station, called the reference station) was expressed in terms of the displacement gradient matrix, which was assumed to be constant and small over the region of the array. The weight matrix used in the least-squares method was derived on a statistical basis (Menke, 1984) that makes the procedure essentially independent of the selection of the reference station. The three constraint equations used to relate the displacement gradient parameters are valid only at the free surface. The use of recordings at depth should be avoided. When using recordings at surface stations only, the procedure can be considered to be calculating the rotational components induced in a two-dimensional, rigid foundation, whose geometry is defined by the distribution of the stations.

Earthquake records from dense arrays such as Parkfield in central California and Lotung in Taiwan have also been used to study the spatial variability of ground motion. The description of the displacement field computed from the recordings of a strong-motion array generally involves the cross-correlation of free-field surface accelerations at nearby stations. Castellani and Zembaty (1996) showed the cross-correlation in vertical motion is related to the power spectrum of the rocking motion and reported the ratio of the peak ordinates of rocking to translational (horizontal) spectra can differ by an order of magnitude between the near field and far field. Using data recorded at surface stations of the Large Scale Seismic Testing (LSST) array in Lotung (Taiwan), Laouami and Labbe (2002) computed the torsional component for each station pair by dividing the difference between the recorded horizontal acceleration histories along the direction normal to the line connecting the stations by the distance between the two stations. Assuming stationarity and identifying the strong-motion phase for each station pair, the spatial variability was then studied by defining a normalizing parameter that is proportional to the separation distance and the ratio of the standard deviation of the torsional motion to the average standard deviation of the

horizontal motions used in calculating the torsional motion. The authors reported that torsional motion decreases and the normalizing parameter increases as the separation distance increases; the greater the intensity of shaking, the greater the torsional motion and the smaller the normalizing parameter.

Other researchers have used the GM of Spudich et al. (1995) to estimate rotational components of ground motion (e.g., Bodin et al., 1997; Ghayamghamian and Nouri, 2007). Estimates of rotational components and dynamic strains computed using the GM and data reconstructed from a single recording station have been compared (Gomberg, 1997; Castellani and Boffi, 1989; Singh et al., 1997) and the reported differences were relatively small. However, the estimates of rotational response from the GM should be deficient at higher frequencies because of the averaging effect of the rigid foundation assumed with its use. The small differences reported by these authors are possibly due to two sources: 1) an incorrect value of the apparent wave velocity, and 2) the parameters chosen for the comparison, rotation and dynamic strain, may not be very sensitive to high frequency content. If rotational acceleration response spectra had been chosen as the basis of the comparison, the general expectations would have been: a) the spectra should match well at lower frequencies, and b) the spectral ordinates obtained using the GM will be underestimated at higher frequencies.

Bodin et al. (1997) concluded that an array dimension of one-quarter of the wavelength of the dominant mode would provide an estimate of the gradient that was within 10% of the true value. They compared the numerical gradient with the actual gradient calculated per Lomnitz (1997). This comparison of gradients is correct at a single station and based on a single station pair. The gradient returned by the GM is, in some sense, the weighted average of those computed using several station pairs sharing one common station. Depending upon the shape of the wave train at the instant of recording, each of these gradients does not necessarily have the same sign and the resulting average gradient can be significantly less than the individual estimates.

The GM computes the best-fit plane surface across the array at every instant of recording. An analogous concept exists in the frequency domain wherein f-k (frequency-wave number) transformation of array recordings is used to characterize spatial variability of the recorded motion and develop attenuation relationships and coherency functions. Since the stations in a seismic array are rarely uniformly spaced, analysis should be based on the non-uniform discrete Fourier Transform and care should be taken to minimize the spatial aliasing (e.g., Kerekes, 2001; Zwartjes and Sacchi, 2007).

A somewhat similar problem exists in the area of acoustic emission and signal processing involving one or multiple emitters and an array of polarized or omni-directional antennas (receivers). Procedures (e.g., multiple signal classification, MUSIC (Schmidt, 1981); estimation of signal parameters via a rotational invariance technique, ESPRIT (Roy, 1987)) exist to characterize received signals and to compute the number of signals and directions of arrival. A comprehensive review of these procedures may be found in Tuncer and Friedlander (2009). Attempts have been made to translate the concept of MUSIC to the analysis of dense seismic array data (e.g., Goldstein and Archuleta, 1987). However, the stumbling block in such translations is the formation of an array-manifold in the presence of different types of waves propagating with different velocities in a seismic array. Another obstacle is the unknown geometric attenuations for different waves propagating through a highly heterogeneous medium. The procedures used in characterizing the acoustic emission, despite having a solid theoretical and statistical basis, have found little application in extracting rotational components from the data recorded in a dense seismic array.

1.3. Extracting Rotational Excitations—Experimental Studies

Seismic wave fields are usually monitored using two types of measurements: translational ground motion using a standard inertial seismometer, and deformation of the earth (strains) over the surface. In addition to translations, three-component rotations are also required to completely describe the wave fields at any given station (Aki and Richards, 1980; and 2002). Direct measurement of rotations is

extremely difficult because of the desired sensitivity over a wide frequency band. The required range of angular velocity to be measured is expected to vary from 10^{-14} to 1 rad/sec and the frequency bandwidth for the seismic waves is between 3 mHz and 10 Hz (Schreiber et al., 2009). The frequency band spans over 5 orders of magnitude and sensitivity of the rotational measurement is desired over 14 orders of magnitude. These requirements cover scenarios from strong motion during a local earthquake to a weak signal from an earthquake more than 10,000 km away. Even if these two extreme scenarios are excluded, the desired sensitivity range is 10^{-12} to 10^{-4} rad/sec (Schreiber et al., 2009). Aki and Richards (2002) note "…seismology still awaits a suitable instrument for making such measurement." The importance of development and deployment of instruments capable of recording rotational components of ground motion was highlighted at the 2006 Fall meeting of the American Geophysical Union (Igel et al., 2006) and a workshop hosted by the US Geological Survey (Lee et al., 2007).

Direct measurement of the rotational excitation is also required to correct translational time series recorded by the standard seismometer. In the triaxial seismometer, the design of the vertical sensor must differ from those in the horizontal direction due to the presence of gravitational force. An alternative to this sensor orientation is the Galperin or symmetric configuration (Galperin, 1985), wherein the three orthogonal sensors are tilted to the vertical axis at the same angle; each responds equally to gravity. However, most sensors used in strong-motion seismology are the mass-on-rod type and use a North-East-Vertical configuration (Graizer, 2009a). Such pendulums are subject to excitations from all six components during a seismic event and the response of the pendulum, even if its natural frequency is well separated from the frequency band of interest, does not capture pure unidirectional (polarized) translational excitation but is rather contaminated by associated rotational excitations. The degree of contamination has been studied using numerical simulation and in the field during an earthquake (Graizer, 1989; 2005; 2006; and 2010; Kalkan and Graizer, 2007; Graizer and Kalkan, 2008). Graizer (2009a) also investigated the response of this seismometer with a Galperin sensor configuration.

Several instruments have been used to measure the rotational excitation. Some of these are a simple extension of the traditional inertial seismometer and are cost effective, whereas others invoke ideas from a completely different field and are expensive. Graizer (2009b) reviewed the classical methods of measuring rotation. Nigbor (1994) directly measured the rotational components of ground motion near a large explosion using commercial rotational velocity sensors, which were used in the aerospace field. This micro-electromechanical gyroscopic sensor was later deployed in the Borrego Valley in Southern California but did not record any earthquake rotational ground motion above the noise level of the sensor (Nigbor et al., 2009). Takeo (1998) faced similar issues of sensor resolution when recording near-field rotational motion using a similar aerospace sensor caused by small earthquakes.

Ring-laser rotation sensors are the state-of-the-art technology for measuring rotational excitation. These sensors operate on principles of optical interferometry (Schreiber et al., 2009). Successful observations using ring-laser sensors include a study in Christchurch, New Zealand (Mcleod et al., 1998; Pancha et al., 2000), and observation of the earth's rate of rotation at Wetzell, Germany (Schreiber et al., 2006). Other studies are reported by Igel et al., 2005; 2007 and Cochard et al., 2006. A prototype was installed at the Pinon Flat Seismological Observatory in 2005 (Schreiber et al., 2009).

Ring-laser gyroscopes require sophisticated facilities and their operation is complex, which are not compatible with large-scale permanent networks or mobile arrays (Stedman, 1995). Cowsik (2007) and Takamori et al. (2009) identified two new rotational seismometers that provide sufficient resolution and yet appear practical for seismic networks and mobile arrays.

The direct recording of rotational components of ground motion remains a research topic. Widespread deployment of such instruments is likely decades away. In the near term, engineers will have to extract rotational components from recorded translational data using single station or multistation procedures to study their effect on structural response.

1.4. Effect of Rotational Excitations on Structural Response

Newmark (1969) showed that a symmetrical building could be excited by the torsional component of ground motion on the basis of a travelling wave propagating with a constant velocity. Hart et al. (1975) attributed the torsional response of most high-rise buildings during the 1971 San Fernando earthquake to rotational components of the ground motion. Bycroft (1980) associated the differential longitudinal motion that he described as responsible for the collapse of bridges during the 1971 San Fernando earthquake and the 1978 Miyagi-Ken-Oki earthquake with rotational components of ground motion.

Wolf et al. (1983) discussed the effect of rocking excitation on a base-isolated nuclear power plant. Politopoulos (2010) identified the excitation of the rocking mode in a base-isolated building due to rocking excitations. Both studies were based on simplified assumptions including horizontally propagating waves in bedrock and vertically propagating shear waves. Zembaty and Boffi (1994) and Zembaty (2009b) identified the contribution of rocking motion to bending moments along the height of a 160 m tall tower using horizontal and rocking spectra computed using Eurocode 8 (EC8.1, 2005; EC8.6, 2005).

Unlike rocking, torsional vibration can be a consequence of structural asymmetry. The torsional response of a structure is thus more complicated than its rocking response. The sources of asymmetry can be generally classified into two groups: natural (inherent) and accidental (uncertain). Natural torsion is due to the difference in the calculated location of the centers of mass and stiffness. These values are computed using the structural and loading properties assumed in a design. However, the true values will be different from those assumed in design and the effect of the differences is addressed through the use of accidental torsion. In total, accidental torsion is associated with: 1) the differences in the assumed and true distributions of mass, stiffness and strength, 2) the torsional component of ground motion, and 3) any other source of torsion not explicitly accounted for in the analysis and design.

1.5. Building Code Treatment of Torsional Response

The Equivalent Lateral Force (ELF) procedure is used for the seismic design of most low-rise buildings. The ELF procedure found in many seismic codes (e.g., ASCE 7-10, Section 12.8) addresses both natural (inherent) and accidental torsion, and involves the following key steps:

1. Determine the reactive weight of the building
2. Calculate the design base shear as the product of a seismic coefficient and the reactive weight, where the coefficient is a function of the site characteristics, the chosen framing system, and the first mode translational period (ASCE 7-10 Equations 12.8-1, 12.8-2, 12.8-3, 12.8-4)
3. Distribute the base shear over the height of the building using a code-specified lateral force profile, producing lateral forces at each floor level (Equations 12.8-11, 12.8-12)
4. Analyze the building for horizontal earthquake effects by applying the lateral force at each floor level at the center of mass of that floor, thereby capturing the natural (inherent) torsion [but without consideration of dynamic amplification] (ASCE 7-10 Section 12.8.4.1)

Accidental torsion is addressed by adding a torsional moment at each floor level by moving the center of mass from its actual location by a distance equal to 5% of the dimension of the structure perpendicular to direction of the applied forces (ASCE 7-10 Section 12.8.4.2). The accidental torsional moment is increased for torsionally irregular buildings using a factor A, greater than 1 and less than 3, that is a function of the peak lateral displacement of a floor due to torsion. The maximum effect of accidental torsion is equivalent to moving the center of mass by 15% of the floor dimension perpendicular to the applied forces.

The ELF procedure does not require the analyst to compute the center of stiffness of each floor level. Dynamic amplification of natural torsion is not considered although procedures are available to do so (e.g., Tso 1990; Goel and Chopra, 1993; Basu and Jain, 2007). When dynamic analysis is required by

seismic codes (e.g., buildings with horizontal and/or vertical setbacks, seismically isolated structures) natural torsion should be accounted for implicitly. However, guidance to account for accidental torsion in dynamic analysis is unclear. The current practice in the United States is to shift the center of mass at each floor level by 5% of the building dimension perpendicular to the direction of excitation, and is identical in concept to the rules for ELF analysis. Many studies have addressed accidental torsion, with significant contributions from Chopra and his co-workers. Based on data recorded in three nominally symmetric, instrumented buildings during three California earthquakes, De La Llera and Chopra (1994a) estimated the dynamic eccentricity (identical to the instantaneous accidental eccentricity) at each floor level and concluded that 5% accidental eccentricity was adequate. De La Llera and Chopra (1994b) investigated the effects of accidental torsion due to uncertainty in the in-plane stiffness of lateral-load-resisting elements in one-story systems and due to base rotational motion (1994c), and compared torsional amplification associated with the ELF and dynamic analysis (1994d). De La Llera and Chopra (1997) developed a five-step procedure to determine the increase in edge displacement due to accidental torsion by utilizing the data recorded at the base and floor levels of an instrumented building, which was later evaluated by Lin et al. (2001). De La Llera and Almazan (2003) studied accidental torsion in two, three-story, base-isolated models: one was nominally symmetric and the other was mass eccentric. Hernandez and Lopez (2004) performed a similar study to that of De La Llera and Chopra (1995). Shakib and Tohidi (2002) evaluated accidental eccentricity due to torsional inputs similar to De La Llera and Chopra (1994c).

Shifting the center of mass by a percentage of the building dimension is widely accepted means to account for accidental torsion in both static and dynamic analysis. However, since the dynamic characteristics of a building change with a shift in the center of mass, the accuracy of the approach warrants review. A reasonable, simplified procedure suitable for implementation in a building code should result in an increase in edge displacement with an increase in accidental eccentricity.

1.6. Objectives of the Report

Given that recording instruments are not available to record rotational components of earthquake ground motion, the first objective of this report is to develop robust analytical procedures to extract these components of ground motion from translational time series. The second objective is to provide the technical basis for the design of a dense array of translational recording instruments to enable an accurate extraction of rotational components of ground motion. The third objective is to impose extracted rotational components of ground motion on sample structures to judge, in a preliminary sense, the relative importance of translational and rotational components of ground motion on response and performance. The fourth objective of this report is to propose a more robust definition for accidental eccentricity, which will achieve the desired outcome, namely, an increase in rotational response with an increase in accidental eccentricity.

1.7. Report Organization

Chapter 2 describes the Large Scale Seismic Testing (LSST) array at Lotung, Taiwan. The translational acceleration time series recorded from one strong-motion event in the array is used throughout this report for consistency and presentation. The widely used Geodetic Method (GM) is described and sample results are presented for later use as benchmark data.

Chapter 3 develops a procedure to extract rotational components of ground motion from translational time series recorded at a single station. The Single Station Procedure (SSP) requires site-specific information. Information on the rupture process can be used to account for finite fault size.

The SSP of Chapter 3 cannot account for spatial variability of ground motion. This variability can be characterized using data recorded in dense seismic arrays such as the Lotung array. Chapter 4 presents a significant extension of the GM that better addresses spatial variability: the Acceleration Gradient Method

(AGM). The GM and AGM require data from multiple recording stations and each is described as a Multiple Station Procedure (MSP).

Chapter 5 presents a Surface Distribution Method (SDM), a MSP, that captures high frequency content in rotational components of ground motion.

Rotational components extracted from translational data recorded in a dense array may be influenced by the analyst's selection of stations for analysis. Chapter 6 presents a study on station selection that leads to a set of design recommendations for the design of a dense array with the objective of accurately extracting rotational ground motions.

Chapter 7 assesses the current practice of addressing torsional ground motion through the use of accidental eccentricity. An improved definition of accidental eccentricity is proposed.

Three test bed structures, a chimney, a base-isolated building and an associated fixed-base building, are analyzed in Chapter 8 to provide insight into the importance of rotational components of ground motion on response and performance.

Chapter 9 summarizes this report, presents its key conclusions, and identifies recommendations for design practice and future research. A list of references is provided in Chapter 10.

Appendix A calculates the threshold frequency addressed in Chapter 4, above which the AGM fails to capture high frequency content in rotational motion. Appendix B re-assesses the utility of the AGM, based on theory developed in Chapter 6. Appendix C presents the state-space algorithm used in Chapter 8. Appendix D presents the finite-difference algorithm used in Chapter 9. The MATLAB source codes for the SSP, AGM2 and SDM are presented in Appendix E.

CHAPTER 2
DENSE SEISMIC ARRAY AND EARTHQUAKE GROUND MOTION

2.1. Introduction

A dense array of seismic accelerometers provides a unique opportunity to characterize the spatial variability of ground motion over a small geographic region. Earthquake data collected from such an array enables the characterization of rotational and translational components of ground motion, evaluation of ground motion predictive (attenuation) relationships, evaluation of seismic wave passage effects and distribution of soil dynamic strain with depth, among many others.

The Large Scale Seismic Test (LSST) array at Lotung, Taiwan is one of the few dense arrays deployed to date. The LSST array is described below because data collected from the array are used later in this report to validate numerical tools and characterize rotational components of earthquake ground motion. Much additional information on the LSST array can be found at www.earth.sinica.edu.tw/~smdmc/llsst/llsst.htm.

The Lotung LSST array is part of the larger SMART1 array. Figure 2-1 shows the location of the SMART1 array, which was deployed near the city of Lotung in northeastern Taiwan on the east coast. The SMART1 array is sited on the Lanyang plain in Ilan County. The plain is bordered by the Mount Syue ridge to the west and the Central ridge to the south. The LSST array is located between the M and O rings of the SMART1 array and within 300 m of the O08 station.

The construction of the Lotung LSST array was a joint project of the Taiwan Power Company (Taipower) and the US Electric Power Research Institute (EPRI). The Institute of Earth Science, Adademic Sinica (IESAS) served as a contractor to Taipower to install and maintain seismic instruments, and collect, reduce and analyze data. The LSST array became operational in October 1985 and closed in

early 1991. During this period, signals from approximately 30 earthquakes were recorded. Information is provided at the above website.

2.2. Instrumentation

The LLSST array was composed of thirty-seven stations. Of these, fifteen were surface stations (see Figure 2-2), eight were downhole stations (see Figure 2-3) and fourteen stations were located in or on two scale models (1/4 and 1/2 scale) of containment vessels for Pressurized Water Reactors (PWR) (see Figures 2-4 and 2-5). A description of the each station (location, elevation, instrument type and period of operation [year_month_day] are presented in Table 2-1. All fifteen free-surface accelerometers were positioned along the three radial arms of the array that made an angle of approximately 120 degrees with each other. Each arm was about 50 m long and the spacing between the surface stations along each arm varied between 3 m and 90 m.

The typical station was instrumented with a three-component Kinematic Force-Balance Accelerometer (FBA) and a DSA-3 cassette digital recorder for the data acquisition. Two types of accelerometers were used: FBA-13 and FBA-13DH. The specifications for the sensors (model: FBA-13 and FBA-13DH) were: i) orthogonally oriented triaxial (L, V, T) force balance accelerometer, ii) natural frequency of 50 Hz, iii) damping ratio of 70 % of critical, and iv) range of measurement of 2.5 volt=2 g (zero to peak). The specifications for the digital recorder were: i) 12 bits resolution, ii) dynamic range of 66 dB (zero to peak), iii) pre-event memory of 5.12 seconds, iv) sampling rate of 200 samples/second, and v) a frequency response to 50 Hz.

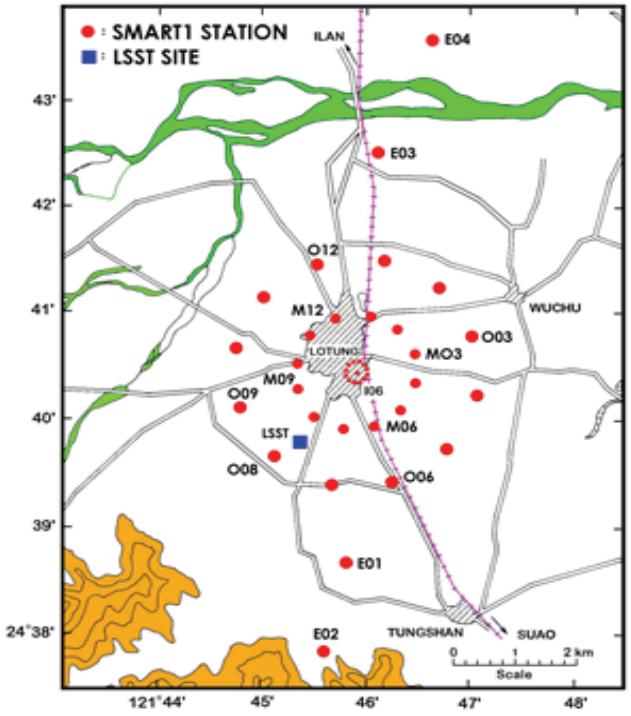

Figure 2-1: Location of the LSST array in Lotung, Taiwan
(www.earth.sinica.edu.tw/~smdmc/llsst/llsst.htm)

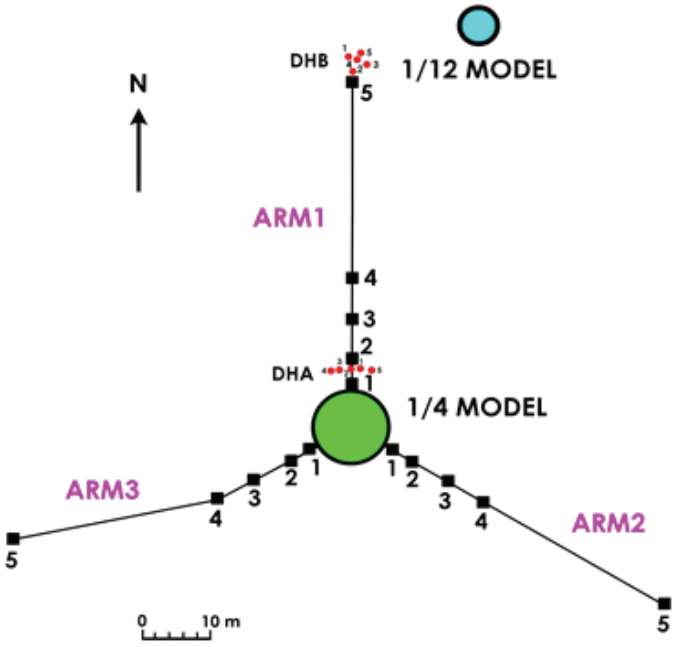

Figure 2-2: Location of the free surface stations
(www.earth.sinica.edu.tw/~smdmc/llsst/llsst.htm)

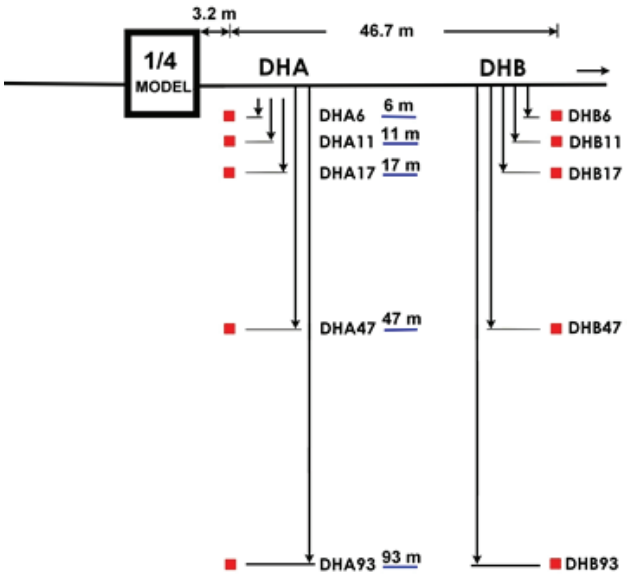

Figure 2-3: Location of the bore-hole stations
(www.earth.sinica.edu.tw/~smdmc/llsst/llsst.htm)

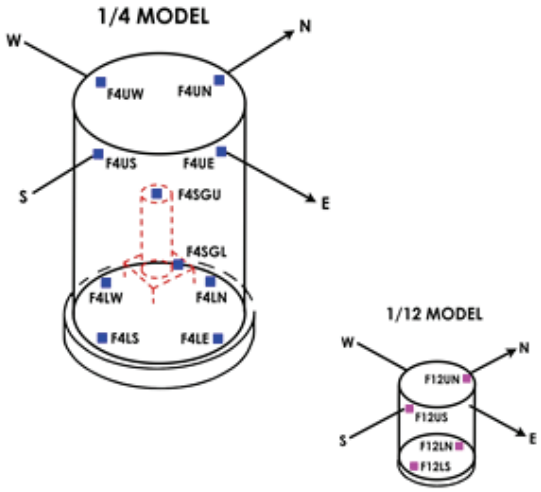

Figure 2-4: Placement of accelerometers on the containment structure
(www.earth.sinica.edu.tw/~smdmc/llsst/llsst.htm)

Figure 2-5: Lotung model containment structure
(www.earth.sinica.edu.tw/~smdmc/llsst/llsst.htm)

2.3. Geological Characteristics of the Site

The Lanyang (Ilan) plain in northeastern Taiwan is a very flat delta-like alluvial plain of about 300 km^2 (Chung, 2007). Seismic surveying and drilling (e.g., Chiang, 1976) indicate that the Lanyang plain is constructed of a soil layer, a layer of alluvium, a Pleistocene stratum and a Miocene basement. The basement surface is concave upward and inclines eastwards reaching a maximum depth of 1500 m at the central section of the coastline (Chung, 2007). Wen and Yeh (1984) conducted a seismic refraction survey for the SMART1 array region and reported the cross-sections that are reproduced in Figure 2-6. The reported spatial variations in wave velocity are shown in Figure 2-7. The soil layer, which varies in thickness between 3 m and 18 m, has a P-wave velocity that ranges between 430 and 760 m/sec and S-wave velocity between 120 and 160 m/sec. The alluvium that ranges in thickness between 30 m and 60 m has a P-wave velocity that varies between 1400 and 1700 m/sec and S-wave velocity between 190 and 320 m/sec. The spatial variation of the wave velocities is similar in the EW and NS directions and the soil properties may be considered to be laterally homogeneous for up to 60 m below the free surface. Boreholes were drilled near the array to determine the spatial heterogeneity in the vertical direction (Moh,

Table 2-1: Description of stations

Station code	Coordinates		Elevation	Instrument type	Operational Period
	Longitude (E)	Latitude (N)	(m)		
F4UN	121 45 18.37	24 39 35.76	0	FBA-13, DSA-3	19850920-19930813
F4UE	121 45 18.37	24 39 35.76	0	FBA-13, DSA-3	19850920-19930813
F4US	121 45 18.37	24 39 35.76	0	FBA-13, DSA-3	19850920-19930813
F4UW	121 45 18.37	24 39 35.76	0	FBA-13, DSA-3	19851026-19930813
F4LN	121 45 18.37	24 39 35.76	0	FBA-13, DSA-3	19850920-19930813
F4LE	121 45 18.37	24 39 35.76	0	FBA-13, DSA-3	19850920-19930813
F4LS	121 45 18.37	24 39 35.76	0	FBA-13, DSA-3	19850920-19930813
F4LW	121 45 18.37	24 39 35.76	0	FBA-13, DSA-3	19851026-19930813
F4SGU	121 45 18.37	24 39 35.76	0	FBA-13, DSA-3	19850920-19930813
F4SGL	121 45 18.37	24 39 35.76	0	FBA-13, DSA-3	19850920-19930813
F12UN	121 45 18.37	24 39 35.76	0	FBA-13, DSA-3	19851026-19930813
F12US	121 45 18.37	24 39 35.76	0	FBA-13, DSA-3	19851026-19930813
F12LN	121 45 18.37	24 39 35.76	0	FBA-13, DSA-3	19851026-19930813
F12LS	121 45 18.37	24 39 35.76	0	FBA-13, DSA-3	19851026-19930813
FA1-1	121 45 18.37	24 39 35.97	0	FBA-13, DSA-3	19851026-19930813
FA1-2	121 45 18.37	24 39 36.07	0	FBA-13, DSA-3	19851026-19930813
FA1-3	121 45 18.37	24 39 36.27	0	FBA-13, DSA-3	19851030-19930813
FA1-4	121 45 18.37	24 39 36.47	0	FBA-13, DSA-3	19851030-19930813
FA1-5	121 45 18.38	24 39 37.42	0	FBA-13, DSA-3	19851030-19930813
FA2-1	121 45 18.58	24 39 35.64	0	FBA-13, DSA-3	19851026-19930813
FA2-2	121 45 18.67	24 39 35.60	0	FBA-13, DSA-3	19851026-19930813
FA2-3	121 45 18.86	24 39 35.49	0	FBA-13, DSA-3	19851026-19930813
FA2-4	121 45 19.06	24 39 35.39	0	FBA-13, DSA-3	19851030-19930813
FA2-5	121 45 19.98	24 39 34.89	0	FBA-13, DSA-3	19851030-19930813
FA3-1	121 45 18.16	24 39 35.65	0	FBA-13, DSA-3	19851026-19930813
FA3-2	121 45 18.07	24 39 35.60	0	FBA-13, DSA-3	19851026-19930813
FA3-3	121 45 17.87	24 39 35.50	0	FBA-13, DSA-3	19851026-19930813
FA3-4	121 45 17.69	24 39 35.40	0	FBA-13, DSA-3	19851026-19930813
FA3-5	121 45 16.64	24 39 35.21	0	FBA-13, DSA-3	19851026-19930813
DHA-1	121 45 18.42	24 39 36.03	6.27	FBA-DH13, DSA-3	19851030-19930812
DHA-2	121 45 18.36	24 39 36.04	11.13	FBA-DH13, DSA-3	19851030-19930812
DHA-3	121 45 18.31	24 39 36.03	17.00	FBA-DH13, DSA-3	19851026-19881026
DHA-4	121 45 18.26	24 39 36.02	46.37	FBA-DH13, DSA-3	19851030-19881026
DHB-1	121 45 18.35	24 39 37.53	6.26	FBA-DH13, DSA-3	19851026-19881026
DHB-2	121 45 18.40	24 39 37.51	11.16	FBA-DH13, DSA-3	19851026-19881026
DHB-3	121 45 18.44	24 39 37.49	17.31	FBA-DH13, DSA-3	19851026-19881026
DHB-4	121 45 18.38	24 39 37.46	46.01	FBA-DH13, DSA-3	19851026-19881026

1986; Chen et al., 1990). The borehole locations are shown in Figure 2-8. Figure 2-9 presents data from boreholes S1, S4, and E2 (see Figure 2-8 for locations). The data include a description of the core sample, its composition, and the SPT-N count. Chen et al (1990) reported the variation of the shear wave velocity (using maximum shear modulus) for locations L2, L6 and L7 (see Figure 2-10). They analyzed the shear modulus and damping ratio for the soil samples from the LSST boreholes. The reduced data (normalized shear modulus and damping ratio) are compared with standard curves in Figure 2-11.

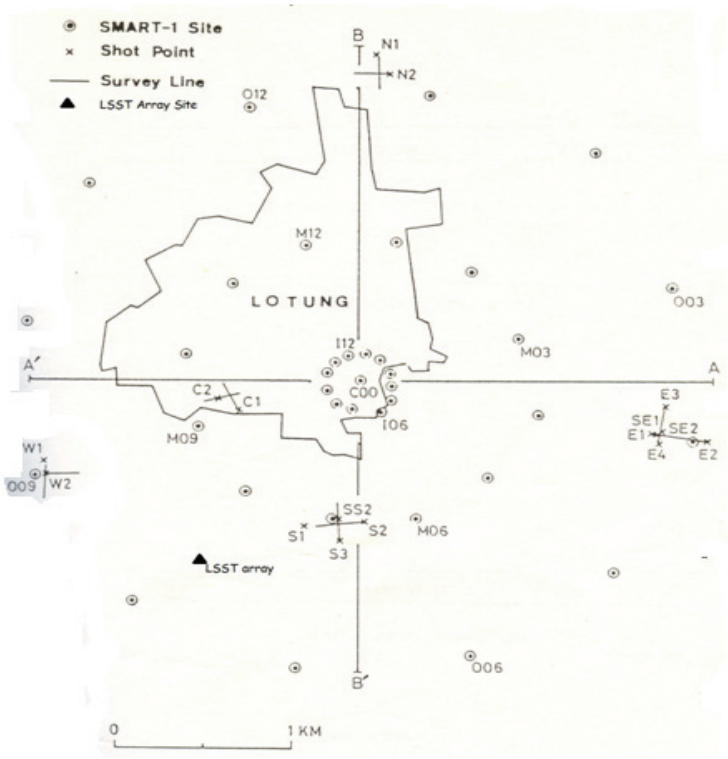

Figure 2-6: Seismic refraction cross-sections (adapted from Wen and Yeh, 1984)

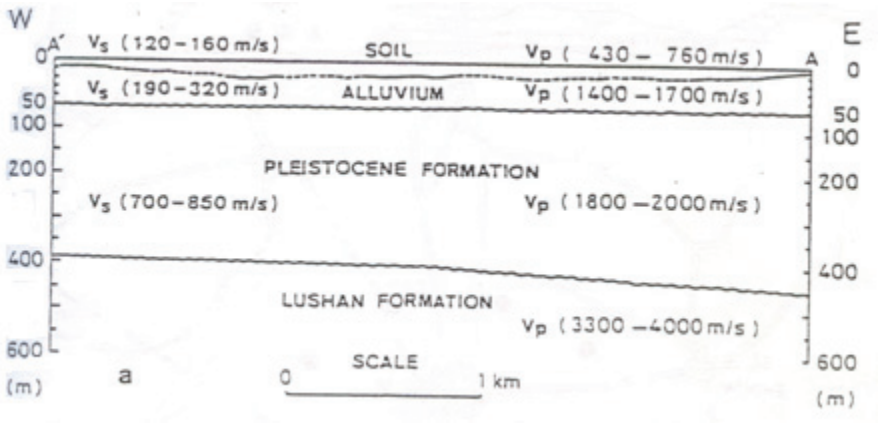

(a) Profile along East-West direction

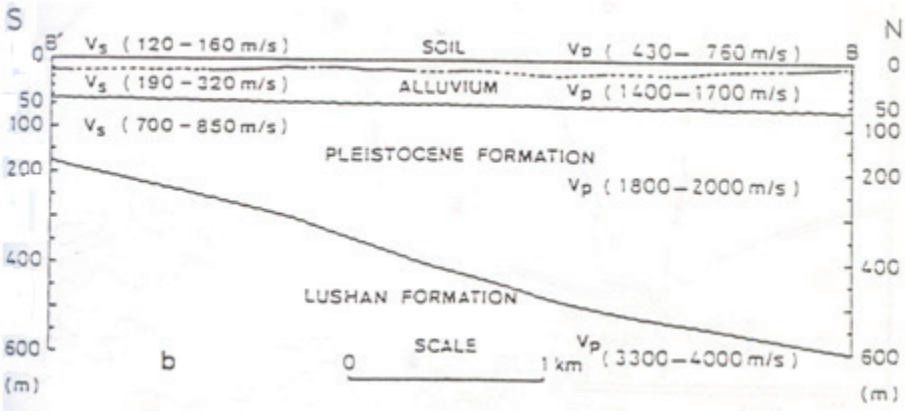

(b) Profile along North-South direction

Figure 2-7: Velocity profile near the LSST array (Wen and Yeh, 1984)

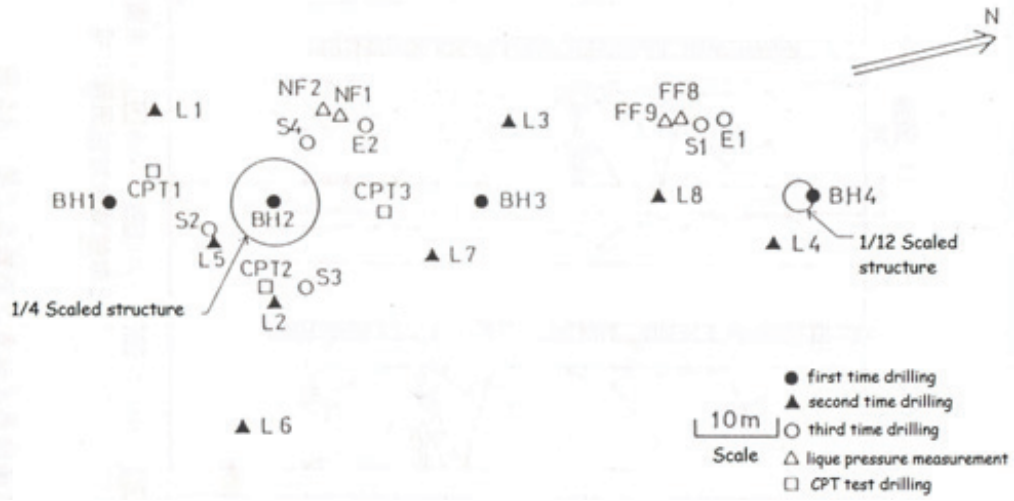

Figure 2-8: Location of boreholes and the containment structure models (Chen et al. 1990)

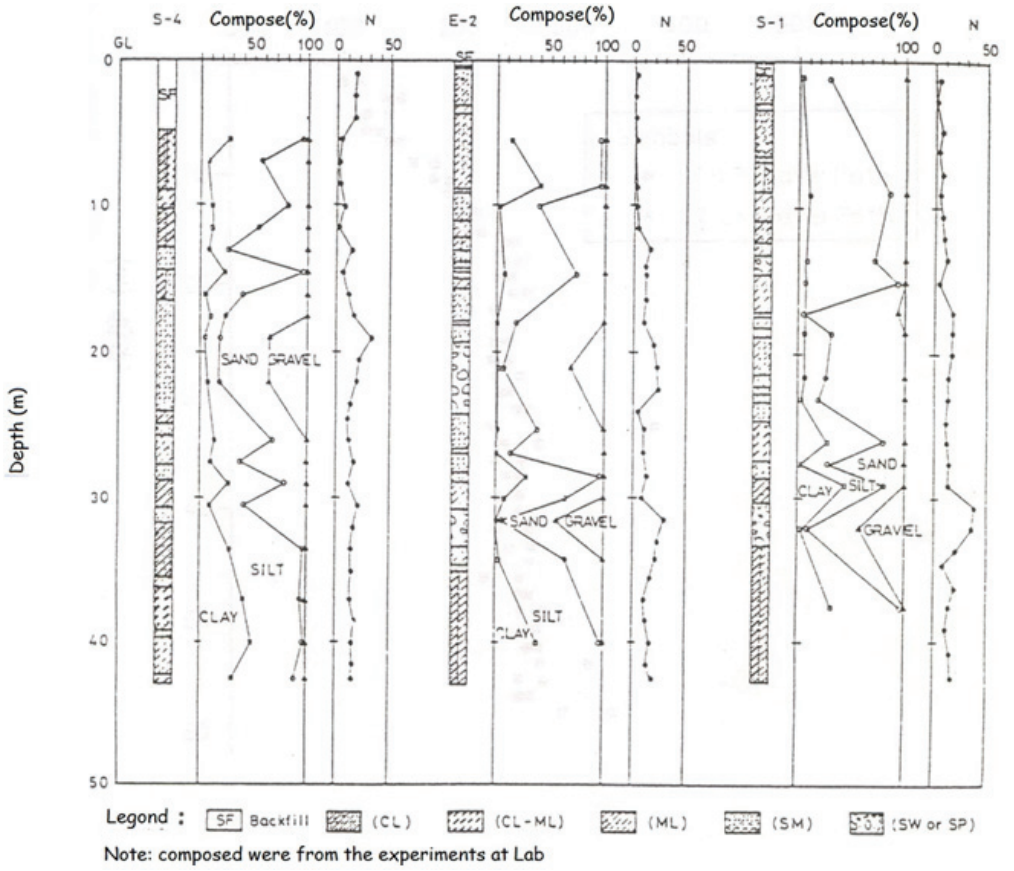

Figure 2-9: Sample borehole data (locations S-4, E-2 and S-1; Moh, 1986)

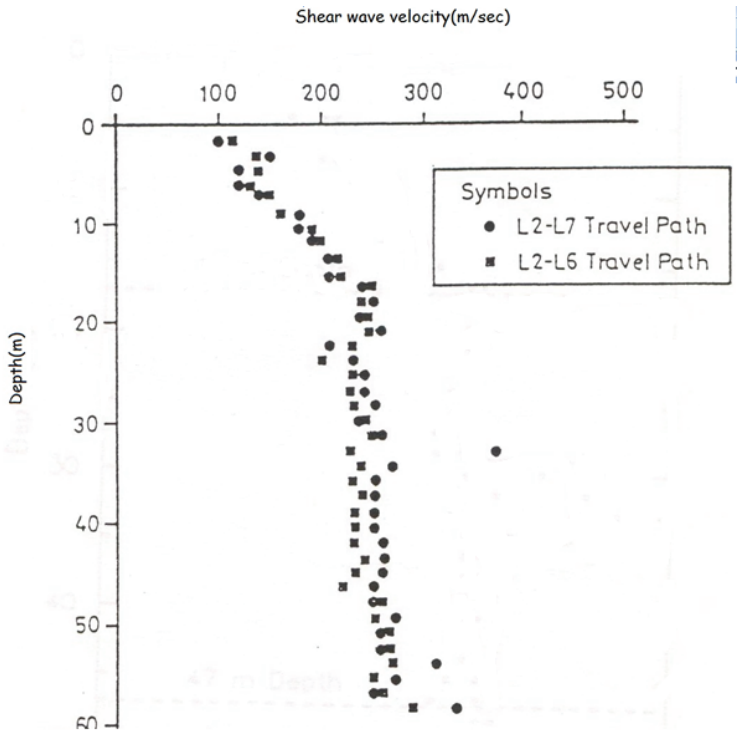

Figure 2-10: Distribution of the shear wave velocity at locations L2, L6 and L7 (Chen et al., 1990)

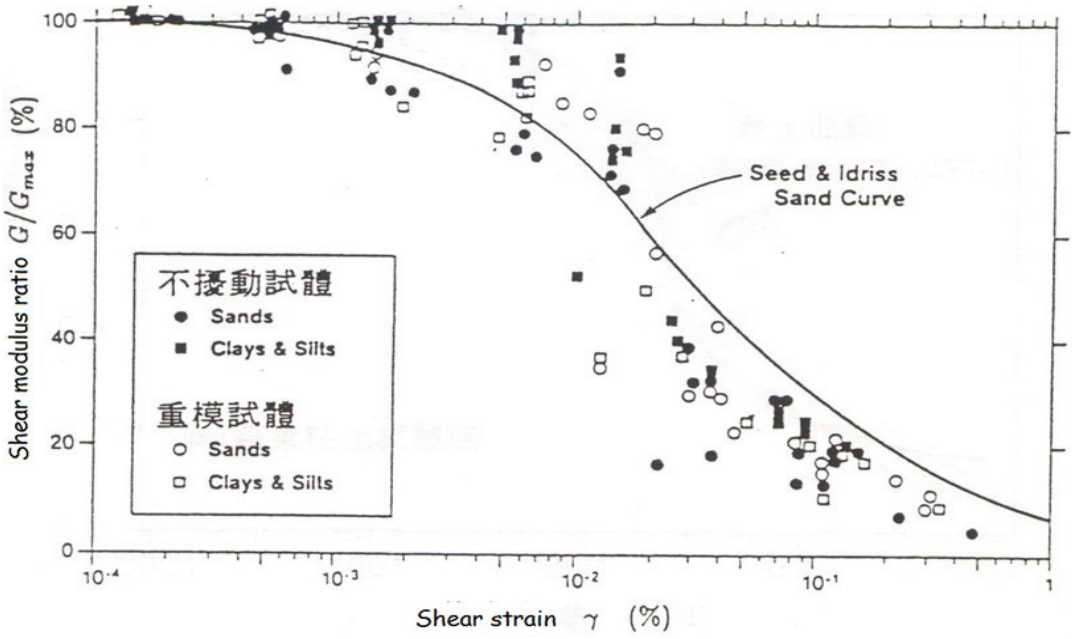

(a) Variation of shear modulus ratio

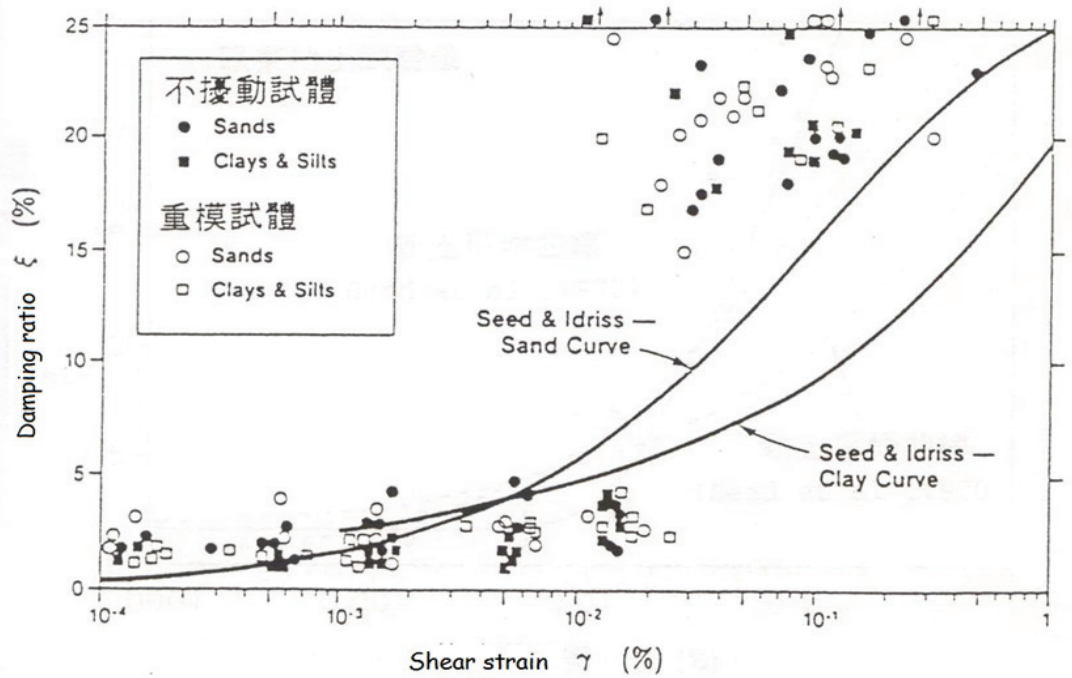

(b) Variation of damping ratio

Figure 2-11: Shear modulus ratio and damping ratio test for soil (Chen et al., 1990) (cont.)

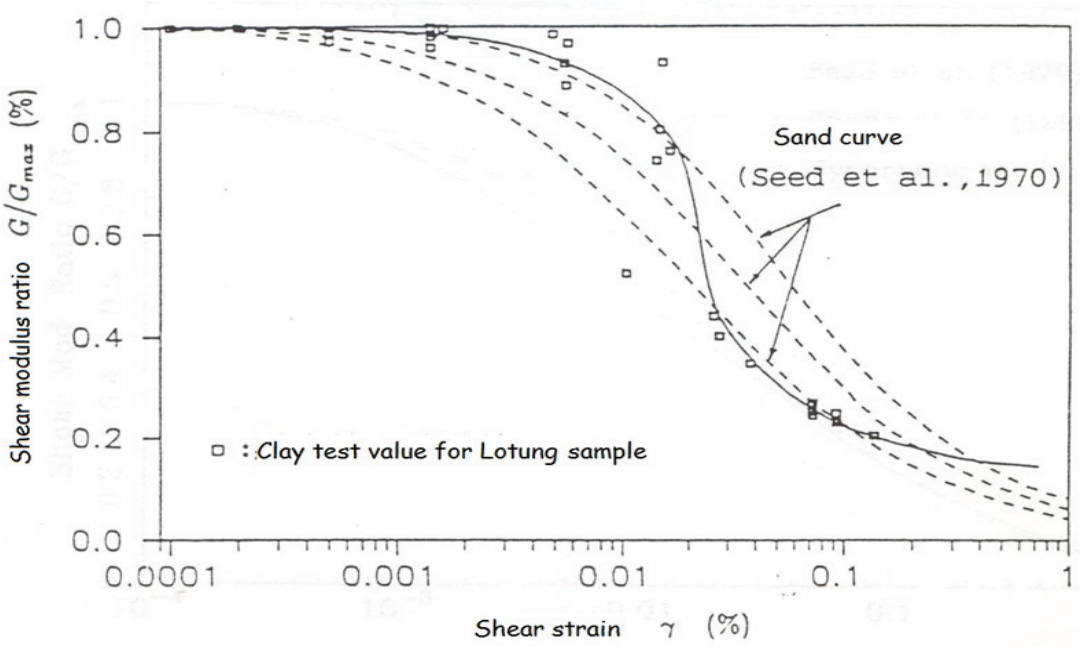

(c) Variation of shear modulus ratio

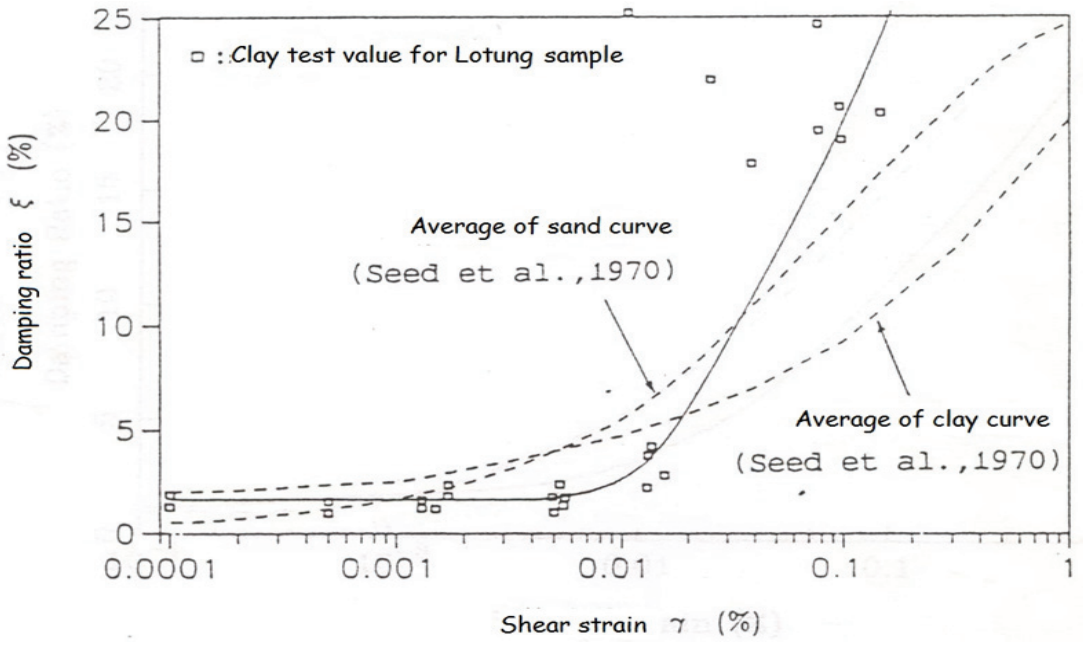

(d) Variation of damping ratio

Figure 2-11: Shear modulus ratio and damping ratio test for soil (Chen et al., 1990)

2.4. Data Processing

The data recorded at the LLSST array was processed in two steps: 1) the 1 second of pre-event mean response was removed (a baseline correction), and 2) the remaining data were high-pass filtered at a frequency of 0.1 Hz (Ryosuke Sato et al., 1979).

2.5. Translational Components of Ground Motion

The M6.1 event of January 16, 1986, recorded at the Lotung-LSST (LLSST) site provides the earthquake ground motions used in the reminder of this report. The focal depth of the event was 10 km. The recorded translational (EW, NS and vertical) acceleration histories are shown in Figure 2-12 for all fifteen surface stations. The associated peak ground motion parameters (acceleration and velocity) are listed in Table 2-2. Significant spatial variability across the array is evident.

2.6. Rotational Components of Ground Motion

2.6.1. Geodetic Method

The rotational components of ground motion are extracted here using the Geodetic Method (GM), originally developed by Spudich et al. (1995), to provide a baseline to be used later. The theoretical background of the procedure is presented below.

Consider the right-handed Cartesian coordinate system (x_1, x_2, x_3) of Figure 2-13, with x_3 representing the vertical direction. Assume there are N stations at which recorded acceleration histories are available along the three orthogonal directions: x_1, x_2, and x_3. Let the reference or at-rest position vector of any two stations, i and j, be given by $r^i = \begin{pmatrix} r_1^i & r_2^i & r_3^i \end{pmatrix}^T$ and $r^j = \begin{pmatrix} r_1^j & r_2^j & r_3^j \end{pmatrix}^T$, respectively. At any time t during the seismic event, the displacements of these two stations with respect to their

reference position are $u^i = \begin{pmatrix} u_1^i & u_2^i & u_3^i \end{pmatrix}^T$ and $u^j = \begin{pmatrix} u_1^j & u_2^j & u_3^j \end{pmatrix}^T$, respectively. Assuming a small and uniform displacement gradient $\left[u_{i,j}\right]$ over the region of interest,

$$\begin{Bmatrix} u_1^j - u_1^i \\ u_2^j - u_2^i \\ u_3^j - u_3^i \end{Bmatrix} = \begin{bmatrix} u_{1,1} & u_{1,2} & u_{1,3} \\ u_{2,1} & u_{2,2} & u_{2,3} \\ u_{3,1} & u_{3,2} & u_{3,3} \end{bmatrix} \begin{Bmatrix} r_1^j - r_1^i \\ r_2^j - r_2^i \\ r_3^j - r_3^i \end{Bmatrix} \tag{2-1}$$

Applying the plane stress condition along the vertical direction and writing the independent unknown displacement gradient parameters in the vector form, Eq (2-1) may be expressed as

$$\begin{Bmatrix} u_1^j - u_1^i \\ u_2^j - u_2^i \\ u_3^j - u_3^i \end{Bmatrix} = \begin{bmatrix} r_1^j - r_1^i & r_3^j - r_3^i & 0 & 0 & r_2^j - r_2^i & 0 \\ 0 & 0 & r_2^j - r_2^i & r_3^j - r_3^i & 0 & r_1^j - r_1^i \\ -\eta\left(r_3^j - r_3^i\right) & -\left(r_1^j - r_1^i\right) & -\eta\left(r_3^j - r_3^i\right) & -\left(r_2^j - r_2^i\right) & 0 & 0 \end{bmatrix} \begin{Bmatrix} u_{1,1} \\ u_{1,3} \\ u_{2,2} \\ u_{2,3} \\ u_{1,2} \\ u_{2,1} \end{Bmatrix} \tag{2-2}$$

Here, the soil in the region of interest is assumed to be a homogeneous, isotropic material with Poisson's ratio ν and $\eta = \nu/(1-\nu)$. If the i^{th} station is fixed as the reference station and by varying the j^{th} station to account for the remaining $(N-1)$ stations, one at a time, a set of $(N-1)$ equations similar to Eq (2-2) may be developed as

$$\Delta u_i^j = A_i^j p,\ i = 1,\ j = 2,...N \tag{2-3}$$

where, Δu_i^j and p are the 3×1 and 6×1 vectors on the left and right sides of Eq (2-2), respectively, and A_i^j is the 3×6 matrix on the right side of Eq (2-2).

The set of $(N-1)$ equations is then assembled as:

$$\left\{\Delta u_1^{2T} \quad \Delta u_1^{3T} \quad . \quad \Delta u_1^{NT}\right\}^T = \left\{A_1^{2T} \quad A_1^{3T} \quad . \quad A_1^{NT}\right\}^T p \tag{2-4}$$

which leads to an overdetermined problem of the form

$$\{\Delta u\} = [A]\{p\} \tag{2-5}$$

The vector $\{\Delta u\}$ is known from the double integration of the measured translational acceleration time series data. The matrix $[A]$, the data kernel, is known from the relative location of the stations. The time varying vector $\{p\}$ comprises the six unknown displacement gradient parameters.

The actual solution p does not exist and the least-square solution $\bar{p}$ of Eq (2-5) may be expressed in the form (Menke, 1984)

$$\bar{p} = \left[A^T W_e A\right]^{-1} A^T W_e \{\Delta u\} \tag{2-6}$$

where the weight matrix $W_e = \left[\mathrm{cov}(\Delta u)\right]^{-1}$ is not diagonal as $\{\Delta u\}$ is not the measured data (or integration of the measured data with respect to time). Instead, this is linearly related to the measured data through $\Delta u = Du$ and hence,

$$\mathrm{cov}(\Delta u) = D\left[\mathrm{cov}(u)\right]D^T = DC_u D^T \tag{2-7}$$

Assuming the measured data have a multivariate Gaussian distribution with equal variance σ_u^2, the covariance matrix reduces to $C_u = \sigma_u^2 [I]_{3N\times 3N}$, where I denotes the identity matrix. The torsional rotation is then given by $\frac{1}{2}(u_{2,1} - u_{1,2}) = \frac{1}{2}\left[\bar{p}(6) - \bar{p}(5)\right]$. Utilizing the plane stress condition along the vertical direction, the rocking rotations on the *xz* and *yz* planes are $u_{1,3} = \bar{p}(2)$ and $-u_{2,3} = -\bar{p}(4)$, respectively.

Finally, with the assumed distribution of the measured data, the solution vector [Eq (2-6)] is independent of σ_u^2 and hence, the weight matrix may be considered as $W_e = \left[DD^T\right]^{-1}$.

2.6.2. Extracted Rotational Components

Only surface stations are considered in this analysis. The rotational time series computed using the GM are presented in Figure 2-14 (panels a, c and e). The associated Fourier amplitude spectra for the torsional (0-10 Hz) and for the rocking (0-20 Hz) accelerations are also shown (panels b, d and f). Figure 2-14b shows that the torsional acceleration is dominated by a single narrow frequency-band that is also apparent from the FFT of the representative horizontal accelerations recorded at station FA1_1 (panels g and h). Panels d and f show multiple frequency contributions to the rocking accelerations, which is expected because the recorded vertical accelerations are richer in higher frequencies than the recorded horizontal accelerations (see Figure 2-12).

Table 2-2: Peak translational accelerations and velocities at the surface stations for the January 16, 1986 earthquake recorded in the LSST array, Lotung

Station	Peak translational acceleration (cm/sec^2)			Peak translational velocity (cm/sec)		
	EW	NS	Vertical	EW	NS	Vertical
FA1_1	136.5	195.0	132.5	23.4	25.6	4.9
FA1_2	142.1	188.0	115.7	23.1	26.6	5.8
FA1_3	152.0	250.3	107.4	23.1	32.8	7.8
FA1_4	148.2	253.3	105.9	23.4	31.3	6.5
FA1_5	142.3	258.0	104.3	24.2	30.5	5.8
FA2_1	148.1	193.4	92.7	22.0	27.7	8.1
FA2_2	149.6	227.7	96.1	20.9	28.5	7.9
FA2_3	158.7	257.0	141.9	26.0	29.7	5.4
FA2_4	---	---	---	---	---	---
FA2_5	138.9	231.1	82.8	21.8	30.5	5.9
FA3_1	142.5	183.5	118.0	23.0	27.5	8.3
FA3_2	---	---	---	---	---	---
FA3_3	186.9	263.3	127.0	26.6	34.4	6.1
FA3_4	---	---	---	---	---	---
FA3_5	223.1	278.0	212.6	29.8	19.3	5.3

--- These stations did not function throughout during the event

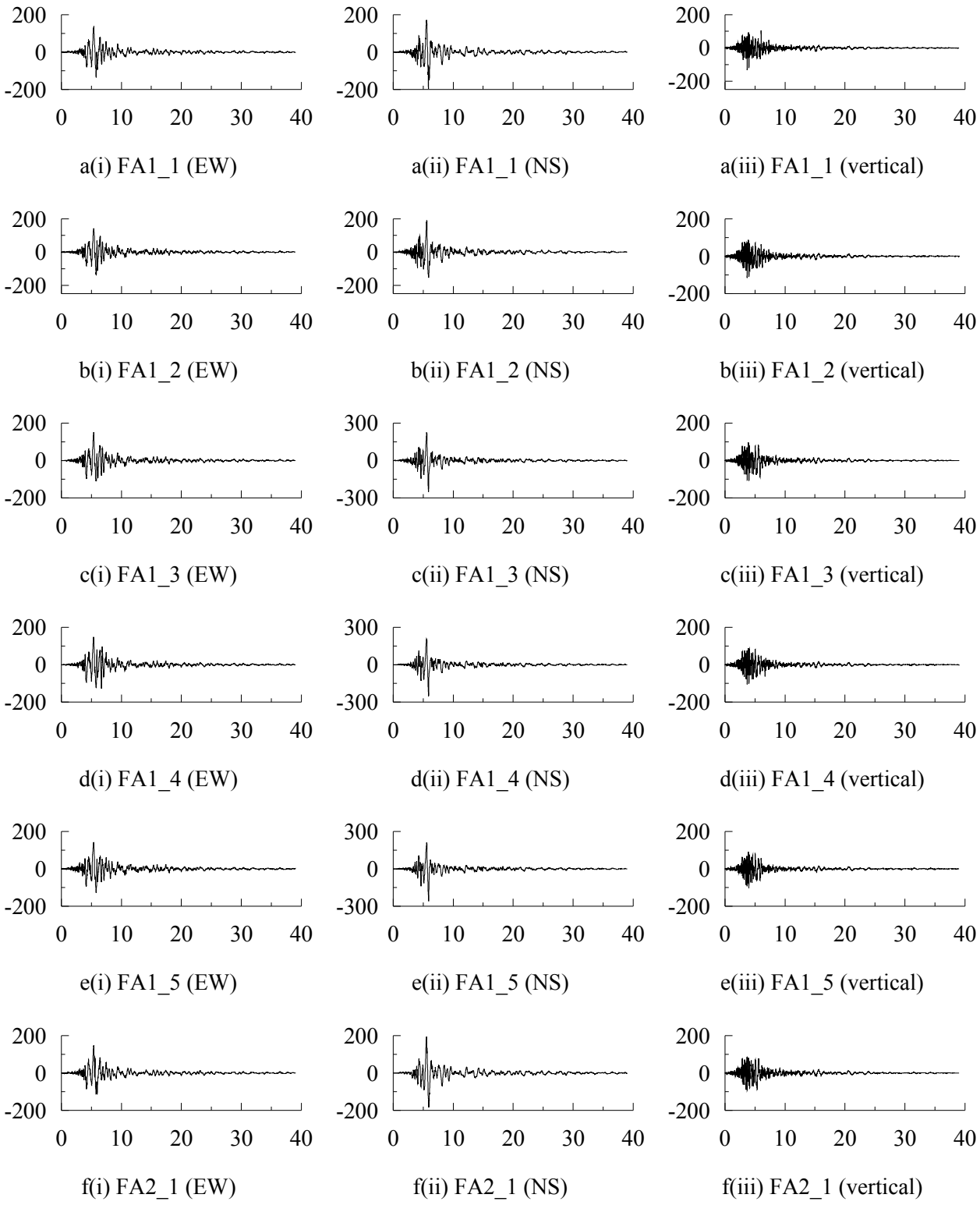

Figure 2-12: Translational acceleration records at all 15 surface stations (cont.)

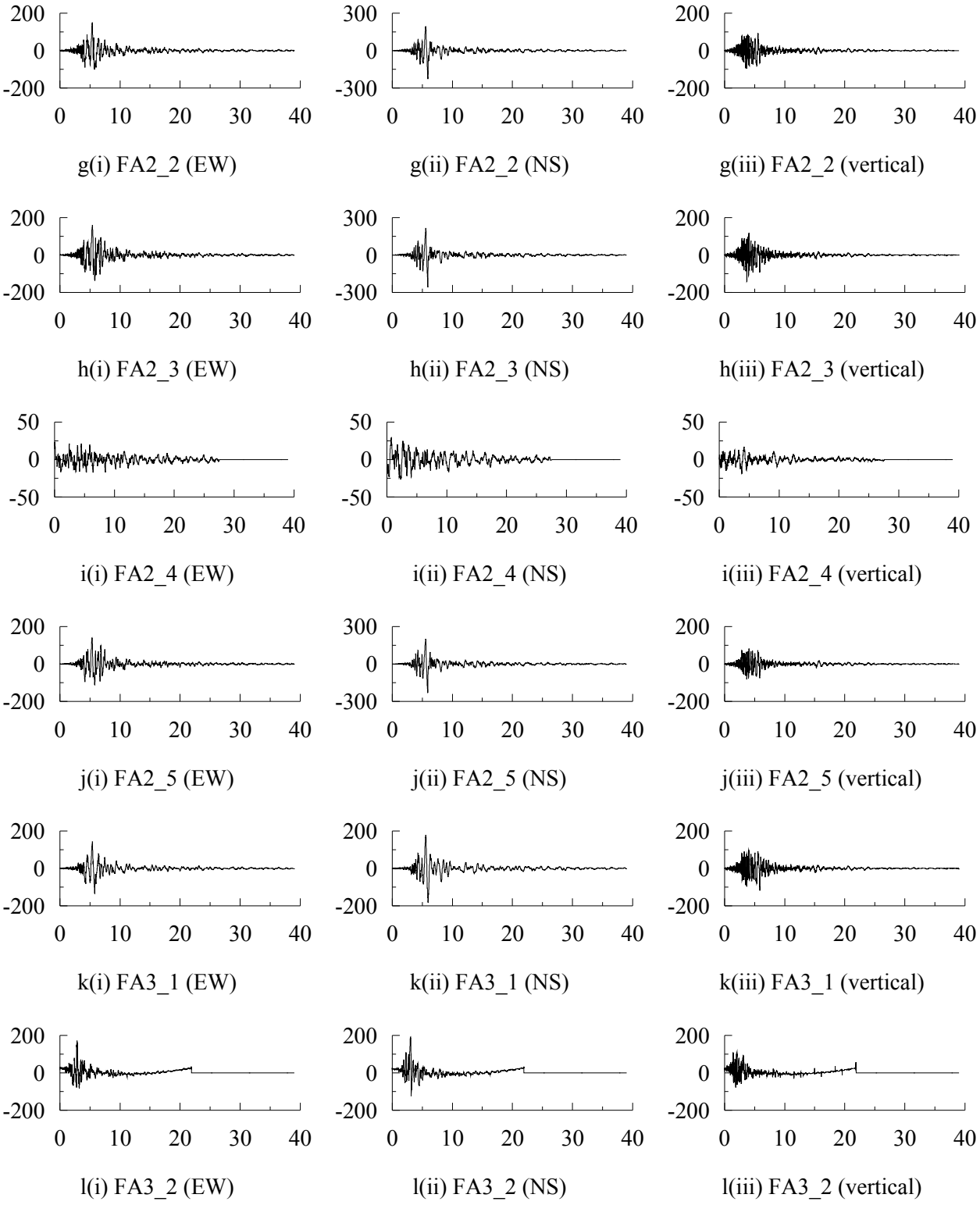

Figure 2-12: Translational acceleration records at all 15 surface stations (cont.)

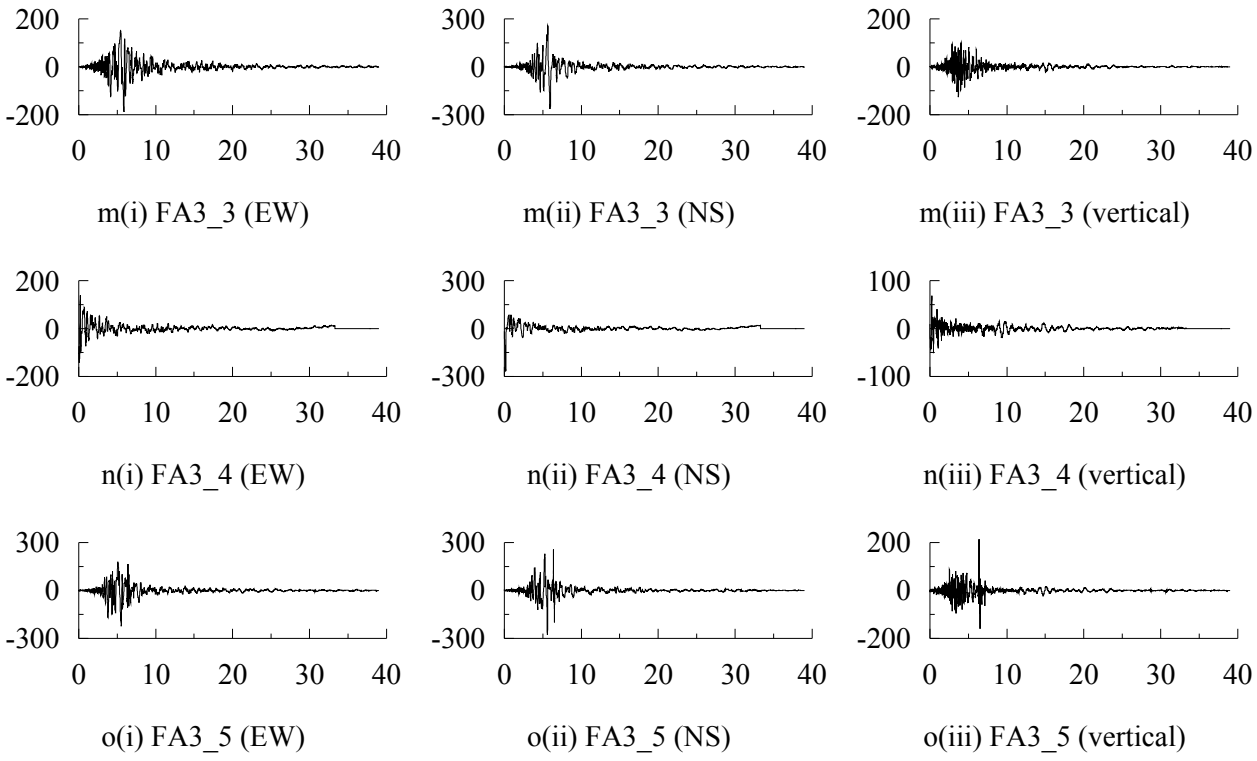

Figure 2-12: Translational acceleration records at all 15 surface stations

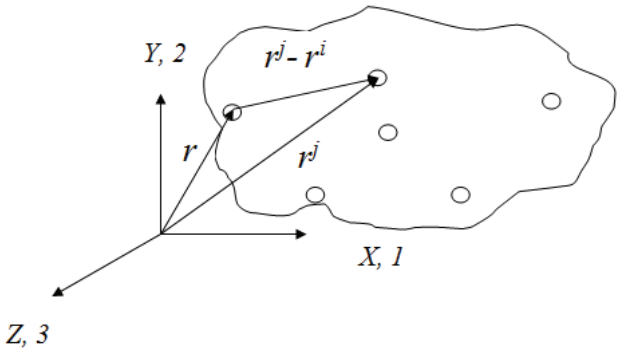

Figure 2-13: Coordinate system

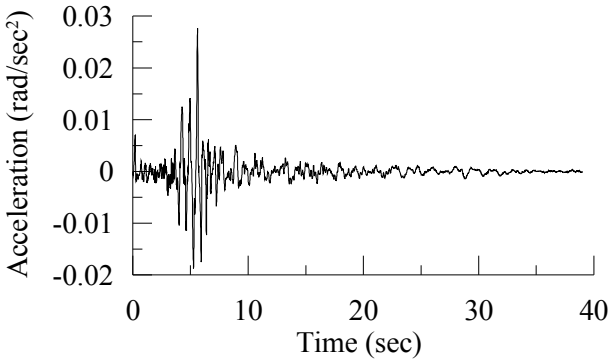

(a) Torsional acceleration using GM

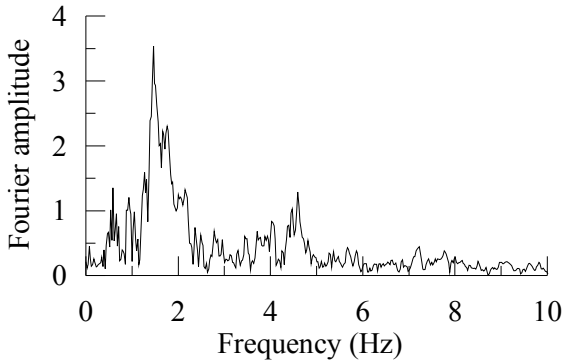

(b) FFT of (a)

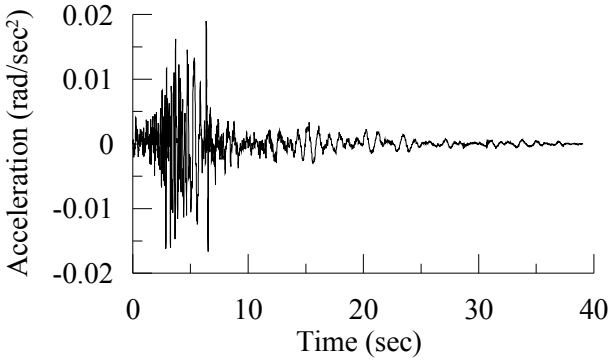

(c) Rocking (xz plane) acceleration using GM

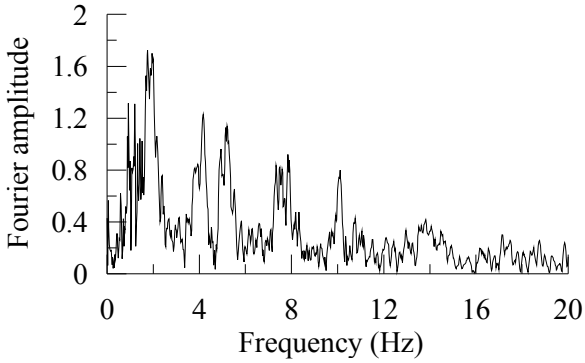

(d) FFT of (c)

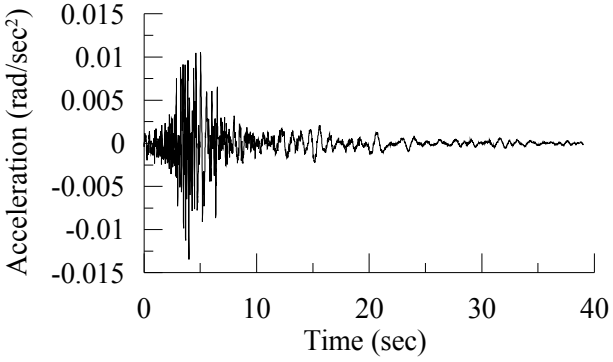

(e) Rocking (yz plane) acceleration using GM

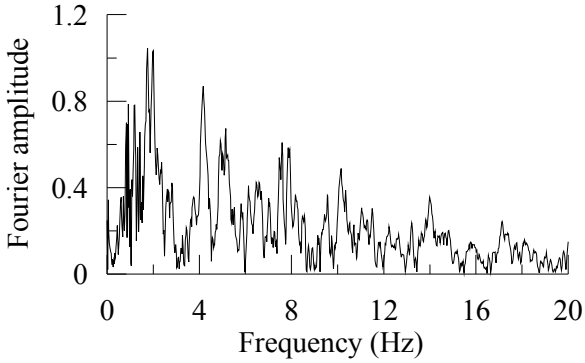

(f) FFT of (e)

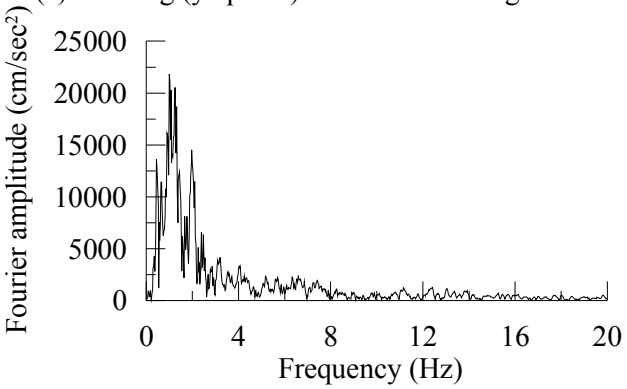

(g) FFT of EW acceleration at station FA1_1

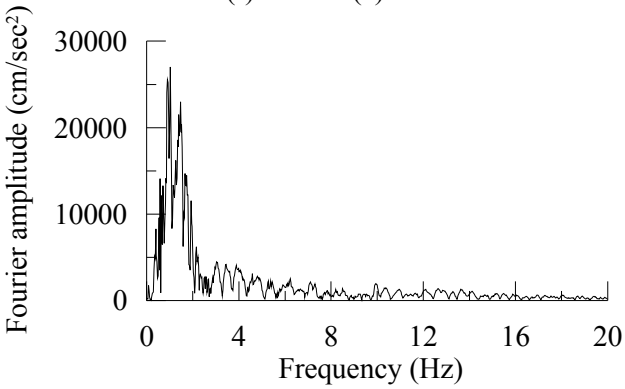

(h) FFT of NS acceleration at station FA1_1

Figure 2-14: Rotational accelerations using GM and FFT of horizontal accelerations at station FA1_1

CHAPTER 3

ESTIMATING ROTATIONAL COMPONENTS OF GROUND MOTION USING A SINGLE STATION APPROACH

3.1. Introduction

In this chapter, a method is presented to develop rotational time series by first decomposing the three translational time series of a ground motion recorded at one station into body waves: P (compressional), SH (shear wave, horizontal particle motion) and SV (shear wave, vertical particle motion). It is assumed that there is no contribution from surface waves. The method is described below as a Single Station Procedure (SSP) to distinguish it from those based on data collected at multiple recording stations. The body waves are then reassembled to generate the rotational time series. Theory is presented first assuming a point source for the earthquake and then extended to address finite fault rupture length and symmetrical and unsymmetrical bilateral rupture. The point-source assumption is reasonable for small site-to-source distances if the earthquake magnitude is small and large site-to-source distances if the earthquake magnitude is large.

The MATLAB source code developed for the SSP is presented in Appendix E, together with an explanation and examples.

3.2. Deconstructing Translational Time Series and Reconstructing Rotational Time Series

Figure 3-1 provides a basis for the discussion that follows and collapses the rupture plane to a point source. Figure 3-1(a) shows the travel path from the hypocenter to the recording station per the seminal paper by Penzien and Watabe (1975). The vertical plane passing through the hypocenter and the recording station is defined as the *principal plane*. The projection of the principal plane onto the ground surface (x_1

direction here) is defined as the *principal direction* and the perpendicular direction on the horizontal plane is defined as the *normal direction*. The reflections of the incident body waves from the free surface are illustrated in Figures 3-1(b), (c) and (d). There are two types of incident body waves: P waves with particle displacement along the direction of propagation, and S waves with particle displacement normal to the direction of propagation but arbitrarily polarized. The S waves are decomposed into SV (vertically polarized) and SH (horizontally polarized) waves. For the incident P and SV waves, the reflected waves are also P and SV, whereas the incident SH wave produces only a reflected SH wave.

An inverse problem with nine unknown parameters is solved here: amplitude, phase and incidence angle for each of the P (assumed homogeneous unless noted otherwise), SV and SH waves. The number of known quantities is six: amplitude and phase of three orthogonal translational components of the recorded acceleration histories, thus the problem is indeterminate to an order of three. The amplification in amplitude due to the reflection of the SH wave from the free surface is two (Achenbach, 1973) and is independent of its incidence angle. The characteristics of the incident SH wave (amplitude and phase) can be determined using the resultant of the components of the recorded horizontal acceleration histories normal to the principal direction. The remaining seven unknown parameters must be estimated from the remaining four known quantities and three additional relationships must be assumed or established. It is now assumed that the phase and incidence angle are the same for the SV and SH waves. These assumptions may be reasonable if the incident S wave is a plane wave with arbitrary polarization, and the problem can be reduced to one degree of indeterminacy for which one final assumption is needed.

Two alternatives are investigated here. Each alternative underpins a procedure to estimate the rotational components and uses wave propagation theory that is presented in the following sections.

3.3. Propagation of Harmonic Plane Waves

With reference to Figure 3-1, consider x_1x_2 as the polarized plane. The propagation of a harmonic plane wave on the polarized plane may be expressed in index form as (Achenbach, 1970)

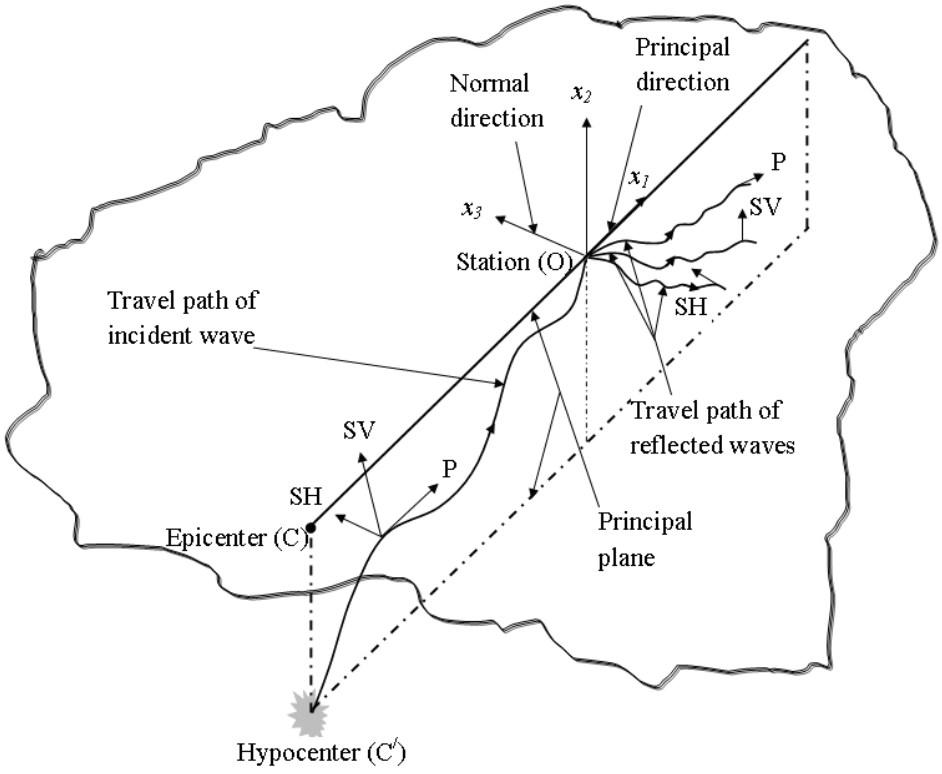

(a) Incident and reflected waves propagating on the principal plane

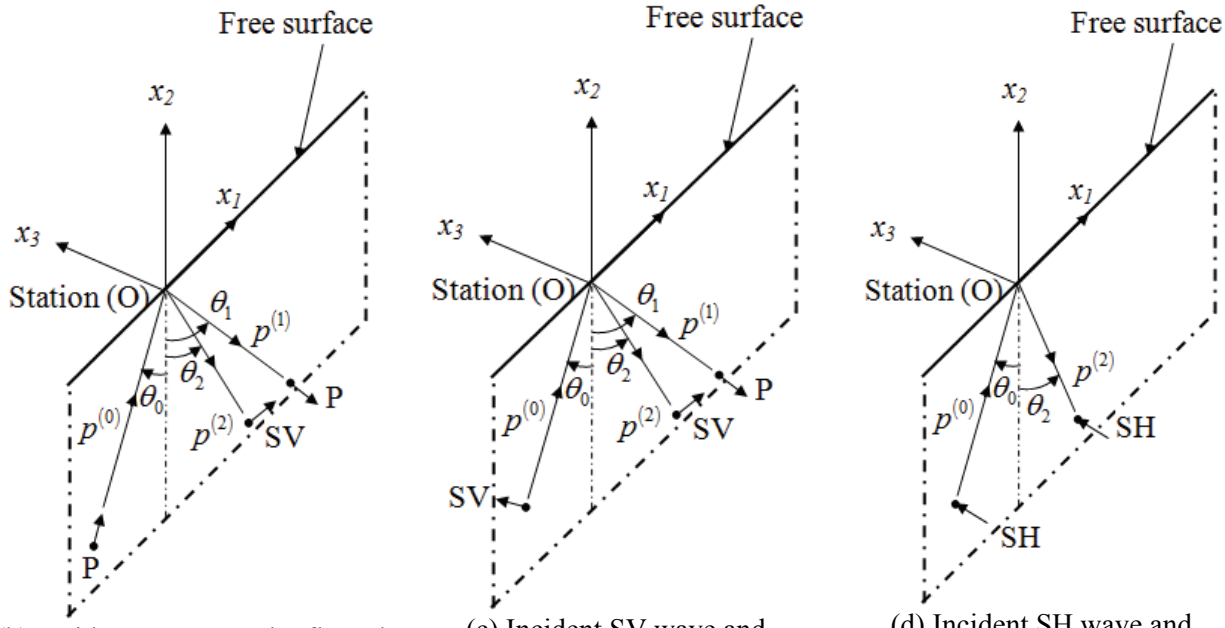

(b) Incident P wave and reflected waves

(c) Incident SV wave and reflected waves

(d) Incident SH wave and reflected wave

Figure 3-1: Waves propagating from the source (hypocenter) to the recording station through principal plane and reflection of the incident wave from the free surface

$$
\begin{aligned}
&{}_r u_l = A_r d_l \exp(i\eta) \\
&\eta = rk(x_m p_m - ct) - \phi_r
\end{aligned}
\tag{3-1}
$$

where p, d denote the vectors of propagation and particle movement, respectively; u is the resultant particle displacement along any of the three orthogonal directions; c is the wave velocity of propagation; r is the mode of propagation or harmonic (r^{th}); k and rk are the wave numbers associated with the fundamental and r^{th} modes, respectively; $kc = \omega$ is the fundamental frequency; $r\omega$ is the frequency of the r^{th} mode, and A_r, ϕ_r are the displacement amplitude and associated phase in the r^{th} mode, respectively. In vector form Eq (3-1) may be written as

$$
\begin{aligned}
&{}_r u = A_r d \exp(i\eta) \\
&\eta = rk(x.p - ct) - \phi_r
\end{aligned}
\tag{3-2}
$$

The stress tensor associated with the r^{th} mode of propagation is

$$
\tau_{lm} = \left[\lambda \delta_{lm}(p_k d_k) + \mu(p_l d_m + p_m d_l)\right] i A_r rk \exp(i\eta) \tag{3-3}
$$

where, λ, μ are Lame's constants and δ is the Dirac delta function, and all other terms have been previously defined.

3.4. Reflection of SV Wave: Incidence Angle Less than or Equal to Critical Angle

By introducing an index n, which is equal to 0, 1 and 2 for the incident wave, reflected P wave and reflected SV wave, respectively; the displacement field of the associated wave in the r^{th} mode may be completely defined as

$$
\begin{aligned}
&{}_r u^{(n)} = A_r^{(n)} d^{(n)} \exp(i\eta) \\
&\eta_n = rk_n\left(x_1 p_1^{(n)} + x_2 p_2^{(n)} - c_n t\right) - \alpha_n
\end{aligned}
\tag{3-4}
$$

where α_n denotes the phase angle.

3.4.1. Incident Wave (n=0)

For this case, the vectors of propagation and particle movement, respectively, are given by

$$p^{(0)} = \sin\theta_0 \hat{i} + \cos\theta_0 \hat{j} \tag{3-5}$$

$$d^{(0)} = \hat{k} \otimes p^{(0)} = -\cos\theta_0 \hat{i} + \sin\theta_0 \hat{j} \tag{3-6}$$

Denoting the shear wave velocity as $c_0 = c_T$ and considering the phase of the incident wave as $\alpha_0 = -\phi_r$, the associated displacement field may be expressed as

$${}_r u^{(0)} = A_r^{(0)} \exp\left[irk_0\left(x_1 \sin\theta_0 + x_2 \cos\theta_0 - c_T t\right) + i\phi_r\right] d^{(0)} \tag{3-7}$$

The displacement field at the free surface $\left(x_2 = 0\right)$ is thus given by

$${}_r u^{(0)} = A_r^{(0)} \exp\left[i\overline{\eta_0}\right] d^{(0)} \tag{3-8}$$

$$\overline{\eta_0} = rk_0\left(x_1 \sin\theta_0 - c_T t\right) + \phi_r \tag{3-9}$$

Substituting Eq (3-5) and Eq (3-6) into Eq (3-3), the stresses at the free surface associated with this displacement field may be obtained as

$$\begin{aligned} \tau_{21}^{(0)} &= -i\mu rk_0 \cos 2\theta_0 A_r^{(0)} \exp\left(i\overline{\eta_0}\right) \\ \tau_{22}^{(0)} &= i\mu rk_0 \sin 2\theta_0 A_r^{(0)} \exp\left(i\overline{\eta_0}\right) \end{aligned} \tag{3-10}$$

3.4.2. Reflected P Wave (n=1)

For this case, the vectors of propagation and particle movement, respectively, are given by

$$d^{(1)} = p^{(1)} = \sin\theta_1 \hat{i} - \cos\theta_1 \hat{j} \tag{3-11}$$

Denoting the P wave velocity as $c_1 = c_L$, the associated displacement field may be expressed as

$${}_r u^{(1)} = A_r^{(1)} \exp\left[-i\left(\alpha_1 + \phi_r\right)\right] \exp\left[irk_1\left(x_1 \sin\theta_1 - x_2 \cos\theta_1 - c_L t\right) + i\phi_r\right] d^{(1)} \tag{3-12}$$

The displacement field at the free surface $\left(x_2 = 0\right)$ is thus given by

$${}_r u^{(1)} = A_r^{(1)} \exp\left[-i\left(\alpha_1 + \phi_r\right)\right] \exp\left[i\overline{\eta_1}\right] d^{(1)} \tag{3-13}$$

$$\overline{\eta_1} = rk_1\left(x_1 \sin\theta_1 - c_L t\right) + \phi_r \tag{3-14}$$

Substituting Eq (3-11) into Eq (3-3), the stresses at the free surface associated with this displacement field are

$$\begin{aligned}\tau_{21}^{(1)} &= -i\mu r k_1 \sin 2\theta_1 A_r^{(1)}\left[\cos\left(\alpha_1 + \phi_r\right) - i\sin\left(\alpha_1 + \phi_r\right)\right]\exp\left(i\overline{\eta_1}\right)\\ \tau_{22}^{(1)} &= i\left(\lambda + 2\mu\cos^2\theta_1\right) r k_1 A_r^{(1)}\left[\cos\left(\alpha_1 + \phi_r\right) - i\sin\left(\alpha_1 + \phi_r\right)\right]\exp\left(i\overline{\eta_1}\right)\end{aligned} \tag{3-15}$$

3.4.3. Reflected SV Wave (n=2)

For this case, the vectors of propagation and particle movement, respectively, are given by

$$p^{(2)} = \sin\theta_2 \hat{i} - \cos\theta_2 \hat{j} \tag{3-16}$$

$$d^{(2)} = \hat{k} \otimes p^{(2)} = \cos\theta_2 \hat{i} + \sin\theta_2 \hat{j} \tag{3-17}$$

Noting that $c_2 = c_T$, the associated displacement field may be expressed as

$${}_r u^{(2)} = A_r^{(2)} \exp\left[-i\left(\alpha_2 + \phi_r\right)\right]\exp\left[irk_2\left(x_1 \sin\theta_2 - x_2 \cos\theta_2 - c_T t\right) + i\phi_r\right] d^{(2)} \tag{3-18}$$

The displacement field at the free surface $\left(x_2 = 0\right)$ is thus given by

$${}_r u^{(2)} = A_r^{(2)} \exp\left[-i\left(\alpha_2 + \phi_r\right)\right]\exp\left[i\overline{\eta_2}\right] d^{(2)} \tag{3-19}$$

$$\overline{\eta_2} = rk_2\left(x_1 \sin\theta_2 - c_T t\right) + \phi_r \tag{3-20}$$

Substituting Eq (3-16) and Eq (3-17) into Eq (3-3), the stresses at the free surface associated with this displacement field are

$$\begin{aligned}\tau_{21}^{(2)} &= -i\mu r k_2 \cos 2\theta_2 A_r^{(2)}\left[\cos\left(\alpha_2 + \phi_r\right) - i\sin\left(\alpha_2 + \phi_r\right)\right]\exp\left(i\overline{\eta_2}\right)\\ \tau_{22}^{(2)} &= -i\mu r k_2 \sin 2\theta_2 A_r^{(2)}\left[\cos\left(\alpha_2 + \phi_r\right) - i\sin\left(\alpha_2 + \phi_r\right)\right]\exp\left(i\overline{\eta_2}\right)\end{aligned} \tag{3-21}$$

3.4.4. Zero Traction at the Free Surface and Amplification Factors

Since the traction at the free surface must be zero,

$$\tau_{21} = \tau_{21}^{(0)} + \tau_{21}^{(1)} + \tau_{21}^{(2)} = 0$$
$$\tau_{22} = \tau_{22}^{(0)} + \tau_{22}^{(1)} + \tau_{22}^{(2)} = 0 \tag{3-22}$$

For a time-independent solution of Eq (3-22),

$$\overline{\eta_0} = \overline{\eta_1} = \overline{\eta_2} \tag{3-23}$$

Substituting Eq (3-9), Eq (3-14) and Eq (3-20) into Eq (3-23), it can be shown that

$$k_1 = k_0 / \beta,\ k_2 = k_0,\ \sin\theta_1 = \beta \sin\theta_0,\ \theta_2 = \theta_0 \tag{3-24}$$

Substituting Eq (3-10), Eq (3-15) and Eq (3-21) into Eq (3-22), thereafter utilizing Eq (3-24) and separating out the real and imaginary parts leads to the following four equations:

$$\frac{A_r^{(1)}}{A_r^{(0)}}\left[\frac{1}{\beta}\sin 2\theta_1 \sin\left(\alpha_1 + \phi_r\right)\right] + \frac{A_r^{(2)}}{A_r^{(0)}}\left[\cos 2\theta_0 \sin\left(\alpha_2 + \phi_r\right)\right] = 0 \tag{3-25}$$

$$\frac{A_r^{(1)}}{A_r^{(0)}}\left[\frac{1}{\beta}\sin 2\theta_1 \cos\left(\alpha_1 + \phi_r\right)\right] + \frac{A_r^{(2)}}{A_r^{(0)}}\left[\cos 2\theta_0 \cos\left(\alpha_2 + \phi_r\right)\right] = -\cos 2\theta_0 \tag{3-26}$$

$$\frac{A_r^{(1)}}{A_r^{(0)}}\left[\beta \cos 2\theta_0 \sin\left(\alpha_1 + \phi_r\right)\right] - \frac{A_r^{(2)}}{A_r^{(0)}}\left[\sin 2\theta_0 \sin\left(\alpha_2 + \phi_r\right)\right] = 0 \tag{3-27}$$

$$\frac{A_r^{(1)}}{A_r^{(0)}}\left[\beta \cos 2\theta_0 \cos\left(\alpha_1 + \phi_r\right)\right] - \frac{A_r^{(2)}}{A_r^{(0)}}\left[\sin 2\theta_0 \cos\left(\alpha_2 + \phi_r\right)\right] = -\sin 2\theta_0 \tag{3-28}$$

After eliminating $\left(A_r^{(2)} / A_r^{(0)}\right) \Big/ \left(A_r^{(1)} / A_r^{(0)}\right)$ from Eq (3-25) and Eq (3-27),

$$\frac{\sin\left(\alpha_1 + \phi_r\right)}{\sin\left(\alpha_2 + \phi_r\right)}\left[\frac{\beta \cos 2\theta_0}{\sin 2\theta_0} + \frac{\sin 2\theta_1}{\beta \cos 2\theta_0}\right] = 0 \tag{3-29}$$

If $\alpha_2 \neq -\phi_r$, to satisfy Eq (3-29) for all θ_0, $\alpha_1 = -\phi_r$. Similarly, Eq (3-29) can be recast in a different form to show that for $\alpha_1 \neq -\phi_r$, $\alpha_2 = -\phi_r$. Therefore, at least one of either α_1 or α_2 is equal to $-\phi_r$. Eq (3-25) shows that the other α_i is also equal to $-\phi_r$. Therefore,

$$\alpha_1 = \alpha_2 = -\phi_r \tag{3-30}$$

Substituting Eq (3-30) into Eq (3-26) and Eq (3-28) gives

$$\frac{A_r^{(1)}}{A_r^{(0)}}\left[\sin 2\theta_1\right]+\frac{A_r^{(2)}}{A_r^{(0)}}\left[\beta\cos 2\theta_0\right]=-\beta\cos 2\theta_0 \tag{3-31}$$

$$\frac{A_r^{(1)}}{A_r^{(0)}}\left[\beta\cos 2\theta_0\right]-\frac{A_r^{(2)}}{A_r^{(0)}}\left[\sin 2\theta_0\right]=-\sin 2\theta_0 \tag{3-32}$$

Denoting $A_r^{(1)}/A_r^{(0)}=M_{SP}$ and $A_r^{(2)}/A_r^{(0)}=M_{SS}$, the solution of Eq (3-31) and Eq (3-32) may be expressed as

$$\begin{aligned} M_{SP}&=\frac{-\beta\sin 4\theta_0}{\sin 2\theta_0\sin 2\theta_1+\beta^2\cos^2 2\theta_0}\\ M_{SS}&=\frac{\sin 2\theta_0\sin 2\theta_1-\beta^2\cos^2 2\theta_0}{\sin 2\theta_0\sin 2\theta_1+\beta^2\cos^2 2\theta_0}\end{aligned} \tag{3-33}$$

3.4.5. Resultant Displacement Field

Denoting $A_r^{(0)}=A_{rs}$, the resultant displacement field may be obtained by summing up the fields given by Eq (3-7), Eq (3-12) and Eq (3-18). Substituting Eq (3-6), Eq (3-11), Eq (3-17), Eq (3-24) and Eq (3-30), into the resultant displacement field, the horizontal and vertical components may be expressed as

$${}_r^s u_{x_1}(x,t)=A_{rs}\begin{bmatrix}-\cos\theta_0\exp\left\{irk_0\left(x_1\sin\theta_0+x_2\cos\theta_0-c_Tt\right)+i\phi_r\right\}\\ +M_{SP}\sin\theta_1\exp\left\{irk_0\left(x_1\sin\theta_0-x_2\dfrac{\cos\theta_1}{\beta}-c_Tt\right)+i\phi_r\right\}\\ +M_{SS}\cos\theta_0\exp\left\{irk_0\left(x_1\sin\theta_0-x_2\cos\theta_0-c_Tt\right)+i\phi_r\right\}\end{bmatrix} \tag{3-34}$$

$${}_r^s u_{x_2}(x,t)=A_{rs}\begin{bmatrix}\sin\theta_0\exp\left\{irk_0\left(x_1\sin\theta_0+x_2\cos\theta_0-c_Tt\right)+i\phi_r\right\}\\ -M_{SP}\cos\theta_1\exp\left\{irk_0\left(x_1\sin\theta_0-x_2\dfrac{\cos\theta_1}{\beta}-c_Tt\right)+i\phi_r\right\}\\ +M_{SS}\sin\theta_0\exp\left\{irk_0\left(x_1\sin\theta_0-x_2\cos\theta_0-c_Tt\right)+i\phi_r\right\}\end{bmatrix} \tag{3-35}$$

3.4.6. Plane Stress Condition and Estimation of Rocking

The displacement fields given by Eq (3-34) and Eq (3-35) satisfy the plane-stress condition along the vertical direction at the free surface and hence

$$\left(\frac{\partial}{\partial x_1}\left[{}^{s}_{r}u_{x_2}(x,t)\right]+\frac{\partial}{\partial x_2}\left[{}^{s}_{r}u_{x_1}(x,t)\right]\right)\Bigg|_{x_2=0}=0 \tag{3-36}$$

Consequently, the rocking rotation on the x_1x_2 plane at the free surface is given by

$$\begin{aligned}{}^{s}_{r}\theta_{x_1x_2}(x,t)&=\frac{1}{2}\left(\frac{\partial}{\partial x_1}\left[{}^{s}_{r}u_{x_2}(x,t)\right]\Big|_{x_2=0}-\frac{\partial}{\partial x_2}\left[{}^{s}_{r}u_{x_1}(x,t)\right]\Big|_{x_2=0}\right)\\&=\frac{\partial}{\partial x_1}\left[{}^{s}_{r}u_{x_2}(x,t)\right]\Big|_{x_2=0}=-\frac{\partial}{\partial x_2}\left[{}^{s}_{r}u_{x_1}(x,t)\right]\Big|_{x_2=0}\end{aligned} \tag{3-37}$$

Substituting Eq (3-34) and Eq (3-35) into the first equality of Eq (3-37) gives

$${}^{s}_{r}\theta_{x_1x_2}(x,t)=\frac{A_{rs}}{2}(1+M_{SS})(irk_0)\exp\left[irk_0(x_1\sin\theta_0-c_Tt)+i\phi_r\right] \tag{3-38}$$

3.4.7. Rocking at Surface Incident Point

At the incident point on the surface $(x_1=x_2=0)$, the rocking rotation may be obtained from Eq (3-38) as

$${}^{s}_{r}\theta_{x_1x_2}(t)=\frac{A_{rs}}{2}(1+M_{SS})\left(\frac{i\omega_r}{c_T}\right)\exp\left[-i(\omega_rt-\phi_r)\right] \tag{3-39}$$

Here $\omega_r=rk_0c_T$ is the frequency of the r^{th} mode. The associated rocking acceleration is

$${}^{s}_{r}\ddot{\theta}_{x_1x_2}(t)=-\frac{A_{rs}}{2}(1+M_{SS})\left(\frac{i\omega_r^3}{c_T}\right)\exp\left[-i(\omega_rt-\phi_r)\right] \tag{3-40}$$

3.4.8. Relationship between Rocking and Vertical Accelerations at the Surface Incident Point

At the incident point on the surface $(x_1=x_2=0)$, the vertical displacement is given by Eq (3-35)

$${}^{s}_{r}u_{x_2}(t)=A_{rs}\left[\sin\theta_0-M_{SP}\cos\theta_1+M_{SS}\sin\theta_0\right]\exp\left(-irk_0c_Tt+i\phi_r\right) \tag{3-41}$$

Using Eq (3-31) and after some trigonometric rearrangements, Eq (3-41) can be written as

$${}^{s}_{r}u_{x_2}(t)=\frac{A_{rs}}{2\sin\theta_0}\left[1+M_{SS}\right]\exp\left[-i(\omega_rt-\phi_r)\right] \tag{3-42}$$

Taking three successive derivatives with respect to time,

$$ {}^{s}_{r}\dddot{u}_{x_2}(t) = \frac{A_{rs}}{2\sin\theta_0}\left[1+M_{SS}\right]\left(i\omega_r^3\right)\exp\left[-i\left(\omega_r t-\phi_r\right)\right] \tag{3-43} $$

Comparing Eq (3-40) with Eq (3-43),

$$ {}^{s}_{r}\ddot{\theta}_{x_1x_2}(t) = -\frac{\sin\theta_0}{c_T}\,{}^{s}_{r}\dddot{u}_{x_2}(t) \tag{3-44} $$

3.4.9. Relationship between Rocking and Horizontal Accelerations at the Surface Incident Point

At the incident point on the surface $\left(x_1 = x_2 = 0\right)$, the horizontal displacement is given by Eq (3-34)

$$ {}^{s}_{r}u_{x_1}(t) = A_{rs}\left[-\cos\theta_0 + M_{SP}\sin\theta_1 + M_{SS}\cos\theta_0\right]\exp\left(-irk_0c_T t + i\phi_r\right) \tag{3-45} $$

Using Eq (3-31) and Eq (3-32), and after some trigonometric rearrangements, Eq (3-45) can be written as

$$ {}^{s}_{r}u_{x_1}(t) = -\frac{A_{rs}\beta\cos 2\theta_0}{4\sin^2\theta_0\cos\theta_1}\left[1+M_{SS}\right]\exp\left[-i\left(\omega_r t-\phi_r\right)\right] \tag{3-46} $$

Taking three successive derivatives with respect to time,

$$ {}^{s}_{r}\dddot{u}_{x_1}(t) = -\frac{A_{rs}}{2}\left[1+M_{SS}\right]\frac{\beta\cos 2\theta_0}{2\sin^2\theta_0\cos\theta_1}\left(i\omega_r^3\right)\exp\left[-i\left(\omega_r t-\phi_r\right)\right] \tag{3-47} $$

Comparing Eq (3-40) with Eq (3-47),

$$ {}^{s}_{r}\ddot{\theta}_{x_1x_2}(t) = \frac{2\sin^2\theta_0}{\beta c_T}\frac{\left(1-\beta^2\sin^2\theta_0\right)^{0.5}}{1-2\sin^2\theta_0}\,{}^{s}_{r}\dddot{u}_{x_1}(t) \tag{3-48} $$

3.4.10. Translational Accelerations at the Surface Incident Point

The horizontal and vertical acceleration histories at the incident point on the surface $\left(x_1 = x_2 = 0\right)$ can be obtained by taking two successive derivatives of Eq (3-46) and Eq (3-42), respectively. After some trigonometric rearrangements, these acceleration histories may be expressed as

$$
\begin{aligned}
&{}^{s}_{r}\ddot{u}_{x_1}(t) = R_{SH}\exp\left[-i\left(\omega_r t-\phi_r\right)\right]\\
&R_{SH} = A_{rs}\omega_r^2\left[\frac{2\beta\cos\theta_0\cos 2\theta_0}{2\sin\theta_0\sin 2\theta_0\left(1-\beta^2\sin^2\theta_0\right)^{0.5}+\beta\cos^2 2\theta_0}\right]
\end{aligned}
\tag{3-49}
$$

$$
\begin{aligned}
&{}^{s}_{r}\ddot{u}_{x_2}(t) = R_{SV}\exp\left[-i\left(\omega_r t-\phi_r\right)\right]\\
&R_{SV} = -A_{rs}\omega_r^2\left[\frac{2\sin 2\theta_0\left(1-\beta^2\sin^2\theta_0\right)^{0.5}}{2\sin\theta_0\sin 2\theta_0\left(1-\beta^2\sin^2\theta_0\right)^{0.5}+\beta\cos^2 2\theta_0}\right]
\end{aligned}
\tag{3-50}
$$

The acceleration histories given by Eq (3-49) and Eq (3-50) will be real for $\beta\sin\theta_0 \le 1$. Accordingly, the incidence angle θ_0 should not exceed the critical angle $\theta_{cr} = \sin^{-1}\left(1/\beta\right)$.

3.5. Reflection of SV Wave: Incidence Angle Exceeds Critical Angle

When $\theta_0 > \theta_{cr}$, and noting $\sin\theta_1 = \beta\sin\theta_0$, the reflection angle for the reflected P wave, θ_1, becomes imaginary. The associated propagation vector is imaginary, which leads to an inhomogeneous reflected P wave field. However, the displacement fields for the incident wave and reflected SV wave, and the associated stress fields at the free surface are the same as those presented in the previous section.

3.5.1. Reflected P Wave (n=1)

Since θ_1 is imaginary and letting $\cos\theta_1 = i\sigma$ with σ real, the vectors of propagation and particle movement, both are given by

$$
d^{(1)} = p^{(1)} = \left(1+\sigma^2\right)^{\frac{1}{2}}\hat{i} - i\sigma\hat{j} \tag{3-51}
$$

The associated displacement field may be expressed as

$$
{}_{r}u^{(1)} = A_r^{(1)}\exp\left[rk_1x_2\sigma\right]\exp\left[-i\left(\alpha_1+\phi_r\right)\right]\exp\left[irk_1\left(x_1\left(1+\sigma^2\right)^{\frac{1}{2}}-c_L t\right)+i\phi_r\right]d^{(1)} \tag{3-52}
$$

The displacement field at the free surface $\left(x_2 = 0\right)$ is thus given by

$$ {}_r u^{(1)} = A_r^{(1)} \exp\left[-i\left(\alpha_1 + \phi_r\right)\right] \exp\left[i\overline{\eta_1}\right] d^{(1)} \tag{3-53} $$

$$ \overline{\eta_1} = r k_1 \left(x_1 \left(1+\sigma^2\right)^{\frac{1}{2}} - c_L t \right) + \phi_r \tag{3-54} $$

Substituting Eq (3-51) into Eq (3-3), the stresses at the free surface associated with this displacement field may be obtained as

$$ \begin{aligned} \tau_{21}^{(1)} &= 2\mu\sigma\left(1+\sigma^2\right)^{\frac{1}{2}} r k_1 A_r^{(1)} \left[\cos\left(\alpha_1 + \phi_r\right) - i\sin\left(\alpha_1 + \phi_r\right)\right] \exp\left(i\overline{\eta_1}\right) \\ \tau_{22}^{(1)} &= i\left(\lambda - 2\mu\sigma^2\right) r k_1 A_r^{(1)} \left[\cos\left(\alpha_1 + \phi_r\right) - i\sin\left(\alpha_1 + \phi_r\right)\right] \exp\left(i\overline{\eta_1}\right) \end{aligned} \tag{3-55} $$

3.5.2. Zero Traction at the Free Surface and Amplification Factors

For zero traction at the free surface, the required conditions are given by Eq (3-22) and for a time-independent solution of Eq (3-22), Eq (3-23) needs to be satisfied. By substituting Eq (3-9), Eq (3-20) and Eq (3-54) into Eq (3-23), it can be shown that

$$ k_1 = k_0 / \beta,\ k_2 = k_0,\ \sigma = \left(\beta^2 \sin^2\theta_0 - 1\right)^{\frac{1}{2}},\ \theta_2 = \theta_0 \tag{3-56} $$

Substituting Eq (3-10), Eq (3-21) and Eq (3-55) into Eq (3-22), thereafter utilizing Eq (3-56) and separating out the real and imaginary parts leads to the following four equations:

$$ \frac{A_r^{(1)}}{A_r^{(0)}} \left[2\sin\theta_0 \left(\beta^2 \sin^2\theta_0 - 1\right)^{\frac{1}{2}} \cos\left(\alpha_1 + \phi_r\right) \right] - \frac{A_r^{(2)}}{A_r^{(0)}} \left[\cos 2\theta_0 \sin\left(\alpha_2 + \phi_r\right)\right] = 0 \tag{3-57} $$

$$ \frac{A_r^{(1)}}{A_r^{(0)}} \left[2\sin\theta_0 \left(\beta^2 \sin^2\theta_0 - 1\right)^{\frac{1}{2}} \sin\left(\alpha_1 + \phi_r\right) \right] + \frac{A_r^{(2)}}{A_r^{(0)}} \left[\cos 2\theta_0 \cos\left(\alpha_2 + \phi_r\right)\right] = -\cos 2\theta_0 \tag{3-58} $$

$$ \frac{A_r^{(1)}}{A_r^{(0)}} \left[\left(\frac{\lambda - 2\mu\sigma^2}{\beta} \right) \sin\left(\alpha_1 + \phi_r\right) \right] - \frac{A_r^{(2)}}{A_r^{(0)}} \left[\mu \sin 2\theta_0 \sin\left(\alpha_2 + \phi_r\right)\right] = 0 \tag{3-59} $$

$$ \frac{A_r^{(1)}}{A_r^{(0)}} \left[\left(\frac{\lambda - 2\mu\sigma^2}{\beta} \right) \cos\left(\alpha_1 + \phi_r\right) \right] - \frac{A_r^{(2)}}{A_r^{(0)}} \left[\mu \sin 2\theta_0 \cos\left(\alpha_2 + \phi_r\right)\right] = -\mu \sin 2\theta_0 \tag{3-60} $$

Denoting $A_r^{(1)}/A_r^{(0)} = \overline{M}_{SP}$ and $A_r^{(2)}/A_r^{(0)} = \overline{M}_{SS}$, the solution of Eq (3-57) through Eq (3-60) may be expressed as

$$\tan\left(\alpha_1 + \phi_r\right) = \frac{2\left(\beta^2 \sin^2\theta_0 \text{-} 1\right)^{\frac{1}{2}} \sin\theta_0 \sin 2\theta_0}{\beta \cos^2 2\theta_0} \tag{3-61}$$

$$\alpha_2 = 2\alpha_1 + \phi_r \tag{3-62}$$

$$M_{SP} = -\frac{\sin 4\theta_0}{\left[4\left(\beta^2 \sin^2\theta_0 \text{-} 1\right)\sin^2\theta_0 \sin^2 2\theta_0 + \beta^2 \cos^4 2\theta_0\right]^{\frac{1}{2}}} \tag{3-63}$$

$$M_{SS} = -1 \tag{3-64}$$

3.5.3. Resultant Displacement Field

Denoting $A_r^{(0)} = A_{rs}$, the resultant displacement field may be obtained by summing the fields given by Eq (3-7), Eq (3-18) and Eq (3-52). Substituting Eq (3-6), Eq (3-17), Eq (3-51), Eq (3-56) and Eq (3-62) into the resultant displacement field, the horizontal and vertical components may be expressed as

$$\begin{aligned} {}_r^s u_{x_1}(x,t) = A_{rs} \Bigg[& -\cos\theta_0 \exp\left(i\phi_r\right) \exp\left\{irk_0\left(x_1 \sin\theta_0 + x_2 \cos\theta_0 - c_T t\right)\right\} \\ & + \overline{M}_{SP} \beta \sin\theta_0 \exp\left\{\frac{rk_0 x_2}{\beta}\left(\beta^2 \sin^2\theta_0 \text{-} 1\right)^{\frac{1}{2}}\right\} \exp\left(-i\alpha_1\right) \\ & * \exp\left\{irk_0\left(x_1 \sin\theta_0 - c_T t\right)\right\} \\ & + \overline{M}_{SS} \cos\theta_0 \exp\left\{-i\left(2\alpha_1 + \phi_r\right)\right\} \exp\left\{irk_0 \begin{pmatrix} x_1 \sin\theta_0 - \\ x_2 \cos\theta_0 - c_T t \end{pmatrix}\right\} \Bigg] \end{aligned} \tag{3-65}$$

$$\begin{aligned} {}_r^s u_{x_2}(x,t) = A_{rs} \Bigg[& \sin\theta_0 \exp\left(i\phi_r\right) \exp\left\{irk_0\left(x_1 \sin\theta_0 + x_2 \cos\theta_0 - c_T t\right)\right\} \\ & + \overline{M}_{SP} \left\{-i\left(\beta^2 \sin^2\theta_0 \text{-} 1\right)^{\frac{1}{2}}\right\} \exp\left\{\frac{rk_0 x_2}{\beta}\left(\beta^2 \sin^2\theta_0 \text{-} 1\right)^{\frac{1}{2}}\right\} \\ & * \exp\left(-i\alpha_1\right) \exp\left\{irk_0\left(x_1 \sin\theta_0 - c_T t\right)\right\} \\ & + \overline{M}_{SS} \sin\theta_0 \exp\left\{-i\left(2\alpha_1 + \phi_r\right)\right\} \\ & * \exp\left\{irk_0\left(x_1 \sin\theta_0 - x_2 \cos\theta_0 - c_T t\right)\right\} \Bigg] \end{aligned} \tag{3-66}$$

3.5.4. Plane Stress Condition and Estimation of Rocking

It is possible to show that the displacement fields given by Eq (3-65) and Eq (3-66) satisfy the plane-stress condition [Eq (3-36)] along the vertical direction at the free surface. However, this is not straightforward and it should be shown that the real and imaginary parts vanish separately. Consequently, the rocking rotation on the x_1x_2 plane at the free surface is given by Eq (3-37). Now, substituting Eq (3-65) and Eq (3-66) into the first equality of Eq (3-37), it can be shown that

$$ {}^{s}_{r}\theta_{x_1x_2}(x,t) = \frac{A_{rs}}{2}\left(1 + M_{SS}\exp\left\{-i\left(2\alpha_1 + 2\phi_r\right)\right\}\right)\left(irk_0\right)\exp\left[irk_0\left(x_1\sin\theta_0 - c_T t\right) + i\phi_r\right] \tag{3-67} $$

3.5.5. Rocking at the Surface Incident Point

At the incident point on the surface $\left(x_1 = x_2 = 0\right)$, the rocking rotation may be obtained from Eq (3-67). Considering the real part only and making use of Eq (3-61), the rocking rotation history is given by

$$ {}^{s}_{r}\theta_{x_1x_2}(t) = -\frac{A_{rs}\omega_r}{c_T}\sin\left(\alpha_1 + \phi_r\right)\cos\left(\omega_r t + \alpha_1\right) \tag{3-68} $$

The associated rocking acceleration is

$$ {}^{s}_{r}\ddot{\theta}_{x_1x_2}(t) = \frac{A_{rs}\omega_r^3}{c_T}\sin\left(\alpha_1 + \phi_r\right)\cos\left(\omega_r t + \alpha_1\right) \tag{3-69} $$

3.5.6. Relationship between Rocking and Vertical Accelerations at the Surface Incident Point

At the incident point on the surface $\left(x_1 = x_2 = 0\right)$, the vertical displacement may be obtained from Eq (3-66). Considering the real part only and after some trigonometric rearrangements, it can be shown that

$$ {}^{s}_{r}u_{x_2}(t) = A_{rs}\frac{\sin\left(\alpha_1 + \phi_r\right)}{\sin\theta_0}\sin\left(\omega_r t + \alpha_1\right) \tag{3-70} $$

Taking three successive derivatives with respect to time,

$$ {}^{s}_{r}\dddot{u}_{x_2}(t) = -A_{rs}\omega_r^3 \frac{\sin(\alpha_1+\phi_r)}{\sin\theta_0}\cos(\omega_r t+\alpha_1) \tag{3-71} $$

By comparing Eq (3-69) with Eq (3-71), Eq (3-44) can be established.

3.5.7. Relationship between Rocking and Horizontal Accelerations at the Surface Incident Point

At the incident point on the surface $(x_1 = x_2 = 0)$, the horizontal displacement may be obtained from Eq (3-65). Considering the real part only and after some trigonometric rearrangements, it can be shown that

$$ {}^{s}_{r}u_{x_1}(t) = -2A_{rs}\frac{\cos(\alpha_1+\phi_r)\cos\theta_0}{\cos 2\theta_0}\cos(\omega_r t+\alpha_1) \tag{3-72} $$

Taking three successive derivatives with respect to time,

$$ {}^{s}_{r}\dddot{u}_{x_1}(t) = -2A_{rs}\omega_r^3\frac{\cos(\alpha_1+\phi_r)\cos\theta_0}{\cos 2\theta_0}\sin(\omega_r t+\alpha_1) \tag{3-73} $$

By comparing Eq (3-69) with Eq (3-73),

$$ {}^{s}_{r}\ddot{\theta}_{x_1x_2}(t) = \frac{2\sin^2\theta_0}{\beta c_T}\frac{\left(1-\beta^2\sin^2\theta_0\right)^{0.5}}{1-2\sin^2\theta_0}\,{}^{s}_{r}\dddot{u}_{x_1}\left(t-\frac{\pi}{2}\right) \tag{3-74} $$

At this stage, it is instructive to compare Eq (3-74) with Eq (3-48).

3.5.8. Translational Accelerations at the Surface Incident Point

The horizontal and vertical acceleration histories at the incident point on the surface $(x_1 = x_2 = 0)$ may be obtained by taking two successive derivatives of Eq (3-72) and Eq (3-70), respectively, as follows:

$$ \begin{aligned} &{}^{s}_{r}\ddot{u}_{x_1}(t) = R_{SH}\cos(\omega_r t+\alpha_1) \\ &R_{SH} = A_{rs}\omega_r^2\left[\frac{2\cos(\alpha_1+\phi_r)\cos\theta_0}{\cos 2\theta_0}\right] \end{aligned} \tag{3-75} $$

$$
\begin{aligned}
&{}^{s}_{r}\ddot{u}_{x_2}(t) = -R_{SV}\sin(\omega_r t + \alpha_1) \\
&R_{SV} = A_{rs}\omega_r^2\left[\frac{\sin(\alpha_1 + \phi_r)}{\sin\theta_0}\right]
\end{aligned}
\tag{3-76}
$$

3.5.9. Change of Variables

Without losing generality, a change in variable is made, namely, $\alpha_1 \rightarrow \alpha_1 - \phi_r$, for future convenience. This leads to the following changes in the previously derived relationships:

$$
\tan\alpha_1 = \frac{2\left(\beta^2\sin^2\theta_0\text{-}1\right)^{\frac{1}{2}}\sin\theta_0\sin 2\theta_0}{\beta\cos^2 2\theta_0}
\tag{3-77}
$$

$$
\begin{aligned}
&{}^{s}_{r}\ddot{u}_{x_1}(t) = R_{SH}\cos(\omega_r t + \alpha_1 - \phi_r) \\
&R_{SH} = A_{rs}\omega_r^2\left[\frac{2\cos\alpha_1\cos\theta_0}{\cos 2\theta_0}\right]
\end{aligned}
\tag{3-78}
$$

$$
\begin{aligned}
&{}^{s}_{r}\ddot{u}_{x_2}(t) = -R_{SV}\sin(\omega_r t + \alpha_1 - \phi_r) \\
&R_{SV} = A_{rs}\omega_r^2\left[\frac{\sin\alpha_1}{\sin\theta_0}\right]
\end{aligned}
\tag{3-79}
$$

3.6. Reflection of a Homogeneous P Wave

The displacement fields and stress fields due to reflected P and SV waves are the same as those formulated earlier for the reflection of SV waves with incidence angles that do not exceed the critical value. The fields associated with the incident P wave are derived first.

3.6.1. Incident Wave (n=0)

For this case, the vectors of propagation and particle movement are both given by

$$
d^{(0)} = p^{(0)} = \sin\theta_0\,\hat{i} + \cos\theta_0\,\hat{j}
\tag{3-80}
$$

Considering the phase of the incident wave as $\alpha_0 = -\phi_r$, the associated displacement field may be expressed as

$$ {}_r u^{(0)} = A_r^{(0)} \exp\left[irk_0 \left(x_1 \sin\theta_0 + x_2 \cos\theta_0 - c_L t \right) + i\phi_r \right] d^{(0)} \tag{3-81} $$

The displacement field at the free surface $\left(x_2 = 0\right)$ is thus given by

$$ {}_r u^{(0)} = A_r^{(0)} \exp\left[i\overline{\eta_0} \right] d^{(0)} \tag{3-82} $$

$$ \overline{\eta_0} = rk_0 \left(x_1 \sin\theta_0 - c_L t \right) + \phi_r \tag{3-83} $$

Substituting Eq (3-80) into Eq (3-3), the stresses at the free surface associated with this displacement field may be obtained as

$$ \begin{aligned} \tau_{21}^{(0)} &= i\mu rk_0 \sin 2\theta_0 A_r^{(0)} \exp\left(i\overline{\eta_0} \right) \\ \tau_{22}^{(0)} &= i\left(\lambda + 2\mu \cos^2\theta_0 \right) rk_0 A_r^{(0)} \exp\left(i\overline{\eta_0} \right) \end{aligned} \tag{3-84} $$

3.6.2. Zero Traction at the Free Surface and Amplification Factors

For zero traction at the free surface, the required conditions are given by Eq (3-22). For a time-independent solution of Eq (3-22), Eq (3-23) must be satisfied. Substituting Eq (3-14), Eq (3-20) and Eq (3-83) into Eq (3-23), it is seen that

$$ k_1 = k_0,\ k_2 = k_0\beta,\ \theta_1 = \theta_0,\ \sin\theta_2 = \sin\theta_0 / \beta \tag{3-85} $$

Substituting Eq (3-15), Eq (3-21) and Eq (3-84) into Eq (3-22), thereafter utilizing Eq (3-85) and separating out the real and imaginary parts, leads to the following four equations:

$$ \frac{A_r^{(1)}}{A_r^{(0)}} \left[\sin 2\theta_0 \sin\left(\alpha_1 + \phi_r \right) \right] + \frac{A_r^{(2)}}{A_r^{(0)}} \left[\beta \cos 2\theta_2 \sin\left(\alpha_2 + \phi_r \right) \right] = 0 \tag{3-86} $$

$$ \frac{A_r^{(1)}}{A_r^{(0)}} \left[\sin 2\theta_0 \cos\left(\alpha_1 + \phi_r \right) \right] + \frac{A_r^{(2)}}{A_r^{(0)}} \left[\beta \cos 2\theta_2 \cos\left(\alpha_2 + \phi_r \right) \right] = \sin 2\theta_0 \tag{3-87} $$

$$ \frac{A_r^{(1)}}{A_r^{(0)}} \left[\left(\beta^2 - 2\sin^2\theta_0 \right) \sin\left(\alpha_1 + \phi_r \right) \right] - \frac{A_r^{(2)}}{A_r^{(0)}} \left[\beta \sin 2\theta_2 \sin\left(\alpha_2 + \phi_r \right) \right] = 0 \tag{3-88} $$

$$\frac{A_r^{(1)}}{A_r^{(0)}}\left[-\left(\beta^2-2\sin^2\theta_0\right)\cos\left(\alpha_1+\phi_r\right)\right]+\frac{A_r^{(2)}}{A_r^{(0)}}\left[\beta\sin 2\theta_2\cos\left(\alpha_2+\phi_r\right)\right] = \left(\beta^2-2\sin^2\theta_0\right) \tag{3-89}$$

Now eliminating $\left(A_r^{(2)}/A_r^{(0)}\right)\Big/\left(A_r^{(1)}/A_r^{(0)}\right)$ from Eq (3-86) and Eq (3-88), one can write

$$\frac{\sin\left(\alpha_1+\phi_r\right)}{\beta\sin\left(\alpha_2+\phi_r\right)}\left[\frac{\sin 2\theta_0}{\cos 2\theta_2}+\frac{\left(\beta^2-2\sin^2\theta_0\right)}{\sin 2\theta_2}\right]=0 \tag{3-90}$$

If $\alpha_2 \neq -\phi_r$, $\alpha_1 = -\phi_r$ to satisfy Eq (3-90) for all θ_0. Similarly, Eq (3-90) may be recast in a different form to show that if $\alpha_1 \neq -\phi_r$ then $\alpha_2 = -\phi_r$. Therefore, at least one of α_1 and α_2 is equal to $-\phi_r$. Moreover Eq (3-86) shows that the other variable is also equal to $-\phi_r$ and hence, Eq (3-30) can be derived. Now, substituting Eq (3-30) into Eq (3-87) and Eq (3-89),

$$\frac{A_r^{(1)}}{A_r^{(0)}}\left[\sin 2\theta_0\right]+\frac{A_r^{(2)}}{A_r^{(0)}}\left[\beta\cos 2\theta_2\right]=\sin 2\theta_0 \tag{3-91}$$

$$-\frac{A_r^{(1)}}{A_r^{(0)}}\left(\beta^2-2\sin^2\theta_0\right)+\frac{A_r^{(2)}}{A_r^{(0)}}\left[\beta\sin 2\theta_2\right]=\left(\beta^2-2\sin^2\theta_0\right) \tag{3-92}$$

Denoting $A_r^{(1)}/A_r^{(0)}=M_{PP}$ and $A_r^{(2)}/A_r^{(0)}=M_{PS}$, the solution of Eq (3-91) and Eq (3-92) can be expressed as

$$\begin{aligned} M_{PP} &= \frac{\sin 2\theta_0\sin 2\theta_2-\beta^2\cos^2 2\theta_2}{\sin 2\theta_0\sin 2\theta_2+\beta^2\cos^2 2\theta_2} \\ M_{PS} &= \frac{2\beta\sin 2\theta_0\cos 2\theta_2}{\sin 2\theta_0\sin 2\theta_2+\beta^2\cos^2 2\theta_2} \end{aligned} \tag{3-93}$$

3.6.3. Resultant Displacement Field

Denoting $A_r^{(0)}=A_{rp}$, the resultant displacement field may be obtained by summing the fields given by Eq (3-12), Eq (3-18) and Eq (3-81). Substituting Eq (3-11), Eq (3-17), Eq (3-30), Eq (3-80) and Eq (3-85) into the resultant displacement field, the horizontal and vertical components may be expressed as

$$
{}^{p}_{r}u_{x_1}(x,t) = A_{rp}\begin{bmatrix} \sin\theta_0 \exp\left\{irk_0\left(x_1\sin\theta_0 + x_2\cos\theta_0 - c_L t\right) + i\phi_r\right\} \\ +M_{PP}\sin\theta_0 \exp\left\{irk_0\left(x_1\sin\theta_0 - x_2\cos\theta_0 - c_L t\right) + i\phi_r\right\} \\ +M_{PS}\cos\theta_2 \exp\left\{irk_0\left(x_1\sin\theta_0 - x_2\beta\cos\theta_2 - c_L t\right) + i\phi_r\right\} \end{bmatrix} \tag{3-94}
$$

$$
{}^{p}_{r}u_{x_2}(x,t) = A_{rp}\begin{bmatrix} \cos\theta_0 \exp\left\{irk_0\left(x_1\sin\theta_0 + x_2\cos\theta_0 - c_L t\right) + i\phi_r\right\} \\ -M_{PP}\cos\theta_0 \exp\left\{irk_0\left(x_1\sin\theta_0 - x_2\cos\theta_0 - c_L t\right) + i\phi_r\right\} \\ +M_{PS}\sin\theta_2 \exp\left\{irk_0\left(x_1\sin\theta_0 - x_2\beta\cos\theta_2 - c_L t\right) + i\phi_r\right\} \end{bmatrix} \tag{3-95}
$$

3.6.4. Plane Stress Condition and Estimation of Rocking

It can be shown that the displacement fields given by Eq (3-94) and Eq (3-95) satisfy the plane-stress condition along the vertical direction at the free surface. Accordingly,

$$
\left(\frac{\partial}{\partial x_1}\left[{}^{p}_{r}u_{x_2}(x,t)\right] + \frac{\partial}{\partial x_2}\left[{}^{p}_{r}u_{x_1}(x,t)\right]\right)\Bigg|_{x_2=0} = 0 \tag{3-96}
$$

Consequently, the rocking rotation on the x_1x_2 plane at the free surface is given by

$$
\begin{aligned}
{}^{p}_{r}\theta_{x_1x_2}(x,t) &= \frac{1}{2}\left(\frac{\partial}{\partial x_1}\left[{}^{p}_{r}u_{x_2}(x,t)\right]\Bigg|_{x_2=0} - \frac{\partial}{\partial x_2}\left[{}^{p}_{r}u_{x_1}(x,t)\right]\Bigg|_{x_2=0}\right) \\
&= \frac{\partial}{\partial x_1}\left[{}^{p}_{r}u_{x_2}(x,t)\right]\Bigg|_{x_2=0} = -\frac{\partial}{\partial x_2}\left[{}^{p}_{r}u_{x_1}(x,t)\right]\Bigg|_{x_2=0}
\end{aligned} \tag{3-97}
$$

Now, substituting Eq (3-94) and Eq (3-95) into the first equality of Eq (3-97), it can be shown that

$$
{}^{p}_{r}\theta_{x_1x_2}(x,t) = \frac{A_{rp}}{2}M_{PS}\beta\left(irk_0\right)\exp\left[irk_0\left(x_1\sin\theta_0 - c_L t\right) + i\phi_r\right] \tag{3-98}
$$

3.6.5. Rocking at Surface the Incident Point

At the incident point on the surface $\left(x_1 = x_2 = 0\right)$, the rocking rotation can be obtained from Eq (3-98) as

$$
{}^{p}_{r}\theta_{x_1x_2}(t) = \frac{A_{rp}M_{PS}\beta}{2}\left(\frac{i\omega_r}{c_L}\right)\exp\left[-i\left(\omega_r t - \phi_r\right)\right] \tag{3-99}
$$

The associated rocking acceleration is

$$ {}^{p}_{r}\ddot{\theta}_{x_1x_2}(t) = -\frac{A_{rp}M_{PS}\beta}{2}\left(\frac{i\omega_r^3}{c_L}\right)\exp\left[-i\left(\omega_r t - \phi_r\right)\right] \tag{3-100} $$

3.6.6. Relationship between Rocking and Vertical Accelerations at the Surface Incident Point

At the incident point on the surface $\left(x_1 = x_2 = 0\right)$, the vertical displacement is given by Eq (3-95)

$$ {}^{p}_{r}u_{x_2}(t) = A_{rp}\left[\cos\theta_0 - M_{PP}\cos\theta_0 + M_{PS}\sin\theta_2\right]\exp\left(-i\omega_r t + i\phi_r\right) \tag{3-101} $$

Using Eq (3-91) and after some trigonometric rearrangements, Eq (3-101) can be rewritten as

$$ {}^{p}_{r}u_{x_2}(t) = \frac{A_{rp}M_{PS}\beta}{2\sin\theta_0}\exp\left[-i\left(\omega_r t - \phi_r\right)\right] \tag{3-102} $$

Taking three successive derivatives with respect to time,

$$ {}^{p}_{r}\dddot{u}_{x_2}(t) = \frac{A_{rp}M_{PS}\beta}{2\sin\theta_0}\left(i\omega_r^3\right)\exp\left[-i\left(\omega_r t - \phi_r\right)\right] \tag{3-103} $$

Now, comparing Eq (3-100) with Eq (3-103),

$$ {}^{p}_{r}\ddot{\theta}_{x_1x_2}(t) = -\frac{\sin\theta_0}{c_L}\,{}^{p}_{r}\dddot{u}_{x_2}(t) \tag{3-104} $$

3.6.7. Relationship between Rocking and Horizontal Accelerations at the Surface Incident Point

At the incident point on the surface $\left(x_1 = x_2 = 0\right)$, the horizontal displacement is given by Eq (3-94)

$$ {}^{p}_{r}u_{x_2}(t) = A_{rp}\left[\sin\theta_0 + M_{PP}\sin\theta_0 + M_{PS}\cos\theta_2\right]\exp\left(-i\omega_r t + i\phi_r\right) \tag{3-105} $$

Using Eq (3-91) and Eq (3-92), and after some trigonometric rearrangements, Eq (3-105) may be rewritten as

$$ {}^{p}_{r}u_{x_1}(t) = \frac{A_{rp}M_{PS}\beta^2\cos\theta_2}{\beta^2 - 2\sin^2\theta_0}\exp\left[-i\left(\omega_r t - \phi_r\right)\right] \tag{3-106} $$

Taking three successive derivatives with respect to time,

$$ {}^{p}_{r}\dddot{u}_{x_1}(t) = \frac{A_{rp} M_{PS} \beta^2 \cos\theta_2}{\beta^2 - 2\sin^2\theta_0} \left(i\omega_r^3\right) \exp\left[-i\left(\omega_r t - \phi_r\right)\right] \tag{3-107} $$

Now, comparing Eq (3-100) with Eq (3-107), it can be shown that

$$ {}^{p}_{r}\ddot{\theta}_{x_1 x_2}(t) = -\frac{\left(\beta^2 - 2\sin^2\theta_0\right)}{2c_L\left(\beta^2 - \sin^2\theta_0\right)^{\frac{1}{2}}} {}^{p}_{r}\dddot{u}_{x_1}(t) \tag{3-108} $$

3.6.8. Translational Accelerations at the Surface Incident Point

The horizontal and vertical acceleration histories at the incident point on the surface $\left(x_1 = x_2 = 0\right)$, can be obtained by taking two successive derivatives of Eq (3-106) and Eq (3-102), respectively. After some trigonometric rearrangements, these acceleration histories can be written as

$$ \begin{aligned} {}^{p}_{r}\ddot{u}_{x_1}(t) &= R_{PH} \exp\left[-i\left(\omega_r t - \phi_r\right)\right] \\ R_{PH} &= -A_{rp}\omega_r^2 \left[\frac{2\beta^2 \sin 2\theta_0 \left(\beta^2 - \sin^2\theta_0\right)^{\frac{1}{2}}}{2\sin\theta_0 \sin 2\theta_0 \left(\beta^2 - \sin^2\theta_0\right)^{\frac{1}{2}} + \left(\beta^2 - 2\sin^2\theta_0\right)^2}\right] \end{aligned} \tag{3-109} $$

$$ \begin{aligned} {}^{p}_{r}\ddot{u}_{x_2}(t) &= R_{PV} \exp\left[-i\left(\omega_r t - \phi_r\right)\right] \\ R_{PV} &= -A_{rp}\omega_r^2 \left[\frac{2\beta^2 \left(\beta^2 - 2\sin^2\theta_0\right)\cos\theta_0}{2\sin\theta_0 \sin 2\theta_0 \left(\beta^2 - \sin^2\theta_0\right)^{\frac{1}{2}} + \left(\beta^2 - 2\sin^2\theta_0\right)^2}\right] \end{aligned} \tag{3-110} $$

3.7. Reflection of an Inhomogeneous P Wave

The inhomogeneous P wave is defined here as the incident P wave that propagates with an imaginary vector of propagation. The incidence angle θ_0 is assumed such that $\cos\theta_0 = i\sigma$. This represents a valid wave propagation problem with an imaginary vector of propagation for the reflected P wave and a real vector of propagation for the reflected SV wave, as shown later. To do so, the

propagation vectors for both the reflected P wave and reflected SV wave are first assumed to be real. In this case, the associated displacement fields and stress fields are the same as those formulated earlier for the reflection of SV wave with an incidence angle that does not exceed the critical angle. The displacement fields associated with the incident P wave are derived first.

3.7.1. Incident Wave (n=0)

For this case, the vectors of propagation and particle movement are both given by

$$d^{(0)} = p^{(0)} = \left(1+\sigma^2\right)^{\frac{1}{2}}\hat{i} + i\sigma\hat{j} \tag{3-111}$$

Considering the phase of the incident wave as $\alpha_0 = -\phi_r$, the associated displacement field can be expressed as

$${}_r u^{(0)} = A_r^{(0)} \exp\left[irk_0\left(x_1\left(1+\sigma^2\right)^{\frac{1}{2}} + x_2\left(i\sigma\right) - c_L t\right) + i\phi_r\right] d^{(0)} \tag{3-112}$$

The displacement field at the free surface $\left(x_2 = 0\right)$ is thus given by

$${}_r u^{(0)} = A_r^{(0)} \exp\left[i\overline{\eta_0}\right] d^{(0)} \tag{3-113}$$

$$\overline{\eta_0} = rk_0\left(x_1\left(1+\sigma^2\right)^{\frac{1}{2}} - c_L t\right) + \phi_r \tag{3-114}$$

Substituting Eq (3-111) into Eq (3-3), the stresses at the free surface associated with this displacement field are

$$\begin{aligned} \tau_{21}^{(0)} &= -2\mu\sigma\left(1+\sigma^2\right)^{\frac{1}{2}} rk_0 A_r^{(0)} \exp\left(i\overline{\eta_0}\right) \\ \tau_{22}^{(0)} &= i\left(\lambda - 2\mu\sigma^2\right) rk_0 A_r^{(0)} \exp\left(i\overline{\eta_0}\right) \end{aligned} \tag{3-115}$$

3.7.2. Zero Traction at the Free Surface and Amplification Factors

For zero traction at the free surface, the required conditions are given by Eq (3-22). For a time-independent solution of Eq (3-22), Eq (3-23) must be satisfied. Substituting Eq (3-14), Eq (3-20) and Eq (3-114) into Eq (3-23),

$$k_1 = k_0,\ k_2 = k_0\beta,\ \cos\theta_1 = \cos\theta_0 = i\sigma,\ \cos\theta_2 = \left(\beta^2 - \sigma^2 - 1\right)^{\frac{1}{2}} \Big/ \beta \tag{3-116}$$

The propagation vector for the reflected P wave is also imaginary. For $\beta^2 < \sigma^2 + 1$, the problem no longer represents a valid wave propagation phenomenon, therefore, $\beta^2 \geq \sigma^2 + 1$ and the propagation vector for the reflected SV wave is real.

Substituting Eq (3-15), Eq (3-21) and Eq (3-115) into Eq (3-22), thereafter utilizing Eq (3-116) and separating out the real and imaginary parts, leads to the following four equations:

$$\frac{A_r^{(1)}}{A_r^{(0)}}\left[2\sigma\left(1+\sigma^2\right)^{\frac{1}{2}}\sin\left(\alpha_1+\phi_r\right)\right] + \frac{A_r^{(2)}}{A_r^{(0)}}\left[\left(\frac{\beta^2-2\sigma^2-2}{\beta}\right)\cos\left(\alpha_2+\phi_r\right)\right] = 0 \tag{3-117}$$

$$\frac{A_r^{(1)}}{A_r^{(0)}}\left[-2\sigma\left(1+\sigma^2\right)^{\frac{1}{2}}\cos\left(\alpha_1+\phi_r\right)\right] + \frac{A_r^{(2)}}{A_r^{(0)}}\left[\left(\frac{\beta^2-2\sigma^2-2}{\beta}\right)\sin\left(\alpha_2+\phi_r\right)\right] = -2\sigma\left(1+\sigma^2\right)^{\frac{1}{2}} \tag{3-118}$$

$$\frac{A_r^{(1)}}{A_r^{(0)}}\left[\left(\frac{\beta^2-2\sigma^2-2}{\beta}\right)\sin\left(\alpha_1+\phi_r\right)\right] + \frac{A_r^{(2)}}{A_r^{(0)}}\left[\frac{2}{\beta^2}\left(1+\sigma^2\right)^{\frac{1}{2}}\left(\beta^2-\sigma^2-1\right)^{\frac{1}{2}}\sin\left(\alpha_2+\phi_r\right)\right] = 0 \tag{3-119}$$

$$\frac{A_r^{(1)}}{A_r^{(0)}}\left[\left(\frac{\beta^2-2\sigma^2-2}{\beta}\right)\cos\left(\alpha_1+\phi_r\right)\right] - \frac{A_r^{(2)}}{A_r^{(0)}}\left[\frac{2}{\beta^2}\left(1+\sigma^2\right)^{\frac{1}{2}}\left(\beta^2-\sigma^2-1\right)^{\frac{1}{2}}\cos\left(\alpha_2+\phi_r\right)\right] = -\left(\frac{\beta^2-2\sigma^2-2}{\beta}\right) \tag{3-120}$$

Denoting $A_r^{(1)} \big/ A_r^{(0)} = \overline{M}_{PP}$ and $A_r^{(2)} \big/ A_r^{(0)} = \overline{M}_{PS}$, the solutions of Eq (3-117) through Eq (3-120) may be expressed as

$$\tan\left(\alpha_2+\phi_r\right)=-\frac{\left(\beta^2-2\sigma^2-2\right)^2}{4\sigma\left(1+\sigma^2\right)\left(\beta^2-\sigma^2-1\right)^{\frac{1}{2}}} \tag{3-121}$$

$$\alpha_1=2\alpha_2+\phi_r \tag{3-122}$$

$$\overline{M}_{PP}=1 \tag{3-123}$$

$$\overline{M}_{PS}=\frac{4\sigma\beta\left(1+\sigma^2\right)^{\frac{1}{2}}\left(\beta^2-2\sigma^2-2\right)}{\left[\left(\beta^2-2\sigma^2-2\right)^4+16\sigma^2\left(1+\sigma^2\right)^2\left(\beta^2-\sigma^2-1\right)\right]^{\frac{1}{2}}} \tag{3-124}$$

3.7.3. Resultant Displacement Field

Denoting $A_r^{(0)}=A_{rp}$, the resultant displacement field may be obtained by summing up the fields given by Eq (3-12), Eq (3-18) and Eq (3-112). Substituting Eq (3-11), Eq (3-17), Eq (3-111), Eq (3-116) and Eq (3-122) into the resultant displacement field, the horizontal and vertical components may be expressed as

$${}_r^p u_{x_1}\left(x,t\right)=A_{rp}\begin{bmatrix}\left(1+\sigma^2\right)^{\frac{1}{2}}\exp\left(i\phi_r\right)\exp\left\{irk_0\left(x_1\left(1+\sigma^2\right)^{\frac{1}{2}}+x_2\left(i\sigma\right)-c_Lt\right)\right\}\\+\overline{M}_{PP}\left(1+\sigma^2\right)^{\frac{1}{2}}\exp\left[-i\left(2\alpha_2+\phi_r\right)\right]\\*\exp\left\{irk_0\left(x_1\left(1+\sigma^2\right)^{\frac{1}{2}}-x_2\left(i\sigma\right)-c_Lt\right)\right\}\\+\overline{M}_{PS}\dfrac{\left(\beta^2-\sigma^2-1\right)^{\frac{1}{2}}}{\beta}\exp\left(-i\alpha_2\right)\\*\exp\left\{irk_0\left(x_1\left(1+\sigma^2\right)^{\frac{1}{2}}-x_2\left(\beta^2-\sigma^2-1\right)^{\frac{1}{2}}-c_Lt\right)\right\}\end{bmatrix} \tag{3-125}$$

$$
{}^{p}_{r}u_{x_2}(x,t) = A_{rp}\left[\begin{array}{l}
(i\sigma)\exp(i\phi_r)\exp\left\{irk_0\left(x_1\left(1+\sigma^2\right)^{\frac{1}{2}}+x_2(i\sigma)-c_Lt\right)\right\} \\
+\overline{M}_{PP}(-i\sigma)\exp\left[-i(2\alpha_2+\phi_r)\right] \\
*\exp\left\{irk_0\left(x_1\left(1+\sigma^2\right)^{\frac{1}{2}}-x_2(i\sigma)-c_Lt\right)\right\} \\
+\overline{M}_{PS}\dfrac{\left(1+\sigma^2\right)^{\frac{1}{2}}}{\beta}\exp(-i\alpha_2) \\
*\exp\left\{irk_0\left(x_1\left(1+\sigma^2\right)^{\frac{1}{2}}-x_2\left(\beta^2-\sigma^2-1\right)^{\frac{1}{2}}-c_Lt\right)\right\}
\end{array}\right] \tag{3-126}
$$

3.7.4. Plane Stress Condition and Estimation of Rocking

It is possible to show that the displacement fields given by Eq (3-125) and Eq (3-126) satisfy the plane-stress condition along the vertical direction at the free surface as given by Eq (3-96). Consequently, the rocking rotation on the x_1x_2 plane at the free surface is given by Eq (3-97). Substituting Eq (3-125) and Eq (3-126) into the first part of Eq (3-97),

$$
{}^{p}_{r}\theta_{x_1x_2}(x,t) = \frac{A_{rp}}{2}\overline{M}_{PS}\beta(irk_0)\exp\left[irk_0\left(x_1\left(1+\sigma^2\right)^{\frac{1}{2}}-c_Lt\right)-i\alpha_2\right] \tag{3-127}
$$

3.7.5. Rocking at the Surface Incident Point

At the incident point on the surface $(x_1 = x_2 = 0)$, the rocking rotation can be obtained from Eq (3-127). Considering the real part only

$$
{}^{p}_{r}\theta_{x_1x_2}(t) = \frac{A_{rp}\overline{M}_{PS}\beta}{2}\left(\frac{\omega_r}{c_L}\right)\sin(\omega_r t+\alpha_2) \tag{3-128}
$$

The associated rocking acceleration is

$$
{}^{p}_{r}\ddot{\theta}_{x_1x_2}(t) = -\frac{A_{rp}\overline{M}_{PS}\beta}{2}\left(\frac{\omega_r^3}{c_L}\right)\sin(\omega_r t+\alpha_2) \tag{3-129}
$$

3.7.6. Relationship between Rocking and Vertical Accelerations at the Surface Incident Point

At the incident point on the surface $\left(x_1 = x_2 = 0\right)$, the vertical displacement may be obtained from Eq (3-126). Considering only the real part

$$ {}^{p}_{r}u_{x_2}\left(t\right) = \frac{-2\sigma\beta^2}{\beta^2 - 2\sigma^2 - 2} A_{rp} \sin\left(\alpha_2 + \phi_r\right)\cos\left(\omega_r t + \alpha_2\right) \tag{3-130} $$

Using Eq (3-121) and after some trigonometric rearrangements, Eq (3-130) can be rewritten as

$$ {}^{p}_{r}u_{x_2}\left(t\right) = \frac{A_{rp}\overline{M}_{PS}\beta}{2\left(1+\sigma^2\right)^{\frac{1}{2}}}\cos\left(\omega_r t + \alpha_2\right) \tag{3-131} $$

Taking three successive derivatives with respect to time,

$$ {}^{p}_{r}\dddot{u}_{x_2}\left(t\right) = \frac{A_{rp}\omega_r^3\overline{M}_{PS}\beta}{2\left(1+\sigma^2\right)^{\frac{1}{2}}}\sin\left(\omega_r t + \alpha_2\right) \tag{3-132} $$

Comparing Eq (3-129) with Eq (3-132), it can be shown that

$$ {}^{p}_{r}\ddot{\theta}_{x_1x_2}\left(t\right) = -\frac{\left(1+\sigma^2\right)^{\frac{1}{2}}}{c_L}\,{}^{p}_{r}\dddot{u}_{x_2}\left(t\right) \tag{3-133} $$

3.7.7. Relationship between Rocking and Horizontal Accelerations at the Surface Incident Point

At the incident point on the surface $\left(x_1 = x_2 = 0\right)$, the horizontal displacement can be obtained from Eq (3-125). Considering only the real part

$$ {}^{p}_{r}u_{x_1}\left(t\right) = \frac{\beta^2}{\left(1+\sigma^2\right)^{\frac{1}{2}}} A_{rp} \cos\left(\alpha_2 + \phi_r\right)\cos\left(\omega_r t + \alpha_2\right) \tag{3-134} $$

Using Eq (3-121) and after some trigonometric rearrangements, Eq (3-134) can be rewritten as

$$ {}^{p}_{r}u_{x_1}\left(t\right) = \frac{A_{rp}\overline{M}_{PS}\beta\left(\beta^2 - \sigma^2 - 1\right)^{\frac{1}{2}}}{\left(\beta^2 - 2\sigma^2 - 2\right)}\cos\left(\omega_r t + \alpha_2\right) \tag{3-135} $$

Taking three successive derivatives with respect to time,

$$ {}^{p}_{r}\dddot{u}_{x_1}(t) = \frac{A_{rp}\omega_r^3 \overline{M}_{PS}\beta\left(\beta^2-\sigma^2-1\right)^{\frac{1}{2}}}{\left(\beta^2-2\sigma^2-2\right)}\sin\left(\omega_r t+\alpha_2\right) \tag{3-136} $$

Now, comparing Eq (3-129) with Eq (3-136),

$$ {}^{p}_{r}\ddot{\theta}_{x_1x_2}(t) = -\frac{\left(\beta^2-2\sigma^2-2\right)}{2c_L\left(\beta^2-\sigma^2-1\right)^{\frac{1}{2}}}\,{}^{p}_{r}\dddot{u}_{x_1}(t) \tag{3-137} $$

Noting, $\sin\theta_0 = \left(1+\sigma^2\right)^{\frac{1}{2}}$ but greater than unity, it can be shown that Eq (3-137) and Eq (3-133) are the same as those derived for the homogeneous P wave, Eq (3-108) and Eq (3-104), respectively.

3.7.8. Translational Accelerations at the Surface Incident Point

The horizontal and vertical acceleration histories at the incident point on the surface $\left(x_1 = x_2 = 0\right)$, can be obtained by taking two successive derivatives of Eq (3-135) and Eq (3-131), respectively. After some trigonometric rearrangements, these acceleration histories may be expressed as

$$ {}^{p}_{r}\ddot{u}_{x_1}(t) = R_{PH}\cos\left(\omega_r t+\alpha_2\right) $$
$$ R_{PH} = -A_{rp}\omega_r^2\left[\frac{4\sigma\beta^2\left(1+\sigma^2\right)^{\frac{1}{2}}\left(\beta^2-\sigma^2-1\right)^{\frac{1}{2}}}{\left(\beta^2-2\sigma^2-2\right)^4+16\sigma^2\left(1+\sigma^2\right)^2\left(\beta^2-\sigma^2-1\right)}\right] \tag{3-138} $$

$$ {}^{p}_{r}\ddot{u}_{x_2}(t) = R_{PV}\cos\left(\omega_r t+\alpha_2\right) $$
$$ R_{PV} = -A_{rp}\omega_r^2\left[\frac{2\sigma\beta^2\left(\beta^2-2\sigma^2-2\right)}{\left(\beta^2-2\sigma^2-2\right)^4+16\sigma^2\left(1+\sigma^2\right)^2\left(\beta^2-\sigma^2-1\right)}\right] \tag{3-139} $$

3.7.9. Change of Variables

Without losing generality, a change of variable, namely, $\alpha_2 = -\phi_{rp}$ is employed for future convenience, where ϕ_{rp} is the phase of the acceleration histories contributed from the inhomogeneous P wave. This leads to the following changes in the previously derived relationships:

$$\tan\left(\phi_r - \phi_{rp}\right) = -\frac{\left(\beta^2 - 2\sigma^2 - 2\right)^2}{4\sigma\left(1+\sigma^2\right)\left(\beta^2 - \sigma^2 - 1\right)^{\frac{1}{2}}} \tag{3-140}$$

$${}^{p}_{r}\ddot{u}_{x_1}(t) = R_{PH}\cos\left(\omega_r t - \phi_{rp}\right) \tag{3-141}$$

$${}^{p}_{r}\ddot{u}_{x_2}(t) = R_{PV}\cos\left(\omega_r t - \phi_{rp}\right) \tag{3-142}$$

3.8. Reflection of an SH Wave

Denoting A_{rn} as the displacement amplitude of the r^{th} mode, the resulting displacement field after reflection from the free surface is

$${}_{r}u_{x_3}(x,t) = 2A_{rn}\cos\left(rk_0 x_2\cos\theta_0\right)\exp\left[irk_0\left(x_1\sin\theta_0 - c_T t\right) + i\phi_r\right]\hat{k} \tag{3-143}$$

This represents a standing wave along the vertical direction but a propagating wave along the horizontal x_3 direction. Rocking on the x_2x_3 plane is therefore zero at the free surface. However, the SH wave contributes to the torsional rotation on the x_1x_3 plane. At the surface incident point, the torsional acceleration and the associated translational acceleration along the x_3 direction are related through

$${}^{sh}_{r}\ddot{\theta}_{x_1x_3}(t) = \frac{1}{2}\frac{\sin\theta_0}{c_T}\,{}^{sh}_{r}\ddot{u}_{x_3}(t) \tag{3-144}$$

Moreover, at the surface incident point, the translational acceleration along the x_3 direction can be expressed as

$$ {}_r\ddot{u}_{x_3}(x,t) = -2A_{rn}\omega_r^2 \exp\left[-i(\omega_r t - \phi_r)\right] \tag{3-145} $$

Here the factor of 2 is the amplification factor, which is independent of the angle of incidence.

3.9. Compatibility/Consistency Condition

Body waves are treated independently above in Sections 3.4 through 3.8 so a compatibility/consistency condition is established below for the simultaneous incidence of P, SH and SV waves. Consider Figure 3-1 that shows the incidence and reflection of a plane wave from the earth's surface. The angles of incidence and reflection are shown in the figure. Calculations are performed on the polarized or principal plane and thus only the incidence of P and SV waves are considered. Further, consider only the r^{th} harmonic component in which: a) θ_{0p} and θ_{0s} denote the incidence angles at the surface for the P and SV waves, respectively, b) ϕ_{rs} denotes the phase of the incident SV wave, which is the same as that of the SH wave, and is known from the FFT of the acceleration history along the x_3 direction, and c) ϕ_{rp} is the phase of the acceleration history (along x_1 and x_2 directions) contributed from the P wave (homogeneous or inhomogeneous). The horizontal direction assumed here, unless noted otherwise, is x_1. In addition, (a_{rh}, b_{rh}) and (a_{rv}, b_{rv}) are denoted as the real and imaginary parts of the Fourier coefficients of the horizontal and vertical accelerations, respectively, for the r^{th} harmonic. Two cases are discussed below, namely, $\theta_{0s} \le \theta_{cr}$ and $\theta_{0s} > \theta_{cr}$, where θ_{cr} is the critical angle. If the incidence angle of the SV wave exceeds the critical angle, the reflected P wave remains plane but inhomogeneous; that is, one of the components of its wave vector is imaginary.

3.9.1. SV Wave Incidence Angle Not Exceeding the Critical Angle

If the SV wave incidence angle is less than or equal to the critical angle, using Eq (3-109) or Eq (3-141) for the P wave, as the case may be, and Eq (3-49) for the SV wave, it may be shown for horizontal acceleration that

$$R_{PH}\cos\phi_{rp} + R_{SH}\cos\phi_{rs} = 2a_{rh} \tag{3-146}$$

$$R_{PH}\sin\phi_{rp} + R_{SH}\sin\phi_{rs} = 2b_{rh} \tag{3-147}$$

Similarly, using Eq (3-110) or Eq (3-142) for the P wave, and Eq (3-50) for the SV wave, it may be shown for the vertical acceleration that

$$R_{PV}\cos\phi_{rp} + R_{SV}\cos\phi_{rs} = 2a_{rv} \tag{3-148}$$

$$R_{PV}\sin\phi_{rp} + R_{SV}\sin\phi_{rs} = 2b_{rv} \tag{3-149}$$

Assuming $\phi_{rp} \neq \phi_{rs}$, R_{PH}, R_{SH}, R_{PV} and R_{SV} may be expressed as

$$R_{PH} = \frac{2\left(a_{rh}\sin\phi_{rs} - b_{rh}\cos\phi_{rs}\right)}{\sin\left(\phi_{rs} - \phi_{rp}\right)} \tag{3-150}$$

$$R_{SH} = \frac{2\left(a_{rh}\sin\phi_{rp} - b_{rh}\cos\phi_{rp}\right)}{\sin\left(\phi_{rp} - \phi_{rs}\right)} \tag{3-151}$$

$$R_{PV} = \frac{2\left(a_{rv}\sin\phi_{rs} - b_{rv}\cos\phi_{rs}\right)}{\sin\left(\phi_{rs} - \phi_{rp}\right)} \tag{3-152}$$

$$R_{SV} = \frac{2\left(a_{rv}\sin\phi_{rp} - b_{rv}\cos\phi_{rp}\right)}{\sin\left(\phi_{rp} - \phi_{rs}\right)} \tag{3-153}$$

Consequently, the Fourier coefficients associated with the P and SV wave contributions to the horizontal acceleration are

$$\begin{aligned} a_{rhp} &= 0.5R_{PH}\cos\phi_{rp,}\; b_{rhp} = 0.5R_{PH}\sin\phi_{rp} \\ a_{rhs} &= 0.5R_{SH}\cos\phi_{rs,}\; b_{rhs} = 0.5R_{SH}\sin\phi_{rs} \end{aligned} \tag{3-154}$$

Similarly, for vertical acceleration

$$\begin{aligned} a_{rvp} &= 0.5R_{PV}\cos\phi_{rp,}\; b_{rvp} = 0.5R_{PV}\sin\phi_{rp} \\ a_{rvs} &= 0.5R_{SV}\cos\phi_{rs,}\; b_{rvs} = 0.5R_{SV}\sin\phi_{rs} \end{aligned} \tag{3-155}$$

3.9.2. SV Wave Incidence Angle Exceeding the Critical Angle

When the SV wave incidence angle exceeds the critical angle, and using Eq (3-109) or Eq (3-141) for the P wave and Eq (3-78) for the SV wave, it can be shown for the horizontal acceleration that

$$R_{PH}\cos\phi_{rp} + R_{SH}\cos\left(\alpha_1 - \phi_{rs}\right) = 2a_{rh} \tag{3-156}$$

$$R_{PH}\sin\phi_{rp} - R_{SH}\sin\left(\alpha_1 - \phi_{rs}\right) = 2b_{rh} \tag{3-157}$$

Similarly, using Eq (3-110) or Eq (3-142) for the P wave and Eq (3-79) for the SV wave, it may be shown for the vertical acceleration that

$$R_{PV}\cos\phi_{rp} - R_{SV}\sin\left(\alpha_1 - \phi_{rs}\right) = 2a_{rv} \tag{3-158}$$

$$R_{PV}\sin\phi_{rp} - R_{SV}\cos\left(\alpha_1 - \phi_{rs}\right) = 2b_{rv} \tag{3-159}$$

Here α_1 is given by

$$\tan\alpha_1 = \frac{2\left(\beta^2\sin^2\theta_{0s}\text{-}1\right)^{\frac{1}{2}}\sin\theta_{0s}\sin 2\theta_{0s}}{\beta\cos^2 2\theta_{0s}} \tag{3-160}$$

Assuming $\cos\left(\alpha_1 - \phi_{rs} + \phi_{rp}\right) \neq 0$ and $\sin\left(\alpha_1 - \phi_{rs} + \phi_{rp}\right) \neq 0$, R_{PH}, R_{SH}, R_{PV} and R_{SV} can be expressed as

$$R_{PH} = \frac{2\left[a_{rh}\sin\left(\alpha_1 - \phi_{rs}\right) + b_{rh}\cos\left(\alpha_1 - \phi_{rs}\right)\right]}{\sin\left(\alpha_1 - \phi_{rs} + \phi_{rp}\right)} \tag{3-161}$$

$$R_{SH} = \frac{2\left(a_{rh}\sin\phi_{rp} - b_{rh}\cos\phi_{rp}\right)}{\sin\left(\alpha_1 - \phi_{rs} + \phi_{rp}\right)} \tag{3-162}$$

$$R_{PV} = \frac{2\left[a_{rv}\cos\left(\alpha_1 - \phi_{rs}\right) - b_{rv}\sin\left(\alpha_1 - \phi_{rs}\right)\right]}{\cos\left(\alpha_1 - \phi_{rs} + \phi_{rp}\right)} \tag{3-163}$$

$$R_{SV} = \frac{2\left(a_{rv}\sin\phi_{rp} - b_{rv}\cos\phi_{rp}\right)}{\cos\left(\alpha_1 - \phi_{rs} + \phi_{rp}\right)} \tag{3-164}$$

Consequently, the Fourier coefficients associated with the P and SV wave contributions to the horizontal acceleration are given by

$$a_{rhp} = 0.5R_{PH}\cos\phi_{rp,}\, b_{rhp} = 0.5R_{PH}\sin\phi_{rp}$$
$$a_{rhs} = 0.5R_{SH}\cos(\alpha_1 - \phi_{rs}),\, b_{rhs} = -0.5R_{SH}\sin(\alpha_1 - \phi_{rs}) \quad (3\text{-}165)$$

Similarly, for vertical acceleration

$$a_{rvp} = 0.5R_{PV}\cos\phi_{rp,}\, b_{rvp} = 0.5R_{PV}\sin\phi_{rp}$$
$$a_{rvs} = -0.5R_{SV}\sin(\alpha_1 - \phi_{rs}),\, b_{rvs} = -0.5R_{SV}\cos(\alpha_1 - \phi_{rs}) \quad (3\text{-}166)$$

In both of these cases, an additional relationship is required to solve the problem. It is assumed that neither both R_{PH} and R_{PV}, nor both R_{SH} and R_{SV}, are zero; otherwise, the inverse problem addressed here collapses to a single type of wave incidence, which is discussed below prior to introducing the general case.

3.10. Special Cases

Two special cases are presented below in which the phase angles of the recorded horizontal and vertical motions are the same. In first case, this phase angle is the same as that of the incident SV (also SH) wave. A single type of wave incidence is likely in both cases, although other possibilities are mathematically possible. To eliminate these other possibilities, the following two assumptions must be made: i) single type of wave incidence, and ii) if there is SV wave incidence, then $\theta_{0s} \leq \theta_{cr}$. These two assumptions, denoted A1 and A2 hereafter, must be distinguished from the other assumptions made in this chapter. While other assumptions are made to reduce the indeterminacy of the inverse problem solved here, A1 and A2 are required for the mathematical uniqueness of the solution in the two special cases considered above. These special cases arise with one additional condition that compensates the, otherwise, one degree indeterminacy of the problem, and, hence, no further assumption is required.

3.10.1. Case 1: Incident SV (also SH) Wave has the Same Phase

Case 1 may be expressed as

$$\tan^{-1}\left(\frac{b_{rh}}{a_{rh}}\right)=\tan^{-1}\left(\frac{b_{rv}}{a_{rv}}\right)=\phi_{rs} \tag{3-167}$$

where all terms have been defined previously. To decide the type of wave incidence, simultaneous incidence of both the P and SV waves is considered first and per A2, $\theta_{0s} \le \theta_{cr}$. Denoting ϕ_h and ϕ_v as the phase of the horizontal and vertical accelerations, respectively, from Eq (3-146) and Eq (3-147),

$$\begin{aligned}\tan\phi_h &= \frac{R_{PH}\sin\phi_{rp}+R_{SH}\sin\phi_{rs}}{R_{PH}\cos\phi_{rp}+R_{SH}\cos\phi_{rs}}\\ R_{PH}\sin\left(\phi_h-\phi_{rp}\right)&=R_{SH}\sin\left(\phi_{rs}-\phi_h\right)\end{aligned} \tag{3-168}$$

Similarly, from Eq (3-148) and Eq (3-149),

$$\begin{aligned}\tan\phi_v &= \frac{R_{PV}\sin\phi_{rp}+R_{SV}\sin\phi_{rs}}{R_{PV}\cos\phi_{rp}+R_{SV}\cos\phi_{rs}}\\ R_{PV}\sin\left(\phi_v-\phi_{rp}\right)&=R_{SV}\sin\left(\phi_{rs}-\phi_v\right)\end{aligned} \tag{3-169}$$

Since $\phi_h=\phi_v=\phi_{rs}$, it is clear that either $\phi_{rs}=\phi_{rp}$ or $R_{PH}=R_{PV}=0$. It is easy to verify that $\phi_{rs}=\phi_{rp}$ leads to an indeterminate problem and discarding this, $R_{PH}=R_{PV}=0$. This shows the possibility of only SV wave incidence with the angle of incidence not exceeding the critical angle.

SV Wave Incidence Only with $\theta_{0s} \le \theta_{cr}$

To confirm this, let

$$\overline{G}=\left(a_{rv}^2+b_{rv}^2\right)^{\frac{1}{2}}\Big/\left(a_{rh}^2+b_{rh}^2\right)^{\frac{1}{2}} \tag{3-170}$$

Using Eq (3-49), Eq (3-50) and Eq (3-170), and setting $\sin^2\theta_{0s}=x$

$$\begin{aligned}\frac{R_{SV}}{R_{SH}}&=-\frac{2\sin\theta_{0s}\left(1-\beta^2\sin^2\theta_{0s}\right)^{\frac{1}{2}}}{\beta\left(1-2\sin^2\theta_{0s}\right)}=\overline{G}\\ x^2-\frac{\beta^2\overline{G}^2+1}{\beta^2\left(\overline{G}^2+1\right)}x&+\frac{\overline{G}^2}{4\left(\overline{G}^2+1\right)}=0\end{aligned} \tag{3-171}$$

If the real root exists, it is easy to verify that both the roots of Eq (3-171) lie between 0 and 1. Moreover, the smaller of the two roots is given by

$$x = \frac{1}{2}\left[\frac{\beta^2\overline{G}^2+1}{\beta^2\left(\overline{G}^2+1\right)}\right] - \frac{1}{2}\left[\frac{\left(\beta^2\overline{G}^2+1\right)^2}{\beta^4\left(\overline{G}^2+1\right)^2} - \frac{\overline{G}^2}{\left(\overline{G}^2+1\right)}\right]^{\frac{1}{2}} \tag{3-172}$$

It can be shown that the solution given by Eq (3-172) will be real if

$$\overline{G}^2 \le \left[\left(\beta^2-1\right)^2-1\right]^{-1} \tag{3-173}$$

Finally, it is possible to show that if a real x exists, then it will be bounded by $0 < x \le 1/\beta^2$. This implies that if Eq (3-173) is satisfied, then θ_{0s} will be bounded by $0 < \theta_{0s} \le \theta_{cr}$.

Inhomogeneous P Wave Incidence

If Eq (3-173) is not satisfied, then it is regarded as a case of the incidence of an inhomogeneous P wave. The possibility of only SV wave incidence with $\theta_{0s} > \theta_{cr}$ is set aside because, in that case, the horizontal and vertical motions would be separated by a phase angle of 90 degrees. Using Eq (3-138), Eq (3-139) and Eq (3-170),

$$\frac{R_{PV}}{R_{PH}} = \frac{\left(\beta^2-2\sigma^2-2\right)}{2\left(1+\sigma^2\right)^{\frac{1}{2}}\left(\beta^2-\sigma^2-1\right)^{\frac{1}{2}}} = \overline{G} \tag{3-174}$$

Rearrangement of Eq (3-174) leads to a quadratic equation in σ^2 and the resulting solutions may be shown to be real for all $\overline{G}^2$. Considering the smaller of the two solutions

$$\sin^2\theta_{0p} = 1+\sigma^2 = \frac{\beta^2}{2}\left[1-\sqrt{\overline{G}^2/\left(\overline{G}^2+1\right)}\right] \tag{3-175}$$

3.10.2. Case 2: Incident SV (also SH) Wave has a Different Phase

Case 2 may be expressed as

$$\tan^{-1}\left(\frac{b_{rh}}{a_{rh}}\right)=\tan^{-1}\left(\frac{b_{rv}}{a_{rv}}\right)\neq\phi_{rs} \tag{3-176}$$

Similar to case 1, consider the simultaneous incidence of both P and SV waves and $\theta_{0s}\leq\theta_{cr}$. Here, there are two options: the phase angle in Eq (3-176) is either equal or not equal to ϕ_{rp}. First assume that the phase angle in Eq (3-176) is not equal to ϕ_{rp}. Substituting Eq (3-176) into Eq (3-168) and Eq (3-169),

$$\frac{R_{PV}}{R_{PH}}=\frac{R_{SV}}{R_{SH}} \tag{3-177}$$

Equating R_{PV}/R_{PH} from Eq (3-150) and Eq (3-152), and from Eq (3-110) and Eq (3-109) (assuming homogeneous P wave incidence), and letting

$$G=\frac{a_{rv}\sin\phi_{rs}-b_{rv}\cos\phi_{rs}}{a_{rh}\sin\phi_{rs}-b_{rh}\cos\phi_{rs}} \tag{3-178}$$

results in

$$\frac{\left(\beta^2-2\sin^2\theta_{0p}\right)}{2\sin\theta_{0p}\left(\beta^2-\sin^2\theta_{0p}\right)^{\frac{1}{2}}}=G \tag{3-179}$$

Eq (3-179) is valid for inhomogeneous P wave also and, in that case $\sin\theta_{0p}>1$. Letting $\sin^2\theta_{0p}=x$, Eq (3-179) leads to a quadratic equation in x, which has real roots for all G^2. Furthermore, the lesser of the two solutions can be expressed as

$$x=\sin^2\theta_{0p}=\frac{\beta^2}{2}\left[1-\sqrt{G^2/\left(G^2+1\right)}\right] \tag{3-180}$$

It may be shown that $\sin\theta_{0p}\leq 1$, that is, the contributing P wave is homogeneous, if

$$G^2\geq\left(\beta^2-2\right)^2/4\left(\beta^2-1\right) \tag{3-181}$$

If Eq (3-181) is not satisfied, then $\sin\theta_{0p}$ can be computed using the Eq (3-180) assuming that the contributing P wave is inhomogeneous.

To compute θ_{0s}, substituting Eq (3-49) and Eq (3-50) into Eq (3-177) and thereafter using Eq (3-179), results in

$$-\frac{2\sin\theta_{0s}\left(1-\beta^2\sin^2\theta_{0s}\right)^{\frac{1}{2}}}{\beta\left(1-2\sin^2\theta_{0s}\right)}=G \tag{3-182}$$

where G is given by Eq (3-178). If $\sin^2\theta_{0s}=x$, Eq (3-182) leads to a quadratic equation in x which has real roots if,

$$G^2\le\frac{1}{\left(\beta^2-1\right)^2-1} \tag{3-183}$$

Further, if the real roots exist, both the roots of x will be positive and for the smaller of the two roots $x\le 1/\beta^2$, that is, $\theta_{0s}\le\theta_{cr}$. Therefore, if Eq (3-183) is satisfied, θ_{0s} will be real and $\theta_{0s}\le\theta_{cr}$.

Further, it may be shown that the limit given by Eq (3-183) is less than that given by Eq (3-181) if Poisson's ratio is less than 0.293. If G^2 is greater than the limit given by Eq (3-183), then the problem does not represent a physical phenomenon and the assumption of a phase angle in Eq (3-176) being different from ϕ_{rp} is incorrect. If Eq (3-183) is satisfied, then: i) if Eq (3-181) is satisfied, the problem is a simultaneous incidence of homogeneous P and SV waves with $\theta_{0s}\le\theta_{cr}$ **,** and ii) if Eq (3-181) is not satisfied then the problem is a simultaneous incidence of inhomogeneous P and SV waves with $\theta_{0s}\le\theta_{cr}$. In either case, A1 is not satisfied. Therefore, it is concluded that the phase angle in Eq (3-176) must be equal to ϕ_{rp}.

After this conclusion, it may be shown from Eq (3-168) and Eq (3-169) that $R_{SH}=R_{SV}=0$**,** which otherwise implies that only the P wave incidence and A1 is satisfied. Next, defining

$$G=\left(a_{rv}^2+b_{rv}^2\right)^{\frac{1}{2}}\Big/\left(a_{rh}^2+b_{rh}^2\right)^{\frac{1}{2}} \tag{3-184}$$

instead of Eq (3-178), Eq (3-180) and Eq (3-181) may be re-calculated for the incidence angle and the associated bound to distinguish between homogeneous and inhomogeneous P wave incidence.

3.11. General Case

The general case developed below holds when the two cases above do not. One additional assumption is required for a solution. Two hypotheses (H1 and H2) are offered for the additional condition as follows: H1 assumes an equal angle of incidence of the P and SV waves, and H2 assumes power compatibility.

3.11.1. Hypothesis H1: Equal Angle of Incidence of the P and SV Waves

Here the additional condition is an equal angle of incidence for the P and SV waves in any mode of propagation: $\theta_{0s} = \theta_{0p} = \theta_0$. The solution proceeds differently depending upon whether θ_{0s} exceeds θ_{cr}.

3.11.1.1. SV Wave Incidence Angle Not Exceeding the Critical Angle

For this case, using Eq (3-146) through Eq (3-149), and letting G be given by Eq (3-178), Eq (3-179) can be solved for θ_{0p} as shown in Eq (3-180). However, the limit shown in Eq (3-181) needs to be recomputed as follows. Since, $\theta_{0s} = \theta_{0p}$ and $\theta_{0s} \le \theta_{cr}$, a check must be made to ensure that $\sin\theta_{0p} \le 1/\beta$. To satisfy this limit, it may be shown that

$$G^2 \ge \left(\beta^4 - 2\right)^2 \Big/ 4\left(\beta^4 - 1\right) \tag{3-185}$$

If the limit in Eq (3-185) is satisfied, equating R_{SV}/R_{SH} computed from Eq (3-151) and Eq (3-153) and from Eq (3-49) and Eq (3-50) leads to

$$-\frac{2\sin\theta_{0s}\left(1-\beta^2\sin^2\theta_{0s}\right)^{\frac{1}{2}}}{\beta\left(1-2\sin^2\theta_{0s}\right)} = \frac{a_{rv}\sin\phi_{rp} - b_{rv}\cos\phi_{rp}}{a_{rh}\sin\phi_{rp} - b_{rh}\cos\phi_{rp}} \tag{3-186}$$

Using $\theta_{0s} = \theta_{0p} = \theta_0$ (as computed above) in Eq (3-186), ϕ_{rp} may be computed as follows:

$$\tan\phi_{rp} = \frac{J_2 b_{rv} + J_1 b_{rh}}{J_2 a_{rv} + J_1 a_{rh}};\; J_1 = 2\sin\theta_0\left(1-\beta^2\sin^2\theta_0\right)^{\frac{1}{2}};\; J_2 = \beta\cos 2\theta_0 \tag{3-187}$$

Knowing ϕ_{rp}, Eq (3-150) through Eq (3-153) can be used to compute R_{PH}, R_{SH}, R_{PV} and R_{SV}, respectively. Finally, the real and complex parts of the Fourier coefficients may be calculated using Eq (3-154) and Eq (3-155). If the limit in Eq (3-185) is not satisfied, the procedure in Section 3.11.1.2 must be followed.

3.11.1.2. SV Wave Incidence Angle Exceeding the Critical Angle

With reference to Eq (3-156) through Eq (3-160), equating R_{PV}/R_{PH} computed from Eq (3-161) and Eq (3-163) and from Eq (3-109) and Eq (3-110), and after some rearrangement using $\theta_{0s} = \theta_{0p} = \theta_0$, it can be shown that

$$\tan\phi_{rp} = \frac{b_{rv}\tan^2(\alpha_1 - \phi_{rs}) + (a_{rh}D - a_{rv})\tan(\alpha_1 - \phi_{rs}) + b_{rh}D}{a_{rh}D\tan^2(\alpha_1 - \phi_{rs}) + (b_{rh}D - b_{rv})\tan(\alpha_1 - \phi_{rs}) + a_{rv}} \tag{3-188}$$

where α_1 is given by Eq (3-77) and

$$D = \frac{\beta^2 - 2\sin^2\theta_0}{2\sin\theta_0\left(\beta^2 - \sin^2\theta_0\right)^{\frac{1}{2}}} \tag{3-189}$$

Similarly, equating R_{SV}/R_{SH} computed from Eq (3-162) and Eq (3-164) and from Eq (3-78) and Eq (3-79), and after some rearrangement using $\theta_{0s} = \theta_{0p} = \theta_0$ and Eq (3-77), it can be shown that

$$\begin{aligned}
&H_1\tan^2\phi_{rp} + H_2\tan\phi_{rp} + H_3 = 0 \\
&H_1 = a_{rv} + Ea_{rh}\tan(\alpha_1 - \phi_{rs}) \\
&H_2 = (a_{rv} - Eb_{rh})\tan(\alpha_1 - \phi_{rs}) - (b_{rv} + Ea_{rh}) \\
&H_3 = -b_{rv}\tan(\alpha_1 - \phi_{rs}) + Eb_{rh} \\
&E = \frac{2\sin\theta_0\left(\beta^2\sin^2\theta_0 - 1\right)^{\frac{1}{2}}}{\beta\cos 2\theta_0}
\end{aligned} \tag{3-190}$$

The angle of incidence θ_0 can be calculated by eliminating ϕ_{rp} from Eq (3-188) and Eq (3-190) and thereafter making use of Eq (3-77). However, the solution procedure is iterative and may be performed as follows: i) assume θ_0; ii) compute α_1 from Eq (3-77); iii) compute ϕ_{rp} from Eq (3-188), and iv) evaluate

Eq (3-190) and, if not zero, revise θ_0. Once θ_0 is computed, α_1 and ϕ_{rp} can be estimated from Eq (3-77) and Eq (3-188), respectively. It may be seen that computed θ_0 will be greater than θ_{cr}.

Further, if θ_0 is less than $\pi/2$, then the following three cases may arise:

i) $\cos\left(\alpha_1 - \phi_{rs} + \phi_{rp}\right) \neq 0$ *and* $\sin\left(\alpha_1 - \phi_{rs} + \phi_{rp}\right) \neq 0$

For this case, compute R_{PH}, R_{SH}, R_{PV} and R_{SV} using Eq (3-161) through Eq (3-164), respectively. Next, compute the real and imaginary parts of the Fourier coefficients using Eq (3-165) and Eq (3-166).

ii) $\sin\left(\alpha_1 - \phi_{rs} + \phi_{rp}\right) = 0$

For this case

$$\alpha_1 = \phi_{rs} - \phi_{rp} \tag{3-191}$$

Accordingly, Eq (3-161) and Eq (3-162) do not hold. This implies the assumption of $\theta_{0s} = \theta_{0p} = \theta_0$ does not lead to a physical solution. However, Eq (3-191) may be used as the required additional condition instead of the assumption of an equal angle of incidence for the P and SV waves. From Eq (3-156) and Eq (3-157),

$$\phi_{rp} = \tan^{-1}\left(b_{rh}/a_{rh}\right) \tag{3-192}$$

$$R_{PH} + R_{SH} = \begin{cases} 2a_{rh}/\cos\phi_{rp} & \text{if } \cos\phi_{rp} \neq 0 \\ 2b_{rh} & \text{otherwise} \end{cases} \tag{3-193}$$

First, compute ϕ_{rp} from Eq (3-192) and then calculate α_1 using Eq (3-191). Now, setting $\tan\alpha_1 = F$ and $\sin^2\theta_{0s} = x$, Eq (3-77) may be expressed as

$$x^4 - \left(1 + \frac{1}{\beta^2}\right)x^3 + \left(\frac{1}{\beta^2} + \frac{F^2}{4}\right)x^2 - \frac{F^2}{4}x + \frac{F^2}{16} = 0 \tag{3-194}$$

The real solution exists and is bounded by $\frac{1}{\beta^2} < x < 1$.Therefore $\theta_{cr} < \theta_{0s} < \pi/2$. Substituting Eq (3-191) into Eq (3-158) and Eq (3-159),

$$R_{PV} = 2\left[a_{rv}\cos\left(\alpha_1 - \phi_{rs}\right) - b_{rv}\sin\left(\alpha_1 - \phi_{rs}\right)\right] \tag{3-195}$$

$$R_{SV} = 2\left(a_{rv}\sin\phi_{rp} - b_{rv}\cos\phi_{rp}\right) \tag{3-196}$$

Knowing, R_{PV} and R_{SV}, R_{SH} can be obtained from

$$\frac{R_{SV}}{R_{SH}} = \frac{\tan\alpha_1}{\tan 2\theta_{0s}} = \frac{2\left(\beta^2\sin^2\theta_{0s} - 1\right)^{\frac{1}{2}}\sin\theta_{0s}}{\beta\cos 2\theta_{0s}} \tag{3-197}$$

The last part of Eq (3-197) is obtained from Eq (3-78) and Eq (3-79) where the last term is due to Eq (3-77). Next, R_{PH} can be computed using Eq (3-193). Knowing, R_{PH}, R_{SH}, R_{PV} and R_{SV}, the real and imaginary parts of the Fourier coefficients can be calculated using Eq (3-165) and Eq (3-166) with the use of Eq (3-191). Finally, defining $G = R_{PV}/R_{PH}$, the angle of incidence for the P wave, θ_{0p}, may be computed using Eq (3-180) and the homogeneous or inhomogeneous nature of the P wave is decided based on the limit given by Eq (3-181). Care is required to solve when $\left|\phi_{rs} - \phi_{rp}\right| \approx \pi/2$.

iii) $\cos\left(\alpha_1 - \phi_{rs} + \phi_{rp}\right) = 0$

For this case

$$\alpha_1 = \frac{\pi}{2} + \phi_{rs} - \phi_{rp} \tag{3-198}$$

Accordingly, Eq (3-163) and Eq (3-164) do not hold and the assumption that $\theta_{0s} = \theta_{0p} = \theta_0$ does not lead to a physical solution. Hence, Eq (3-198) can be used as the required additional condition. From Eq (3-158) and Eq (3-159),

$$\phi_{rp} = \tan^{-1}\left(b_{rv}/a_{rv}\right) \tag{3-199}$$

$$R_{PV} - R_{SV} = \begin{cases} 2a_{rv}/\cos\phi_{rp} & \text{if } \cos\phi_{rp} \neq 0 \\ 2b_{rv} & \text{otherwise} \end{cases} \tag{3-200}$$

First, compute ϕ_{rp} from Eq (3-199) and then calculate α_1 using Eq (3-188). Setting $\tan\alpha_1 = F$ and $\sin^2\theta_{0s} = x$, Eq (3-77) may be solved for θ_{0s} in the form of Eq (3-194) and once again $\theta_{cr} < \theta_{0s} < \pi/2$. Substituting Eq (3-198) into Eq (3-156) and Eq (3-157),

$$R_{PH} = 2\left[a_{rh}\sin\left(\alpha_1 - \phi_{rs}\right) + b_{rh}\cos\left(\alpha_1 - \phi_{rs}\right)\right] \tag{3-201}$$

$$R_{SH} = 2\left(a_{rh}\sin\phi_{rp} - b_{rh}\cos\phi_{rp}\right) \tag{3-202}$$

Knowing R_{PH} and R_{SH}, R_{SV} can be obtained from Eq (3-197). Next, R_{PV} can be computed using Eq (3-200). Knowing R_{PH}, R_{SH}, R_{PV} and R_{SV}, the real and imaginary parts of the Fourier coefficients may be calculated using Eq (3-165) and Eq (3-166) after making use of Eq (3-198). Finally, defining $G = R_{PV}/R_{PH}$, the angle of incidence for the P wave, θ_{0p}, can be computed using Eq (3-180). The homogeneous or inhomogeneous nature of the P wave is determined based on the limit given by Eq (3-181). Care is required to solve when $\left|\phi_{rs} - \phi_{rp}\right| \approx 0$.

If θ_0 computed by solving Eq (3-188) and Eq (3-190) is not less than $\pi/2$, proceed with the following procedure.

3.11.1.3. SV Wave Incidence at Critical Angle (SVcrP)

If θ_0 computed by solving Eq (3-188) and Eq (3-190) is not less than $\pi/2$, then the assumption of $\theta_{0s} = \theta_{0p} = \theta_0$ does not lead to a physical solution. In general, the number of harmonics in which this case arises is insignificant when compared to the total number of harmonics. For the sake of completeness, assume $\theta_{0s} = \theta_{cr}$ with no theoretical basis. The additional error associated with this assumption will be insignificant when compared with the other assumptions involved in the procedure.

The assumption of $\theta_{0s} = \theta_{cr}$ leads to $R_{SV} = 0$, $\phi_{rp} = \tan^{-1}\left(b_{rv}/a_{rv}\right)$. Next, R_{PV} may be computed from Eq (3-148) or Eq (3-149), as appropriate (whether $\cos\phi_{rp} = 0$). Variable R_{PH} and R_{SH} may then be

computed using the Eq (3-150) and Eq (3-151), respectively. Next, defining $G = R_{PV}/R_{PH}$, the angle of incidence for the P wave, θ_{0p}, can be computed using Eq (3-180). Whether the P wave is homogeneous or inhomogeneous is decided based on the limit given by Eq (3-181). The real and complex parts of the Fourier coefficients can be calculated using Eq (3-154) and Eq (3-155).

3.11.2. Hypothesis H2: Power Compatibility

The alternate hypothesis, H2, is based on power compatibility. Two cases are considered, namely, 1) the angle of incidence of the SV wave does not exceed the critical angle, and 2) the angle of incidence of the SV wave exceeds the critical angle.

3.11.2.1. SV Wave Incidence Angle Not Exceeding the Critical Angle

Power associated with any discrete frequency of a time series is proportional to the square of the associated Fourier amplitude (and also with the square of the frequency). Defining the power associated with the r^{th} discrete frequency of the recorded horizontal acceleration and the decomposed P and SV wave contributions as E_H, E_{HP}, and E_{HS}, respectively,

$$E_H = a_{rh}^2 + b_{rh}^2,\ E_{HP} = a_{rhp}^2 + b_{rhp}^2,\ E_{HS} = a_{rhs}^2 + b_{rhs}^2 \tag{3-203}$$

The difference in the power in the recorded and decomposed motion in the horizontal direction, after making use of Eq (3-154), can be written as

$$\begin{aligned} \Delta E_h &= E_H - \left(E_{HP} + E_{HS}\right) = 2\left(a_{rhp}a_{rhs} + b_{rhp}b_{rhs}\right) \\ &= \frac{1}{2} R_{PH} R_{SH} \cos\left(\phi_{rp} - \phi_{rs}\right) \end{aligned} \tag{3-204}$$

Similarly, for the vertical acceleration,

$$\begin{aligned} \Delta E_v &= E_V - \left(E_{VP} + E_{VS}\right) = 2\left(a_{rvp}a_{rvs} + b_{rvp}b_{rvs}\right) \\ &= \frac{1}{2} R_{PV} R_{SV} \cos\left(\phi_{rp} - \phi_{rs}\right) \end{aligned} \tag{3-205}$$

Defining, $\Pi = \left(\Delta E_h\right)^2 + \left(\Delta E_v\right)^2$, the required additional condition is obtained by minimizing Π with respect to ϕ_{rp}. The square of the differential power is considered here as the intent is to minimize the absolute value of the differential power, which leads to $\phi_{rp} - \phi_{rs} = \pm\pi/2$. It is assumed that R_{PH}, R_{SH}, R_{PV} and R_{SV} are not zero. The minimum value of Π is zero and power is conserved in both the horizontal and vertical accelerations. Without loss of generality and taking the positive sign, the required additional condition for $\theta_{0s} \le \theta_{cr}$ is considered as

$$\phi_{rp} = \phi_{rs} + \pi/2 \tag{3-206}$$

Therefore, the procedure to be followed for this case ($\theta_{0s} \le \theta_{cr}$) can be summarized as follows: i) compute R_{PH}, R_{SH}, R_{PV} and R_{SV} from Eq (3-150) through Eq (3-153) after making use of Eq (3-206); ii) define $\overline{G} = R_{SV}/R_{SH}$, and if the limit in Eq (3-173) is satisfied, θ_{0s} may be calculated by solving Eq (3-171); iii) define $G = R_{PV}/R_{PH}$, the angle of incidence for the P wave, θ_{0p} can be computed using Eq (3-180) and whether the P wave is homogeneous or inhomogeneous is decided based on the limit given by Eq (3-181); and iv) calculate the real and complex parts of the Fourier coefficients using Eq (3-154) and Eq (3-155). If the limit in Eq (3-173) is not satisfied, use the procedure for $\theta_{0s} > \theta_{cr}$ that is presented below.

3.11.2.2. SV Wave Incidence Angle Exceeding the Critical Angle

For this case, Eq (3-204) and Eq (3-205) may be expressed as (after substituting Eq (3-165) and Eq (3-166))

$$\Delta E_h = \frac{1}{2} R_{PH} R_{SH} \cos\left(\alpha_1 + \phi_{rp} - \phi_{rs}\right) \tag{3-207}$$

$$\Delta E_v = -\frac{1}{2} R_{PV} R_{SV} \sin\left(\alpha_1 + \phi_{rp} - \phi_{rs}\right) \tag{3-208}$$

where α_1 is given by Eq (3-77). Here, R_{PH}, R_{SH}, R_{PV} and R_{SV} are assumed to be non-zero. Defining, as before, $\Pi = (\Delta E_h)^2 + (\Delta E_v)^2$, the required additional condition is obtained by minimizing Π with respect to ϕ_{rp}, which leads to Eq (3-198) if $(R_{PH}R_{SH})^2 > (R_{PV}R_{SV})^2$ or Eq (3-191) if it is not.

Therefore, the procedure to follow when $\theta_{0s} > \theta_{cr}$ is outlined in Hypothesis H1 in connection with Eq (3-198) and Eq (3-191), respectively, depending upon whether $(R_{PH}R_{SH})^2 > (R_{PV}R_{SV})^2$. The procedure associated with Eq (3-191) should be used first and then a check performed to examine whether $(R_{PH}R_{SH})^2 \le (R_{PV}R_{SV})^2$. If the check is not satisfied, the procedure associated with Eq (3-198) should be used. In a rare instance, the solution might flip-flop: after implementing the procedure associated with Eq (3-198), $(R_{PH}R_{SH})^2 \le (R_{PV}R_{SV})^2$. In this case, use the results obtained using the procedure associated with Eq (3-198).

3.12. Deriving Rotational Components of Ground Motion from a Point Source

The Single Station Procedure described in Sections 3.2 through 3.11 is used here to extract rotational components of motion from translational time series. The translational time series presented in Section 2.5 from the M6.1 event of 1986 are used for this purpose. A point source is assumed. Rotational components of ground motion calculated assuming the (H1) case of equal angle of incidence of P and SV waves, and the (H2) case of power compatibility, are compared below. In each case, the computed rotational acceleration time series is first processed by: i) low-pass filtering the resultant time series with a cut-off frequency of 20 Hz, ii) cosine tapering the first and last 1 second of the recording, and iii) removing the mean of the resultant time series. This processing eliminates the contributions of numerically-induced high frequency response, the source of which is explained as follows.

Consider a harmonic that has almost negligible amplitude (or energy) in the translational motion: real and imaginary parts of the associated Fourier coefficient are close to zero. In this harmonic, the P and SV wave decomposition procedure described above may lead to nearly equal and opposite Fourier coefficients for the P and SV wave but not necessarily of negligible amplitude. This is true for both low and high frequency harmonics. However, its effect may be significant in the high frequency content of the rotational motion because the rotational motion is obtained from the derivative of the translational motion and the process of taking derivative involves multiplication of the Fourier coefficient by the frequency with a phase shift of 90 degrees.

The associated response spectra are then used as the basis for a comparison. A comparison for the torsional spectra and rocking spectra on the *xz* plane (EW direction) and *yz* plane (NS direction) is shown in Figures 3-2 through 3-4.

The two hypotheses differ only in terms of deriving the required additional condition that is used to compute the P and SV wave contributions to the total horizontal and vertical accelerations on the principal plane. The SH wave contribution is the acceleration history along the direction normal to the principal axis and is identical for both methods. Since torsional motion is calculated from the SH wave contribution only, and despite its dependency on the angle of incidence and thereby on the P and SV wave decomposition, it is expected that the torsional motion computed using the two methods will not differ significantly, which is confirmed by a comparison of the torsional spectra presented in Figure 3-2.

The rocking motion is computed from the vertical acceleration and thus depends on the P and SV wave contributions to the vertical acceleration. The two hypotheses are expected to produce different rocking motions. This is evident from comparisons of the rocking spectra on the *xz* plane (Figure 3-3) and on the *yz* plane (Figure 3-4). Further, the spectral demand predicted assuming an equal angle of incidence for the P and SV waves (H1) is significantly greater than that predicted assuming power compatibility (H2) if the time period is small. For large time periods, the spectra are nearly the same. This observation

is attributed to the power compatibility criterion that ensures the differential power between the recorded and decomposed motion is minimized.

3.13. A Composite Method (H3)

The physical interpretation of the H1 hypothesis is a point source within a homogeneous halfspace. In reality, wave scattering along the source-to-station travel path due to variations in the layers and material properties in each layer will result in different angles of incidence for the P and SV waves at the free surface. This difference increases at higher frequencies as the effect of scattering is generally more pronounced at shorter wavelengths. The assumption of equal angle of incidence for the P and SV waves (H1) should therefore be limited to the low frequency harmonics. The power compatibility criteria (H2) is more suitable for the high frequency harmonics.

On this basis, a composite method (H3) is presented that assumes the H2 hypothesis at higher harmonics and the H1 hypothesis at lower harmonics. The geometric mean (geomean) spectrum of the horizontal and vertical spectra on the principal plane is used to establish the transition period between the lower and higher harmonics. Regions of constant acceleration and constant velocity are then used to idealize the geomean spectrum. The transition period, TP, is set equal to the time period at the midpoint of the constant acceleration region. Figure 3-5 illustrates the calculation of the transition period for station FA1_1.

The TP is closely associated with the P and SV wave decomposition of the horizontal and vertical accelerations on the principal plane and has a greater influence on the rocking motion than the torsional motion. Horizontal and vertical motions contribute to rocking on the principal plane and so the geometric mean spectrum best characterizes the combined effects. However, the selection of the mid-point of the constant acceleration region as the transition period is subjective and influences the resulting spectral shape in the immediate vicinity. The TPs associated with each station are listed in Table 3-1.

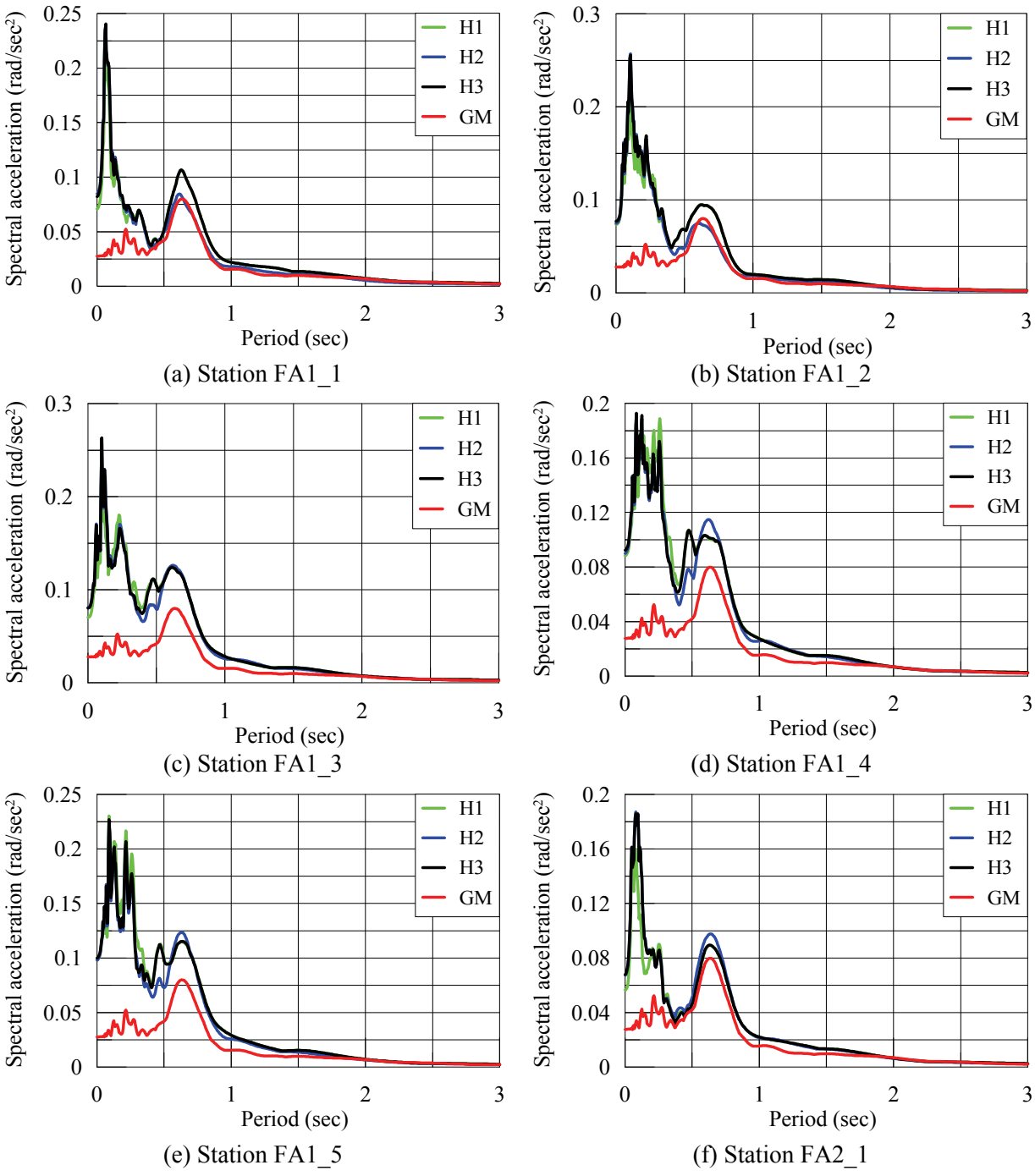

Figure 3-2: Torsional spectra computed using three different hypotheses and geodetic method (cont.)

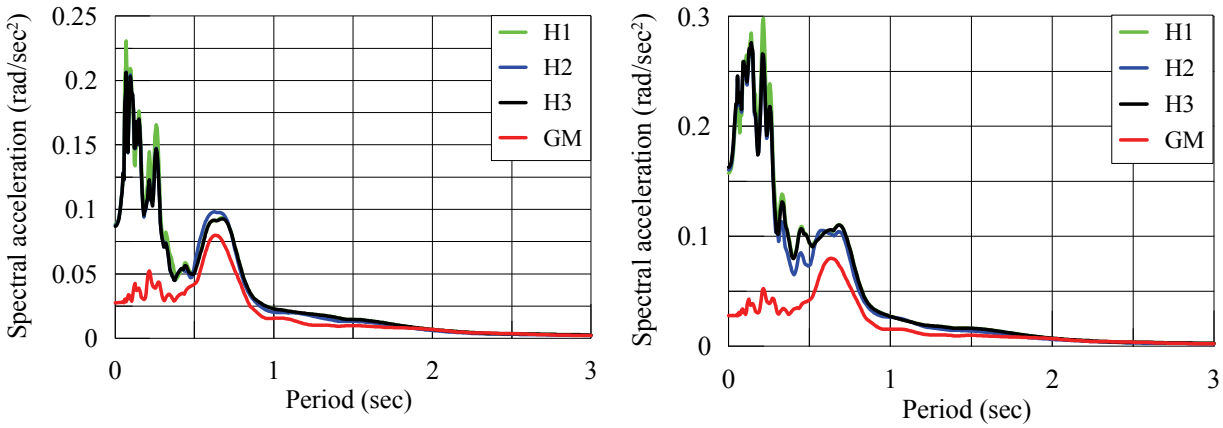

(g) Station FA2_2

(h) Station FA2_3

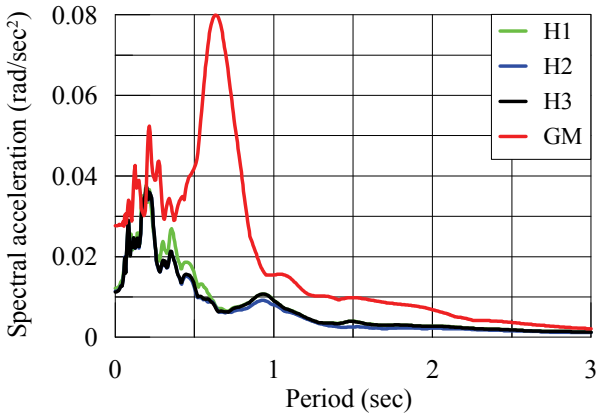

(i) Station FA2_4

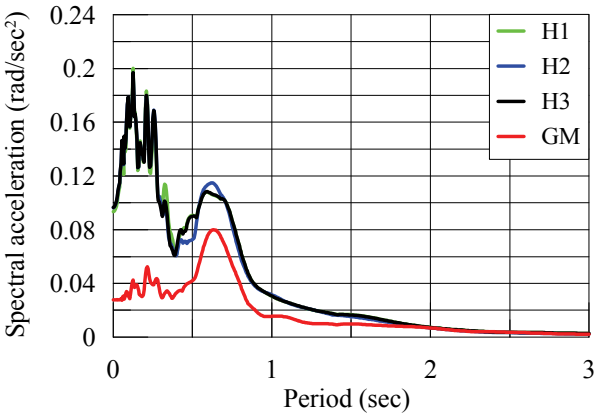

(j) Station FA2_5

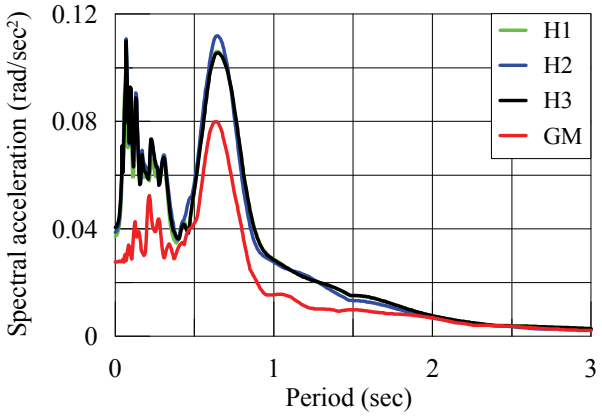

(k) Station FA3_1

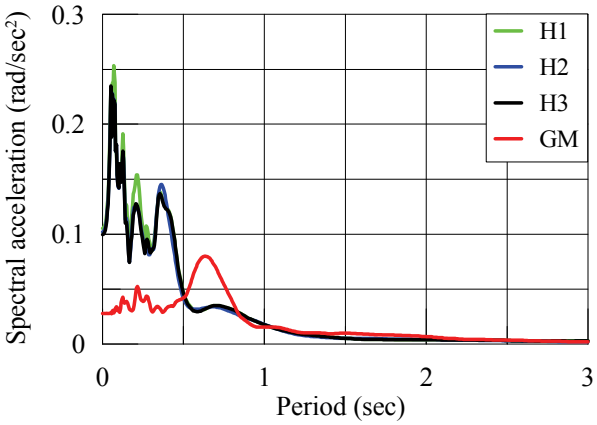

(l) Station FA3_2

Figure 3-2: Torsional spectra computed using three different hypotheses and geodetic method (cont.)

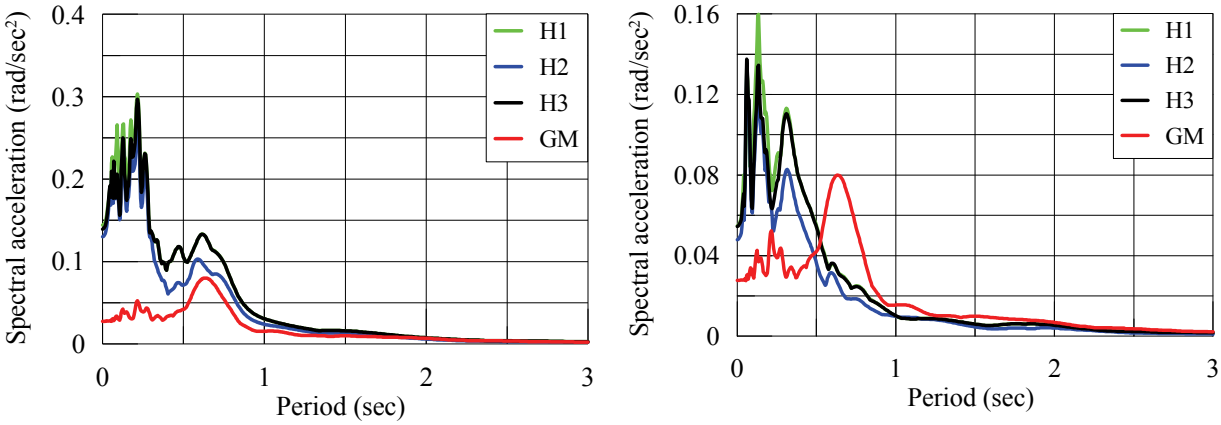

(m) Station FA3_3

(n) Station FA3_4

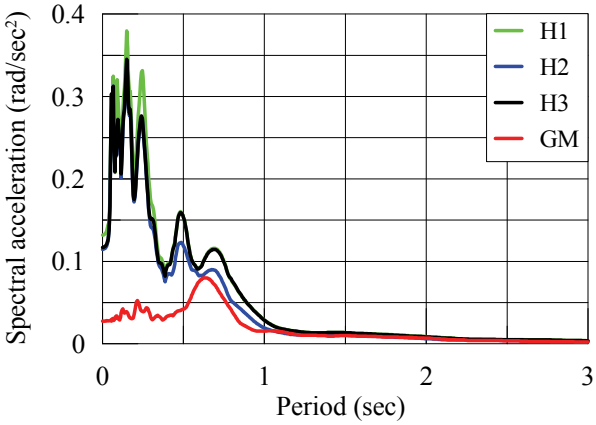

(o) Station FA3_5

Figure 3-2: Torsional spectra computed using three different hypotheses and geodetic method

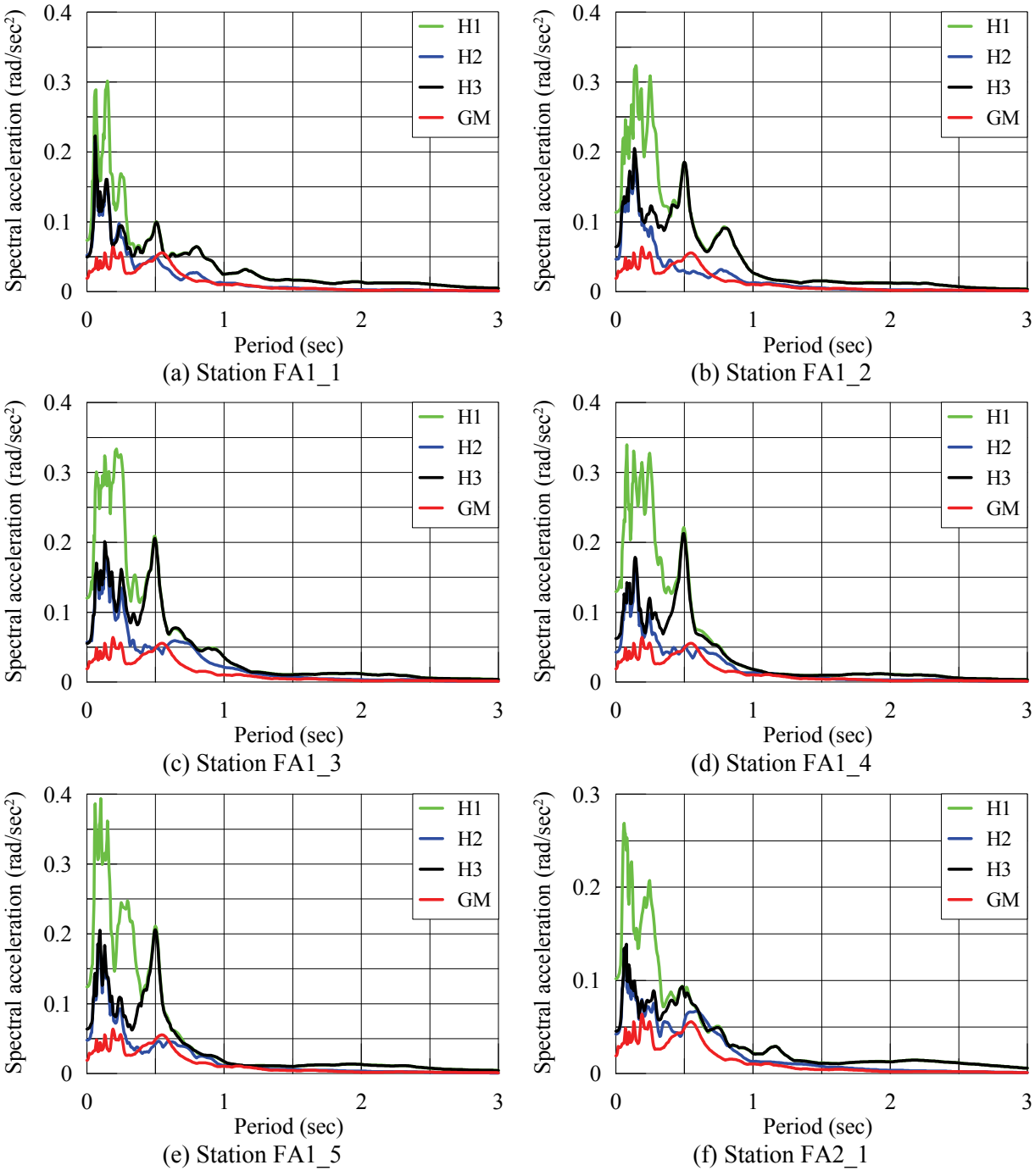

Figure 3-3: Rocking (*xz* plane) spectra computed using three different hypotheses and geodetic method (cont.)

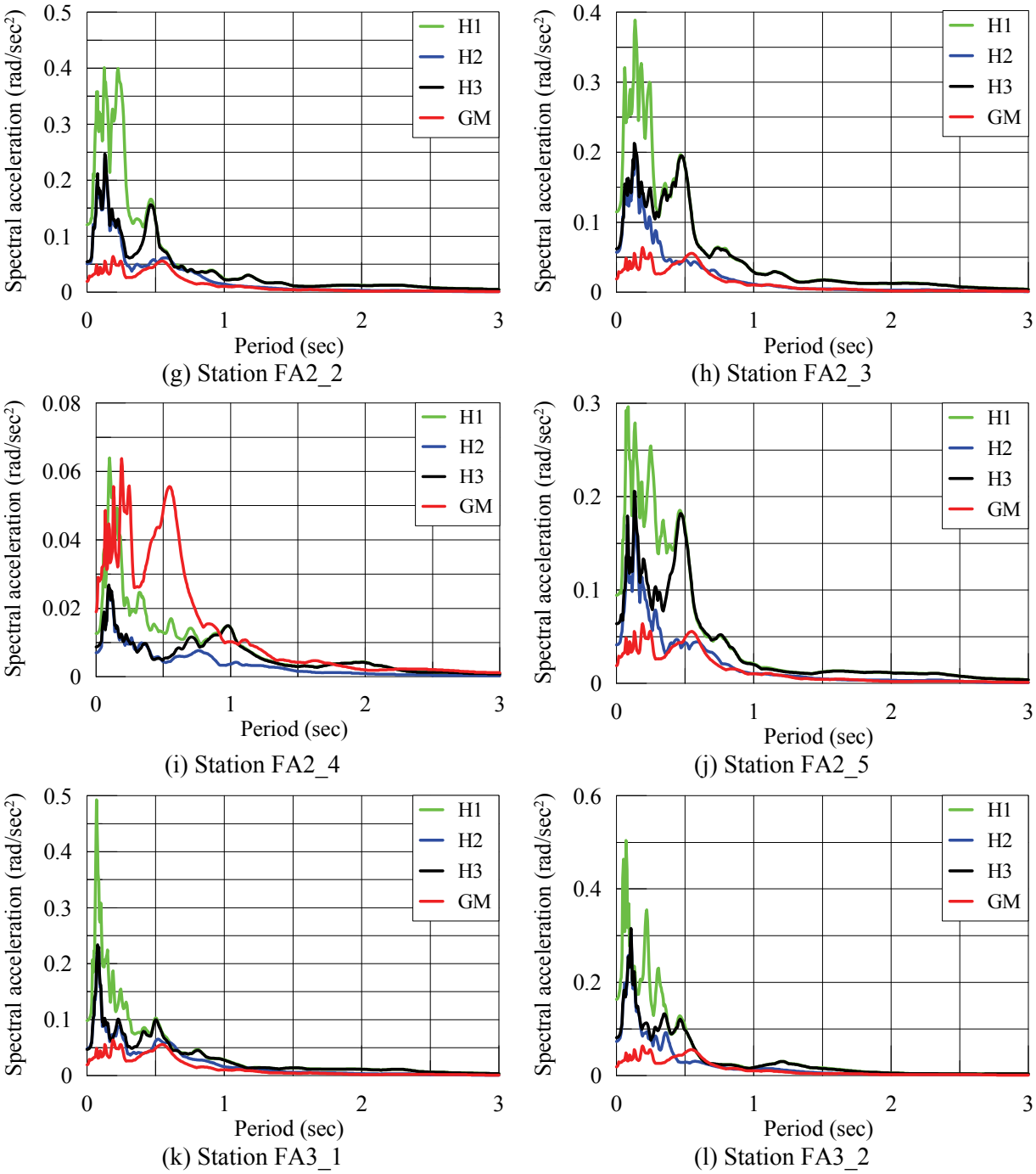

Figure 3-3: Rocking (*xz* plane) spectra computed using three different hypotheses and geodetic method (cont.)

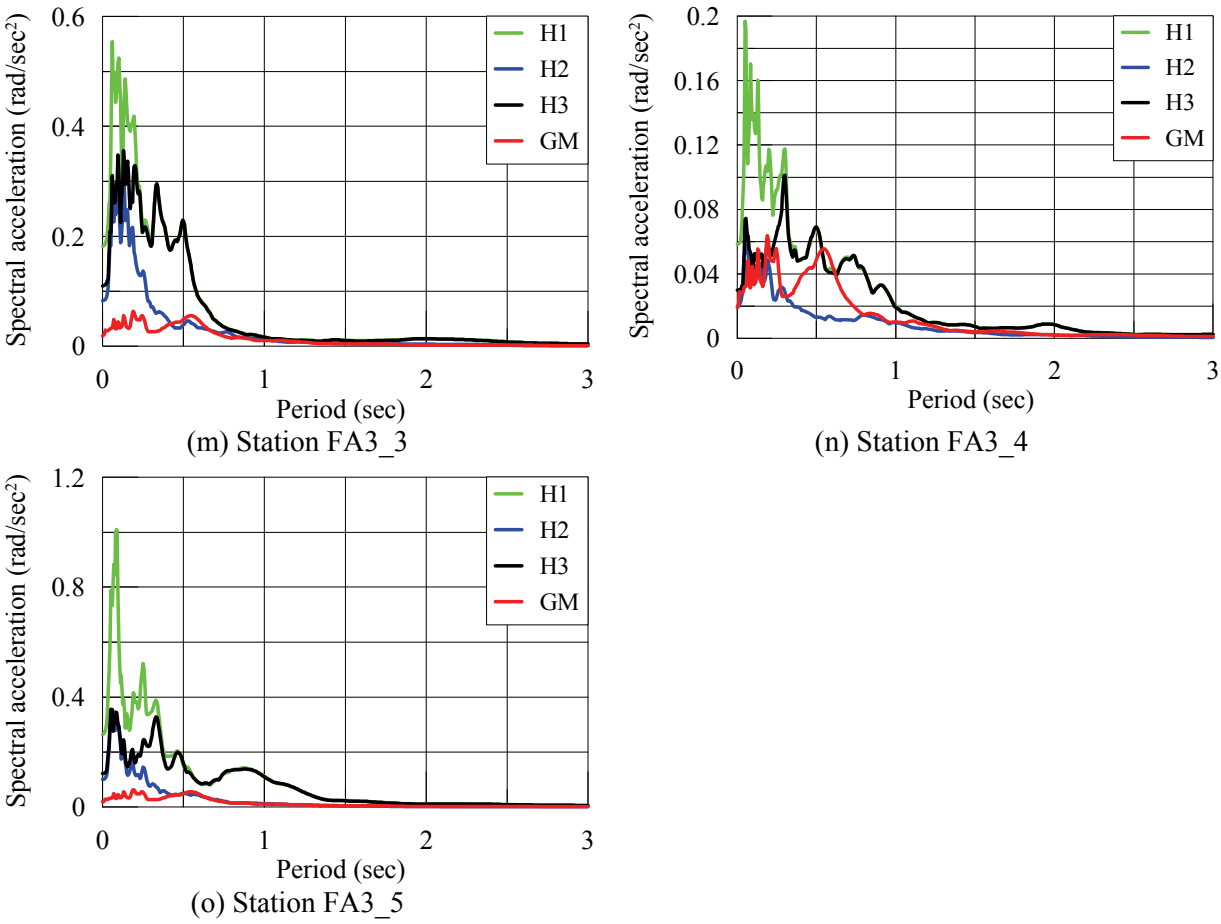

Figure 3-3: Rocking (*xz* plane) spectra computed using three different hypotheses and geodetic method

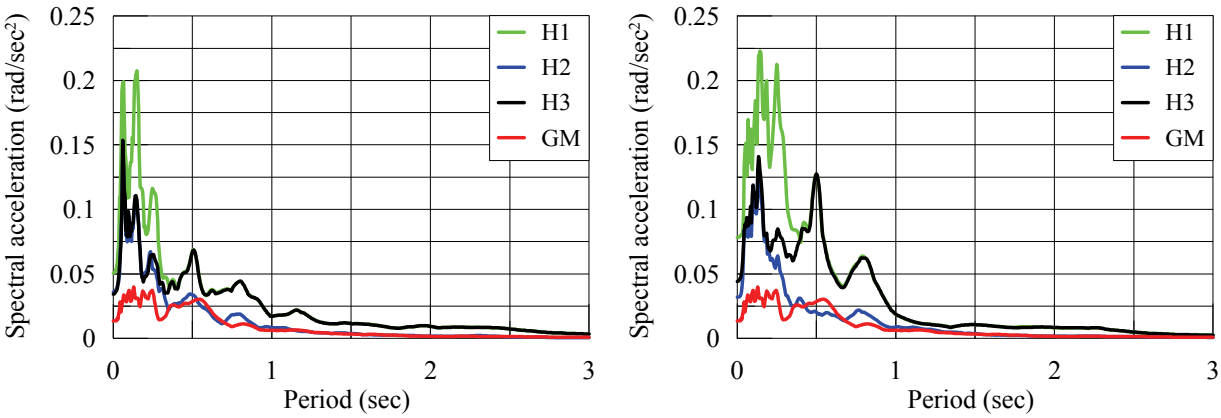

(a) Station FA1_1

(b) Station FA1_2

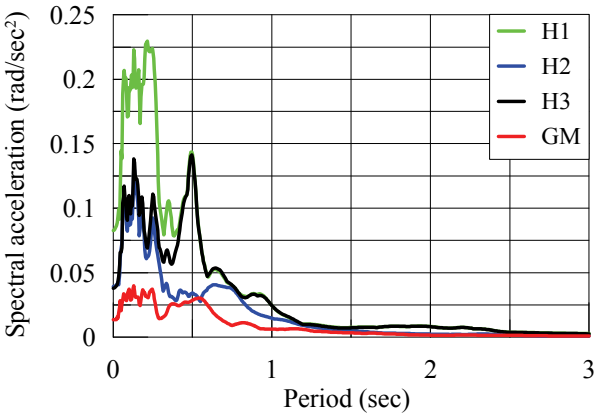

(c) Station FA1_3

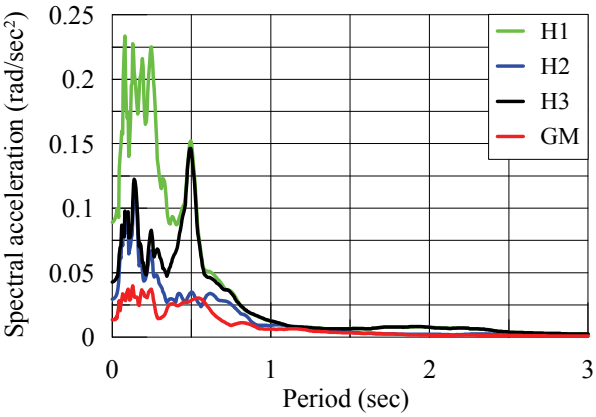

(d) Station FA1_4

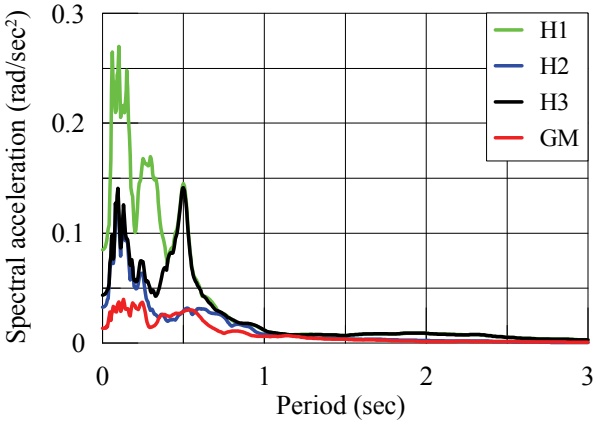

(e) Station FA1_5

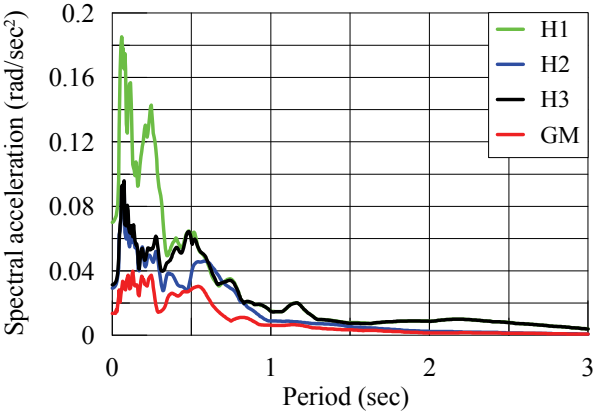

(f) Station FA2_1

Figure 3-4: Rocking (*yz* plane) spectra computed using three different hypotheses and geodetic method (cont.)

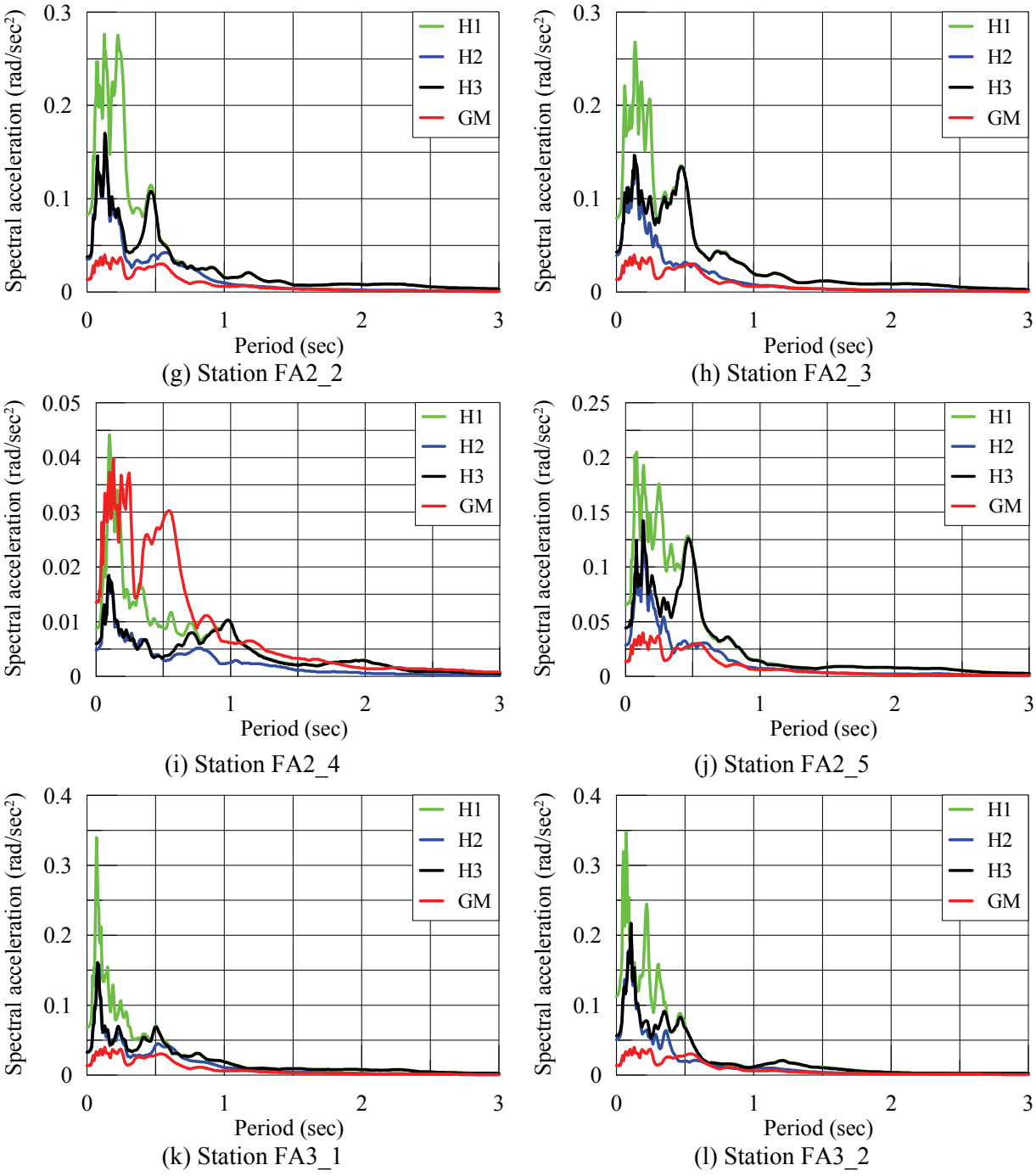

Figure 3-4: Rocking (*yz* plane) spectra computed using three different hypotheses and geodetic method (cont.)

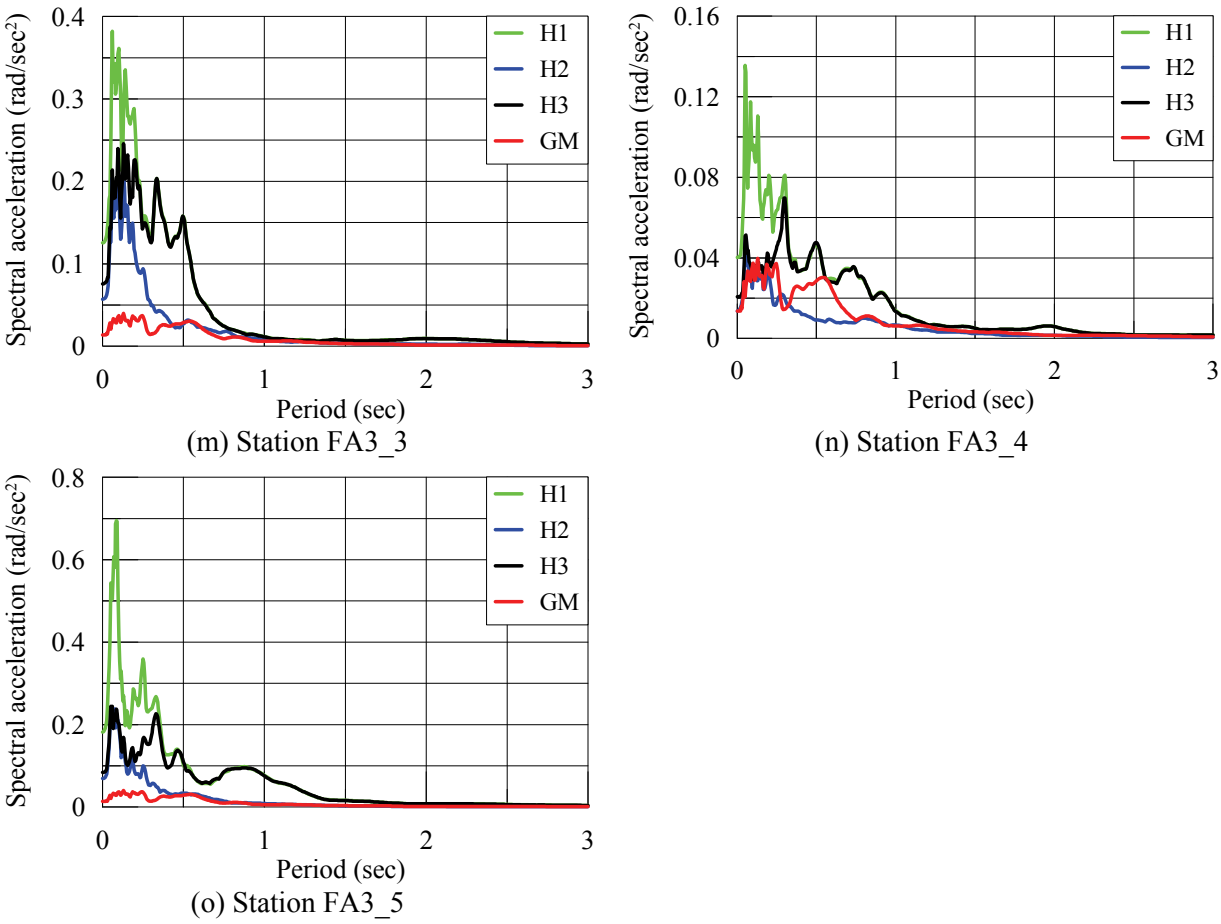

Figure 3-4: Rocking (*yz* plane) spectra computed using three different hypotheses and geodetic method

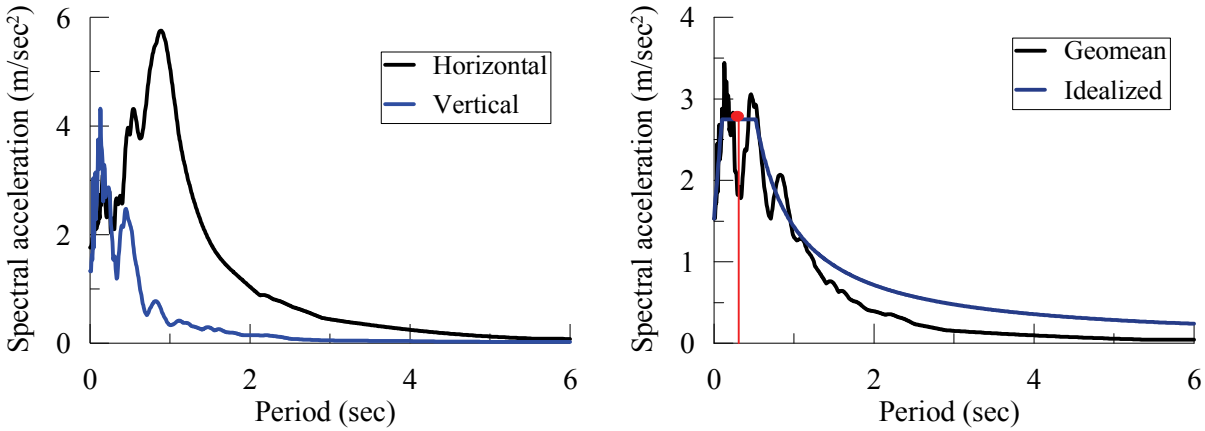

(a) Horizontal and vertical spectra on principal plane

(b) Geomean spectra and its idealization

Figure 3-5: Calculation of transition period at station FA1_1

Table 3-1: Critical Time Period (CTP) associated with different stations

Station	Critical Time Period (sec)
FA1_1	0.31
FA1_2	0.34
FA1_3	0.41
FA1_4	0.38
FA1_5	0.37
FA2_1	0.39
FA2_2	0.40
FA2_3	0.34
FA2_4	0.60
FA2_5	0.37
FA3_1	0.39
FA3_2	0.32
FA3_3	0.20
FA3_4	0.28
FA3_5	0.30

3.14. Comparison of Composite Method (H3) and Hypothesis 1 and 2

The resulting rotational acceleration spectra computed based on H3 are shown in Figures 3-2 through 3-4. As expected, the torsional spectra (Figure 3-2) are identical in all three cases. For rocking motion, the spectra for H3 follow those of H2 for short time periods and H1 for medium to long time periods. This trend is seen for both rocking on the *xz* plane (the vertical plane in the EW direction, see Figure 3-3) and on the *yz* plane (the vertical plane in the NS direction, see Figure 3-4). On the basis of these data, the composite method (H3) is used in the remainder of this chapter.

3.15. Finite Rupture Length

The procedure developed in the previous section assumes the fault to be a point source, with the previously described limitations. This assumption is set aside here and the composite (H3) procedure is extended to consider a finite length of fault rupture, which extends its applicability to large magnitude earthquakes and/or small site-to-source distances. Two scenarios are considered: 1) bi-lateral rupture symmetric about the principal plane, and 2) bi-lateral rupture offset about the principal plane (arbitrary location of the hypocenter).

3.15.1. Symmetric Bi-lateral Fault Rupture

Figure 3-6 describes the fault plane and source-to-site travel path. In this figure, C' is considered as the point representation of the source (fault) with focal depth D and C as the associated epicenter. Let the rupture initiate at C', the mid-point of the observed ruptured length L, and propagate with uniform velocity V_r along the fault plane on each side of C'. Seismic energy will be generated first at point C' and the resulting waves will propagate along the principal plane $C'CO$ (or simply *C*) to reach the site. After some finite time, equal to the distance between B' and C' divided by V_r, the rupture will have

propagated to point B' and the resulting waves will propagate along the principal plane $B'BO$ (or simply B) to reach the site.

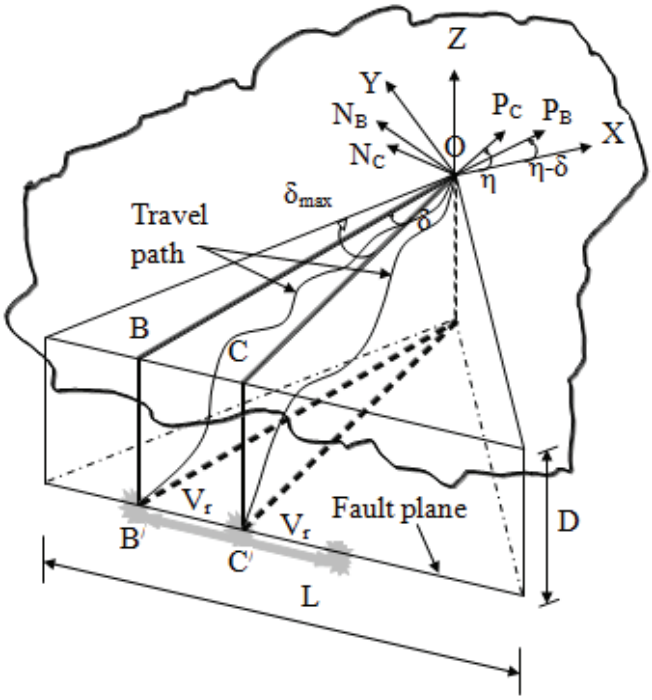

Figure 3-6: Evolution of principal planes with the propagation of fault rupture

There is a time delay at the recording site between the arrival times in the waves travelling on the principal planes *B* and *C*. Let this time delay be $t_B = t_{B1} + t_{B2}$, where t_{B1} is due to the propagation of rupture from point C' to point B' and t_{B2} is the difference in time for waves traveling from the points B' and C' to the site *O* following the actual travel paths as indicated in Figure 3-6. For simplicity, consider: a) the travel path as the straight line joining the point of rupture to the site, b) in computing t_{B2}, the wave velocity as the average of the P and S wave velocity, c) the wave velocity is constant in the region, and d) the rupture velocity is constant. Accordingly,

$$t_{B1} = \overline{B'C'}/V_r = S\tan\delta_B/V_r$$
$$t_{B2} = \frac{2}{\left(C_L + C_T\right)}\left[\left\{\left(\frac{S}{\cos\delta_B}\right)^2 + D^2\right\}^{\frac{1}{2}} - \left(S^2 + D^2\right)^{\frac{1}{2}}\right] \tag{3-209}$$

where $S = \overline{CO}$ is the epicentral distance, which is assumed to be normal to the fault plane in the absence of site-specific information.

For any incident wave travelling along the principal plane C, the associated displacement field due to the r^{th} mode of wave propagation is given by

$$\begin{aligned} {}^{c}_{r}u_l &= A_r d_l \exp\left(i\eta^c\right) \\ \eta^c &= rk\left(x_m p_m - ct\right) - \phi_r \end{aligned} \tag{3-210}$$

Here the superscript c denotes the principal plane along which the wave has travelled. Note that the resulting particle displacement (horizontal) will be along P_C due to P and SV waves and along N_C due to the SH waves.

On the basis of the assumptions made above, the displacement field (r^{th} harmonic) due to waves travelling along principal plane B is given by

$$\begin{aligned} {}^{b}_{r}u_l &= A_r d_l \exp\left(i\eta^b\right) \\ \eta^b &= rk\left[x_m p_m - c\left(t - t_B\right)\right] - \phi_r \end{aligned} \tag{3-211}$$

However, the associated particle displacement (horizontal) will be along P_B due to P and SV waves and along N_B due to SH waves. Eq (3-210) and Eq (3-211) differ from each other only in terms of time delay t_B. Denote $\bar{a}_{pc}(\omega_r)$, $\bar{a}_{nc}(\omega_r)$ and $\bar{a}_{vc}(\omega_r)$ as the FFT of the particle acceleration along P_C, N_C and the vertical directions, respectively, in the r^{th} harmonic due to a wave travelling along the principal plane C. Using a shift theorem, the FFT of the particle acceleration along P_B, N_B and vertical directions in the r^{th} mode of propagation due to wave travelling along the principal plane B are given by $\exp\left(-i\omega_r t_B\right)\bar{a}_{pc}(\omega_r)$, $\exp\left(-i\omega_r t_B\right)\bar{a}_{nc}(\omega_r)$ and $\exp\left(-i\omega_r t_B\right)\bar{a}_{vc}(\omega_r)$, respectively.

Now, let $\delta_{\max} = \tan^{-1}\left(0.5L/S\right)$ be the angle between the bounding principal plane and the principal plane C. Discretizing the angle $\delta_{\max}$ into *m* uniform intervals, consider a total of m principal planes on either side of the principal plane C. Computing the FFT of accelerations for all the principal planes and then equating the sum along the *x*, *y* and *z* directions with the FFT of the respective measured accelerations [$A_x(\omega_r)$, $A_y(\omega_r)$ and $A_z(\omega_r)$],

$$\begin{aligned}
\bar{a}_{pc}(\omega_r) &= \frac{1}{\sigma}\left[A_x(\omega_r)\cos\eta + A_y(\omega_r)\sin\eta\right] \\
\bar{a}_{nc}(\omega_r) &= \frac{1}{\sigma}\left[A_y(\omega_r)\cos\eta - A_x(\omega_r)\sin\eta\right] \\
\bar{a}_{vc}(\omega_r) &= \frac{1}{\sigma}\left[A_z(\omega_r)\right]
\end{aligned} \tag{3-212}$$

where

$$\begin{aligned}
\sigma &= 1 + 2\sum_{i=1}^{m}\exp\left(-i\omega_r t_i\right)\cos\delta_i \\
\bar{\sigma} &= 1 + 2\sum_{i=1}^{m}\exp\left(-i\omega_r t_i\right)
\end{aligned} \tag{3-213}$$

Here, δ_i is the orientation angle of the i^{th} principal plane with respect to the principal plane C; and t_i is the associated time delay given by

$$t_i = \frac{S\tan\delta_i}{V_r} + \frac{2}{\left(C_L + C_T\right)}\left[\left\{\left(\frac{S}{\cos\delta_i}\right)^2 + D^2\right\}^{\frac{1}{2}} - \left(S^2 + D^2\right)^{\frac{1}{2}}\right] \tag{3-214}$$

and η is the orientation angle of the principal plane C with respect to the x axis in a counterclockwise direction. Knowing the FFT of the horizontal acceleration along and normal to the principal plane, and also that of the associated vertical component due to the wave propagation only along the principal plane C [from Eq (3-212)], the FFT of the accelerations associated with the wave propagation along any other principal plane (say i^{th}) may be computed as

$$\begin{aligned}
\bar{a}_{pi}(\omega_r) &= \exp(-i\omega_r t_i)\bar{a}_{pc}(\omega_r) \\
\bar{a}_{ni}(\omega_r) &= \exp(-i\omega_r t_i)\bar{a}_{nc}(\omega_r) \\
\bar{a}_{vi}(\omega_r) &= \exp(-i\omega_r t_i)\bar{a}_{vc}(\omega_r)
\end{aligned} \tag{3-215}$$

Eq (3-215) can then be used to estimate the associated rotational acceleration components. For the torsional component, the algebraic sum of the contributions from each principal plane leads to the total torsional component at the site (station). However, in the case of rocking motion on the *xz* and *yz* planes, the vector sum of the contributions from each principal plane needs to be computed.

3.15.2. Asymmetrical Bi-lateral Fault Rupture

In the previous case, the initiation of rupture was assumed to be at the mid-point of the ruptured length of the fault. This assumption is relaxed here. Consider the rupture initiating at point C' and extending over different distances on either side of the principal plane C. Discretize the total angle made by the two bounding principal planes at the site into $(m+n)$ equal intervals so there are m and n principal planes on the left and right sides, respectively, of the principal plane C. Now following the same procedure presented above for symmetric rupture, Eq (3-212) may be expressed as

$$\begin{aligned}
\bar{a}_{pc}(\omega_r) &= \frac{1}{\sigma_1^2+\sigma_2^2}\left[\sigma_1 A_x(\omega_r)+\sigma_2 A_y(\omega_r)\right] \\
\bar{a}_{nc}(\omega_r) &= \frac{1}{\sigma_1^2+\sigma_2^2}\left[\sigma_1 A_y(\omega_r)-\sigma_2 A_x(\omega_r)\right] \\
\bar{a}_{vc}(\omega_r) &= \frac{1}{\sigma^*}\left[A_z(\omega_r)\right]
\end{aligned} \tag{3-216}$$

where

$$\begin{aligned}
\sigma_1 &= \cos\eta + \sum_{i=1}^{m}\exp(-i\omega_r t_i)\cos(\eta+\delta_i) + \sum_{j=1}^{n}\exp(-i\omega_r t_j)\cos(\eta-\delta_j) \\
\sigma_2 &= \sin\eta + \sum_{i=1}^{m}\exp(-i\omega_r t_i)\sin(\eta+\delta_i) + \sum_{j=1}^{n}\exp(-i\omega_r t_j)\sin(\eta-\delta_j) \\
\sigma^* &= 1 + \sum_{i=1}^{m}\exp(-i\omega_r t_i) + \sum_{j=1}^{n}\exp(-i\omega_r t_j)
\end{aligned} \tag{3-217}$$

The remainder of the procedure is identical to that discussed in the Section 3.15.1 for symmetrical rupture.

3.15.3. Results and Discussions on Effect of Fault Rupture

To account for finite rupture length, the rupture length and the angle of orientation of the fault with respect to the principal plane *C* are estimated first. In the absence of recorded information, the empirical relationship reported in the literature by Wells and Coppersmith (1994) is used to estimate the rupture length. For the case studied here, the ruptured length is approximately 10 km. The fault plane is assumed to be perpendicular to the principal plane *C* and the rupture velocity is assumed to be 2 km/sec on either side of the hypocenter.

Rotational spectra resulting from four different assumptions are compared: 1) the fault as a point source (H3), 2) fault rupture that propagates symmetrically on either side of the principal plane *C*, 3) rupture initiates at the left-quarter point (denoted here as *left offset*), and 4) rupture initiates at the right-quarter point (denoted here as *right offset*). The torsional spectra and rocking spectra on the *xz* and *yz* planes are shown in Figures 3-7 through 3-9, respectively. The computer program with illustrations on the single station procedure are presented in Appendix E.

The rotational spectra (torsion and both rocking components) resulting from the point-source modeling and symmetric fault rupture modeling are similar, which is expected because of the assumptions of uniform rupture mechanism and symmetry of the ruptured length on either side of the principal plane, *C*. Unsymmetrical fault rupture has an effect on the rotational spectra: small for the torsional spectra but significant for the rocking spectra, especially rocking on the *yz* plane. The effect of the initiation point, in general, depends on the recorded motion and cannot be generalized. If the information on the rupture process is known (as is generally is the case after an earthquake), this procedure presents a simple way to account for such information and computing the rotational components of ground motion at a site.

3.16. A Comparison of the Single Station Procedure and the Geodetic Method

The geodetic method (GM) of Spudich et al. (1995) calculates one torsional motion and two rocking motions for an entire array of recording stations. Rotational spectra computed using the geodetic method, as presented in Chapter 2, are reproduced in Figures 3-2 through 3-4. The results are compared here with those obtained using H3. The spectral ordinates are similar at longer periods (i.e., periods greater than 1 sec) but the spectral ordinates computed using the geodetic method are significantly smaller at shorter periods. Figures 3-10 through 3-12 enable a comparison of the torsional and rocking histories at four selected stations. The high frequency contents of the H3 histories are much richer than those of the GM because:

1) Rotational spectra computed using the geodetic method with surface stations are independent of material properties and thus wave velocities (to be discussed in Chapter 4). The SSP employed here is sensitive to the wave velocities. The values used per Wen and Yeh (1984) appear to be too low.
2) At any time instant, the distribution surface of the recorded data on the horizontal plane takes the form of a wave that is approximated as a best-fit plane surface in the geodetic method. The high frequency components are averaged, leading to the underestimation of the spectral ordinates at low periods.

It can be argued that neglecting the surface wave contributions has some effects on the mismatch noted above at shorter periods. However, note that the epicentral distance in this case (20 km) is similar to that of the study of Castellani and Boffi (1989) and they note that the contribution of the surface waves at frequencies greater than 1 Hz is negligible.

To support the second statement, the H3 rotational histories (one torsional and two rocking) are averaged over all 15 surface stations. The averaged histories are plotted in Figure 3-13 together with histories generated using the GM. There is a better match between the averaged H3 time series and the

GM times series than at individual stations (Figures 3-10 through 3-12) because the GM delivers rotational components that are effectively a weighted average of the free field components at all surface stations considered.

The SSP method assumes the soil medium is a homogeneous, elastic half space. The soil profile at the Lotung site is layered (Wen and Yeh, 1984) and thus inhomogeneous. The body waves arriving at the surface recording stations will likely have many angles of incidence associated with reflections and refractions at the boundaries of the layers in the soil profile.

For completeness, the translational acceleration histories recorded at the station FA1_1 are presented in Figure 3-14. These translational histories could be used with the rotational histories presented in the panels a of Figures 3-10, 3-11 and 3-12 to fully describe the *free field* earthquake ground motion at station FA1_1.

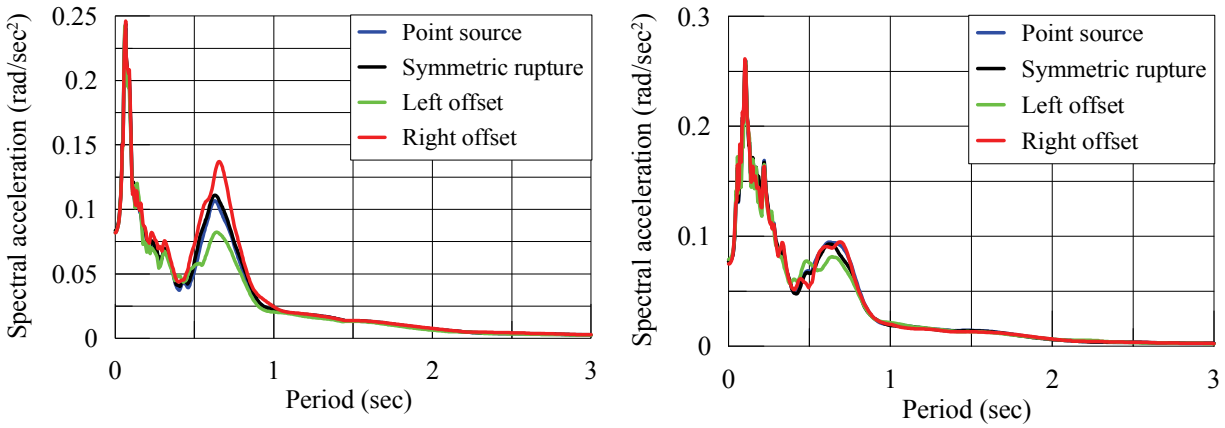

(a) Station FA1_1

(b) Station FA1_2

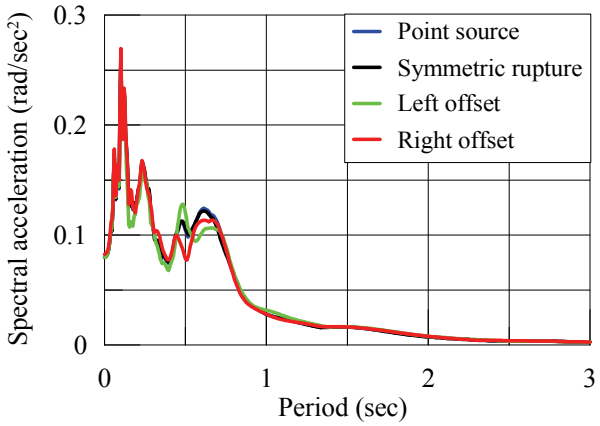

(c) Station FA1_3

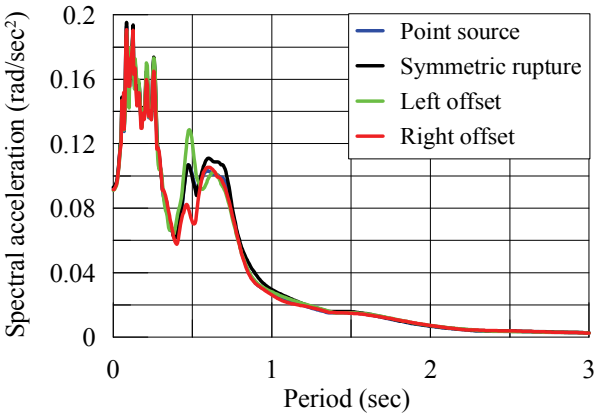

(d) Station FA1_4

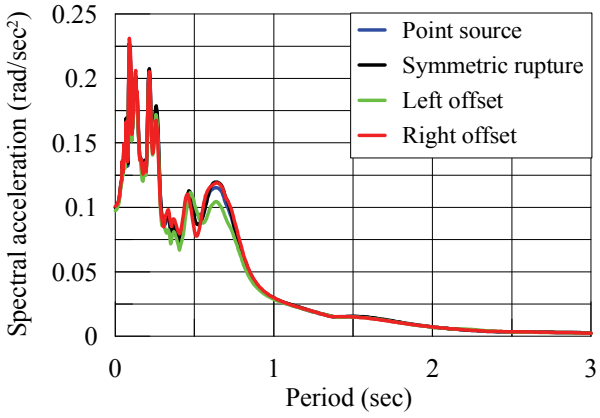

(e) Station FA1_5

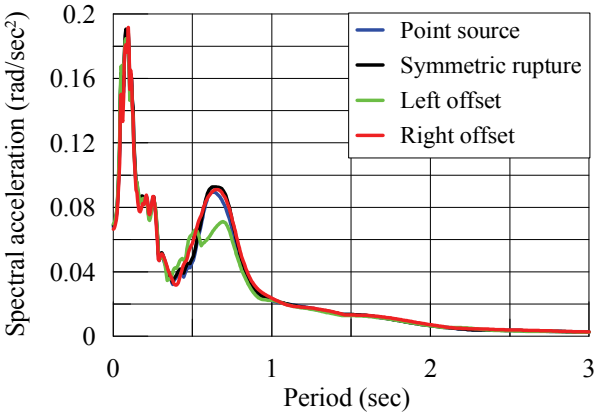

(f) Station FA2_1

Figure 3-7: Effect of rupture on torsional spectra (cont.)

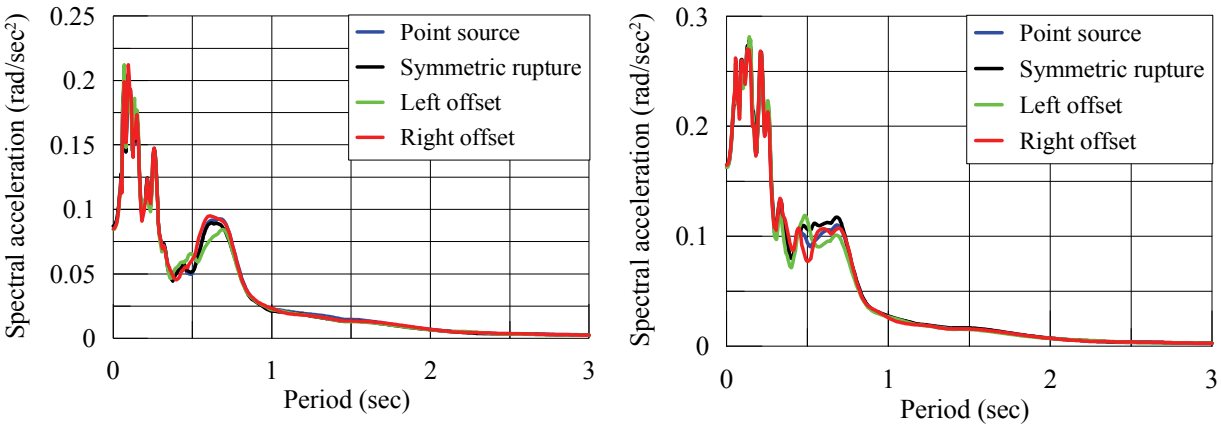

(g) Station FA2_2

(h) Station FA2_3

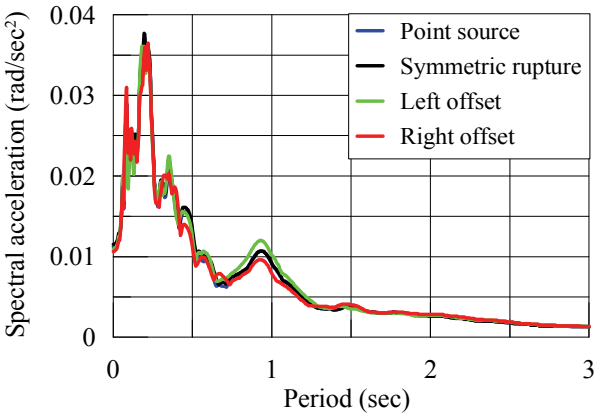

(i) Station FA2_4

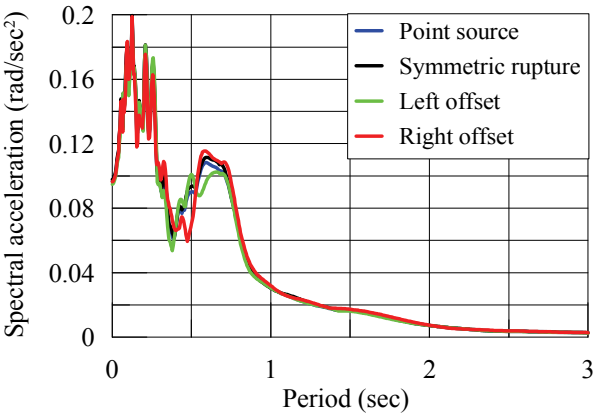

(j) Station FA2_5

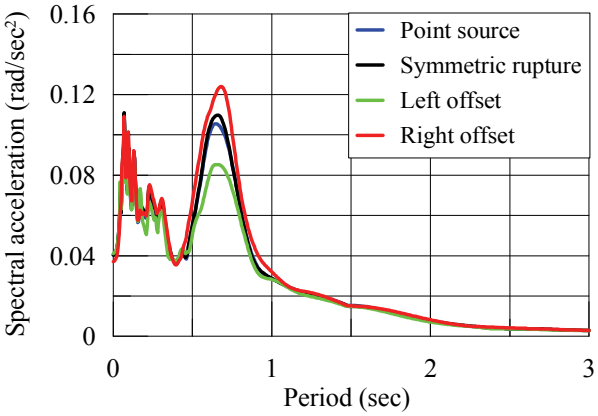

(k) Station FA3_1

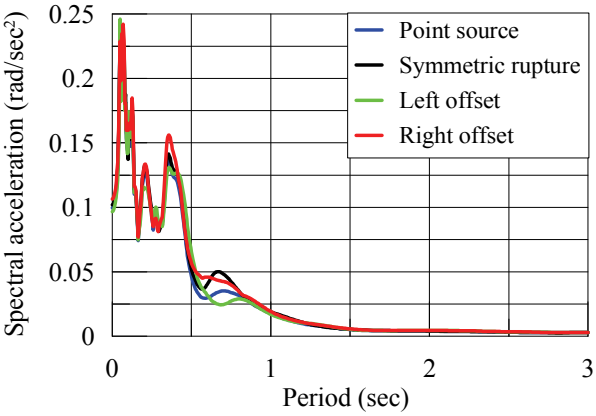

(l) Station FA3_2

Figure 3-7: Effect of rupture on torsional spectra (cont.)

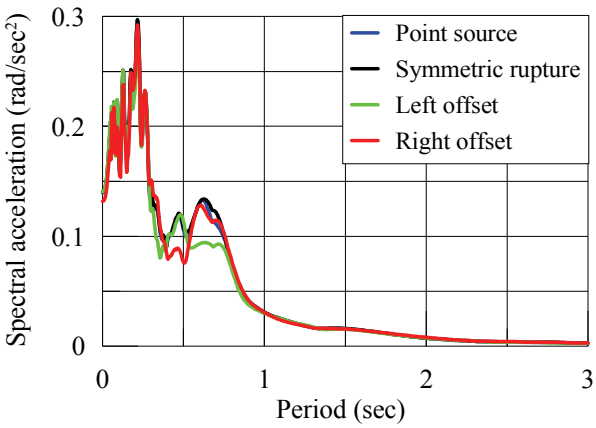

(m) Station FA3_3

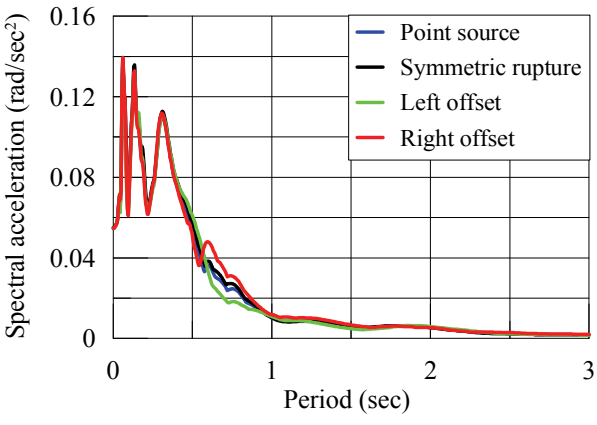

(n) Station FA3_4

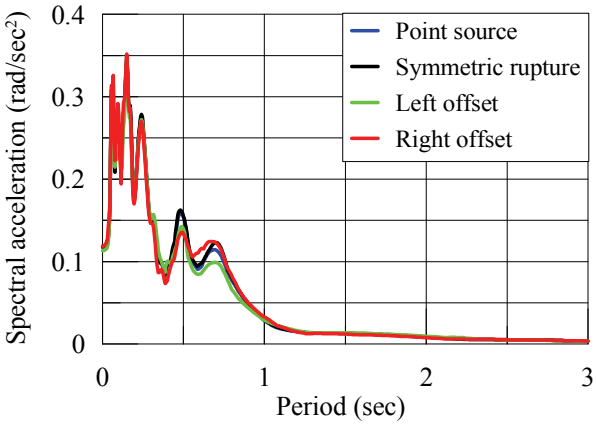

(o) Station FA3_5

Figure 3-7: Effect of rupture on torsional spectra

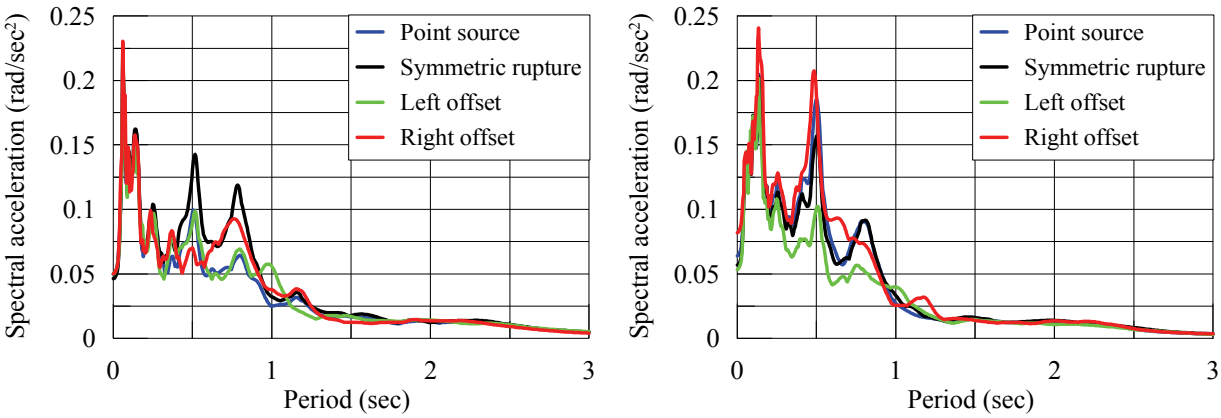

(a) Station FA1_1

(b) Station FA1_2

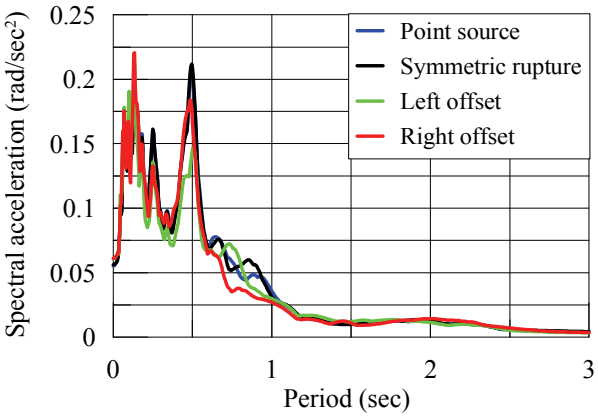

(c) Station FA1_3

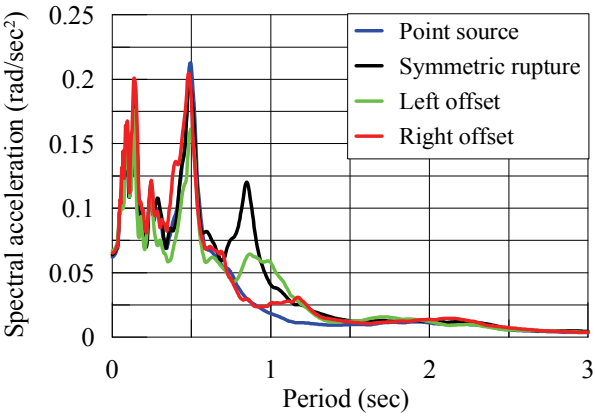

(d) Station FA1_4

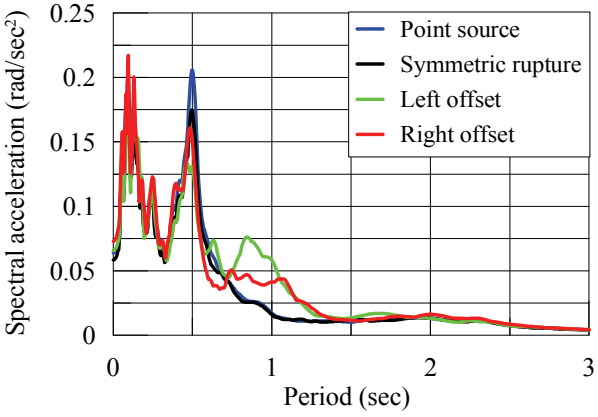

(e) Station FA1_5

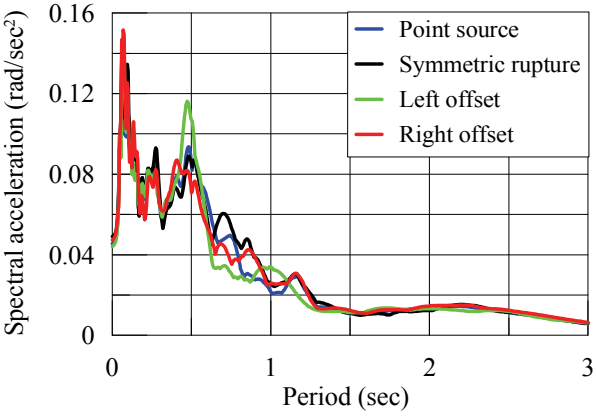

(f) Station FA2_1

Figure 3-8: Effect of rupture on rocking (*xz* plane) spectra (cont.)

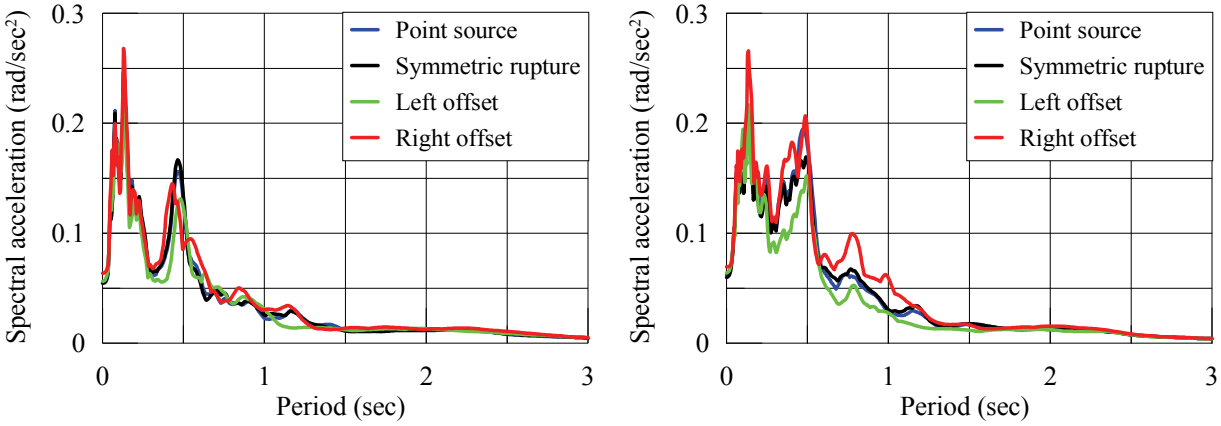

(g) Station FA2_2 (h) Station FA2_3

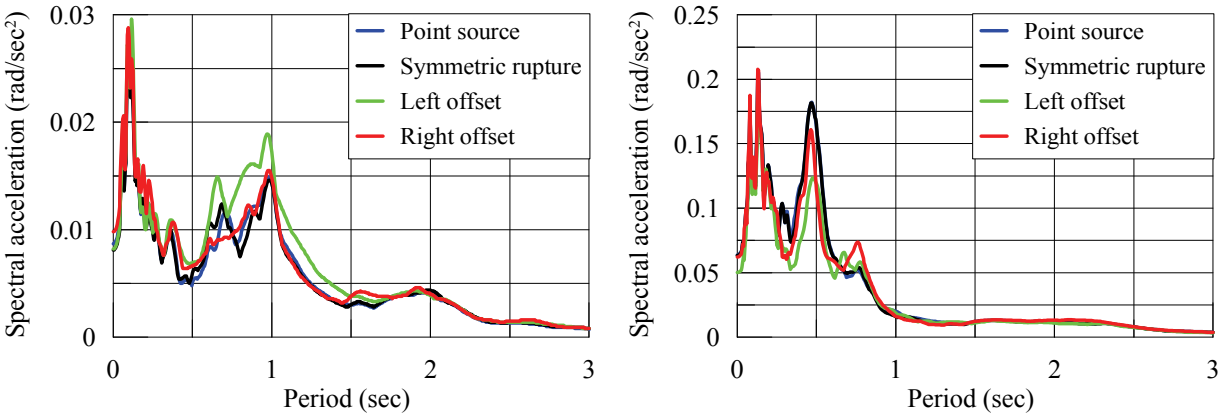

(i) Station FA2_4 (j) Station FA2_5

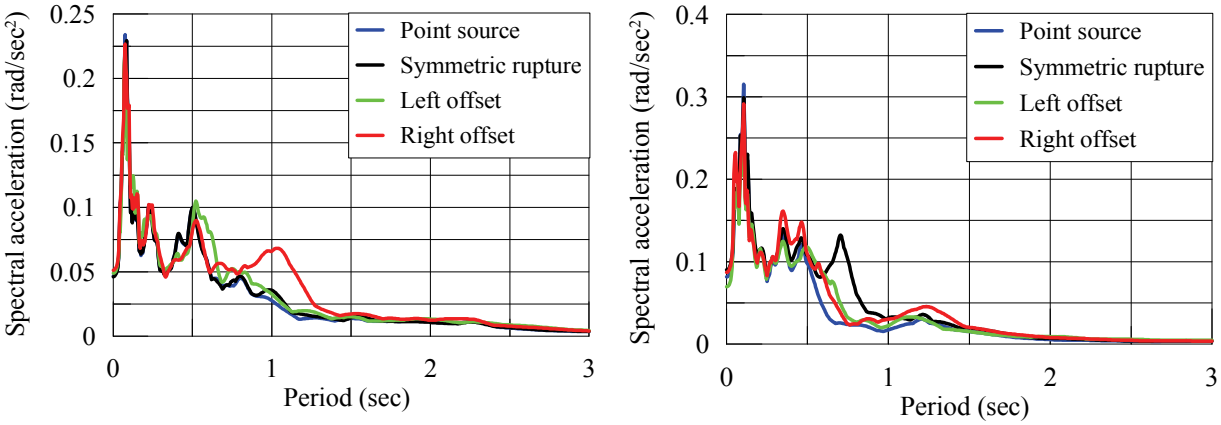

(k) Station FA3_1 (l) Station FA3_2

Figure 3-8: Effect of rupture on rocking (*xz* plane) spectra (cont.)

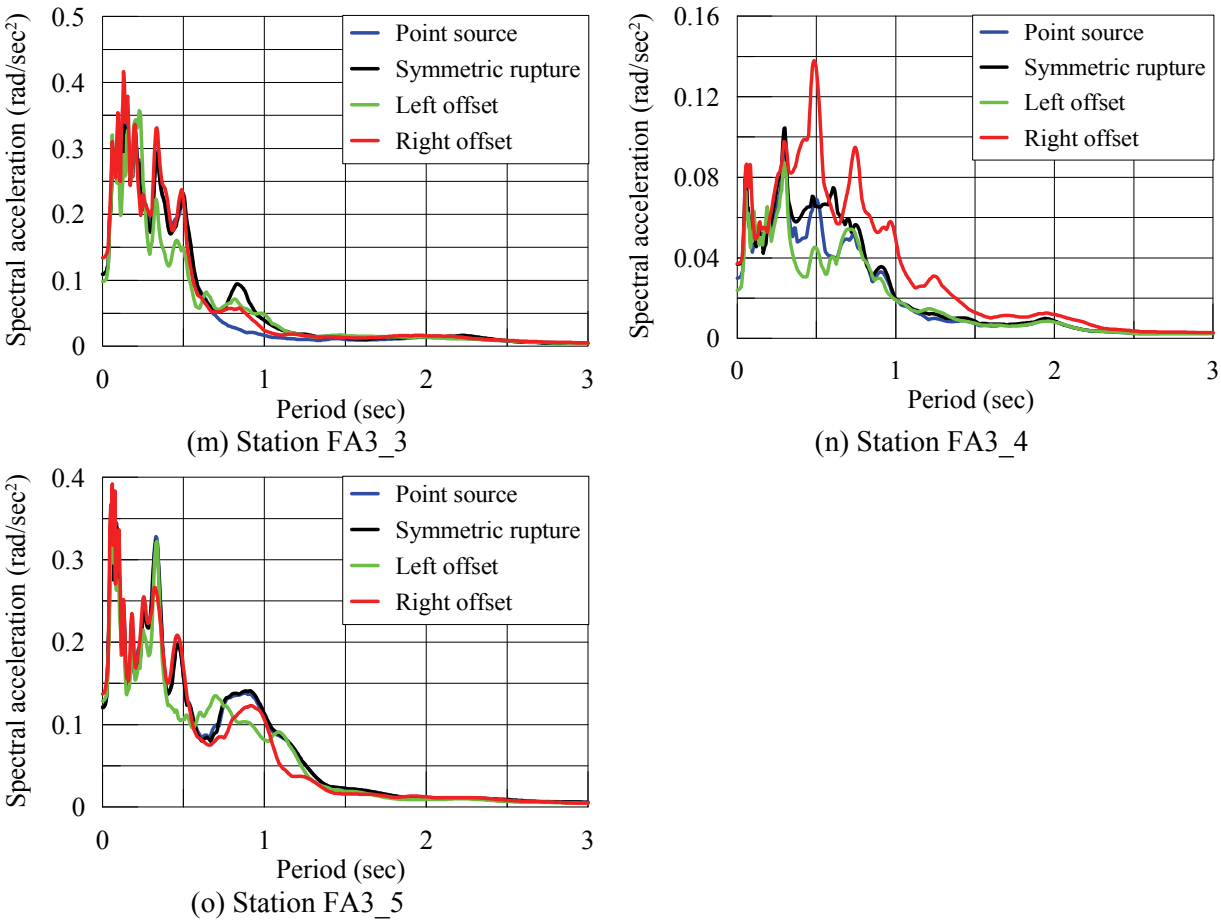

Figure 3-8: Effect of rupture on rocking (*xz* plane) spectra

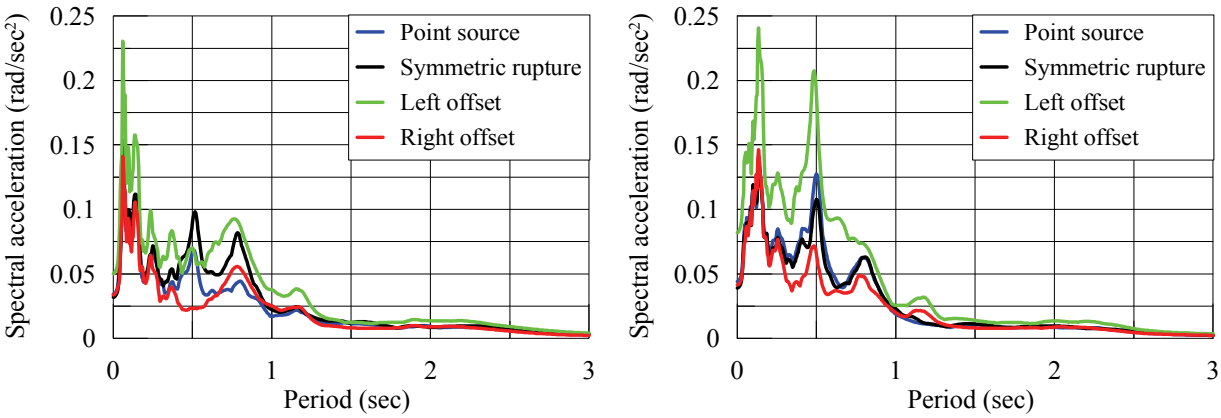

(a) Station FA1_1

(b) Station FA1_2

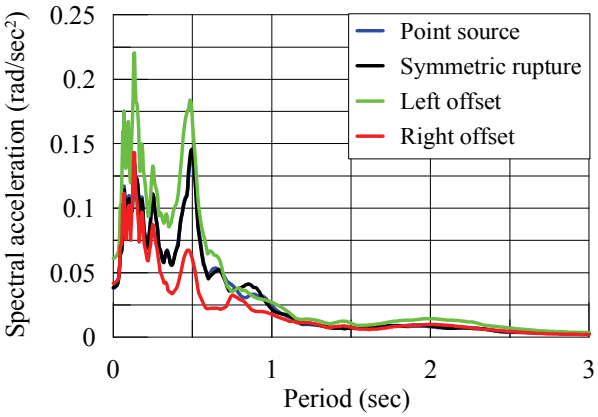

(c) Station FA1_3

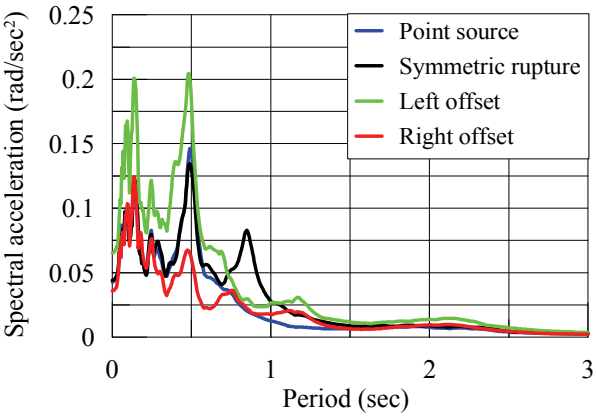

(d) Station FA1_4

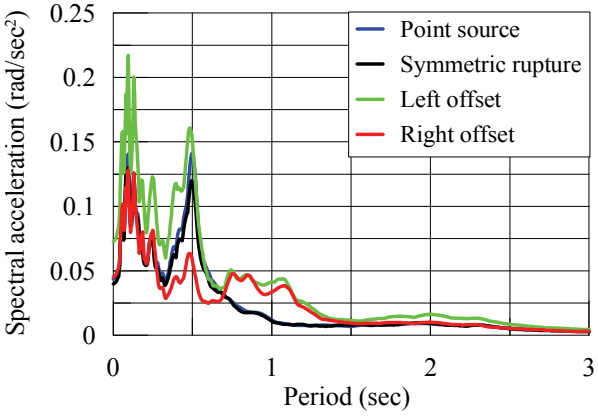

(e) Station FA1_5

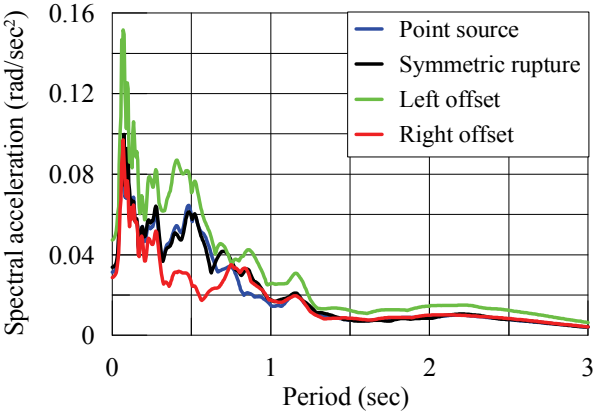

(f) Station FA2_1

Figure 3-9: Effect of rupture on rocking (*yz* plane) spectra (cont.)

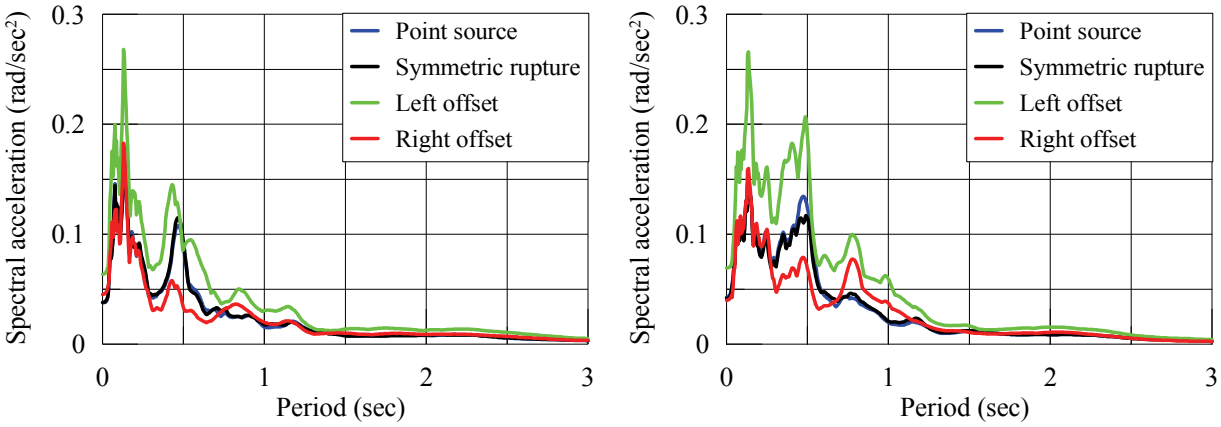

(g) Station FA2_2 (h) Station FA2_3

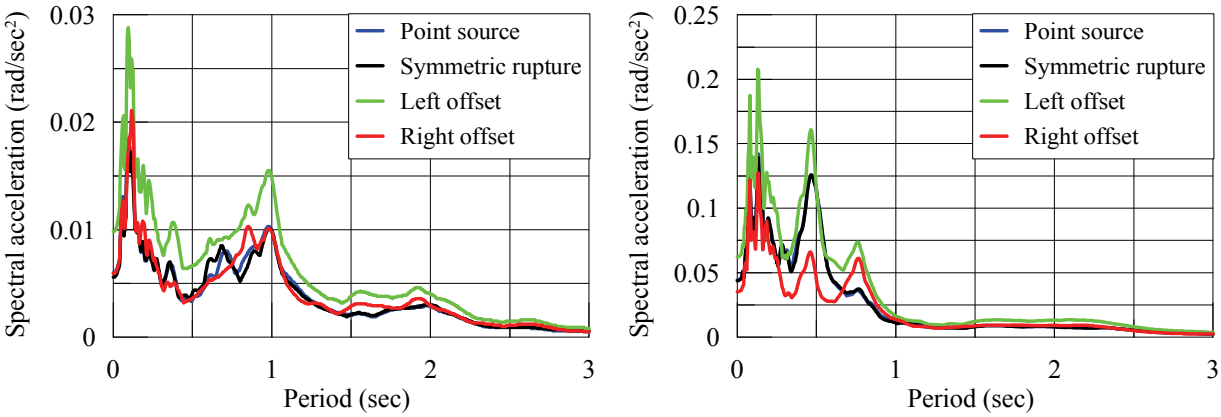

(i) Station FA2_4 (j) Station FA2_5

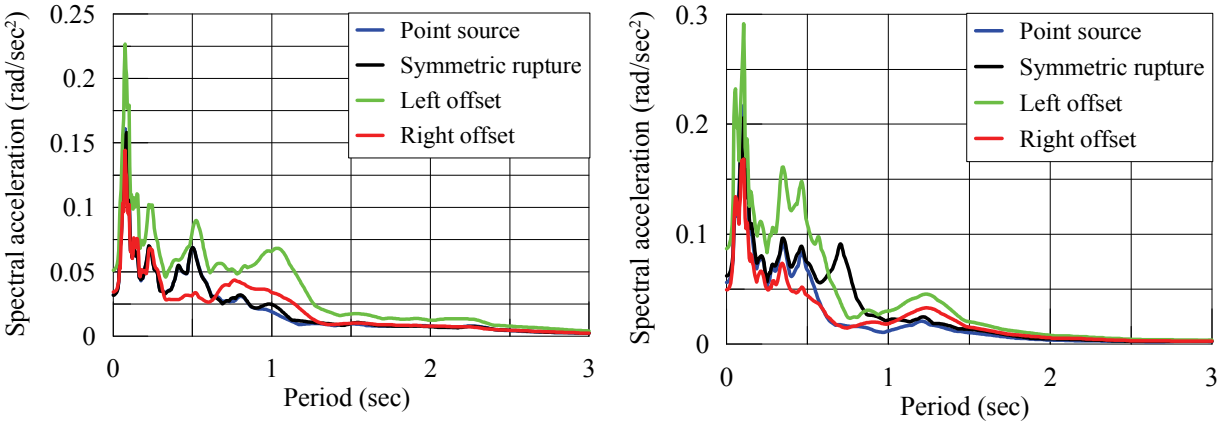

(k) Station FA3_1 (l) Station FA3_2

Figure 3-9: Effect of rupture on rocking (*yz* plane) spectra (cont.)

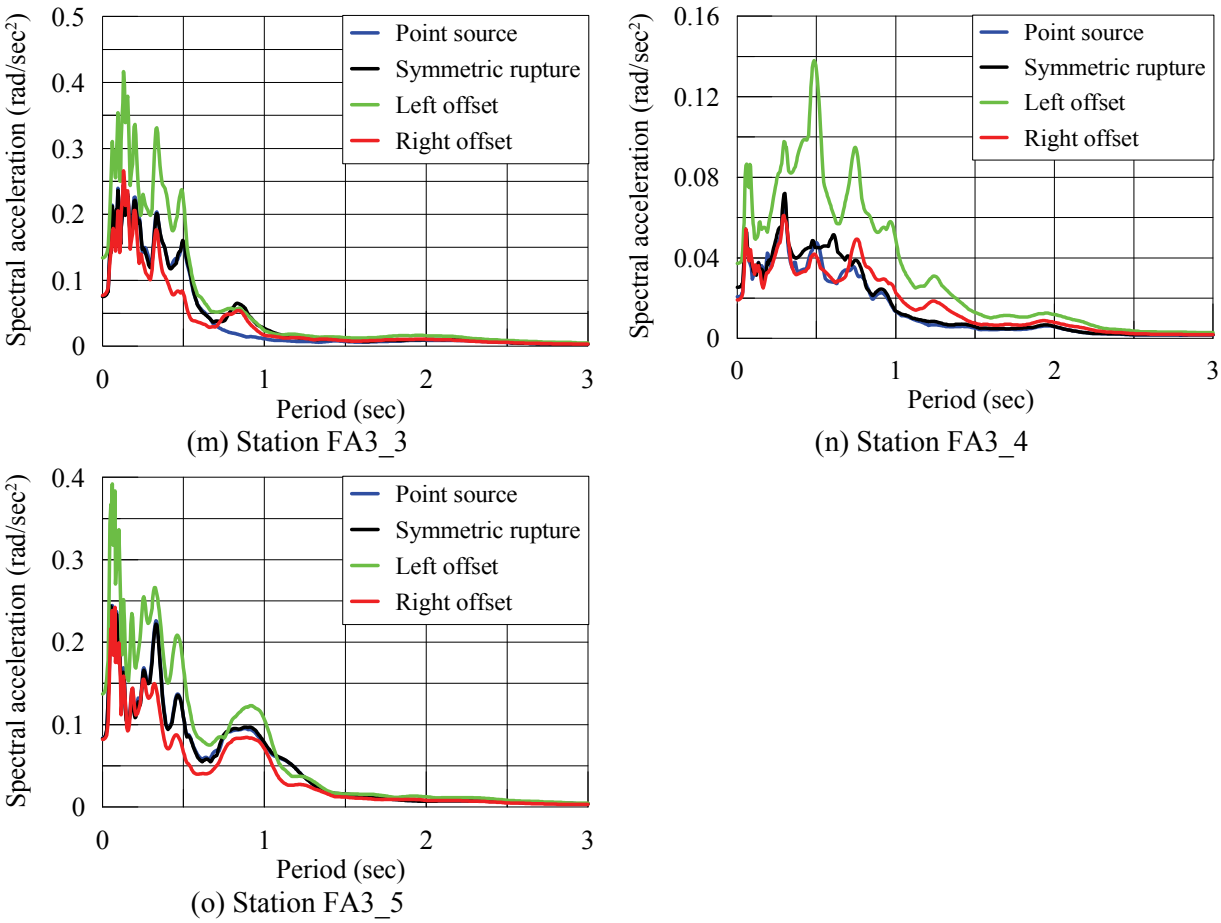

Figure 3-9: Effect of rupture on rocking (*yz* plane) spectra

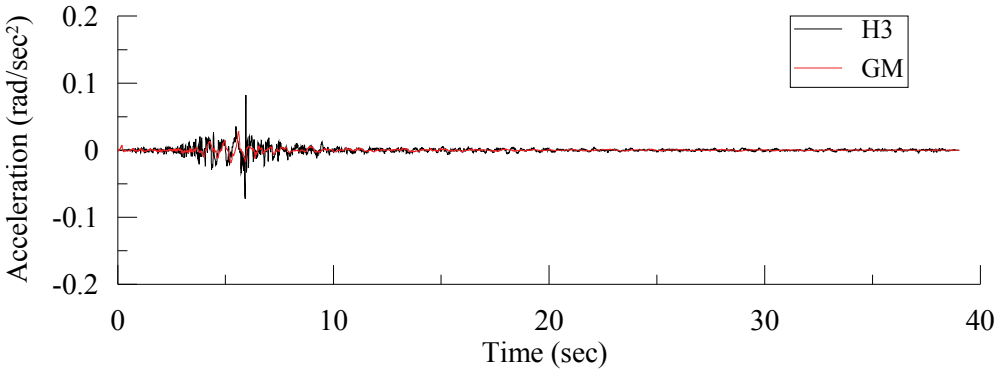

(a) Station FA1_1

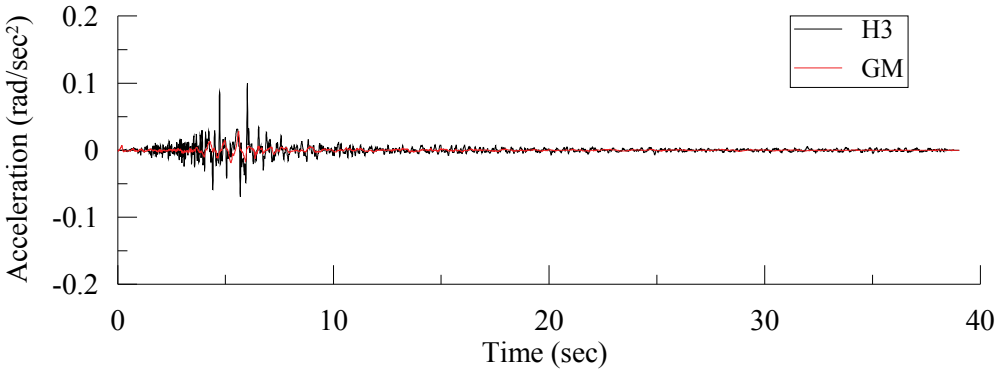

(b) Station FA1_5

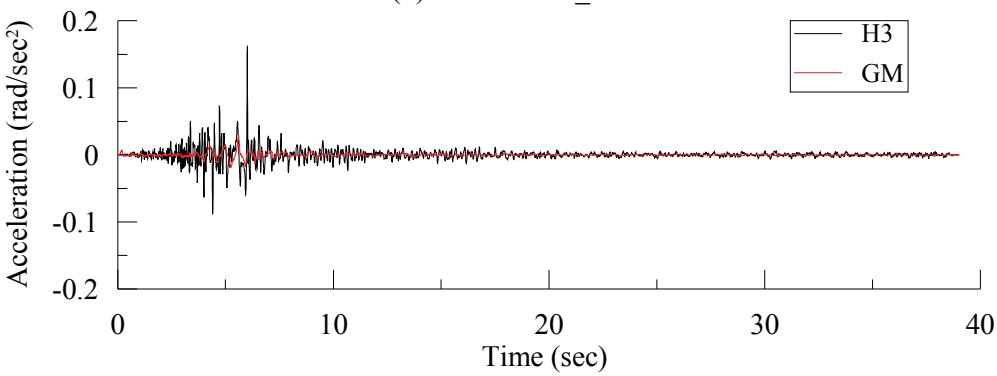

(c) Station FA2_3

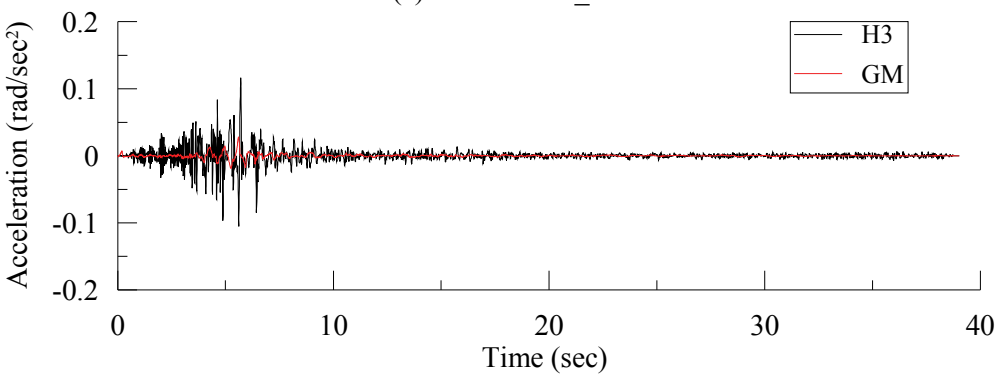

(d) Station FA3_5

Figure 3-10: Torsional histories computed using SSP (H3) and GM

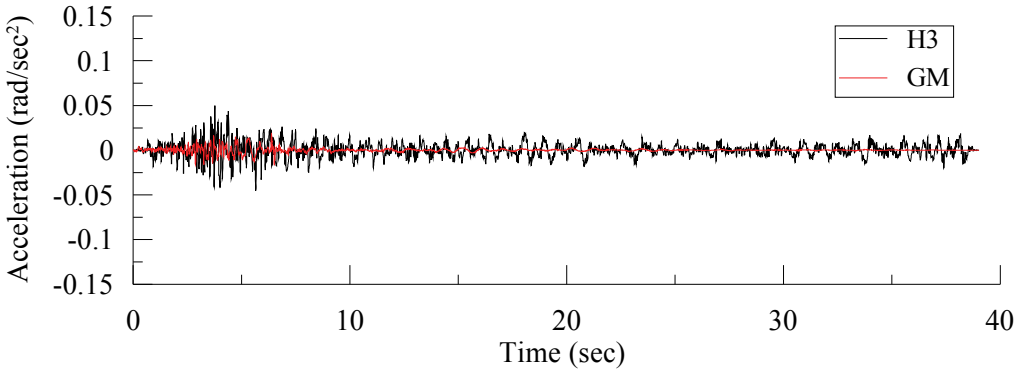

(a) Station FA1_1

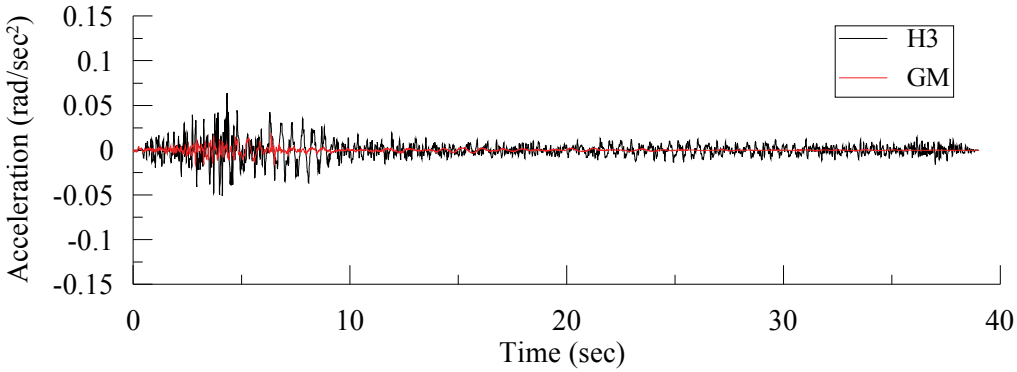

(b) Station FA1_5

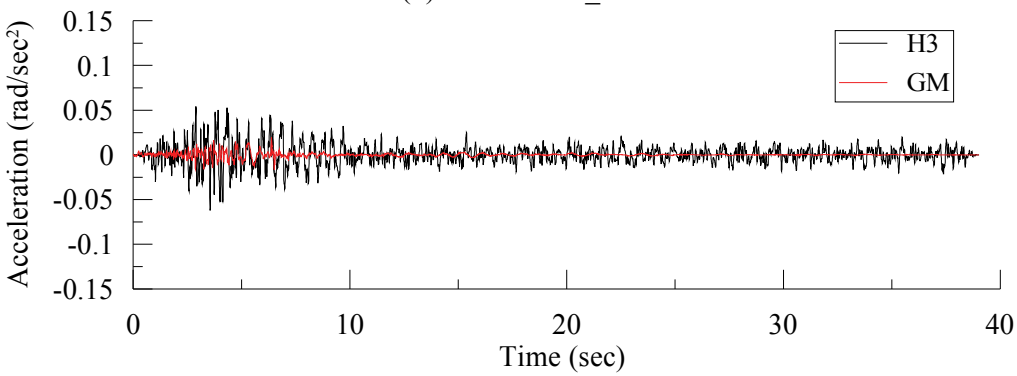

(c) Station FA2_3

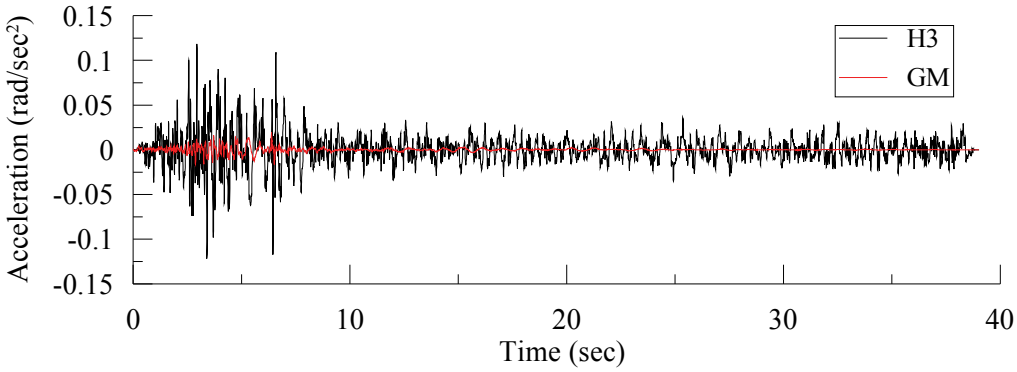

(d) Station FA3_5

Figure 3-11: Rocking histories on the *xz* plane computed using SSP (H3) and GM

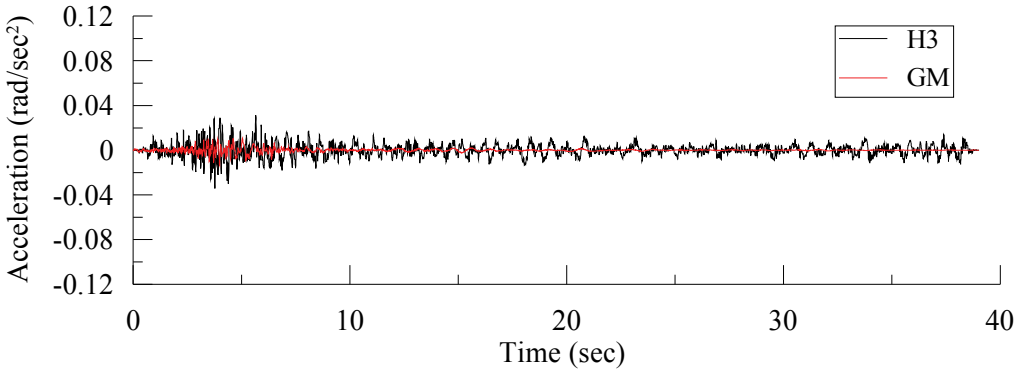

(a) Station FA1_1

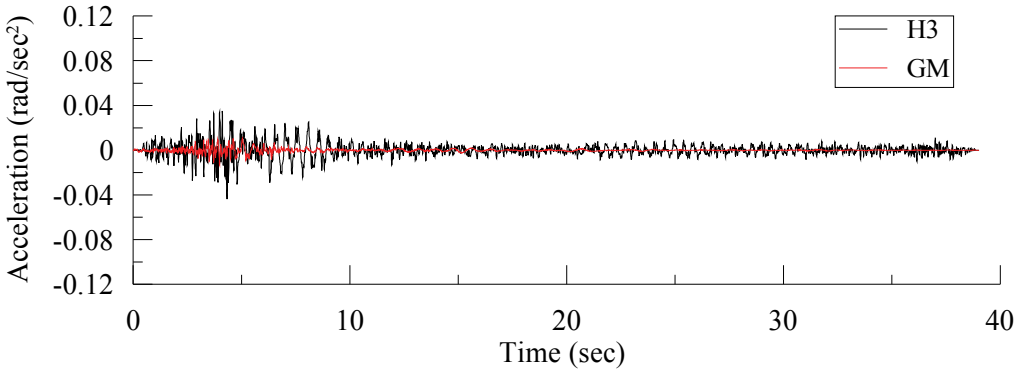

(b) Station FA1_5

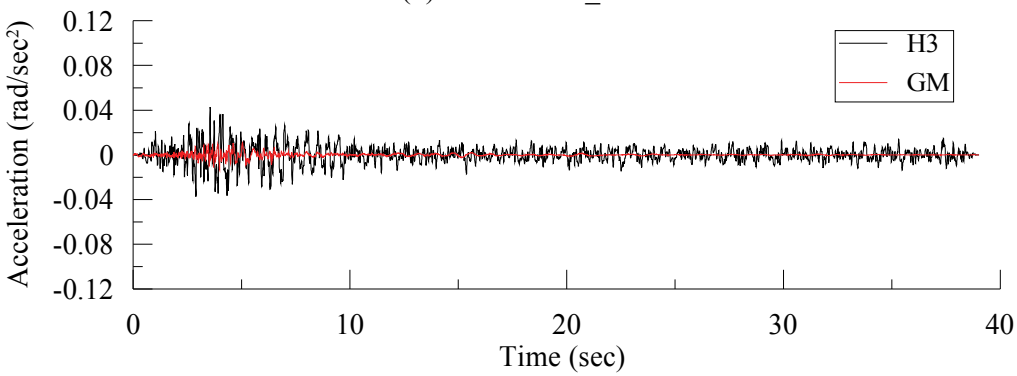

(c) Station FA2_3

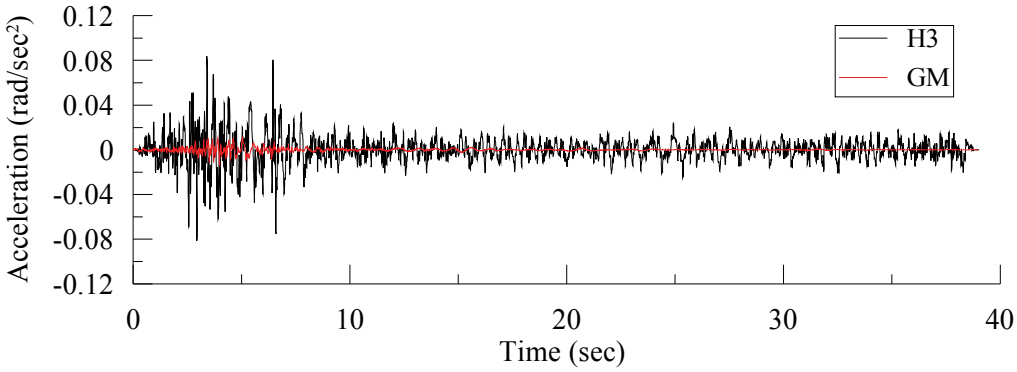

(d) Station FA3_5

Figure 3-12: Rocking histories on the *yz* plane computed using SSP (H3) and GM

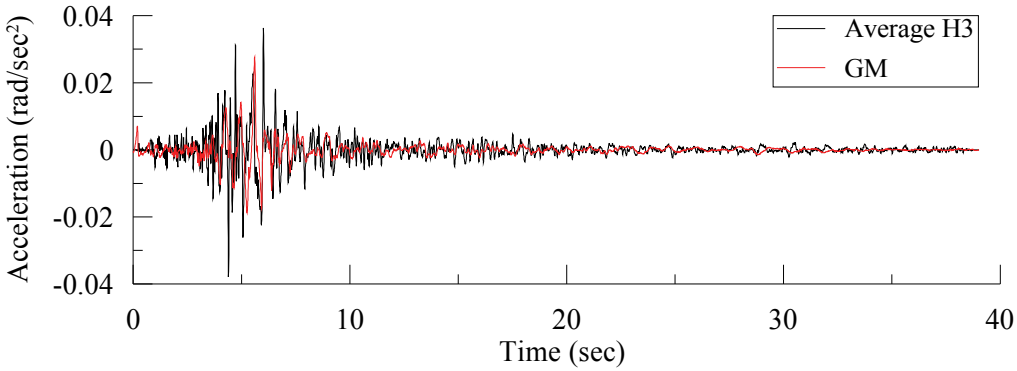

(a) Torsional

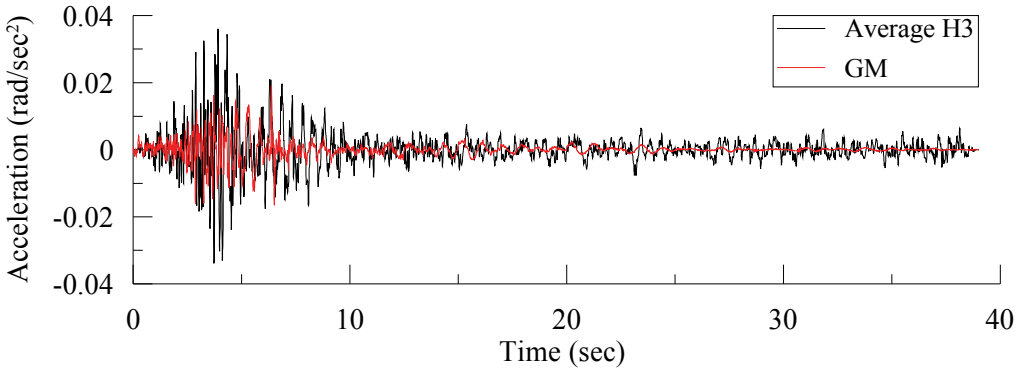

(b) Rocking on *xz* plane

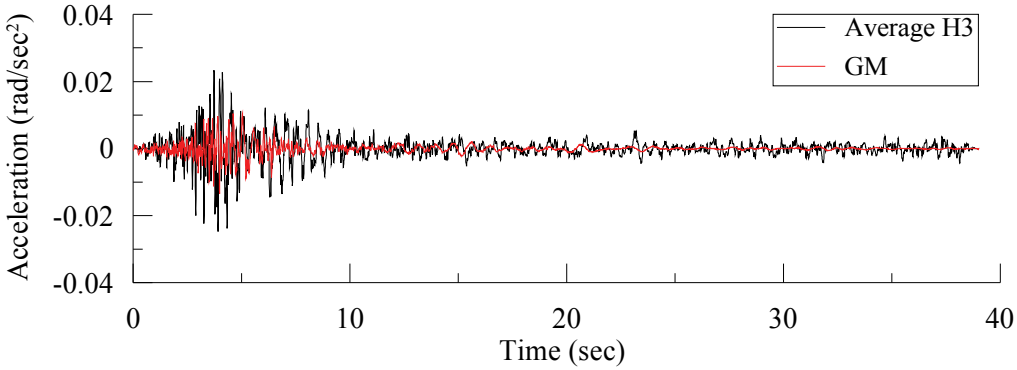

(c) Rocking on *yz* plane

Figure 3-13: Averaged rotational histories computed using SSP (H3) and GM

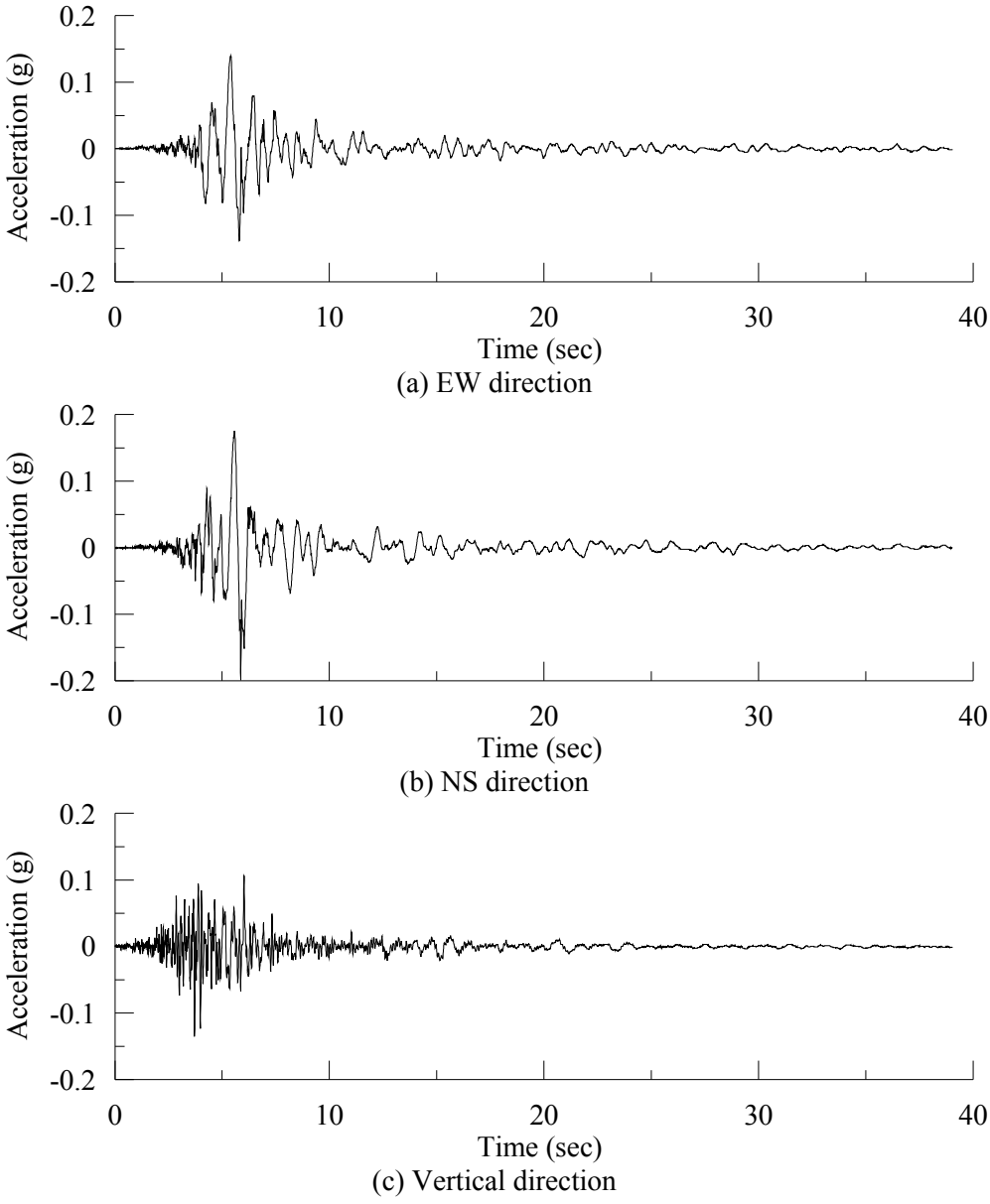

Figure 3-14: Recorded translational acceleration at Station FA1_1

CHAPTER 4
ESTIMATING ROTATIONAL COMPONENTS OF GROUND MOTION USING DATA FROM MULTIPLE RECORDING STATIONS

4.1. Introduction

This chapter describes a procedure to compute the rotational components of ground motion using data recorded in a set of closely spaced recording stations, the so-called *dense array*. The procedure is based on the Geodetic Method (Spudich et al., 1995), which was introduced in Chapter 2. The Geodetic Method (GM) is revisited using data recorded at only surface stations and an uncoupled version of the method is developed. The underestimation of higher frequency content in the rotational motions computed using the GM is illustrated. Section 4.3 presents a higher order Acceleration Gradient Method (AGM) that is capable of capturing higher frequency content in rotational time-series. A physical interpretation of the different orders of the method is presented in Section 4.4 and an optimal order is recommended. Section 4.5 discusses the source of numerical errors associated with the orders higher than two. Results are presented in Section 4.6 for the proposed procedure, geodetic method, and the single-station procedure discussed in Chapter 3, all using data recorded at the Lotung array in Taiwan.

The Matlab source code developed for the AGM is presented in Appendix E, together with an explanation and examples.

4.2. Formulation of the Uncoupled Geodetic Method

The plane-stress condition utilized in the formulation of the GM in the vertical direction must be restricted only at the free surface. Accordingly, only data recorded at the surface stations can be used with the GM. In this case, and noting that $r_3^j - r_3^i = 0$ for any station pair, Eq (2-1) can be reduced to

$$\begin{Bmatrix} u_1^j - u_1^i \\ u_2^j - u_2^i \\ u_3^j - u_3^i \end{Bmatrix} = \begin{bmatrix} u_{1,1} & u_{1,2} \\ u_{2,1} & u_{2,2} \\ u_{3,1} & u_{3,2} \end{bmatrix} \begin{Bmatrix} r_1^j - r_1^i \\ r_2^j - r_2^i \end{Bmatrix} \tag{4-1}$$

Eq (4-1) represents three uncoupled equations, one for each orthogonal direction. Each uncoupled equation involves one distinct pair of displacement gradient parameters. Therefore, recorded data at all the stations along any orthogonal direction can be analyzed separately (independent of the other two orthogonal directions) through an overdetermined problem and the associated two gradient parameters can be calculated. For this purpose, Eq (2-6) can still be used with the reduced data kernel $[A]$, the reduced data $\{\Delta u\}$ and the reduced solution vector $\{p\}$

Of the nine displacement gradient parameters in Eq (2-1), only six are independent, due to the free surface that provides three constraint equations through the plane-stress condition. When the plane-stress condition is applied along the vertical direction and includes the stations at depth, as is the case with the GM, the constraint equations couple the orthogonal directions. In contrast, if only surface stations are considered, the constraint equations are identically satisfied, which uncouples the calculations in the orthogonal directions. Accordingly, the results computed using the original and uncoupled geodetic methods will be identical if only data from surface stations are used for the computations. Importantly, the computed rotational components are independent of the soil properties in this case. The use of the data recorded only at the surface stations for computing rotational components has two distinct advantages, namely, 1) the uncertainty associated with the estimation of soil properties is eliminated, and 2) the uncoupling of the calculations in the orthogonal directions reduces the complexities in the higher order methods that are discussed later in this chapter.

Figure 4-1 illustrates a hypothetical product of the uncoupled geodetic method for a linear array of length *L*, with 11 equally-spaced stations, namely, C0, B1 through B5 and A1 through A5. In this figure, length is normalized by *L*. At any instant in time, a snapshot of the ordinates of the translational accelerations at these stations, perpendicular to the axis of the array, are those shown in Figure 4-1a.

Consider C0 as the reference station and subtract the value recorded at this station from the values at the remaining stations. The resulting distribution surface (a line in this case) is shown in Figure 4-1b. Note that the number of data points shown is 10 and not 11. The GM returns a linear fit to the data (10 data points), as illustrated in Figure 4-1b. In this example, the linear fit underestimates the peak rotational motion across the array.

Consider the translational strong motion data from the M6.1 event recorded by the Lotung array, which is reported in Chapter 2. Five snapshots of vertical acceleration along Arm 1 are presented in Figure 4-2a at 5.8 sec, 5.9 sec, 6.0 sec, 6.1 sec and 6.2 sec. Figure 4-2b presents the Fourier amplitude spectra of the recorded vertical acceleration at one of the stations, FA1_1, located on the same arm. Similar results for Arm 2 and Arm 3 are also presented in Figure 4-2 (panels c through f). Panels a, c and e support the wavy nature of the snapshots as opposed to the linear fit assumed in the GM. Further, panels b, d and f illustrate that the recorded vertical acceleration does not have frequency content significantly beyond 10 Hz. The Fourier amplitude spectra of the rocking motion computed using GM (panels d and f, Figure 2-14) show little frequency content beyond 10 Hz. This comparison illustrates that the increase in frequency content in rocking motion when compared to the vertical motion is not significant, which is unusual as the rocking motion is obtained from the spatial derivative of the vertical motion. The linear fit associated with the GM underestimates high frequency contributions to the resulting rotational components.

4.3. Acceleration Gradient Method (AGM)

4.3.1. First-Order Method

If the coupled (original) or uncoupled GM is used to generate rotational acceleration time series, two successive numerical integrations of translational acceleration time series at multiple stations in the dense array are performed followed by two successive numerical differentiations of the resulting rotational time series. To avoid numerical errors associated with these operations, Eq (2-6) may be recast as

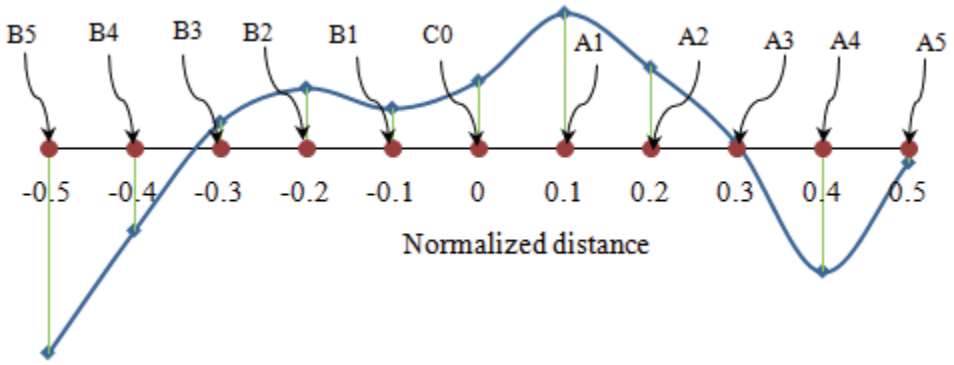

(a) Distribution of recorded data in a linear array

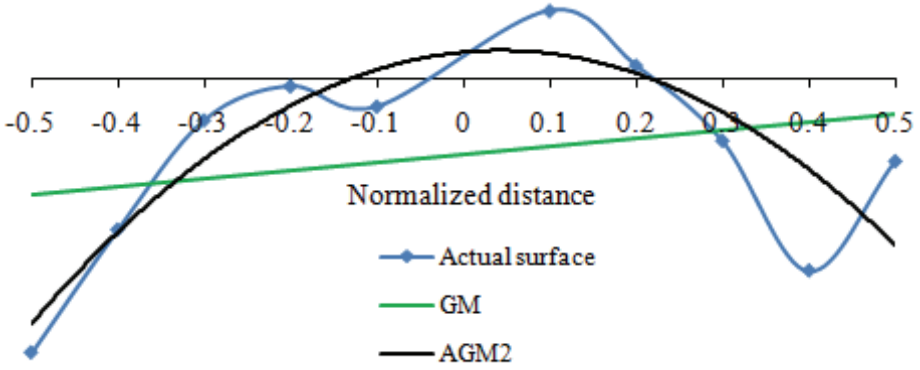

(b) Best-fit surface using GM and AGM2

Figure 4-1: Schematic comparison of GM and AGM2

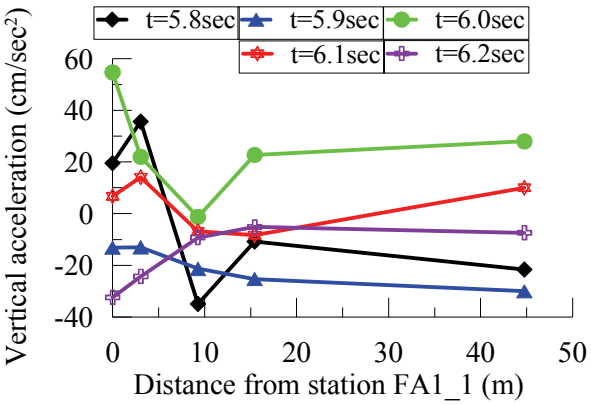

(a) Snapshot of vertical acceleration along Arm 1

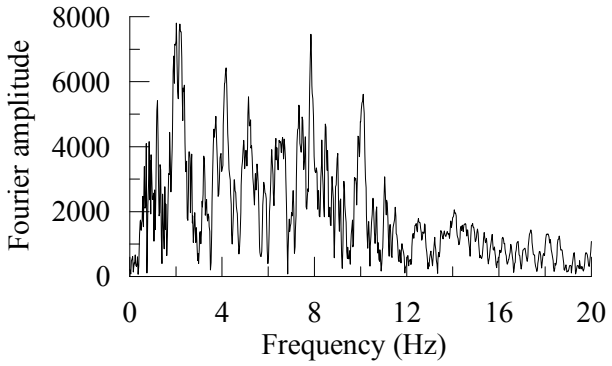

(b) FFT of vertical acceleration at station FA1_1

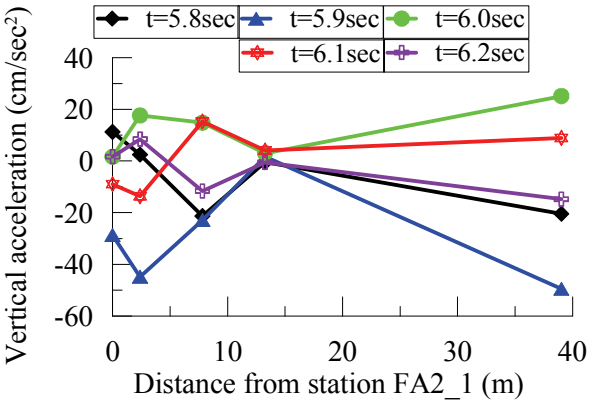

(c) Snapshot of vertical acceleration along Arm 2

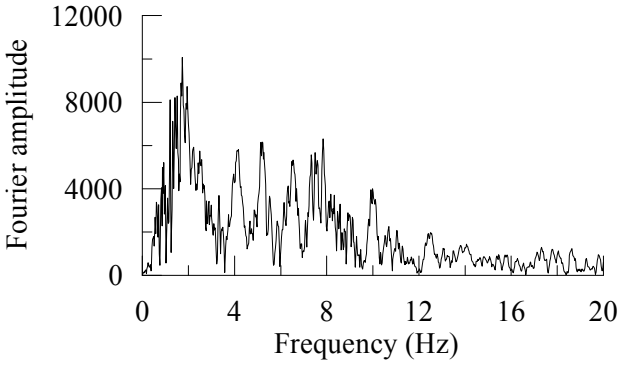

(d) FFT of vertical acceleration at station FA2_2

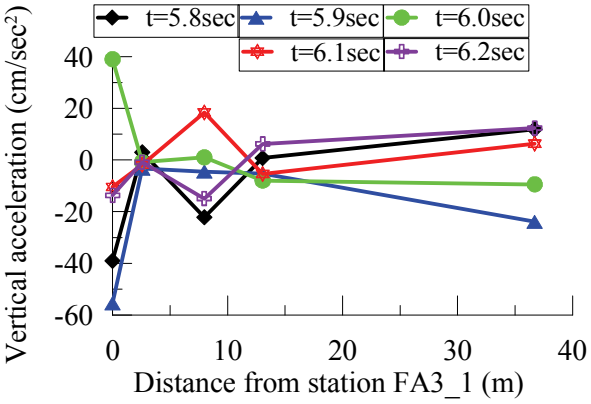

(e) Snapshot of vertical acceleration along Arm 3

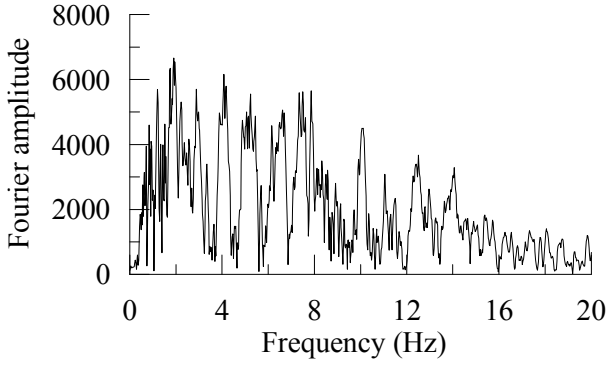

(f) FFT of vertical acceleration at station FA3_3

Figure 4-2: Snapshots of acceleration along each arm and FFT of acceleration at one station on each arm

$$\ddot{\bar{p}} = \left[A^T W_e A\right]^{-1} A^T W_e \left(\Delta\ddot{u}\right) \tag{4-2}$$

In the process of taking derivatives, Δu on the right side of Eq (2-6) is changed to $\Delta\ddot{u}$ in Eq (4-2). All other terms are unchanged. This action is equivalent to taking two successive derivatives with respect to time in Eq (2-2). The associated gradient parameters are now the acceleration gradients. The desired rotational acceleration may now be derived directly from $\ddot{\bar{p}}$ without numerical differentiation.

Equation (4-2) and not Eq (2-6) is the governing expression for computing the rotational acceleration histories. This procedure is described as an Acceleration Gradient Method (AGM) of the first order: AGM1. A rotational acceleration history obtained using AGM1 will be identical to that obtained using the GM if the errors accumulated by the numerical differentiation and integration are insignificant. However, the full potential of the AGM is realized when expanded to the second order, AGM2, as presented next.

4.3.2. Second-Order Method

The physical interpretation of the solution vector computed using Eq (2-6) or Eq (4-2) (the GM) is a planar surface best-fit through the measured dataset at every time step. Figure 4-1 illustrates this for a linear array where the planer surface collapses to a line. However, as shown in the figure, the actual surface is wavy. The rotational components computed using the GM do therefore not necessarily characterize free-field motion but rather inputs to a rigid foundation with a footprint described by the spatial distribution of the recording stations in the array. The curvature of the distribution surface must be computed to enable a comparison of rotational motions with estimates obtained using a single station procedure (see Chapter 3). The curvature of the surface is established using a second-order Taylor expansion of the displacement field about the reference station. The second-order method is denoted as AGM2 hereafter. A sample curved surface is also shown in Figure 4-1.

Denote the displacement field at any instant of time with respect to a suitable Cartesian coordinate system as

$$\Pi(x,y,z) = u(x,y,z)\hat{i} + v(x,y,z)\hat{j} + w(x,y,z)\hat{k} \tag{4-3}$$

Next, define a reference point R with coordinates (x_0, y_0, z_0), take the Taylor expansion of $\Pi(x,y,z)$ about R and retain terms up to the second order derivative:

$$\Delta\Pi = \{\Delta u \quad \Delta v \quad \Delta w\}^T = T\Delta q \tag{4-4}$$

$$\Delta q = \left\{\Delta x \quad \Delta y \quad \Delta z \quad \Delta x\Delta y \quad \Delta y\Delta z \quad \Delta z\Delta x \quad \frac{(\Delta x)^2}{2} \quad \frac{(\Delta y)^2}{2} \quad \frac{(\Delta z)^2}{2}\right\}^T \tag{4-5}$$

$$\Delta x = x - x_0 \quad \Delta y = y - y_0 \quad \Delta z = z - z_0 \tag{4-6}$$

$$T = \begin{bmatrix} \frac{\partial u}{\partial x} & \frac{\partial u}{\partial y} & \frac{\partial u}{\partial z} & \frac{\partial^2 u}{\partial x\partial y} & \frac{\partial^2 u}{\partial y\partial z} & \frac{\partial^2 u}{\partial z\partial x} & \frac{\partial^2 u}{\partial x^2} & \frac{\partial^2 u}{\partial y^2} & \frac{\partial^2 u}{\partial z^2} \\ \frac{\partial v}{\partial x} & \frac{\partial v}{\partial y} & \frac{\partial v}{\partial z} & \frac{\partial^2 v}{\partial x\partial y} & \frac{\partial^2 v}{\partial y\partial z} & \frac{\partial^2 v}{\partial z\partial x} & \frac{\partial^2 v}{\partial x^2} & \frac{\partial^2 v}{\partial y^2} & \frac{\partial^2 v}{\partial z^2} \\ \frac{\partial w}{\partial x} & \frac{\partial w}{\partial y} & \frac{\partial w}{\partial z} & \frac{\partial^2 w}{\partial x\partial y} & \frac{\partial^2 w}{\partial y\partial z} & \frac{\partial^2 w}{\partial z\partial x} & \frac{\partial^2 w}{\partial x^2} & \frac{\partial^2 w}{\partial y^2} & \frac{\partial^2 w}{\partial z^2} \end{bmatrix} \tag{4-7}$$

The Taylor matrix T contains a total of 27 gradient parameters that are not independent due to the plane-stress condition along the vertical direction. The plane-stress condition for this case not only yields three relations involving the gradient parameters as in case of the GM, but also generates additional relations involving their spatial derivatives. These relations are summarized in Eq (4-8) through Eq (4-10):

$$\frac{\partial u}{\partial z} + \frac{\partial w}{\partial x} = 0 \quad \frac{\partial^2 u}{\partial z\partial x} + \frac{\partial^2 w}{\partial x^2} = 0 \quad \frac{\partial^2 u}{\partial y\partial z} + \frac{\partial^2 w}{\partial x\partial y} = 0 \quad \frac{\partial^2 u}{\partial z^2} + \frac{\partial^2 w}{\partial z\partial x} = 0 \tag{4-8}$$

$$\frac{\partial v}{\partial z} + \frac{\partial w}{\partial y} = 0 \quad \frac{\partial^2 v}{\partial z\partial x} + \frac{\partial^2 w}{\partial x\partial y} = 0 \quad \frac{\partial^2 v}{\partial y\partial z} + \frac{\partial^2 w}{\partial y^2} = 0 \quad \frac{\partial^2 v}{\partial z^2} + \frac{\partial^2 w}{\partial y\partial z} = 0 \tag{4-9}$$

$$\begin{aligned} &\frac{\partial w}{\partial z} = -\eta\left(\frac{\partial u}{\partial x} + \frac{\partial v}{\partial y}\right) \quad \frac{\partial^2 w}{\partial z\partial x} = -\eta\left(\frac{\partial^2 u}{\partial x^2} + \frac{\partial^2 v}{\partial x\partial y}\right) \quad \frac{\partial^2 w}{\partial y\partial z} = -\eta\left(\frac{\partial^2 u}{\partial x\partial y} + \frac{\partial^2 v}{\partial y^2}\right) \\ &\frac{\partial^2 w}{\partial z^2} = -\eta\left(\frac{\partial^2 u}{\partial z\partial x} + \frac{\partial^2 v}{\partial y\partial z}\right) \end{aligned} \tag{4-10}$$

The plane-stress condition leads to 12 relations and hence Eq (4-4) contains only 15 independent gradient parameters.

Returning to the indicial notation used with the GM and using 1, 2, and 3 instead of x, y, and z, respectively, and denoting u as the displacement field, the following are selected as the 15 independent gradient parameters:

$$p=\begin{Bmatrix} u_{1,1}, & u_{1,3}, & u_{2,2}, & u_{2,3}, & u_{1,23}, & u_{1,13}, & u_{2,23}, & u_{1,11}, \\ u_{1,22}, & u_{1,33}, & u_{2,11}, & u_{2,22}, & u_{2,33}, & u_{1,2}, & 0.5\left(u_{2,1}-u_{1,2}\right) \end{Bmatrix}^T \tag{4-11}$$

Following the same procedure used for the GM, the time-varying displacement at the i^{th} and j^{th} stations may be related through Eq (2-2) where Δu_i^j is given by the left side of Eq (2-3) and $\{p\}$ is given by Eq (4-11). The matrix A_i^j takes the form as follows:

$$A_i^j=\begin{bmatrix} A_1^T & A_2^T & A_3^T \end{bmatrix}^T$$

$$A_1=\begin{Bmatrix} \left(r_1^j-r_1^i\right),\left(r_3^j-r_3^i\right),0,0,\left(r_2^j-r_2^i\right)\left(r_3^j-r_3^i\right),\left(r_3^j-r_3^i\right)\left(r_1^j-r_1^i\right),0,0.5\left(r_1^j-r_1^i\right)^2, \\ 0.5\left(r_2^j-r_2^i\right)^2,0.5\left(r_3^j-r_3^i\right)^2,0,-\left(r_1^j-r_1^i\right)\left(r_2^j-r_2^i\right),\left(r_1^j-r_1^i\right)\left(r_2^j-r_2^i\right)/\eta,\left(r_2^j-r_2^i\right),0 \end{Bmatrix}$$

$$A_2=\begin{Bmatrix} 0,0,\left(r_2^j-r_2^i\right),\left(r_3^j-r_3^i\right),\left(r_3^j-r_3^i\right)\left(r_1^j-r_1^i\right),0,\left(r_2^j-r_2^i\right)\left(r_3^j-r_3^i\right),-\left(r_1^j-r_1^i\right)\left(r_2^j-r_2^i\right), \\ 0,\left(r_1^j-r_1^i\right)\left(r_2^j-r_2^i\right)/\eta,0.5\left(r_1^j-r_1^i\right)^2,0.5\left(r_2^j-r_2^i\right)^2,0.5\left(r_3^j-r_3^i\right)^2,\left(r_1^j-r_1^i\right),2\left(r_1^j-r_1^i\right) \end{Bmatrix}$$

$$A_3=\begin{Bmatrix} -\eta\left(r_3^j-r_3^i\right),-\left(r_1^j-r_1^i\right),-\eta\left(r_3^j-r_3^i\right),-\left(r_2^j-r_2^i\right),-\left(r_1^j-r_1^i\right)\left(r_2^j-r_2^i\right),-\left[0.5\left(r_1^j-r_1^i\right)^2+0.5\eta\left(r_3^j-r_3^i\right)^2\right], \\ -\left[0.5\left(r_2^j-r_2^i\right)^2+0.5\eta\left(r_3^j-r_3^i\right)^2,0,0,-\left(r_3^j-r_3^i\right)\left(r_1^j-r_1^i\right),0,0,-\left(r_2^j-r_2^i\right)\left(r_3^j-r_3^i\right),0,0\right] \end{Bmatrix} \tag{4-12}$$

Next, Station 1 is considered to be the i^{th} station and fixed, and the j^{th} station is varied to account for the remaining $(N-1)$ stations, one at a time. A set of $(N-1)$ equations is therefore obtained, which can be assembled per Eq (2-4). The solution vector can be written by Eq (4-2) by differentiating the resulting equation twice with respect to time and solving the associated overdetermined problem. The solution vector contains the double derivative of the gradient quantities shown in Eq (4-11). The torsional and rocking rotations can be derived from the solution vector without numerical differentiation.

The gradient quantities computed here correspond to those at the reference station. To compute these gradient quantities at any other station, particularly those involving the first-order derivative only, their first order Taylor expansions can be used. As examples, the resulting torsional rotation ($\ddot{\theta}_{xy}$) and rocking rotations on the *xz* and *yz* planes ($\ddot{\theta}_{xz}$ and $\ddot{\theta}_{yz}$, respectively) are presented in Eq (4-13) through Eq (4-15), respectively:

$$\begin{aligned}\ddot{\theta}_{xy}^{ref} &= \ddot{\bar{p}}(15)\\ \ddot{\theta}_{xy}^{i} &= \ddot{\theta}_{xy}^{ref} + 0.5\left[\left(\ddot{\bar{p}}(11)+\ddot{\bar{p}}(12)-\ddot{\bar{p}}(13)/\eta\right)\left(r_1^i - r_1^{ref}\right)-\left(\ddot{\bar{p}}(8)+\ddot{\bar{p}}(9)-\ddot{\bar{p}}(10)/\eta\right)\left(r_2^i - r_2^{ref}\right)\right]\end{aligned} \tag{4-13}$$

$$\begin{aligned}\ddot{\theta}_{xz}^{ref} &= \ddot{\bar{p}}(2)\\ \ddot{\theta}_{xz}^{i} &= \ddot{\theta}_{xz}^{ref} + \left(r_1^i - r_1^{ref}\right)\ddot{\bar{p}}(6)+\left(r_2^i - r_2^{ref}\right)\ddot{\bar{p}}(5)+\left(r_3^i - r_3^{ref}\right)\ddot{\bar{p}}(10)\end{aligned} \tag{4-14}$$

$$\begin{aligned}\ddot{\theta}_{yz}^{ref} &= -\ddot{\bar{p}}(4)\\ \ddot{\theta}_{yz}^{i} &= \ddot{\theta}_{yz}^{ref} - \left(r_1^i - r_1^{ref}\right)\ddot{\bar{p}}(5)-\left(r_2^i - r_2^{ref}\right)\ddot{\bar{p}}(7)-\left(r_3^i - r_3^{ref}\right)\ddot{\bar{p}}(13)\end{aligned} \tag{4-15}$$

The superscripts *ref* and *i* denote the reference and any arbitrary stations, respectively, in Eq (4-13) through (4-15).

Another procedure for calculating rotations at a station other than the reference station is to reanalyze the problem assuming the particular station to be the reference station. The results will be identical because, similar to the GM, the least-square surface is independent of the selection of the reference station.

4.3.3. Uncoupled Second-Order AGM (AGM2)

Since the plane-stress condition is strictly applicable only at the free surface, the surface stations in a dense array are only considered here, which reduces Eq (4-4) to

$$\begin{Bmatrix} \Delta u \\ \Delta v \\ \Delta w \end{Bmatrix} = \begin{bmatrix} \frac{\partial u}{\partial x} & \frac{\partial u}{\partial y} & \frac{\partial^2 u}{\partial x \partial y} & \frac{\partial^2 u}{\partial x^2} & \frac{\partial^2 u}{\partial y^2} \\ \frac{\partial v}{\partial x} & \frac{\partial v}{\partial y} & \frac{\partial^2 v}{\partial x \partial y} & \frac{\partial^2 v}{\partial x^2} & \frac{\partial^2 v}{\partial y^2} \\ \frac{\partial w}{\partial x} & \frac{\partial w}{\partial y} & \frac{\partial^2 w}{\partial x \partial y} & \frac{\partial^2 w}{\partial x^2} & \frac{\partial^2 w}{\partial y^2} \end{bmatrix} \begin{Bmatrix} (x - x_0) \\ (y - y_0) \\ (x - x_0)(y - y_0) \\ \frac{(x - x_0)^2}{2} \\ \frac{(y - y_0)^2}{2} \end{Bmatrix} \tag{4-16}$$

Accordingly, each orthogonal direction can be analyzed independently and each analysis will involve only five gradient parameters. Using indicial notation, the *x* displacement at i^{th} and j^{th} stations may be related as

$$\Delta u_i^j = A_i^j p$$

$$\left\{u_1^j - u_1^i\right\} = \begin{bmatrix} \left(r_1^j - r_1^i\right) & \left(r_2^j - r_2^i\right) & \left(r_1^j - r_1^i\right)\left(r_2^j - r_2^i\right) & \frac{\left(r_1^j - r_1^i\right)^2}{2} & \frac{\left(r_2^j - r_2^i\right)^2}{2} \end{bmatrix} \begin{Bmatrix} u_{1,1} \\ u_{1,2} \\ u_{1,12} \\ u_{1,11} \\ u_{1,22} \end{Bmatrix} \tag{4-17}$$

Now, considering Station 1 as the i^{th} station and fixed, and varying the j^{th} station to account for the remaining $(N-1)$ stations, one at a time, a set of $(N-1)$ equations can be obtained in the form of Eq (4-17). These $(N-1)$ equations can be assembled per Eq (2-4). By differentiating the resulting equation twice with respect to time and solving the associated overdetermined problem, the solution vector can be written by Eq (4.2). The solution vector contains the second derivative (with respect to time) of the gradient parameters included in Eq (4-17). A similar analysis can be performed along the *y* and *z* directions. These steps complete the evaluation of the second derivative with respect to time of all 15 gradient parameters in Eq (4-16). The torsional acceleration and the rocking accelerations on the *xz* and *yz* planes, at the reference station and any other station, are derived as follows:

$$\ddot{\theta}_{xy}^{ref} = \frac{1}{2}\left(\ddot{u}_{2,1} - \ddot{u}_{1,2}\right)$$
$$\ddot{\theta}_{xy}^{i} = \ddot{\theta}_{xy}^{ref} + \frac{1}{2}\left[\left(\ddot{u}_{2,11} - \ddot{u}_{1,12}\right)\left(r_1^i - r_1^{ref}\right) + \left(\ddot{u}_{2,12} - \ddot{u}_{1,22}\right)\left(r_2^i - r_2^{ref}\right)\right] \tag{4-18}$$

$$\ddot{\theta}_{xz}^{ref} = -\ddot{u}_{3,1}$$
$$\ddot{\theta}_{xz}^{i} = \ddot{\theta}_{xz}^{ref} - \ddot{u}_{3,11}\left(r_1^i - r_1^{ref}\right) - \ddot{u}_{3,12}\left(r_2^i - r_2^{ref}\right) \tag{4-19}$$

$$\ddot{\theta}_{yz}^{ref} = \ddot{u}_{3,2}$$
$$\ddot{\theta}_{yz}^{i} = \ddot{\theta}_{yz}^{ref} + \ddot{u}_{3,12}\left(r_1^i - r_1^{ref}\right) + \ddot{u}_{3,22}\left(r_2^i - r_2^{ref}\right) \tag{4-20}$$

The rotational acceleration at any station other than the reference station may be obtained by reanalyzing the problem by considering the particular station as the reference station. As noted previously, the results will be identical.

The computation of the torsional and rocking accelerations in the uncoupled formulation does not require knowledge of soil properties. The uncoupled formulation can be extended to higher orders as described below.

4.3.4. Uncoupled AGM of Order n

Eq (4-16) can be rewritten as a recursive formula to account for the n^{th} order derivative:

$$\Delta u(x,y) = \sum_{k=1}^{n}\left[\sum_{l=0}^{k}\frac{\partial^k u}{\partial x^{k-l}\partial y^l}\frac{(dx)^{k-l}}{(k-l)!}\frac{(dy)^l}{l!}\right] \tag{4-21}$$

Using indicial notation, the x displacement at the i^{th} and j^{th} stations can be related per Eq (2-3) where Δu_i^j, A_i^j and p are shown in Box 1.

The total number of gradient parameters involved in the analysis along one orthogonal direction is $n(n+3)/2$. By considering Station 1 as the i^{th} station and fixed, and varying the j^{th} station to account for the remaining $(N-1)$ stations, one at a time, a set of $(N-1)$ equations is obtained. This equation set

Box 1: Calculation of Δu_i^j, A_i^j and p in AGMn

$$\Delta u_i^j = u_1^j - u_1^i$$
$$q = 0$$
$$for\ k = 1:n$$
$$\quad for\ \mathrm{l}=0:k$$
$$\qquad \mathrm{q} = q + 1$$
$$A_i^j(1,q) = \frac{\left(r_1^j - r_1^i\right)^{k-l}}{(k-l)!}\frac{\left(r_2^j - r_2^i\right)^{l}}{l!}$$
$$p(q) = u_{k,(k-l)l}$$
$$\quad end$$
$$end$$

can be assembled as shown in Eq (2-4). The solution vector can be written per Eq (4-2) by differentiating the resulting equation twice with respect to time and solving the associated overdetermined problem. The solution vector contains the second derivative with respect to time of the gradient parameters shown in Box 1. Denoting v and w as the displacements along the *y* and *z* directions, respectively, a similar analysis can be performed to compute the associated solution vector. These will complete the evaluation of the second derivative with respect to time of the $3n(n+3)/2$ gradient parameters. The next step is to derive the rotational accelerations from the computed solution vectors, which may be expressed as follows:

$$\ddot{\theta}_{xy}^{ref} = 0.5\left(\ddot{v}_{1,10} - \ddot{u}_{1,01}\right)$$
$$\ddot{\theta}_{xy}^{i} = \ddot{\theta}_{xy}^{ref} + 0.5\sum_{k=1}^{n-1}\sum_{l=0}^{k}\left(\ddot{v}_{(k+1),(k-l+1)l} - \ddot{u}_{(k+1),(k-l)(l+1)}\right)\frac{\left(r_1^i - r_1^{ref}\right)^{k-l}}{(k-l)!}\frac{\left(r_2^i - r_2^{ref}\right)^{l}}{l!} \tag{4-22}$$

$$\ddot{\theta}_{xz}^{ref} = -\ddot{w}_{1,10}$$
$$\ddot{\theta}_{xz}^{i} = \ddot{\theta}_{xz}^{ref} - \sum_{k=1}^{n-1}\sum_{l=0}^{k}\ddot{w}_{(k+1),(k-l+1)l}\frac{\left(r_1^i - r_1^{ref}\right)^{k-l}}{(k-l)!}\frac{\left(r_2^i - r_2^{ref}\right)^{l}}{l!} \tag{4-23}$$

$$\ddot{\theta}_{yz}^{ref} = \ddot{w}_{1,01}$$

$$\ddot{\theta}_{yz}^{i} = \ddot{\theta}_{yz}^{ref} + \sum_{k=1}^{n-1}\sum_{l=0}^{k} \ddot{w}_{(k+1),(k-l)(l+1)} \frac{\left(r_1^i - r_1^{ref}\right)^{k-l}}{(k-l)!} \frac{\left(r_2^i - r_2^{ref}\right)^{l}}{l!} \tag{4-24}$$

The rotational acceleration at any station other than the reference station can also be obtained by reanalyzing the problem assuming the station to be the reference station. As noted previously for other formulations, soil properties are not required to compute the rotational components if the dataset involves only surface stations.

A procedure for developing the Acceleration Gradient Method of different orders has been developed and documented. Below is a physical interpretation of the different orders followed by a recommendation regarding the appropriate order for further analysis. Data recorded at the surface stations only are used for this interpretation.

4.4. Physical Interpretation of the AGM with Different Orders

Consider recorded acceleration data along any of the three orthogonal directions. If Eq (4-2) is used to compute the solution vector of the *n*th order AGM, AGMn, it effectively calculates the best-fit surface (minimizes the least-squares error) of order n through the measured dataset. For a linear array, if $n=1$, the line (surface) is linear; if $n=2$, the line (surface) is quadratic. Equation (4-21) may be considered as the distribution of the best-fit surface on the *xy* plane and the unknowns involved in defining the best-fit surface are computed in Eq (4-2). Once the best-fit surface is computed, the gradient parameters at any other location can be obtained through successive spatial derivatives at that location.

As noted previously, for AGM1 (or the uncoupled GM), the best-fit surface is a plane and the associated gradient parameters are two first-order terms. Moreover, these gradient parameters are constant over the region of interest. The actual surface is expected to be wavy due to contributions from waves of many frequencies as illustrated in Figure 4-1 and verified in Figure 4-2 (for the vertical acceleration). At any instant of time, AGM1 (and uncoupled GM) averages the actual spatial distribution of the rotational

acceleration and returns a representative value for the entire array. Therefore, the AGM1 (or the GM) should underestimate the contributions from higher frequencies in the computed rotational accelerations as discussed earlier. It is unknown whether this is important in terms of response of or damage to structures.

One way to consider higher frequencies in the rotational time series is to introduce curvature in the distribution surface; that is, by increasing the order of the AGM. The best-fit surface in AGM2 is quadratic, as shown in the Figure 4-1 (hypothetically), and the associated gradient parameters include two first-order and three second-order terms. Among the gradient parameters, the second-order terms remain constant over the footprint of the array and the first-order terms vary linearly with distance. Accordingly, the rotational acceleration (torsional and rocking) at any arbitrary station is linearly related to that computed at the reference station. However, this may not reflect the true characteristics of an earthquake if the distance between the reference and other stations is great.

Consider Figure 4-1, where L is the length of the array. Define c as the apparent wave velocity. Appendix A of this report shows that AGM2 cannot include contributions from frequencies higher than $c/2L$, defined here as a *threshold frequency*, in the recorded acceleration data because the higher modes introduce at least one change of sign in the curvature of the surface within the length of the array. However, because the assumed best-fit surface is second order, it cannot capture this change of sign in the curvature and averages out the contributions from the higher frequencies in the recorded data. The threshold frequency is constant regardless of the phase of the instantaneous wave train. This loss of high frequency content does not become significant until the number of changes of sign in the curvature of the surface within the length of the array exceeds two. In this case, the accumulated error also depends on the phase of the instantaneous wave train. Appendix A also provides the technical basis for these observations. The rotational acceleration computed using AGM2 may underestimate contributions from frequencies higher than the threshold frequency. However, this error will remain small if the recorded

translational acceleration data has little frequency content beyond twice the threshold frequency, equal to c/L . AGM2 is an improvement over AGM1.

The recovery of higher frequencies using AGM2 is partial. The computation of the second-order gradient terms in AGM2 involves additional numerical errors and the errors increase with the square of the increase in the distance between the reference station and the most distant station (separation distance) in the array. Errors also accumulate with the use of AGM1 (and GM) but the error is linearly proportional to the separation distance. The use of AGM2 represents a trade-off between the partial recovery of high-frequency contributions and additional numerical errors associated with the computation of higher order terms.

The AGMs of order three and higher require similar trade-offs: higher frequency contributions versus additional numerical errors. In general, AGMn cannot account for the contributions from the frequencies greater than $(n-1)c/2L$ and the error may become significant if the frequency content of the recorded data is rich beyond $nc/2L$. However, AGMn introduces numerical errors that are proportional to the n^{th} power of the separation distance. The challenge is to establish a threshold frequency beyond which the contributions to response and damage are insignificant.

For the Lotung array considered here, the maximum possible order of the AGM is 4, as the number of surface station is 15. At the instant of 5.995 sec, best-fit surfaces computed using AGM2, AGM3 and AGM4 are presented in Figures 4-3 through 4-5, respectively, for the recorded vertical acceleration data. Comparing the maximum ordinate of the best-fit surfaces over the array dimension, for the third and higher order AGMs, it can be seen that: i) the resulting best-fit surface closely satisfies the acceleration data recorded at the stations due to the underlying theory of the least squares method, but ii) at points other than the recording stations, the use of the best-fit surface leads to accelerations several times greater than the maximum acceleration recorded at all the stations (at the same instant of time). This is attributed to the numerical error associated with the computation of the higher order gradients as described above

and can be explained using the spectral value decomposition (SVD) of the data kernel, which depends on the relative location of the stations but not on the recorded data, as presented next.

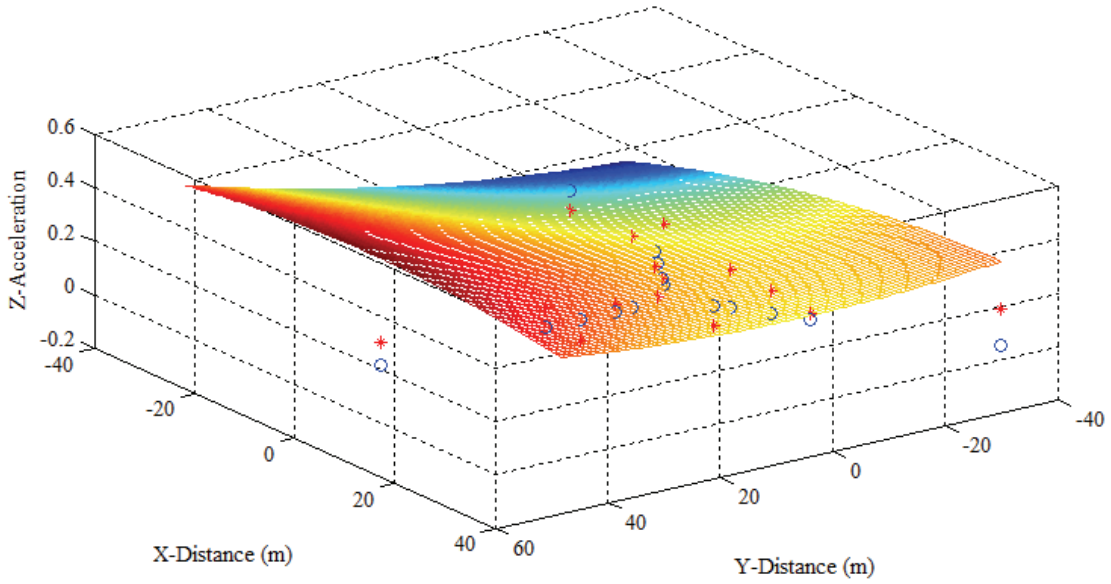

Figure 4-3: Best-fit surface for the distribution of the vertical acceleration (m/sec^2) at time instant 5.995sec using AGM2

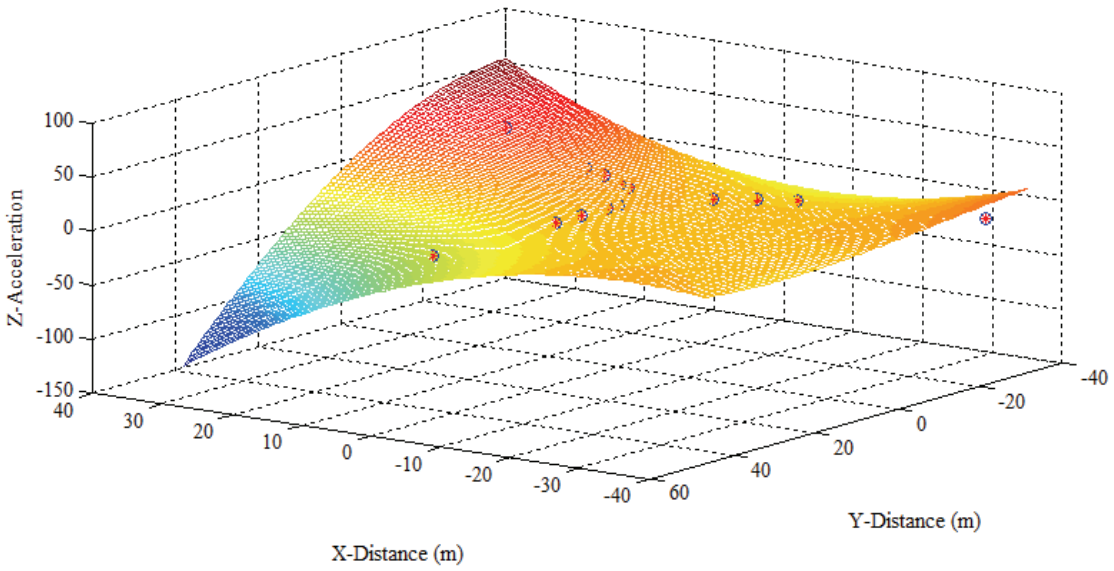

Figure 4-4: Best-fit surface for the distribution of the vertical acceleration (m/sec^2) at time instant 5.995sec using AGM3

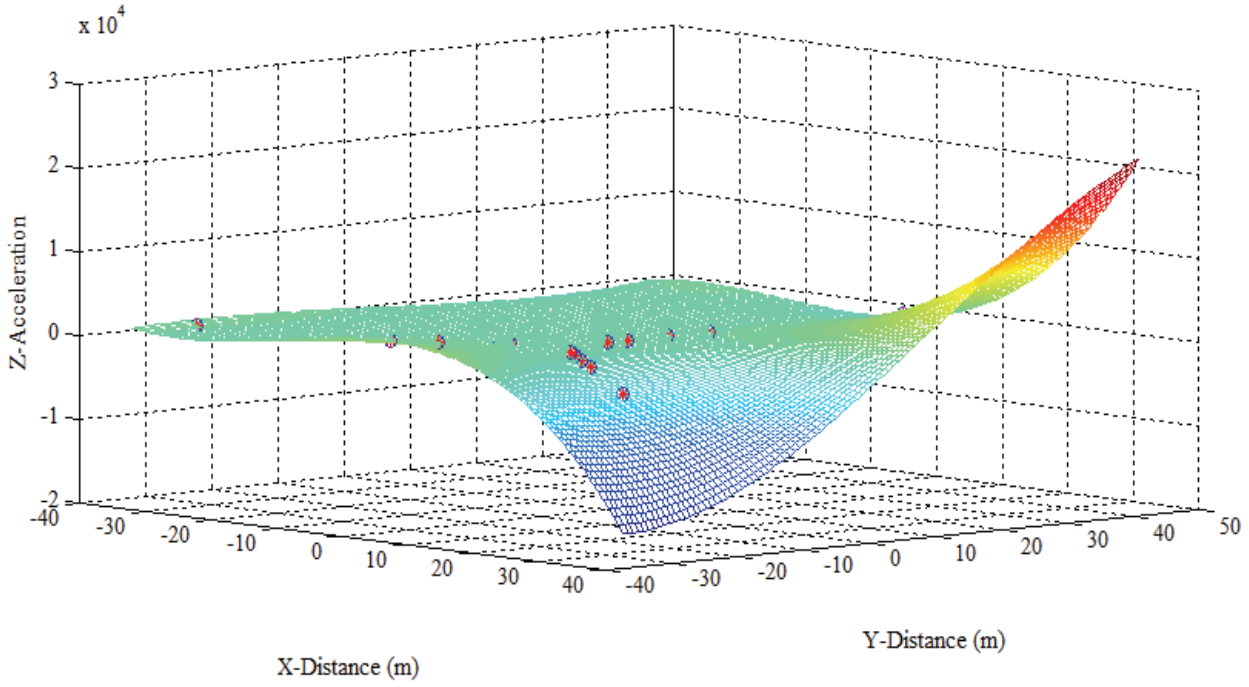

Figure 4-5: Best-fit surface for the distribution of the vertical acceleration (m/sec^2) at time instant 5.995sec using AGM4

4.5. Numerical Error in Higher Order AGMs and Recommendations

The problem *tends to singularity* with the inclusion of higher order derivatives in the computation. Here, the phrase *tends to singularity* implies either that a mathematical solution does not exist or even if it exists, it is not feasible. To show this, Eq (2-5) is rewritten as

$$[A][S][S]^{-1}\{\ddot{p}\} = [AS]\{S^{-1}\ddot{p}\} = \{\Delta\ddot{u}\} \tag{4-25}$$

Here the matrix $[S]$ is diagonal such that in the matrix $[AS]$, the first two columns of matrix $[A]$ are normalized by a characteristic length (defined later), the next three columns are normalized by the square of the characteristic length, the next four columns are normalized by the cube of the characteristic length, and so on. This converts the matrix $[AS]$ to a dimensionless form and all the entries of $\{S^{-1}\ddot{p}\}$ to the dimension of the translational acceleration. The solution of Eq (4-25), similar to Eq (4-2), may be expressed as

$$S^{-1}\ddot{\bar{p}} = \left[S^T A^T W_e A S\right]^{-1} S^T A^T W_e \left(\Delta\ddot{u}\right) \tag{4-26}$$

Eq (4-2) and Eq (4-26) are exactly identical, but the latter considers $\left\{S^{-1}\ddot{p}\right\}$ as the solution vector instead of $\left\{\ddot{p}\right\}$. Clearly, the numerical stability of the solution given by Eq (4-26) depends on the existence of the inverse of $\left[G\right] = \left[S^T A^T W_e A S\right]$. Here, it is noted that $\left[G\right]$ is dimensionless, real and symmetric. Therefore, the eigenvalues of $\left[G\right]$ will be dimensionless and real. Also, the matrix $\left[G\right]$ can be calculated using the data kernel only, without using the measured data; hence, the computed eigenvalues will be valid regardless of the time instant. Moreover, if the matrix $\left[G\right]$ is found to be singular or close to singularity, then at least one or more unknowns in the solution vector $\left\{S^{-1}\ddot{p}\right\}$ no longer remains overdetermined.

A brief investigation of the same issue will be presented here but using spectral value decomposition. Note that Eq (4-26) is derived as the solution of Eq (4-25) by minimizing the weighted second norm of the error. The same solution can also be obtained by minimizing the simple (not weighted) second norm of the error where the data are transformed into a different coordinate system. For example, if $\left[\sigma\right]$ denotes a diagonal matrix containing the eigenvalues of the weight matrix $\left[W_e\right]$ and $\left[\Phi\right]$ is the associated modal matrix, then noting $\left[W_e\right]$ as real and symmetric, it may be shown that

$$\begin{aligned} \left[W_e\right] &= \left[\Phi\right]\left[\sigma\right]\left[\Phi\right]^T = \left[T_w\right]^T\left[T_w\right] \\ \left[T_w\right] &= \left[\sigma\right]^{1/2}\left[\Phi\right]^T \end{aligned} \tag{4-27}$$

Now, the overdetermined problem given by Eq (4-25) is transformed as follows:

$$\left[T_w\right]\left[AS\right]\left\{S^{-1}\ddot{p}\right\} = \left[T_w\right]\left\{\Delta\ddot{u}\right\} \tag{4-28}$$

Identifying $\left[T_w AS\right]$ as the transformed data kernel and $\left\{T_w \Delta\ddot{u}\right\}$ as the transformed data, Eq (4-26) may be readily derived by minimizing the second norm of the error. Moreover, using spectral value decomposition,

$$[Q]=[T_w AS]=[U][\lambda][V]^T=\sum_{i=1}^{m}\lambda_i u_i v_i^T \tag{4-29}$$

Since $[Q]$ is a rectangular matrix of order $(n-1=\kappa)\times m$, $[U]$ and $[V]$ are the square matrices such that $[U]^T[U]$ and $[V]^T[V]$ are the identity matrices of order κ and m, respectively, and $[\lambda]$ is a $\kappa\times m$ rectangular matrix containing the spectral values (real and non-negative, by definition) of $[Q]$ in m leading diagonals in a descending order and all other elements are zero. Further, u_i and v_i are the i^{th} column of $[U]$ and $[V]$, respectively. If Eq (4-28) represents a completely overdetermined problem, its solution may be expressed as

$$S^{-1}\ddot{\bar{p}}=[V_m][\lambda_m]^{-1}[U_m]^T[T_w]\{\Delta\ddot{u}\}=\left[\sum_{i=1}^{m}\frac{1}{\lambda_i}v_i u_i^T\right][T_w]\{\Delta\ddot{u}\} \tag{4-30}$$

where $[\lambda_m]$ is the leading diagonal matrix of order m derived from $[\lambda]$, whereas $[U_m]$ and $[V_m]$ are derived from $[U]$ and $[V]$, respectively, taking the first m columns only. It may be noted that Eq (4-30) is exactly identical to Eq (4-26). Noting that $[G]=[Q]^T[Q]$, it is readily seen that spectral values of $[Q]$ will be same as the square root of the eigenvalues of $[G]$.

Among the set of m unknowns in $\{S^{-1}\ddot{p}\}$, if m_o are overdetermined and $m_u=m-m_o$ are underdetermined, then $[\lambda]$ will have zeros in the last m_u entries in the leading diagonal. This shows that $[G]$ cannot be inverted and Eq (4-26) cannot be used as the solution of Eq (4-25). Since $[S]$ can be inverted, underdeterminacy (precisely, mixed determinacy) implies that Eq (4-2) also will not hold. In such a case, Eq (4-29) remains the same if m is replaced by m_o. The natural solution of such a mixed determined problem is given by Eq (4-30) with m replaced by m_o. The mixed determinacy of the problem can be tested by taking the spectral value decomposition of the transformed data kernel and checking the existence of zero spectral values. In the presence of such mixed determinacy, the natural

solution can be obtained as discussed above. However, the most critical part of the problem is treating spectral values that are not exactly zero but very close to zero. It is always possible to have all the spectral values of the transformed data kernel close to zero by selecting very large characteristic length but this will be quite misleading. Before proceeding further, it is necessary to comment on the selection of the characteristic length.

The characteristic length is considered as the SRSS of the dimensions of the dense array along the *x* and *y* directions. The spectral values of the transformed data kernel are then calculated from AGM1. The chosen characteristic length is then scaled so that the first (higher of the two) spectral value becomes close to but less than unity, say 0.99. The vertical acceleration is analyzed with this characteristic length and results are presented at an arbitrarily selected time instant of 5.995 sec, using the AGM with orders 1 through 4. Table 4-1 presents the results of the AGM1. Note that the spectral values are independent of the selected time instant but not the estimated gradient parameters ($\ddot{\bar{p}}$). From column 2 of Table 4-1, it is seen that the highest spectral value is close to unity as targeted. Table 4-2 shows the results obtained using AGM2. Of the five spectral values (column 2, Table 4-2), the first two are close to those obtained using AGM1. Further, the gradient parameters estimated using all five spectral values in AGM2 are presented in column 4 of the table. The gradient parameters computed using the first two spectral values are shown in column 5 of the table. It is important to compare the first two gradient parameters (being common) in AGM1 and AGM2. The estimated values are quite different in AGM1 and AGM2 when the contributions of all spectral values are taken into account. However, this difference is significantly reduced when only the contributions of first two spectral values are considered in AGM2. Table 4-3 presents the results using AGM3. It is evident from column 2 of this table that, of nine spectral values, the first five are nearly the same as obtained in AGM2. The gradient parameters computed using all nine spectral values are presented in column 4. The gradient parameters computed using the first five and first two spectral values are shown in columns 5 and 6, respectively. Again, the gradient parameters computed using all spectral values (column 4, Table 4-3) are compared with those obtained using the lower order

AGM. For example, the first five gradient parameters computed using all spectral values (column 4) are substantially different from those obtained using AGM2 (with all five spectral values). Similarly, the first two gradient parameters in column 4 are substantially different from those computed for AGM1. However, if only the first five spectral values are considered for AGM3, then the first five gradient parameters (column 5, Table 4-3) are close to those obtained for AGM2 with all five spectral values taken into account (column 4, Table 4-2). Similarly, if only the first two spectral values are included for AGM3, the first two gradient parameters (column 6, Table 4-3) are close to those estimated for AGM1 (column 4, Table 4-1). AGM4 is considered next and it involves 14 gradient parameters. The results are presented in Table 4-4. The trends identified above for AGM2 and AGM3 are also seen for AGM4 and are not repeated here. Therefore, if the data kernel is scaled as described above, it can be concluded that: i) if the spectral values are computed using the AGM of two consecutive orders, the set associated with the lower order is approximately retained within the set computed using the higher order, ii) if the gradient parameters are estimated using any lower order AGMn but taking all associated $n(n+3)/2$ spectral values into account, the estimated set is nearly preserved in any higher order AGMm $(m>n)$ when using the contributions from the first $n(n+3)/2$ spectral values, and iii) the difference in the estimated gradient parameters using the AGM of two consecutive orders is mostly due to the contributions of the additional spectral values associated with the higher order AGM. Therefore, significantly low spectral values associated with third and fourth order AGM (when compared to AGM1 and AGM2) may be considered as the source of mixed determinacy in the problem that leads to an impractical solution.

These conclusions will not hold if the data kernel is not normalized or if the characteristic length is arbitrarily selected. To show this, the same set of analyses described above is repeated but using a characteristic length of unity. This case may also be thought of using the data kernel that is not normalized. Results are presented in Table 4-5 through Table 4-8. The trends seen in Table 4-1 through Table 4-4 are not evident in Table 4-5 through Table 4-8. However, when all the spectral values are taken into account in estimating the gradient parameters, Table 4-5 through Table 4-8 list results (column 4 in

each table) that are identical to those presented in Table 4-1 through Table 4-4, respectively. Accordingly, if all the spectral values are to be taken into account, regardless of how close to zero they are, that is, treating the problem as completely overdetermined, the selection of the characteristic length does not affect the estimation of the gradient parameters.

The definition of the characteristic length in such a way that the highest (first) spectral value is close to, but less than, unity is useful to separate out the *near singularity case* from the apparently overdetermined problem. Again note that the *near singularity case* is not a true mathematical singularity but rather implies a case where the solution is not feasible. If the gradient parameters are estimated without using characteristic length [Eq 4-2] or using characteristic length but accounting for the all the spectral values [Eq (4-26) or Eq (4-30)], both the AGM3 and AGM4 do not show a true mathematical singularity and the estimated gradient parameters are not feasible. This was noted previously by the comparison of Figures 4-3 through Figure 4-5.

Even though the above observations are specific to the Lotung array, it is expected to be valid for other seismic arrays due to the finite number and finite spacing of the recording stations in these arrays. On this basis, the AGM of order two (AGM2) is recommended.

4.6. Computations using Recordings from the Lotung Array

Rotational components obtained from the translational strong motion records described in Chapter 2 are compared below. The computer program implementing AGM2 with illustrations are provided in Appendix E.

Comparison of rotational spectra using GM, AGM2 and SSP

The rotational spectra computed using GM and AGM1 are compared in Figure 4-6. Panel a compares the torsional spectra. Similar data for rocking motions on the *xz* and *yz* planes are presented in panels b and c, respectively. In all three cases, the spectra obtained using the GM match well with those resulting

Table 4-1. AGM1 using normalized data kernel

Spectral values		Gradient parameters	
Mode	Magnitude	Type	Values
1	9.8970E-01	$\ddot{w}_{1,10}$	3.1000E-03
2	8.3600E-01	$\ddot{w}_{1,01}$	9.0800E-04

Table 4-2. AGM2 using normalized data kernel

Spectral values		Gradient parameters		
Mode	Magnitude	Type	All spectral values	First order spectral values
1	1.0026E+00	$\ddot{w}_{1,10}$	2.4000E-03	2.8000E-03
2	8.8340E-01	$\ddot{w}_{1,01}$	2.0000E-03	8.9536E-04
3	2.1490E-01	$\ddot{w}_{2,20}$	6.8357E-05	-2.2773E-06
4	7.3200E-02	$\ddot{w}_{2,11}$	-4.6356E-05	-1.3275E-05
5	5.9700E-02	$\ddot{w}_{2,02}$	-8.1133E-05	2.9385E-06

Table 4-3. AGM3 using normalized data kernel

Spectral values		Gradient parameters			
Mode	Magnitude	Type	All spectral values	Second order spectral values	First order spectral values
1	1.0045E+00	$\ddot{w}_{1,10}$	-1.5440E-01	2.6000E-03	2.8000E-03
2	8.8540E-01	$\ddot{w}_{1,01}$	-1.0700E-02	1.9000E-03	8.9483E-04
3	2.2210E-01	$\ddot{w}_{2,20}$	-1.8000E-02	5.4394E-05	-2.2697E-06
4	7.8700E-02	$\ddot{w}_{2,11}$	-2.2800E-02	-3.1492E-05	-1.3213E-05
5	6.4000E-02	$\ddot{w}_{2,02}$	-1.5255E-05	-7.3875E-05	2.9331E-06
6	5.0000E-03	$\ddot{w}_{3,30}$	6.6950E-04	-7.4612E-09	1.9879E-08
7	2.9000E-03	$\ddot{w}_{3,21}$	-9.0082E-04	-3.5817E-07	4.6029E-09
8	1.2000E-03	$\ddot{w}_{3,12}$	-1.7000E-03	1.3009E-07	3.4095E-08
9	2.2522E-04	$\ddot{w}_{3,03}$	6.9961E-05	-3.2727E-07	4.8566E-09

Table 4-4. AGM4 using normalized data kernel

Spectral values		Gradient parameters				
Mode	Magnitude	Type	All spectral values	Third order spectral values	Second order spectral values	First order spectral values
1	1.0045E+00	$\ddot{w}_{1,10}$	3.6397E+00	-1.4260E-01	2.6000E-03	2.8000E-03
2	8.8550E-01	$\ddot{w}_{1,01}$	-7.7900E-02	-9.8000E-03	1.9000E-03	8.9488E-04
3	2.2250E-01	$\ddot{w}_{2,20}$	4.3910E-01	-1.8100E-02	5.4150E-05	-2.2691E-06
4	7.8900E-02	$\ddot{w}_{2,11}$	1.2116E+00	-2.0700E-02	-3.0945E-05	-1.3210E-05
5	6.4300E-02	$\ddot{w}_{2,02}$	-1.0500E-02	8.5969E-05	-7.3834E-05	2.9332E-06
6	5.1000E-03	$\ddot{w}_{3,30}$	-1.8640E-01	5.7553E-04	-8.8318E-09	1.9875E-08
7	3.1000E-03	$\ddot{w}_{3,21}$	3.7400E-02	-8.8658E-04	-3.5595E-07	4.6014E-09
8	1.3000E-03	$\ddot{w}_{3,12}$	2.5660E-01	-1.5000E-03	1.2753E-07	3.4088E-08
9	2.3327E-04	$\ddot{w}_{3,03}$	1.0000E-02	2.0343E-05	-3.2579E-07	4.8575E-09
10	5.2260E-05	$\ddot{w}_{4,40}$	4.2000E-03	-3.0915E-06	3.3588E-10	-1.1913E-11
11	3.4140E-05	$\ddot{w}_{4,31}$	-1.0800E-02	4.2182E-07	-1.2761E-10	-1.0293E-10
12	6.4112E-06	$\ddot{w}_{4,22}$	1.8000E-03	-3.4283E-07	1.1067E-09	7.7796E-12
13	9.0594E-07	$\ddot{w}_{4,13}$	2.4400E-02	5.2632E-06	-3.5378E-10	-6.1226E-11
14	1.1789E-07	$\ddot{w}_{4,04}$	-1.6000E-03	3.1341E-06	-5.0668E-10	2.0628E-11

Table 4-5. AGM1 using original data kernel

Spectral values		Gradient parameters	
Mode	Magnitude	Type	Values
1	7.0947E+01	$\ddot{w}_{1,10}$	3.1000E-03
2	5.9928E+01	$\ddot{w}_{1,01}$	9.0800E-04

Table 4-6. AGM2 using original data kernel

Spectral values		Gradient parameters		
Mode	Magnitude	Type	All spectral values	First order spectral values
1	1.6094E+03	$\ddot{w}_{1,10}$	2.4000E-03	4.5626E-06
2	1.0586E+03	$\ddot{w}_{1,01}$	2.0000E-03	-6.6414E-07
3	7.6200E+02	$\ddot{w}_{2,20}$	6.8357E-05	-2.9038E-05
4	3.4841E+01	$\ddot{w}_{2,11}$	-4.6356E-05	-1.1463E-04
5	1.2819E+01	$\ddot{w}_{2,02}$	-8.1133E-05	-1.8655E-05

Table 4-7. AGM3 using original data kernel

Spectral values		Gradient parameters			
Mode	Magnitude	Type	All spectral values	Second order spectral values	First order spectral values
1	3.0478E+04	$\ddot{w}_{1,10}$	-1.5440E-01	-2.5815E-05	1.7214E-08
2	2.2133E+04	$\ddot{w}_{1,01}$	-1.0700E-02	6.8843E-05	4.5253E-09
3	1.3853E+04	$\ddot{w}_{2,20}$	-1.8000E-02	-1.9901E-04	-1.4219E-07
4	1.2589E+03	$\ddot{w}_{2,11}$	-2.2800E-02	2.7216E-04	-4.3830E-07
5	1.8055E+02	$\ddot{w}_{2,02}$	-1.5255E-05	-5.5144E-04	3.8127E-08
6	4.9828E+01	$\ddot{w}_{3,30}$	6.6950E-04	-8.3265E-05	3.8829E-06
7	2.8635E+01	$\ddot{w}_{3,21}$	-9.0082E-04	-1.3232E-06	2.5773E-06
8	1.4927E+01	$\ddot{w}_{3,12}$	-1.7000E-03	8.1873E-05	5.8162E-06
9	1.1356E+00	$\ddot{w}_{3,03}$	6.9961E-05	3.4510E-05	5.4294E-07

Table 4-8. AGM4 using original data kernel

Spectral values		Gradient parameters				
Mode	Magnitude	Type	All spectral values	Third order spectral values	Second order spectral values	First order spectral values
1	4.8871E+05	$\ddot{w}_{1,10}$	3.6397E+00	-2.1789E-04	-5.2446E-08	6.1095E-11
2	3.2063E+05	$\ddot{w}_{1,01}$	-7.7900E-02	-9.6785E-05	1.6469E-07	1.5059E-11
3	1.5985E+05	$\ddot{w}_{2,20}$	4.3910E-01	-3.0864E-04	-6.3719E-07	-6.2764E-10
4	1.2622E+04	$\ddot{w}_{2,11}$	1.2116E+00	1.2000E-03	7.2323E-07	-1.5551E-09
5	3.3779E+03	$\ddot{w}_{2,02}$	-1.0500E-02	1.7002E-05	-7.0658E-07	1.1550E-11
6	5.4810E+02	$\ddot{w}_{3,30}$	-1.8640E-01	1.9000E-03	-1.3385E-06	1.4467E-08
7	2.4524E+02	$\ddot{w}_{3,21}$	3.7400E-02	1.8000E-03	7.5166E-06	1.2530E-08
8	7.7100E+01	$\ddot{w}_{3,12}$	2.5660E-01	-8.0764E-04	-3.6971E-06	2.0407E-08
9	3.3667E+01	$\ddot{w}_{3,03}$	1.0000E-02	-2.5661E-04	7.7570E-06	1.3169E-09
10	2.6219E+01	$\ddot{w}_{4,40}$	4.2000E-03	-5.9424E-04	2.0988E-05	-8.5151E-08
11	5.3897E+00	$\ddot{w}_{4,31}$	-1.0800E-02	3.0135E-04	-4.6916E-07	-3.6835E-07
12	1.6556E+00	$\ddot{w}_{4,22}$	1.8000E-03	2.5380E-04	-6.8882E-06	-1.0860E-07
13	7.3060E-01	$\ddot{w}_{4,13}$	2.4400E-02	-3.0622E-04	-5.7535E-06	-1.8351E-07
14	1.5400E-02	$\ddot{w}_{4,04}$	-1.6000E-03	2.9134E-05	-4.7952E-07	1.8435E-08

from AGM1. The error associated with the numerical integrations and differentiations in using GM is small. The results of analysis using the GM, SSP and AGM2 are presented next.

The AGM2 and SSP compute spectra at multiple stations in an array whereas the GM returns one spectrum as representative of the entire array. Even though the results are presented for all 15 surface stations from the Lotung array, only six stations are selected for the detailed comparison of procedures, namely, FA1_1, FA1_2, FA2_1, FA3_1, FA1_5 and FA2_5. The first four stations are located in the interior of the array and the remaining two are in the outer ring.

Torsional Spectra

Figure 4-7 enables a comparison of the torsional spectra. There are two important observations: 1) for the interior stations, the ordinates of the three spectra are similar at intermediate to high periods but at lower periods, the ordinates computed using the GM are much smaller than those computed using AGM2, which in turn are less than those computed using the SSP; and 2) at the exterior stations (for example, FA1_5 (panel e), FA2_5 (Panel j) and FA3_5 (panel o)), the relative values of the ordinate of the GM and SSP are similar to those computed for the interior stations, but the spectral demands computed using the AGM2 are quite different from those at the interior stations and are greater than the demands calculated using either the GM or SSP.

If it is assumed that the frequency content of the recorded ground motion is preserved in the SSP, the first observation indicates the AGM2 preserves the high frequency content, which are lost in the GM. As noted previously, high frequency errors may accumulate with AGM2 if the SH wave component of the ground motion (which dictates the torsional motion, as noted in Chapter 3) has significant frequency content beyond the threshold frequency ($= c/2L$), but the error may not be significant unless there is substantial frequency content beyond twice the threshold frequency ($= c/L$). To verify this hypothesis, the apparent wave velocity for the SH wave was first calculated using the results of the SSP analysis (Chapter 3): half the ratio of the absolute peak of the derivative of the acceleration history contributed

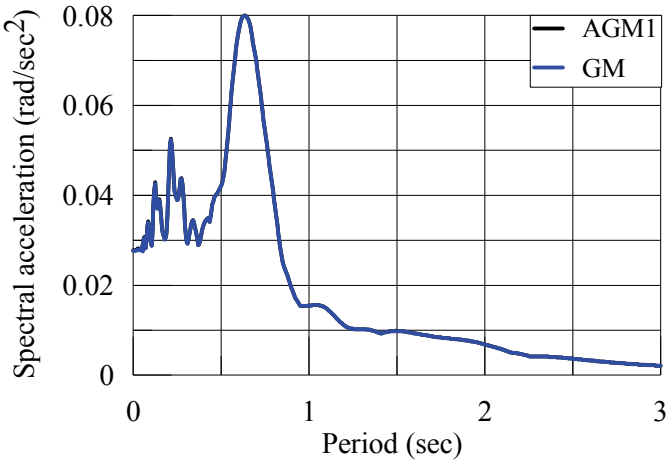

(a) Torsional spectra

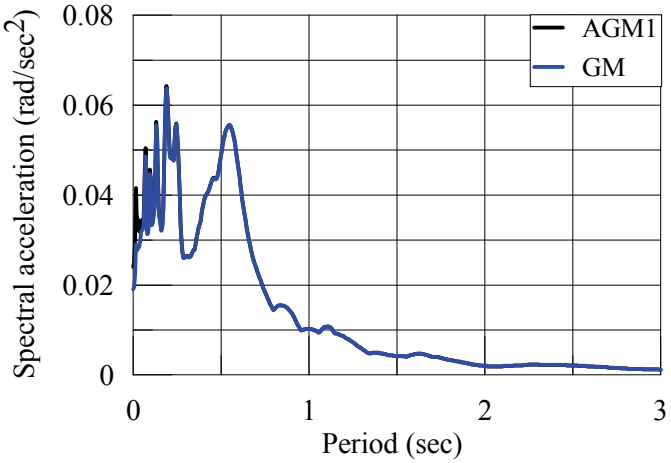

(b) Rocking (*xz* plane) spectra

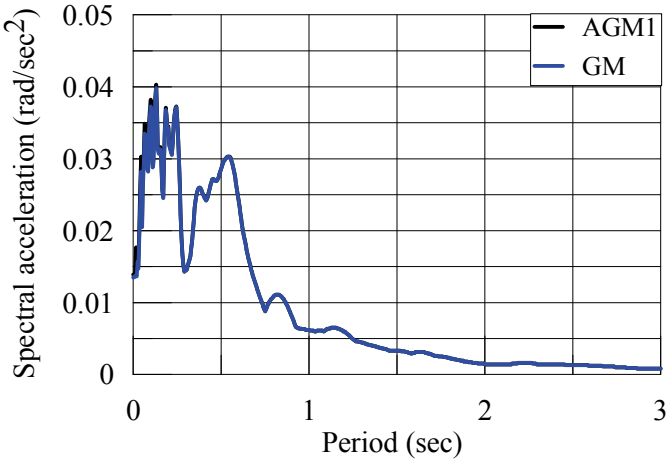

(c) Rocking (*yz* plane) spectra

Figure 4-6: Spectra computed using AGM1 and GM

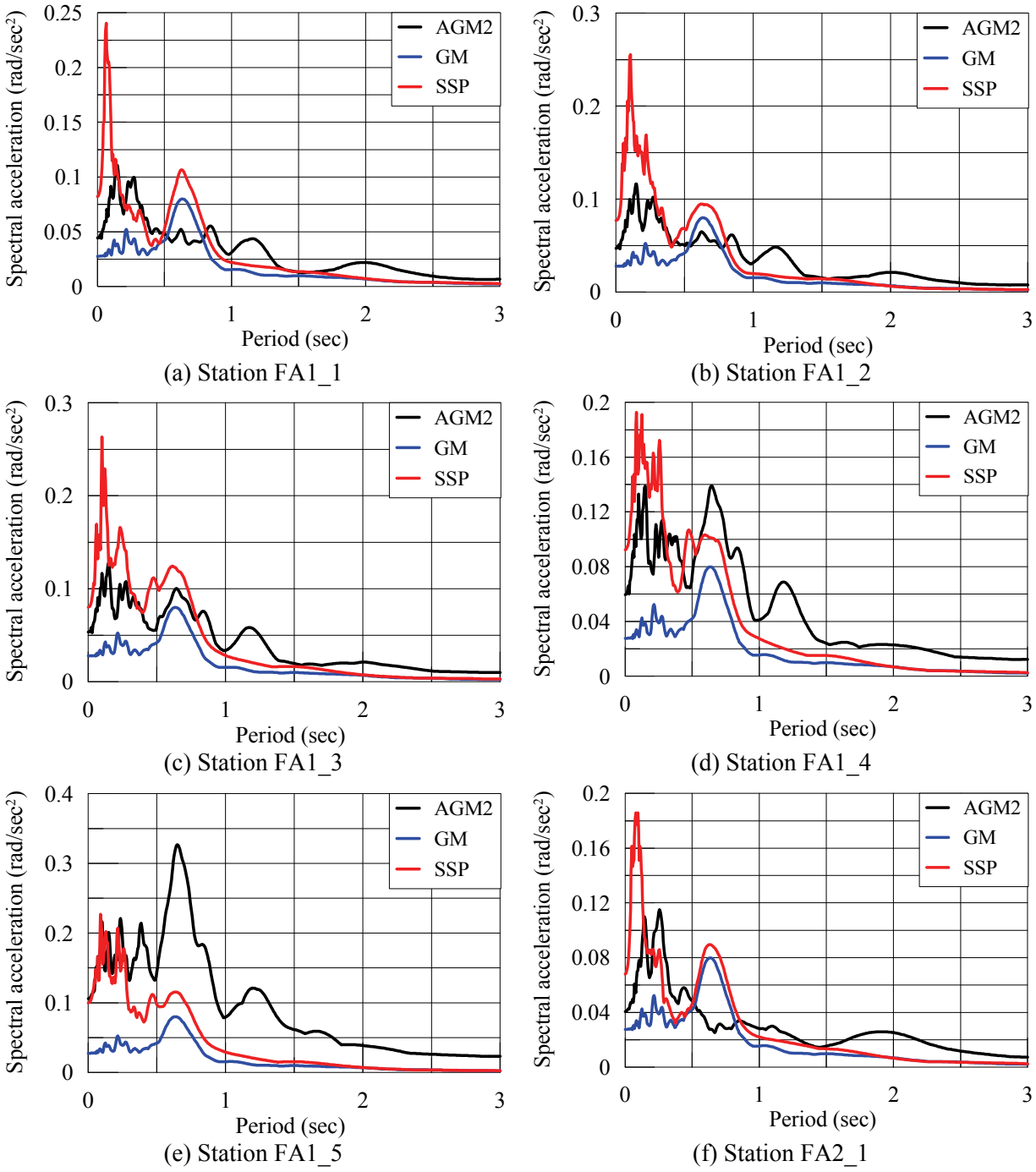

Figure 4-7: Torsional spectra computed using three different methods (cont.)

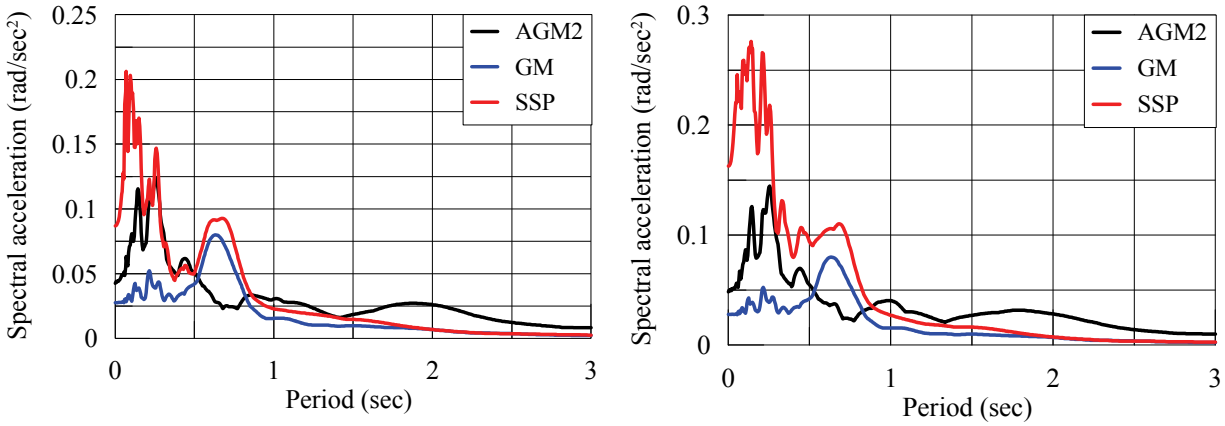

(g) Station FA2_2

(h) Station FA2_3

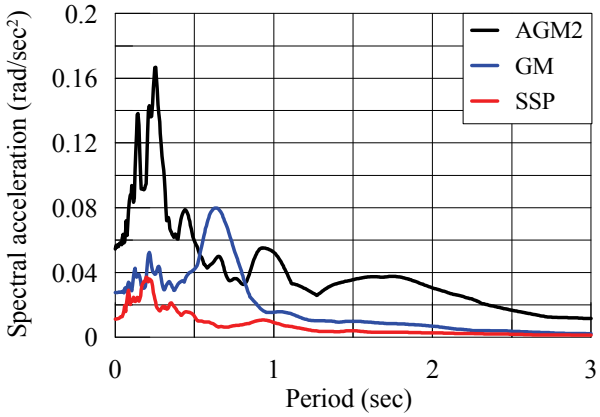

(i) Station FA2_4

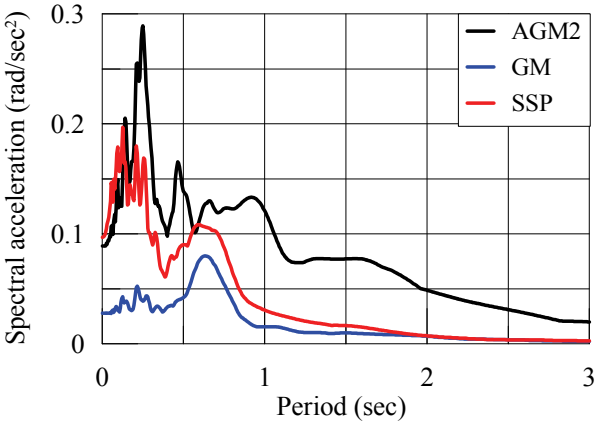

(j) Station FA2_5

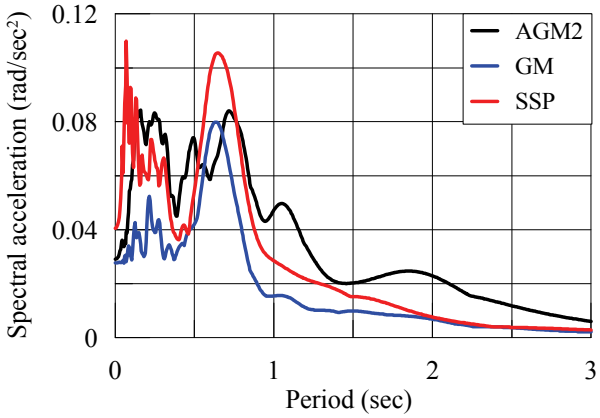

(k) Station FA3_1

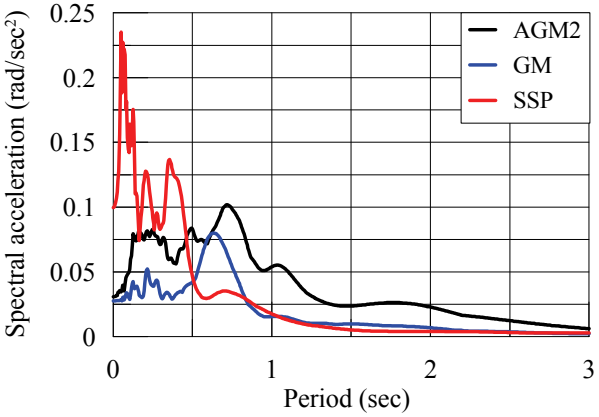

(l) Station FA3_2

Figure 4-7: Torsional spectra computed using three different methods (cont.)

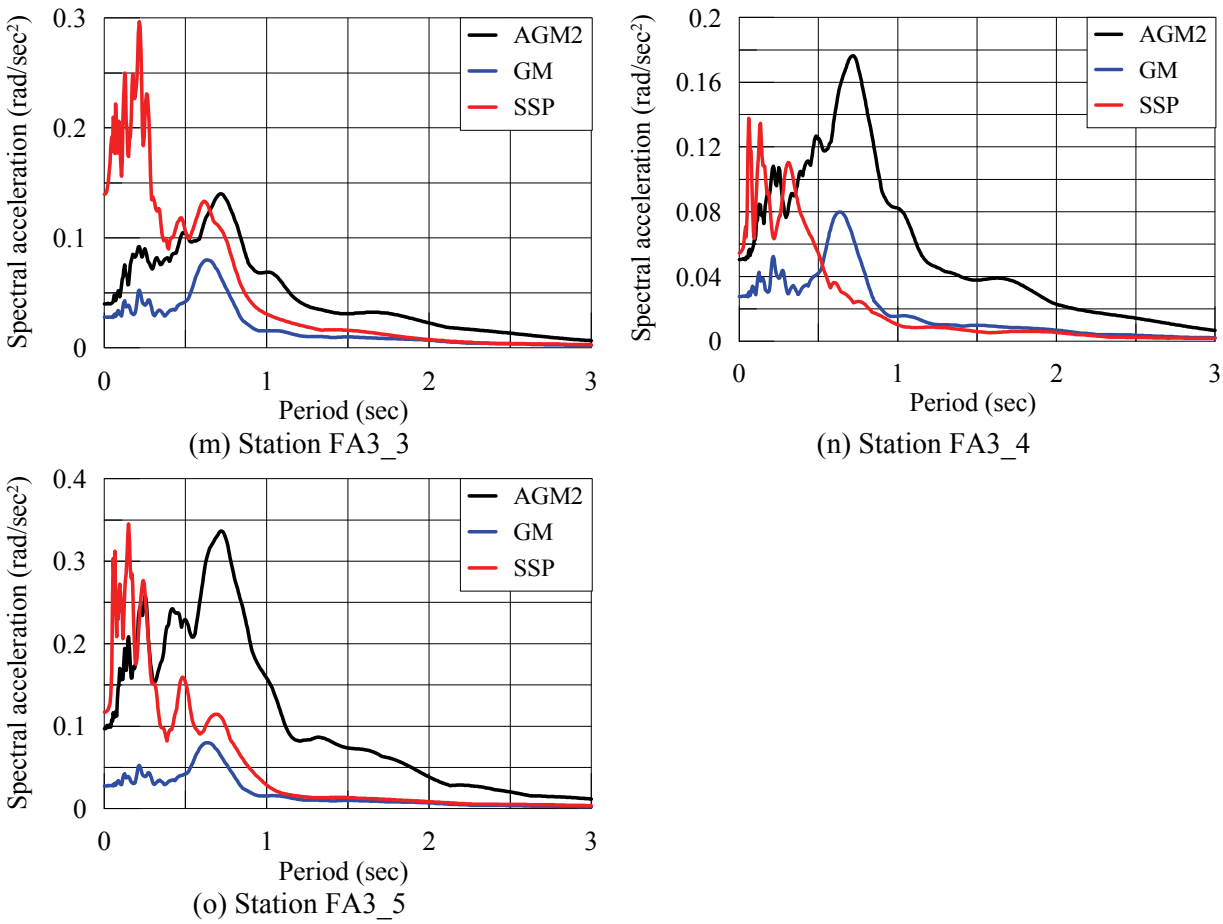

(m) Station FA3_3

(n) Station FA3_4

(o) Station FA3_5

Figure 4-7: Torsional spectra computed using three different methods

from the SH wave to the resulting absolute peak torsional acceleration. Table 4-9 presents the apparent wave velocities for the SH wave computed at different stations. The average velocity is 249 m/sec with a coefficient of variation (COV) of 6%. The length of the array is 75 m as calculated from the spatial distribution of the recording stations; see Chapter 6 for further details. The threshold frequency is 1.66 Hz ($= 249/(2\times 75)$). The torsional spectra computed using AGM2 should not include high frequency errors for periods greater than 0.6 sec (1.66 Hz) but the error may be significant for periods smaller than 0.3 sec.

The second observation is associated with the error norm in the Taylor expansion. To explain this, consider an interior and an exterior reference station. Recall that the computed best-fit surface in the AGM2 is independent of the selection of the reference station and that the gradient parameters computed by the least-squares solution are those of the reference point. However, the magnitude of the error increases with the distance between the most distant station considered in the calculation and the reference station (separation distance). Since the separation distance for the exterior reference station is greater than for the interior reference station, the error in the estimated gradient parameters will be greater for the exterior station. The spectral shape at the exterior stations obtained using AGM2 is different from that at the interior stations due to these errors in the computation.

Rocking Spectra

Comparisons for the rocking spectra on the *xz* and *yz* planes are presented in Figures 4-8 and 4-9, respectively. For the interior stations, the ordinates of the three spectra are similar at the intermediate to high periods, which are the same observations made for the torsional spectra of Figure 4-7. For interior stations and low periods, the ordinates of the AGM2 spectra are not necessarily smaller than those of the SSP, which is different from that observed for the torsional spectra. The spectral ordinates at stations, for example, FA2_1 (panel f) and FA3_1 (panel k) in Figure 4-9, computed using the AGM2 are greater than those obtained using the SSP. This outcome is due to the influence of the orientation of the principal plane considered in the SSP (Chapter 3). In the SSP, rocking motion on the plane normal to the principal

Table 4-9: Apparent wave velocity

Station	Wave velocity (m/sec)					
	Horizontal motion	Vertical motion				
	SH wave	Recorded	SV wave	P wave	Homogeneous P wave	Inhomogeneous P wave
FA1_1	260	1103	189	1231	1421	388
FA1_2	250	780	176	999	1410	409
FA1_3	239	836	193	1111	1215	396
FA1_4	267	783	184	1073	1394	401
FA1_5	249	715	181	1167	1345	425
FA2_1	241	1050	196	1291	1704	416
FA2_2	255	821	198	833	1068	413
FA2_3	238	1016	182	1181	1548	411
FA2_4*	284	490	220	530	1095	344
FA2_5	257	558	176	893	1161	419
FA3_1	230	956	200	1088	1338	407
FA3_2*	237	491	196	866	1125	380
FA3_3	240	517	180	705	1112	389
FA3_4*	242	419	163	712	829	313
FA3_5	241	436	199	591	805	416
Mean	249	731	189	951	1238	395
Standard deviation	14	235	13	239	248	30
COV	0.06	0.32	0.07	0.25	0.20	0.08

* Based on the partial data registered at these stations

plane is zero and thus the motion (rocking) on the *xz* and *yz* plane is the cosine and sine component of that which exists on the principal plane. Clearly, the selection of the orientation of the principal plane affects the relative spectral ordinates on the *xz* and *yz* planes. To eliminate this influence, a unified spectral representation for the rocking component is required to enable a comparison. Two such representations namely, the SRSS (square root sum of the squares) and geomean spectra computed on the *xz* and *yz* planes, are considered in Figures 4-10 and 4-11, respectively. The spectral ordinates at the interior stations show similar trends to those noted for the torsional spectra.

The threshold frequency (period) below (above) which the three procedures provide similar rocking spectra is calculated again. This frequency is difficult to compute as both SV waves and P waves (homogeneous and inhomogeneous) contribute to the rocking motion and these waves propagate at different apparent velocities. Table 4-9 shows the computed apparent velocities for each type of wave

contributing to the vertical motion and also for the case in which the vertical motion is the recorded motion (i.e., not decomposed). The calculation procedure is similar to that used for the SH wave: ratio of the absolute peak of the derivative of the acceleration history contributed from any particular wave to the resulting absolute peak rocking acceleration. The COV of the apparent wave velocity computed directly from the recorded motion is 32%, which suggests that a simple estimate of the threshold frequency is not possible for rocking spectra. When the vertical motion is decomposed into the P wave (without distinguishing homogeneous and inhomogeneous) and SV wave, Table 4-9 shows that the value for the SV wave is stable with a COV of 7%. The COV for the P wave is 25%. When the P wave contribution is decomposed into its homogeneous and inhomogeneous parts (see Chapter 3), the inhomogeneous P wave is somewhat stable with a COV of 8% whereas that of the homogeneous part is 20%. The mean apparent velocities of Table 4-9 are used to compute the threshold frequencies for the respective waves. Results are 1.26 Hz, 8.25 Hz and 2.63 Hz for the SV, homogeneous and inhomogeneous P waves, respectively. There should be no high frequency error associated with the SV wave at periods greater than 0.8 sec (1.26 Hz) but the error is expected to be significant for periods of less than 0.4 sec. The period-pair for the homogeneous P wave is 0.12 sec and 0.06 sec, and for the inhomogeneous P wave is 0.38 sec and 0.19 sec. Clearly, the deviation of the spectra computed using the AGM2 from that obtained using the SSP depends on the relative contributions of theses waves. However, regardless of the relative contributions, both the spectra (AGM2 and SSP) should not differ appreciably at periods greater than 0.8 sec. See, for example, panels a, b, d and f of Figures 4-10 and 4-11. At periods equal to or greater than approximately 0.8 sec, the spectral demand computed using AGM2 and SSP are very similar. This outcome is attributed to the low COV associated with the computation of the apparent velocity of the SV wave. If the vertical motion is contributed mostly by the SV wave, the high frequency error is expected to be significant for periods less than 0.4 sec provided there is substantial frequency content in the recorded vertical motion beyond 2.5 Hz. Similarly, if the vertical motion is contributed mostly by the inhomogeneous (homogeneous) P wave, the high frequency error may be significant for periods less than 0.19 sec (0.06 sec) if the frequency content is substantial beyond 5.25 Hz (17Hz). However, regardless of the relative

contributions from the individual type of waves, a high frequency error is expected to be significant for periods less than 0.06 sec if the recorded motion has significant frequency content above 17 Hz. For most of the interior stations, there is a significant difference in spectral demand at periods considerably greater than 0.1 sec. This is attributed to: a) the high COV in the computed apparent velocity of the homogeneous P wave, b) unknown relative contributions from the two P waves and SV waves, and c) spectra computed using the SSP is low-pass-filtered of a cut-off frequency of 20 Hz (Chapter 3).

At the exterior stations (Figures 4-10 and 4-11, for example, panels e, j and o), the spectral ordinates computed using AGM2 exceed those obtained using the SSP for reasons as discussed above for torsional spectra.

Note that stations FA1_4, FA3_2 and FA3_4 acquired data for only part of the earthquake. The peak ground acceleration at FA1_4 is about one-tenth of that recorded in the adjacent stations, which is physically unrealistic. These three stations should be ignored when comparing the results obtained with different procedures.

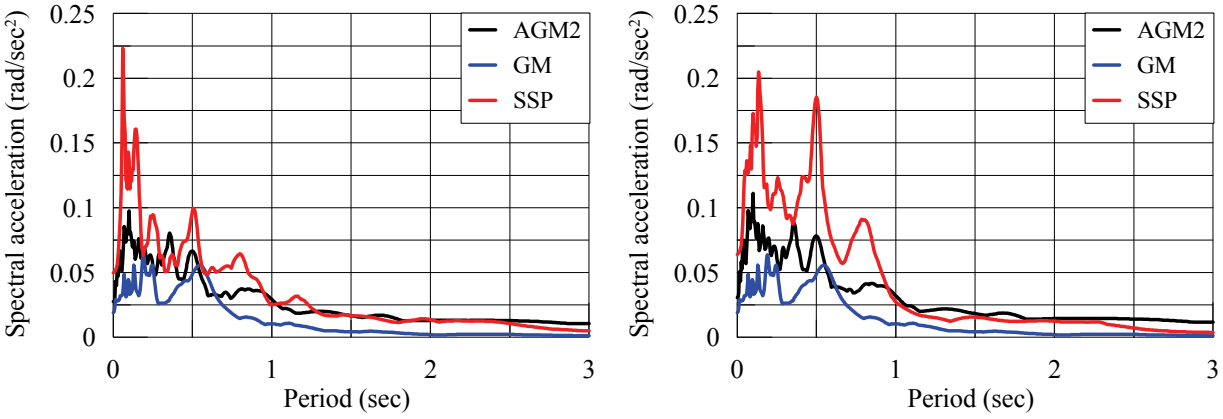

(a) Station FA1_1

(b) Station FA1_2

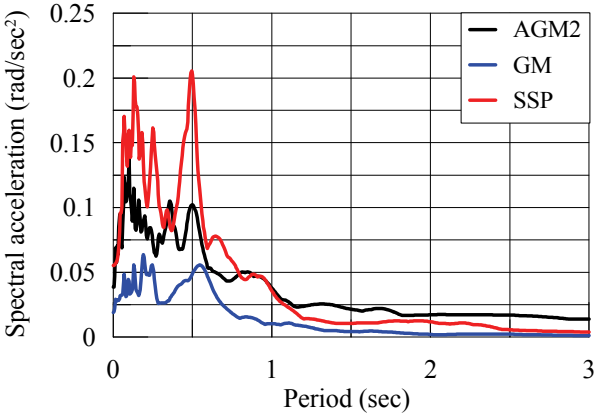

(c) Station FA1_3

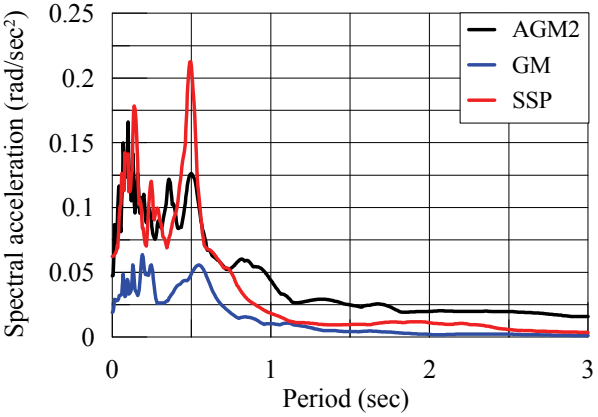

(d) Station FA1_4

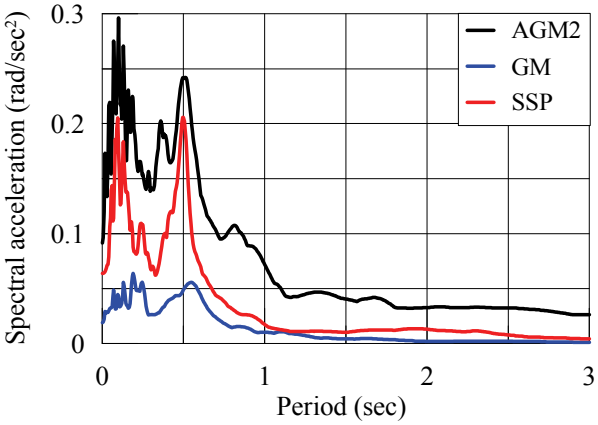

(e) Station FA1_5

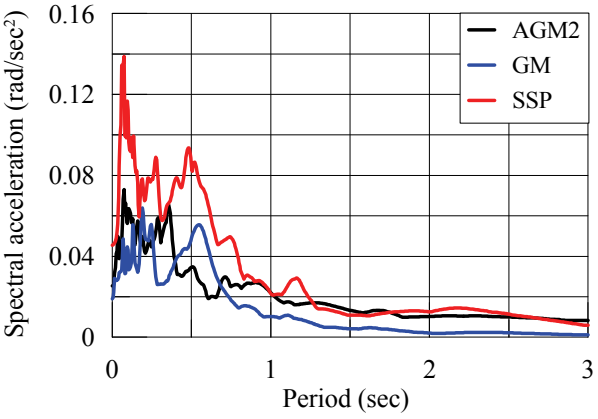

(f) Station FA2_1

Figure 4-8: Rocking (*xz* plane) spectra computed using three different methods (cont.)

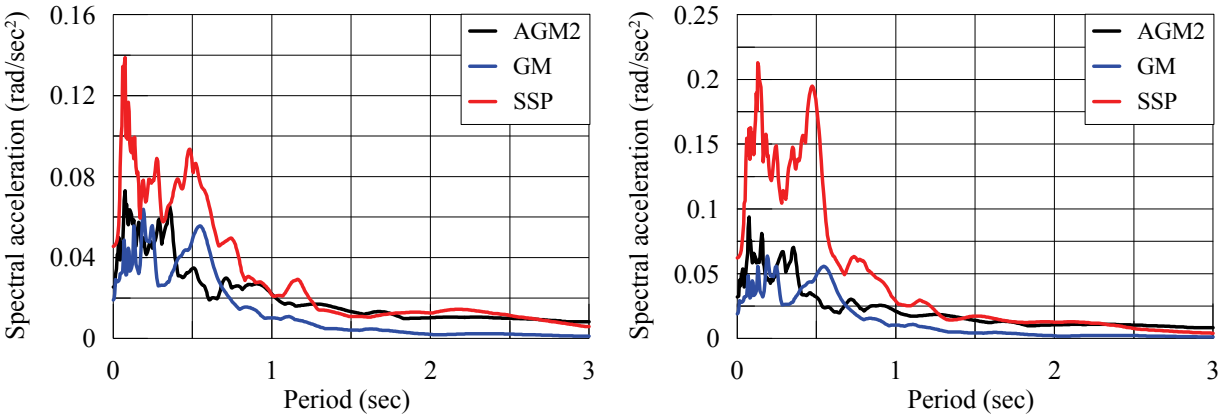

(g) Station FA2_2

(h) Station FA2_3

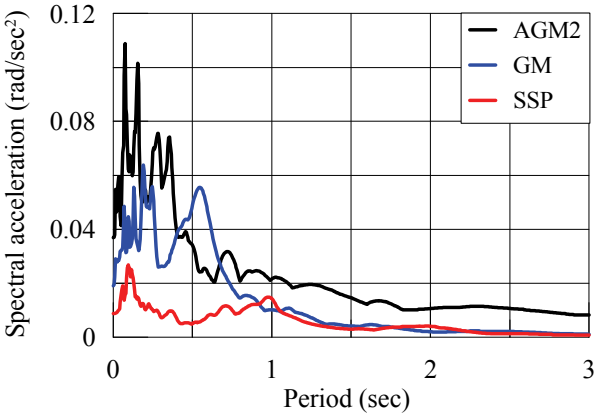

(i) Station FA2_4

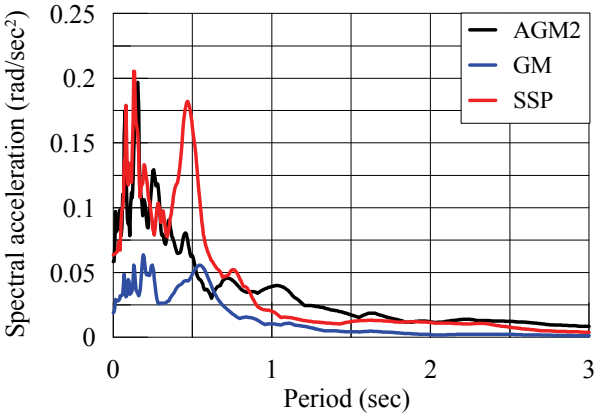

(j) Station FA2_5

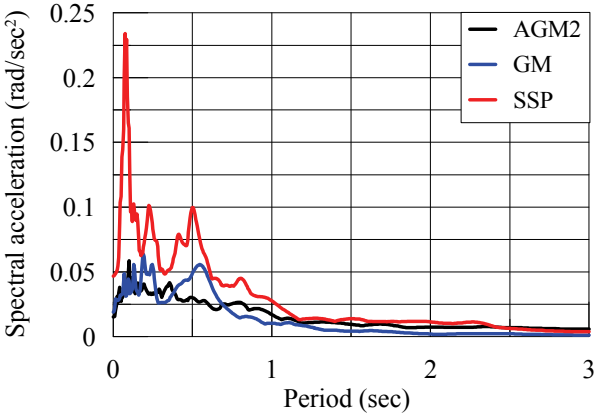

(k) Station FA3_1

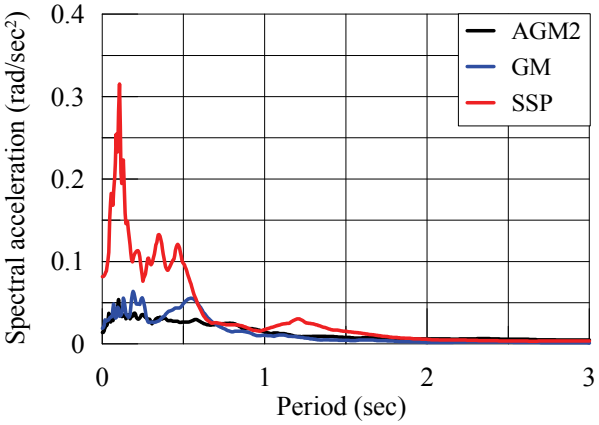

(l) Station FA3_2

Figure 4-8: Rocking (*xz* plane) spectra computed using three different methods (cont.)

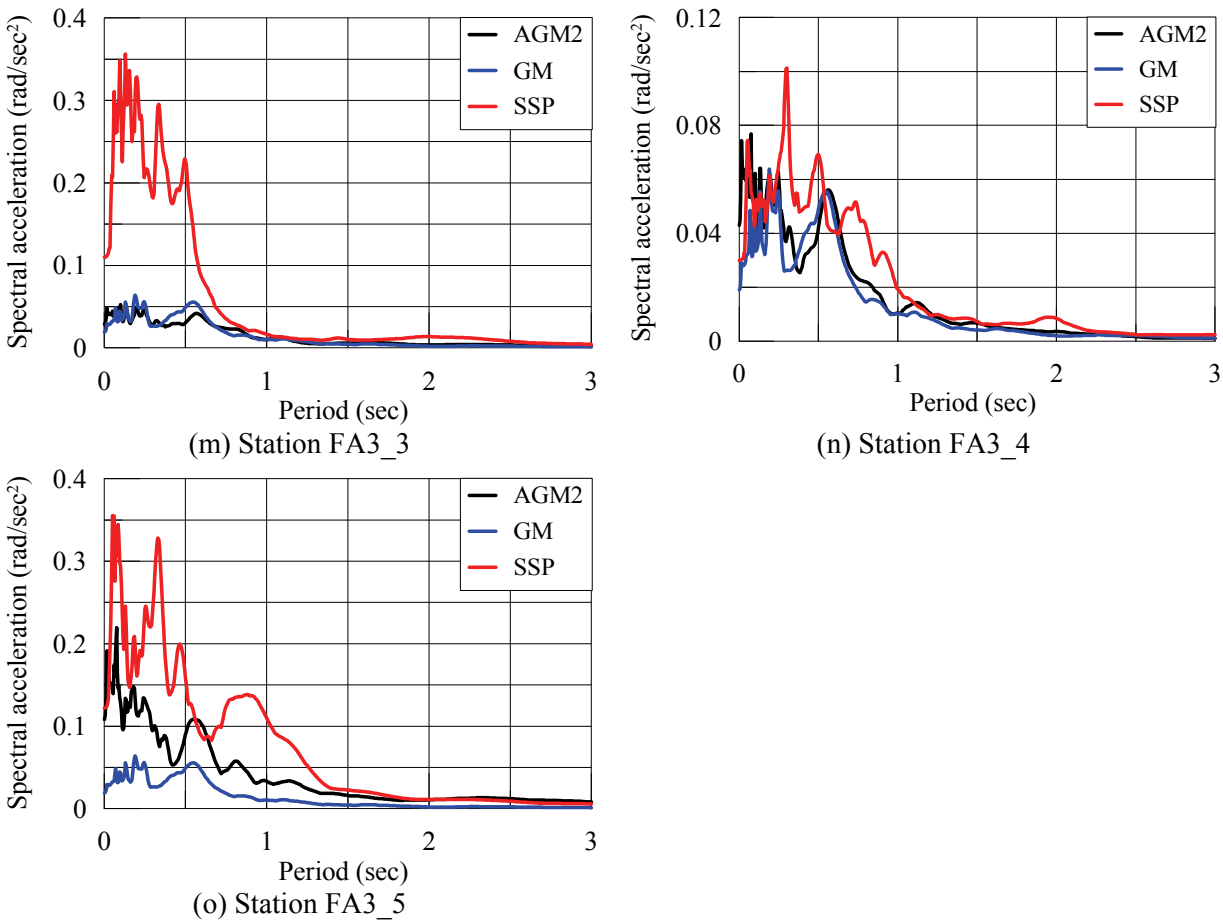

Figure 4-8: Rocking (*xz* plane) spectra computed using three different methods

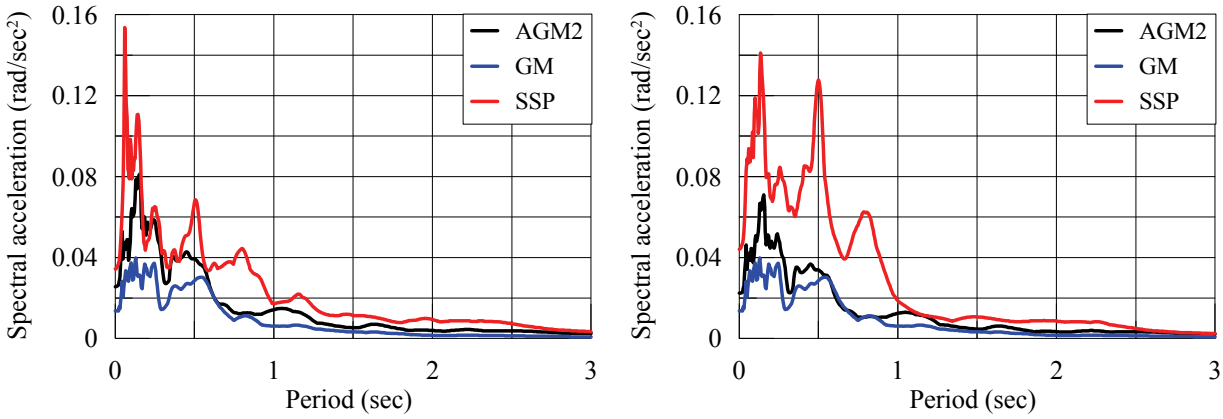

(a) Station FA1_1

(b) Station FA1_2

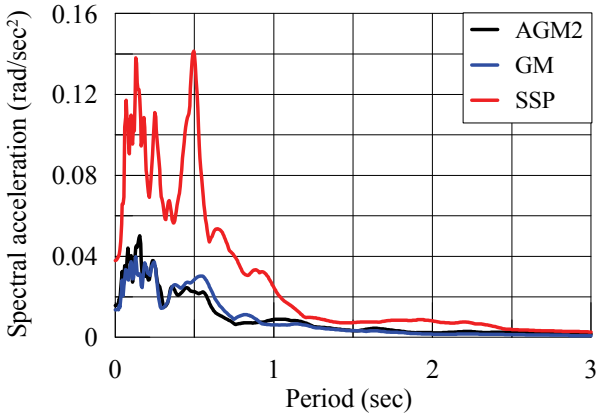

(c) Station FA1_3

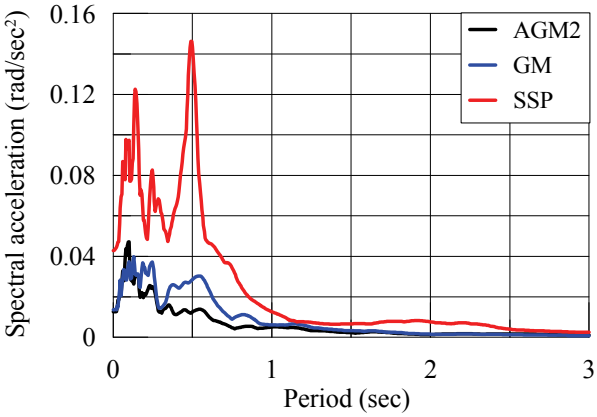

(d) Station FA1_4

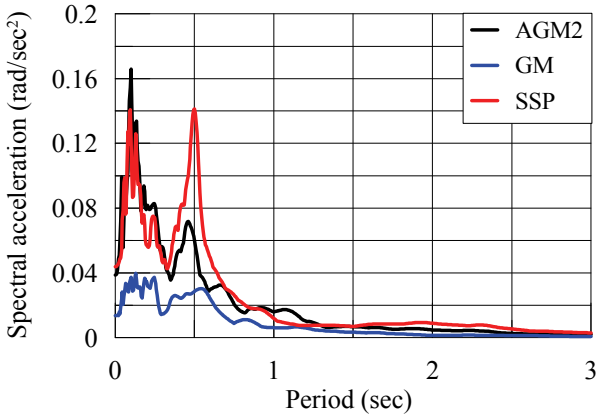

(e) Station FA1_5

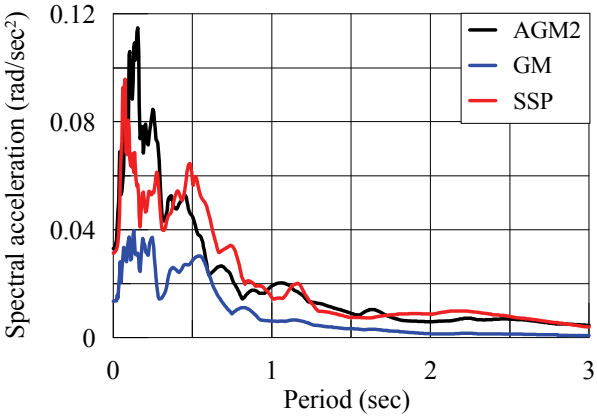

(f) Station FA2_1

Figure 4-9: Rocking (*yz* plane) spectra computed using three different methods (cont.)

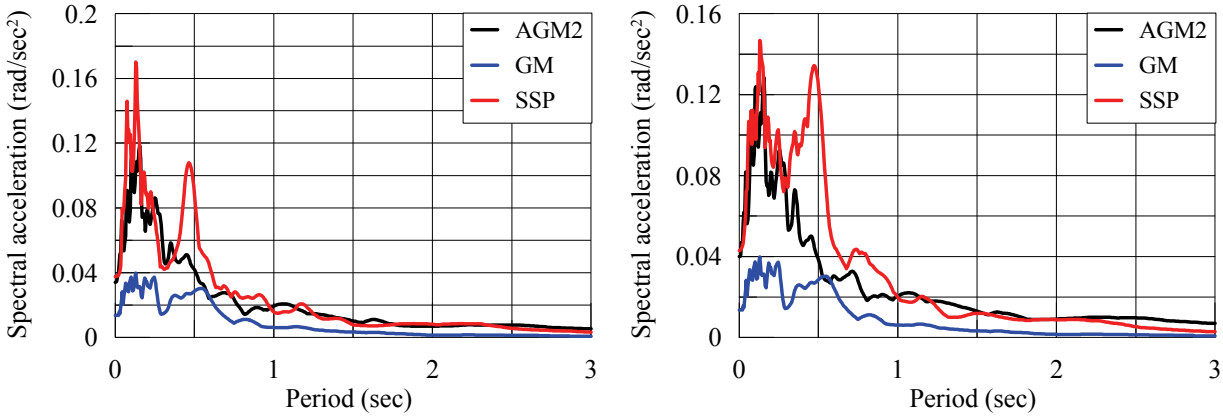

(g) Station FA2_2

(h) Station FA2_3

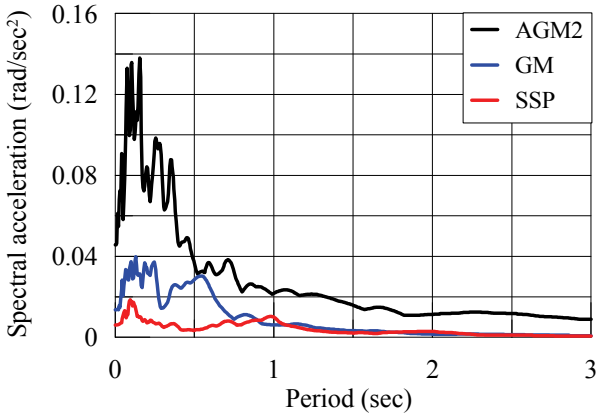

(i) Station FA2_4

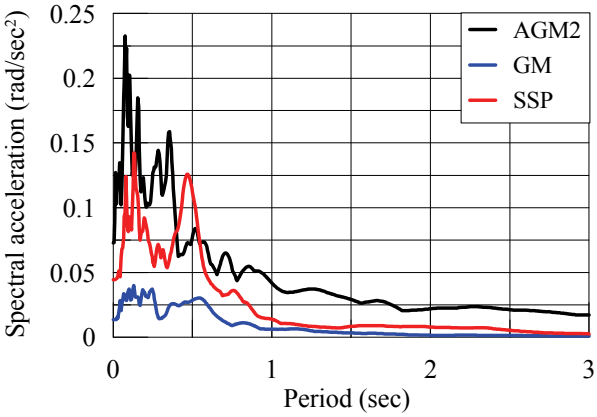

(j) Station FA2_5

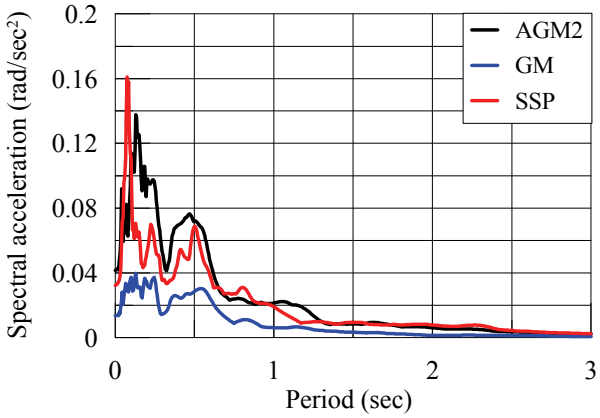

(k) Station FA3_1

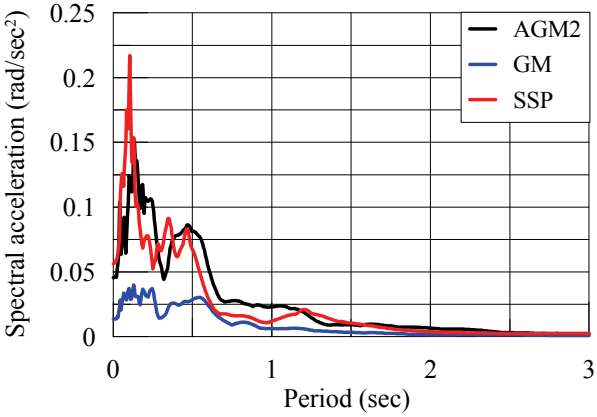

(l) Station FA3_2

Figure 4-9: Rocking (*yz* plane) spectra computed using three different methods (cont.)

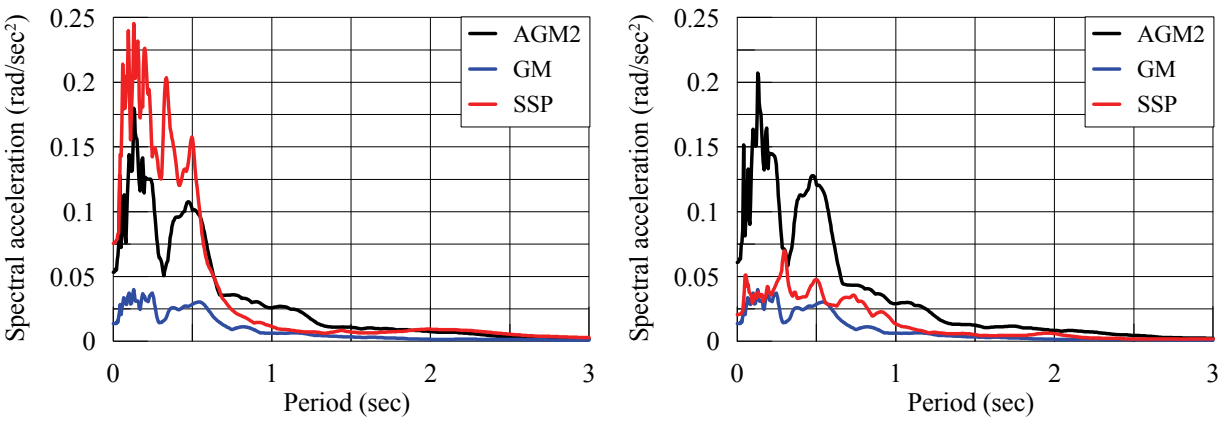

(m) Station FA3_3

(n) Station FA3_4

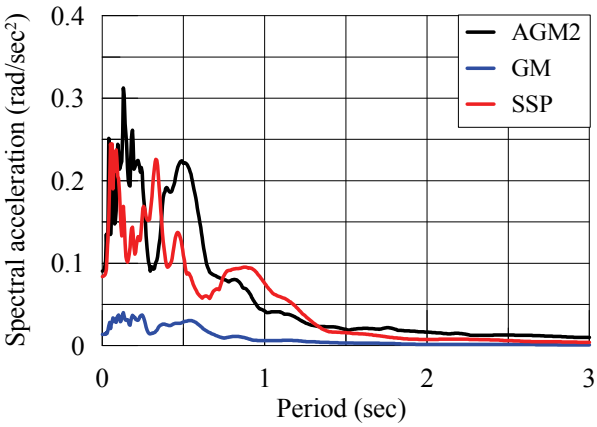

(o) Station FA3_5

Figure 4-9: Rocking (*yz* plane) spectra computed using three different methods

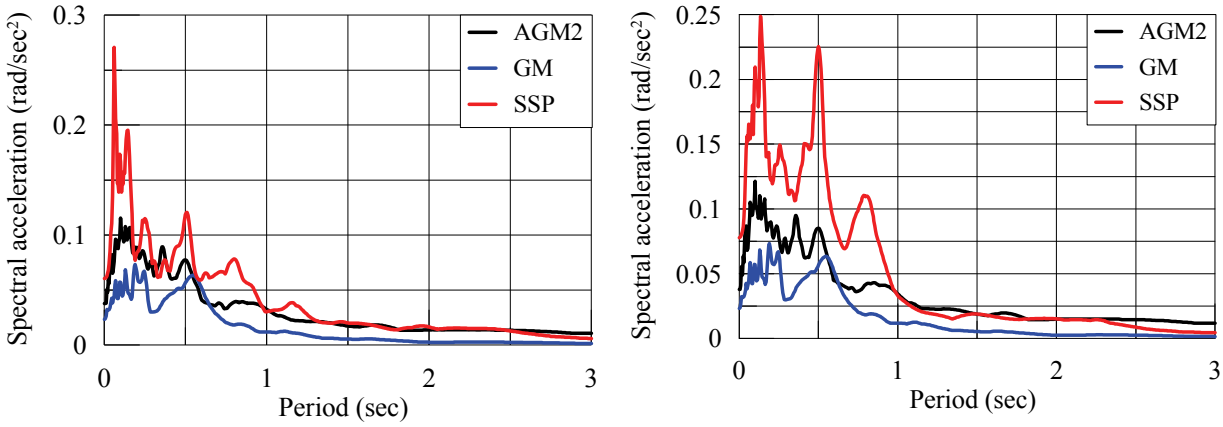

(a) Station FA1_1

(b) Station FA1_2

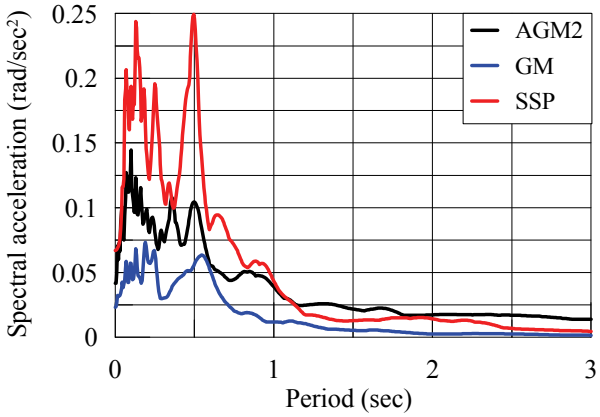

(c) Station FA1_3

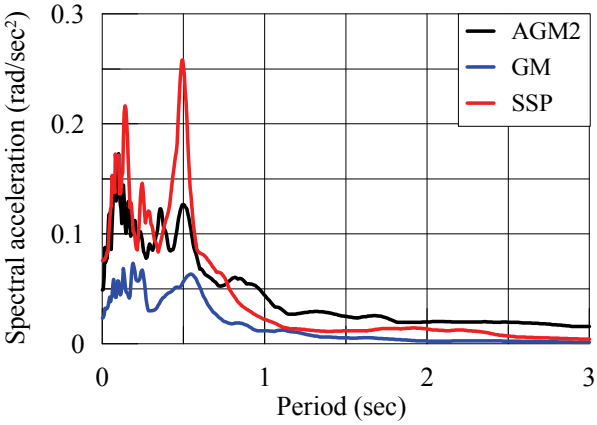

(d) Station FA1_4

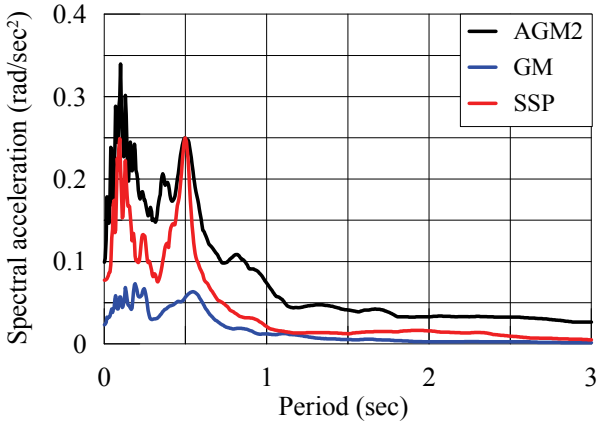

(e) Station FA1_5

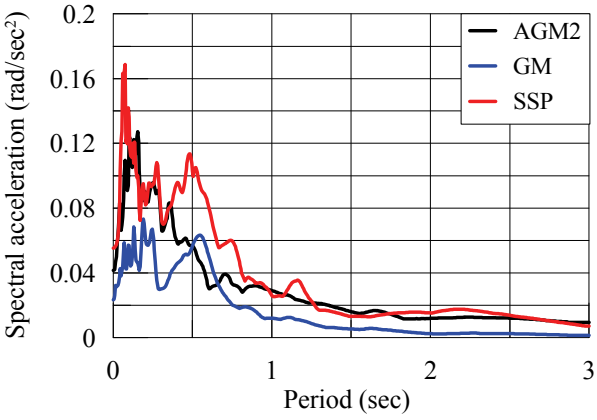

(f) Station FA2_1

Figure 4-10: Rocking (SRSS) spectra computed using three different methods (cont.)

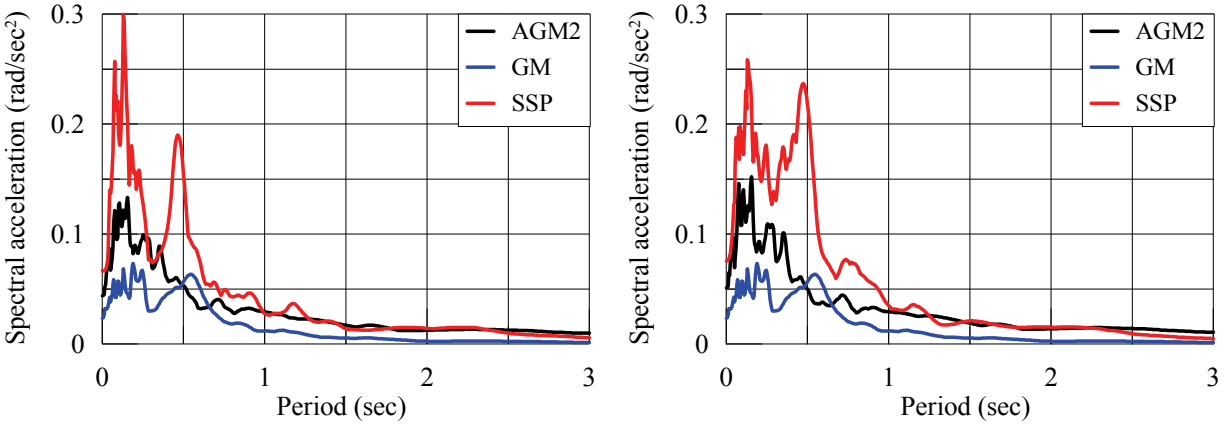

(g) Station FA2_2

(h) Station FA2_3

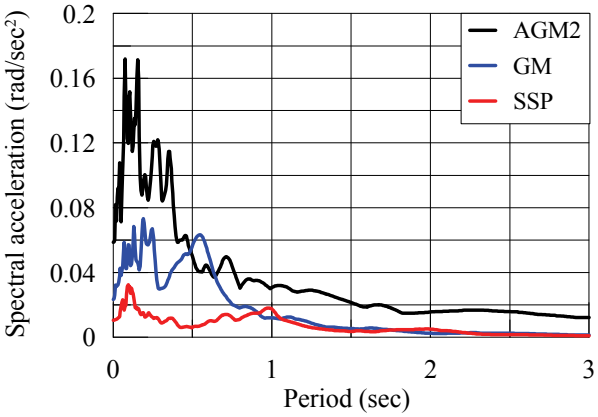

(i) Station FA2_4

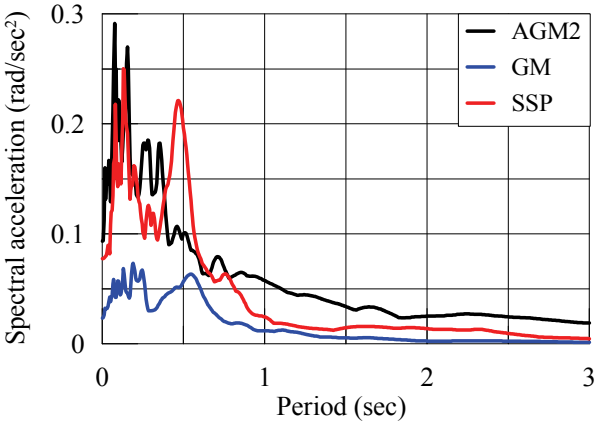

(j) Station FA2_5

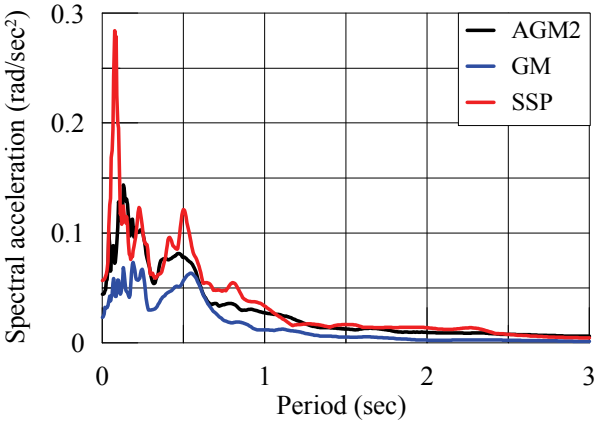

(k) Station FA3_1

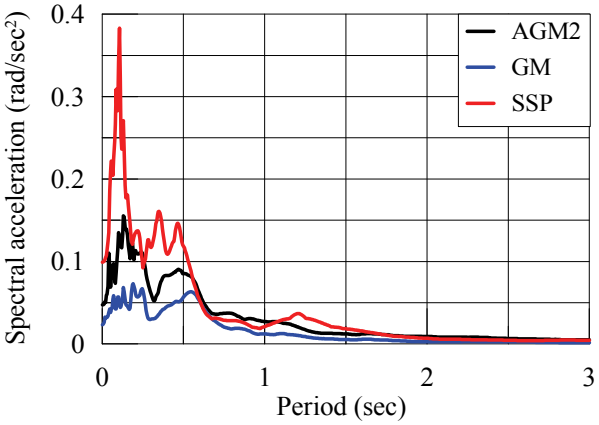

(l) Station FA3_2

Figure 4-10: Rocking (SRSS) spectra computed using three different methods (cont.)

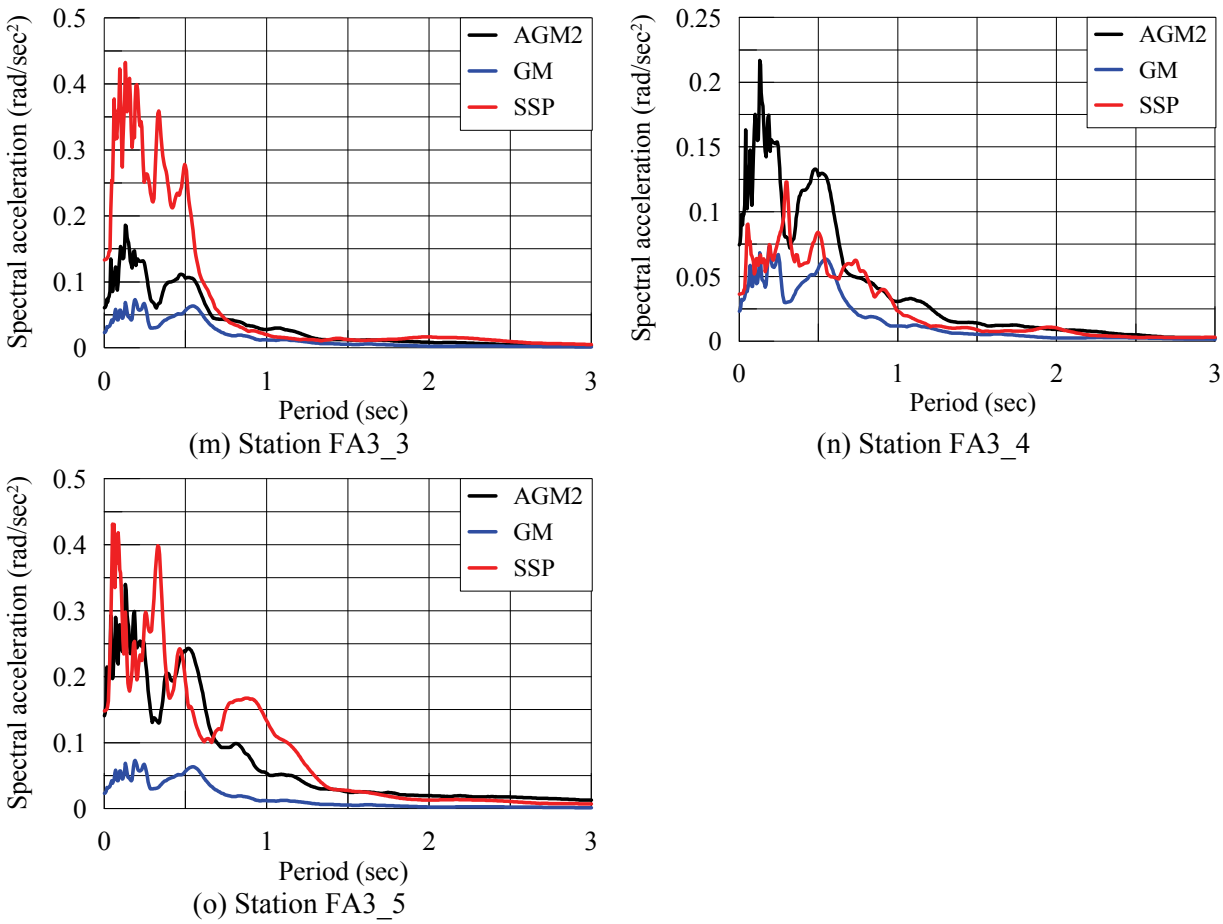

(m) Station FA3_3

(n) Station FA3_4

(o) Station FA3_5

Figure 4-10: Rocking (SRSS) spectra computed using three different methods

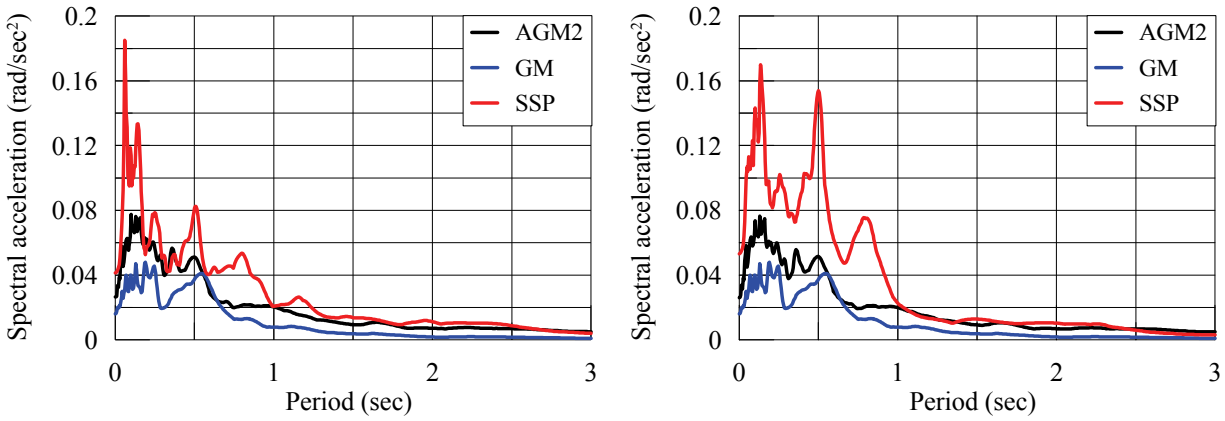

(a) Station FA1_1

(b) Station FA1_2

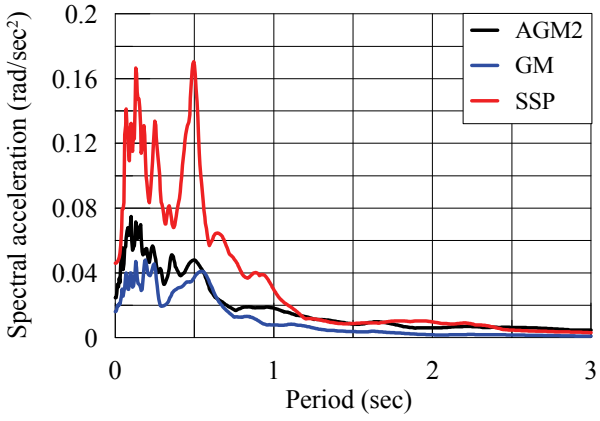

(c) Station FA1_3

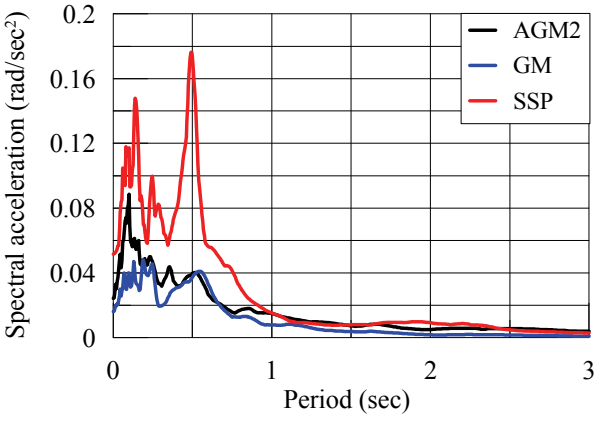

(d) Station FA1_4

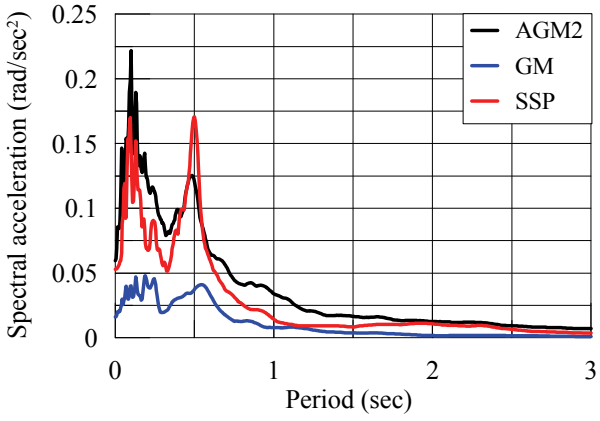

(e) Station FA1_5

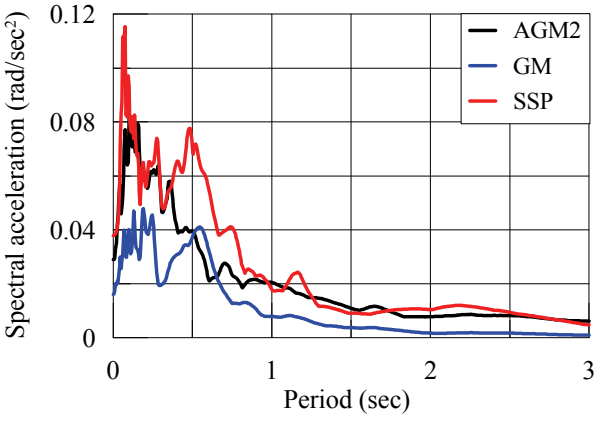

(f) Station FA2_1

Figure 4-11: Rocking (Geomean) spectra computed using three different methods (cont.)

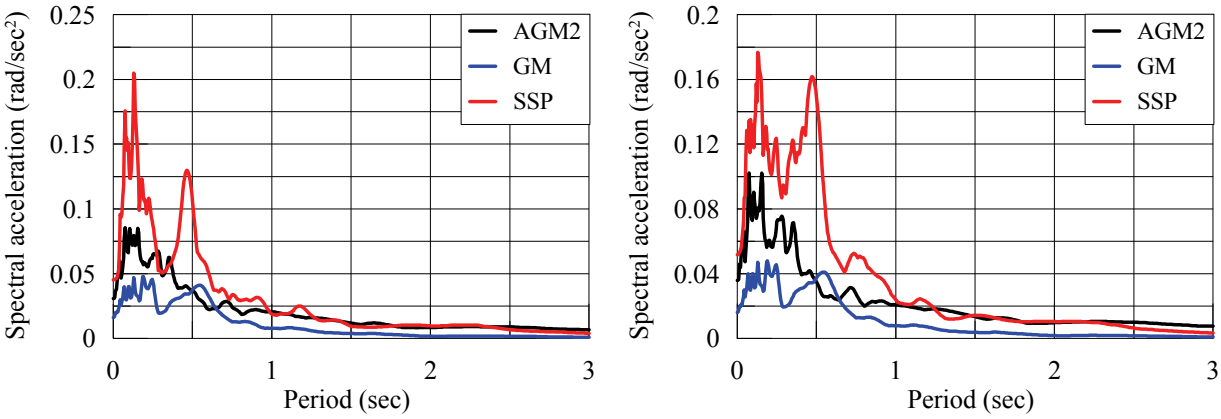

(g) Station FA2_2

(h) Station FA2_3

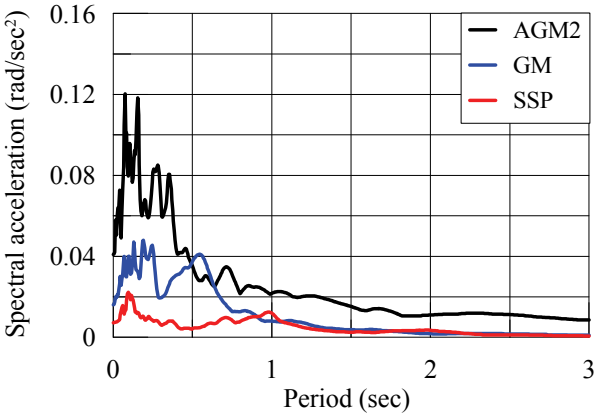

(i) Station FA2_4

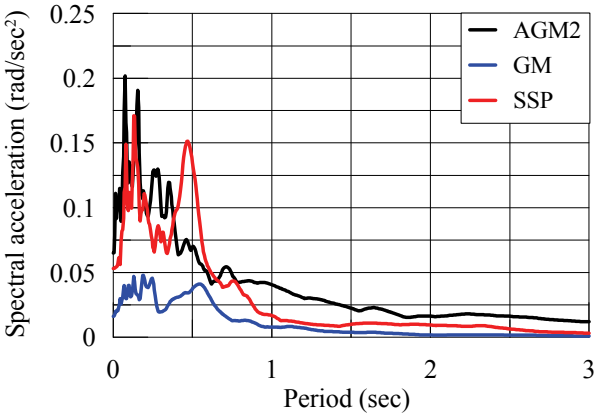

(j) Station FA2_5

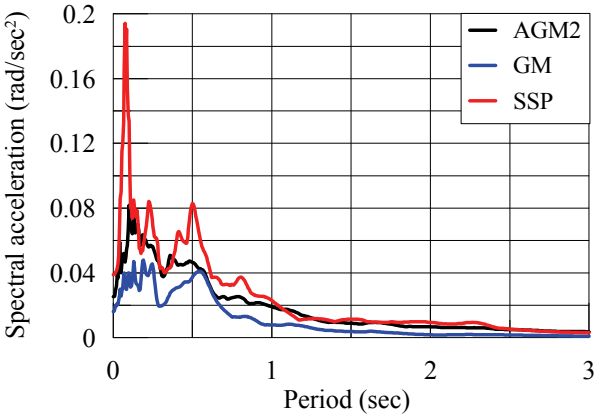

(k) Station FA3_1

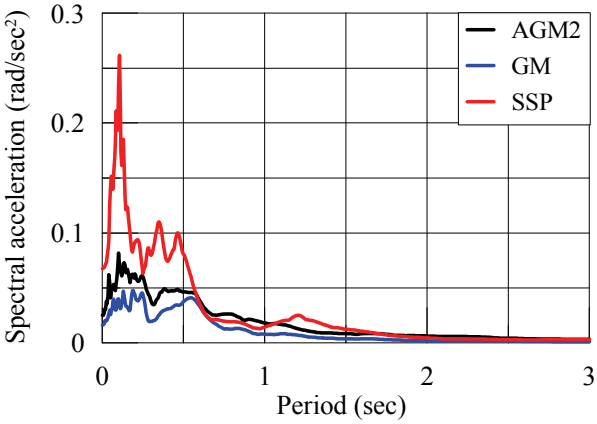

(l) Station FA3_2

Figure 4-11: Rocking (Geomean) spectra computed using three different methods (cont.)

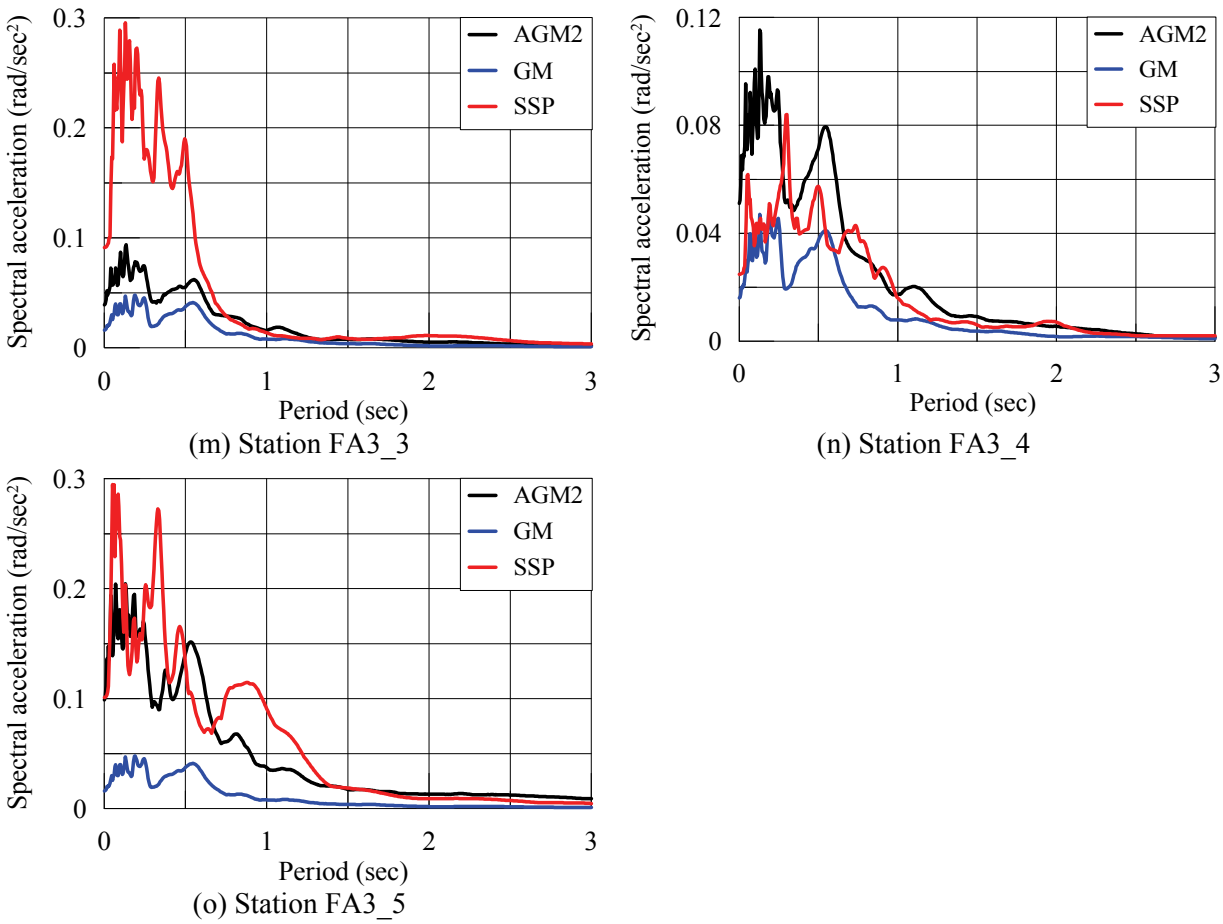

Figure 4-11: Rocking (Geomean) spectra computed using three different methods

CHAPTER 5

ESTIMATING ROTATIONAL COMPONENTS OF GROUND MOTION USING A SURFACE DISTRIBUTION METHOD

5.1. Introduction

The single station procedure (SSP) described in Chapter 3 enables the computation of rotational components of ground motion from the translational data recorded at a single station. The SSP involves a number of uncertainties and assumptions, including plane wave propagation, existence of a principal plane, lateral homogeneity of the soil medium, a frequency-dependent angle of incidence, the effect of dispersion, and the indeterminacy involved in the deconstruction of the recorded translational time series to the contributions from different types of body and surface waves. An alternative to the SSP involves the use of data from a number of closely spaced, spatially distributed stations; that is the so-called dense seismic array. These Multiple Station Procedures (MSP) are presented in Chapters 2 and 4. The Geodetic Method (GM), originally proposed by Spudich et al. (1995) is discussed in Chapter 2. Rotational components calculated using GM are deficient at higher frequencies due to the assumption of a planar best-fit surface. A higher-order MSP, called the Acceleration Gradient Method (AGM), is introduced in Chapter 4. The AGM is capable of retaining higher frequencies than the GM with the upper limit on frequency being a function of the physical dimensions of the seismic array. The second-order best-fit surface in AGM results in a linear variation of the computed rotational components across a seismic array, which is unrealistic. These shortcomings of the AGM can be addressed in the frequency domain. One approach is a frequency-wave number (f-k) transformation that requires the dense seismic array to span a large area. Since the stations in a seismic array are rarely uniformly spaced, analysis should be based on non-uniform discrete Fourier Transform and care should be taken to minimize the spatial aliasing (e.g., Kerekes, 2001; Zwartjes and Sacchi, 2007).

An alternative to the f-k transformation is to first take the Discrete Fourier transform of the recorded data with respect to time. A suitable process of wave propagation (e.g., plane wave propagation) over the footprint of the array is then assumed to calculate the best-fit spatial distribution of the Fourier coefficients in every harmonic, although the choice requires knowledge of site-specific parameters, such as wave velocity, number of waves, directions of arrival and geometric attenuation.

A somewhat similar problem exists in the field of acoustic emission and signal processing involving one or multiple emitters and an array of polarized or omni-directional antennas (receivers). Procedures (e.g., multiple signal classification, MUSIC (Schmidt, 1981); estimation of signal parameters via rotational invariance technique, ESPRIT (Roy, 1987)) exist to characterize received signals and to compute the number of signals and directions of arrival. A comprehensive review of these procedures is presented by Tuncer and Friedlander (2009). Attempts have been made to translate the concept of MUSIC to the analysis of dense-array data. (e.g., Goldstein and Archuleta, 1987). However, the stumbling block in such translations is the formation of an array-manifold in the presence of different types of waves propagating with different velocities in a seismic array. Another obstacle is the unknown geometric attenuations for different waves propagating through a highly heterogeneous medium. The procedures used in characterizing the acoustic emission, despite having a solid theoretical and statistical basis, have found little application in extracting rotational components from data recorded in dense seismic arrays.

In this chapter, a procedure called the Surface Distribution Method (SDM) is presented to extract the rotational components of ground motion from dense seismic array records by operating in the frequency domain and using the assumptions of plane wave propagation on the horizontal plane with a known apparent wave velocity. The directions of the propagation are considered to be parallel and normal to the principal plane. Apparent wave velocities are estimated using the results of the SSP described in Chapter 3. Geometric attenuation over the footprint of the array is neglected. The procedure is formulated in Section 5.2 and its potential limitations when applied to data recorded in a dense seismic array are

discussed in Section 5.3. Section 5.4 illustrates its application and the results are compared with the GM, AGM and SSP in Section 5.5.

The Matlab source code developed for the SDM is presented in Appendix E, together with an explanation and examples.

5.2. Formulation of the SDM

For simplicity, it is assumed that a single wave propagates on the horizontal plane (*xy*) and all stations are located on a straight line spanning in the direction of propagation (i.e., the x direction). The resulting particle displacements (U, V and W) along the three orthogonal directions (x, y and z) are, respectively,

$$\left\{U(x,t) \quad V(x,t) \quad W(x,t)\right\} = \sum_{r=1}^{N} \left\{D_r^u \quad D_r^v \quad D_r^w\right\} \cos\left(k_r x - \omega_r t + \phi_r\right) \tag{5-1}$$

where r is the r^{th} harmonic, N is the total number of harmonics, and D, ϕ, ω and k denote the amplitude, phase, frequency and wave number, respectively, in the respective harmonic. The particle displacement along one or two directions can be zero in Eq (5-1) depending upon the nature of the propagating wave. Without a loss of generality, and considering the particle displacement in one direction only, say W, the last part of Eq (5-1) for the r^{th} harmonic (but in the form of particle acceleration) can be expressed as

$$\ddot{W}_r(x,t) = A_r \cos\left(k_r x + \phi_r\right)\cos\left(\omega_r t\right) + A_r \sin\left(k_r x + \phi_r\right)\sin\left(\omega_r t\right) \tag{5-2}$$

where $A_r = -\omega_r^2 D_r^w$ is the amplitude of the particle acceleration. Taking the FFT of the recorded acceleration data along the same direction at the j^{th} station and denoting $a_j - ib_j$ as the Fourier coefficient associated with the r^{th} discrete positive frequency, it may be shown that

$$a_j = \frac{1}{2} A_r \cos\left(k_r x_j + \phi_r\right),\ b_j = \frac{1}{2} A_r \sin\left(k_r x_j + \phi_r\right) \tag{5-3}$$

where x_j is the location of the j^{th} station with respect to the reference point at the source of excitation. Assuming that the length of the array is much smaller than the source-to-site distance, and the soil at the surface layer is homogeneous within the length of the array, the reference point can be moved from the source to any station within the array by applying an additive phase to all the recording stations. This additive phase may be computed based on the arrival time at the selected reference station. Assuming the distance between the adjacent stations tends to zero, Eq (5-3) may be expressed as

$$a(x)=\frac{1}{2}A_r\cos\left(k_r x+\bar{\phi}_r\right),\ b(x)=\frac{1}{2}A_r\sin\left(k_r x+\bar{\phi}_r\right) \tag{5-4}$$

Note that the phase ϕ_r in Eq (5-3) is changed to $\bar{\phi}_r$ in Eq (5-4) to account for the additive phase described above. It is useful to rewrite Eq (5-4) as

$$\begin{aligned} &a(x)=C_r\cos k_r x+D_r\sin k_r x\ ,\ b(x)=E_r\cos k_r x+F_r\sin k_r x \\ &C_r=\frac{1}{2}A_r\cos\bar{\phi}_r,\ \mathrm{D}_r=-\frac{1}{2}A_r\sin\bar{\phi}_r,\ E_r=\frac{1}{2}A_r\sin\bar{\phi}_r,\ \mathrm{F}_r=\frac{1}{2}A_r\cos\bar{\phi}_r \end{aligned} \tag{5-5}$$

where all the terms are as previously described. The real and imaginary parts of the Fourier coefficient, associated with any discrete frequency, are distributed along the direction of propagation in the form of a wave. The wavelength of this distribution is the same as that of the propagating wave in the corresponding harmonic.

Next, the assumption of the location of the stations is relaxed and they are scattered along the *xy* plane (Figure 5-1). The direction of wave propagation ξ is considered to be at an arbitrary angle η (see Figure 5-1) with respect to the x axis. In the r^{th} harmonic, the wavelength λ_r along the direction of the propagation can be related to that along the x and y directions as $\lambda_{xr}=\lambda_r/\cos\eta$ and $\lambda_{yr}=\lambda_r/\sin\eta$, respectively. The associated wave numbers are related as

$$k_r\xi=k_{xr}x+k_{yr}y \tag{5-6}$$

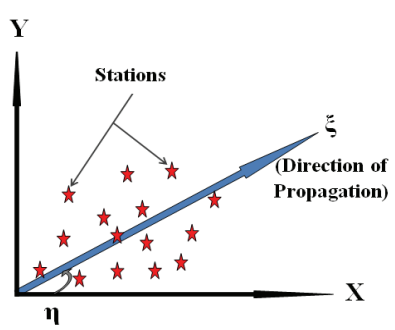

(a) Location of stations and direction of wave propagation

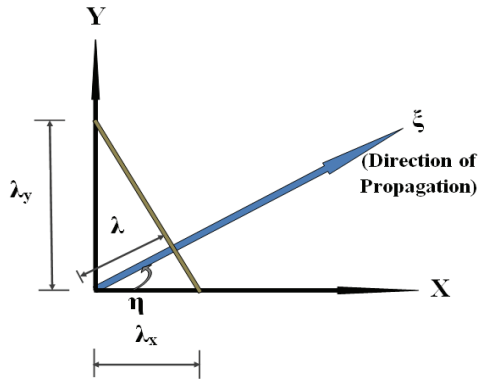

(b) Equivalent wavelength along x- and y-directions

Figure 5-1: Wave propagation on a horizontal (*xy*) plane

The spatial distribution of the Fourier coefficients can be obtained from Eq (5-5) by substituting $k_{xr}x + k_{yr}y$ in place of $k_r x$, leading to

$$\begin{aligned} a(x,y) &= C_r \cos\left(k_{xr}x + k_{yr}y\right) + D_r \sin\left(k_{xr}x + k_{yr}y\right) \\ b(x,y) &= E_r \cos\left(k_{xr}x + k_{yr}y\right) + F_r \sin\left(k_{xr}x + k_{yr}y\right) \\ k_{xr} &= k_r \cos\eta,\ k_{yr} = k_r \cos\eta,\ k_r = 2\pi/\lambda_r \end{aligned} \tag{5-7}$$

To date, only a single wave has been considered. However, in reality, wave propagation is complex because of the dispersive nature of the wave and the inhomogeneity in the spatial distribution of material properties. Finite fault size adds another complexity by questioning the existence of a principal plane, especially for near-fault sites. Therefore, instead of a single wave propagating along the principal direction, which is assumed in the SSP (see Chapter 3), two waves of different amplitudes and phases are assumed to be propagating on the horizontal plane with the same apparent wave velocity, c. The direction of propagation of one wave is along the principal direction, whereas that of the other wave is normal to the principal direction. The objective here is to approximately account for finite fault size leading to the existence of multiple principal planes. Denoting η as the orientation of the principal direction with respect to the x axis in the counter-clockwise direction, the spatial distribution of the real and imaginary parts of the Fourier coefficient for the r^{th} discrete frequency may be expressed as

$$\begin{Bmatrix} a(x,y) & b(x,y) \end{Bmatrix} = \begin{Bmatrix} G_1 & G_2 & G_3 & G_4 \end{Bmatrix} \begin{bmatrix} P_{ar} & Q_{ar} & R_{ar} & S_{ar} \\ P_{br} & Q_{br} & R_{br} & S_{br} \end{bmatrix}^T \tag{5-8}$$

where the elements of $\{G\}$ are given by

$$\begin{aligned} G_1 &= \cos(xk_r \cos\eta + yk_r \sin\eta);\ G_2 = \sin(xk_r \cos\eta + yk_r \sin\eta) \\ G_3 &= \cos(-xk_r \sin\eta + yk_r \cos\eta);\ G_4 = \sin(-xk_r \sin\eta + yk_r \cos\eta) \end{aligned} \tag{5-9}$$

The second matrix on the right side of Eq (5-8) represents terms analogous to $C_r(E_r)$ and $D_r(F_r)$ as discussed above. The first two rows of this matrix are the contributions from the wave propagating along the principal direction and the next two rows account for the other wave. It is important to note $C_r = F_r$ and $D_r = -E_r$ in Eq (5-5), leading to $P_{ar} = Q_{br}$, $Q_{ar} = -P_{br}$, $R_{ar} = S_{br}$ and $S_{ar} = -R_{br}$ in Eq (5-8). Since wave phenomenon in the field may be very different from that assumed here, and noting the primary objective of Eq (5-8) is to form the pattern of the distribution surface, without a loss of generality, the above relationships are set aside and all eight variables are considered to be independent. Considering the left side as a complex parameter and the second matrix on the right side as a vector of complex parameters, Eq (5-8) can be considered to be the distribution of the complex Fourier coefficients on the *xy* plane.

Setting the origin at the reference station and substituting the x and y coordinates of any station in Eq (5-8) associated with any discrete frequency, say the r^{th}, $\{G\}$ is known completely and the left side is also known from the FFT of the recorded acceleration data. Repeating the same procedure at all other stations, including the reference station, and assembling the resulting equations in matrix form, it may be shown that

$$[A]\{p\} = \{d\} \tag{5-10}$$

where $[A]$ represents the data kernel associated with the r^{th} harmonic. Each row of $[A]$ represents the row-vector $\{G\}$ calculated for a particular station in Eq (5-8). The vector $\{d\}$ is the vector of Fourier coefficients associated with the r^{th} discrete frequency at all the stations, and $\{p\}$ represents the vector of unknown complex parameters associated with the spatial distribution of the Fourier coefficients at the r^{th} discrete frequency on the *xy* plane. If the number of recording stations (surface stations) is greater than four, Eq (5-10) becomes an overdetermined problem. The overdetermined problem is then solved using a least-squares method such that the distribution surface is constrained to pass through the Fourier coefficient at the reference station. This is done by selecting a diagonal weight matrix W and assigning a weight associated with the reference station (e.g., 1000) that is significantly greater than that associated with the other stations (e.g., 1). The least-squares solution of Eq (5-10) may be expressed as

$$\bar{p} = \left[A^T W A\right]^{-1} A^T W \{d\} \tag{5-11}$$

The vector $\bar{p}$ computed from Eq (5-11), when substituted into Eq (5-8), represents the best-fit surface for the distribution of the Fourier coefficient associated with the r^{th} discrete frequency on the *xy* plane.

Accordingly, the spatial derivative at any point on this distribution surface may be expressed as

$$\begin{aligned}
\left\{\frac{\partial a(x,y)}{\partial x} \quad \frac{\partial b(x,y)}{\partial x}\right\} &= \left\{\frac{\partial G_1}{\partial x} \quad \frac{\partial G_2}{\partial x} \quad \frac{\partial G_3}{\partial x} \quad \frac{\partial G_4}{\partial x}\right\}\{\bar{p}\} \\
\left\{\frac{\partial a(x,y)}{\partial y} \quad \frac{\partial b(x,y)}{\partial y}\right\} &= \left\{\frac{\partial G_1}{\partial y} \quad \frac{\partial G_2}{\partial y} \quad \frac{\partial G_3}{\partial y} \quad \frac{\partial G_4}{\partial y}\right\}\{\bar{p}\}
\end{aligned} \tag{5-12}$$

where the left side of Eq (5-12) may be considered as the complex Fourier coefficient associated with the r^{th} discrete frequency of the spatial derivative of the acceleration. The same procedure can be used to compute the spatial derivative of the Fourier coefficients of the horizontal accelerations. The history of the spatial derivatives of the acceleration at any point on the *xy* plane can be computed after calculating the Fourier coefficients at all discrete frequencies and taking the inverse Fourier transform, as discussed below.

5.2.1. Computation of Rotational Acceleration History

The Fourier coefficients along three orthogonal directions are defined with subscripts u, v and w. The coefficients of the torsional acceleration associated with the r^{th} discrete frequency may be expressed as

$$\theta_{xy}(x,y,\omega_r)=\frac{1}{2}\left[\frac{\partial}{\partial y}\left\{a_u(x,y)-ib_u(x,y)\right\}-\frac{\partial}{\partial x}\left\{a_v(x,y)-ib_v(x,y)\right\}\right] \tag{5-13}$$

Similarly, for rocking accelerations on the *xz* and *yz* planes

$$\theta_{xz}(x,y,\omega_r)=-\frac{\partial}{\partial x}\left\{a_w(x,y)-ib_w(x,y)\right\} \tag{5-14}$$

$$\theta_{yz}(x,y,\omega_r)=\frac{\partial}{\partial y}\left\{a_w(x,y)-ib_w(x,y)\right\} \tag{5-15}$$

The associated rotational acceleration histories can be computed at any point on the *xy* plane by calculating the Fourier coefficients using Eq (5-13) through Eq (5-15) for all discrete frequencies and thereafter taking the inverse Fourier transform. Note that Eq (5-13) through Eq (5-15) utilizes the uncoupled nature of the problem identified in Chapter 4 when using the data recorded only at the surface stations. The torsional rotation can be computed from the recordings along the *x* and *y* directions and rocking acceleration from the recording along the vertical direction.

5.2.2. Minimum Seismic Array Dimension

The SDM procedure utilizes the Discrete Fourier Transform. The wave number k_r tends to zero for extremely low frequency harmonics. In this case, and regardless of the array dimension, xk_r and yk_r tend to zero, leading to the singularity in the matrix $[G]$ as $\{G_1\}\approx\{G_3\}$ and $\{G_2\}\approx\{G_4\}$. To avoid this singularity, it is assumed that $0.5Lk_r>\varepsilon$ (= 0.1 in this paper), when the reference station is located close to the center of the array (i.e., $\min(x_{\max},y_{\max})=L/2$ where L is the array dimension). When this

condition is not satisfied (extremely low frequency harmonics), the wave propagating normal to the principal direction should be ignored; that is, only the first two columns of $[G]$ are used. Effectively, this procedure defines a frequency limit of $f_u = \varepsilon c/\pi L$. The full matrix $[G]$ should be used for any harmonic with frequency $f > f_u$; otherwise, only the first two columns should be used. The values of f_u should not exceed an upper bound that restricts the minimum dimension of the seismic array (see Chapter 6).

5.3. Application of the Surface Distribution Method

The formulation of the SDM depends upon several assumptions that, in a strict sense, are rarely satisfied by the data recorded in a seismic array. For example, the SDM assumes the recorded data are due to the propagation of two waves of the same type propagating orthogonal to each other at the same apparent velocity. Reality is far more complex. Body waves (P, SV and SH) propagate with different velocities and strike the free surface at different angles of incidence. The angle of incidence may vary in different harmonics, which theoretically precludes the existence of an apparent wave velocity for any type of body wave. The situation will be further complicated by the presence of surface waves: Rayleigh and Love. Finally, the assumption of plane wave propagation is not strictly valid due to material inhomogeneity and finite fault size with source-to-site distance comparable to or less than the rupture length. The assumptions may limit the utility of the SDM at extracting rotational components of ground motion from dense array translational time series. Potential limitations are discussed below.

First, the rupture process, including its type, length, and source-to-site distance, should be such that the assumption of plane wave propagation can be satisfied in an approximate sense. Second, the propagating wave over the footprint of the array should be non-dispersive (i.e., frequency independent wave velocity) and propagate without geometric attenuation. Third, the incidence angles for the body waves should be frequency independent. When these three conditions are nearly satisfied, the history of the spatial and temporal derivatives of the acceleration due to any particular type of body wave will be similar in shape; one can be approximately obtained from another by using a scale factor and then

applying a phase shift. In this case, the ratio of the absolute peak temporal derivative to the peak spatial derivative may be taken as the apparent wave velocity. It is also assumed that the apparent velocity of any type of body wave will remain constant over the footprint of the array.

These conditions are necessary but not sufficient to use the SDM to compute rotational components from translational data recorded in a seismic array. A sufficient condition is when each rotational component is formed by a single type of body or surface wave, which is discussed next.

5.3.1. Estimation of Torsional Motion

The SH wave (body wave) and Love wave (surface wave) contribute to the torsional motion. For near-fault records, the contribution from Love waves can be assumed to be negligible (Castellani and Boffi, 1989). The SH wave contribution is computed first by rotating the recorded horizontal motions along the direction normal to the principal plane. Next, its components along the *x* and *y* directions are calculated to compute the horizontal acceleration field. Note this computation assumes the direction of propagation is along the principal direction and the resulting acceleration in the same direction is zero. This acceleration field is considered as input to the SDM, wherein it is considered as the result of two SH waves (with different amplitude and phase) propagating with the same apparent velocity along and normal to the principal direction. The SDM approximately accounts for the spatial variability in the computed SH wave contributions and also the effect of multiple principal planes that are associated with a fault of finite size.

Let c_{sh} be the apparent SH wave velocity and L be the dimension of the array. If the AGM (see Chapter 4) is used to compute the torsional spectra, the spectral ordinate at periods $T < L/c_{sh}$ will be underestimated if the SH wave contribution to the horizontal motions involves frequency content significantly beyond c_{sh}/L. Smaller underpredictions are expected with the AGM for periods in the range $L/c_{sh} \leq T < 2L/c_{sh}$ (Chapter 4). If the SDM is used with a reasonably good estimate of c_{sh}, no spectral content at the low period is lost.

For far-field (distant) records, torsional motion is assumed to be due to the Love wave only. Thus, a procedure similar to the one described above can be used together with an estimate of the frequency-independent Love wave velocity to estimate torsional motion.

5.3.2. Estimation of Rocking Motion

Rocking motion is due to the P and SV (body) waves and Rayleigh (surface) waves. The contribution from the Rayleigh wave is negligible for near-fault records. Even then, the sufficient condition is not satisfied, since both P and SV waves contribute to the recorded vertical motion with different apparent velocities. The spatial and temporal derivatives of the recorded vertical motions cannot be derived from one another by scaling and a phase shift. The frequency content of the P wave contribution to the vertical acceleration involves higher frequencies than the SV wave. Accordingly, it is assumed that only the P wave contributes to the frequency content of the recorded vertical motion above a certain frequency, say f_e. The apparent velocity of the P wave can be used for the vertical motion in these higher harmonics ($f \geq f_e$). However, if the same apparent velocity is used for the lower harmonics ($f < f_e$), the results may be inaccurate, depending upon the relative contributions of the SV and P waves.

The apparent P and SV wave velocities are defined as c_p and c_{sv}, respectively. If the AGM is used to compute the rocking motion, the error in the spectral demand at a period greater than $2L/c_{sv}$, due to the presence of high frequencies in the recorded vertical motion, will be negligible (see Chapter 4). Using the same theory, it is seen that the error at periods $2L/c_p \leq T \leq 2L/c_{sv}$ is entirely due to the presence of high frequencies in the SV wave. Therefore, the error at periods $T \leq 2L/c_p$ is primarily due to the high frequencies in the P wave unless $f_e > c_p/2L$. In such a case, the SV wave will also contribute. Finally, if $c_p > 2c_{sv}$ (i.e., $2L/c_p < L/c_{sv}$, which is usually satisfied), it is assumed that the spectra computed using the AGM will be acceptable for any period $T \geq L/c_{sv}$, under the assumption that the P wave is the primary contributor to the recorded vertical motion.

The use of the SDM will lead to acceptable rocking acceleration spectra for periods $T \leq 1/f_e$. Moreover, if any harmonic is considered for which the wavelength associated with the P and SV waves ($\lambda_p = c_p/f$, $\lambda_{sv} = c_{sv}/f$) is significantly greater than the array dimension, the solution of the associated overdetermined problem becomes nearly independent of the apparent wave velocity used, c_p or c_{sv}, because the shape of the distribution surface within the length of the array does not significantly vary. This is apparent from Eq (5-8) and Eq (5-9), and is considered to be true if the wavelength associated with the SV wave (being smaller than the P wave) is greater than twice the length of the array. Hence, the SDM using c_p as the apparent wave velocity will produce acceptable results for harmonics with frequencies of less than $c_{sv}/2L$. Accordingly, the spectral ordinates computed using the SDM and AGM are expected to be similar for $T \geq 2L/c_{sv}$. Again, this limit can be relaxed for the analysis with the SDM if the P wave is the primary contributor to the recorded vertical motion. Thus, it is concluded that: a) the error in the spectral ordinates computed using the AGM at low periods, $T \leq 1/f_e$, is recovered using the SDM with c_p as the apparent wave velocity, b) the spectral ordinate computed using the SDM and AGM should not differ for periods $T \geq 2L/c_{sv}$, and c) the spectral ordinates computed using the SDM for periods in the range $1/f_e \leq T \leq 2L/c_{sv}$ may also be considered reasonable if the P wave is the primary contributor to the recorded vertical motion; in this case, the SDM and AGM should not differ much in the period range $L/c_{sv} \leq T \leq 2L/c_{sv}$.

An analysis of the far-field data is straightforward as the body wave contribution can be assumed to be small but an estimate of the Rayleigh wave velocity is then required.

5.4. Computations using Recordings from a Strong Motion Array

The translational strong motion data of the M6.1 event recorded by the Lotung array, as described in Chapter 2, is used for the computations presented below.

5.4.1. Apparent Wave Velocity

Estimates of the apparent wave velocities for the body waves (c_p, c_{sh} and c_{sv}) are required to apply the SDM to compute the rotational components. In the absence of data, the procedure briefly described in Chapter 4 can be used. The procedure is illustrated below with results presented in Table 4-9. Relevant portions of the data presented in Table 4-9 are reproduced in Table 5-1 for convenience.

Table 5-1: Apparent wave velocities

Station	Wave velocity (m/sec)			
	Horizontal motion	Vertical motion		
	SH wave (c_{sh})	Recorded	SV wave (c_{sv})	P wave (c_p)
FA1_1	260	1103	189	1231
FA1_2	250	780	176	999
FA1_3	239	836	193	1111
FA1_4	267	783	184	1073
FA1_5	249	715	181	1167
FA2_1	241	1050	196	1291
FA2_2	255	821	198	833
FA2_3	238	1016	182	1181
FA2_4	284	490	220	530
FA2_5	257	558	176	893
FA3_1	230	956	200	1088
FA3_2	237	491	196	866
FA3_3	240	517	180	705
FA3_4	242	419	163	712
FA3_5	241	436	199	591
Mean	249	731	189	951
Standard deviation	14	235	13	239
Coefficient of variation	0.06	0.32	0.07	0.25

1. SH wave: Compute the torsional acceleration history using the SSP (Chapter 3), wherein the SH wave contribution to the horizontal motion is also computed by rotating the recorded horizontal motion normal to principal direction. Let the absolute peak torsional acceleration be $\left|\ddot{\theta}_{xy}\right|$. Next, the time derivative of the acceleration history produced by the SH wave is computed and the absolute

peak value, $|\ddot{u}_n|$ is identified. The apparent SH wave velocity is then calculated as $c_{sh} = 0.5|\ddot{u}_n| / |\ddot{\theta}_{xy}|$. The procedure is implemented at all the recording stations and the resulting apparent SH wave velocities are reported in column 2 of Table 5-1, which shows a fairly stable trend with a mean velocity of 249 m/sec and coefficient of variation (COV) as 6%. To assess the quality of these estimates, $\ddot{\theta}_{xy}(t)$ (Rotational) and $\ddot{u}_n(t)/2c_{sh}$ (From translational) are compared in panel a of Figure 5-2 for the interior station FA1_1. Panel b presents a time window near the peak. The time series are similar, although a time shift is evident. Similar data are presented for exterior station FA2_5 in panels c and d. These data indicate an acceptable level of accuracy for the estimate of the apparent SH wave velocity. The spatial variability of the SH wave velocity is low and approximately satisfies the assumption of plane wave propagation.

2. SV wave: Compute the rocking acceleration history on the principal plane using the SSP. Let the absolute peak rocking acceleration be $|\ddot{\theta}_{pp}|$. Next compute the time derivative of the SV wave contribution to the vertical acceleration history and identify the absolute peak value, $|\dddot{u}_{pp}|$. The apparent SV wave velocity is then calculated as $c_{sv} = |\ddot{u}_{pp}| / |\ddot{\theta}_{pp}|$. The resulting apparent wave velocities are presented in column 4 of Table 5-1: the mean velocity is 189 m/sec with a COV of 7%. To assess the quality of these estimates of c_{sv}, $\ddot{\theta}_{pp}(t)$ (Rotational) and $\dddot{u}_{pp}(t)/c_{sv}$ (From translational) are compared in panel a of Figure 5-3 for the interior station FA1_1. Panel b presents a time window near the peak. The time series are in good agreement although a time shift is once again evident. Similar data are presented for exterior station FA2_5 in panels c and d. These data and the low spatial variability of c_{sv} indicate that the SV wave closely satisfies the assumption of plane wave propagation.

3. P wave: Follow the SV wave calculation procedure but consider the contribution of the P wave. The apparent wave velocities are tabulated in column 5 of Table 5-1. Significant spatial variability is

observed: the mean velocity is 951 m/sec with a COV of 25%. However, the quality of the predictions per Figure 5-4 is fairly good. The spatial variability is attributed to geometric attenuation over the footprint of the array and it is assumed that plane wave propagation holds at the individual stations.

4. Recorded vertical motion (not decomposed): Calculate the apparent wave velocity for the vertical motion without decomposition. The apparent wave velocities are presented in column 3 of Table 5-1: the mean velocity is 731 m/sec with a COV of 32%. Figure 5-5 enables an evaluation of the quality of the predictions at Station FA1_1 and FA2_5. As expected, the quality of the predictions is poorer than those calculations involving both P waves (Figure 5-4) and SV waves (Figure 5-3).

Note that any acceleration history computed using the SSP is processed before it is used in the calculation of apparent wave velocities. The processing involves: 1) low pass filtering with a cut-off frequency of 20 Hz, 2) applying a 1 sec taper at the beginning and end of the time series, and 3) removal of the mean.

5.4.2. Relative Contributions of the P and SV Waves to the Vertical Motion

Before applying the SDM to compute the rotational components of motion, the relative contributions of the P and SV waves to the vertical acceleration history are compared. Figure 5-6 presents the results for Station FA1_1. The decomposition is performed using the SSP (see Chapter 3). The contribution of the SV wave is much smaller than that of the P wave. It is also apparent that the P wave is relatively rich in high frequency content.

5.4.3. Maximum Frequency Content of the SV Wave

A maximum frequency for SV wave content, f_e, is required to compute the period interval over which the SDM recovers the high frequency contributions to the rocking spectra lost using the AGM. One simple way to compute this frequency is to use the Fourier amplitude spectrum of the contribution of the SV wave to the vertical acceleration. An alternative approach is adopted to avoid the peak-to-valley variations in this spectrum. First, the rocking spectrum is calculated on the principal plane using the SSP.

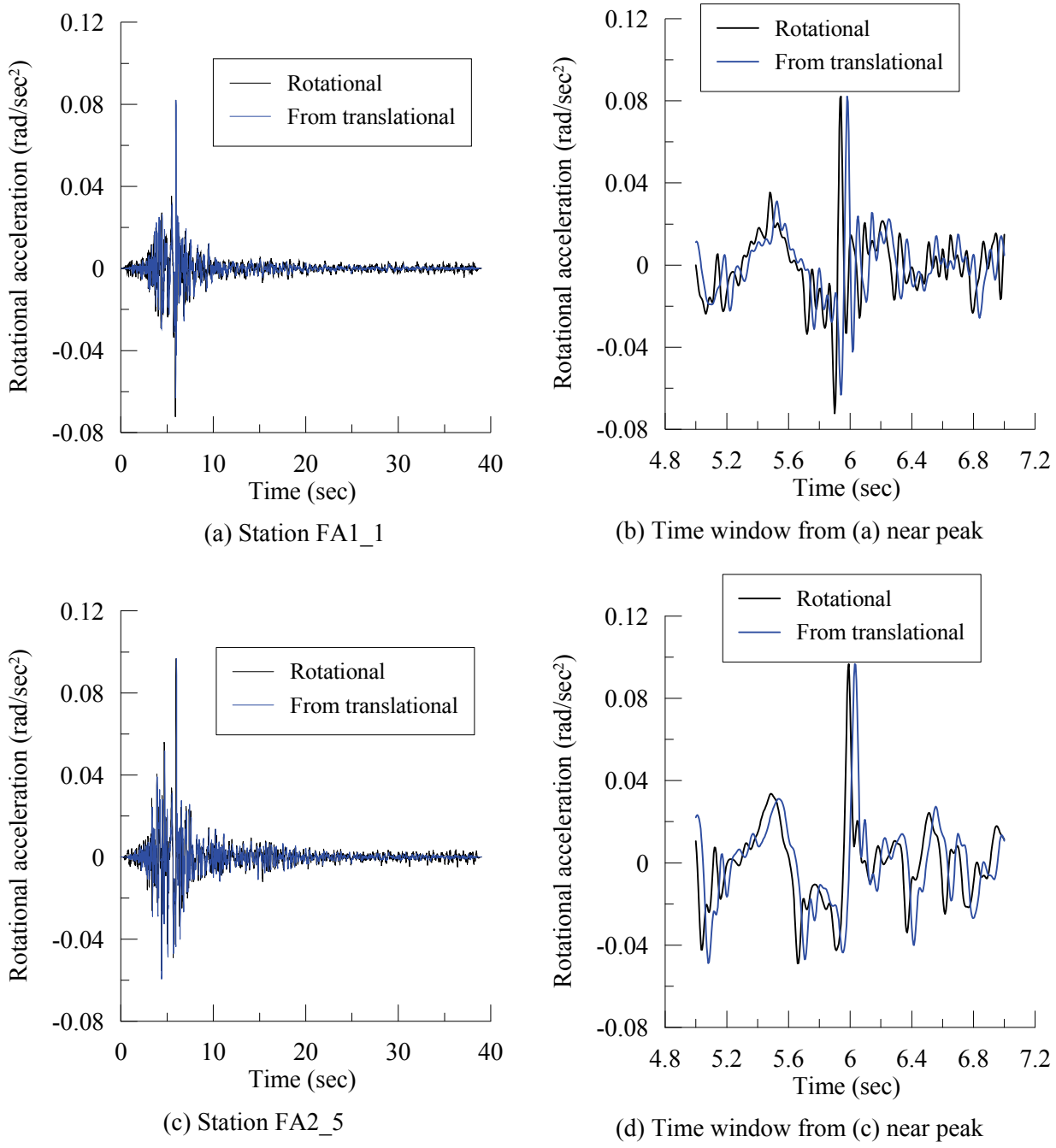

(a) Station FA1_1

(b) Time window from (a) near peak

(c) Station FA2_5

(d) Time window from (c) near peak

Figure 5-2: Comparison of torsional acceleration and derivative of SH wave component of horizontal acceleration scaled by the apparent SH wave velocity

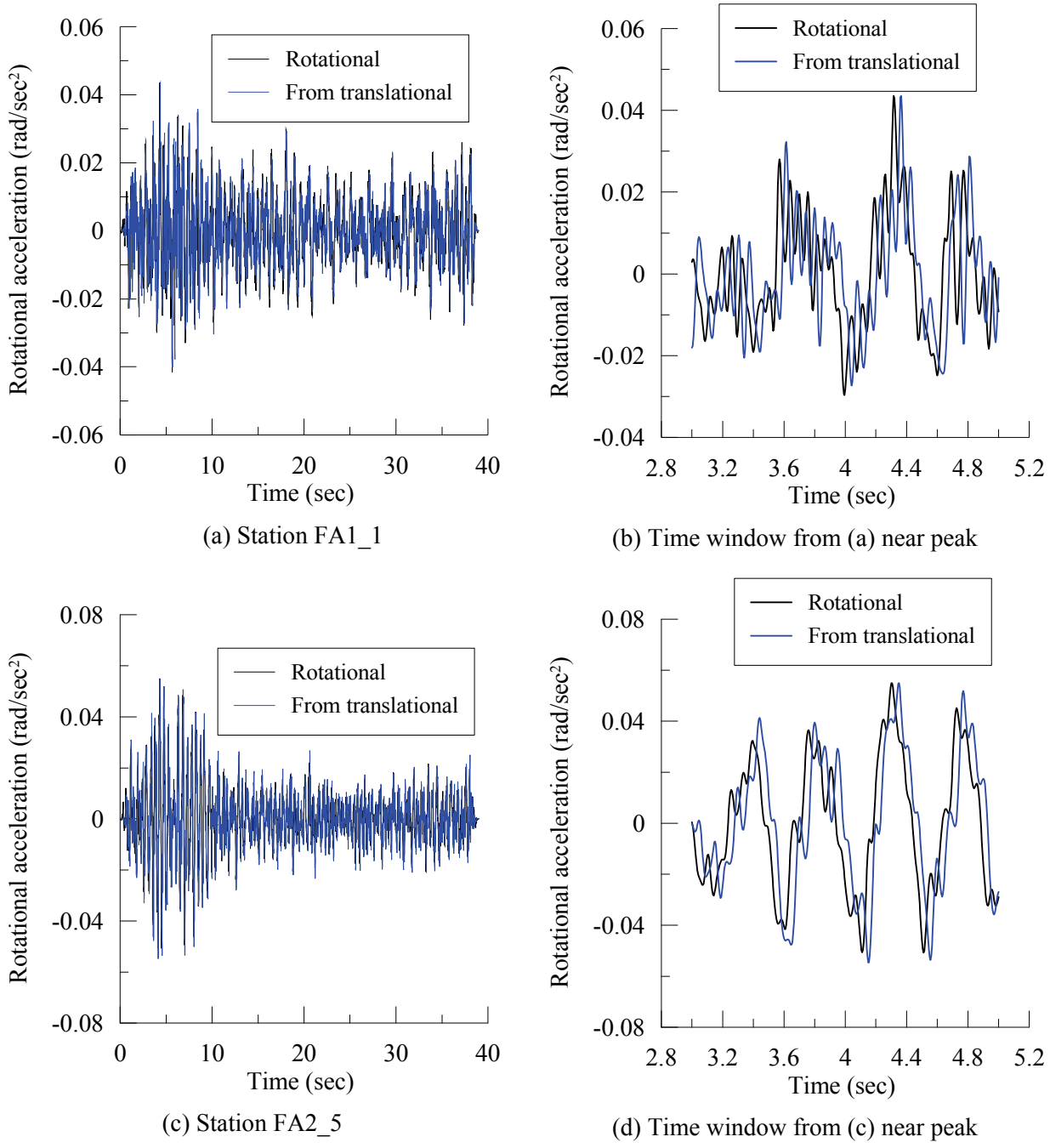

(a) Station FA1_1

(b) Time window from (a) near peak

(c) Station FA2_5

(d) Time window from (c) near peak

Figure 5-3: Comparison of SV wave contribution to rocking acceleration and derivative of SV wave contribution to the vertical acceleration scaled by the apparent SV wave velocity

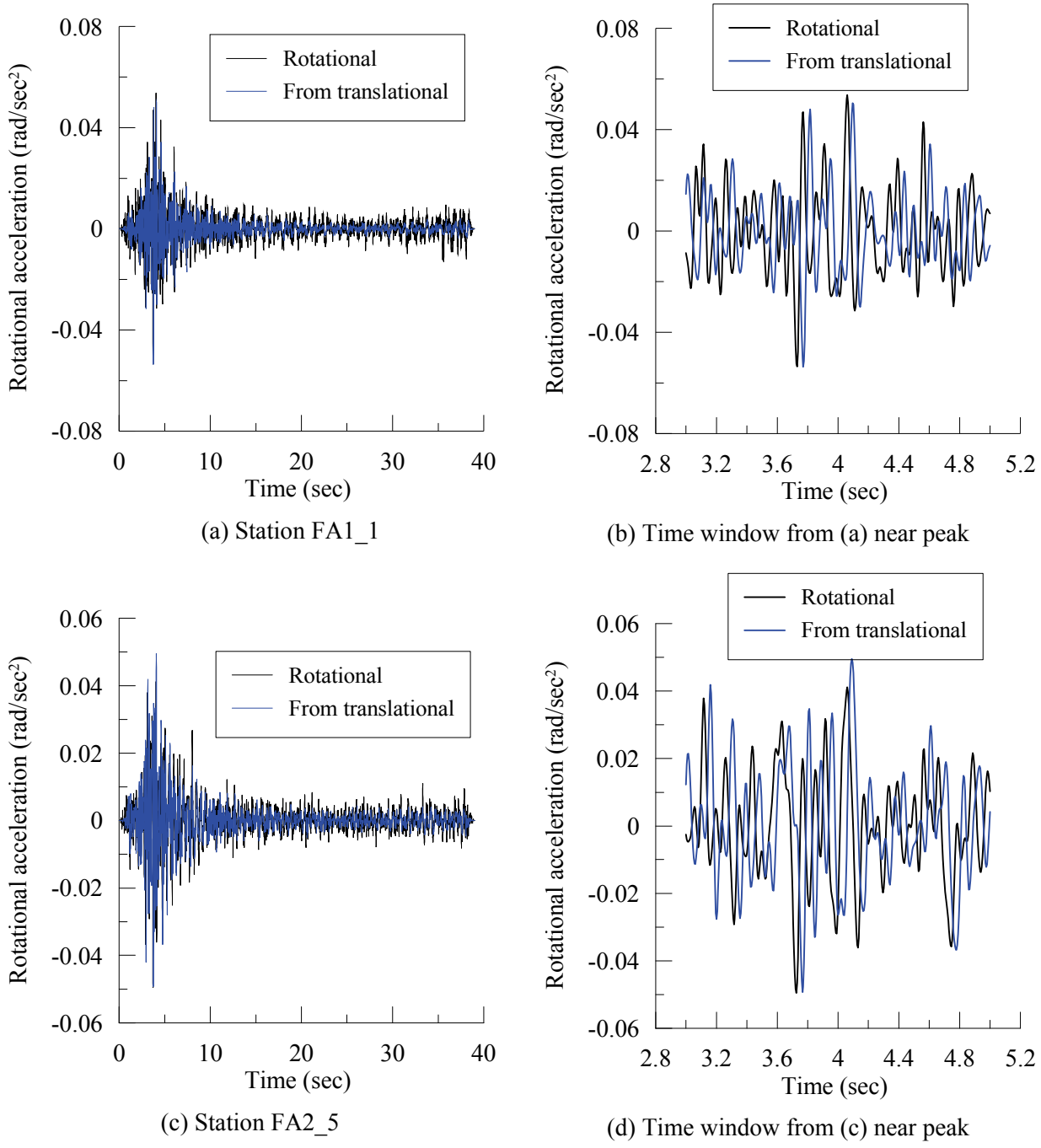

(a) Station FA1_1

(b) Time window from (a) near peak

(c) Station FA2_5

(d) Time window from (c) near peak

Figure 5-4: Comparison of P wave contribution to rocking acceleration and derivative of P wave contribution to the vertical acceleration scaled by the apparent P wave velocity

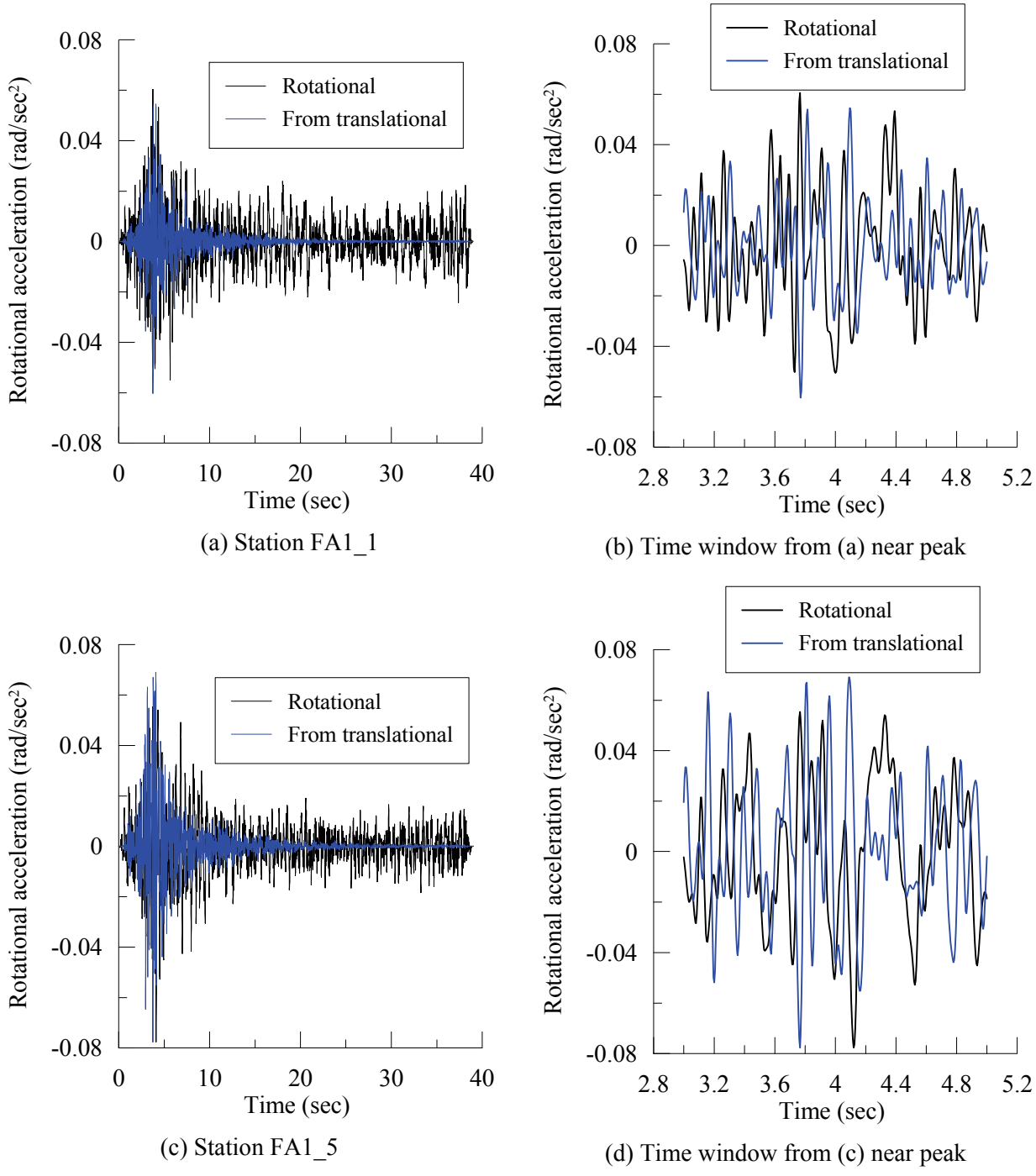

(a) Station FA1_1

(b) Time window from (a) near peak

(c) Station FA1_5

(d) Time window from (c) near peak

Figure 5-5: Comparison of rocking acceleration and derivative of vertical acceleration scaled by the apparent wave velocity

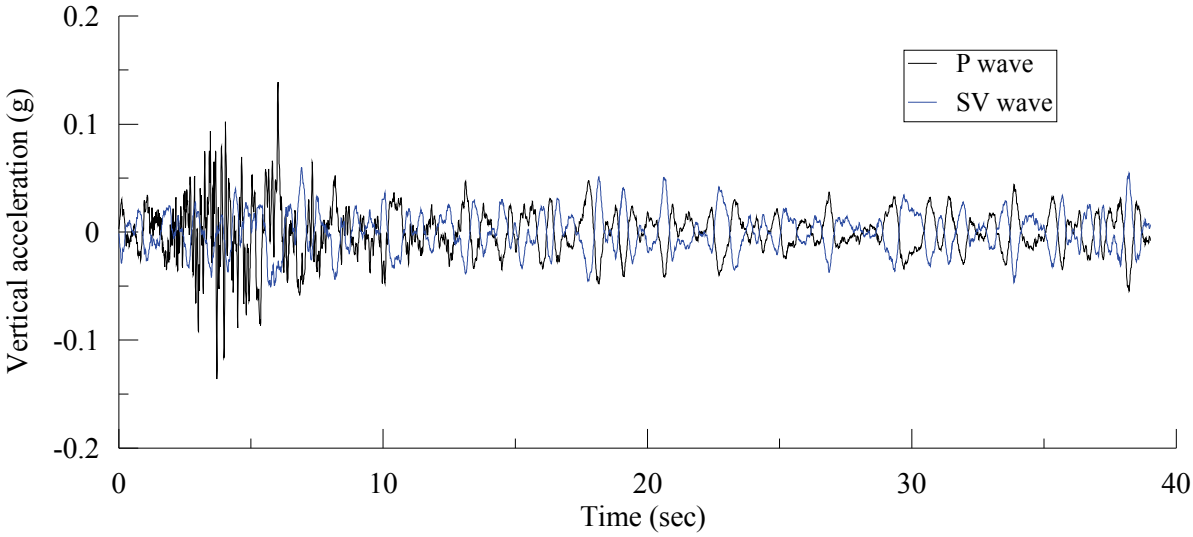

Figure 5-6: Contributions of P and SV wave to the vertical acceleration at Station FA1_1

Then, a derived rotational motion is obtained by dividing the time derivative of the recorded (not decomposed) vertical motion by the apparent P wave velocity and comparing the associated response spectrum with that computed in the first step. These two spectra are expected to be the same at low periods ($T \leq T_e$), as only the P wave will contribute to the vertical motion above the frequency $f_e = 1/T_e$. Figure 5-7 presents data at six stations: four interior stations (FA1_1, FA1_2, FA2_1 and FA3_1) and two exterior stations (FA2_5 and FA3_5). In each case, T_e is approximately 0.2 sec. Similar values of f_e are expected over the footprint of the array as the values of the apparent SV wave velocity computed above did not show significant spatial variability.

5.5. Comparison of Rotational Spectra using SDM, AGM, GM and SSP

A comparison of rotational spectra computed using SDM, AGM, GM and SSP is presented in this section. The same six stations considered above are chosen for the purpose of detailed comparison. A computer program implementing SDM with illustrations are presented in Appendix E.

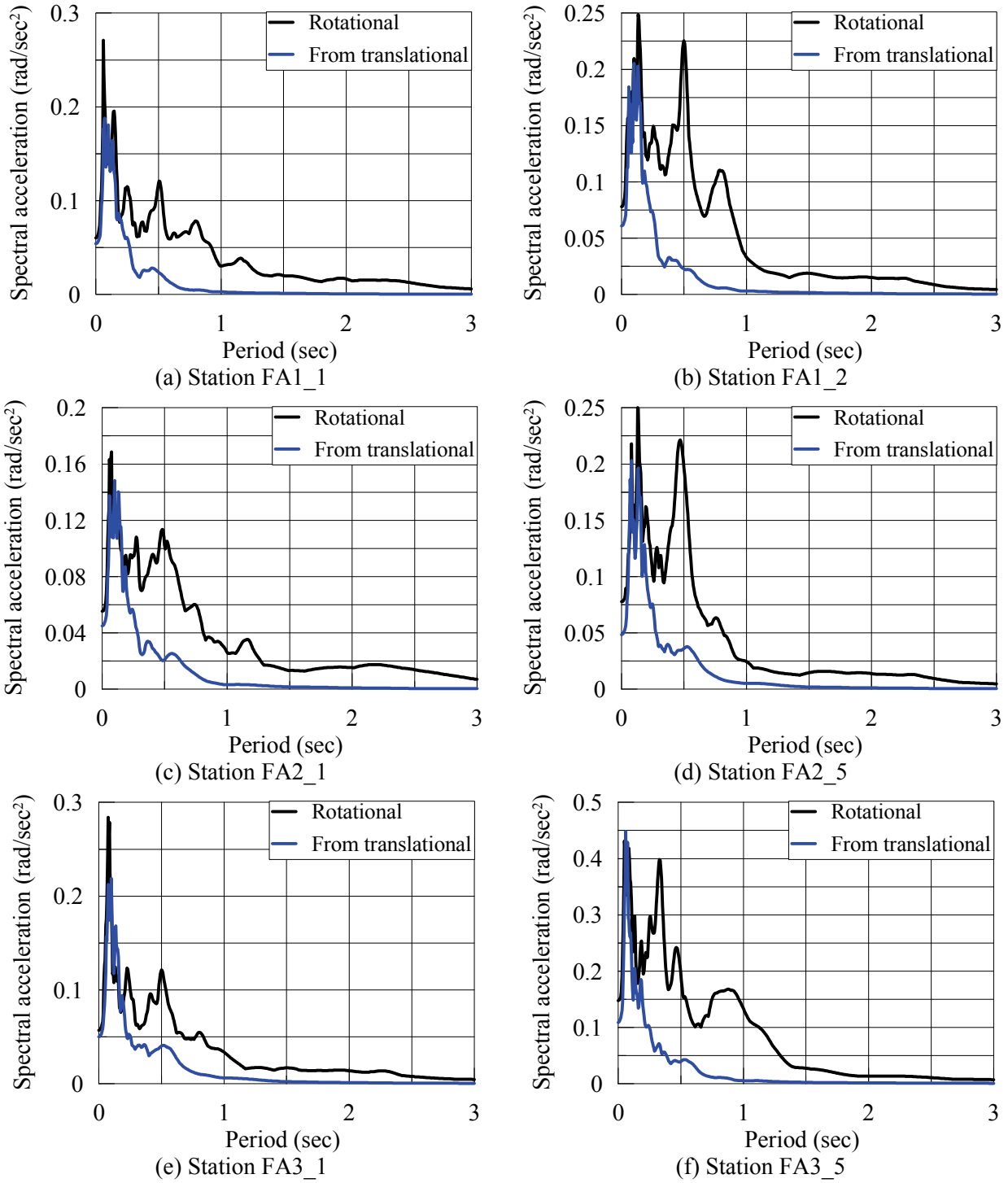

Figure 5-7: Spectra of rocking acceleration and derivative of vertical acceleration scaled by the apparent P wave velocity

5.5.1. Torsional Spectra

Torsional spectra are presented in Figure 5-8. For the interior stations (e.g., panels a, b, f), spectra computed using the SDM closely match those obtained using the AGM. However, the general expectation is that the spectral ordinates per the AGM will be underestimated at periods $T < L/c_{sh}$ sec provided the SH wave contribution to the ground motion has significant frequency content beyond (above) c_{sh}/L Hz (=249/75=3.32 Hz in this case). Figure 5-9 presents the Fourier amplitude spectrum of the SH wave contributions at one interior station (FA1_1) and one exterior station (FA2_5). The frequency content above 3.32 Hz is not sufficiently great to explain the underestimation of the spectral ordinates at low periods using the AGM. For the exterior stations (panel e, j etc.), the spectral ordinates computed using the AGM are greater than those computed using the SDM because of the numerical error associated with the AGM when applied to the exterior stations. The underestimation of spectral demand at all stations by the GM is due to the averaging effect associated with the assumption of a planar best-fit surface (see Chapter 4). Finally, note that the difference in spectral ordinates obtained using the SDM and SSP is attributed to a lack of information on the spatial variability of the recorded motions utilized in the SSP.

5.5.2. Rocking Spectra

Rocking spectra per the SDM, AGM and GM are presented in Figure 5-10 (*xz* plane) and Figure 5-11 (*yz* plane). For the interior stations (panel a, b, f etc., Figures 5-10 and 5-11), the SDM and AGM closely match at high periods, and at low periods, the SDM spectral ordinates are greater than those of the AGM in an average sense. Both trends conform to the discussions presented previously. For the exterior stations (panel e, j etc., Figures 5-10 and 5-11), the AGM spectral ordinates are greater than those of the SDM due to the numerical error associated with the AGM. Spectral ordinates computed using the GM are much smaller than those obtained using SDM, especially at low periods, due to the averaging effect of the planar best-fit surface. Note that the SSP prediction is not included in the above comparison because the relative values of the spectral ordinates on the *xz* and *yz* planes are significantly influenced by the

orientation of the principal plane as the rocking spectra in the SSP are computed on the principal plane and no rocking motion exists on a plane normal to the principal plane.

A more detailed comparison involving the frequency intervals described in the Section 5.3 is presented below along with the results calculated using the SSP. Instead of spectra on the *xz* and *yz* planes, the SRSS of these spectra is considered to be the measure of rocking motion for this comparison. The SRSS rocking spectrum calculated using the SSP physically implies spectrum on the principal plane. Figure 5-12 enables a comparison of results from which the following points are observed:

1. For this seismic array and event, $2L/c_{sv} = 0.8$ sec. The AGM and SDM spectra at the interior stations are very similar for periods greater than 0.8 sec, which is an expected result.
2. The maximum frequency associated with the SV wave contribution to the vertical acceleration is 5 Hz (0.2 sec). At interior stations, the AGM spectral ordinates are less than those of the SDM at periods less than 0.2 sec, as expected.
3. Per Figure 5-6, the amplitude of the P wave contribution to the vertical acceleration is greater than that of the SV wave. For this seismic array and event, $c_p > 2c_{sv}$. As a result, the spectral ordinates computed using the SDM in the period interval $1/f_e \le T \le 2L/c_{sv}$ (0.2 to 0.8 sec, for this case) are considered reasonable. In the interval $L/c_{sv} \le T \le 2L/c_{sv}$ (0.4 to 0.8 sec, for this case), the differences between the SDM and AGM spectra are small.
4. The differences in spectra computed using the SDM and SSP are due to the spatial variability of the recorded ground motions, information that is not used in the SSP.

The first three observations do not hold strictly at the exterior stations because of the numerical error associated with AGM.

The SDM and SSP spectra differ more for rocking than for torsion. This is attributed to the spatial variability of the P wave contribution to the vertical motion and SH wave contribution to the horizontal motion.

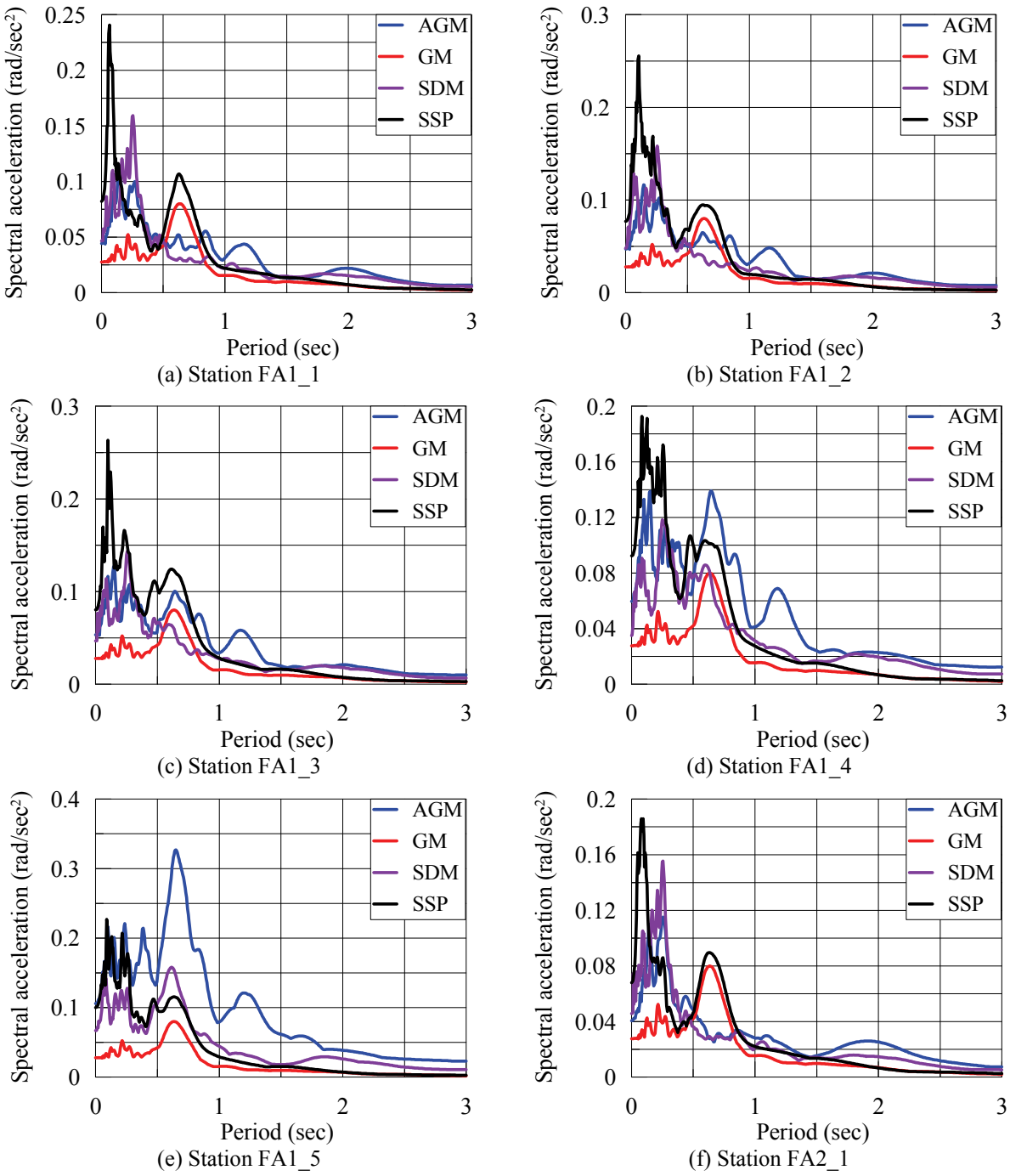

Figure 5-8: Torsional spectra computed using four different methods (cont.)

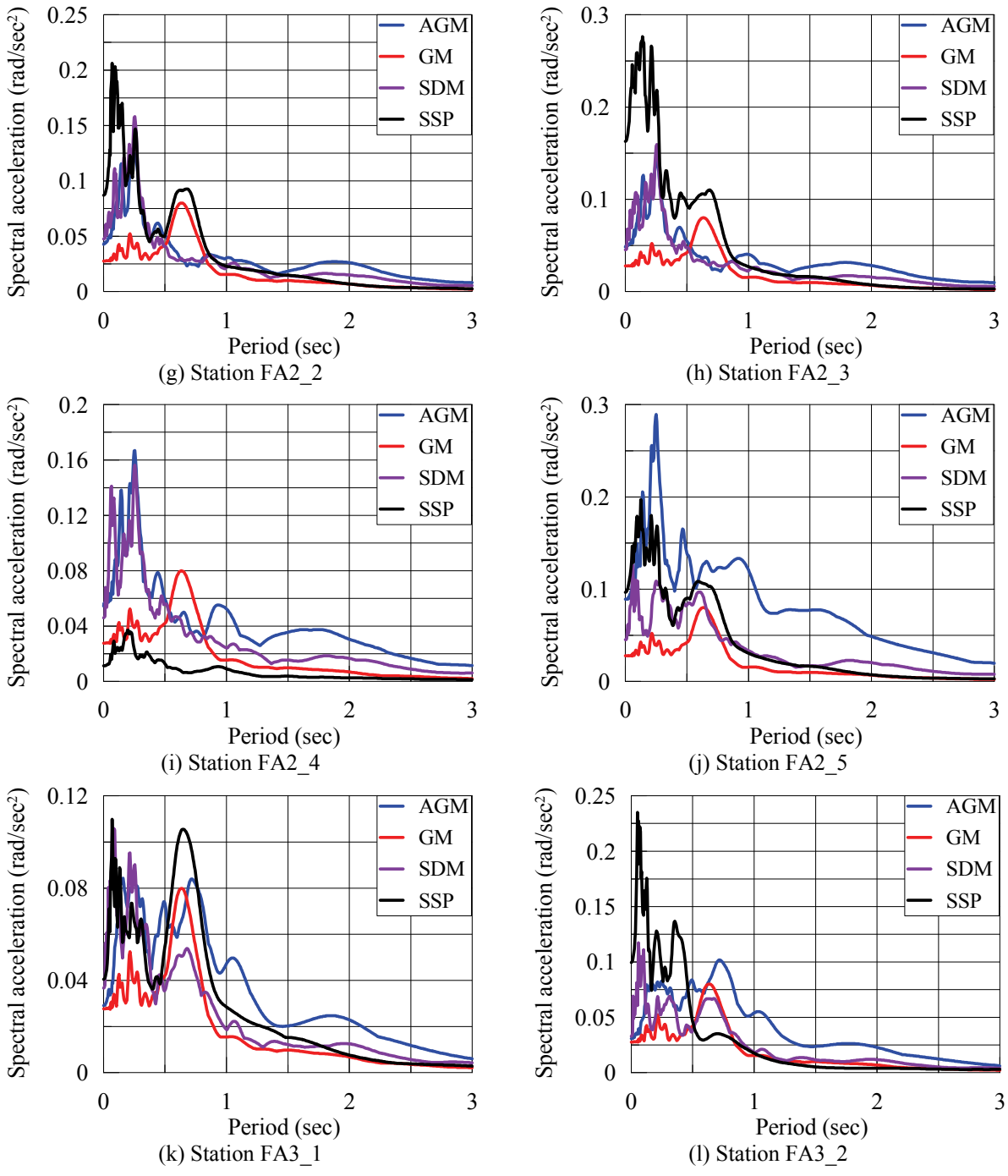

Figure 5-8: Torsional spectra computed using four different methods (cont.)

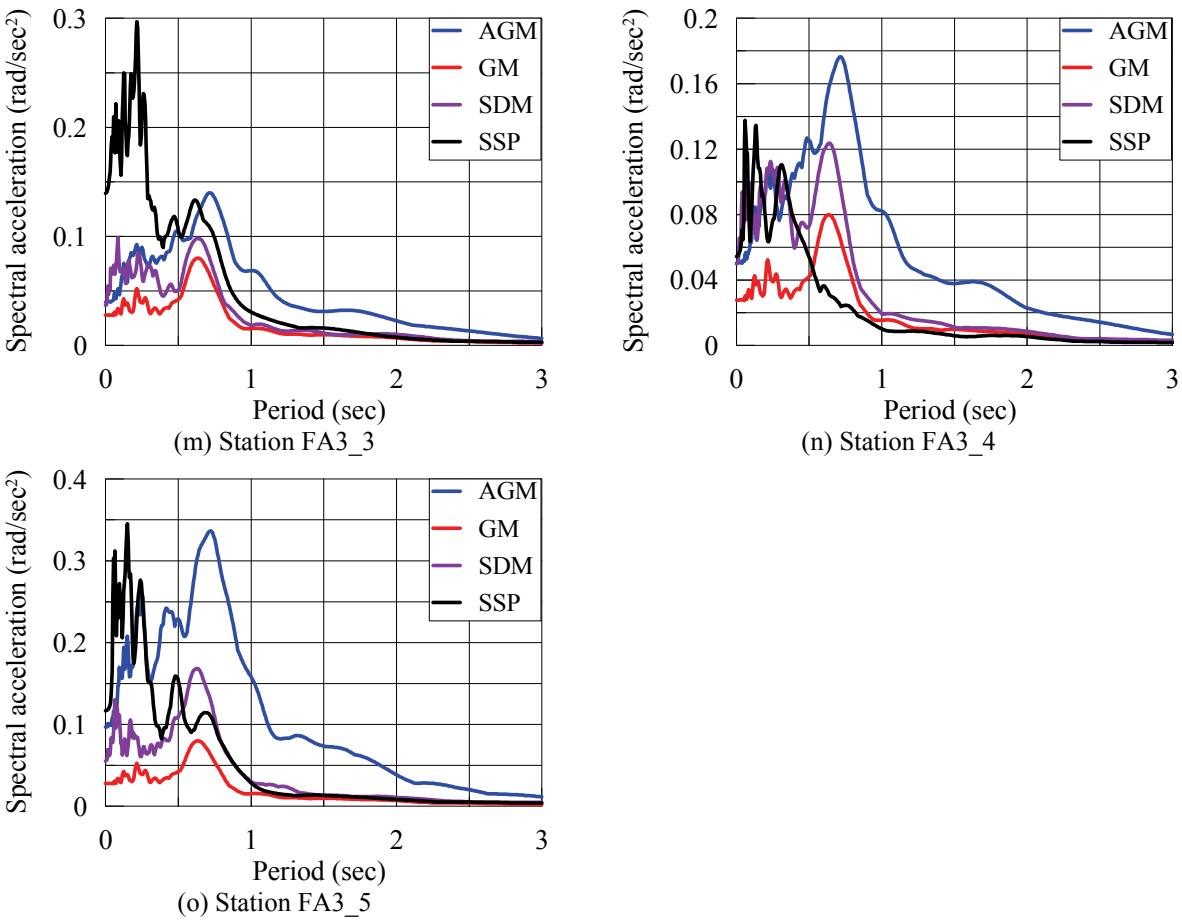

Figure 5-8: Torsional spectra computed using four different methods

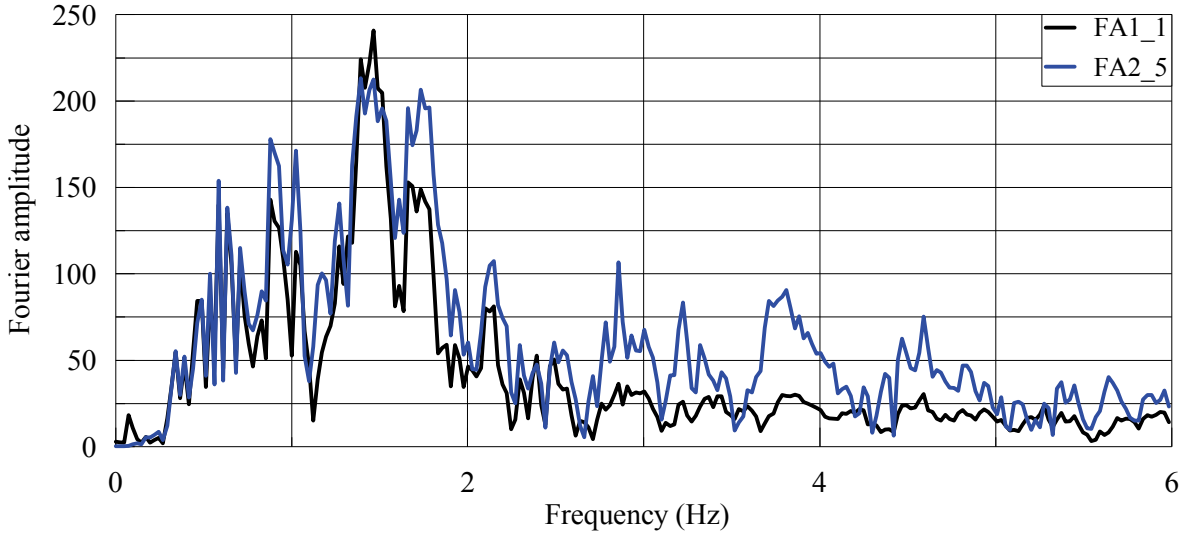

Figure 5-9: Fourier amplitude spectra of the SH wave contribution to the horizontal motion (normal to the principal plane)

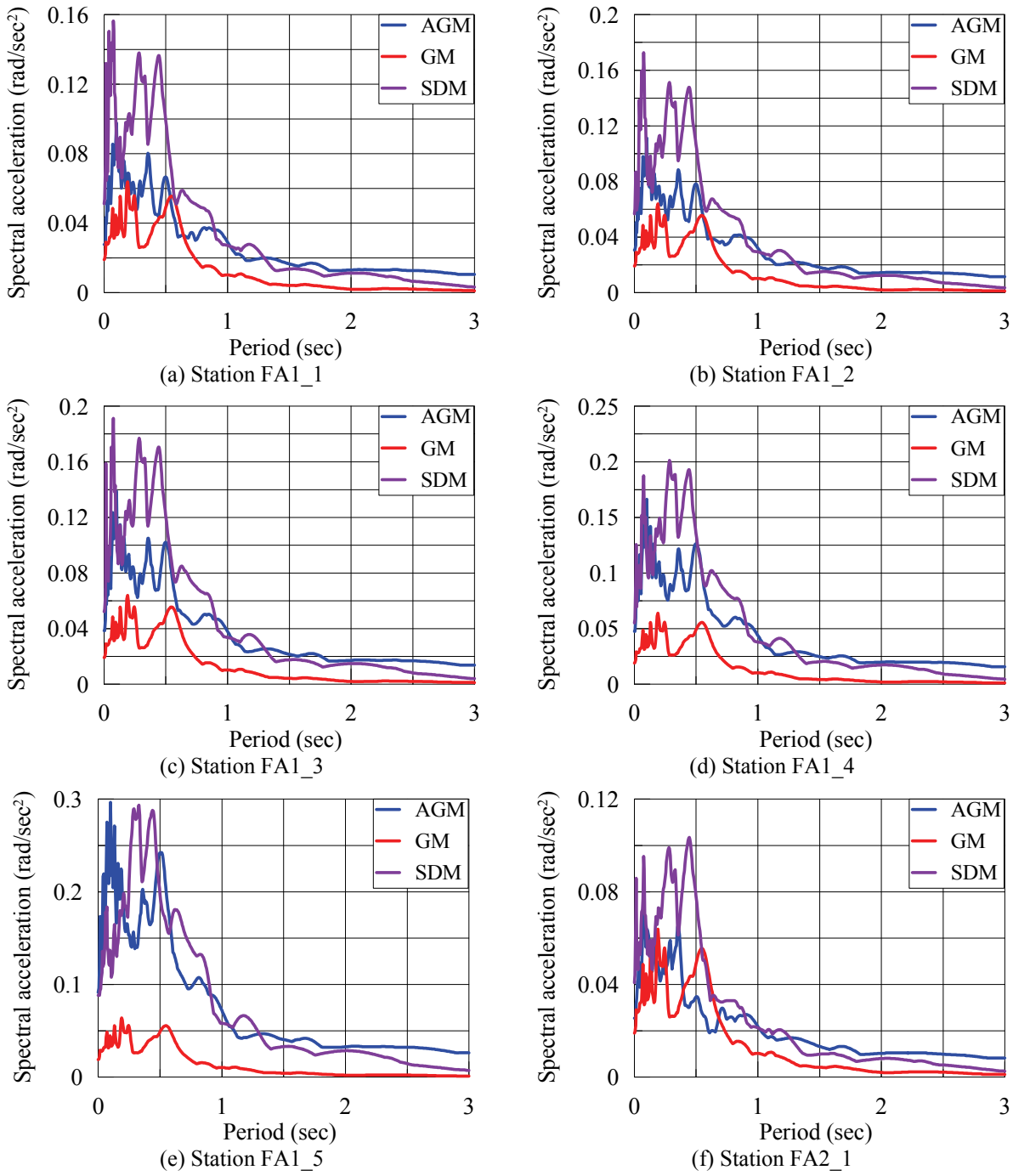

Figure 5-10: Rocking (*xz* plane) spectra computed using three different methods (cont.)

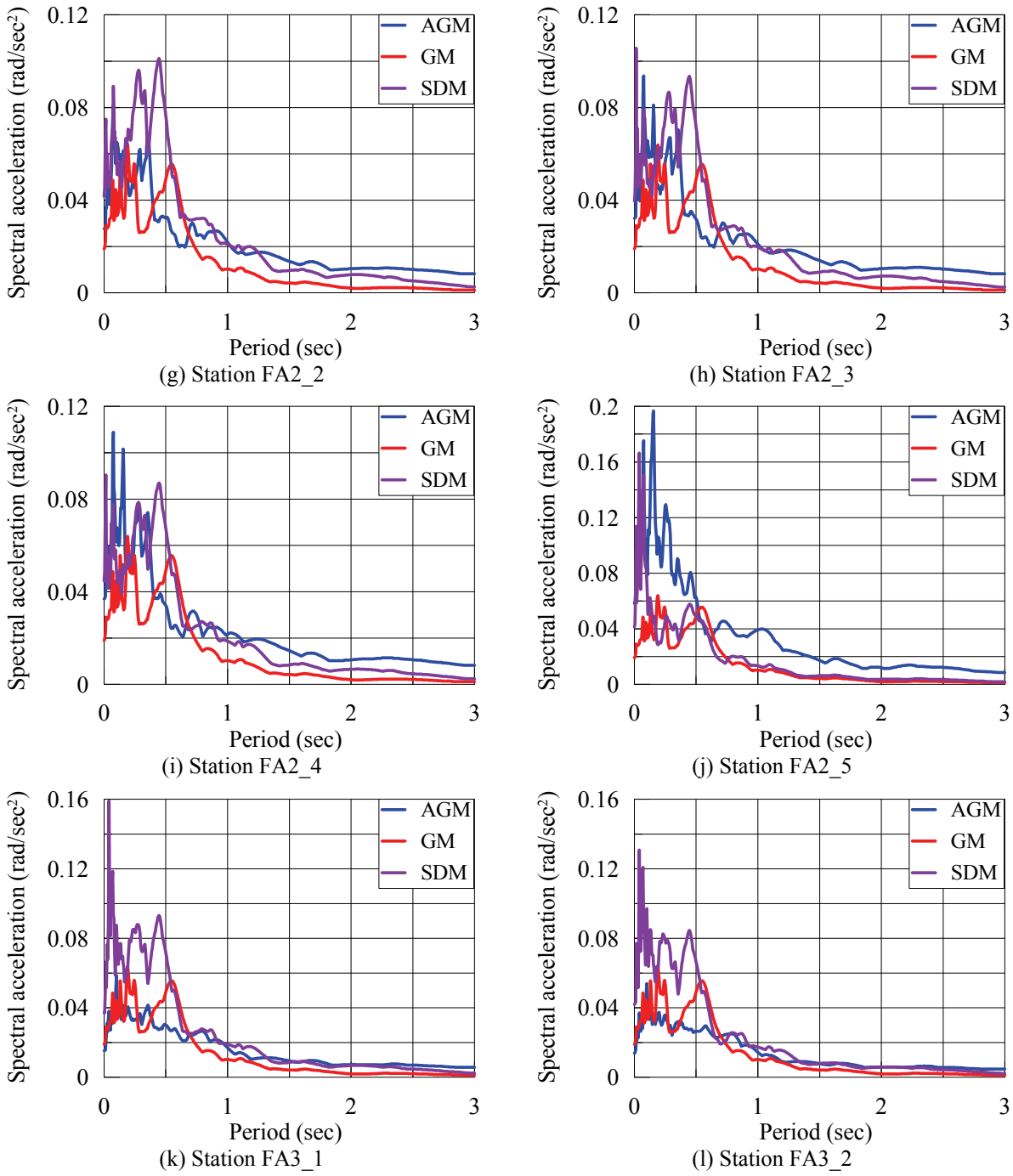

Figure 5-10: Rocking (*xz* plane) spectra computed using three different methods (cont.)

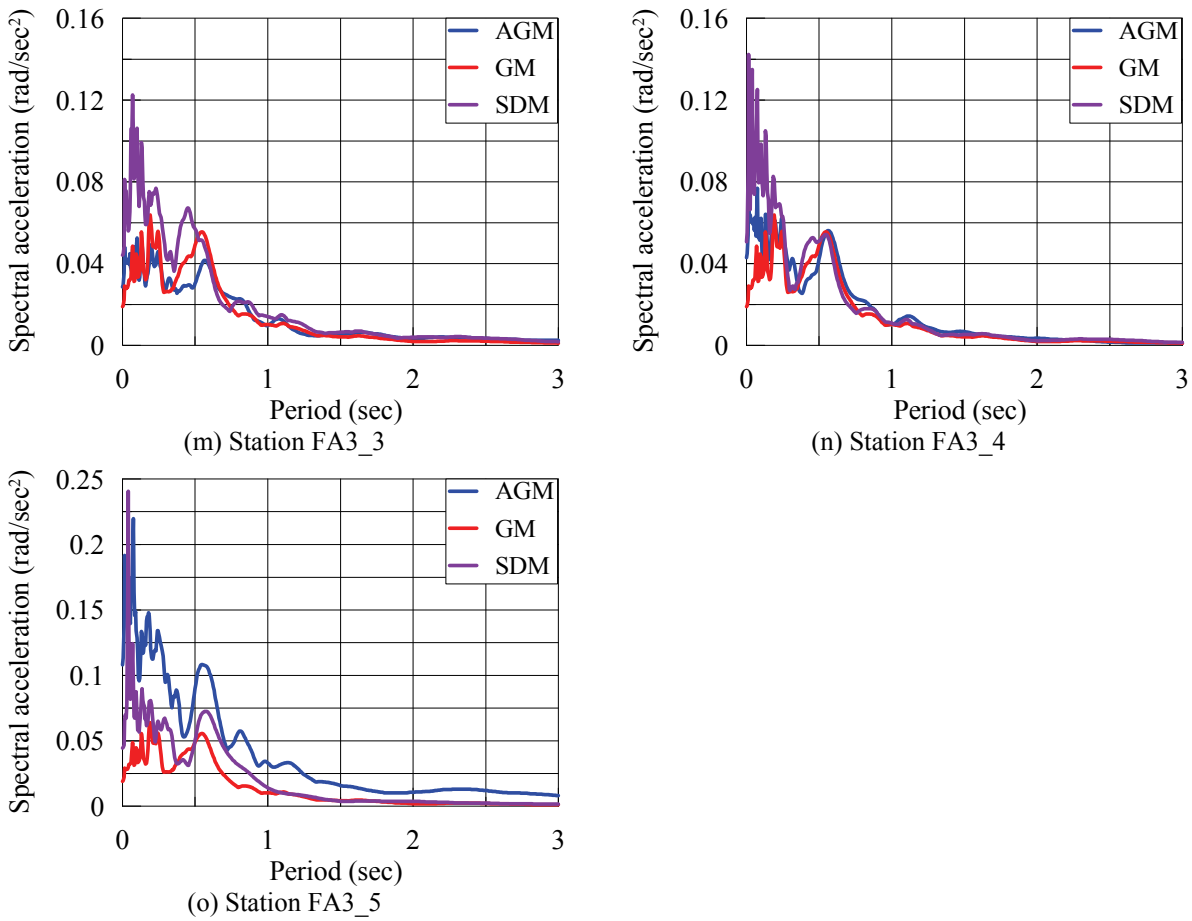

Figure 5-10: Rocking (*xz* plane) spectra computed using three different methods

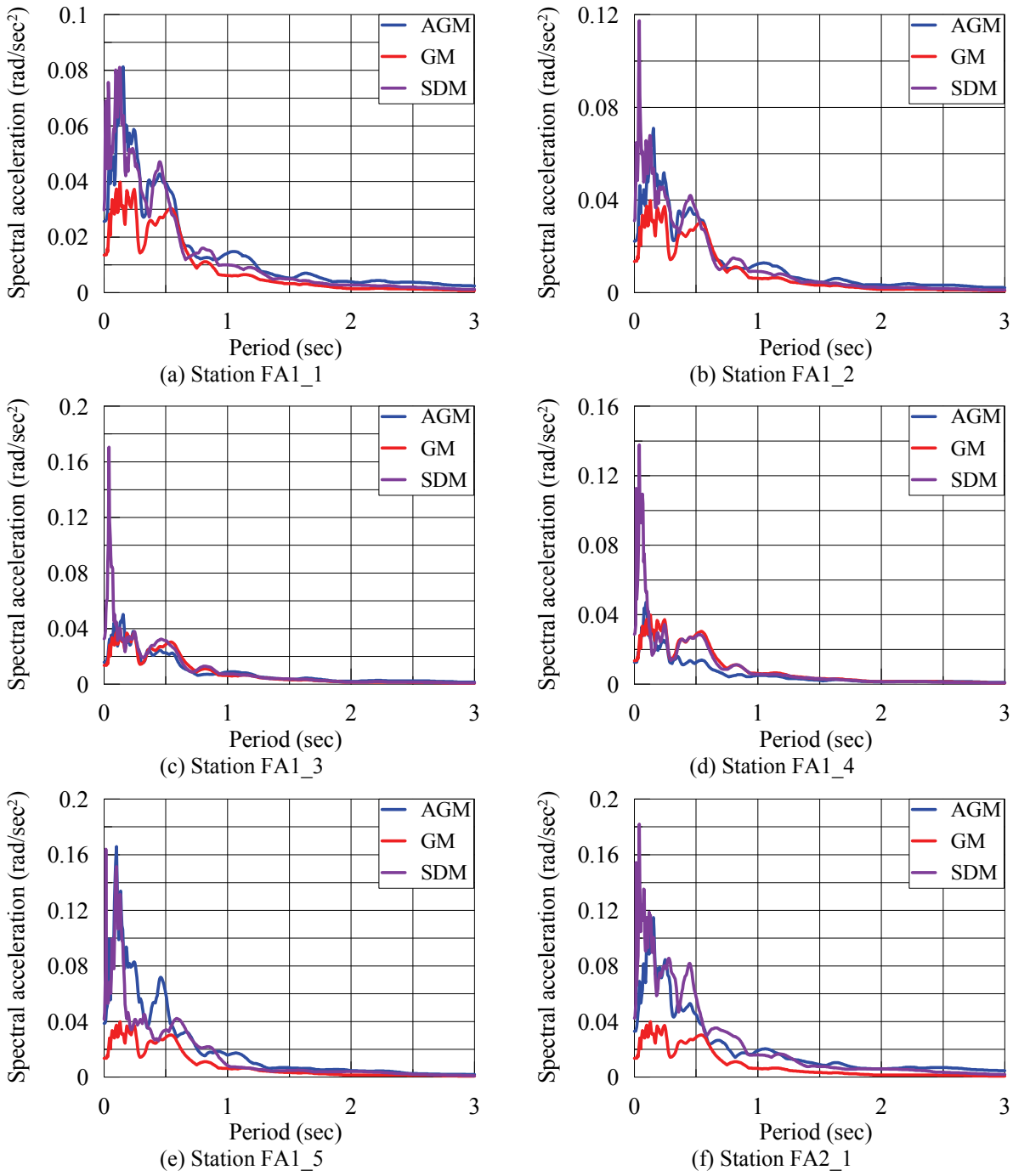

Figure 5-11: Rocking (*yz* plane) spectra computed using three different methods (cont.)

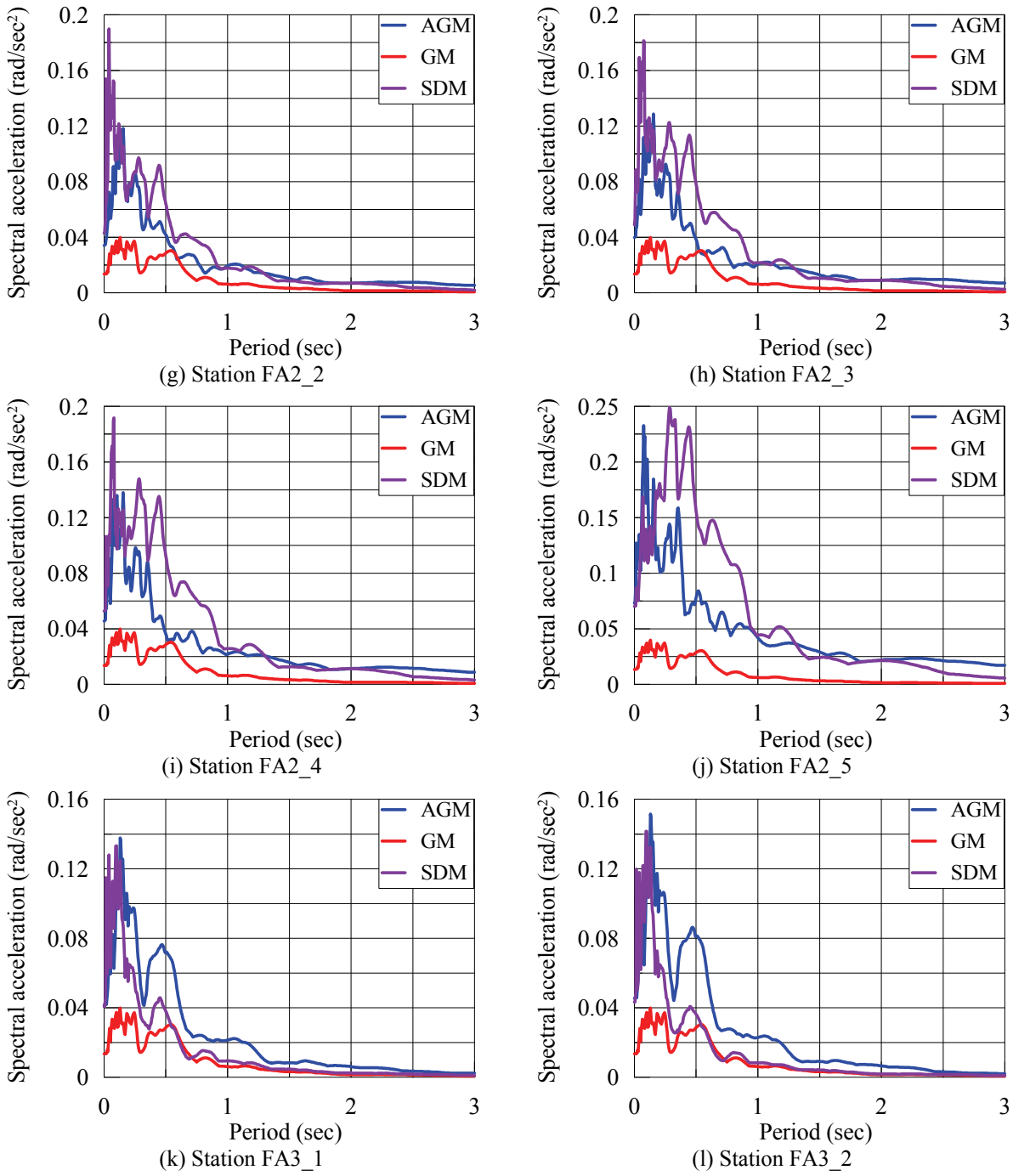

Figure 5-11: Rocking (*yz* plane) spectra computed using three different methods (cont.)

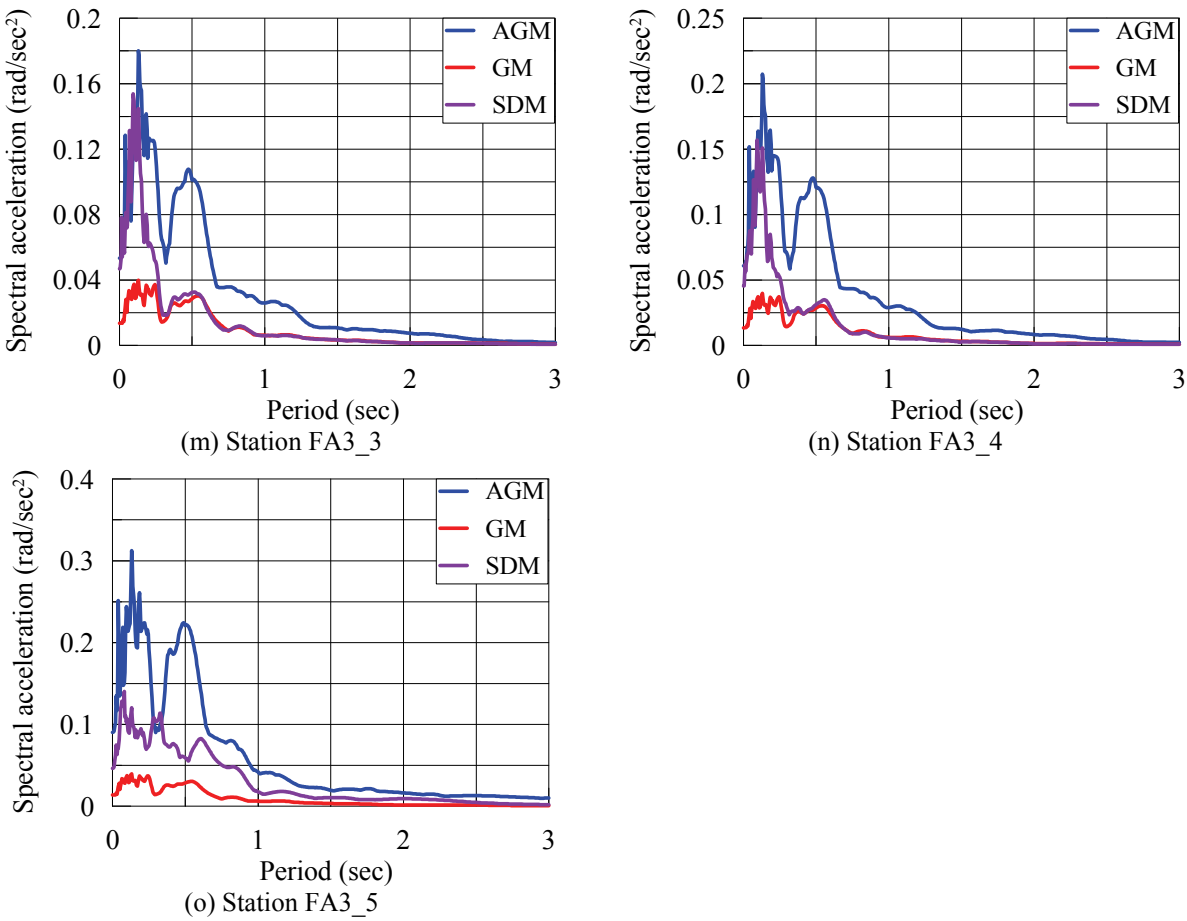

Figure 5-11: Rocking (*yz* plane) spectra computed using three different methods

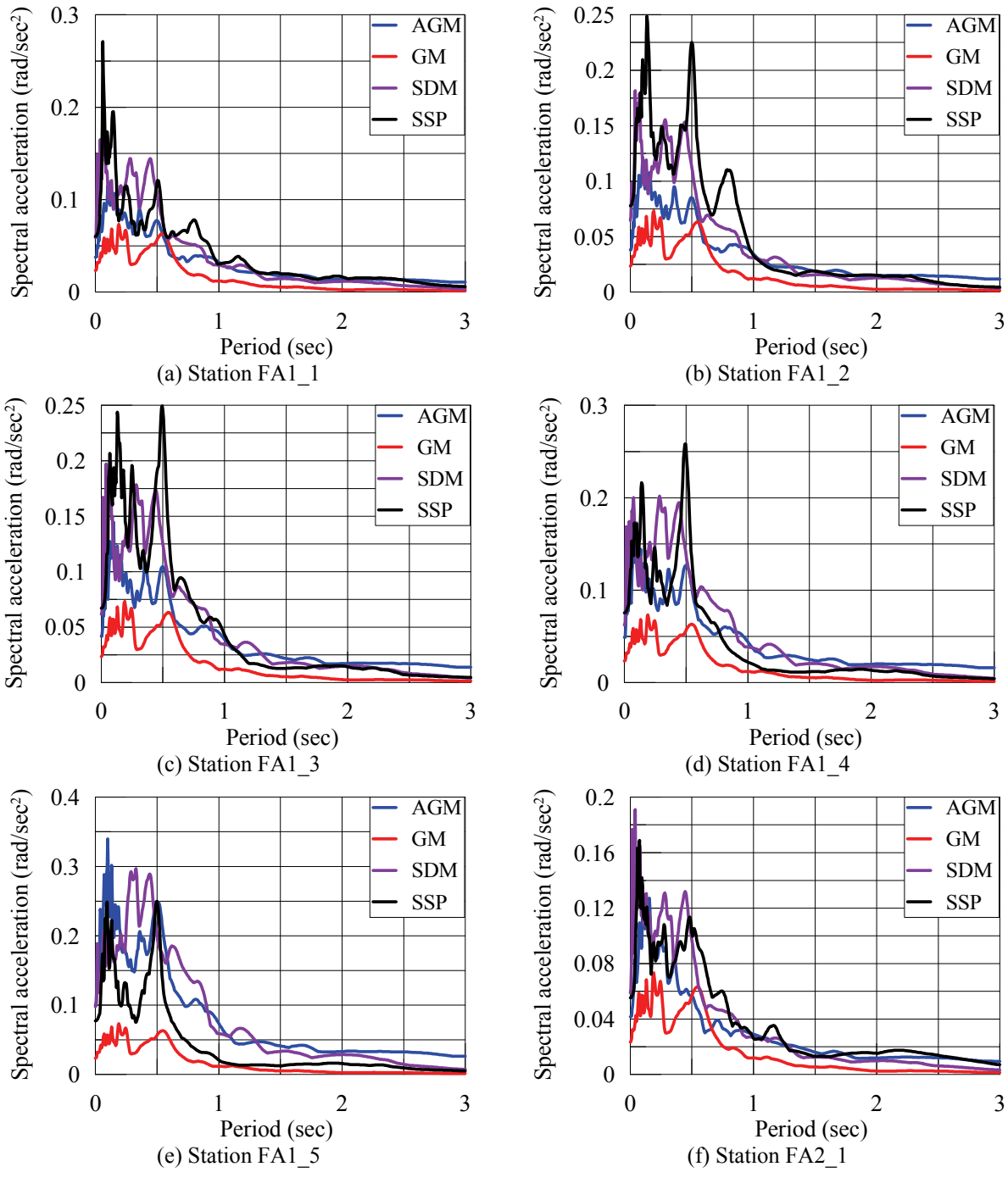

Figure 5-12: Rocking (SRSS) spectra computed using four different methods (cont.)

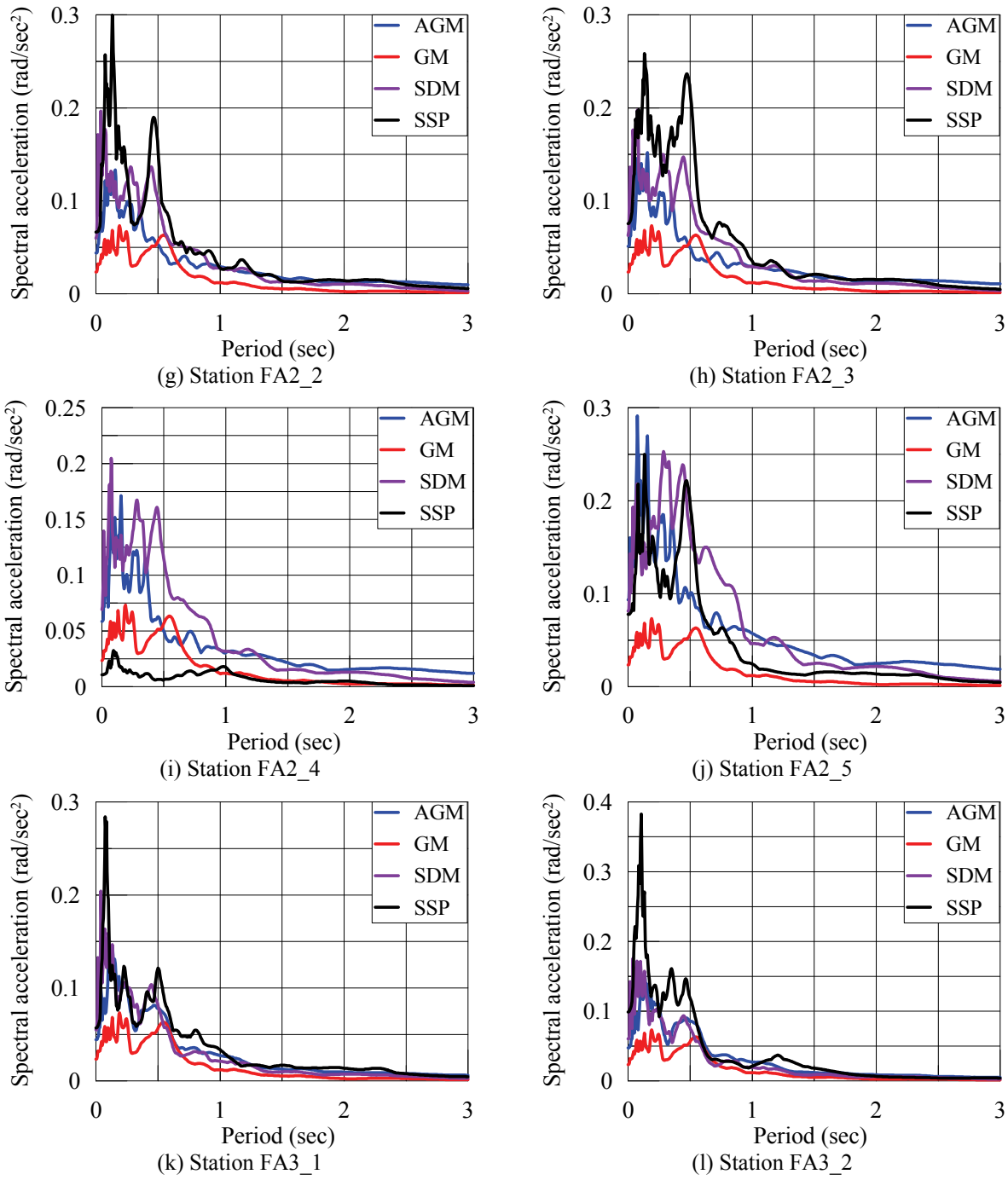

Figure 5-12: Rocking (SRSS) spectra computed using four different methods (cont.)

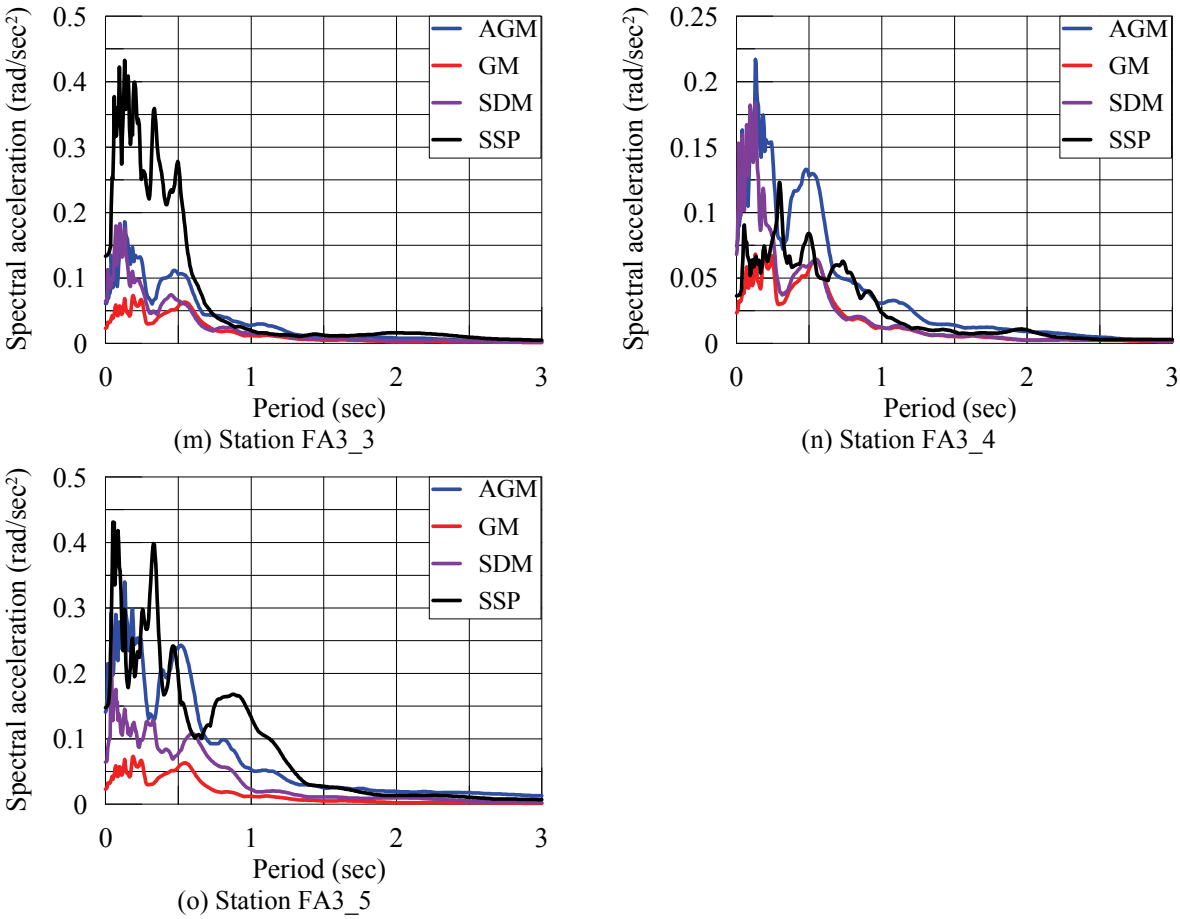

Figure 5-12: Rocking (SRSS) spectra computed using four different methods

CHAPTER 6

DIMENSIONS OF A DENSE ARRAY TO EXTRACT ROTATIONAL COMPONENTS OF EARTHQUAKE GROUND MOTION

6.1. Introduction

There have been very few studies on the effect of the spatial distribution of the recording stations and array dimensions on the computed rotational components of ground motion. Using the Geodetic Method (GM), Bodin et al. (1997) concluded an array dimension of less than one-quarter of the wavelength of the dominant harmonic would provide an estimate of the gradient of the instantaneous displacement field across the array within 10% of the true value. On this basis, the shorter the length of the array, the greater the accuracy of the estimated gradients (i.e., rotational components). As explained in Chapter 4, this comparison is only valid at a single station if based on one pair of stations. The gradient returned by the GM is essentially a weighted average of those computed using several station pairs sharing one common station. Depending upon the shape of the wave train at the instant of recording, each of these gradients does not necessarily have the same sign and the resulting average gradient can be significantly less than the individual estimates. Chung (2007) studied the effect of station selection on the computed dynamic soil strains computed using the GM for earthquakes recorded by the Lotung array in Taiwan. The study compared the results obtained using all the surface stations in the array and a number of station triplets. He concluded that the results obtained using all the stations were nearly the same as those obtained using only three exterior stations. Since a planar best-fit surface across the array is computed at every instant of the recording and the gradients of the surface are used to compute the rotational components, the GM essentially calculates inputs to a hypothetical rigid foundation with a shape defined by spatial distribution of the stations over the footprint of the array. Since the shape of the rigid foundation is essentially the

same for the cases considered by Chung, namely, a) all stations and b) only three exterior stations, this conclusion is expected.

None of the studies performed to date has characterized the effect of: a) the spatial distribution of the stations, and b) the array dimensions, on the extracted free-field rotational components. Such a study is presented in Section 6.2 using the Surface Distribution Method (SDM) (see Chapter 5). The similar study is then presented in Section 6.3 using the Acceleration Gradient Method (AGM) (see Chapter 4) and GM (see Chapter 2). The sensitivity studies confirms that the length of the array is the key design parameter. Design objectives for a dense array are presented in Section 6.4 and followed by the conceptual design of a one-dimensional array in Section 6.5. Design criteria for a two-dimensional array are discussed in Section 6.6. Numerical illustrations are presented in Sections 6.7 and 6.8. Section 6.9 presents a discussion on the calculation of the length of the array from a given spatial distribution of stations. The set of criteria proposed here for the design of a dense seismic array assumes that the SDM is to be used to extract the rotational components of ground motion.

6.2. Sensitivity of the SDM to Station Spatial Distribution

Translational strong motion data from the M6.1 event of January 16, 1986, as recorded at the Large Scale Seismic Testing (LSST) array in Lotung, Taiwan, is used for analysis. A study is performed to understand how rotational spectra computed using the SDM vary with the inclusion of different surface stations in the analysis, that is, the *sensitivity* of the results to different assumptions.

To perform the sensitivity analysis, the stations are grouped into 10 different sets as shown in Table 6-1. The lateral dimension of the array associated with each set of motions, which is determined by the most distant tier included in the set, is calculated next. The lateral dimension is taken as the smaller of the sides of rectangle (or square) centered at (0, 0) per Figure 6-1 that includes all stations in the set. This is described below as the *rectangular approximation* of the length of the array. A circle could also be used with a diameter equal to the lateral dimension, which is described here as the *circular approximation*. A

discussion of each definition is presented later in this chapter. The lateral dimensions of the arrays studied here (per the rectangular approximation) are listed in Table 6-2.

Table 6-1: Sets of motions considered in the sensitivity analysis

	Set									
	1	2	3	4	5	6	7	8	9	Full
Tier	-	-	-	5	5	5	5	5	5	5
	-	-	4	-	4	4	4	-	-	4
	-	3	3	3	-	3	-	3	-	3
	2	2	2	2	2	-	-	-	2	2
	1	1	1	1	1	1	1	1	1	1

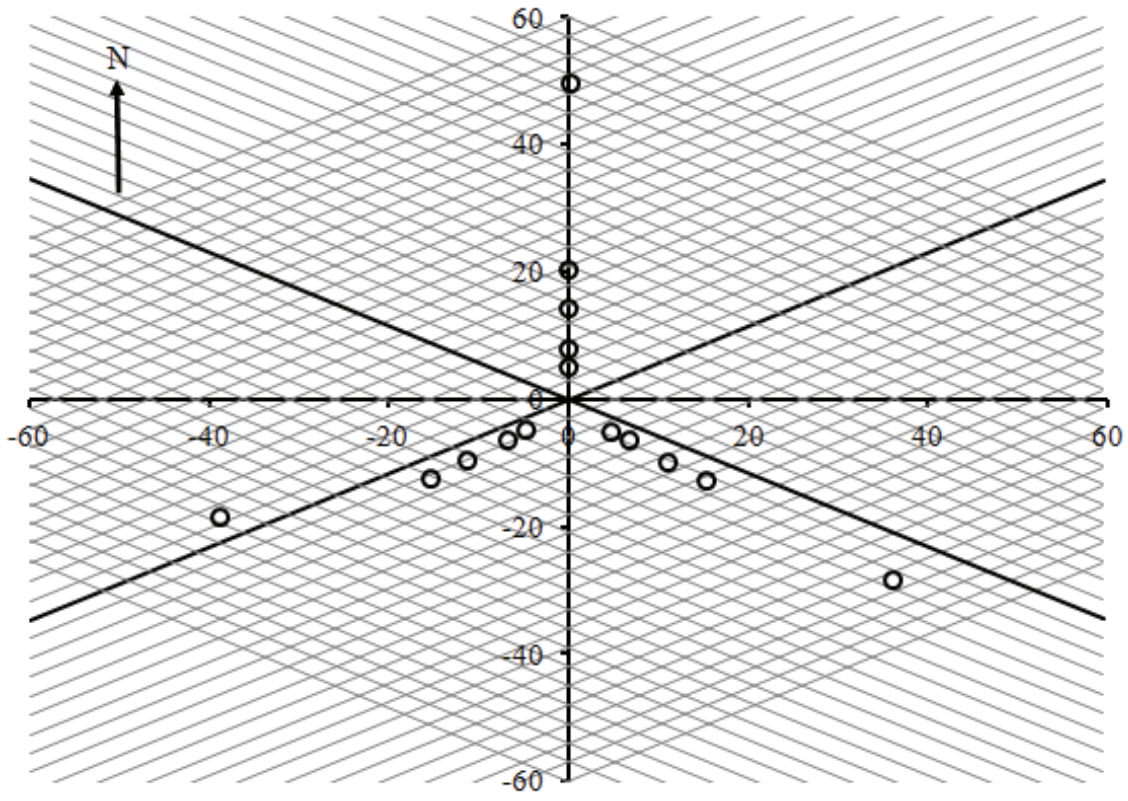

Figure 6-1: The dimensions of the Lotung LSST array

Table 6-2: Array dimensions associated with the inclusion of different tiers

Tier	Array Dimension (m)		
	EW	NS	Lateral [min (EW,NS)]
5	74.9	78.1	75
4	30.7	33.4	30
3	22.2	24.1	22
2	13.5	14.5	13

The sensitivity analysis was performed by comparing the torsional spectra in Figure 6-2: Sets 1, 2 and 3, and the Full Set in panel a; Sets 3, 4, 5 and 6, and the Full Set in panel b; and Sets 2, 7, 8 and 9, and the Full Set in panel c. These comparisons are repeated for the rocking spectra in Figures 6-3 through 6-5: *xz* plane (EW) and *yz* plane (NS) are considered in Figures 6-3 and 6-4, respectively, whereas Figure 6-5 presents the SRSS (square root sum of square) of the spectra on the *xz* and *yz* planes.

It is evident from panel a of Figure 6-2 that the difference in spectral ordinates computed using the Set 2 and Set 3 motions are significantly less than using Set 1 and Set 2. Note that the increase in the array dimension from Set 1 to Set 2 is 9 m, and from Set 2 to Set 3 is 8 m. Considering the difference in spectral ordinates when Set 3 is compared with the Full Set and noting the associated increase in array dimension is 45 m, it is apparent that the sensitivity of the results reduces as the array dimension increases. This trend is also seen for the rocking spectra on the *xz* plane (see Figure 6-3a) but the spectra on the *yz* plane show relatively less sensitivity (see Figure 6-4a). This may be related to the polarization of the propagating wave. To address this, an SRSS spectra on *xz* and *yz* planes is considered to be a unified measure of the rocking motion, which exhibits similar sensitivity (see Figure 6-5a) to the torsional spectra. The observed trend could be due to both the array dimension and the number of stations. The answer is provided in panel b of the Figures 6-2 through 6-5. Sets 3 through 6 comprise 12 stations each, but the spectra computed using Set 3 appear as outliers in Figures 6-2, 6-3 and 6-5 due to the array dimension, which is significantly less in Set 3 than Sets 4 through 6 and the Full Set. The spectra

computed using Sets 4 through 6 are similar to those computed using the Full Set, which includes more stations. This result is due to the array dimension, which is the same for Sets 4, 5 and 6, and the Full Set. Sets 4 through 6 differ in the spacing of the stations.

A similar comparison is presented in panel c of Figures 6-2 through 6-5. Set 2 and Sets 7 through 9 comprise nine stations each but the array dimension is significantly smaller in Set 2 than the others. The spectra computed using Set 2 appear to be outliers but the other three (Set 7 through Set 9) spectra are similar. Further, the spectra computed using Sets 7, 8 and 9 are similar to those generated using the Full Set, which includes more stations. The length of the array remains the governing criterion, which is identical for all four sets.

In summary, the array length (dimension) is a critical design parameter and greater the number of stations in an array of a given dimension, the better the resolution of the wave fields.

6.3. Sensitivity of the AGM and GM to Station Spatial Distribution

The above sensitivity study was repeated using the AGM and GM. Results are presented in Figures 6-6 through 6-9, and Figures 6-10 through 6-13, respectively. The AGM is more sensitive to array length than the SDM; the GM is insensitive to array dimension.

6.4. Design Objectives for a Dense Array

The ordinates of rotational spectra computed using records from dense arrays are sensitive to array length (dimension), which reduces as the array dimension increases. However, the required minimum dimension of an array has not yet been established, in part because the objectives of building a dense array vary, and could include developing attenuation relationships, validating analytically-computed coherency functions, estimating the rotational components of ground motions, and estimating dynamic strains in the soil. The parameters used in the design of a dense array (with the objective of extracting the

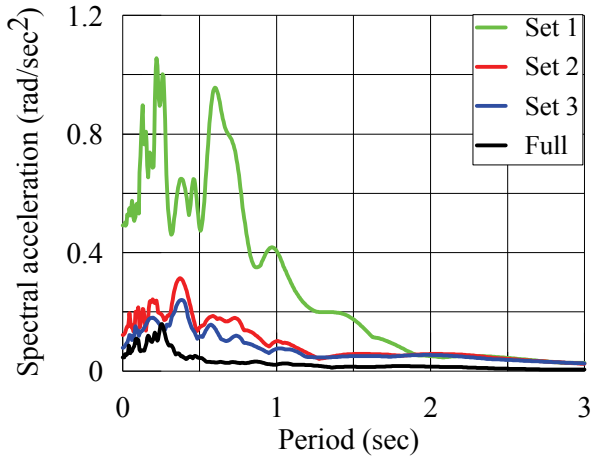

(a) Sets 1, 2, 3 and full

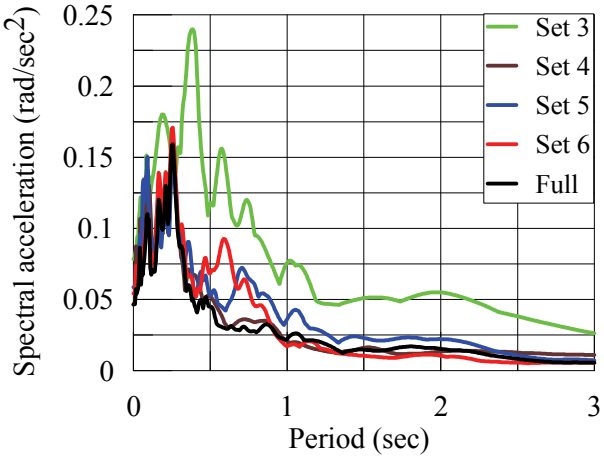

(b) Four tiers in each set and full

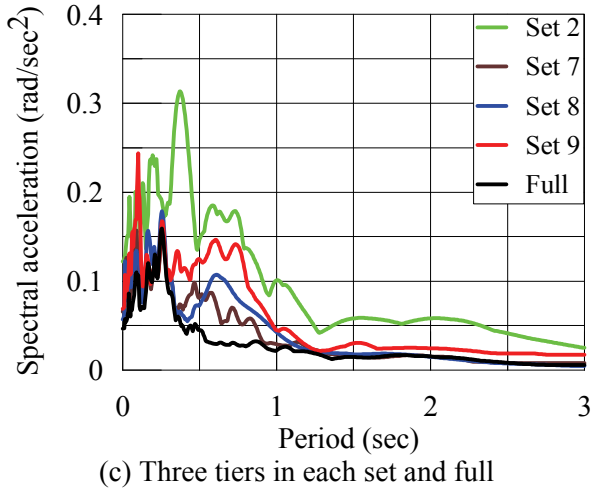

(c) Three tiers in each set and full

Figure 6-2: Torsional spectra computed using different sets of recorded motions, SDM

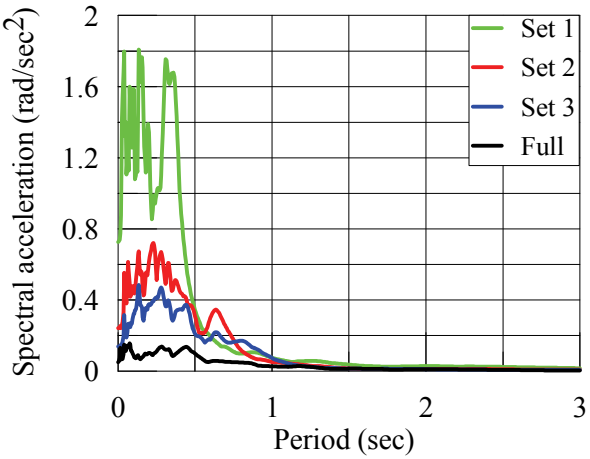

(a) Sets 1, 2, 3 and full

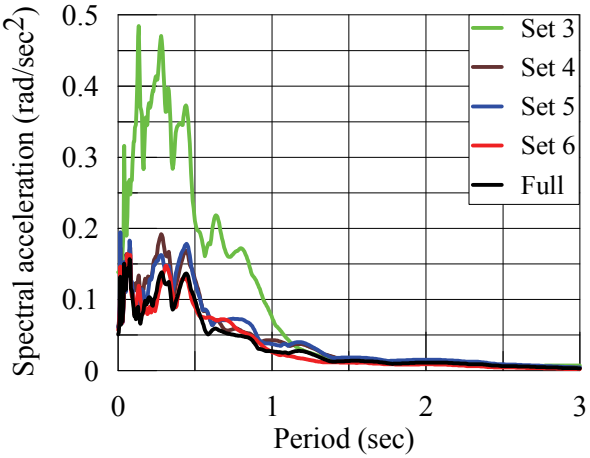

(b) Four tiers in each set and full

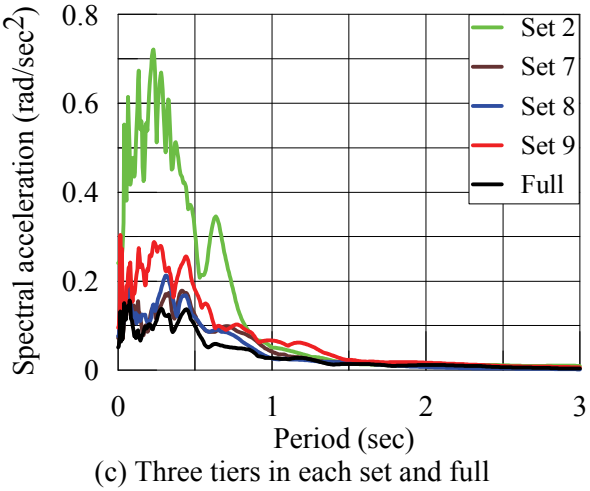

(c) Three tiers in each set and full

Figure 6-3: Rocking (*xz* plane) spectra computed using different sets of recorded motions, SDM

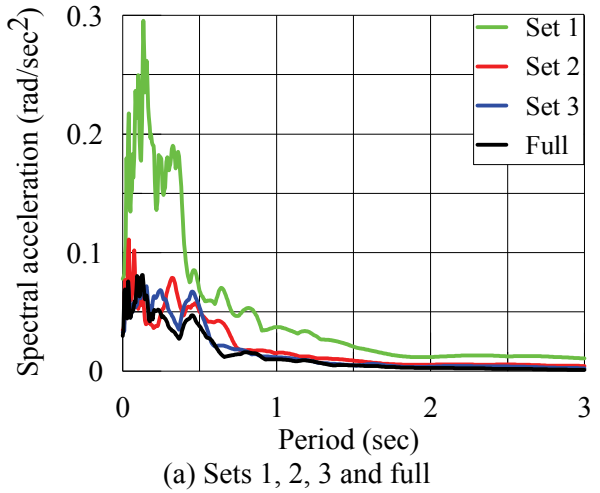

(a) Sets 1, 2, 3 and full

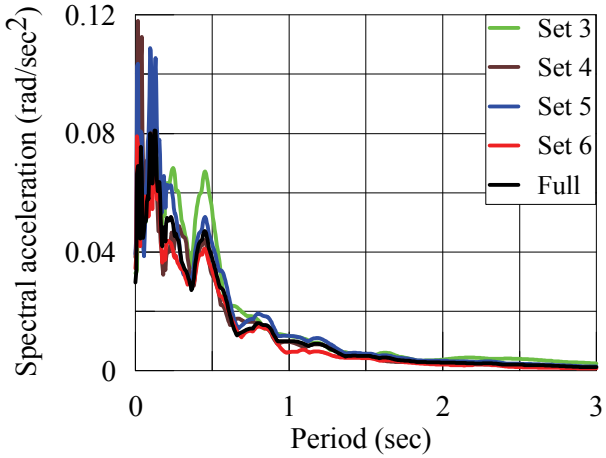

(b) Four tiers in each set and full

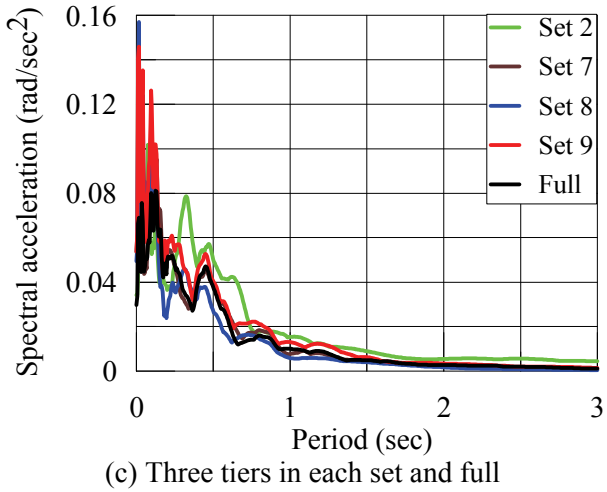

(c) Three tiers in each set and full

Figure 6-4: Rocking (*yz* plane) spectra computed using different sets of recorded motions, SDM

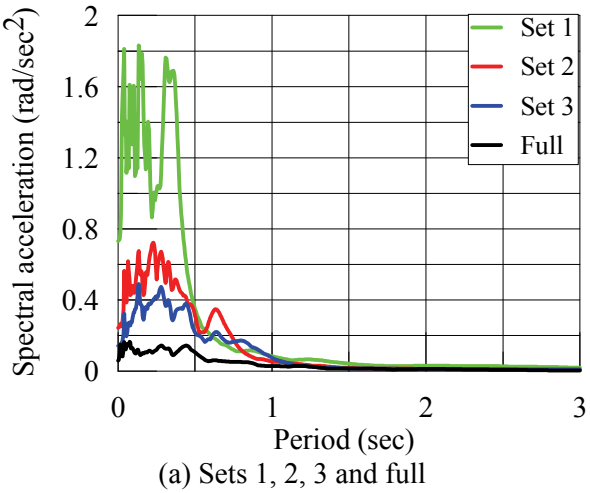

(a) Sets 1, 2, 3 and full

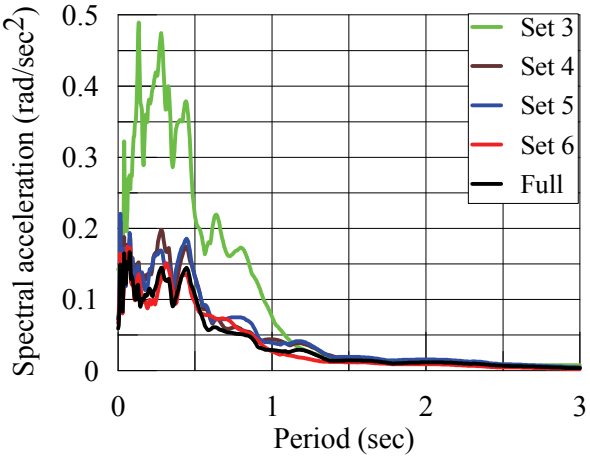

(b) Four tiers in each set and full

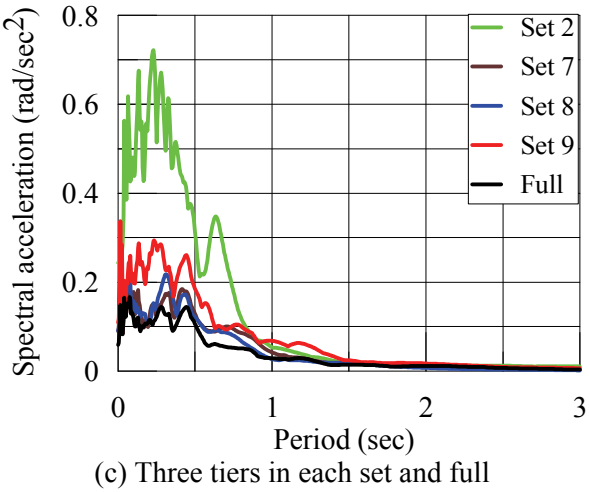

(c) Three tiers in each set and full

Figure 6-5: Rocking (SRSS) spectra computed using different sets of recorded motions, SDM

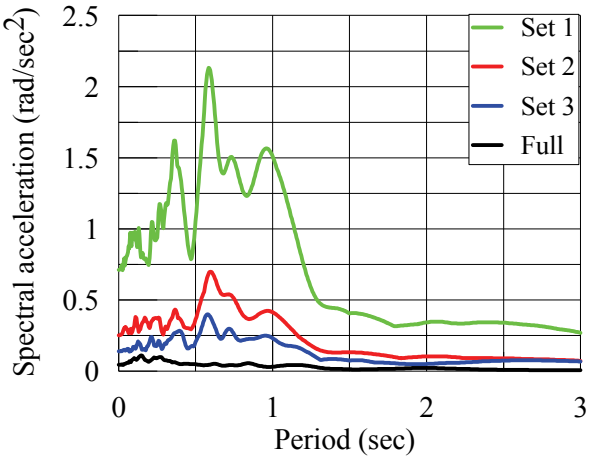

(a) Sets 1, 2, 3 and full

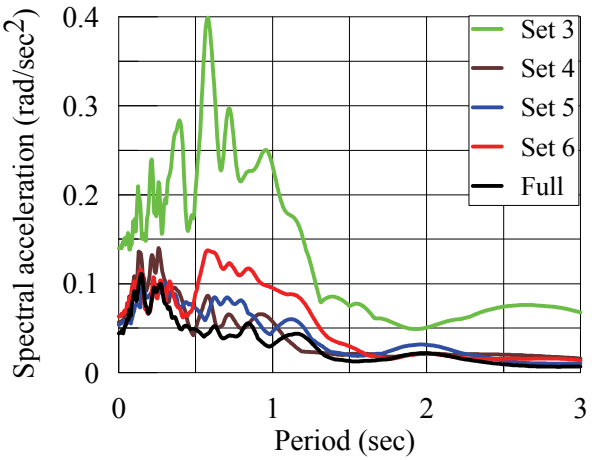

(b) Four tiers in each set and full

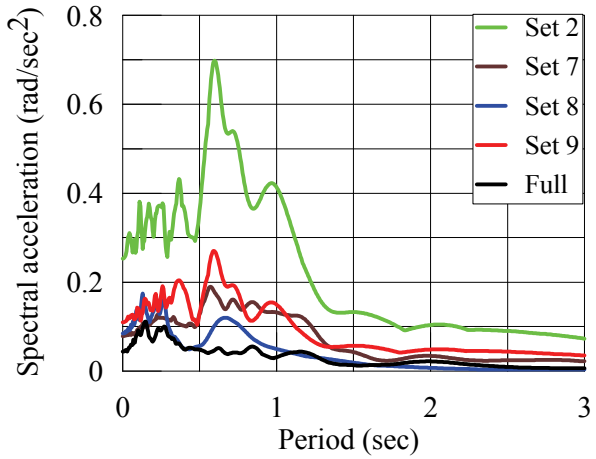

(c) Three tiers in each set and full

Figure 6-6: Torsional spectra computed using different sets of recorded motions, AGM

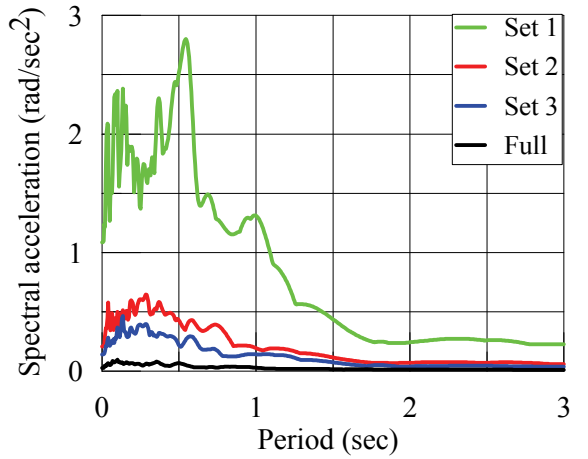

(a) Sets 1, 2, 3 and full

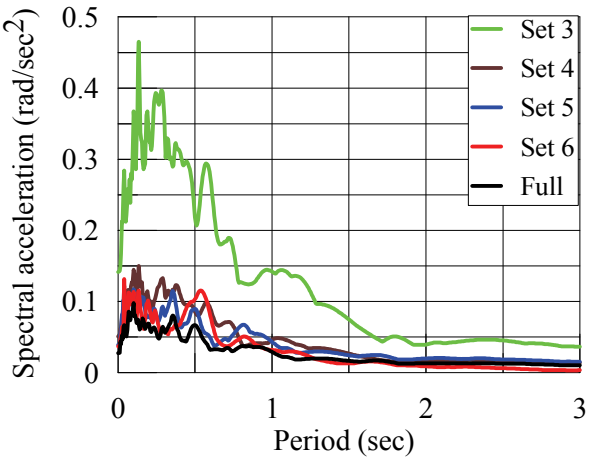

(b) Four tiers in each set and full

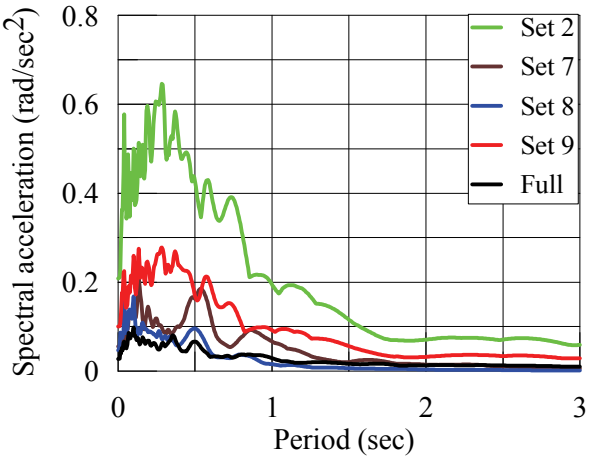

(c) Three tiers in each set and full

Figure 6-7: Rocking (*xz* plane) spectra computed using different sets of recorded motions, AGM

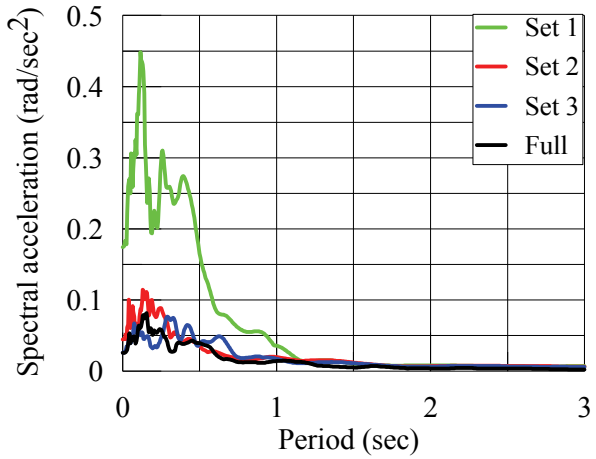

(a) Sets 1, 2, 3 and full

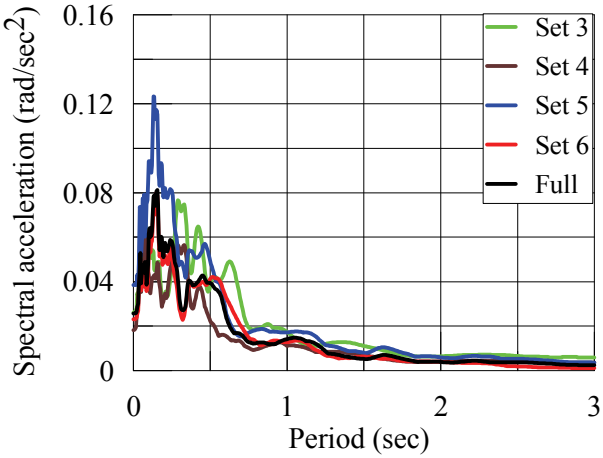

(b) Four tiers in each set and full

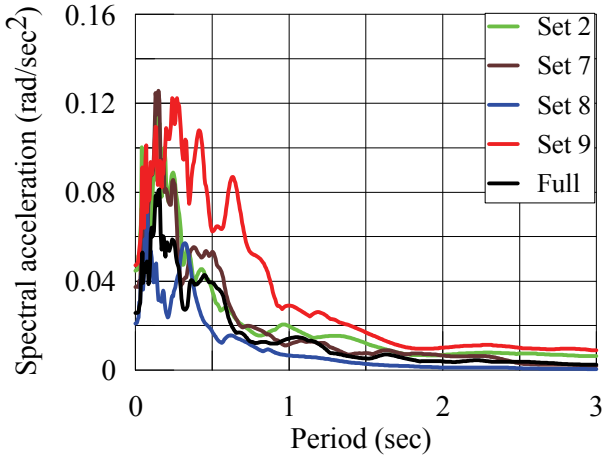

(c) Three tiers in each set and full

Figure 6-8: Rocking (*yz* plane) spectra computed using different sets of recorded motions, AGM

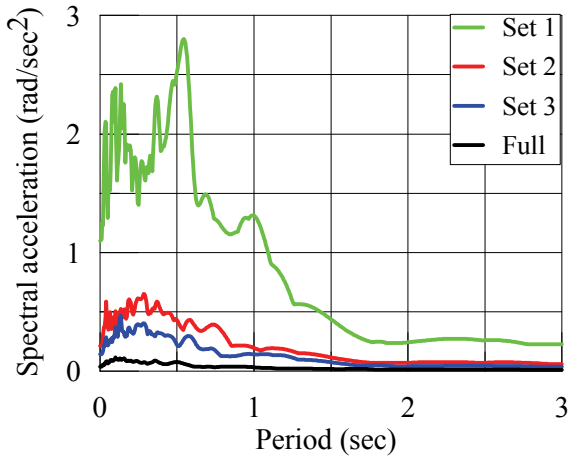

(a) Sets 1, 2, 3 and full

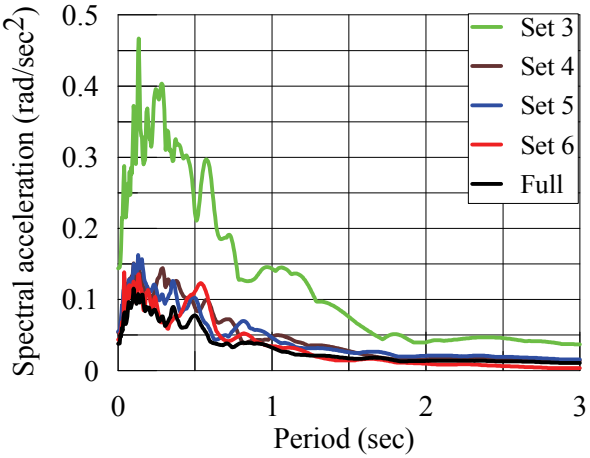

(b) Four tiers in each set and full

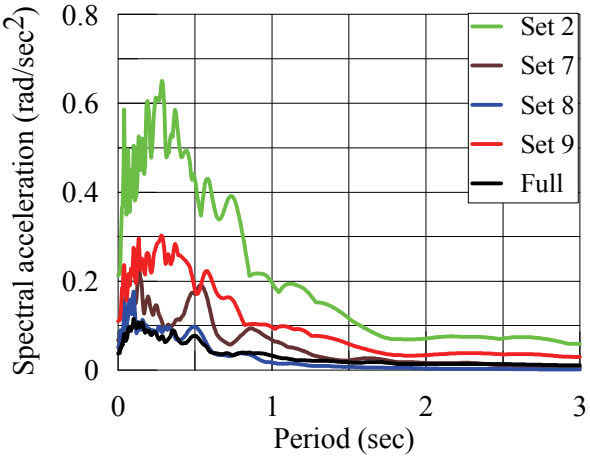

(c) Three tiers in each set and full

Figure 6-9: Rocking (SRSS) spectra computed using different sets of recorded motions, AGM

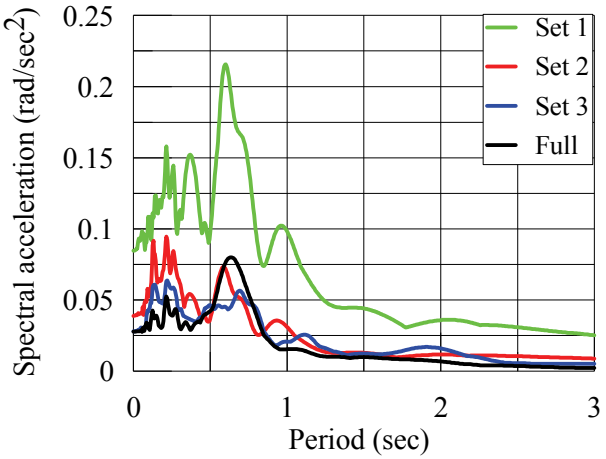

(a) Sets 1, 2, 3 and full

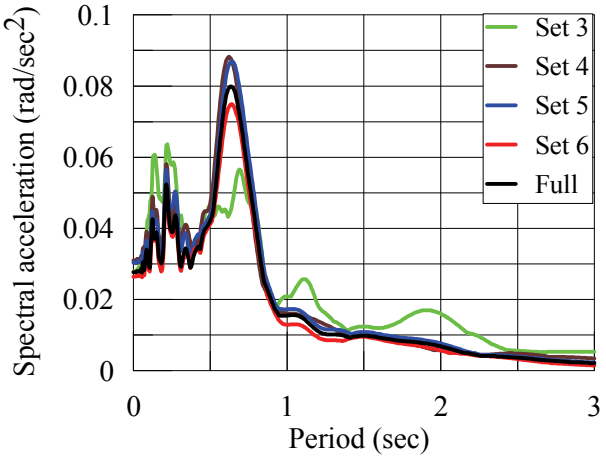

(b) Four tiers in each set and full

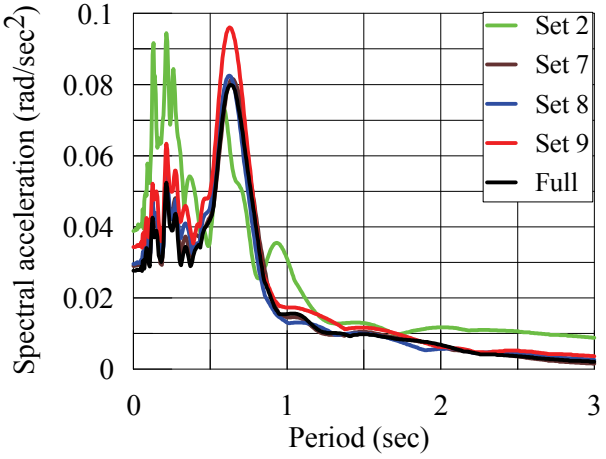

(c) Three tiers in each set and full

Figure 6-10: Torsional spectra computed using different sets of recorded motions, GM

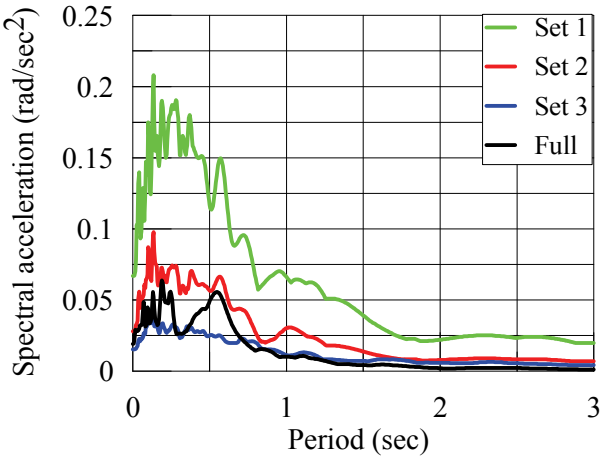

(a) Sets 1, 2, 3 and full

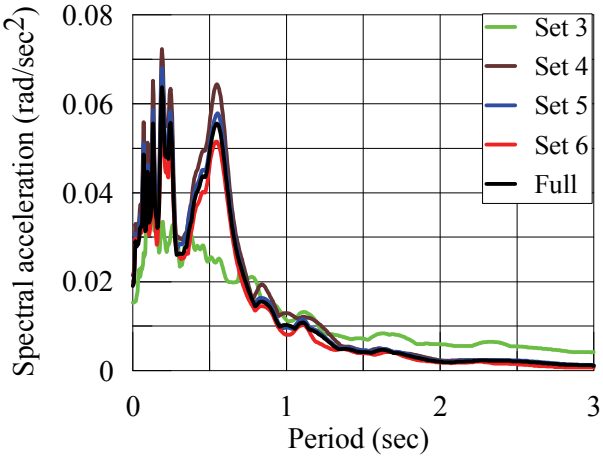

(b) Four tiers in each set and full

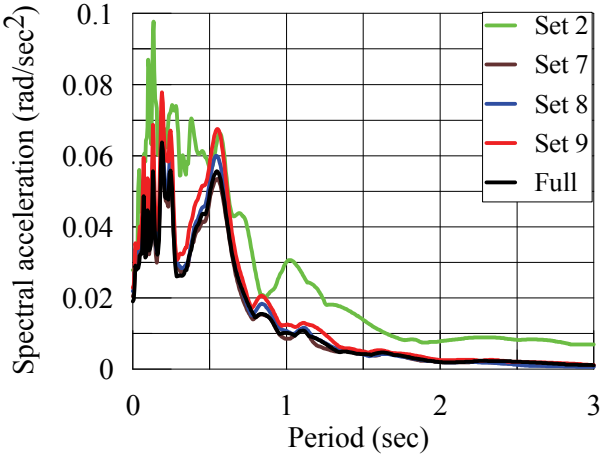

(c) Three tiers in each set and full

Figure 6-11: Rocking (*xz* plane) spectra computed using different sets of recorded motions, GM

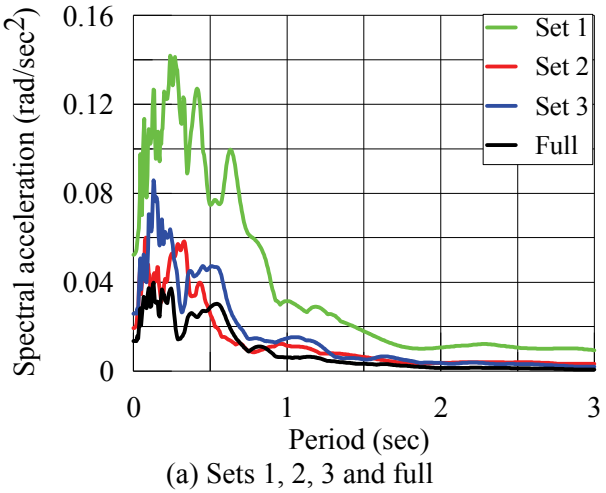

(a) Sets 1, 2, 3 and full

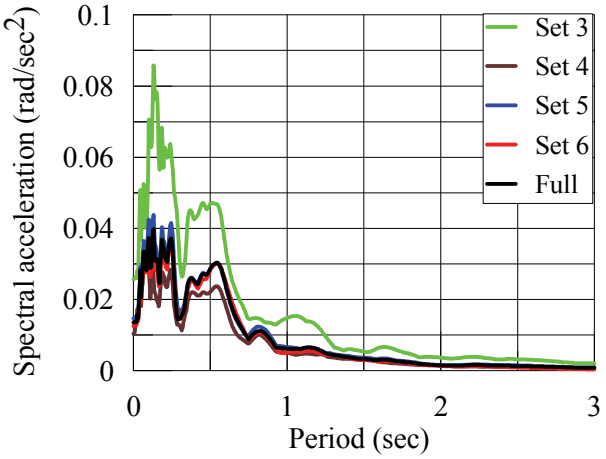

(b) Four tiers in each set and full

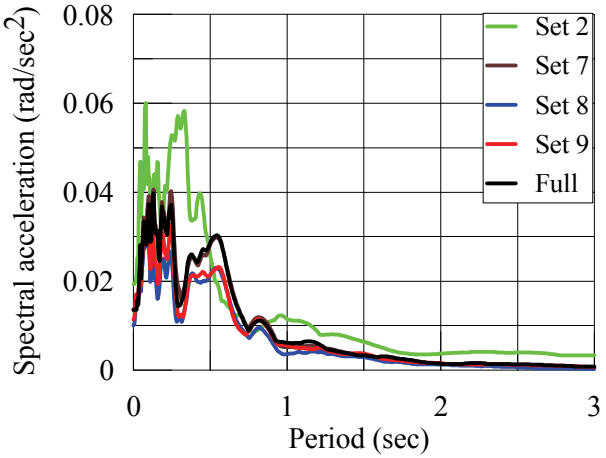

(c) Three tiers in each set and full

Figure 6-12: Rocking (*yz* plane) spectra computed using different sets of recorded motions, GM

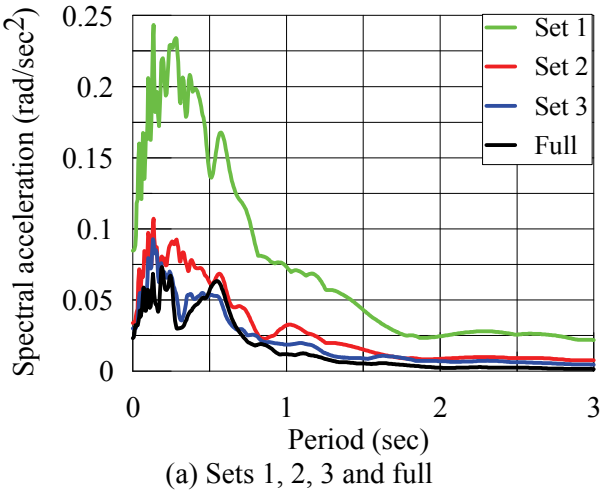

(a) Sets 1, 2, 3 and full

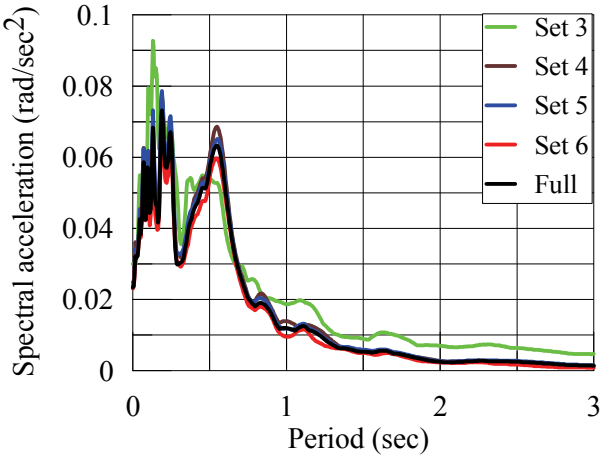

(b) Four tiers in each set and full

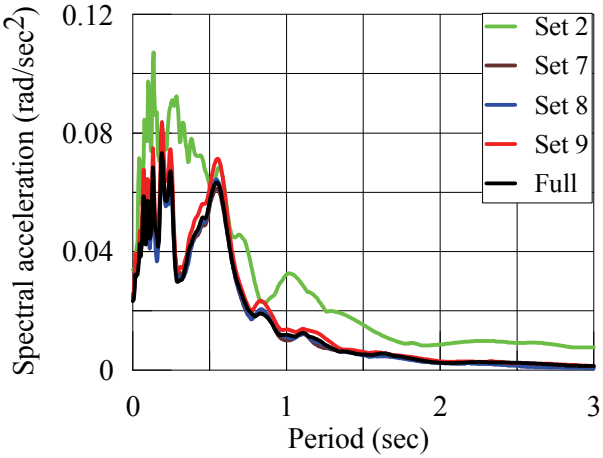

(c) Three tiers in each set and full

Figure 6-13: Rocking (SRSS) spectra computed using different sets of recorded motions, GM

rotational components only) include: a) the apparent seismic wave velocity, and b) the expected (site-specific) frequency content of the future earthquake ground motion.

6.5. Conceptual Design of a Dense Array

Assumptions on the underlying wave propagation theory, geometry of the array and the specification on the data acquisition must be made at the outset. Assume that the governing displacement field is essentially due to the propagation of a non-dispersive plane-wave (P or S) on the horizontal plane along any direction, say *x*. Geometric attenuation within the array is neglected. Stations are assumed to be uniformly spaced (l_s) across the array and located on a straight line (of length L) spanning along the direction of propagation. For data acquisition, the sampling time (t_s) is considered to be the same for all stations and the duration of the earthquake shaking considered for the design of the array is T sec.

The resulting displacement fields along the *x, y* and *z* (vertical) directions are

$$\left\{U(x,t) \quad V(x,t) \quad W(x,t)\right\} = \sum_{r=1}^{N} \left\{D_r^u \quad D_r^v \quad D_r^w\right\} \cos\left(k_r x - \omega_r t + \phi_r\right) \tag{6-1}$$

where r denotes the r^{th} harmonic; N is the total number of harmonics; and D, ϕ, ω and k denote the amplitude, phase, frequency and wave number, respectively, in the respective harmonics of wave propagation. The particle displacement along one or two directions can be zero in Eq (6-1) depending upon the nature of the propagating wave. Considering the particle displacement along one direction only, say W, the particle acceleration in the r^{th} harmonic may be expressed as

$$\ddot{W}_r(x,t) = A_r \cos\left(k_r x - \omega_r t + \phi_r\right) \tag{6-2}$$

where $A_r = -\omega_r^2 D_r^w$ is the amplitude of the particle acceleration.

6.5.1. Case 1: FFT with Respect to Time

Taking the FFT of the recorded acceleration data along the same direction (vertical) at the j^{th} station and denoting $a_j - ib_j$ as the Fourier coefficient associated with the r^{th} discrete positive frequency, it can be shown that

$$a_j = \frac{1}{2} A_r \cos\left(k_r x_j + \phi_r\right);\ b_j = \frac{1}{2} A_r \sin\left(k_r x_j + \phi_r\right) \tag{6-3}$$

where x_j denotes the location of the j^{th} station with respect to the source of excitation, which is the initial point of reference. Assuming the length of the array is much smaller than the source-to-site distance, and the soil at the surface layer is homogeneous within the length of the array, the reference point can be moved from the source to any station within the array by applying an additive phase to all the recording stations. This additive phase may be computed based on the arrival time at the selected reference station. Assuming the distance between the adjacent stations tends to zero, Eq (6-3) may be expressed as

$$a(x) = \frac{1}{2} A_r \cos\left(k_r x + \bar{\phi}_r\right);\ b(x) = \frac{1}{2} A_r \sin\left(k_r x + \bar{\phi}_r\right) \tag{6-4}$$

Note that the phase ϕ_r in Eq (6-3) is changed to $\bar{\phi}_r$ in Eq (6-4) to account for the additive phase as described above. It is useful to rewrite Eq (6-4) as

$$\begin{aligned} &a(x) = C_r \cos k_r x + D_r \sin k_r x;\ b(x) = E_r \cos k_r x + F_r \sin k_r x \\ &C_r = 0.5 A_r \cos\bar{\phi}_r,\ \mathrm{D}_r = -0.5 A_r \sin\bar{\phi}_r,\ E_r = 0.5 A_r \sin\bar{\phi}_r,\ \mathrm{F}_r = 0.5 A_r \cos\bar{\phi}_r \end{aligned} \tag{6-5}$$

In matrix form

$$\begin{Bmatrix} a(x) & b(x) \end{Bmatrix} = \begin{Bmatrix} \cos k_r x & \sin k_r x \end{Bmatrix} \begin{bmatrix} C_r & E_r \\ D_r & F_r \end{bmatrix} \tag{6-6}$$

It is important to note that the relationships $C_r = \mathrm{F}_r$ and $D_r = -\mathrm{E}_r$ as evident from Eq (6-5) are ignored in Eq (6-6) because the primary objective is to form the pattern of the distribution surface and the wave phenomenon in the field is far more complex than is assumed here.

Next, establishing the origin at the reference station and substituting the coordinate of any station in Eq (6-6) associated with any discrete frequency, say the r^{th}, the row vector on the right side is completely known and the left side is also known from the FFT of the recorded acceleration data. Repeating this procedure at all the other stations, including the reference station, and assembling the resulting equations in a matrix form, an overdetermined problem is formed that can be solved using the least-squares method. The overdetermined problem comprises only two sets of unknowns. Therefore, only two recording stations are required to compute the distribution surface. Further, if the assumption made on wave propagation is strictly satisfied, then the least-squares solution calculated using the recorded data at all the stations will be *exactly the same* as that calculated using any two stations. This is due to the existence of a unique (and exact) solution and in such a case, the least-squares method returns the solution with zero error. The Fourier coefficient of the rotational component may be obtained by taking the spatial derivatives once the distribution surface is calculated,. The rotational acceleration history is computed by repeating these steps for all the harmonics of propagation and finally taking the inverse FFT.

6.5.2. Case 2: FFT with Respect to Spatial Coordinates

Consider now the data recorded at a specific time instant t_i at all stations. Here, t_i is the time counted from the triggering at the reference station, not from the triggering of the earthquake at the source. Defining $\bar{a}_{t_i} - i\bar{b}_{t_i}$ as the Fourier coefficient associated with the r^{th} discrete positive wave number, it may be shown that

$$\bar{a}_{t_i} = \frac{1}{2} A_r \cos\left(\omega_r t_i - \bar{\phi}_r\right);\ \bar{b}_{t_i} = \frac{1}{2} A_r \sin\left(\omega_r t_i - \bar{\phi}_r\right) \tag{6-7}$$

At any time t,

$$\bar{a}(t)=\frac{1}{2}A_r\cos\left(\omega_r t-\bar{\phi}_r\right);\ \bar{b}(t)=\frac{1}{2}A_r\sin\left(\omega_r t-\bar{\phi}_r\right) \tag{6-8}$$

Eq (6-8) is now rewritten as

$$\begin{aligned}&\bar{a}(t)=\overline{C}_r\cos\omega_r t+\overline{D}_r\sin\omega_r t;\ \bar{b}(t)=\overline{E}_r\cos\omega_r t+\overline{F}_r\sin\omega_r t\\&\overline{C}_r=0.5A_r\cos\bar{\phi}_r,\ \overline{D}_r=0.5A_r\sin\bar{\phi}_r,\ \overline{E}_r=-0.5A_r\sin\bar{\phi}_r,\ \overline{F}_r=0.5A_r\cos\bar{\phi}_r\end{aligned} \tag{6-9}$$

In matrix form,

$$\left\{\bar{a}(t)\quad\bar{b}(t)\right\}=\left\{\cos\omega_r t\quad\sin\omega_r t\right\}\begin{bmatrix}\overline{C}_r & \overline{E}_r\\ \overline{D}_r & \overline{F}_r\end{bmatrix} \tag{6-10}$$

The relationships $\overline{C}_r=\overline{\mathrm{F}}_r$ and $\overline{D}_r=-\overline{\mathrm{E}}_r$ as evident from Eq (6-9) are ignored in Eq (6-10) because the primary objective is to form the pattern of the distribution surface. The unknowns in Eq (6-10) can be computed using the recorded data at all the stations in two discrete time instants. On the other hand, the solution can also be obtained by solving an overdetermined problem using the recorded data at all time instants. However, if the assumption made on the wave propagation is strictly satisfied, both solution sets will be exactly identical. Once the distribution surface is calculated, that is, the unknowns in Eq (6-10) are evaluated, and selecting any arbitrary time instant, the Fourier coefficient associated with the rotational component may be obtained through multiplying Eq (6-10) by ik_r. The spatial distribution of the rotational acceleration at any time instant is computed by repeating these steps for all harmonics of propagation at the same time instant and thereafter taking the inverse FFT. By varying the selected instant in time, it is possible to generate the rotational acceleration history at any station.

6.5.3. Comparison of Case 1 and Case 2

For Case 1, the solution for the distribution surface is unique and exact, and requires only two recording stations. The computed distribution surface is unique and exact for Case 2 also and requires

recordings at all the stations but at two discrete instants in time. Case 1 and Case 2 will produce identical results, if and only if, there exists a one-to-one mapping in the frequency and wave number. This can be guaranteed if the number of harmonics and the Nyquist frequency are identical in both cases. The Nyquist frequency will be identical if $l_s = ct_s$ and the number of harmonics will be identical if $L = cT$, where c is the velocity of propagation. Further, this will be true only when the assumptions made regarding wave propagation are strictly satisfied. In addition, the existence of the discrete Fourier transformation, finite duration of recording at the array and in turn, the periodicity in any snapshot (instantaneous deformed shape of the free-surface) with a wavelength $L = cT$ are also assumed.

Consider two subsets of Case 2: Case 2a wherein l_s is doubled and Case 2b wherein L is halved.

Case 2a: Spacing is Doubled

In this case, the Nyquist frequency is halved, the number of harmonics is also halved and hence, the frequency interval is unchanged. Therefore, results generated using Case 2a will differ from Case 1 if the frequency content of the motion exceeds the reduced Nyquist frequency.

Case 2b: Length of the Array is Halved

In this case, the Nyquist frequency is unchanged but the results will be affected by aliasing. All harmonics for which the wavelength lies between the reduced and original length of the array will contribute to the aliasing.

Case 1 provides a better way of designing the dense array if the objective is to compute rotational motion because: a) it is more economical as only two stations are required, and b) since the FFT is not taken with respect to the spatial coordinate, the procedure is almost unaffected by the aliasing, provided it is eliminated on the time axis by a suitable means, for example, by cosine tapering (Bendat and Piersol, 1986). Accordingly, only Case 1 is used to design the dense array as described below.

6.5.4. Wave Propagation Assumption Not Satisfied

If the assumption made regarding wave propagation is not strictly satisfied, the unique solution of Eq (6-6) will not exist. In such a case, the overdetermined problem is solved using the least-squares method. The resulting distribution surface will be a best-fit surface. Since the wave characteristics in the field are far more complex than assumed in the analysis, the rotational spectra computed using dense-array records will be somewhat sensitive to the selection and number of stations. A computed best-fit surface should not be extrapolated beyond the furthest recording station used in the analysis because its use would lead to erroneous results.

6.5.5. Design Criteria

The design criteria for a dense array includes the specifications of the array length and the number of stations. Considering the periodicity of the distribution surface associated with any harmonic, it is expected that the sensitivity of the results will be minimized if a large number of stations are distributed over a span of a few wavelengths of that harmonic. This observation implies that the length of the array should span a few wavelengths of the *contributive lowest harmonic* (CLH). At this point of the derivation, the CLH is defined as the harmonic with the lowest frequency that contains non-negligible energy. More than half the wavelength is required to reduce the sensitivity because the sensitivity arises when the distribution surface is computed without capturing the peak in the distribution of the Fourier coefficients within the length of the array. Physically, this implies a lack of information to determine a reasonable distribution surface if the array length is shorter than half the wavelength. By considering half the wavelength, one peak within the length of the array is ensured. At a minimum, at least five stations are required to simulate half the wavelength of the associated harmonic. Therefore, at least five stations should be located within the wavelength of the *contributive highest harmonic* (CHH), where the CHH is defined as the harmonic with the highest frequency that contains non-negligible energy.

These requirements on the length of the array may produce an uneconomical design because the CLH usually contributes much less energy than the *modal harmonic* (MH) to the computed rotational motion. The MH is defined as the harmonic that contains the highest energy. By more heavily weighting the MH, the recommended length of the dense array should be the greater of: a) half of the wavelength associated with the MH, and b) a quarter of the wavelength associated with the CLH.

The limit on the CLH will generally govern the length of the array because most seismic events are not extremely narrow banded.

6.6. Design of a General Two-Dimensional Dense Array

The design of a two-dimensional array adds complexities in terms of the spatial patterns of the stations. Since the computation of rotational spectra essentially involves the calculation of the best-fit surface that is expected to be sensitive to the arrangement of the stations, an optimum configuration involves uniformly spaced stations. The regular hexagon is a possible geometric shape wherein each station is equidistant from the others. Therefore, a vertical line representing the NS direction is constructed first and a point on it is selected as the reference station (see Figure 6-14). Then, two lines are plotted, one at $+30^o$ and other at -30^o with respect to the EW direction, passing through the reference station (solid lines in Figure 6-14). Next, a set of points is plotted at a spacing of s on these two lines. Finally, a line is drawn at either $+30^o$ or -30^o through each of these points (thin lines in Figure 6-14). If each of these intersecting grid-points is selected as the stations, the distance between any two adjacent stations will be the same. In this case, the arrangement will form a set of concentric regular hexagons. Note that the hexagon was also considered by Kerekes (2001) as the basic shape to illustrate the design of a dense array using spatial convolution.

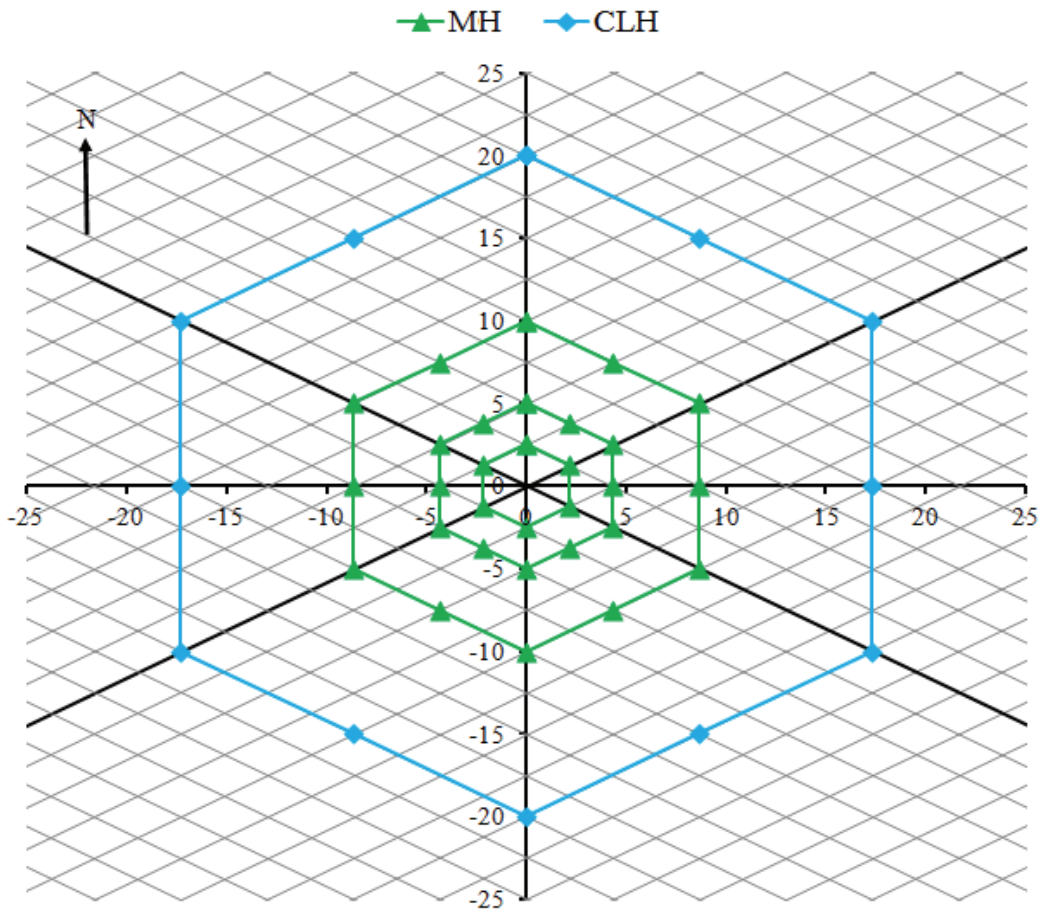

Figure 6-14: Arrangement of stations in the design of a dense array

However, a dense array will likely be uneconomical if a station is located at every grid-point. As an intermediate solution, and in line with the conceptual design of the one-dimensional array presented above,

1) Aside from the reference station, stations should be considered in three hexagons (Δ in Figure 6-14) to cover the half wavelength of the MH, and
2) If the required dimension of the array (half of the wavelength of the MH and a quarter of the wavelength of the CLH, whichever is higher) is governed by CLH, the radial spacing of additional hexagons of stations can be doubled in each successive layer (◊ in Figure 6-14) until the required array length is obtained.

The spacing s of the first hexagon from the reference station is the same as that of the second hexagon from the first. Further, $2s$ is the spacing of the third hexagon from the second. Therefore, the half wavelength of the MH is $8s$ and effectively, there are seven points in the recording directions (EW and NS) within a half wavelength of the MH, which is acceptable as the minimum number is five. Further, note that five points are available along the EW and NS directions in the half wavelength of a harmonic whose frequency is twice that of the MH. This implies that the frequency of the CHH can be as much as twice that of the MH. However, the spacing of the subsequent hexagons up to the required length of the array is somewhat speculative. Moreover, the number of stations in the hexagon beyond the third is also speculative but with a minimum of six, one at each vertex.

6.7. Design of a Specific Two-Dimensional Dense Array

The site-specific characteristics required for this design are computed by analysis of the January 16, 1986 earthquake recorded at the LSST array, including: a) the apparent seismic wave velocity, b) the frequencies associated with the CHH and CLH of the recorded motion, and c) the frequency of the MH. Further, these characteristics differ significantly when estimating torsional and rocking motions from translational data recorded in a dense array. The design of the dense array should therefore be performed separately for the torsional and rocking motions and the final design should satisfy both.

For the specific seismic event considered here, the computation of the apparent wave velocities to be used in the SDM is presented in Chapter 5: 249 m/sec and 951 m/sec for the torsional and rocking motions, respectively. These velocities are the mean values calculated in Chapter 5. The frequencies associated with the CLH, MH and CHH are calculated using the data recorded at the innermost station on Arm 1 (NS direction).

The frequencies associated with the CLH and the MH can be estimated using the Fourier amplitude spectrum, which is a measure of the energy contained in any harmonic. Panel a of Figure 6-15 presents the amplitude spectra for the horizontal motions. Panel b presents the data of panel a in a range from

which the peak amplitude and the frequency associated with the MH can be estimated. Judgment is required to estimate the percentage of the peak amplitude required to compute the frequency of the CLH. Ten percent is assumed here. Similar data are presented in panels c and d for the vertical acceleration. The jaggedness of the Fourier amplitude spectra complicates the calculation of the frequency of the CLH. An alternative is to use response spectra that are smoother than Fourier amplitude spectra. The frequency of the MH is the reciprocal of the time period associated with the peak spectral ordinate. To compute the frequency of the CLH, the (lowest) frequency associated with a spectral ordinate of 10% of the peak value is computed. The calculation is illustrated in Figures 6-16 and 6-17, for the horizontal and vertical motions, respectively. The frequency of the CHH is twice that of the MH as explained in the conceptual design. These frequency characteristics are used to design the dense array per the box below.

The final design must accommodate both rocking and torsional motion. The station layout for this example is presented in Figure 6-18. Figure 6-19 presents the layout of stations considering only those stations located at the vertices of each hexagon. This is defined here as a Level 1 simplification. The station layout presented in Figure 6-19 can be considered as intersecting Y's in the NS direction. The station layout of Figure 6-20 is a simplification of that shown in Figure 6-19: one Y-shaped array is eliminated. This is defined as a Level 2 simplification.

The station layout presented in Figure 6-20 is similar in shape to the Lotung array. The numbers of stations on each arm (six stations) is also similar to that of the Lotung array (five stations). However, in the Lotung array: a) the length of the array is small, and b) the stations are more closely spaced. This closer spacing enables the Lotung array to capture a seismic event that is rich in higher frequencies. The array length smaller than that required explains the sensitivity of the computed rotational components on the selection of stations observed in Figures 6-2 through 6-5.

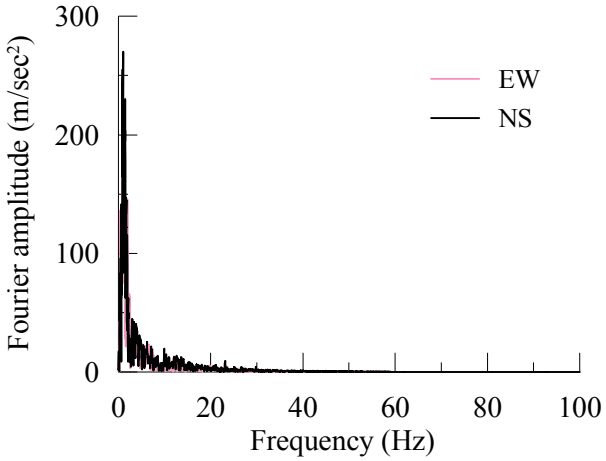

(a) Frequency range 0-100Hz (EW and NS)

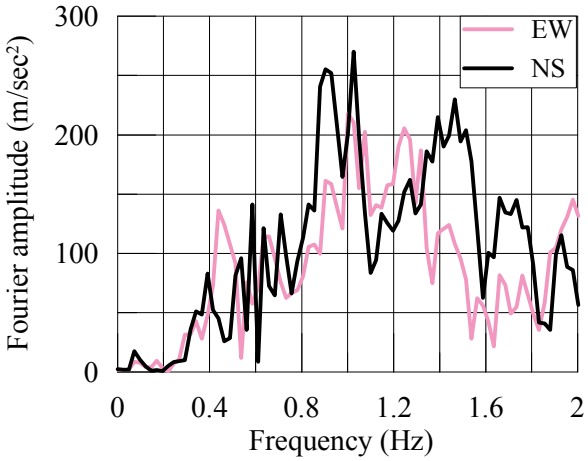

(b) Frequency range 0-2Hz (EW and NS)

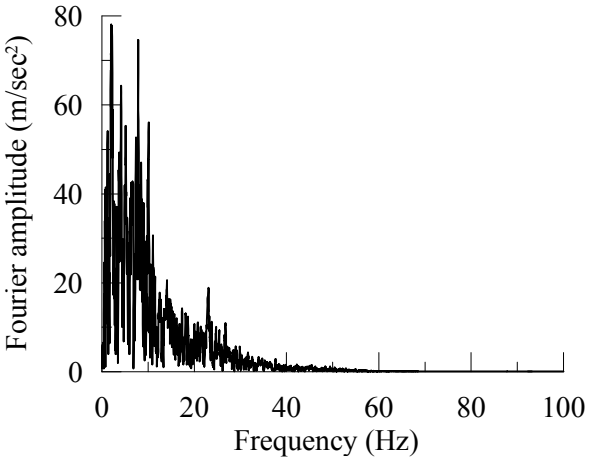

(c) Frequency range 0-100Hz (Vertical)

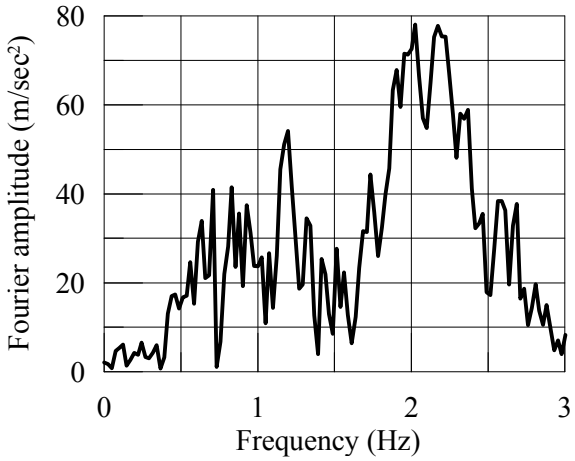

(d) Frequency range 0-2Hz (Vertical)

Figure 6-15: Fourier amplitude spectra for January 16, 1986 event recorded at station FA1_1 of LSST array, Lotung (Taiwan)

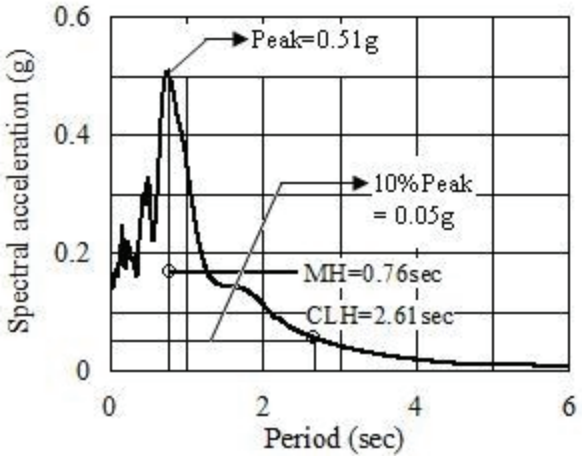

(a) EW direction

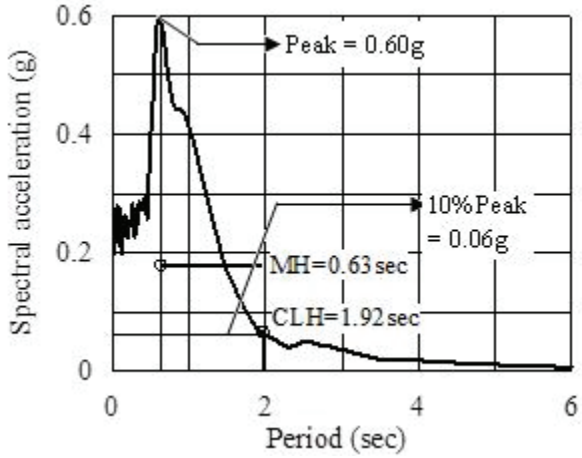

(b) NS direction

Figure 6-16: Identifying MH and CLH for the horizontal motion using response spectra

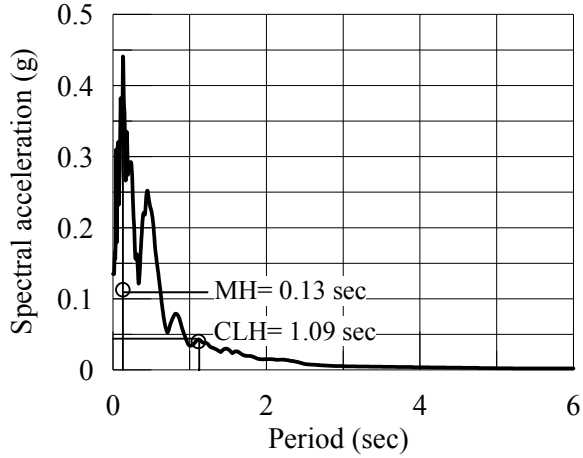

Figure 6-17: Identifying MH and CLH for the vertical motion using response spectra

Example 1: Two-dimensional dense array

Design Criteria	Horizontal Motion	Vertical Motion
Frequency of CLH (Hz)	$f_{CLH} = \min\left(\frac{1}{2.61}, \frac{1}{1.92}\right) = 0.38$	$f_{CLH} = \frac{1}{1.09} = 0.92$
Frequency of MH (Hz)	$f_{MH} = \max\left(\frac{1}{0.76}, \frac{1}{0.63}\right) = 1.59$	$f_{MH} = \frac{1}{0.135} = 7.4$
Frequency of CHH (Hz): $f_{CHH} = 2f_{MH}$	$f_{CHH} = 2 \times 1.59 = 3.18$	$f_{CHH} = 2 \times 7.4 = 14.8$
Array dimension from the MCH Criterion $D_{MH} \geq \frac{1}{2}\lambda_{MH} = \frac{1}{2}\frac{c}{f_{MH}}$	$D_{MH} \geq \frac{1}{2}\left(\frac{249}{1.59}\right) \geq 78.3$ m	$D_{MH} \geq \frac{1}{2}\left(\frac{951}{7.4}\right) \geq 64.3$ m
Array dimension from the CLH Criterion $D_{CLH} \geq \frac{1}{4}\lambda_{CLH} = \frac{1}{4}\frac{c}{f_{CLH}}$	$D_{CLH} \geq \frac{1}{4}\left(\frac{249}{0.38}\right) \geq 163.8$ m	$D_{CLH} \geq \frac{1}{4}\left(\frac{951}{0.92}\right) \geq 258.4$ m
Spacing, $s = \frac{D_{MH}}{8}$	$s = \frac{78}{8} = 9.75$ m	$s = \frac{64}{8} = 8$ m
Design Configuration*	$s = 10$ m Radial distance: $\{10, 20, 40, 60, 80\}$ m $D_{MH} = 80$ m $D_{CLH} = 160$ m	$s = 8$ m Radial distance: $\{8, 16, 32, 64, 96, 128\}$ m $D_{MH} = 64$ m $D_{CLH} = 256$ m

*Governed by rocking motion for this example

6.8. Array Design using Bounded Site Characteristics

The site-specific parameters used to design an array depend on the site topology and vary with the expected seismic events. Lower and upper bounds on design parameters are denoted using the superscripts *L* and *U*, respectively. The following recommendations are made to design an array:

1. Compute $D_{MH}^{L} = 0.5c^{L} / f_{MH}^{U}$ and the spacing $s = D_{MH}^{L} / 8$. Aside from the reference station, provide three hexagonal tiers at a radial spacing of s, s and $2s$.
2. Compute $D_{MH}^{U} = 0.5c^{U} / f_{MH}^{L}$. Provide hexagonal tiers at the radial spacing of $4s$ within the radial distance $D_{MH}^{L} / 2$ and $D_{MH}^{U} / 2$

3. Compute $D^U_{CLH} = 0.25c^U / f^L_{CLH}$. Provide hexagonal tiers at a radial spacing of $4s$ (or the spacing can be doubled in each successive layer) within the radial distance $D^U_{MH}/2$ to $D^U_{CLH}/2$.

The procedure is illustrated in the box below, where the upper and lower bounds chosen for the site specific characteristics are somewhat arbitrary.

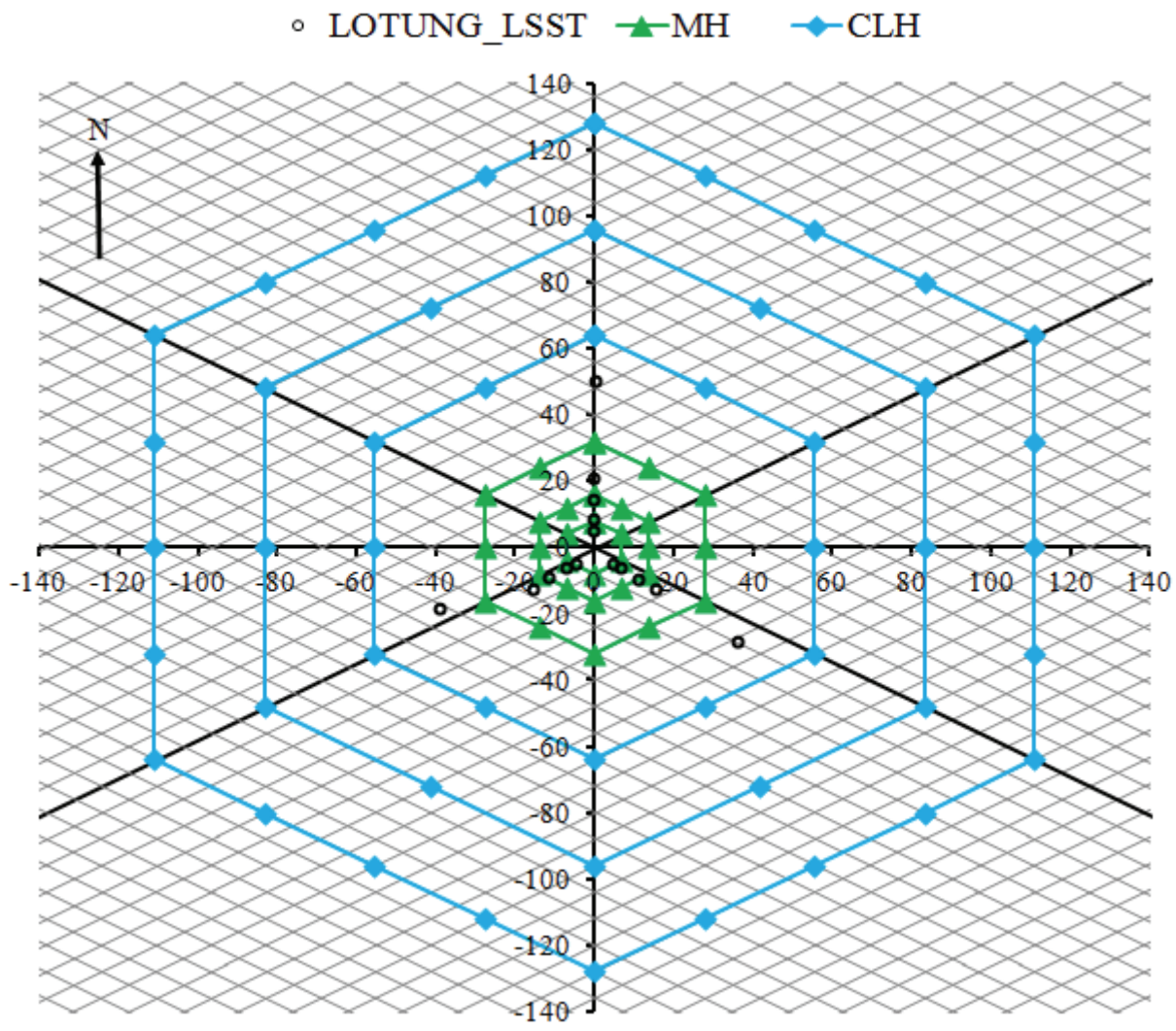

Figure 6-18: Location of the surface-stations when designed using the MH and the CLH of the January 16, 1986 event recorded at LSST, Lotung (Taiwan); all dimensions are in meters

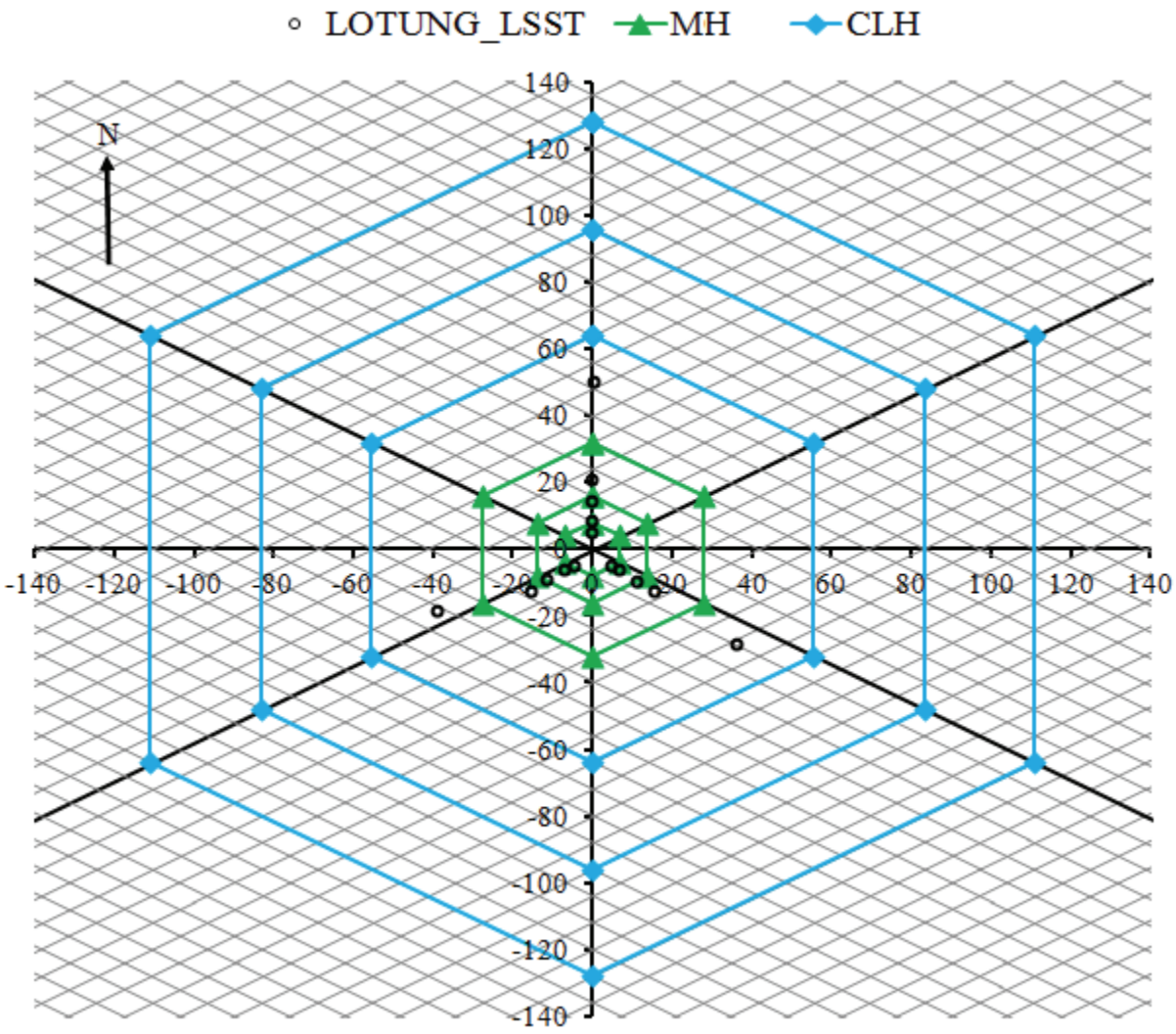

Figure 6-19: Level 1 simplification of the station layout presented in Figure 6-18; all dimensions are in meters

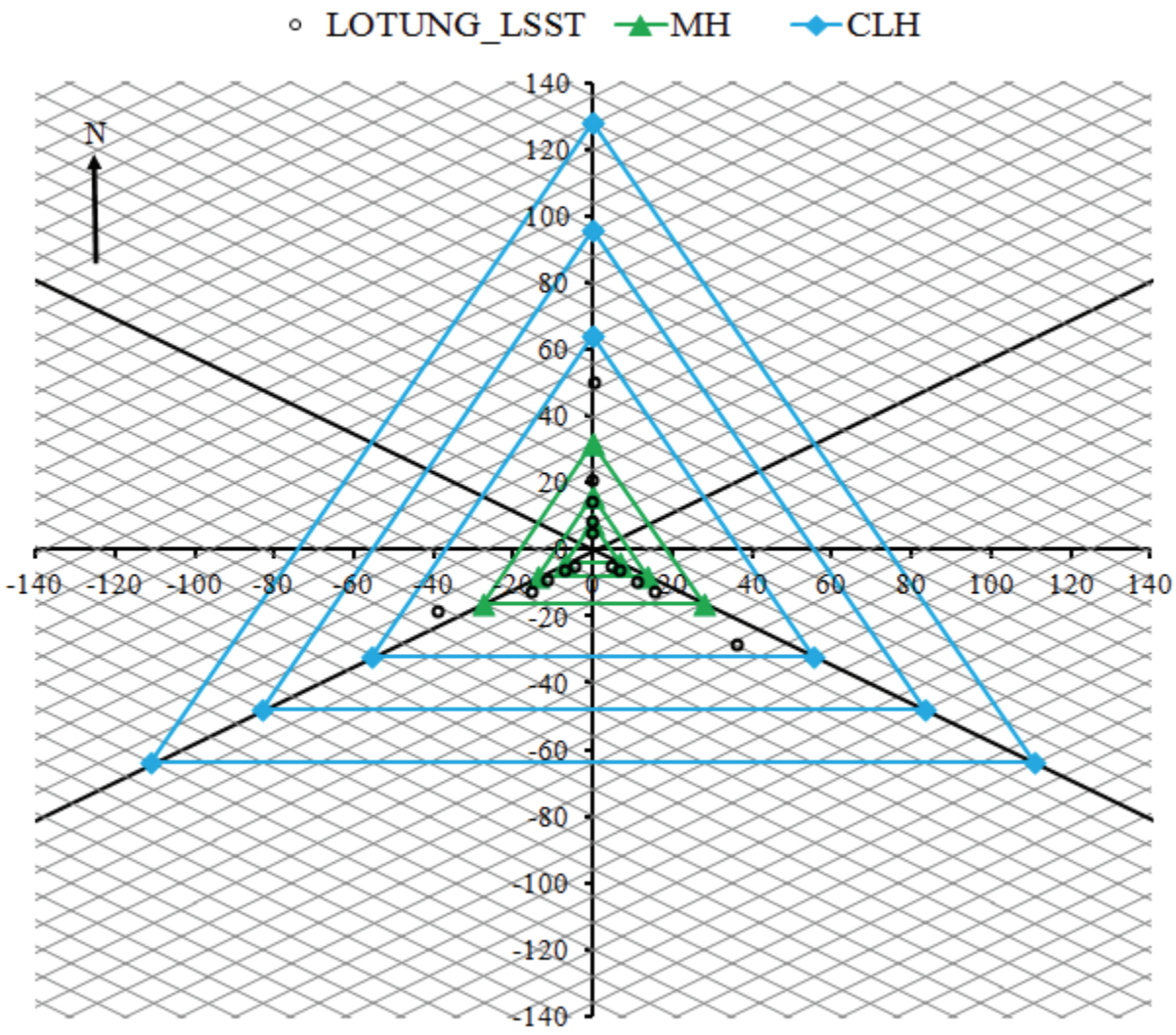

Figure 6-20: Level 2 simplification of the station layout presented in Figure 6-18; all dimensions are in meters

Example 2: Bounded site characteristics

Design Criteria	Horizontal Motion	Vertical Motion
Apparent wave velocity range (m/sec)	200 - 500	750 - 1500
Lower bound frequency of CLH (Hz)	0.25	1.0
Frequency range for MH (Hz)	1.0 - 2.5	5 - 10
Lower bound array dimension from the MH criterion $D_{MH}^{L} = 0.5c^{L} / f_{MH}^{U}$	$D_{MH}^{L} = \frac{1}{2}\left(\frac{200}{2.5}\right)$ =40 m	$D_{MH}^{L} = \frac{1}{2}\left(\frac{750}{10}\right)$ =37.5 m
Upper bound array dimension from the MH criterion $D_{MH}^{U} = 0.5c^{U} / f_{MH}^{L}$	$D_{MH}^{U} = \frac{1}{2}\left(\frac{500}{1.0}\right)$ =250 m	$D_{MH}^{U} = \frac{1}{2}\left(\frac{1500}{5.0}\right)$ =150 m
Upper bound array dimension from the CLH criterion $D_{CLH}^{U} = 0.25c^{U} / f_{CLH}^{L}$	$D_{CLH}^{U} = \frac{1}{4}\left(\frac{500}{0.25}\right)$ =500 m	$D_{CLH}^{U} = \frac{1}{4}\left(\frac{1500}{1.0}\right)$ =375 m
Spacing, $s = \frac{D_{MH}^{L}}{8}$	$s = \frac{40}{8} = 5$ m	$s = \frac{37.5}{8} = 4.7$ m
Design configuration:	$s = 5$ m Radial distance: $\left\{\begin{matrix}5,10,20,40,60,80,100,\\120,160,200,240\end{matrix}\right\}$ m	$s = 5$ m Radial distance: $\left\{\begin{matrix}5,10,20,40,60,\\80,120,160,200\end{matrix}\right\}$ m
Final configuration*	Radial distance: $\{5,10,20,40,60,80,100,120,160,200,240\}$ m	

*Governed by the design for torsional motion

6.9. Length of the Array using Circular and Rectangular Approximations

The circular and rectangular approximations yield an identical array length for the station layout presented in Figure 6-18. Its Level 1 simplification is presented in Figure 6-19. After the Level 2 simplification (see Figure 6-20), the array length computed using the rectangular approximation is three quarters of that calculated using the circular approximation. Even though the circular approximation is more appealing because of its similarity to an expanding wavefront, an adequate number of stations (at least six) must be provided on the perimeter of the circle. For example, if the array is designed for a target length of 256 m, providing only three arms of 128 m length will reduce the effective length of the array to approximately 192 m. Accordingly, the rotational spectra computed using the data recorded in the array will remain sensitive to the arrangement of the stations.

CHAPTER 7
QUANTIFICATION OF ACCIDENTAL ECCENTRICITY DUE TO TORSIONAL GROUND MOTION

7.1. Introduction

The calculation of the seismic response of buildings and safety-related nuclear structures requires consideration of torsion; that is, rotation about a vertical axis. Standards of design practice such as ASCE 7-10 (2010) and ASCE 4-98 (2000) recognize the importance of torsional contributions to horizontal displacement response and simplified procedures have been proposed to estimate these contributions. Two types of torsion are considered: *natural (or inherent)* and *accidental*. Natural torsion is the product of non-coincident centers of mass (CM) and rigidity (CR) at one or more floor levels in a structure. Accidental torsion is used to indirectly account for: a) plan distributions of reactive mass that differ from those assumed in design, b) variations in the mechanical properties of structural components in the seismic force-resisting system, c) non-uniform yielding of components in the seismic force-resisting system, and d) torsional ground motion.

Seismic analysis and design of buildings and safety-related nuclear structures require explicit consideration of natural and accidental torsion. Rules are presented in ASCE Standard 4, *Seismic Analysis of Safety-Related Nuclear Structures and Commentary* (ASCE 2000) and ASCE Standard 7, *Minimum Design Loads for Buildings and Other Structures* (ASCE 2010) for use with Equivalent Lateral Force (ELF) or static analysis, and dynamic analysis. These rules are repeated below for reference.

ASCE Standard 4

Section 3.1.1 (d) and (e) of the 2000 edition of ASCE Standard 4, Seismic Analysis of Safety-Related Nuclear Structures and Commentary, writes the following rules for addressing torsion in analysis:

> "(d) The [mathematical] model shall represent the actual locations of the centers of mass and centers of rigidity, thus accounting for the torsional effects caused by eccentricity, and (e) When

calculating forces in various structural elements, the torsional moments due to accidental eccentricity with respect to the center of rigidity and the effects of non-vertically incident or incoherent waves shall be accounted for. An acceptable means of accounting for these torsional moments is to include an additional torsional moment in the design or evaluation of structural members. This additional moment shall be taken equal to the story shear at the elevation and in the direction of interest times a moment arm equal to 5% of the building plan dimension perpendicular to the direction of motion in the analysis. Consideration of such eccentricity shall be used only to increase the magnitude of the forces."

Subsection (d) addresses natural torsion and (e) accidental torsion. The two subsections apply to static and dynamic analysis but detailed guidance on how to apply the rules is not presented.

ASCE Standard 7

Section 12.8.4 of ASCE 7 presents rules for addressing torsion if the ELF procedure is used to analyze a building. Section 16.1 writes rules for use with dynamic analysis. In the discussion below, it is assumed that floor diaphragms are rigid in their plane.

Section 12.8.4

In the ELF of ASCE 7-10, a period-dependent base shear is computed using Eq 12.8-1. The base shear is distributed over the height of the building per Eq. 12.8-11 and 12.8-12.

For natural (inherent) torsion, Section 12.8.4.1 writes "..the distribution of lateral forces at each level shall consider the effect of the inherent torsional moment, M_t, resulting from eccentricity between the locations of the center of mass and center of rigidity.

For accidental torsion, Section 12.8.4.2 writes "..the design shall include the inherent torsional moment (M_t) resulting from the location of the structure masses plus the accidental torsional moments (M_{ta}) caused by assumed displacement of the center of mass each way from its actual location by a distance equal to 5 percent of the dimension of the structure perpendicular to the

direction of the applied forces. Where earthquake forces are applied concurrently in two orthogonal directions, the required 5 percent displacement of the center of mass need not be applied in both of the orthogonal directions at the same time, but shall be applied in the direction that produces the greatest effect."

If the structure being analyzed is deemed to be torsionally irregular (Type 1a or 1b per Table 12.3-1) and is assigned to Seismic Design Category C, D, E or F, the accidental torsional moment M_{ta} is increased by a torsional amplification factor. The natural torsional moment is not increased. Section 12.8.4.3 writes for these structures "…shall have the effects accounting for by multiplying M_{ta} at each level by a torsional amplification factor (A_x) as illustrated in Figure 12.8-1 [reproduced in Figure 7-1] and determined from the following equation [12.8-14]:

$$A_x = \left(\delta_{\max} / 1.2\delta_{avg}\right)^2 \tag{7-1}$$

where $\delta_{\max}$ is the maximum displacement at Level *x* computed assuming $A_x = 1$ (in. or mm), and δ_{avg} is the average of the displacements at the extreme points of the structure at Level *x* assuming $A_x = 1$ (in. or mm). The torsional amplification factor (A_x) shall not be less than 1 and is not required to exceed 3.0. The most severe loading for each element shall be considered for design."

Section 16.1

Section 16.1.5, Horizontal Shear Distribution, writes "The distribution of horizontal shear shall be in accordance with Section 12.8.4 except that amplification of torsion in accordance with Section 12.8.4.3 is not required where the accidental torsion effects are included in the dynamic analysis model."

Consider the simple three degree-of-freedom system shown in Figure 7-2. The plan dimensions of the single story structure are $a \times b$. The floor plate is supported by six columns that have lateral stiffness K_1, K_2 and K_3 as shown in the figure. The CR is located a distance e from the CM. The calculation of CR is simple for this structure. The offset of the CR from the CM produces the natural or inherent torsional

moment, M_t. The total torsional moment for this structure, including dynamic amplification, can be calculated as the product of the translational inertial force and a design eccentricity, e_d, as follows:

$$e_d = \alpha(e \pm \beta b) \tag{7-2}$$

where α is a dynamic amplification factor, β is a decimal fraction (set equal to 0.05 in ASCE 4 and ASCE 7), and b is the building plan dimension perpendicular to the applied translational force. The product βb is the accidental eccentricity. In ASCE 7, the dynamic amplification factor is applied to the accidental torsion only, and $\alpha = A_x$. The approach adopted in ASCE 7 is straightforward and does not require explicit calculation of the CR at each floor level, with the natural torsion being directly taken into account in the analysis of a mathematical model by applying the code-specified lateral load profile through the CM at each floor level. (The calculation of the CR at each floor level is not straightforward for a multistory building and is dependent on the lateral force profile used for the ELF procedure as discussed in Hejal and Chopra (1987) and Basu and Jain (2007). Although procedures have been developed to account for the dynamic amplification of natural torsion when using an ELF procedure (e.g., Tso, 1990; Goel and Chopra, 1993; Basu and Jain, 2007), they have not been adopted in ASCE 7. De La Llera and Chopra (1994a-e; 1995; 1997) studied different sources of accidental torsion in a probabilistic framework, compared the code specified static and dynamic analysis in context with accounting for the effect of accidental torsion, assessed the adequacy of the code specified 5% accidental eccentricity and recommended simplified procedure to account for the accidental torsion. None of these recommendations has been adopted to date in ASCE 7.

The ASCE 4 and 7 rules for imposing accidental torsion in multistory structures are incomplete. It is unclear whether a shift in the CM of each floor plate is to be ordered or random; namely, is the same shift used at each floor level? If the dominant contributor to accidental torsion is torsional ground motion, an ordered shift in the CM of each floor plate is reasonable. If this is not the case, random shifts are reasonable, with the net effect of accidental torsion likely being small in the lower stories of a medium-to-high-rise structure.

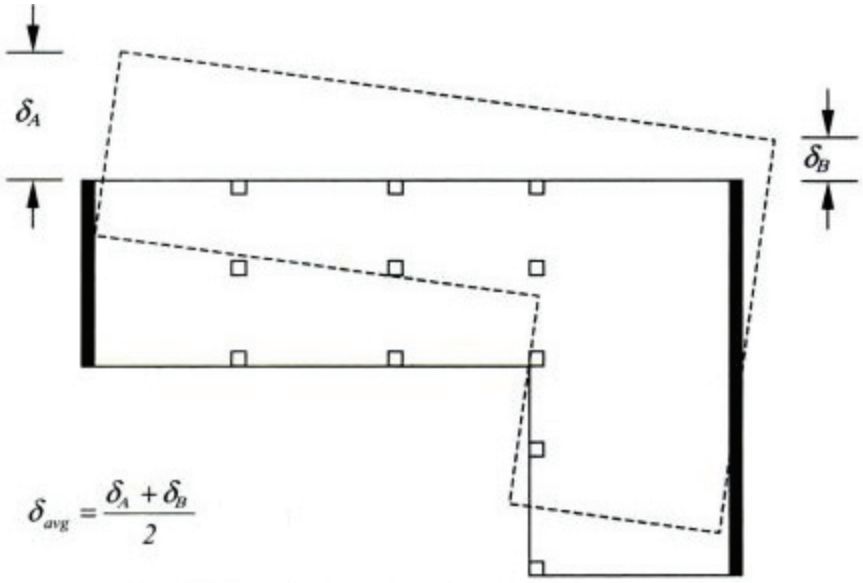

Figure 7-1: Calculation of torsional amplification factor

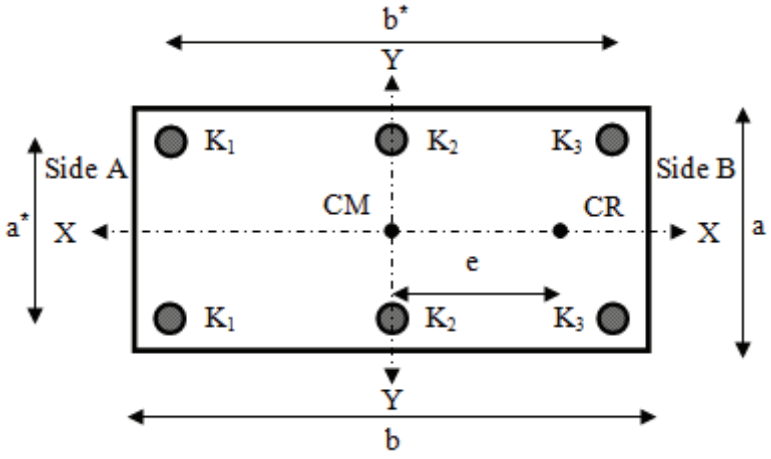

Figure 7-2: Analytical model

Shifting the CM at each floor level to consider the effects of accidental torsion alters the modal properties of a structure and its modal damping ratios if Rayleigh damping is used to describe the inherent damping in the structure. The impact of shifting the CM on the modal properties and structural response has not been discussed in the literature and is studied in the remainder of this chapter. For simplicity, torsional ground motion is assumed to be the dominant contributor to the accidental torsion.

A series of single story elastic systems is subjected to translational and torsional components of seismic excitation to study the conventional treatment of accidental torsion. Section 7.2 presents the description of the model considered in the analysis. Details on the analysis procedure and input ground motions are presented in Section 7.3. The study shows the limitations of the conventional approach when used with response-history analysis. Next, an alternative definition of accidental eccentricity is proposed and verified by a series of analyses of single story elastic systems and nonlinear seismic isolation systems. Sections 7.4 and 7.5 present the analysis of the elastic and nonlinear isolation systems, respectively. Validation of the analysis results and implementation of the proposed method in SAP2000 (CSI, 2009) are presented in Section 7.6.

7.2. Mathematical Model for Dynamic Analysis

The one-story singly symmetric system of Figure 7-2 composed of a rigid deck of mass m supported on six massless lateral-load-resisting elements is used for analysis. The CM of the deck is located at its geometric center and its radius of gyration about a vertical axis passing through the CM is r. Each lateral-load-resisting element has identical translational stiffness in the two orthogonal directions but no torsional stiffness. The system is symmetric about the x axis but has an eccentricity e about the y axis. This system could represent a seismic isolation system supporting a rigid superstructure or a single story singly symmetric building. The system is subjected to both translational seismic excitation along the y axis and torsional ground excitation.

The parameters used to characterize the model are: 1) K_y = total lateral stiffness along the *y* direction (same as that in the *x* direction), 2) $\omega_y = \left(K_y / m\right)^{0.5}$ = uncoupled lateral frequency, 3) $K_{\theta R}$ = torsional stiffness about the CR, 4) $\omega_\theta = \left(K_{\theta R} / mr^2\right)^{0.5}$ = uncoupled torsional frequency, and 5) $\Omega = \left(K_{\theta R} / r^2 K_y\right)^{0.5}$ = ratio of uncoupled torsional frequency to translational frequency.

For a given aspect ratio and location of the elements with respect to the CM, the lateral stiffness of each of the elements may be expressed as

$$
\begin{aligned}
K_1 &= K_y \left[-\frac{1}{2s_x}\left(\frac{e}{b}\right) - \frac{1}{4}\left(\frac{s_y s_a}{s_x}\right)^2 + \Omega^2 R_a^2 + \frac{1}{s_x^2}\left(\frac{e}{b}\right)^2 \right] \\
K_2 &= K_y \left[\frac{1}{2}\left\{ 1 + \left(\frac{s_y s_a}{s_x}\right)^2 \right\} - 2\Omega^2 R_a^2 - \frac{2}{s_x^2}\left(\frac{e}{b}\right)^2 \right] \\
K_3 &= K_y \left[\frac{1}{2s_x}\left(\frac{e}{b}\right) - \frac{1}{4}\left(\frac{s_y s_a}{s_x}\right)^2 + \Omega^2 R_a^2 + \frac{1}{s_x^2}\left(\frac{e}{b}\right)^2 \right]
\end{aligned}
\tag{7-3}
$$

In Eq (7-3), $s_x = b^*/b$, $s_y = a^*/a$, $s_a = a/b$, $R_a = \left[1 + s_a^2\right]^{0.5} \Big/ \left(2\sqrt{3}s_x\right)$. Assuming a unit mass, K_y in Eq (7-3) may be replaced by ω_y^2. Given the dimensions of the deck and location of the elements, this elastic system is uniquely described by three normalized parameters: ω_y, Ω and e/b.

7.3. Conventional Calculation of Accidental Eccentricity

It is common practice to shift the CM at each floor level by a distance equal to the accidental eccentricity to amplify the maximum translational response when performing response-history analysis. This approach is studied herein and its effect on the displacement demand is examined. For convenience, denote the two sides with respect to the CR of the model as Side A and Side B as shown in Figure 7-2. Since the elements located on Side A are expected to sustain more displacement demand than those on Side B, the present study focuses on Side A elements only. The CM is first shifted away from the CR

(increasing the eccentricity) and denoted here as Shift 1. The CM is then shifted to each side in turn and denoted as Shift 2.

7.3.1. Ground Motion Considered

This study of accidental torsion includes consideration of torsional ground motion. Such histories of torsional motions are not recorded and need to be extracted by analysis of earthquake records obtained in dense arrays. The M6.1 earthquake of January 16, 1986, recorded by the Large Scale Seismic Testing (LSST) array in Lotung, Taiwan, is considered for this purpose. The Surface Distribution Method (SDM) presented in Chapter 5 is used to compute the torsional ground motion with the following modifications: i) instead of the SH wave component, the recorded EW (y) and NS (x) components are considered as the horizontal acceleration field, ii) shear wave velocity at the surface layer (140 m/sec) is used instead of the apparent SH wave velocity computed in Chapter 5 (249 m/sec), and iii) the Set3 motions (see Chapter 6) are used in the SDM. These three modifications are to used estimate an upper bound on the torsional ground motion spectra. Since the SDM yields one torsional ground motion for each surface station considered, the torsional acceleration history with the highest peak torsional acceleration is considered here as the torsional ground motion input. The translational acceleration history is considered as that recorded at the interior station FA1_1, which is different from the station where the peak torsional acceleration is noted. The translational acceleration histories along the x and y directions, the torsional acceleration and their respective 5-percent damped response spectra are shown in Figure 7-3. As the system is symmetric about the x axis, the translational acceleration in the NS direction is not input to the model.

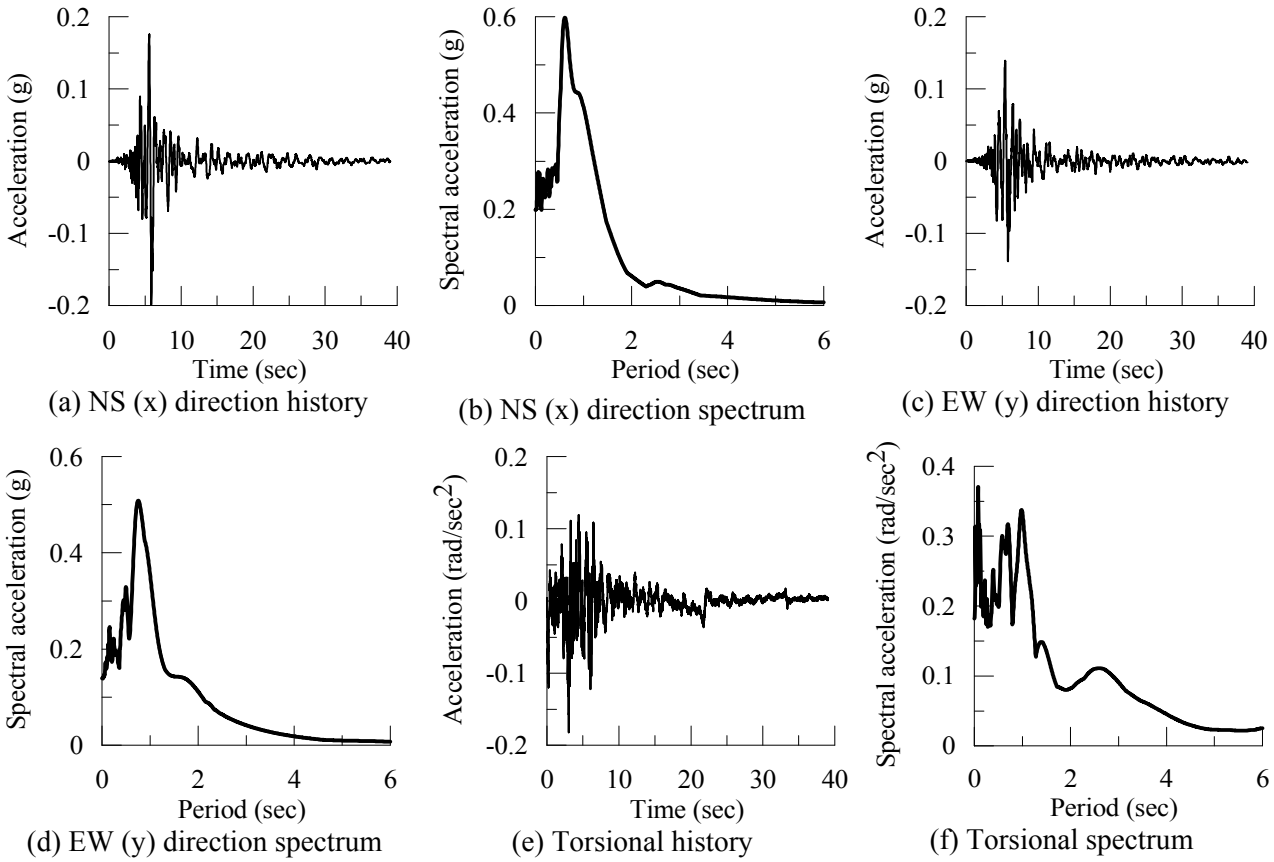

(a) NS (x) direction history (b) NS (x) direction spectrum (c) EW (y) direction history

(d) EW (y) direction spectrum (e) Torsional history (f) Torsional spectrum

Figure 7-3: Input ground acceleration data

7.3.2. Procedure

The steps followed in the analysis and the presentation of results are :

1. Select values for the normalized parameters ω_y, Ω and e/b (e is the actual eccentricity) that uniquely define the elastic system.
2. Apply translational and torsional acceleration histories simultaneously and find the absolute maximum displacement at the farthest element on Side A, U^{fl}.
3. Repeat Step 2 but apply only the translational acceleration history; let the absolute maximum displacement for the same element be $\bar{U}^{fl}$; compute the torsional amplification factor as $R_1 = U^{fl}/\bar{U}^{fl}$.

4. Repeat Steps 2 and 3 but reverse the direction of the torsional acceleration history and compute the torsional amplification factor R_2; select the *target torsional amplification factor* as $R = \max(R_1, R_2)$.

5. a) Shift 1: Shift the CM away from the CR by an offset e_a (an accidental eccentricity) and analyze the system by applying only the translational acceleration history; let the absolute maximum displacement at the furthest element on Side A be $\bar{\bar{U}}^{fl}$.

   b) Shift 2: Repeat '5a' but shift the CM in both directions (that is, away and towards the CR) and compare the two values of $\bar{\bar{U}}^{fl}$; record the greater value.

6. Define the torsional amplification factor associated with offset e_a as $R^* = \bar{\bar{U}}^{fl} / \bar{U}^{fl}$. Repeat Step 5 for a range of values of e_a and generate the associated torsional amplification factor. The required accidental eccentricity for the system considered is given by the offset e_a for which $R^* \geq R$.

7.3.3. Results and Discussions

The procedure outlined above is applied to a variety of elastic systems selected by varying the three normalized parameters ω_y, Ω and e/b. In each case, the aspect ratio of the deck and the location of the elements with respect to the CM of the deck are described by $s_x = 1$, $s_y = 1$, and $s_a = 0.5$. Damping in this three degree-of-freedom (DOF) system is described by Rayleigh damping with 5% critical damping in the first and third modes. Analysis of each system is carried out using a state-space procedure, and target and computed torsional amplification factors are compared to calculate the required e_a. Results for two cases are presented below.

<u>System 1:</u>

For this set of systems the uncoupled translational period ($T_n = 2\pi/\omega_y$) is 1.0 sec and the ratio of the uncoupled torsional to translational frequency (Ω) is 1.25. Figure 7-4 enables a comparison of the target

torsional amplification and that achieved by Shift 1. The torsional amplification does not increase monotonically with the accidental eccentricity (see also Figure 7-5). Note that Figure 7-4 presents the torsional amplification versus the actual eccentricity for various values of the accidental eccentricity. Figure 7-5 presents the same amplification factor versus the accidental eccentricity for various values of the actual eccentricity. Further, the target torsional amplification is not achieved even though the accidental eccentricity is increased to 49%: see panel j of Figure 7-4 for $e/b = 0.10$, wherein the amplification for Shift 1 is approximately 0.8, and only 75% of the target value of 1.08. Note that a shift in the CM of greater than $0.5b$ is meaningless for nearly all framing systems. This example identifies cases where the conventional procedure does not provide the target torsional amplification, albeit conditioned on: i) one pair of translational and torsional ground motions, and ii) the overestimation involved in the computation of the torsional ground motion.

Shift 2 better represents the provisions in Sections 12.8.4.2 of ASCE 7-10 (2010). Results are presented in Figures 7-6 through 7-7. Once again, the system with $e/b = 0.10$ does not deliver the target torsional amplification regardless of the accidental eccentricity used. An interesting situation arises for the system with $e/b = 0.15$: the system meets the target torsional amplification at an accidental eccentricity e_a/b of 0.03 but not at 0.12.

System 2:

System 2 is a family of long period structures, with $T_n = 3$ sec and $\Omega = 1.25$. The results presented in Figures 7-8 through 7-11 show the same trends as seen for System 1.

An increase in accidental eccentricity, say from 3% to 5% of the building dimension, should lead to an increase in torsional response. However, the examples considered above do not exhibit this trend. See Figures 7-5 and 7-7 for System 1 and Figures 7-9 and 7-11 for System 2. These figures do not include the target torsional demand and are independent of the torsional ground motion used for the analysis. These figures are generated by only shifting the CM. The observed trend is therefore not limited to accidental torsion due to the torsional component of ground motion; rather it is applicable to that contributed from

the other sources. The relationship between the torsional amplification and accidental eccentricity shown in these figures is attributed to the change in the dynamic characteristics of the system when the CM is shifted. Shifting the CM in response-history analysis does not appear to deliver the expected increase in displacement response.

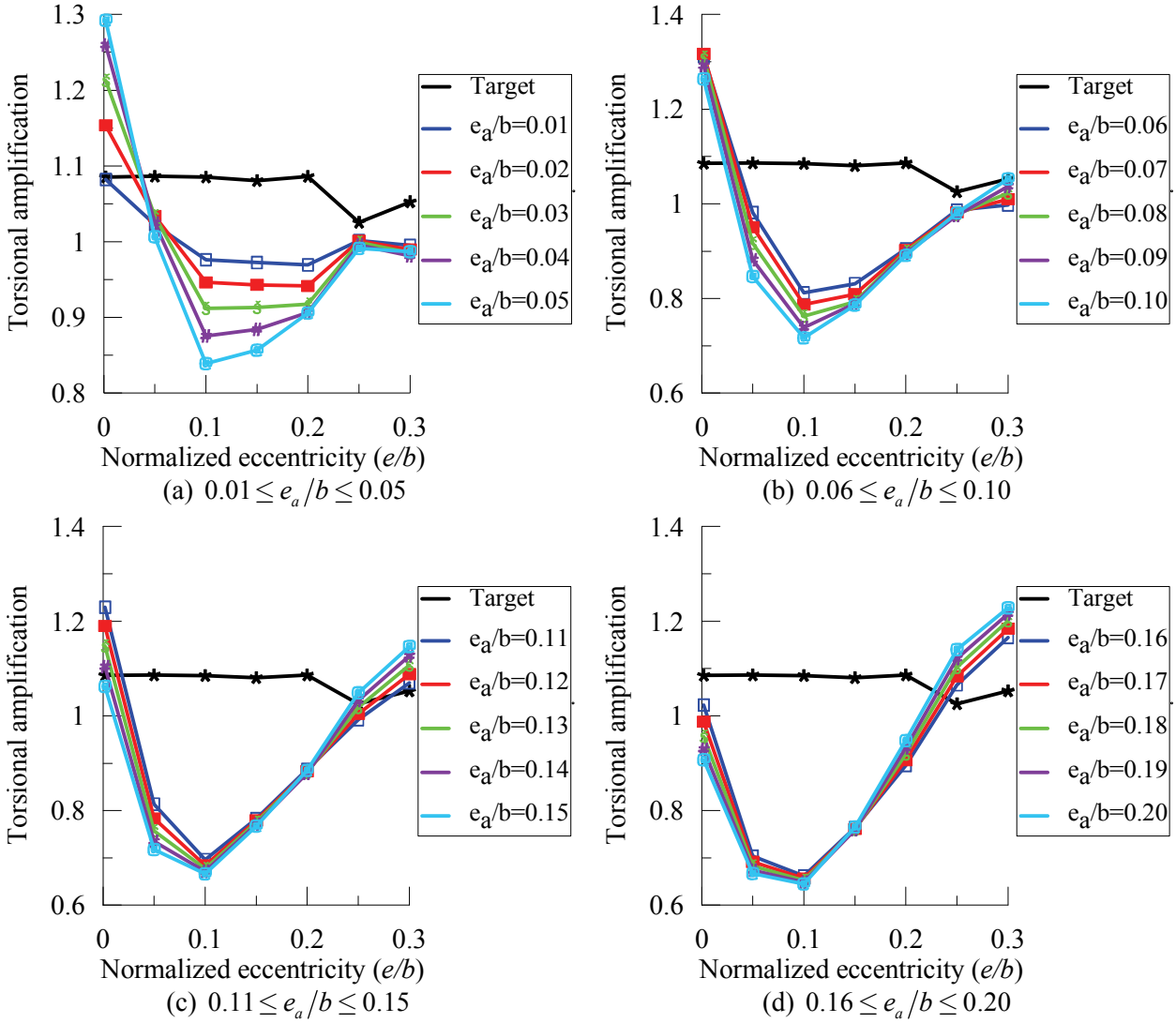

Figure 7-4: Torsional amplification for System 1, Shift 1, conventional approach (cont.)

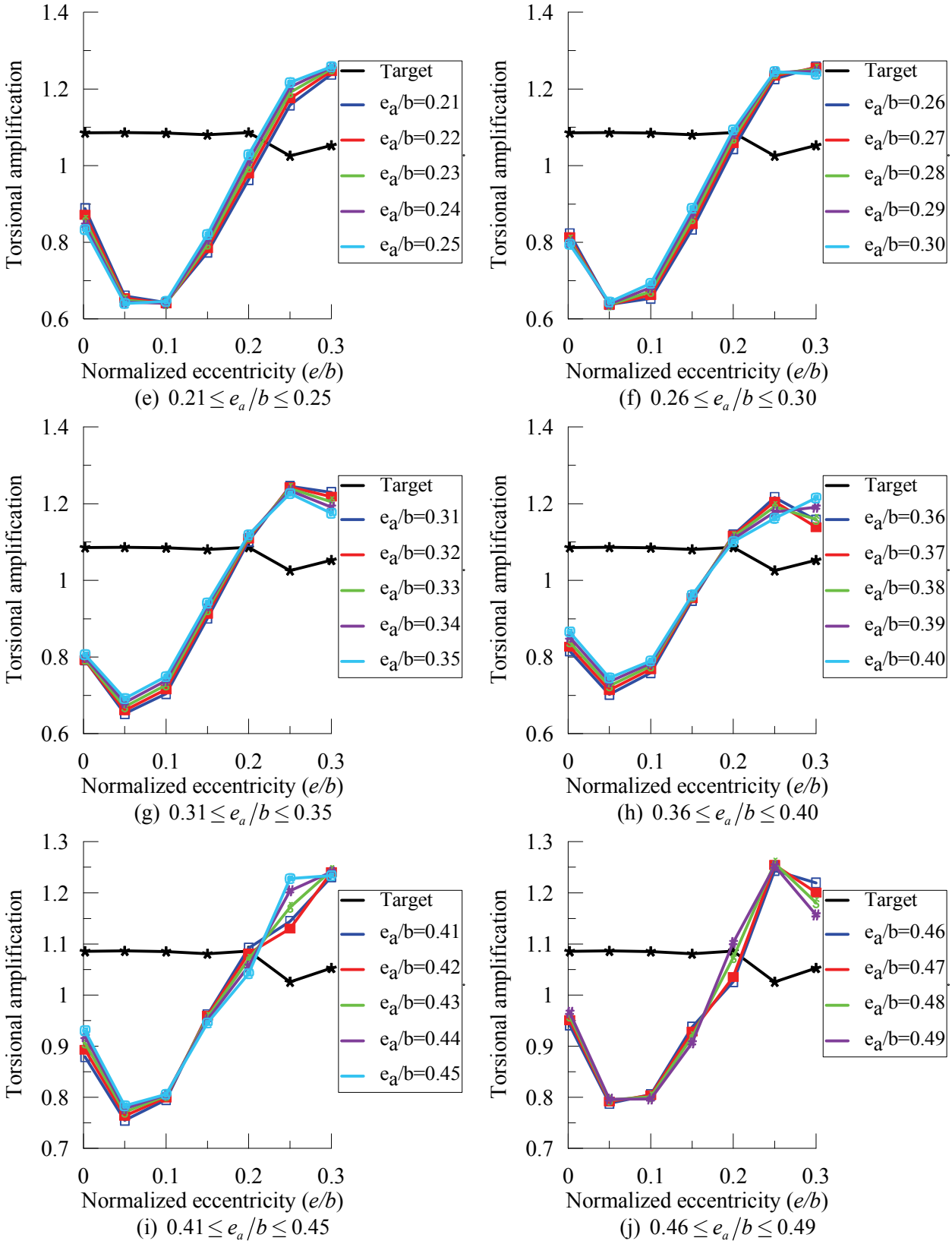

Figure 7-4: Torsional amplification for System 1, Shift 1, conventional approach

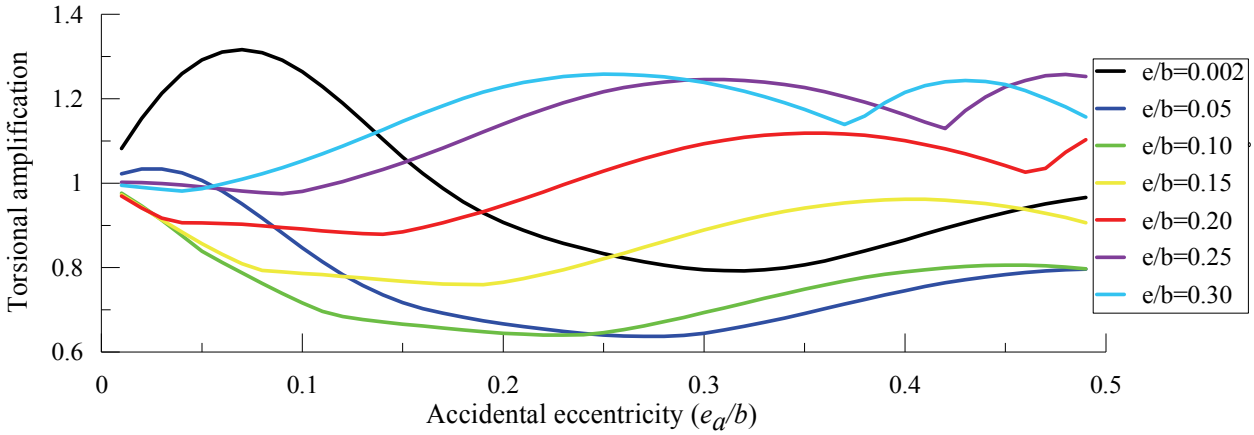

Figure 7-5: Variation of torsional amplification for System 1, Shift 1, conventional approach

7.4. Alternate Definition of Accidental Eccentricity

Recognizing that the current representation of accidental eccentricity does not achieve the desired goal with response-history analysis, an alternate definition is developed below. The equation of motion of the system (Figure 7-2) subjected to seismic acceleration along the *y*-direction (eliminating the uncoupled *x*-direction) with degrees of freedom u_y and u_θ defined at the CM of the deck can be expressed as follows:

$$\begin{bmatrix} m & \\ & mr^2 \end{bmatrix} \begin{Bmatrix} \ddot{u}_y + a_{gy} \\ \ddot{u}_\theta \end{Bmatrix} + \begin{bmatrix} C_y & C_{y\theta} \\ C_{y\theta} & C_\theta \end{bmatrix} \begin{Bmatrix} \dot{u}_y \\ \dot{u}_\theta \end{Bmatrix} + \begin{bmatrix} K_y & K_{y\theta} \\ K_{y\theta} & K_\theta \end{bmatrix} \begin{Bmatrix} u_y \\ u_\theta \end{Bmatrix} = \begin{Bmatrix} 0 \\ 0 \end{Bmatrix} \tag{7-4}$$

When the CM is shifted away from the CR by a distance e_a, Eq (7-4) is modified to

$$\begin{bmatrix} m & -me_a \\ -me_a & m\left(r^2 + e_a^2\right) \end{bmatrix} \begin{Bmatrix} \ddot{u}_y + a_{gy} \\ \ddot{u}_\theta \end{Bmatrix} + \begin{bmatrix} C_y & C_{y\theta} \\ C_{y\theta} & C_\theta \end{bmatrix} \begin{Bmatrix} \dot{u}_y \\ \dot{u}_\theta \end{Bmatrix} + \begin{bmatrix} K_y & K_{y\theta} \\ K_{y\theta} & K_\theta \end{bmatrix} \begin{Bmatrix} u_y \\ u_\theta \end{Bmatrix} = \begin{Bmatrix} 0 \\ 0 \end{Bmatrix} \tag{7-5}$$

The only change is in the mass matrix; the damping and stiffness matrices are unchanged as the reference point, where the degrees of freedom are assigned, does not change. The dynamic characteristics of the system will be altered by shifting the CM. Eq (7-5) can be rewritten as

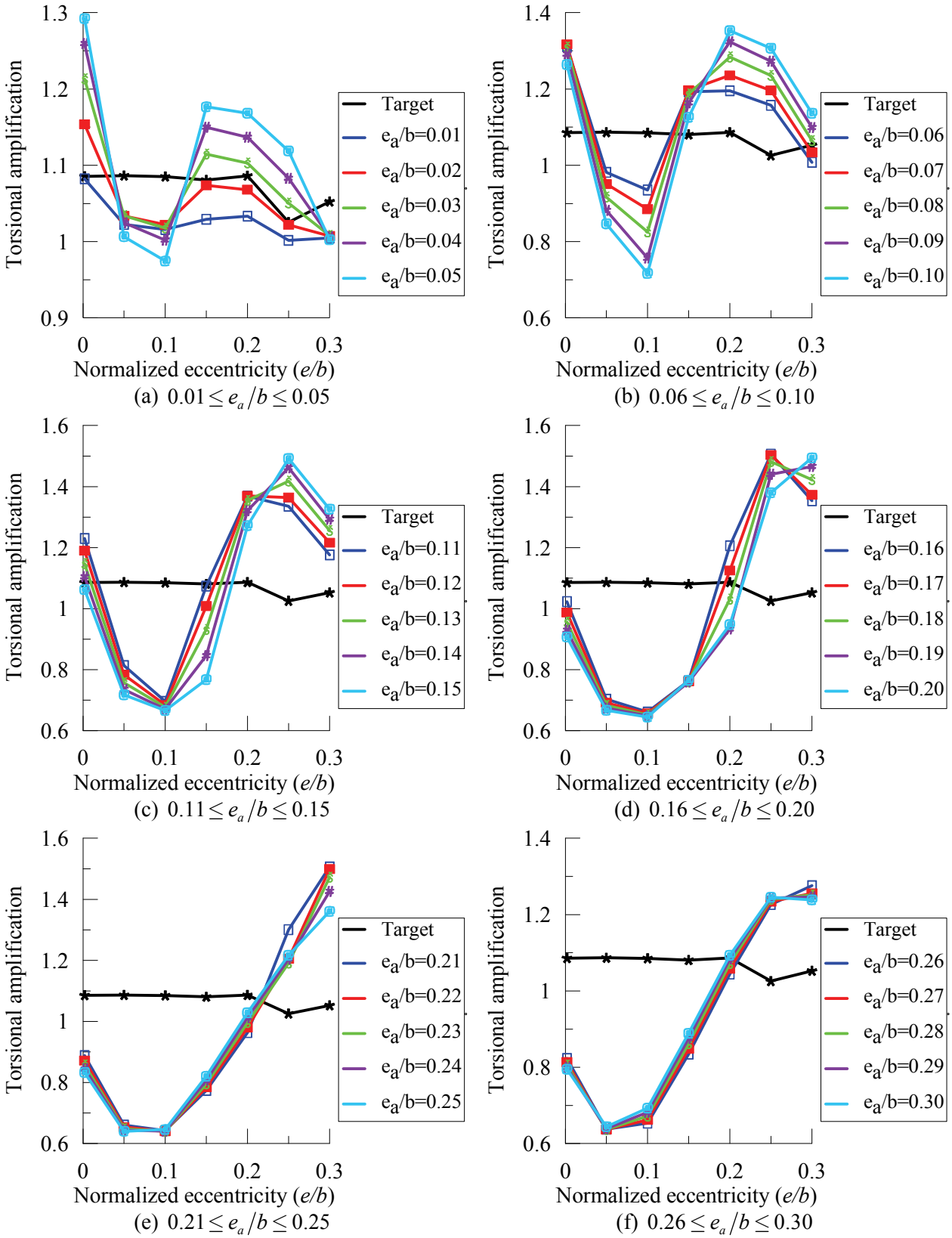

Figure 7-6: Torsional amplification for System 1, Shift 2, conventional approach (cont.)

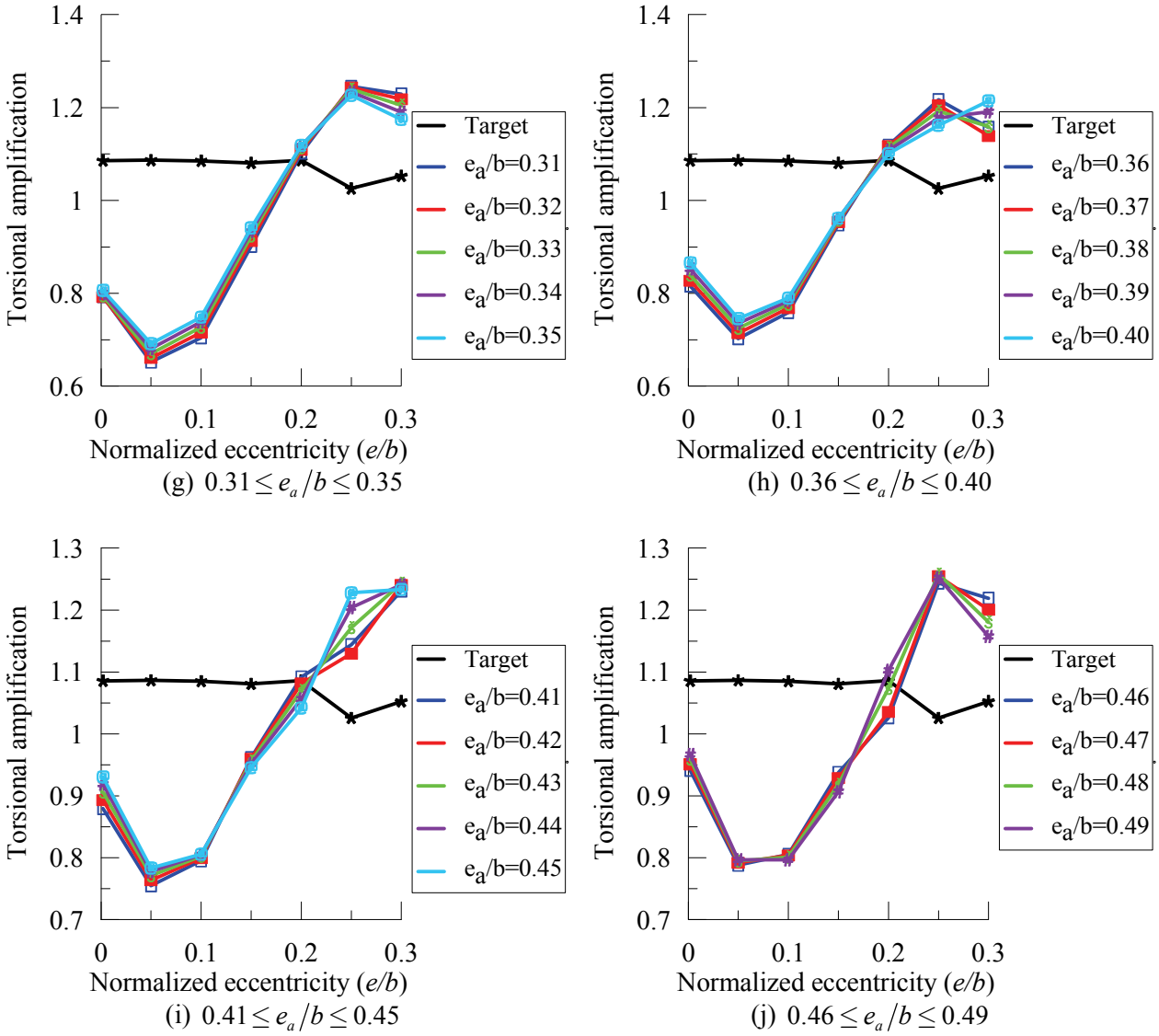

Figure 7-6: Torsional amplification for System 1, Shift 2, conventional approach

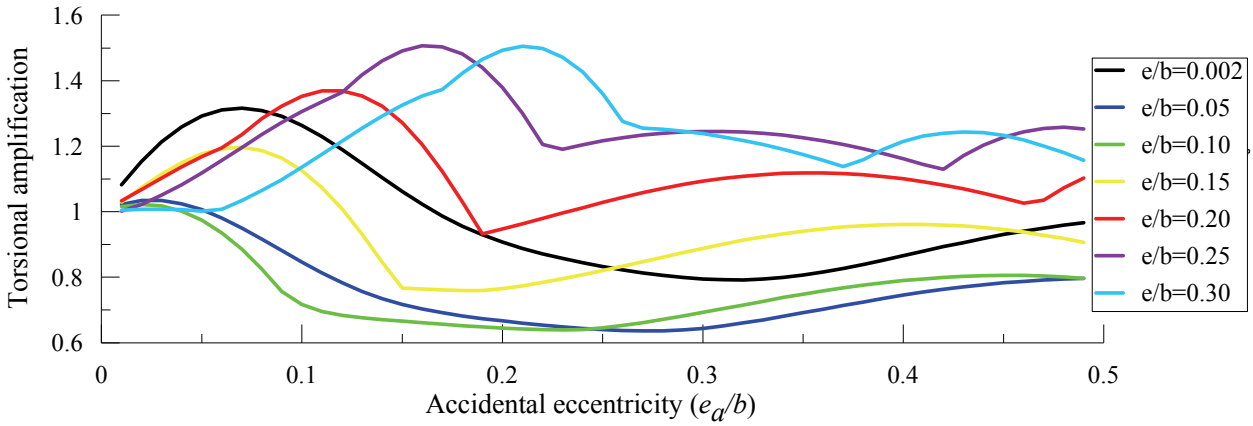

Figure 7-7: Variation of torsional amplification in System 1, Shift 2, conventional approach

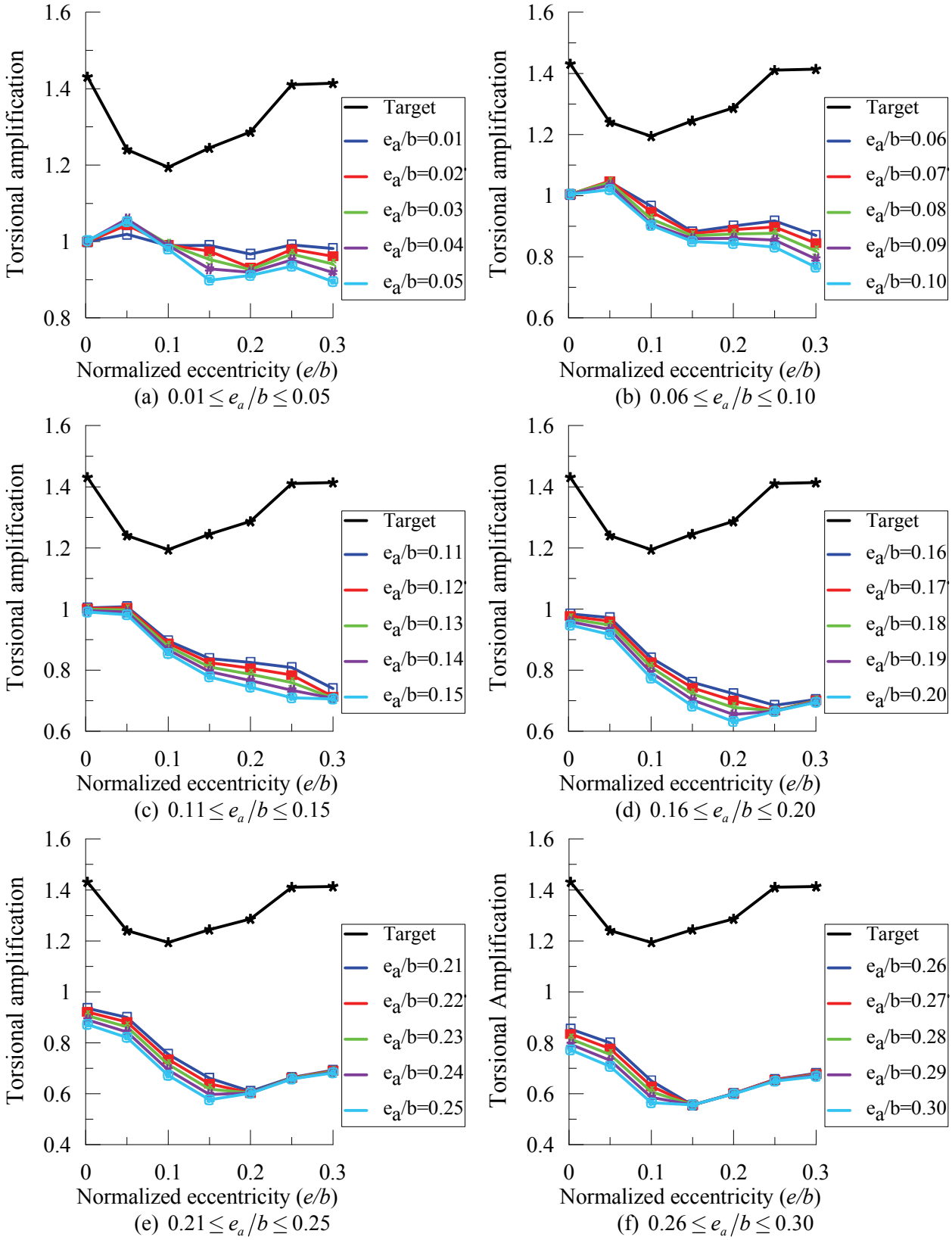

Figure 7-8: Torsional amplification for System 2, Shift 1, conventional approach (cont.)

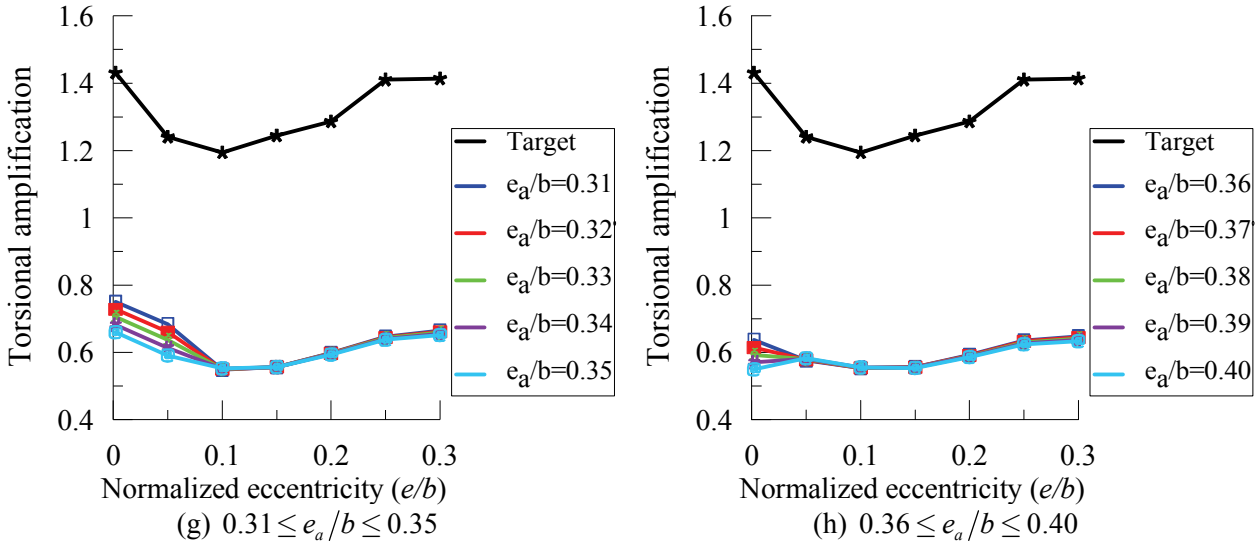

Figure 7-8: Torsional amplification for System 2, Shift 1, conventional approach

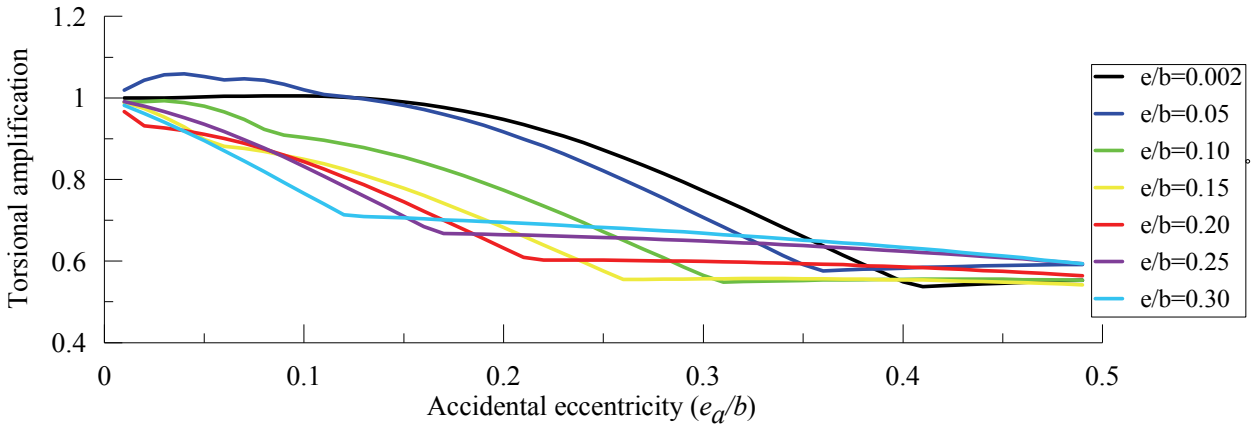

Figure 7-9: Variation of torsional amplification in System 2, Shift 1, conventional approach

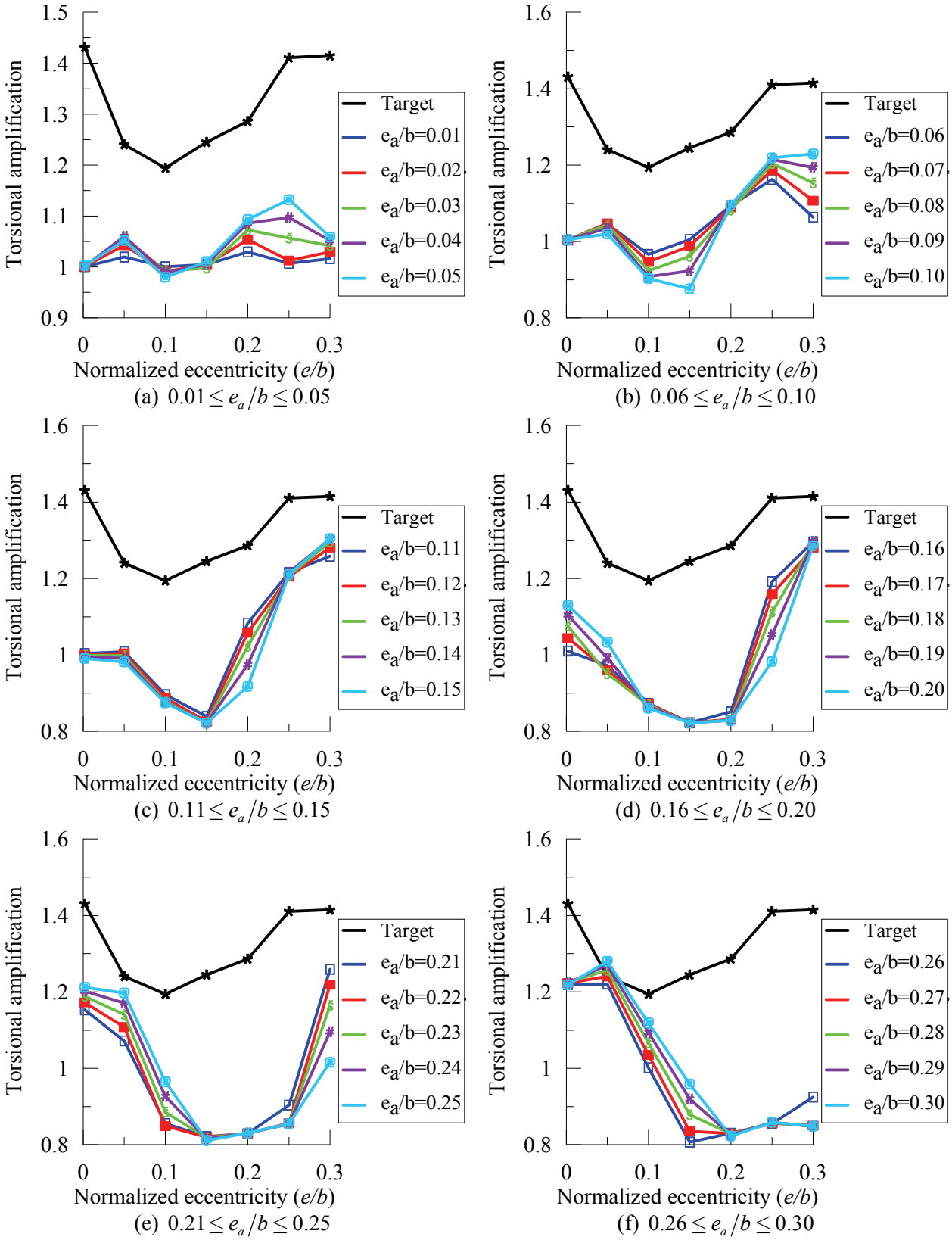

Figure 7-10: Torsional amplification for System 2, Shift 2, conventional approach (cont.)

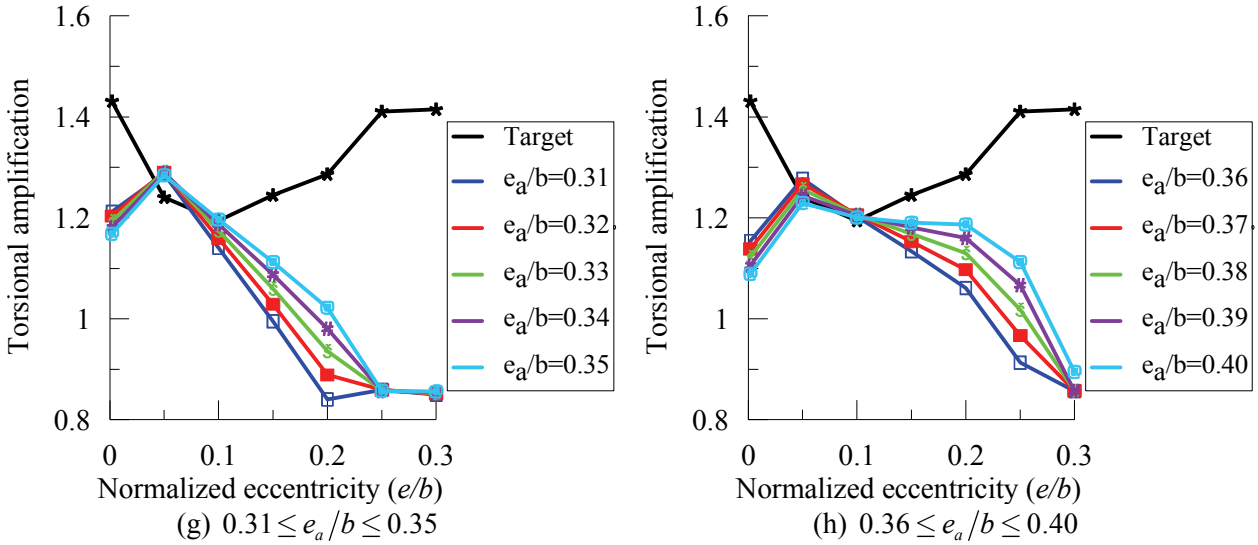

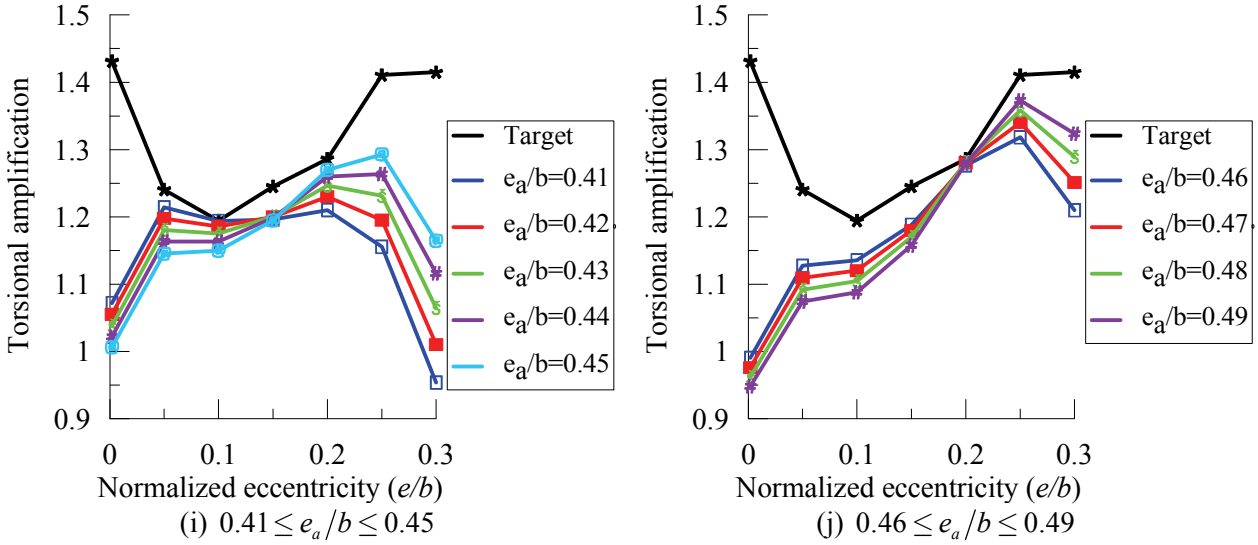

Figure 7-10: Torsional amplification for System 2, Shift 2, conventional approach

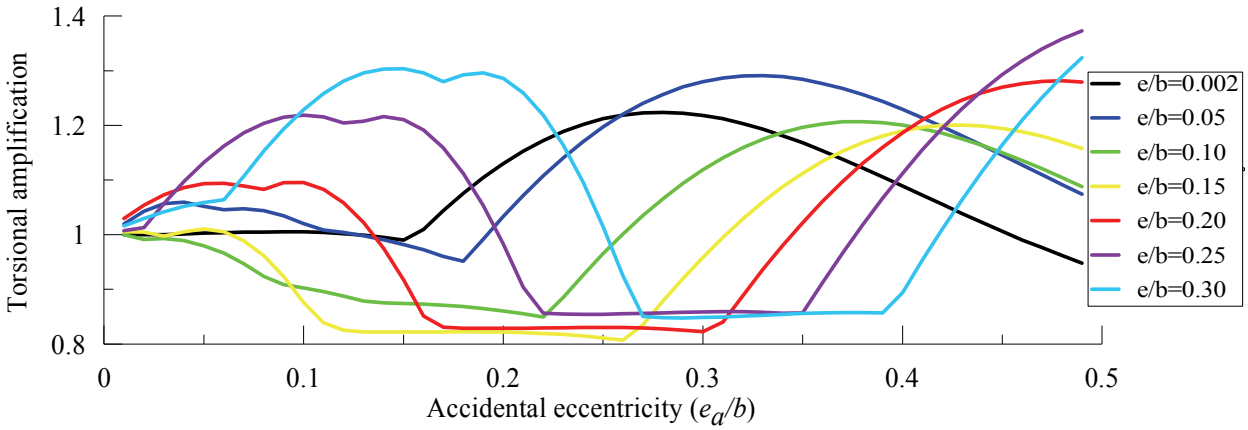

Figure 7-11: Variation of torsional amplification in System 2, Shift 2, conventional approach

$$\begin{bmatrix} m & -me_a \\ -me_a & m\left(r^2+e_a^2\right) \end{bmatrix}\begin{Bmatrix} \ddot{u}_y \\ \ddot{u}_\theta \end{Bmatrix}+\begin{bmatrix} C_y & C_{y\theta} \\ C_{y\theta} & C_\theta \end{bmatrix}\begin{Bmatrix} \dot{u}_y \\ \dot{u}_\theta \end{Bmatrix}+\begin{bmatrix} K_y & K_{y\theta} \\ K_{y\theta} & K_\theta \end{bmatrix}\begin{Bmatrix} u_y \\ u_\theta \end{Bmatrix}=-\begin{bmatrix} m & -me_a \\ -me_a & m\left(r^2+e_a^2\right) \end{bmatrix}\begin{Bmatrix} a_{gy} \\ 0 \end{Bmatrix} \tag{7-6}$$

The solution of Eq (7-6) first requires evaluation of frequencies and mode shapes. To impose the same dynamic characteristics on the two systems, the mass matrix on the left side of Eq (7-6) is modified to that of the original system [Eq 7-4)] without changing the right side. Eq (7-6) is modified to:

$$\begin{bmatrix} m & \\ & mr^2 \end{bmatrix}\begin{Bmatrix} \ddot{u}_y \\ \ddot{u}_\theta \end{Bmatrix}+\begin{bmatrix} C_y & C_{y\theta} \\ C_{y\theta} & C_\theta \end{bmatrix}\begin{Bmatrix} \dot{u}_y \\ \dot{u}_\theta \end{Bmatrix}+\begin{bmatrix} K_y & K_{y\theta} \\ K_{y\theta} & K_\theta \end{bmatrix}\begin{Bmatrix} u_y \\ u_\theta \end{Bmatrix}=-\begin{bmatrix} m & -me_a \\ -me_a & m\left(r^2+e_a^2\right) \end{bmatrix}\begin{Bmatrix} a_{gy} \\ 0 \end{Bmatrix} \tag{7-7}$$

Rearranging the right side, Eq (7-7) can be rewritten as

$$\begin{bmatrix} m & \\ & mr^2 \end{bmatrix}\begin{Bmatrix} \ddot{u}_y \\ \ddot{u}_\theta \end{Bmatrix}+\begin{bmatrix} C_y & C_{y\theta} \\ C_{y\theta} & C_\theta \end{bmatrix}\begin{Bmatrix} \dot{u}_y \\ \dot{u}_\theta \end{Bmatrix}+\begin{bmatrix} K_y & K_{y\theta} \\ K_{y\theta} & K_\theta \end{bmatrix}\begin{Bmatrix} u_y \\ u_\theta \end{Bmatrix}=-\begin{bmatrix} m & \\ & mr^2 \end{bmatrix}\begin{Bmatrix} a_{gy} \\ -\dfrac{e_a}{r^2}a_{gy} \end{Bmatrix} \tag{7-8}$$

The effect of accidental torsion can be accounted for by simultaneously applying the translational acceleration history a_{gy} and an artificial torsional acceleration history given by $-\left(e_a/r^2\right)a_{gy}$.

This alternative approach can also be derived schematically as seen in Figure 7-12 in terms of application of the inertial force. Panel a shows the inertial force and moment acting through the CM of the system when subjected to the translational acceleration along the y direction. The inertial force is

comprised of components $m\ddot{u}_y$ and ma_{gy}. To account for the effect of accidental torsion in the elements located on Side A only, the force ma_{gy} is shifted away from the CR by a distance e_a (see panel b). This is equivalent to applying a torsional moment equal to $me_a a_{gy}$ (see panel c). The inertial force and moment shown in panel c can be considered as resulting from a set of equivalent ground motions acting on the original system as shown in panel d.

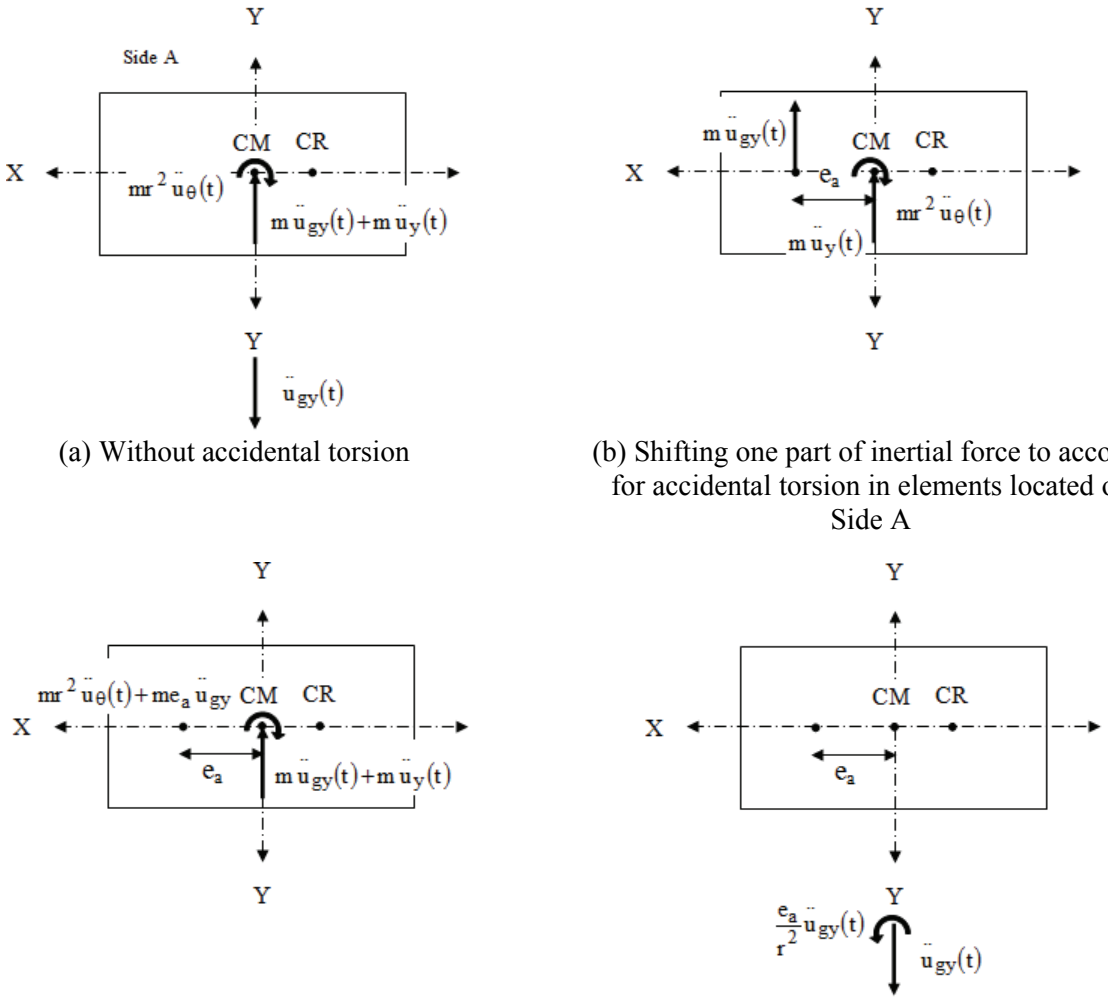

(a) Without accidental torsion

(b) Shifting one part of inertial force to account for accidental torsion in elements located on Side A

(c) Equivalence of (b)

(d) Equivalent ground motion inputs

Figure 7-12: Schematic representation of the alternative definition of accidental eccentricity

7.4.1. Evaluation Procedure

The required steps are identical to those described in Section 7.3.2 except the shifting of the CM is replaced by the application of an artificial torsional acceleration history. Note that the procedure uses two types of torsional acceleration histories: i) an actual record (described in Section 7.3.1) to compute the target torsional amplification, and ii) a record derived by scaling the translational acceleration history using a factor that is a function of the proposed accidental eccentricity. The intensity of the torsional acceleration history is increased by incrementing the accidental eccentricity until the target torsional amplification is obtained.

7.4.2. Scaling of Accidental Eccentricity

The artificial torsional acceleration history described above is $\ddot{u}_{g\theta} = -\left(e_a / r^2\right)\ddot{u}_{gy}$, where e_a is the accidental eccentricity and $\ddot{u}_{gy}$ the translational acceleration history. Alternatively, the torsional acceleration history may be expressed as

$$\ddot{u}_{g\theta} = -\left(\overline{e}_a / r^2\right)\left(b^* / r\right)^2 \ddot{u}_{gy} \tag{7-9}$$

where b^* is the greater of the two plan dimensions, *a* and *b,* and

$$\overline{e}_a = e_a \left(b^* / r\right)^2 \tag{7-10}$$

Note that quantity $\left(b^* / r\right)^2$ is a multiplier larger than unity (for a square plan, it is equal to 6).

7.4.3. Results and Discussions

The systems analyzed previously by shifting the CM are reanalyzed using the proposed definition of accidental eccentricity. The steps in the analysis are identical to those described above except the shifting of the CM is replaced by a torsional acceleration history defined previously. Figures 7-13 and 7-14 present the calculated torsional amplification for System 1. Similar results are presented in Figures 7-15

and 7-16 for System 2. The torsional amplification increases monotonically with increasing accidental eccentricity (Figures 7-14 and 7-16). Therefore, the procedure can be used to develop design recommendations for accidental eccentricity to be used with response history analysis to account for the effects of torsional ground motion. The recommendation should be based on a comparison of calculated torsional amplification and the target torsional amplification obtained using actual torsional ground motion input. Table 7-1 presents values of accidental eccentricity ($\bar{e}_a/b$) as a percentage of the plan dimension normal to the direction of excitation for use in response-history analysis. Note however these values are for elastic systems and are based on analysis using one record of torsional ground motion, which is calculated conservatively.

Table 7-1 Accidental eccentricity $\bar{e}_a/b$ for an elastic system

Ω	T_n (sec)				
	0.5	1.0	1.5	3.0	4.0
1	0.01	0.01	0.02	0.03	0.03
1.25	0.01	0.03	0.03	0.03	0.02
1.5	0.01	0.03	0.02	0.01	0.02

7.5. Accidental Eccentricity in Nonlinear Isolation Systems

The system shown in Figure 7-2 is now assumed to represent a rigid structure that is seismically isolated. The isolation system consists of six axisymmetric isolators such that the system is symmetric about the *x* axis but has an eccentricity about the *y* axis. The mass of the rigid superstructure is lumped at the CM (and geometric center) of the deck. The isolators have the bilinear hysteresis shown in Figure 7-17.

The behavior of the isolators is considered to be uncoupled along the two orthogonal horizontal directions. Analysis of this nonlinear isolation system can be performed using the procedure outlined in Appendix B with a change to the element force-displacement relation, as described below. The model

described in Appendix B is an improved version of the Bouc-Wen model (Wen, 1976) as implemented in the program 3D-BASIS (Nagarajaiah et al., 1989).

$$F = \alpha \frac{F_y}{Y} u + (1-\alpha) F_y Z$$
$$\dot{Z} = \frac{1}{Y}\left[\dot{u} - 0.5\left|\dot{u}\right| Z |Z|^{\eta-1} - 0.5\dot{u}|Z|^{\eta}\right] \tag{7-11}$$

Per Figure 7-17, the post-elastic resistance F of an isolator at displacement u (greater than the yield displacement Y) is

$$F = K_d u + Q \tag{7-12}$$

where K_d is the post-elastic stiffness and Q is the strength of the isolator at zero displacement. The force-displacement relation for the isolator is

$$F = K_d u + QZ \tag{7-13}$$

Comparing Eq (7-13) with Eq (7-11)

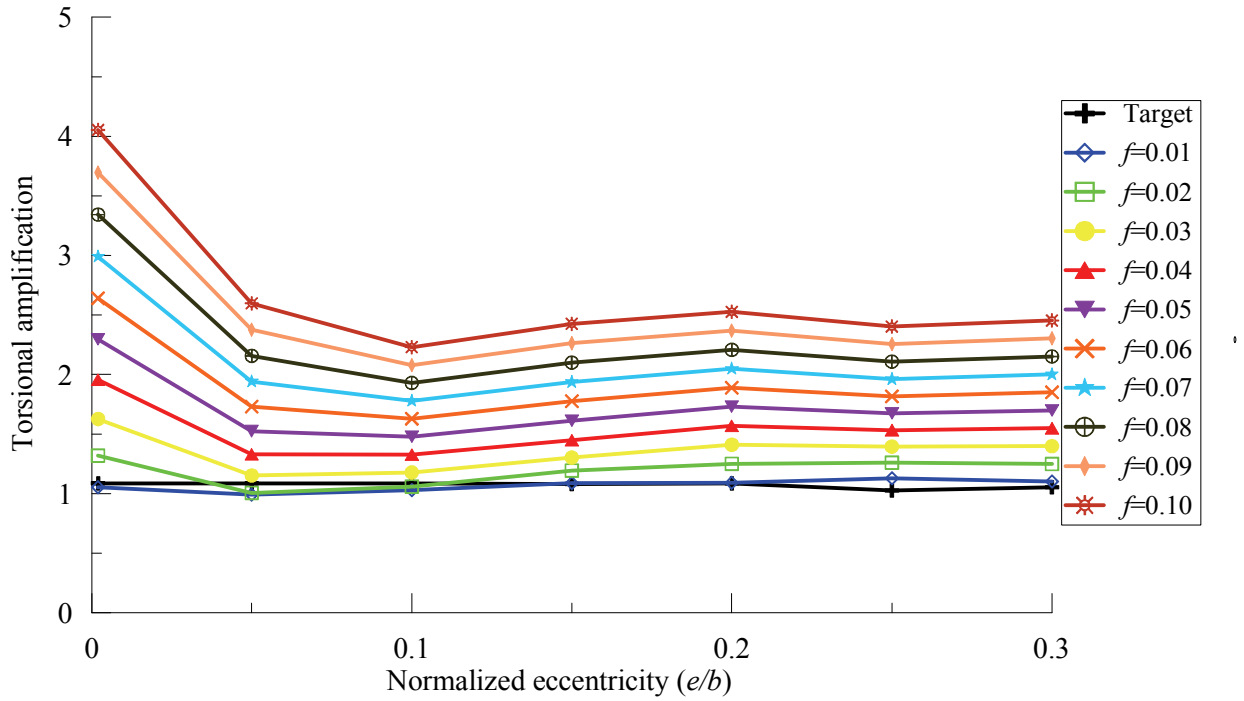

Figure 7-13: Variation of torsional amplification in System 1 as a function of normalized eccentricity, proposed approach, $f = \bar{e}_a / b$

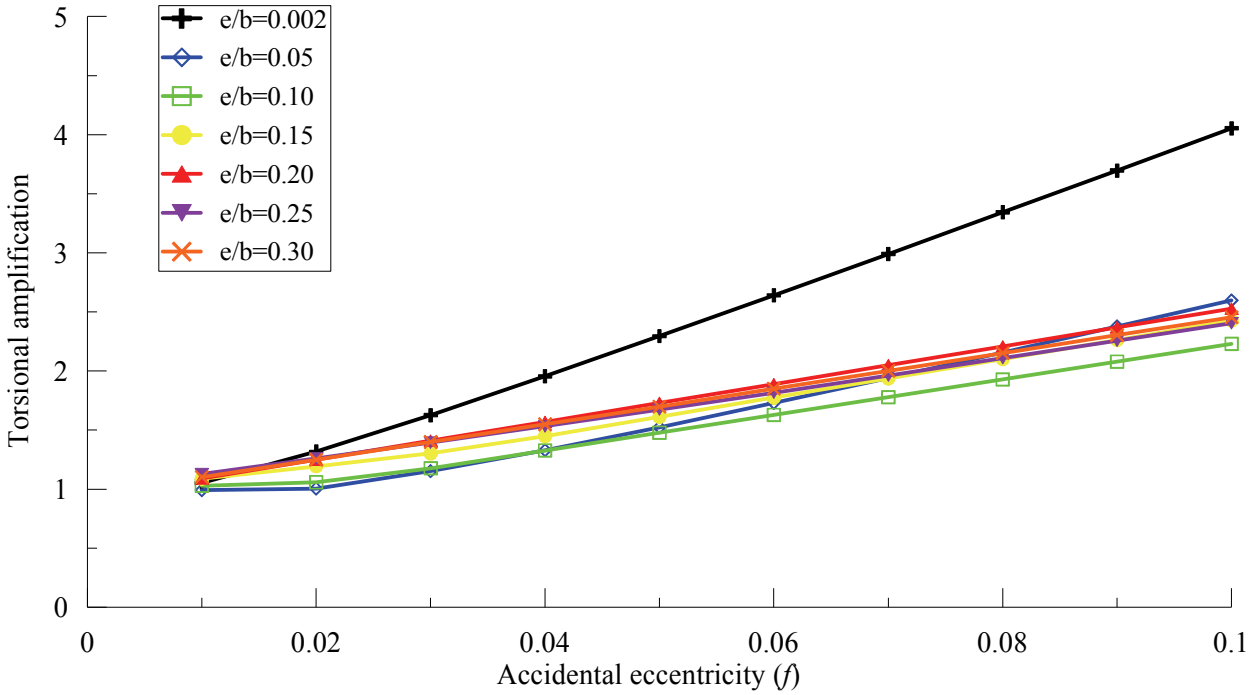

Figure 7-14: Variation of torsional amplification in System 1 as a function of accidental eccentricity, proposed approach, $f = \bar{e}_a / b$

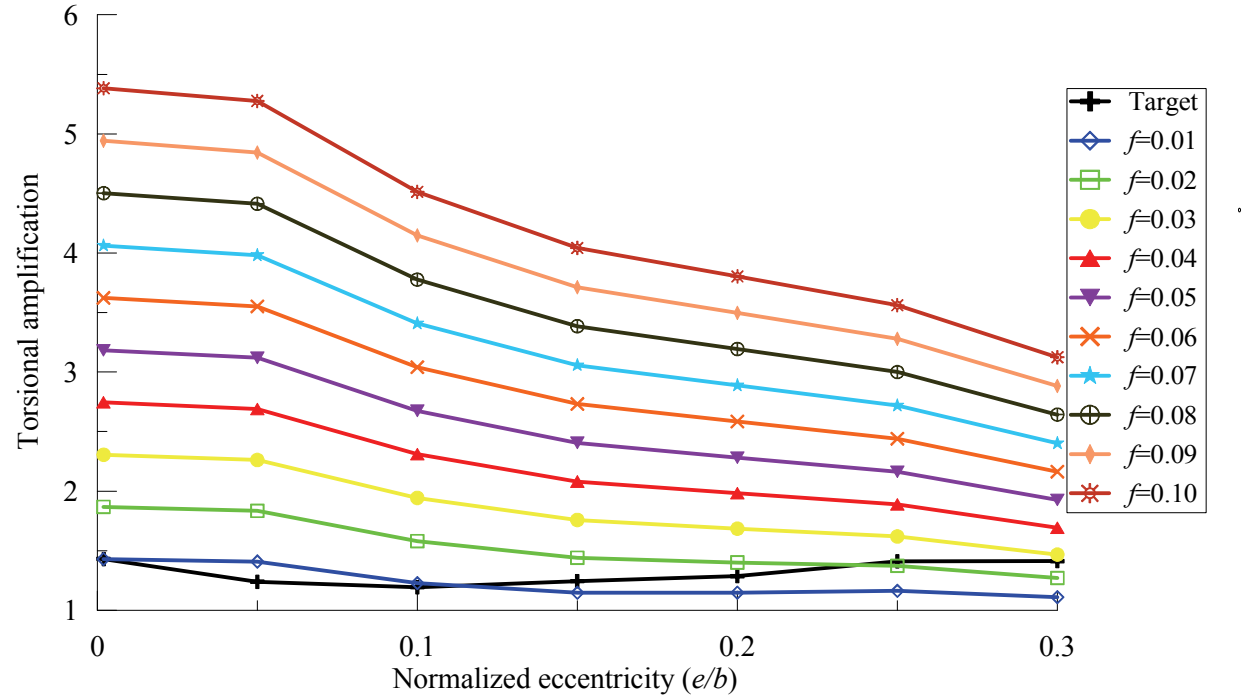

Figure 7-15: Variation of torsional amplification in System 2 as a function of normalized eccentricity, proposed approach, $f = \bar{e}_a / b$

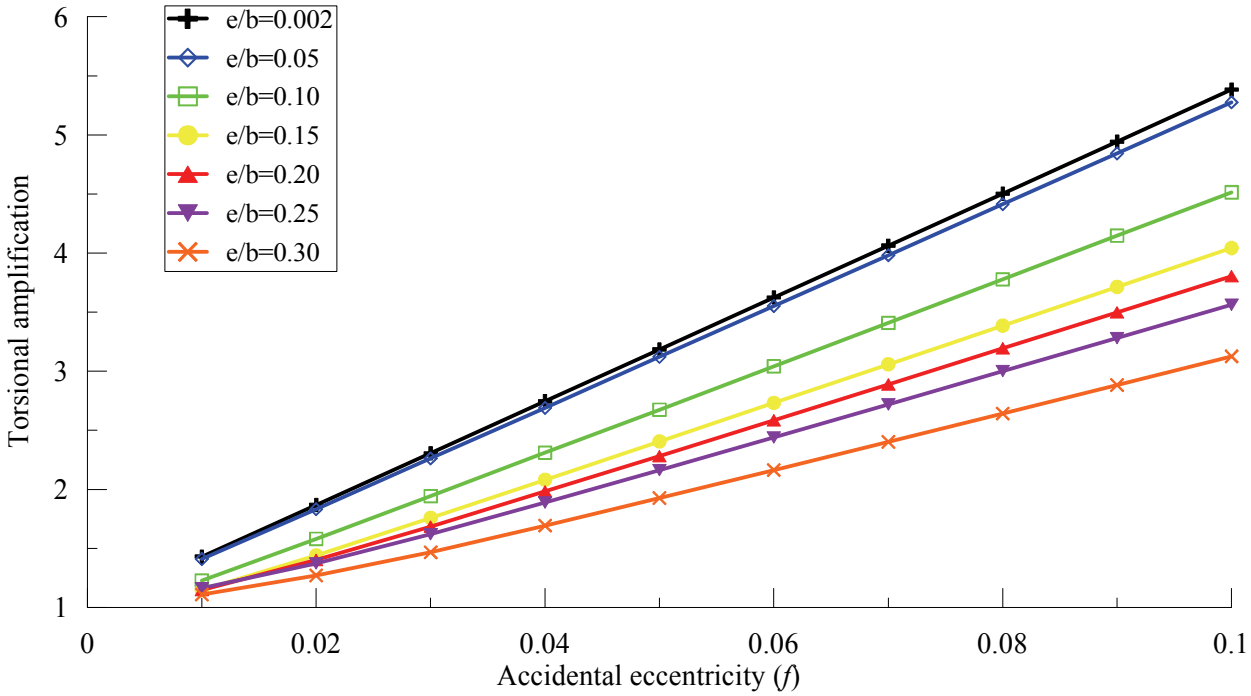

Figure 7-16: Variation of torsional amplification in System 2 as a function of accidental eccentricity, proposed approach, $f = \bar{e}_a / b$

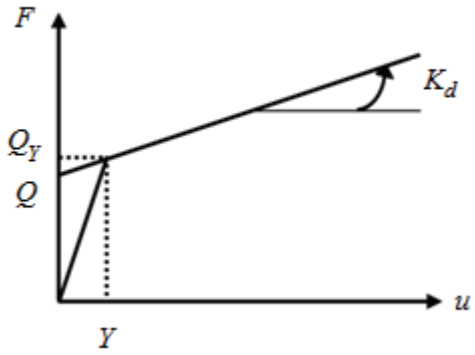

Figure 7-17: Force-displacement relationship for a typical isolator

$$K_d = \alpha \frac{F_y}{Y}$$
$$Q = (1-\alpha) F_y \qquad (7\text{-}14)$$

and the equation of motion presented in Appendix B (Eq (C-10)) can be modified per Eq (7-14). Specifically, $\alpha_x f_{yx} / Y_x$ and $(1-\alpha_x) f_{yx}$ are replaced by K_{dx} and Q_x, respectively. Similarly, $\alpha_y f_{yy} / Y_y$

and $\left(1-\alpha_y\right) f_{yy}$ are replaced by K_{dy} and Q_y, respectively, where α is the post-elastic stiffness ratio and the coefficient η dictates the smoothness of the transition from the elastic to post-elastic regimes.

A broad range of nonlinear isolation systems is considered. Each has the same mass. These systems are characterized per Section 7.2 with the exception that the post-elastic stiffness, K_d, is used instead of the elastic stiffness, K_y. The uncoupled translational time period based on the post-elastic stiffness is denoted as T_d. Two isolation systems are considered with periods of $T_d = 4\,\text{sec}$ and $T_d = 5\,\text{sec}$. The ratios of the uncoupled torsional frequency to translational frequency, based on the post-elastic stiffness, Ω, are 1.0, 1.25 and 1.5. The normalized natural eccentricity (e/b) is increased from zero (rather 0.002), in increments of 0.05, until one of the isolator stiffnesses calculated per Eq (7-3) becomes negative. [Three unknown stiffnesses in the mathematical model are computed by solving three simultaneous equations, one for each specified normalized parameter. Any arbitrary combination of the specified normalized parameters may not always represent a realistic system and in such a case, at least one of the computed values of stiffness is non-positive.] The yield displacement of each isolator is 5 mm. The ratio of characteristic strength to supported weight (Q/W) for each isolator was set equal to 0.04, 0.05 and 0.06, which are reasonable values used in professional practice (e.g., Constantinou et al., 2007). These isolation systems are analyzed using a state-space procedure.

7.5.1. Results and Discussions

The accidental eccentricity computed for all systems considered in this study are reported in Table 7-2. Results from one of these cases, $T_d = 4$ sec, $\Omega = 1.25$ and $Q/W = 0.05$ is presented in Figure 7-18 and the required accidental eccentricity is nearly independent of the natural eccentricity. For a given characteristic strength, the required accidental eccentricity does not depend on the uncoupled translational time period or the ratio of the uncoupled torsional to translational frequency (Table 7-2). Therefore, the required accidental eccentricity does not depend on the post-elastic stiffness and the eccentricity calculated based on it. However, for these conclusions to hold, it is shown in the following section that

the ratio of characteristic strength-to-weight should exceed a lower bound and the yield displacement should not exceed an upper bound.

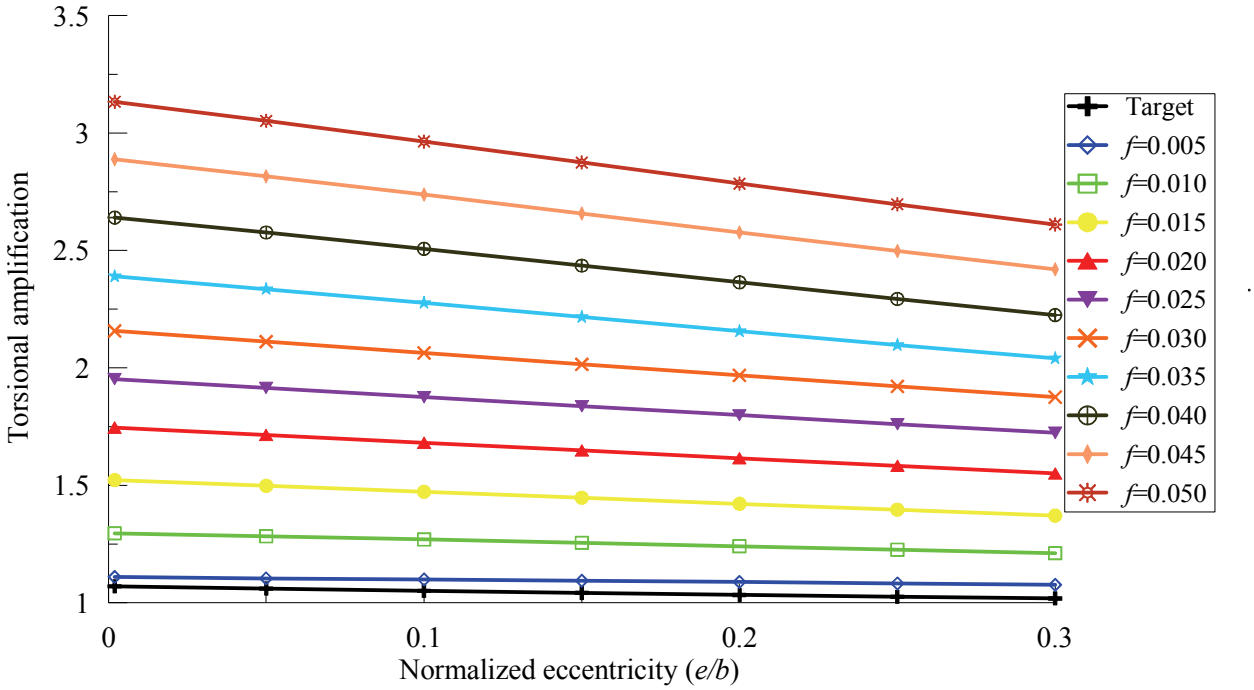

Figure 7-18: Variation of torsional amplification in nonlinear isolation system, $T_d = 4$ sec, $\Omega = 1.25$, $Q/W = 0.05$, $Y = 5$ mm, orthogonally uncoupled, $f = \bar{e}_a / b$

Table 7-2 Accidental eccentricity (%) for an uncoupled isolation system, $Y = 5$ mm

	$T_d = 4\,\text{sec}$			$T_d = 5\,\text{sec}$		
	$\kappa = Q/W\,(\%)$			$\kappa = Q/W\,(\%)$		
Ω	4	5	6	4	5	6
1	0.01	0.005	0.005	0.01	0.005	0.005
1.25	0.01	0.005	0.005	0.01	0.005	0.005
1.5	0.01	0.005	0.005	0.01	0.005	0.005

7.5.2. Properties of the Associated Elastic Systems

An isolation system, comprising N number of isolators with any general arrangement supporting a mass m, is considered. For any isolator, the ratio of characteristic strength to supported weight, and the

yield displacement are assumed to be constant: for the i^{th} isolator, $Q_i/W_i = \kappa$ and $Y_i = Y$. The effective stiffness of the i^{th} isolator at any displacement u_i and the associated elastic stiffness are given by

$$K_{eff}^i = \frac{Q_i}{u_i} + K_{di}$$
$$K_{el}^i = \frac{Q_i}{Y_i} + K_{di} \tag{7-15}$$

The uncoupled translational frequency of the associated elastic system is

$$\omega_{el} = \sqrt{\frac{1}{m}\sum_{i=1}^{N} K_{el}^i} = \omega_d \sqrt{\gamma} \tag{7-16}$$

where ω_d is the frequency based on the post-elastic stiffness and γ is given by

$$\gamma = 1 + \frac{\kappa g}{\omega_d^2 Y} \tag{7-17}$$

The normalized natural eccentricity based on the elastic stiffness is

$$\frac{e_{el}}{b} = \frac{\sum_{i=1}^{N} x_i K_{el}^i}{\sum_{i=1}^{N} K_{el}^i} = \left(\frac{e}{b}\right)\frac{1}{\gamma} \tag{7-18}$$

The torsional stiffness about the CM of the associated elastic system is

$$K_{\theta,el} = \sum_{i=1}^{N}\left(\frac{Q_i}{Y_i} + K_{di}\right)\left(x_i^2 + y_i^2\right) = K_\theta + \frac{\kappa g}{Y}\sum_{i=1}^{N} m_i\left(x_i^2 + y_i^2\right) \tag{7-19}$$

where K_θ is the torsional stiffness about the CM calculated on the post-elastic stiffness. Making the approximation

$$\sum_{i=1}^{N} m_i\left(x_i^2 + y_i^2\right) = \chi I_\theta \tag{7-20}$$

where I_θ is the polar moment of inertia about the CM and χ is a factor close to unity when the number of isolators is large, Eq (7-19) can be reduced to

$$K_{\theta,el} = K_\theta + \frac{\kappa g}{Y}\chi I_\theta \tag{7-21}$$

The torsional stiffness about the CR in the associated elastic system is

$$K_{\theta R,el} = K_{\theta,el} - e_{el}^2 K_{el} \tag{7-22}$$

Now, the ratio of the uncoupled torsional to translational frequency in the associated elastic system can be expressed as

$$\Omega_{el}^2 = \chi\left(1-\frac{1}{\gamma}\right)+\frac{\Omega^2}{\gamma}-\left(\frac{e}{r}\right)^2\frac{1}{\gamma^2} \tag{7-23}$$

Given the normalized parameters of the nonlinear system, which are defined using the post-elastic stiffness, Eq (7-16), Eq (7-18) and Eq (7-23) estimate the normalized parameters required to characterize the associated elastic system. For all the systems considered in Table 7-2 with $T_d = 4$ sec, γ is 33, 41 and 49 for κ equal to 0.04, 0.05 and 0.06, respectively. The periods of the associated elastic systems can be calculated from Eq (7-16) as 0.70 sec, 0.63 sec and 0.57 sec, respectively. Similarly, γ for all the systems considered in Table 7-2 with $T_d = 5$ sec are 51, 63 and 76, respectively. The periods of the associated elastic systems are 0.70 sec, 0.63 sec and 0.57 sec, respectively. These periods do not change with T_d for the same ratio of strength-to-weight, κ. Further, for all the nonlinear systems considered in Table 7-2, the periods of the associated elastic systems range between 0.57 and 0.70 sec. For all these nonlinear systems, associated elastic systems show $e_{el} \approx 0$ and $\Omega_{el} \approx 1.0$ (from Eq (7-18) and Eq (7-23), respectively). If the associated elastic systems are now analyzed, the required accidental eccentricity ($\overline{e}_a/b$) will be 0.01 (see Table 7-1 for $\Omega = 1.0$ and $T = 0.5 \sim 1.0$ sec). However, analysis of the nonlinear systems results in an accidental eccentricity of 0.01 for $\kappa = 0.04$ and 0.005 for $\kappa = 0.05$ and 0.06 (see Table 7-2). In the results presented in Table 7-1, eccentricity is incremented in the units of 0.01 (1%) and a required accidental eccentricity of less than 0.01 is not captured. The required accidental eccentricity computed from the analysis of the nonlinear systems is nearly the same as that obtained from the associated elastic system, justifying the observations made in Section 7.5.1.

However, for this justification to hold, γ should be at least 20 (see above). Otherwise, analysis of each nonlinear system will lead to a different (e_{el} , Ω_{el}) pair leading to a different value of the accidental

eccentricity. Note that the parameter γ drops almost linearly with a reduction in the ratio of characteristic strength-to-weight and with an increase in yield displacement. The conclusions drawn in Section 7.5.1 will not hold if the ratio of characteristic strength-to-weight is less than a lower bound and/or the yield displacement exceeds an upper bound.

7.5.3. Isolator Modeling With Orthogonal Coupling

Isolator hysteresis is coupled along the horizontal axes for low damping rubber, lead-rubber and Friction Pendulum™ seismic isolators. The coupling is described here using the differential equations proposed by Park et al (1985) but as modified and subsequently implemented in program 3D-BASIS (Nagarajaiah et al., 1989):

$$\begin{aligned} \dot{Z}_x &= \frac{1}{Y}\left[\dot{u}_x - 0.5\left|\dot{u}_x Z_x\right| Z_x - 0.5\dot{u}_x Z_x^2 - 0.5\left|\dot{u}_y Z_y\right| Z_x - 0.5\dot{u}_y Z_x Z_y\right] \\ \dot{Z}_y &= \frac{1}{Y}\left[\dot{u}_y - 0.5\left|\dot{u}_y Z_y\right| Z_y - 0.5\dot{u}_y Z_y^2 - 0.5\left|\dot{u}_x Z_x\right| Z_y - 0.5\dot{u}_x Z_y Z_x\right] \end{aligned} \tag{7-24}$$

The equation of motion described in Appendix B [Eq (C-10)] is modified here to account for the modification of Section 7.5 and Eq (7-24). This alters only the last two equations in Eq (C-10) as follows:

For $i, j = 1,..., N$ = number of isolators

$$\begin{aligned} \phi_{i+6}(V) &= \frac{1}{Y_{xi}}\begin{bmatrix} (V_4 - y_i V_6) - 0.5\left|(V_4 - y_i V_6)V_{i+6}\right| V_{i+6} - 0.5(V_4 - y_i V_6)V_{i+6}^2 \\ -0.5\left|(V_5 + x_i V_6)V_{i+6+N}\right| V_{i+6} - 0.5(V_5 + x_i V_6)V_{i+6}V_{i+6+N} \end{bmatrix} \\ \phi_{j+N+6}(V) &= \frac{1}{Y_{yj}}\begin{bmatrix} (V_5 + x_j V_6) - 0.5\left|(V_5 + x_j V_6)V_{j+N+6}\right| V_{j+N+6} - 0.5(V_5 + x_j V_6)V_{j+N+6}^2 \\ -0.5\left|(V_4 - y_j V_6)V_{j+6}\right| V_{j+N+6} - 0.5(V_4 - y_j V_6)V_{j+6}V_{j+N+6} \end{bmatrix} \end{aligned} \tag{7-25}$$

The domain of analyses is broadened by including systems with $T_d = 3\text{sec}$ and $\kappa = 0.07$. Table 7-3 lists the required accidental eccentricities. Figure 7-19 enables a comparison of the target and achieved torsional amplifications for the same set of systems considered in Figure 7-18. A comparison of the results of Table 7-3 and Table 7-2 shows the effect of orthogonal coupling on the required accidental eccentricity. This difference is attributed in part to the selection of the coefficient η. For the uncoupled

calculations $\eta = 5$ (Table 7-2); the coupled model (Park et al., 1985) implicitly assumes $\eta = 2$ (Table 7-3).

Table 7-3 Accidental eccentricity $\bar{e}_a / b$ in nonlinear isolation system, $Y = 5$ mm

	$T_d = 3\,\text{sec}$				$T_d = 4\,\text{sec}$				$T_d = 5\,\text{sec}$			
	$\kappa = Q/W\,(\%)$				$\kappa = Q/W\,(\%)$				$\kappa = Q/W\,(\%)$			
Ω	4	5	6	7	4	5	6	7	4	5	6	7
1	0.01	0.005	0.01	0.01	0.01	0.005	0.01	0.01	0.01	0.005	0.01	0.01
1.25	0.01	0.005	0.01	0.01	0.01	0.005	0.01	0.01	0.01	0.005	0.01	0.01
1.5	0.01	0.005	0.01	0.01	0.01	0.005	0.01	0.01	0.01	0.005	0.01	0.01

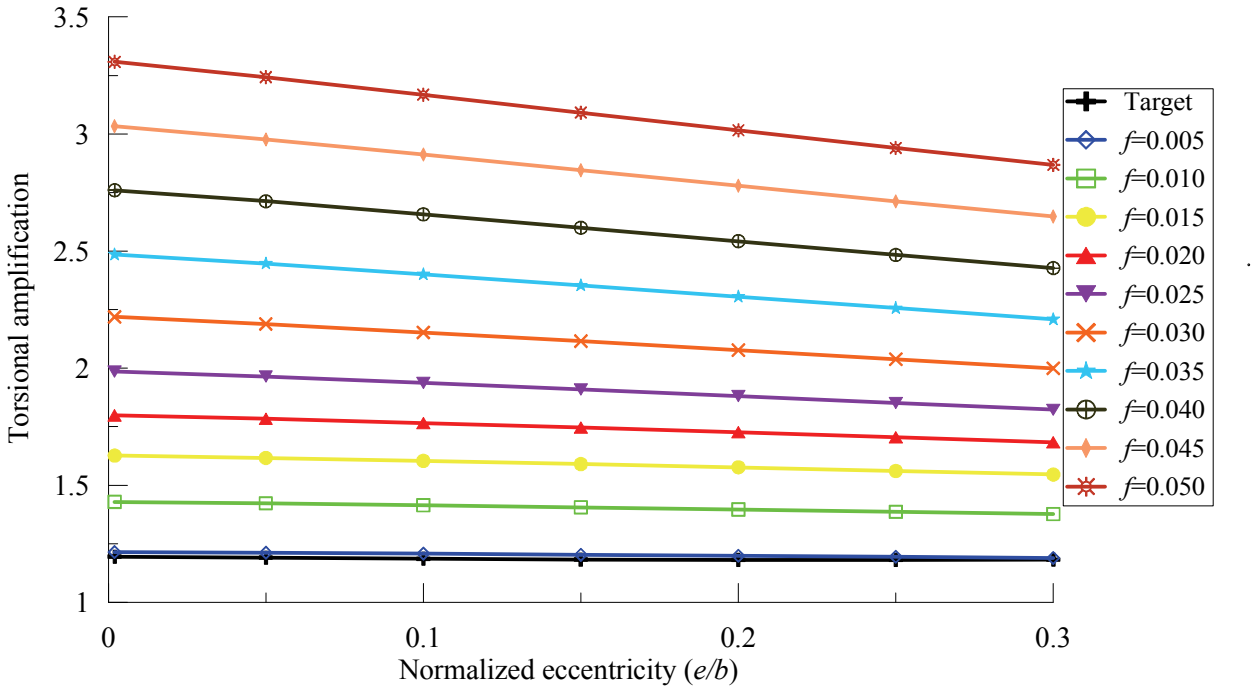

Figure 7-19: Variation of torsional amplification in nonlinear isolation system, $T_d = 4$ sec, $\Omega = 1.25$, $Q/W = 0.05$, $Y = 5$ mm, orthogonally coupled, $f = \bar{e}_a / b$

7.5.4. Effect of Yield Displacement of Isolators on Accidental Eccentricity

If the isolator response is uncoupled, Section 7.5.2 identifies that the yield displacement (Y) plays an important role in calculating the required accidental eccentricity. This section confirms the observation

for coupled isolator response. To date, Y has been set equal to 5 mm. Here, Y is set equal to 1 mm and 10 mm. Results are presented in Table 7-4 ($Y = 1$ mm) and Table 7-5 ($Y = 10$ mm). An evaluation of results presented in Tables 7-3 through 7-5 identifies the yield displacement and ratio of characteristic strength-to-weight as the governing parameters in the computation of the accidental eccentricity.

Table 7-4 Accidental eccentricity $\bar{e}_a/b$ in nonlinear isolation system, Y = 1 mm

	$T_d = 3\text{sec}$				$T_d = 4\text{sec}$				$T_d = 5\text{sec}$			
	$\kappa = Q/W(\%)$				$\kappa = Q/W(\%)$				$\kappa = Q/W(\%)$			
Ω	4	5	6	7	4	5	6	7	4	5	6	7
1	0.005	0.005	0.005	0.005	0.005	0.005	0.005	0.005	0.005	0.005	0.005	0.005
1.25	0.005	0.005	0.005	0.005	0.005	0.005	0.005	0.005	0.005	0.005	0.005	0.005
1.5	0.005	0.005	0.005	0.005	0.005	0.005	0.005	0.005	0.005	0.005	0.005	0.005

Table 7-5 Accidental eccentricity $\bar{e}_a/b$ in nonlinear isolation system, Y = 10 mm

	$T_d = 3\text{sec}$				$T_d = 4\text{sec}$				$T_d = 5\text{sec}$			
	$\kappa = Q/W(\%)$				$\kappa = Q/W(\%)$				$\kappa = Q/W(\%)$			
Ω	4	5	6	7	4	5	6	7	4	5	6	7
1	0.01	0.01	0.01	0.005	0.01	0.01	0.01	0.005	0.01	0.01	0.01	0.005
1.25	0.01	0.01	0.01	0.005	0.01	0.01	0.01	0.005	0.01	0.01	0.01	0.005
1.5	0.01	0.01	0.01	0.005	0.01	0.01	0.01	0.005	0.01	0.01	0.01	0.005

7.6. Analysis and Validation of Results with SAP2000

This section has three objectives, namely, 1) to assess the accuracy of the computer program developed to analyze torsionally coupled systems (elastic or nonlinear) subjected to translational and torsional ground excitations; 2) to identify the role of damping in shifting the CM if standard software, such as SAP 2000, is used; and 3) to illustrate the implementation of the proposed approach in SAP 2000. To validate the elastic analysis, two systems are considered, System 1: $T_n = 1$ sec, $\Omega = 1.25$, and $e/b = 0.15$, and System 2: $T_n = 3$ sec, $\Omega = 1.25$, and $e/b = 0.05$. Rayleigh damping is assumed in both cases with a damping ratio 5% of critical in the first and third modes. Figure 7-20 enables a comparison

for System 1: panel (a) (Shift 1) and panel (b) (Shift 2) suggest that the difference is small if the accidental eccentricity is small. Calculations of the torsional amplification are presented in Table 7-6. The discrepancy in torsional amplification is attributed to the assumed damping. In the analyses performed here, the damping matrix is computed once, before shifting the CM. An identical damping matrix is used for different values of the accidental eccentricity. Exactly the same damping is specified in SAP through mass and stiffness proportionality constants. The damping matrix is changed by shifting the CM as the mass matrix changes, but the associated proportionality constant is not. The greater the accidental eccentricity, the greater the discrepancy due to damping. To confirm this observation, analyses are performed using a damping ratio of 0.1% of critical in the first and third modes. Results are presented in panel (c) and panel (d) of Figure 7-20. Calculations for the amplification factor are presented in Table 7-7. The difference in the torsional amplification diminishes significantly with a reduction in damping. Results for System 2 are presented in Figure 7-21 and Tables 7-8 and 7-9. The observations are essentially identical to those for System 1.

A validation of the proposed procedure is presented next for the elastic systems shown in Figure 7-22 and Tables 7-10 and 7-11. In both cases, close agreement between the computer program developed here (see Appendix A) and SAP2000 is evident because the proposed procedure does not require shifting the CM.

The system selected to validate the nonlinear analysis is $T_d = 4$ sec, $\Omega = 1.25$, $e/b = 0.10$ and $Y = 5$ mm. The mass of the system is 90 tons. The isolators are modeled in SAP2000 with the properties shown in Table 7-12. Uncoupled and coupled behaviors are included in the results presented in Figure 7-23 and Tables 7-13 and 7-14. Good agreement is observed. Assuming coupled response, element hysteresis along the y-direction is compared for element 1 when $\bar{e}_a/b = 0.005$ (Figure 7-24). For the same accidental eccentricity, the displacement history along the *y* direction of the point located at the intersection of the *x* axis and the line joining elements 1 and 4 are plotted in Figure 7-25. In both cases, the agreement is excellent.

7.7. Discussion on the Proposed Definition of Accidental Eccentricity

Instead of the conventional approach of shifting the CM, the proposed definition of accidental eccentricity considers the application of a torsional ground motion, which is derived from the translational ground motion by multiplying it by a factor that is a function of the proposed accidental eccentricity. The required accidental eccentricity is that for which the achieved torsional amplification is greater than or equal to the actual torsional amplification. The displacement of a corner of the building is chosen to define the torsional amplification for the one-story systems. For multistory systems, the number of candidates for defining the torsional amplification, including corner displacement and story drift, is large in number. Each of them is expected to yield different accidental eccentricities in a multistory building. The definition of accidental eccentricity proposed here applies to all sources of accidental torsion but the procedure to quantify the required accidental eccentricity will differ by source.

Table 7-6: Peak displacements for the conventional approach for 5% damped System 1 (all displacements in mm)

$e_a/b = 0$	a_{gy}	$a_{gy} + a_{g\theta}$	$a_{gy} - a_{g\theta}$	Actual torsional amplification
SAP	109.6	100.7	118.6	1.08
Program	109.7	100.9	118.5	1.08
SAP/Program	1.00	1.00	1.00	1.00

e_a/b	Shifting away from CR			Shifting towards CR			Torsional amplification (SAP)	
	SAP	Program	SAP/Program	SAP	Program	SAP/Program	Shift 1	Shift 2
0.01	106.5	106.7	1.00	112.4	112.9	1.00	0.97	1.03
0.05	93.6	93.9	1.00	130.6	129.0	1.01	0.85	1.19
0.10	83.7	86.2	0.97	126.8	123.4	1.03	0.76	1.16
0.15	80.7	84.2	0.96	88.1	82.6	1.07	0.74	0.80
0.20	82.2	83.9	0.98	59.4	48.6	1.22	0.75	0.75
0.25	86.6	89.9	0.96	63.2	52.6	1.20	0.79	0.79
0.30	91.6	97.5	0.94	66.6	56.5	1.18	0.84	0.84
0.35	94.4	103.2	0.92	59.8	51.7	1.16	0.86	0.86
0.40	94.2	105.4	0.89	47.6	42.7	1.12	0.86	0.86
0.45	90.9	103.7	0.88	40.8	37.6	1.09	0.83	0.83
0.49	86.1	99.4	0.87	42.4	40.3	1.05	0.79	0.79

Table 7-7: Peak displacements for the conventional approach for 0.1% damped System 1 (all displacements in mm)

$e_a/b = 0$	a_{gy}	$a_{gy} + a_{g\theta}$	$a_{gy} - a_{g\theta}$	Actual torsional amplification
SAP	178.1	160.6	200.1	1.12
Program	178.5	160.0	198.5	1.11
SAP/Program	1.00	1.00	1.01	1.01

e_a/b	Shifting away from CR			Shifting towards CR			Torsional amplification (SAP)	
	SAP	Program	SAP/Program	SAP	Program	SAP/Program	Shift 1	Shift 2
0.01	167.3	167.5	1.00	181.4	182.3	1.00	0.94	1.02
0.05	135.0	135.0	1.00	211.2	209.5	1.01	0.76	1.19
0.10	110.2	110.2	1.00	227.6	227.5	1.00	0.62	1.28
0.15	103.0	103.7	0.99	151.8	152.2	1.00	0.58	0.85
0.20	114.0	114.4	1.00	123.3	121.9	1.01	0.64	0.69
0.25	150.9	154.6	0.98	88.9	87.7	1.01	0.85	0.85
0.30	124.6	126.0	0.99	91.8	90.5	1.01	0.70	0.70
0.35	113.7	113.9	1.00	78.3	76.9	1.02	0.64	0.64
0.40	117.2	117.6	1.00	56.8	56.3	1.01	0.66	0.66
0.45	115.4	115.8	1.00	59.7	58.6	1.02	0.65	0.65
0.49	125.1	128.7	0.97	65.9	61.9	1.07	0.70	0.70

Table 7-8: Peak displacements for the conventional approach for 5% damped System 2 (all displacements in mm)

$e_a/b=0$	a_{gy}	$a_{gy}+a_{g\theta}$	$a_{gy}-a_{g\theta}$	Actual torsional amplification
SAP	90.6	112.6	81.3	1.24
Program	90.6	112.5	82.3	1.24
SAP/Program	1.00	1.00	0.99	1.00

e_a/b	Shifting away from CR			Shifting towards CR			Torsional amplification (SAP)	
	SAP	Program	SAP/Program	SAP	Program	SAP/Program	Shift 1	Shift 2
0.01	91.8	92.4	0.99	90.6	90.4	1.00	1.01	1.01
0.05	94.0	95.4	0.99	91.2	90.2	1.01	1.04	1.04
0.10	90.6	92.5	0.98	92.3	89.9	1.03	1.00	1.02
0.15	87.2	89.0	0.98	92.0	88.3	1.04	0.96	1.02
0.20	81.5	83.1	0.98	99.2	93.7	1.06	0.90	1.10
0.25	73.2	74.5	0.98	116.5	108.5	1.07	0.81	1.29
0.30	63.4	64.2	0.99	125.8	116.1	1.08	0.70	1.39
0.35	53.5	53.6	1.00	126.8	116.4	1.09	0.59	1.40
0.40	49.8	52.8	0.94	121.1	111.5	1.09	0.55	1.34
0.45	50.1	53.4	0.94	111.8	103.8	1.08	0.55	1.23
0.49	50.3	53.6	0.94	103.9	97.4	1.07	0.56	1.15

Table 7-9: Peak displacements for the conventional approach for 0.1% damped System 2 (all displacements in mm)

$e_a/b=0$	a_{gy}	$a_{gy}+a_{g\theta}$	$a_{gy}-a_{g\theta}$	Actual torsional amplification
SAP	168.3	161.4	203.5	1.21
Program	169.6	160.9	204.0	1.20
SAP/Program	0.99	1.00	1.00	1.01

e_a/b	Shifting away from CR			Shifting towards CR			Torsional amplification (SAP)	
	SAP	Program	SAP/Program	SAP	Program	SAP/Program	Shift 1	Shift 2
0.01	175.1	176.7	0.99	163.9	163.9	1.00	1.04	1.04
0.05	170.7	173.0	0.99	110.5	110.4	1.00	1.01	1.01
0.10	146.2	146.7	1.00	135.7	136.3	1.00	0.87	0.87
0.15	104.3	104.3	1.00	196.6	192.8	1.02	0.62	1.17
0.20	87.7	88.0	1.00	217.8	214.5	1.02	0.52	1.29
0.25	77.8	78.0	1.00	162.7	158.3	1.03	0.46	0.97
0.30	65.7	65.8	1.00	153.7	153.1	1.00	0.39	0.91
0.35	54.3	54.4	1.00	153.4	152.6	1.01	0.32	0.91
0.40	54.8	54.9	1.00	142.8	141.8	1.01	0.33	0.85
0.45	55.4	55.5	1.00	170.6	165.0	1.03	0.33	1.01
0.49	55.7	55.8	1.00	184.0	170.0	1.08	0.33	1.09

Table 7-10: Peak displacements for the proposed approach for 5% damped elastic System 1 (all displacements in mm)

$\overline{e}_a/b=0$	a_{gy}	$a_{gy}+a_{g\theta}$	$a_{gy}-a_{g\theta}$	Actual torsional amplification	
SAP	109.6	100.7	118.6	1.08	
Program	109.7	100.9	118.5	1.08	
SAP/Program	1.00	1.00	1.00	1.00	
$\overline{e}_a/b$	SAP	Program	SAP/Program	Torsional amplification	
				SAP	Program
0.01	119.3	119.4	1.00	1.09	1.09
0.02	130.7	131.0	1.00	1.19	1.19
0.03	142.2	142.8	1.00	1.30	1.30
0.04	158.5	158.8	1.00	1.45	1.45
0.05	176.4	176.7	1.00	1.61	1.61
0.06	194.2	194.6	1.00	1.77	1.77
0.07	212.1	212.5	1.00	1.94	1.94
0.08	230.4	230.4	1.00	2.10	2.10
0.09	248.3	248.2	1.00	2.27	2.26
0.10	265.6	266.1	1.00	2.42	2.43

Table 7-11: Peak displacements for the proposed approach for 5% damped elastic System 2 (all displacements in mm)

$\overline{e}_a/b=0$	a_{gy}	$a_{gy}+a_{g\theta}$	$a_{gy}-a_{g\theta}$	Actual torsional amplification	
SAP	90.6	112.6	81.3	1.24	
Program	90.6	112.5	82.3	1.24	
SAP/Program	1.00	1.00	0.99	1.00	
$\overline{e}_a/b$	SAP	Program	SAP/Program	Torsional amplification	
				SAP	Program
0.01	127.4	127.8	1.00	1.41	1.41
0.02	165.6	166.3	1.00	1.83	1.84
0.03	204.0	205.1	1.00	2.25	2.26
0.04	242.6	243.9	1.00	2.68	2.69
0.05	281.3	282.9	0.99	3.11	3.12
0.06	320.0	322.1	0.99	3.53	3.56
0.07	358.7	361.1	0.99	3.96	3.99
0.08	397.5	400.2	0.99	4.39	4.42
0.09	437.2	439.3	1.00	4.83	4.85
0.10	474.5	478.5	0.99	5.24	5.28

Table 7-12: Element properties used in SAP analysis for nonlinear isolation system[1]

	Effective properties		Nonlinear properties		
	Stiffness	Damping	Stiffness	Yield strength	Post-yield stiffness ratio (K_d/K)
	K_d	C	$K = K_d + Q/u_y$	$F = Q + K_d u_y$	
Element	(kN/m)	(kN-sec/m)	(kN/m)	(kN)	
1	21.1	0	1124.8	5.6	0.0188
2	44.0	0	2251.3	11.3	0.0196
3	45.8	0	1149.4	5.7	0.0398

[1]Exponent used in the Bouc-Wen model is 5 for uncoupled and 2 for coupled orthogonal behavior

Table 7-13: Peak displacements for the proposed approach for nonlinear isolation system—orthogonally uncoupled (all displacements in mm)

$\bar{e}_a/b = 0$	a_{gy}	$a_{gy} + a_{g\theta}$	$a_{gy} - a_{g\theta}$	Actual torsional amplification	
SAP	59.0	57.7	62.1	1.05	
Program	59.0	57.8	62.0	1.05	
SAP/Program	1.00	1.00	1.00	1.00	
$\bar{e}_a/b$	SAP	Program	SAP/Program	Torsional amplification	
				SAP	Program
0.005	64.9	64.9	1.00	1.10	1.10
0.010	74.8	74.9	1.00	1.27	1.27
0.015	86.7	86.9	1.00	1.47	1.47
0.020	98.9	99.3	1.00	1.68	1.68
0.025	110.3	110.7	1.00	1.87	1.88
0.030	121.3	121.8	1.00	2.06	2.06
0.035	133.7	134.4	1.01	2.27	2.28
0.040	147.1	148.0	1.01	2.49	2.51
0.045	160.6	161.6	1.01	2.72	2.74
0.050	173.9	175.0	1.01	2.95	2.97

Table 7-14: Peak displacements for the proposed approach for nonlinear isolation system--orthogonally coupled (all displacements in mm)

$\bar{e}_a/b=0$	a_{gy}	$a_{gy}+a_{g\theta}$	$a_{gy}-a_{g\theta}$	Actual torsional amplification
SAP	57.0	43.2	67.4	1.18
Program	57.0	43.1	67.6	1.19
SAP/Program	1.00	1.00	1.00	1.00

$\bar{e}_a/b$	SAP	Program	SAP/Program	Torsional amplification	
				SAP	Program
0.005	68.7	68.8	1.00	1.21	1.21
0.010	80.4	80.6	1.00	1.41	1.41
0.015	91.2	91.4	1.00	1.60	1.60
0.020	100.4	100.6	1.00	1.76	1.77
0.025	110.0	110.4	1.00	1.93	1.94
0.030	122.1	122.7	1.01	2.14	2.15
0.035	136.0	136.8	1.01	2.39	2.40
0.040	150.5	151.4	1.01	2.64	2.66
0.045	164.9	165.9	1.01	2.89	2.91
0.050	179.3	180.5	1.01	3.15	3.17

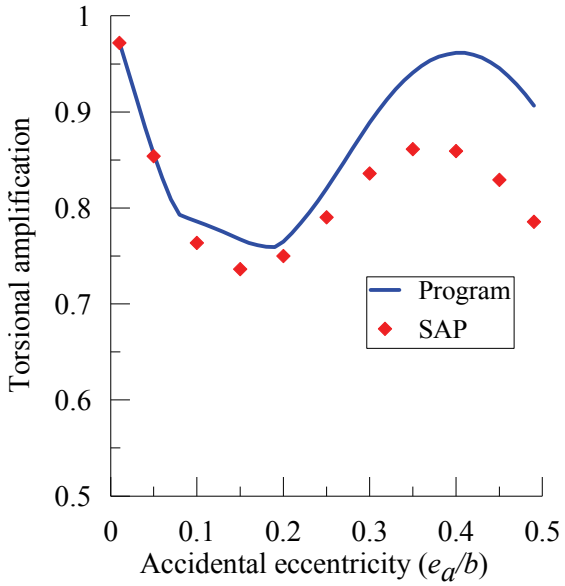

(a) 5% damped elastic system, Shift 1

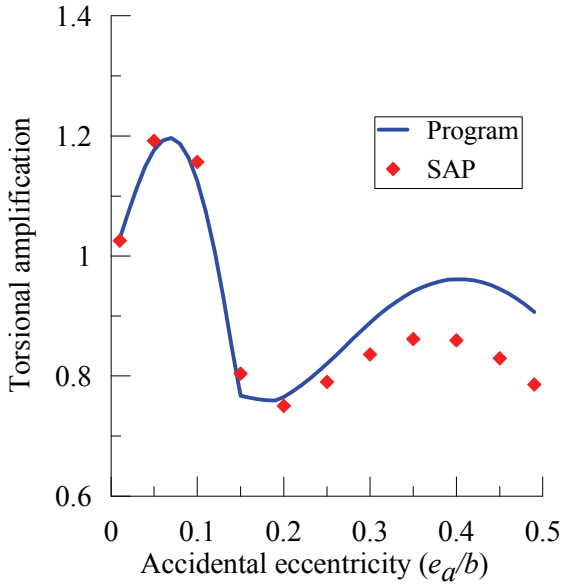

(b) 5% damped elastic system, Shift 2

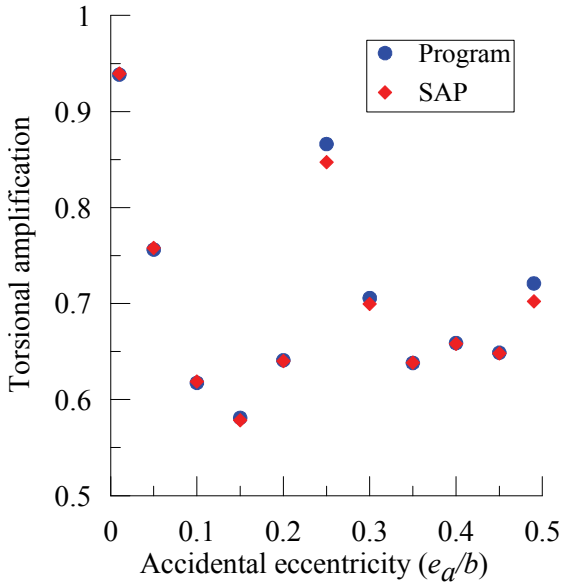

(c) 0.1% damped elastic system, Shift 1

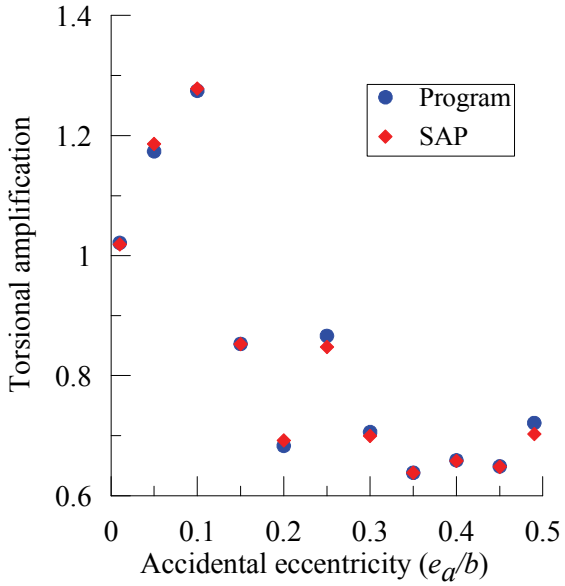

(d) 0.1% damped elastic system, Shift 2

Figure 7-20: Analysis of conventional approach for System 1

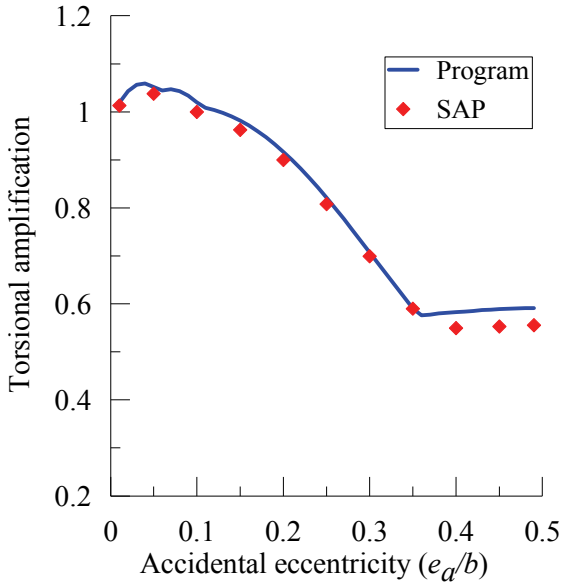

(a) 5% damped elastic system, Shift 1

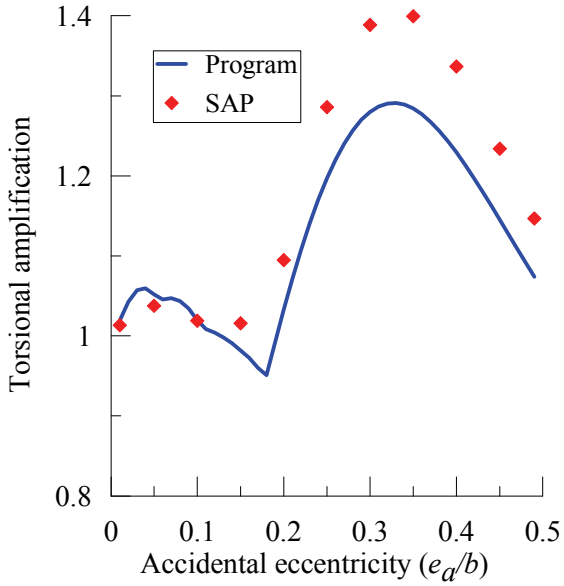

(b) 5% damped elastic system, Shift 2

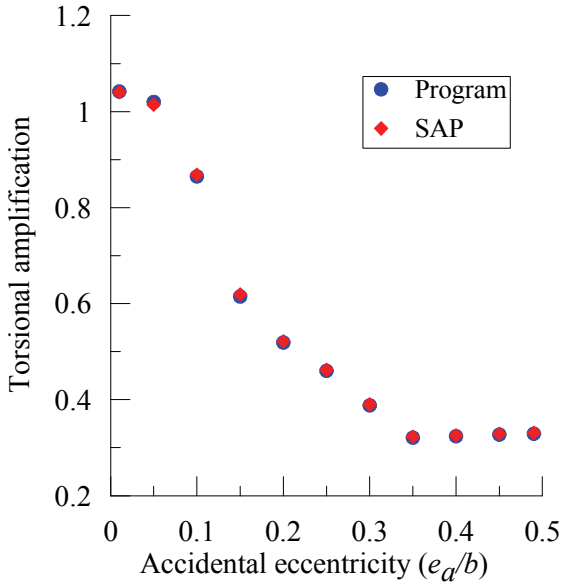

(c) 0.1% damped elastic system, Shift 1

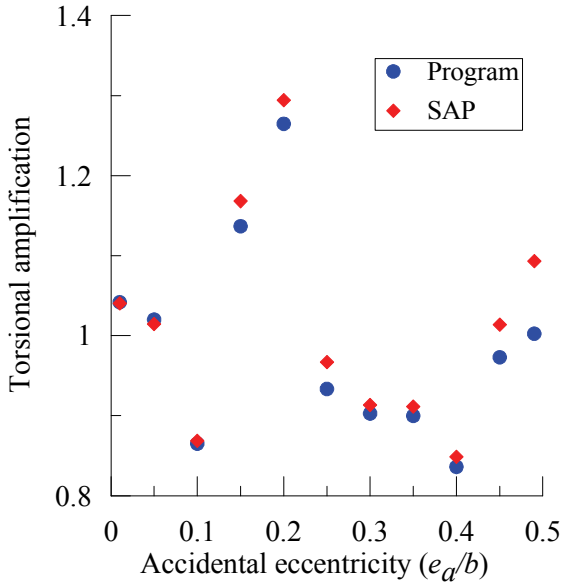

(d) 0.1% damped elastic system, Shift 2

Figure 7-21: Analysis of conventional approach for System 2

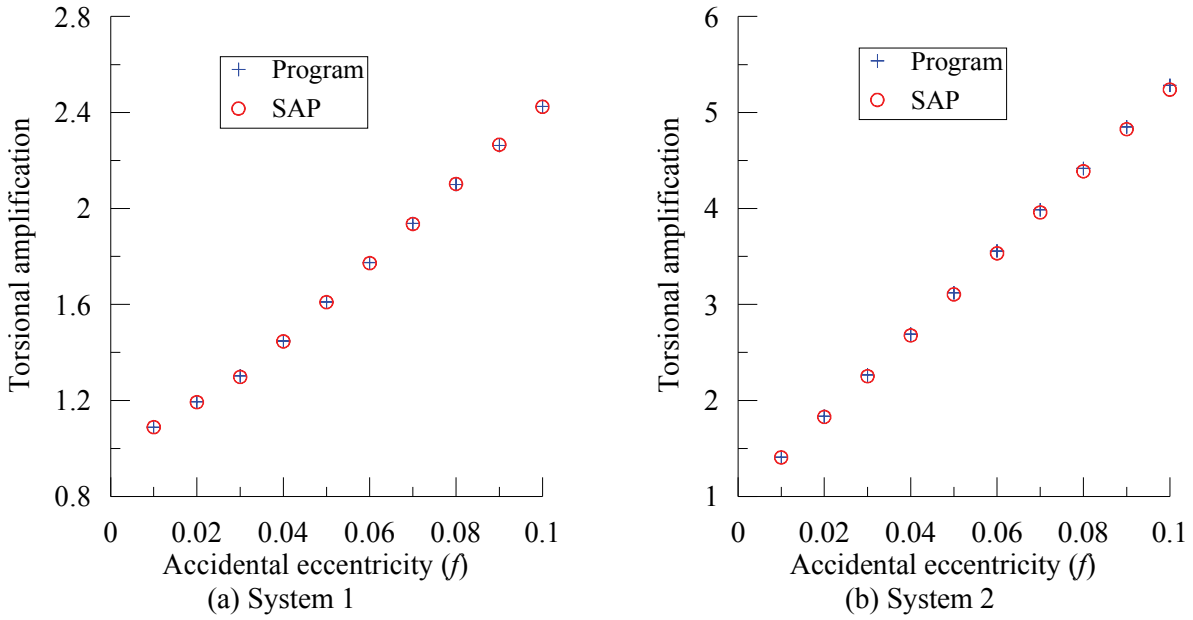

(a) System 1 (b) System 2

Figure 7-22: Proposed approach for 5% damped elastic systems, $f = \bar{e}_a / b$

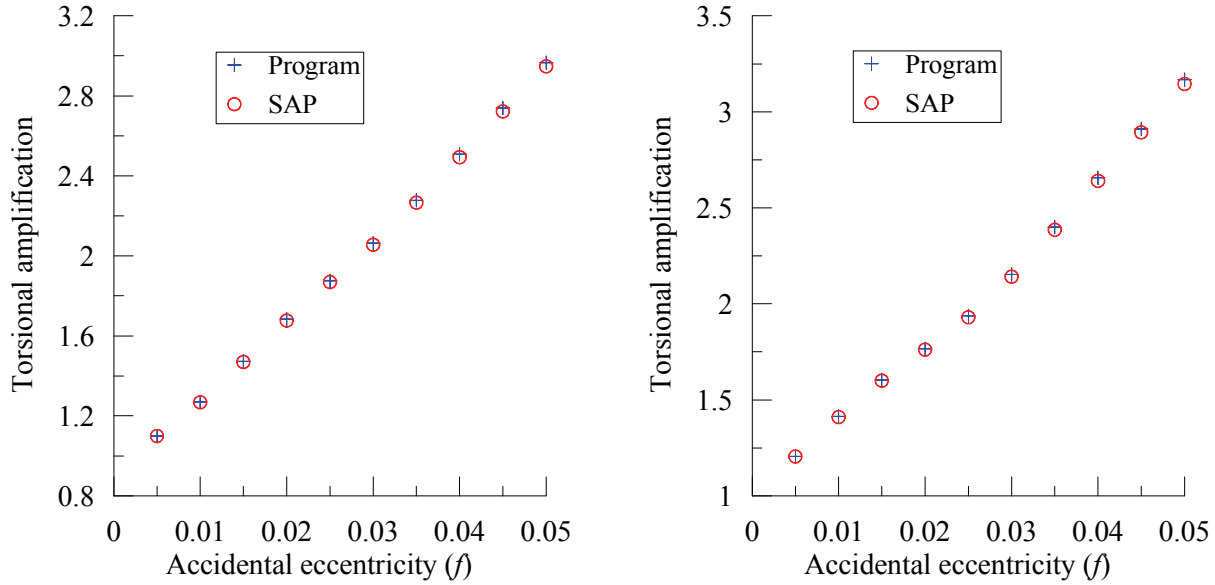

(a) Nonlinear isolation system, $T_d = 4$ sec, $\Omega = 1.25$, $Q/W = 0.05$, $Y = 5$ mm, orthogonally uncoupled

(b) Nonlinear isolation system, $T_d = 4$ sec, $\Omega = 1.25$, $Q/W = 0.05$, $Y = 5$ mm, orthogonally coupled

Figure 7-23: Proposed approach for nonlinear isolation system, $f = \bar{e}_a / b$

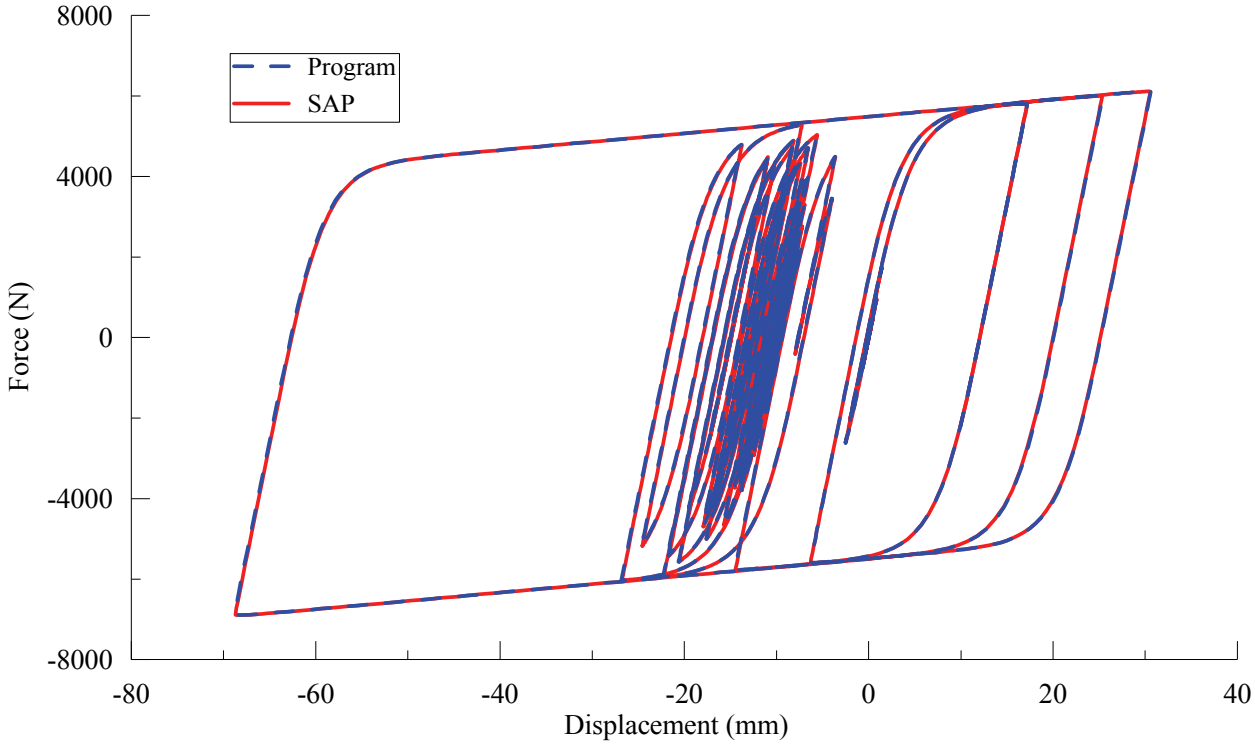

Figure 7-24: Hysteresis for element 1, $T_d = 4$ sec, $\Omega = 1.25$, $Q/W = 0.05$, $Y = 5$ mm, orthogonally coupled

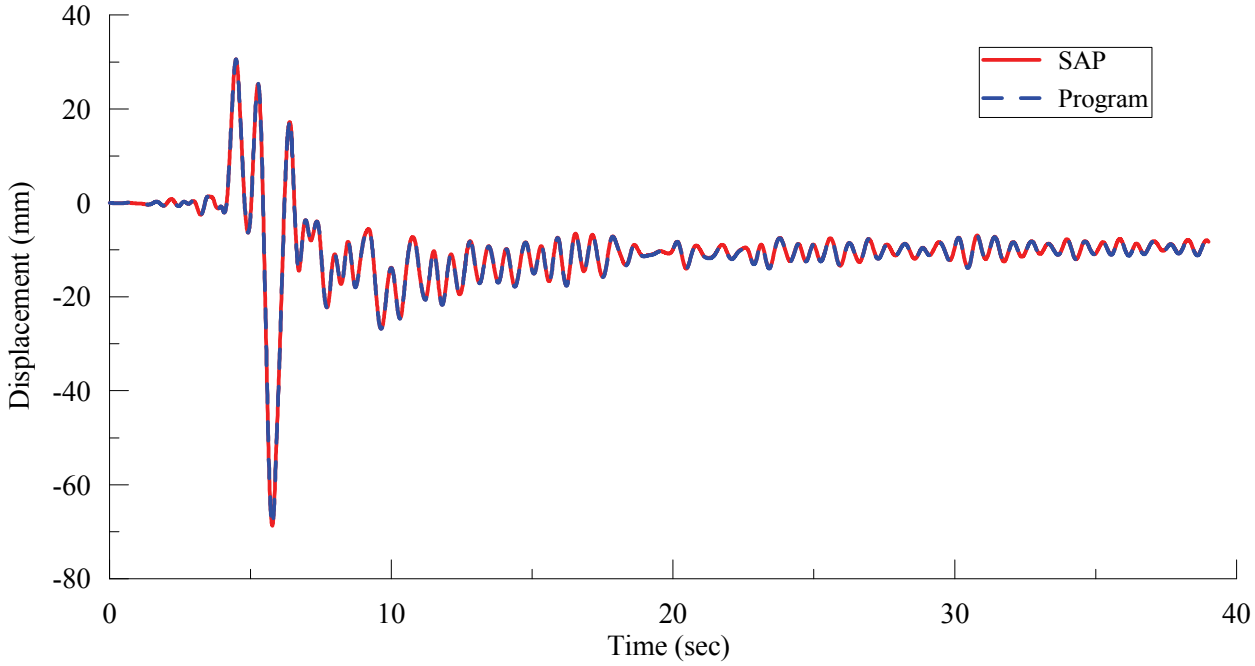

Figure 7-25: *Y*-displacement history at the midpoint (edge) of side A, $T_d = 4$ sec, $\Omega = 1.25$, $Q/W = 0.05$, $Y = 5$ mm, orthogonally coupled

CHAPTER 8

EFFECT OF ROTATIONAL GROUND MOTIONS ON STRUCTURAL RESPONSE

8.1. Introduction

Rotational components of the ground motion are not usually considered in seismic analysis and design of structures. Rocking ground motion is expected to influence the response of tall and slender structures and base-isolated structures (e.g., Wolf et al., 1983; Zembaty and Boffi, 1994; Politopoulos, 2010). The effects of torsional ground motion are expected to be greatest in near-symmetric buildings (De La Llera and Chopra, 1994c).

This chapter investigates the effect of rotational ground motion on the response of three example structures: a chimney (Section 8.2), a base-isolated building (Section 8.3), and a fixed-base building (Section 8.4). The observations made from these studies demonstrate the significance of consideration of the rotational ground motion but, the observations cannot be generalized due to limited scope of the study.

The rotational ground motions used here are the free-field components calculated in Chapter 5. Foundation will generally modify (and reduce) the free-field motions due to incoherency and soil-structure interaction, but those effects are not considered here.

8.2. Description of Ground Motions

The seismic event described in Chapter 2 is considered here for all the analyses. The rotational ground motions are calculated using the surface distribution method (SDM) presented in Chapter 5. In the description of the ground motions, the EW and NS directions are the x and y directions, respectively. Figures 8-1 and 8-2 provide a description of the ground motion: a) translational acceleration time series

recorded at station FA1_1 and the associated 5% damped spectra (Figure 8-1); and b) rotational acceleration time series at the same station and the associated 5% damped spectra (Figure 8-2).

8.3. Seismic Response of a Chimney

The objectives of this study are to assess the contribution of rocking ground motion to the lateral response of a chimney and to study how the contribution varies as the height of the chimney increases.

8.3.1. Continuum Model

A continuum model of a chimney is shown in Figure 8-3. The profile along the vertical direction is arbitrary but continuous. The variation in mass/unit length (m), cross-sectional area (A), flexural rigidity (EI) and inherent damping (c) along the vertical direction are also continuous. The chimney is supported on a flexible foundation of mass m_f and mass moment of inertia I_f. Foundation flexibility is modeled through a set of translational and rocking springs with stiffness K_f and K_{fr}, respectively. Foundation damping is modeled through a set of translational and rocking dashpots with viscous damping coefficients C_f and C_{fr}, respectively.

The differential equation governing the lateral vibration of the chimney when subjected to a set of unidirectional horizontal and rocking ground excitations may be expressed as

$$\begin{aligned} &m(h)\frac{\partial^2 u(h,t)}{\partial t^2}+c(h)\frac{\partial u(h,t)}{\partial t}+\frac{\partial^2}{\partial h^2}\left[EI(h)\frac{\partial^2 u(h,t)}{\partial h^2}\right]+\frac{\partial}{\partial h}\left[F_A(h,t)\frac{\partial u(h,t)}{\partial h}\right]=P_{eff}(h,t) \\ &P_{eff}(h,t)=-m(h)\frac{\partial^2 u_g(t)}{\partial t^2}+hm(h)\frac{\partial^2 \theta_g(t)}{\partial t^2}+\frac{\partial F_A(h,t)}{\partial h}\theta_g(t) \end{aligned} \tag{8-1}$$

In Eq (8-1), $\ddot{u}_g$ and $\ddot{\theta}_g$ (an over dot represents the derivative with respect to time) are the horizontal and rocking ground motions, respectively, and $F_A(h,t)$ is the axial force intensity over the height. The so-

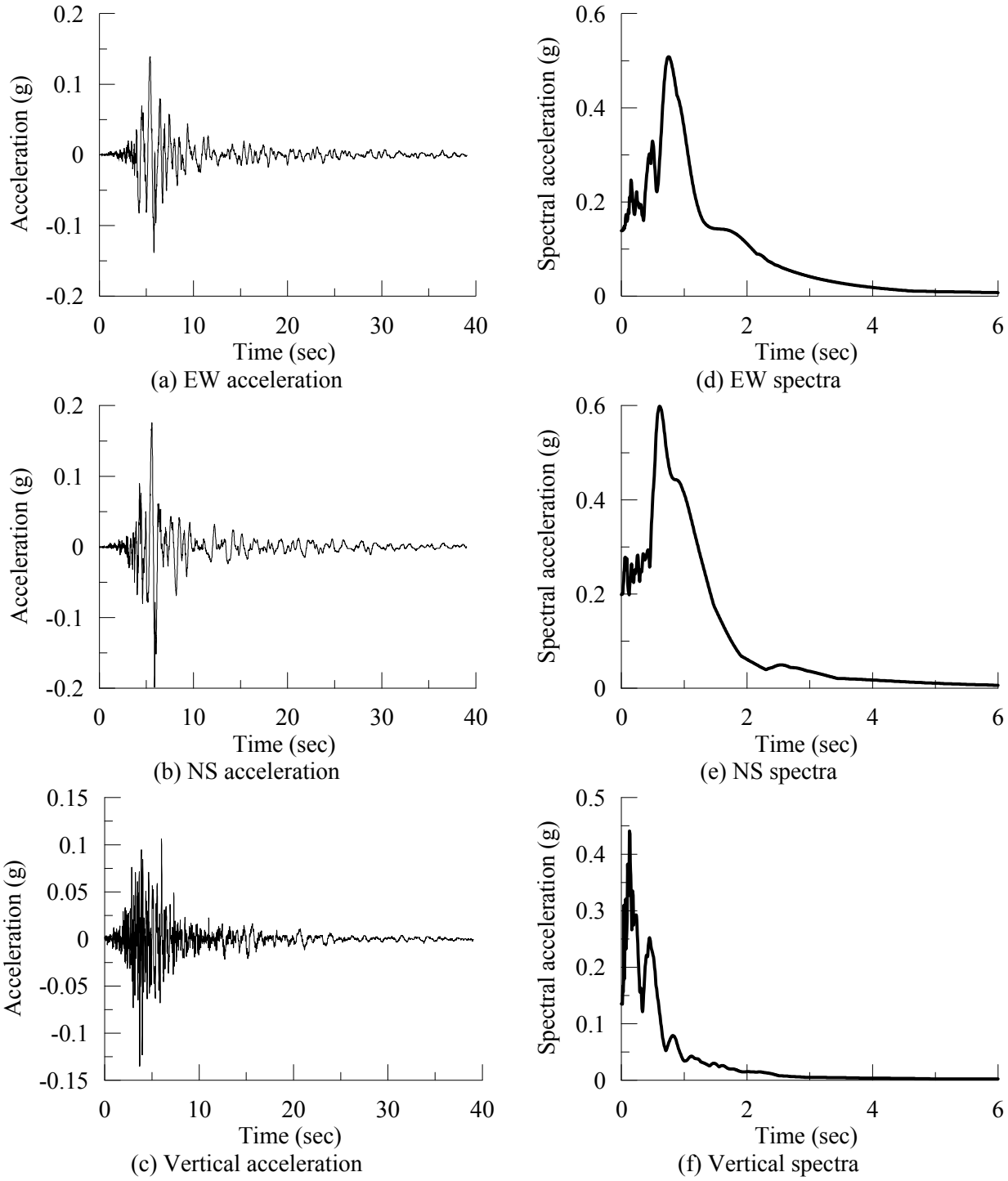

Figure 8-1: Translational ground motions recorded at station FA1_1 and associated 5% damped spectra

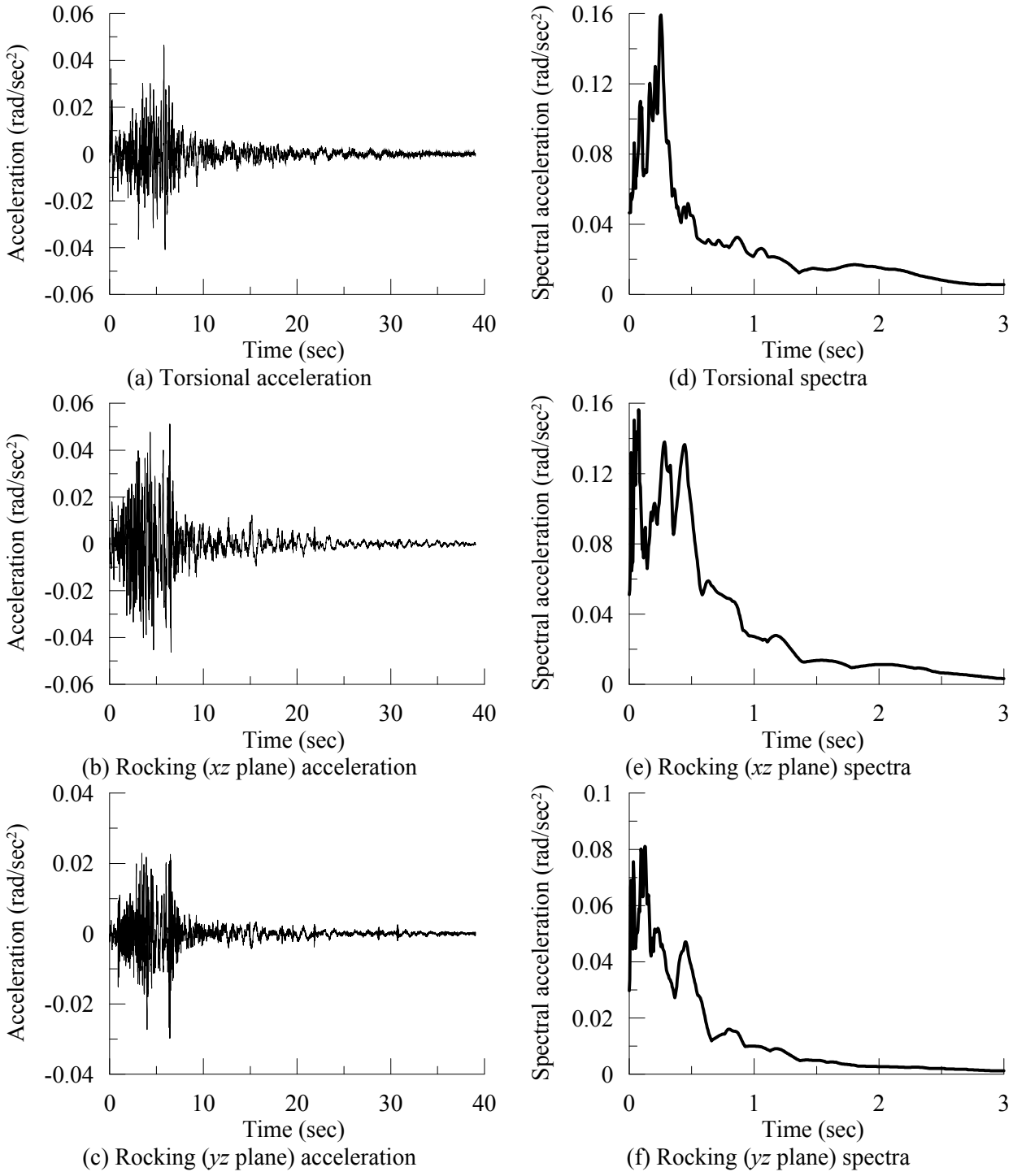

Figure 8-2: Rotational ground motions at station FA1_1 and associated 5% damped spectra

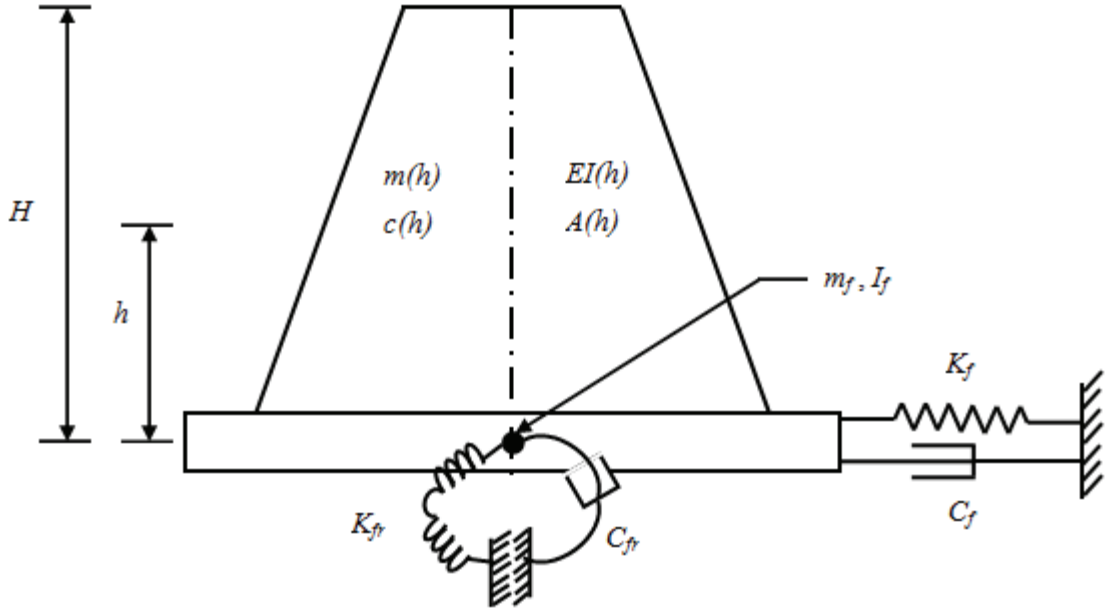

Figure 8-3: Continuum model of a chimney on a flexible foundation

called $P-\Delta$ effect is accounted for directly. The rocking rotation θ_g is an additional input to the problem. The axial load is also time-varying to enable consideration of vertical ground motion.

The associated four boundary conditions are:

$$m_f \frac{\partial^2 u(0,t)}{\partial t^2} + C_f \frac{\partial u(0,t)}{\partial t} + K_f u(0,t) + F_A(0,t)\frac{\partial u(0,t)}{\partial h} + \frac{\partial}{\partial h}\left[EI(0)\frac{\partial^2 u(0,t)}{\partial h^2}\right] = G(t)$$

where (8-2)

$$G(t) = -m_f \frac{\partial^2 u_g(t)}{\partial t^2} + F_A(0,t)\theta_g(t)$$

$$I_f \frac{\partial^3 u(0,t)}{\partial h \partial t^2} + C_{fr} \frac{\partial^2 u(0,t)}{\partial h \partial t} + K_{fr} \frac{\partial u(0,t)}{\partial h} - EI(0)\frac{\partial^2 u(0,t)}{\partial h^2} = R(t) = I_f \frac{\partial^2 u_g(t)}{\partial t^2} \quad (8\text{-}3)$$

$$\frac{\partial}{\partial h}\left[EI(H)\frac{\partial^2 u(H,t)}{\partial h^2}\right] + F_A(H,t)\frac{\partial u(H,t)}{\partial h} = F_A(H,t)\theta_g(t) \quad (8\text{-}4)$$

$$\frac{\partial^2 u(H,t)}{\partial h^2} = 0 \tag{8-5}$$

8.3.2. Ground Motions Used for Analysis

The horizontal and rocking excitations presented in panel a of Figure 8-1 and panel b of Figure 8-2, respectively. The effects of vertical motion (panel c of Figure 8-1) are reported in Appendix D.

8.3.3. Solution of the Differential Equation using Explicit Finite Difference Method

A computer program is developed to solve the governing differential equation using an explicit finite-difference algorithm. The salient features of the program along with a brief description of the algorithm and stability criterion are presented in Appendix D. The results obtained using this computer program are compared with those from the analysis of a stick model in SAP2000 (CSI, 2009) and are reported in that appendix. The verification example includes a straight-sided, annular chimney. Both flexible and fixed bases are considered. The results presented in Appendix D show the vertical excitation does not make any significant contribution to the lateral response of the chimney and so its effects are not reported in this chapter.

8.3.4. Mathematical Models

A series of annular chimneys with a linearly varying profile in the vertical direction is developed; see Figure 8-1. The outer and inner diameters just above the foundation are D_{ob} and D_{ib}, respectively. Let the slope of the outer surface with respect to horizontal axis be θ. Defining the ratio of height-to-outer diameter (or aspect ratio) $\eta = H/D_{ob}$ and normalized height $h^* = h/H$, the outer diameter at any height is given by

$$D_{oh} = D_{ob} f\left(h^*\right); f\left(h^*\right) = \left(1 - \frac{2\eta h^*}{\tan\theta}\right) \tag{8-6}$$

The same profile, $f\left(h^*\right)$, is considered for the inner diameter, which results in a wall thickness that follows the same profile function.

For all the six chimneys considered in this study: i) the outer diameter at the base is 5m; ii) the ratio of thickness to outer diameter at the base is 0.05; iii) the slope of the outer surface with respect to the horizontal axis is 89 degrees, and iv) the foundation is rigidly attached to the ground. Six aspect ratios are considered: 4, 6, 8, 10, 12 and 14. Material density is taken as 24.5 kN/m^3 and Young's modulus is set equal to 2.55×10^7 kN/m^2. The inherent structural damping is taken as 5% of critical. The fundamental periods of the chimneys are 0.13, 0.27, 0.47, 0.70, 0.96, and 1.25 sec for $\eta =$ 4, 6, 8, 10, 12 and 14, respectively. The time step of the input ground motion is 0.005 sec. To satisfy the stability criteria with a fairly large number of elements (see Appendix D), the analysis time step is reduced to 0.001 sec. Cubic interpolation is performed for the ground motion data at intermediate instants of time.

8.3.5. Analysis, Results and Discussion

Each chimney is analyzed with four different sets of ground motion inputs: i) lateral excitation only, ii) lateral plus rocking excitation, iii) lateral minus rocking excitation, and iv) rocking excitation only. The response quantities of interest are the tip lateral displacement, base shear and base moment. Table 8-1 summarizes the results for all six aspect ratios. The histories of calculated responses are presented in Figures 8-4 through 8-6 for $\eta = 14$. The time series are plotted for 12 sec, within which the peak responses occur. The variation of base shear and base moment with increasing aspect ratio does not change monotonically for any of the four sets of ground-motion inputs (Table 8-1).

Table 8-2 identifies the contributions of the rocking component to the response of the chimneys. When the excitation includes rocking and lateral inputs, the maximum response is taken as the greater of Lateral + rocking and Lateral - rocking. The column in Table 8-2 titled 'Lateral and rocking' presents these data; the column titled 'Ratio' presents the ratio of the maximum response to that due to the lateral

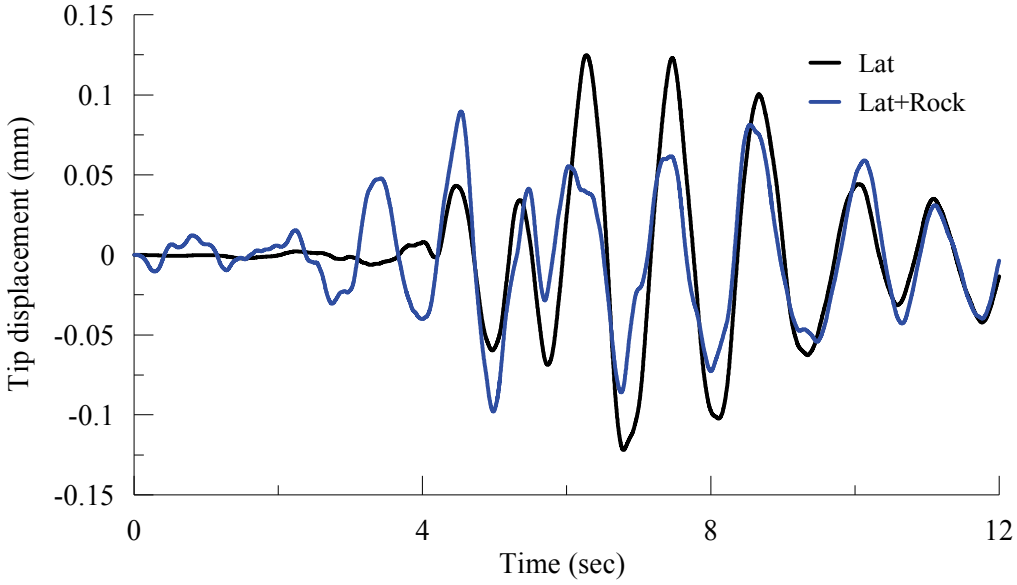

(a) Positive rocking excitation

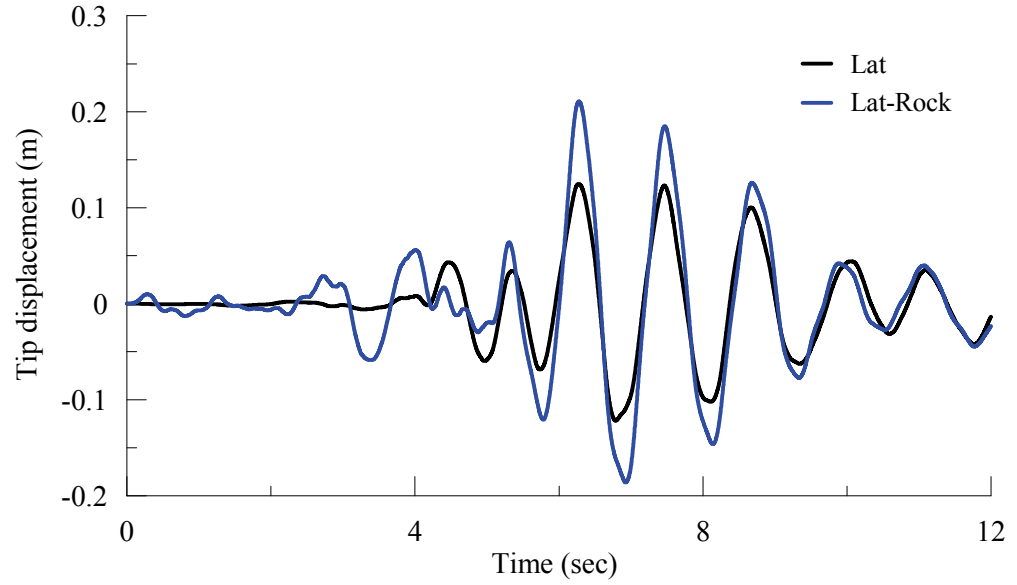

(b) Negative rocking excitation

Figure 8-4: Effect of rocking excitation on tip displacement, $\eta = 14$

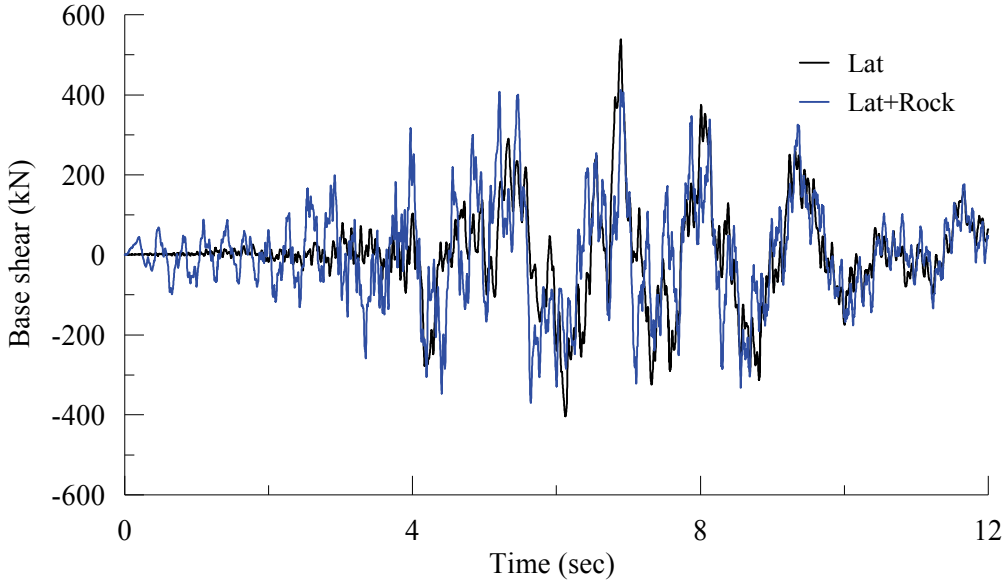

(a) Positive rocking excitation

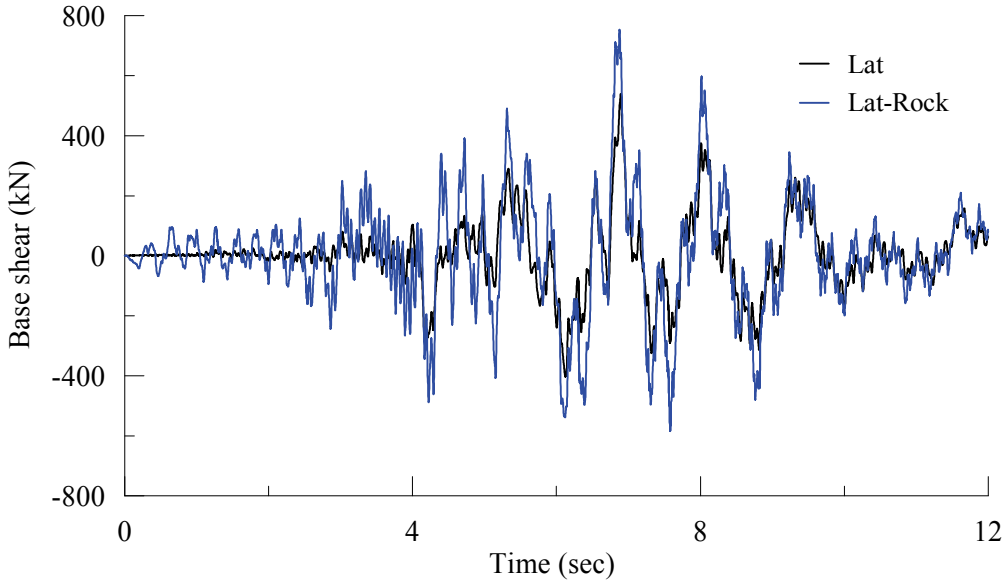

(b) Negative rocking excitation

Figure 8-5: Effect of rocking excitation on base shear, $\eta = 14$

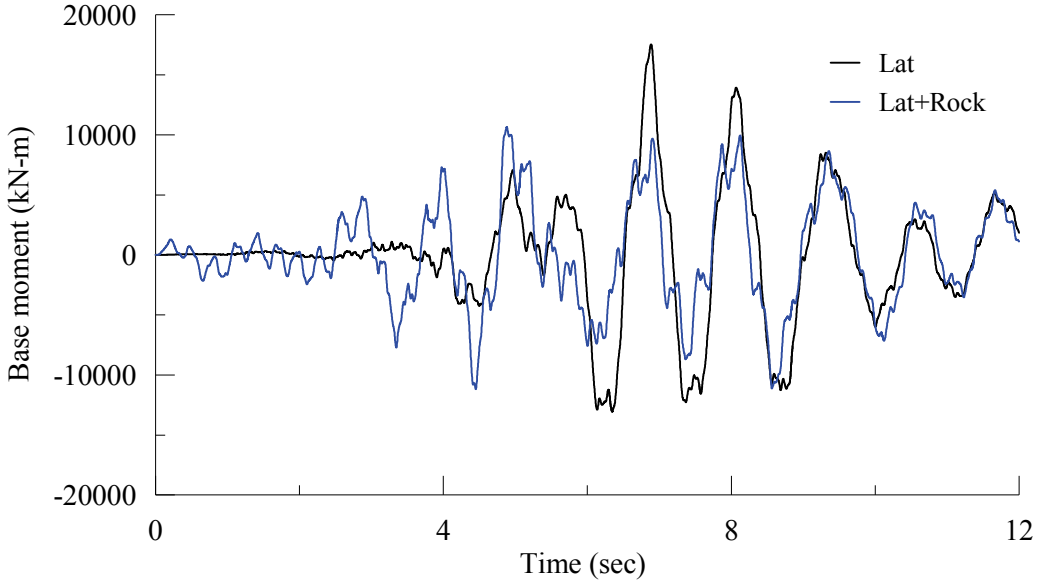

(a) Positive rocking excitation

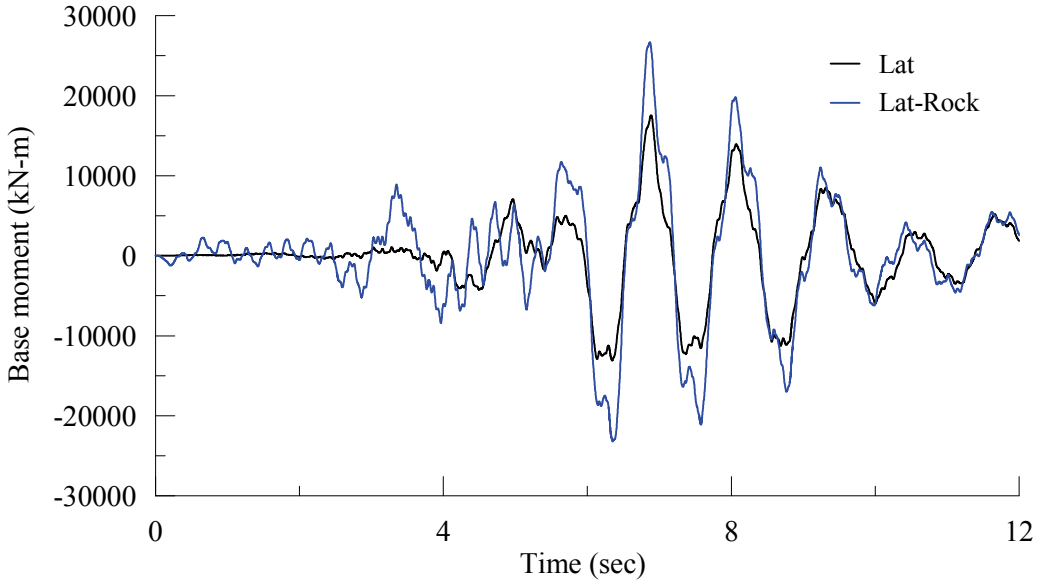

(b) Negative rocking excitation

Figure 8-6: Effect of rocking excitation on base moment, $\eta = 14$

Table 8-1: Response of linearly tapering chimneys to lateral and/or rocking excitation

	Lateral			Lateral + rocking			Lateral - rocking			Rocking		
	Tip Δ	Chimney base		Tip Δ	Chimney base		Tip Δ	Chimney base		Tip Δ	Chimney base	
		Shear	Moment		Shear	Moment		Shear	Moment		Shear	Moment
η^*	(mm)	(kN)	(kN-m)	(mm)	(kN)	(kN-m)	(mm)	(kN)	(kN-m)	(mm)	(kN)	(kN-m)
4	1	304	3035	2	347	3758	2	348	3973	1	142	1758
6	6	334	5257	11	617	10303	13	637	11418	9	426	7992
8	26	565	12391	49	783	21648	47	894	21384	30	552	14201
10	104	969	28485	110	999	30623	99	972	26503	40	331	10518
12	156	653	26021	144	639	23104	168	858	30244	49	275	8773
14	125	539	17534	98	413	11182	211	754	26687	86	339	10815

* $\eta = H/D_{ob}$

Table 8-2: Contributions from the rocking excitation- linearly tapered chimneys

	Tip Δ (mm)			Base shear (kN)			Base moment (kN-m)		
η^*	Lateral	Lateral and rocking	Ratio	Lateral	Lateral and rocking	Ratio	Lateral	Lateral and rocking	Ratio
(1)	(2)	(3)	(4)=(3)/(2)	(5)	(6)	(7)=(6)/(5)	(8)	(9)	(10)=(9)/(8)
4	1	2	1.36	304	348	1.15	3035	3973	1.31
6	6	13	2.18	334	637	1.91	5257	11418	2.17
8	26	49	1.85	565	894	1.58	12391	21648	1.75
10	104	110	1.05	969	999	1.03	28485	30623	1.08
12	156	168	1.07	653	858	1.32	26021	30244	1.16
14	125	211	1.69	539	754	1.40	17534	26687	1.52

* $\eta = H/D_{ob}$

Table 8-3: Response of straight chimneys to lateral and/or rocking excitation

	Lateral			Lateral + rocking			Lateral - rocking			Rocking		
	Tip Δ	Chimney base		Tip Δ	Chimney base		Tip Δ	Chimney base		Tip Δ	Chimney base	
		Shear	Moment		Shear	Moment		Shear	Moment		Shear	Moment
η^*	(mm)	(kN)	(kN-m)	(mm)	(kN)	(kN-m)	(mm)	(kN)	(kN-m)	(mm)	(kN)	(kN-m)
4	1	282	3480	2	326	4199	2	371	4914	1	131	1874
6	7	408	7528	11	605	11842	15	790	15661	10	468	10137
8	30	730	17455	46	941	27156	35	887	21806	25	585	15247
10	126	1599	49055	125	1669	51205	153	1726	57136	47	508	17914
12	111	831	29101	88	531	22164	171	1291	47613	67	499	18574
14	145	624	29248	95	689	19971	197	1204	45015	73	634	15907

* $\eta = H/D$

Table 8-4: Contributions from the rocking excitation to the response of straight chimneys

	Tip Δ (mm)			Base shear (kN)			Base moment (kN-m)		
η^*	Lateral	Lateral and rocking	Ratio	Lateral	Lateral and rocking	Ratio	Lateral	Lateral and rocking	Ratio
(1)	(2)	(3)	(4)=(3)/(2)	(5)	(6)	(7)=(6)/(5)	(8)	(9)	(10)=(9)/(8)
4	1	2	1.42	282	371	1.32	3480	4914	1.41
6	7	15	2.16	408	790	1.94	7528	15661	2.08
8	30	46	1.55	730	941	1.29	17455	27156	1.56
10	126	153	1.21	1599	1726	1.08	49055	57136	1.16
12	111	171	1.54	831	1291	1.55	29101	47613	1.64
14	145	197	1.36	624	1204	1.93	29248	45015	1.54

* $\eta = H/D$

input only. The 'Ratio' shows no definite trend with increasing η. The inclusion of the rocking excitation generally leads to a significant increase in response.

To ensure these changes in the response with the increasing aspect ratio are only due to changes in the dynamic characteristics of the chimneys and not the tapering of the vertical profile, the same set of analyses is repeated for chimneys with the same diameter and thickness over the height. Results are presented in Table 8-3 and Table 8-4. The observations are similar to those presented above.

8.4. Response of a Four-Story, Base-Isolated Building

The primary objectives of this study are to assess the contribution of rotational ground motions to displacement demands on the isolators and its effect on floor acceleration response spectra.

8.4.1. System Descriptions

The example building is that reported by Sarlis and Constantinou (2010). The building comprises three identical longitudinal frames with a center-to-center spacing of 9.75 m. The typical longitudinal frame is shown in Figure 8-7 (panel a); panel b shows the floor plan. The total weight on one longitudinal frame is 24020 kN and is supported by six identical Triple Friction Pendulum (TFP) isolators. The description of a typical isolator is reproduced from Sarlis and Constantinou (2010) in Figure 8-8 and Table 8-5. The typical force-displacement relationship for a typical TFP isolator is shown in Figure 8-9 (from Sarlis and Constantinou, 2010); five distinct sliding regimes are evident. However, for the properties of Table 8-5, sliding regimes II and III occur simultaneously and the regimes IV and V occur simultaneously. Further details on the building and its isolation system can be found in Sarlis and Constantinou (2010). The isolators have a displacement capacity of 934 mm at the onset of stiffening regime IV and an ultimate capacity of 952 mm (end of regime V). The SAP 2000 (CSI, 2009) model of the building developed by Sarlis and Constantinou (2010) is used for the analysis. The longitudinal and transverse directions are denoted *x* and *y*, respectively. The origin of the coordinate system is at the center of the plan area. The building is symmetric about both orthogonal axes.

Table 8-5: Properties of TFP isolator (Sarlis and Constantinou, 2010)[1]

$R_{eff_1} = R_{eff_4}$ (mm)	2096
$R_{eff_2} = R_{eff_3}$ (mm)	191
$d_1^* = d_4^*$ (mm)	452[1]
$d_2^* = d_3^*$ (mm)	24[1]
$\mu_1 = \mu_4$	0.108[2]
$\mu_2 = \mu_3$	0.030[2]
$a_1 = a_2 = a_3 = a_4$ (sec/m)	100

[1] 1. $d_i^* = d_i R_{effi} / R_i$, $R_{effi} = R_i - h_i, i = 1...4$
2. All values are for high speed conditions

8.4.2. Ground Motion Considered

The ground motions considered for analysis are those described by Figures 8-1 and 8-2 but scaled up by a factor equal to 4.5 to increase the isolator displacement demand. Vertical seismic inputs are not considered. The EW and NS motions are applied along the *x* and *y* directions, respectively.

8.4.3. Combination of Input Ground Motions

The ground motions are applied in 15 combinations as shown in Table 8-6. In these combinations, i) 'Lateral' denotes the simultaneous application of EW and NS motions; ii) 'Torsional' denotes the inclusion of torsional motion and the preceding + and – sign defines the direction in a right handed Cartesian coordinate system; and iii) 'Rocking' indicates the inclusion of rocking motion; the plane on which the motion acts and the sense of the motion are indicated by the attached strings. For example, combination 13 is the simultaneous application of the EW and NS motions, torsional motion in a negative sense, and rocking motions in a positive sense on the *xz* plane but in a negative sense on the *yz* plane (p denotes positive and n denotes negative).

(a) Typical longitudinal frame

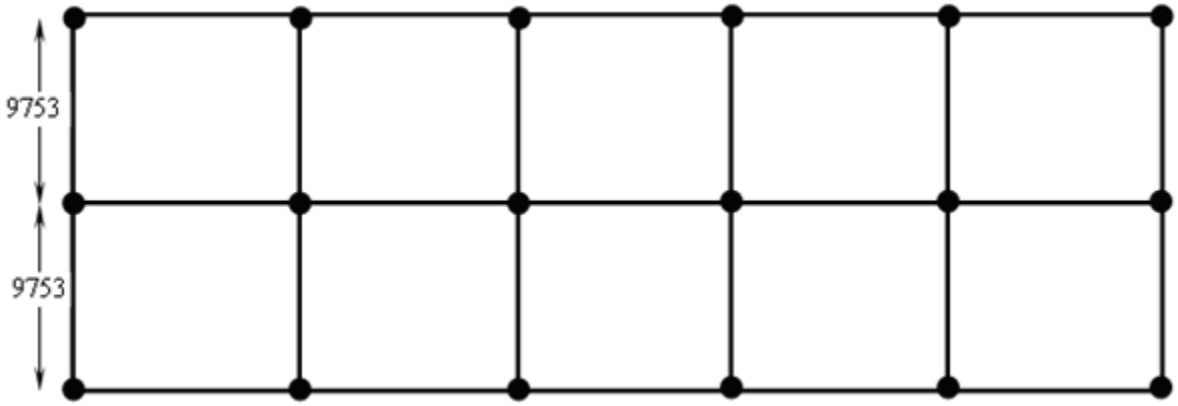

(b) Floor plan

Figure 8-7: Four story, isolated building, all dimensions are in mm (adapted from Sarlis and Constantinou, 2010)

8.4.4. Analysis, Results and Discussions

Analysis is performed using SAP2000 (CSI, 2009), which can accommodate translational and rotational base inputs. The four corners of the building are selected to report responses: A through D in fourth through first quadrant, respectively. Displacement responses are compared at these four corners at the isolator, ground floor and roof levels. Table 8-7 presents the maximum resultant displacement of the isolators at the four corners. Table 8-8 presents the maximum displacements along the *x* and *y* directions at the ground floor level. Table 8-9 presents the same data at the roof level.

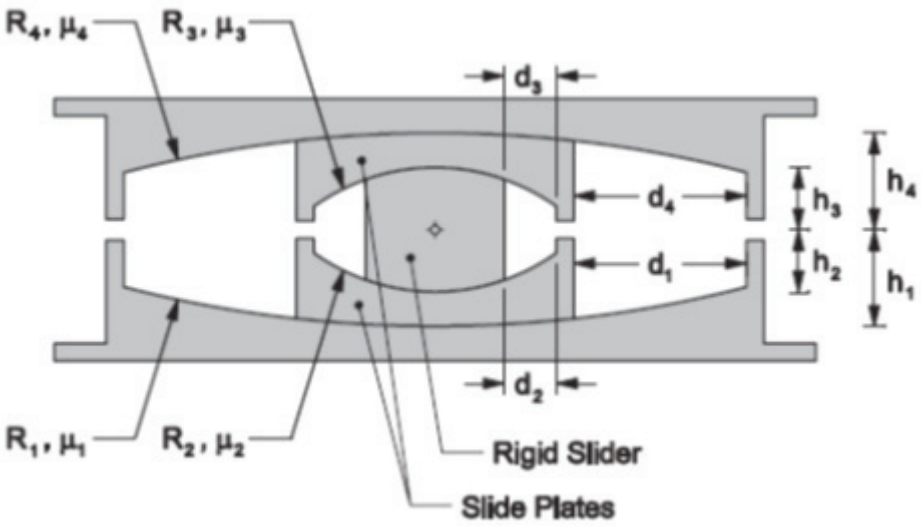

Figure 8-8: Schematic sketch of a Triple Friction Pendulum (TFP) isolator (Sarlis and Constantinou, 2010)

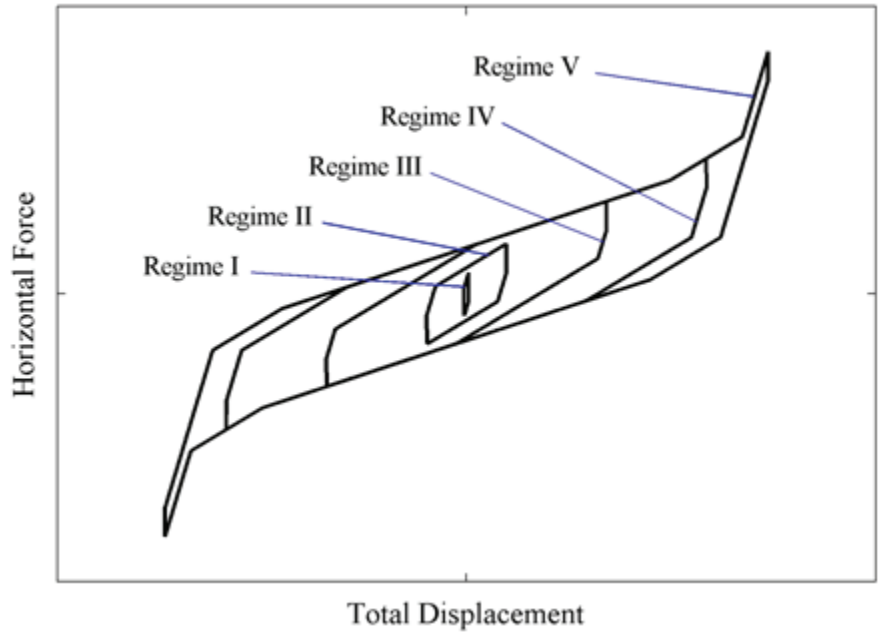

Figure 8-9: Force-displacement loops for a TFP isolator (Sarlis and Constantinou, 2010)

Table 8-6: Load combinations

Combination	Ground motions
1	Lateral
2	Lateral+Torsional
3	Lateral-Torsional
4	Lateral+Rocking_xzp_yzp
5	Lateral+Rocking_xzp_yzn
6	Lateral+Rocking_xzn_yzp
7	Lateral+Rocking_xzn_yzn
8	Lateral+Torsional+Rocking_xzp_yzp
9	Lateral+Torsional+Rocking_xzp_yzn
10	Lateral+Torsional+Rocking_xzn_yzp
11	Lateral+Torsional+Rocking_xzn_yzn
12	Lateral-Torsional+Rocking_xzp_yzp
13	Lateral-Torsional+Rocking_xzp_yzn
14	Lateral-Torsional+Rocking_xzn_yzp
15	Lateral-Torsional+Rocking_xzn_yzn

Effect of Torsional Ground Motion on Displacement Demand

The contribution of torsional ground motion to the response is assessed by comparing the greater of the responses in combinations 2 and 3 with that in combination 1. These two cases are denoted as 'Lat' and 'Lat-Tor', respectively, in Tables 8-7 through 8-9. Torsional ground motion amplifies the isolator displacement demand by as much as 12% (see Table 8-7). The maximum increase in displacement demand at the ground floor level is 6% in the *x* direction and 22% in the *y* direction (see Table 8-8) and 7% and 17%, respectively, at the roof level (see Table 8-9). The torsional contribution along *x* axis is not significant, due in part to the dimension of the building in the transverse direction, which is much smaller than that in the longitudinal direction. The torsional ground motion contributes significantly to the displacement along the *y* direction.

Table 8-7: Maximum resultant isolator displacement (base-isolated building)

	Corner			
	A	B	C	D
Combination	(mm)	(mm)	(mm)	(mm)
1	263	274	292	282
2	295	281	252	269
3	232	274	327	298
4	283	287	297	292
5	278	284	295	289
6	275	288	305	292
7	270	290	314	297
8	313	296	257	276
9	309	293	259	277
10	305	291	274	286
11	304	293	281	289
12	254	283	341	313
13	257	287	342	315
14	249	290	336	303
15	245	291	342	307
Lat	263	274	292	282
Lat-Tor	295	281	327	298
Lat-Rock	283	290	314	297
Lat-Tor-Rock	313	296	342	315
Increase (%)				
Torsional only	12	2	12	6
Rocking only	7	6	8	5
Torsional and Rocking	19	8	17	12

Effect of Rocking Ground Motion on Displacement Demand

The contribution of the rocking ground motion to the response is assessed by comparing the greater of the responses in combinations 4 through 7 with that of combination 1. The former is denoted as 'Lat-Rock' in Tables 8-7 through 8-9. The rocking ground motion amplifies the isolator displacement demand by as much as 8% (see Table 8-7). The maximum increase in displacement demand at the ground floor level is 9% in the *x* direction and 13% in the *y* direction (see Table 8-8), and 15% and 12%, respectively, at the roof level (see Table 8-9). The rocking ground motion contributes more to the displacement demand in the upper floor of the structure than at the isolator level, which is an expected result.

Table 8-8: Maximum displacement at the ground floor level (base-isolated building)

	Displacement along x direction				Displacement along y direction			
	Corner A	Corner B	Corner C	Corner D	Corner A	Corner B	Corner C	Corner D
Combination	(mm)	(mm)	(mm)	(mm)	(mm)	(mm)	(mm)	(mm)
1	239	253	253	239	165	165	198	198
2	252	228	228	252	201	201	166	166
3	219	268	268	219	148	148	233	233
4	228	241	241	228	180	180	192	192
5	230	244	244	230	169	169	186	186
6	256	268	268	256	160	160	210	210
7	256	276	276	256	157	157	222	222
8	241	215	215	241	212	212	155	155
9	245	221	221	245	203	203	151	151
10	268	247	247	268	193	193	195	195
11	269	251	251	269	197	197	209	209
12	213	266	266	213	151	151	234	234
13	217	271	271	217	148	148	231	231
14	238	283	283	238	162	162	234	234
15	236	287	287	236	155	155	245	245
Lat	239	253	253	239	165	165	198	198
Lat-Tor	252	268	268	252	201	201	233	233
Lat-Rock	256	276	276	256	180	180	222	222
Lat-Tor-Rock	269	287	287	269	212	212	245	245
Increase (%)								
Torsional only	5	6	6	5	22	22	18	18
Rocking only	7	9	9	7	9	9	13	13
Torsional and Rocking	12	13	13	12	29	29	24	24

Effect of Rotational Ground Motion on Displacement Demand

The rotational ground motion includes both torsional and rocking components. The contribution of the rotational ground motion to the response is assessed by comparing the greater of the responses in combinations 8 through 15 with that of combination 1. The former is denoted as 'Lat-Tor-Rock' in Tables 8-7 through 8-9. The torsional and rocking ground motions together amplify the isolator displacement demand by as much as 19% (see Table 8-7). The maximum increase in displacement demand at the ground floor level is 13% in the *x* direction and 29% in the *y* direction (see Table 8-8), and 23% and 31%,

Table 8-9: Maximum displacement at the roof level (base-isolated building)

	Displacement along x direction				Displacement along y direction			
	Corner A	Corner B	Corner C	Corner D	Corner A	Corner B	Corner C	Corner D
Combination	(mm)	(mm)	(mm)	(mm)	(mm)	(mm)	(mm)	(mm)
1	236	252	252	236	220	220	264	264
2	251	226	226	251	257	257	226	226
3	216	270	270	216	206	206	303	303
4	271	277	277	271	247	247	273	273
5	272	281	281	272	217	217	250	250
6	230	252	252	230	220	220	275	275
7	231	262	262	231	207	207	275	275
8	285	251	251	285	288	288	233	233
9	288	256	256	288	260	260	211	211
10	244	229	229	244	254	254	248	248
11	244	234	234	244	241	241	247	247
12	255	304	304	255	205	205	317	317
13	259	309	309	259	231	231	298	298
14	211	269	269	211	196	196	308	308
15	210	274	274	210	218	218	308	308
Lat	236	252	252	236	220	220	264	264
Lat-Tor	251	270	270	251	257	257	303	303
Lat-Rock	272	281	281	272	247	247	275	275
Lat-Tor-Rock	288	309	309	288	288	288	317	317
Increase (%)								
Torsional only	6	7	7	6	17	17	15	15
Rocking only	15	11	11	15	12	12	4	4
Torsional and Rocking	22	23	23	22	31	31	20	20

respectively, at the roof level (see Table 8-9). The combined effect of the torsional and rocking ground motions to the displacement demand can be significant.

Vertical Displacement of the Isolators

The vertical displacement histories of all four corner isolators are studied. Each of these isolators experienced uplift whenever the ground motion inputs include the rocking components (combinations 4 through 15). Note that vertical shaking is not imposed on the model. The uplift is not more than 1.7 mm. Hysteresis loops for the isolator at Corner A are shown in Figures 8-10 and 8-11 for the *x* and *y* directions, respectively. All combinations involving rocking input (4 through 15) show fluctuations of

lateral forces in the hysteresis loops, which is attributed to the significant fluctuations of the vertical load on each isolator due to the rocking components of ground motion. This observation is in consistent with De La Llera and Almazan (2003).

Floor Acceleration Spectra

Acceleration response is of particular importance if the performance of nonstructural components is a concern. Floor acceleration spectra at Corner A at the roof level are presented in Figures 8-12 and 8-13 for the *x* and *y* directions, respectively. In these figures, i) 'Lat' represent the spectra due to bidirectional translational excitations; ii) 'Lat-Tor' represents the maximum (envelope) spectra from the combinations 2 and 3; iii) 'Lat-Rock' denotes the maximum (envelope) spectra from the combinations 4 through 7; and iv) 'Lat-Tor-Rock' denotes the maximum (envelope) spectra from the combinations 8 through 15. The influence of the rocking component is seen in Figure 8-12. In this figure, the influence of the torsional motion is not as significant because the transverse direction is the shorter of the two plan dimensions. The influence of the torsional component is evident in Figure 8-13 and the rocking motion also contributes. The torsional and rocking inputs together amplify the acceleration response by 100% for periods less than 1 sec. On the basis of these results, the contribution of rotational ground motion to floor acceleration spectra cannot be neglected.

8.4.5. Torsional Response of the Building at the Stiffening Regime

It is of interest to understand the influence of the stiffening regime (sliding regimes IV and V) of the TFP on the torsional response of the building. To drive the isolator close to onset of regimes IV and V, when subjected to lateral excitations only, the motion is amplitude scaled by a factor 12. The resultant displacement of the isolator at Corner A is 873 mm, which is less than the displacement at the onset of the stiffening regime of 934 mm. Note the diameter of inner sliding surfaces (see Table 8-5) limits the maximum displacement at the end of regime V to 952 mm.

Analysis is performed with bidirectional translational motions and torsional ground motion in a negative sense, all with an amplitude scale factor of 12. Figure 8-14a presents the resultant displacement of the isolator at Corner A. Figure 8-14b presents the torsional rotation of the base mat. The force-displacement response of the isolator at Corner A is shown in Figure 8-15.

The isolator displacement is greater than 934 mm between $t = 5.91\text{sec}$ and $t = 5.99\,\text{sec}$ (see Figure 8-14a). In this period, the torsional rotation is only 0.0005 rad (see Figure 8-14b). The maximum rotation is approximately 0.011 rad, which occurs before the bearing enters the stiffening range. After $t = 5.99\,\text{sec}$, when the bearing unloads, the torsional rotation increases to a maximum of approximately 0.005 rad, which is much less than the peak torsional rotation because the torsional excitation subsides. Apparently the stiffening behavior of the isolators reduced the tendency of the building to rotate.

The maximum resultant displacement of the isolator is 940 mm (Figure 8-14a), which is less than its displacement capacity of 952 mm. Note the contribution of the torsional motion to the displacement demand along the *x* direction is much less than that along the *y* direction because the dimension of the building in the transverse direction is much smaller than in the longitudinal direction.

8.5. Response of Four Story Fixed-Base Building

The four-story building of Section 8.4 is then fixed at the ground floor level and reanalyzed to judge the influence of the rotational motions on displacement response and floor spectra. The ground motion used are those described in Section 8.4.2 without scaling (i.e., scale factor = 1.0). Corner displacements at the roof level are presented in Table 8-10. The contribution of the torsional ground motion in the *x* direction is close to zero but 11% in the *y* direction. The contribution from the rocking ground motion is rotational ground motions is negligible. Note that this behavior is likely the result of the assumed elastic close to zero in both directions. Floor acceleration spectra at Corner A of the roof level are compared in Figures 8-16 and 8-17 for the *x* and *y* directions, respectively. In both cases, the contribution from the behavior of the analyzed fixed-base building. If inelastic behavior had been considered, the behavior

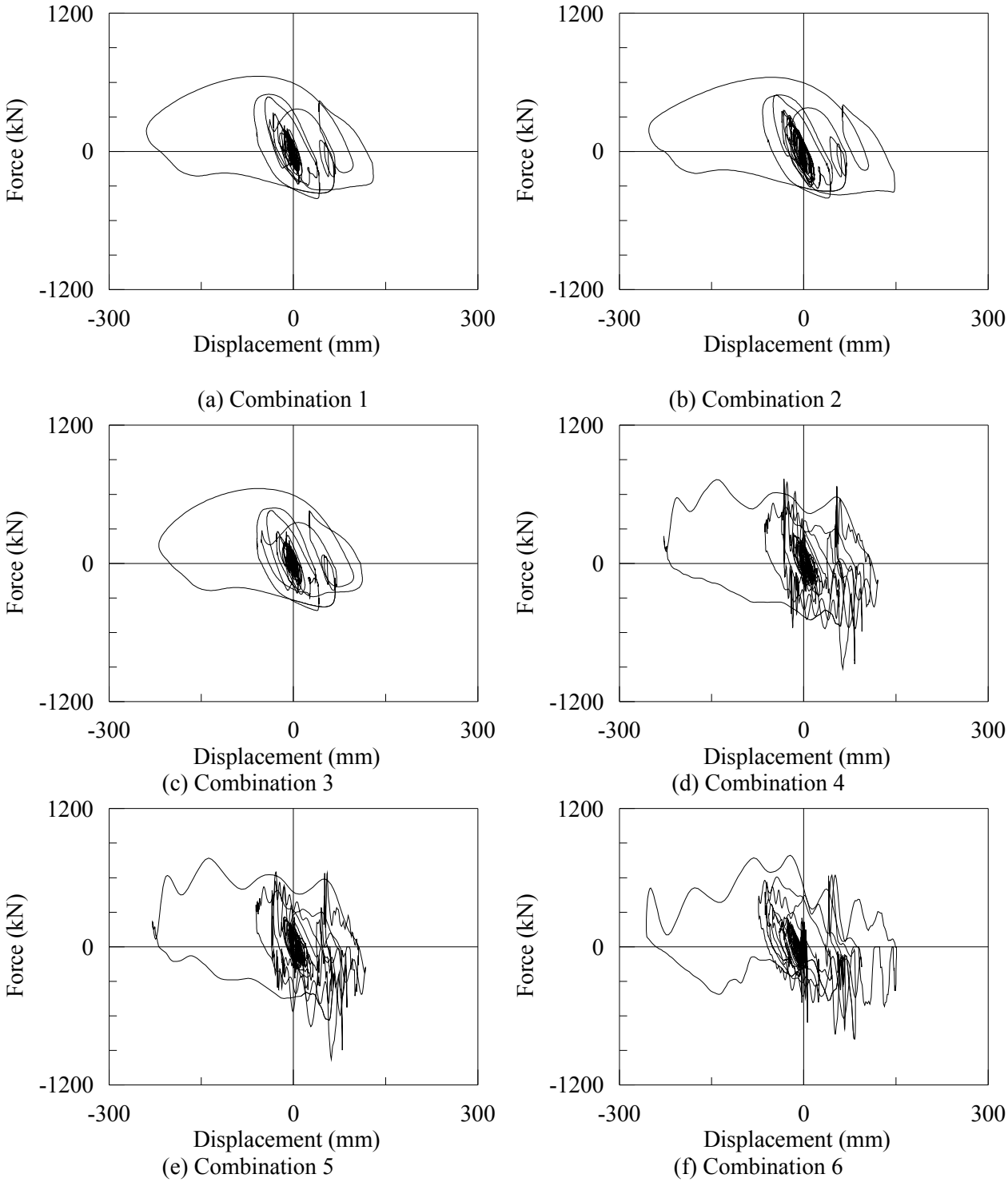

Figure 8-10: Hysteresis along the *x* direction of the isolator at Corner A of the base-isolated building, input scale factor = 4.5 (cont.)

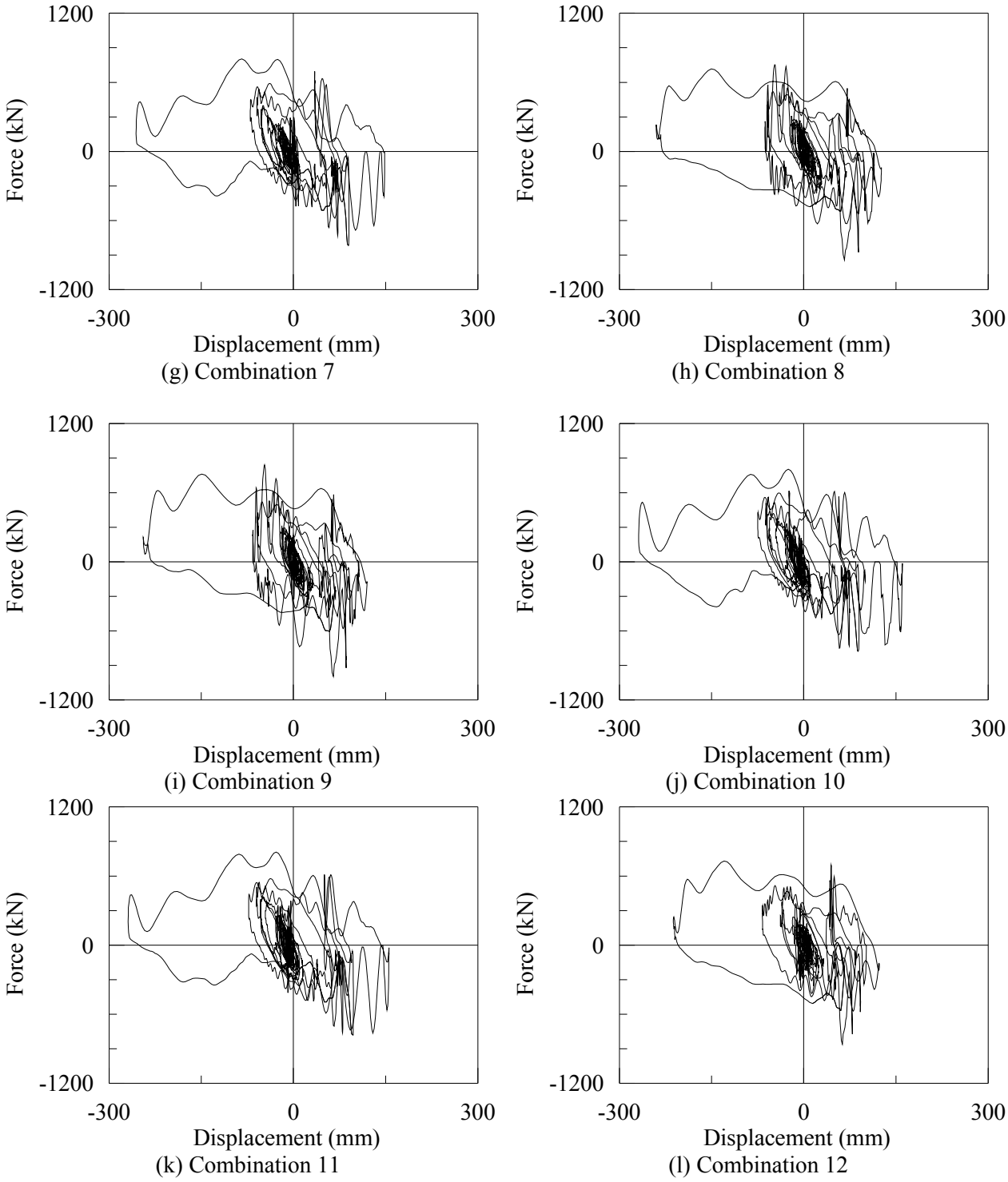

Figure 8-10: Hysteresis along the *x* direction of the isolator at Corner A of the base-isolated building, input scale factor = 4.5 (cont.)

would likely resemble that of the seismically isolated building, of which the behavior is controlled by the nonlinear nature of the isolators.

Note that although the rotational components of ground motion have a marked effect on the floor spectra of the isolated structure, the spectral demands in the isolated building are still significantly smaller than those of the non-isolated building for the same intensity of earthquake shaking.

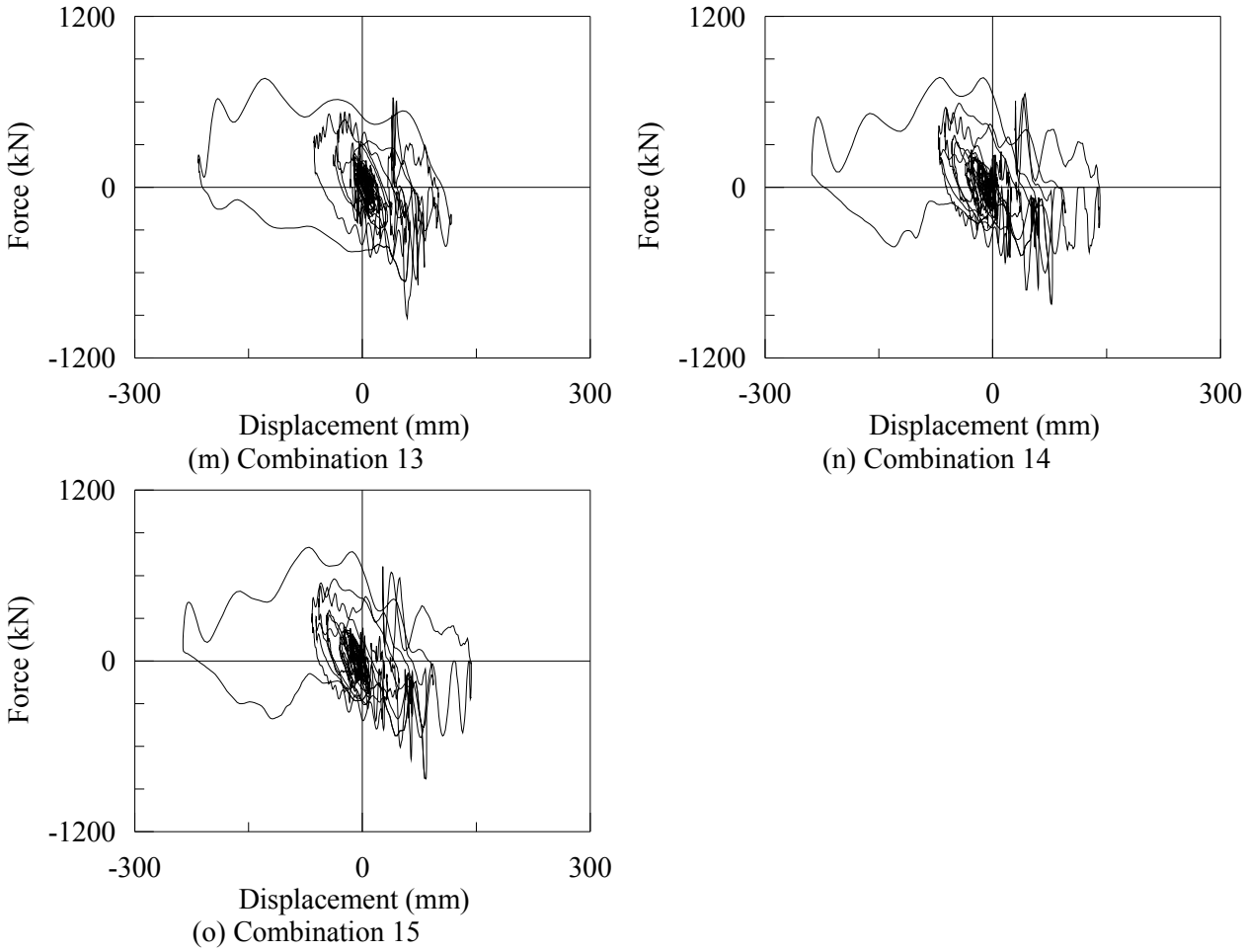

Figure 8-10: Hysteresis along the *x* direction of the isolator at Corner A of the base-isolated building, input scale factor = 4.5

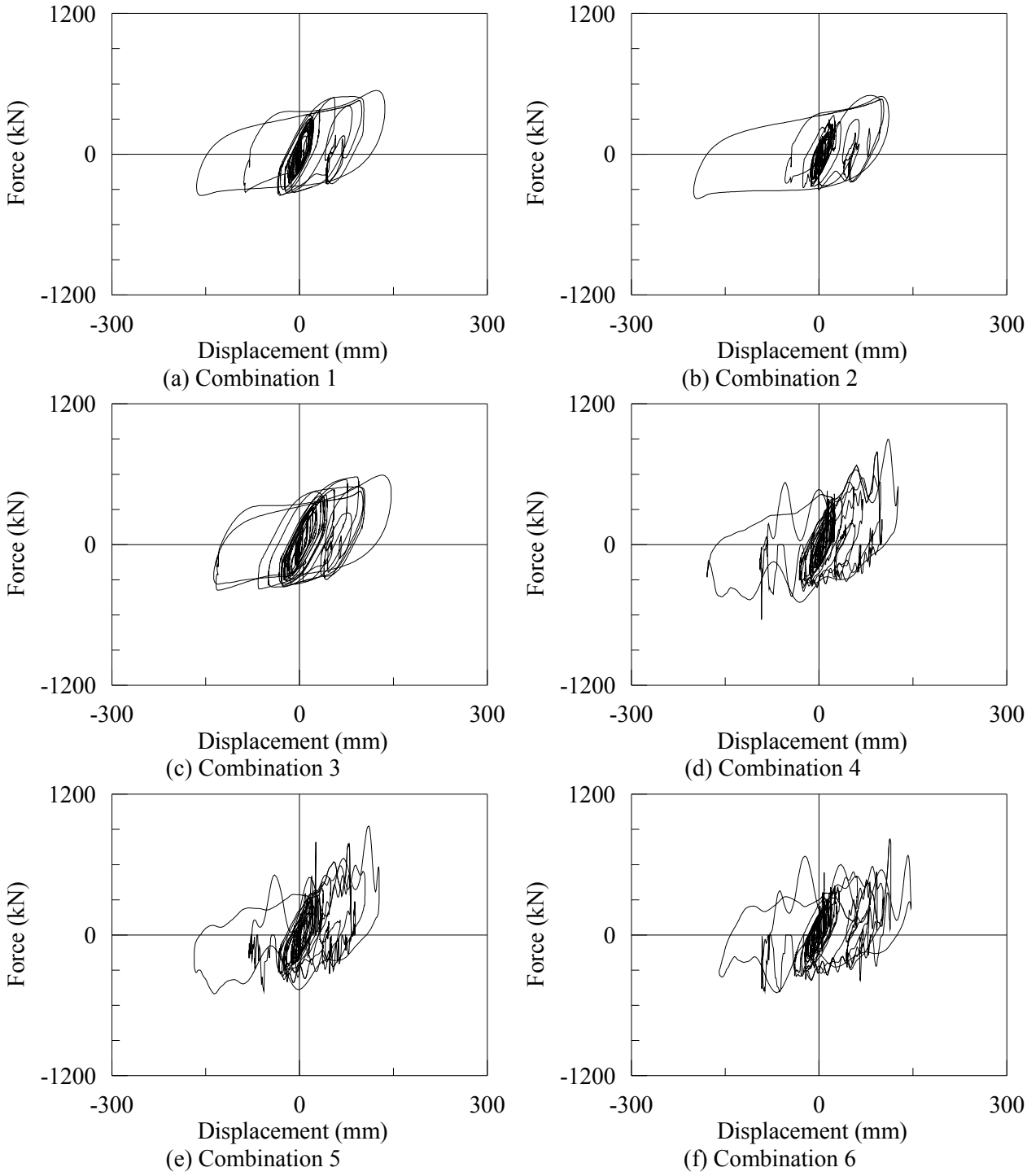

Figure 8-11: Hysteresis along the *y* direction of the isolator at Corner A of the base-isolated building, input scale factor = 4.5 (cont.)

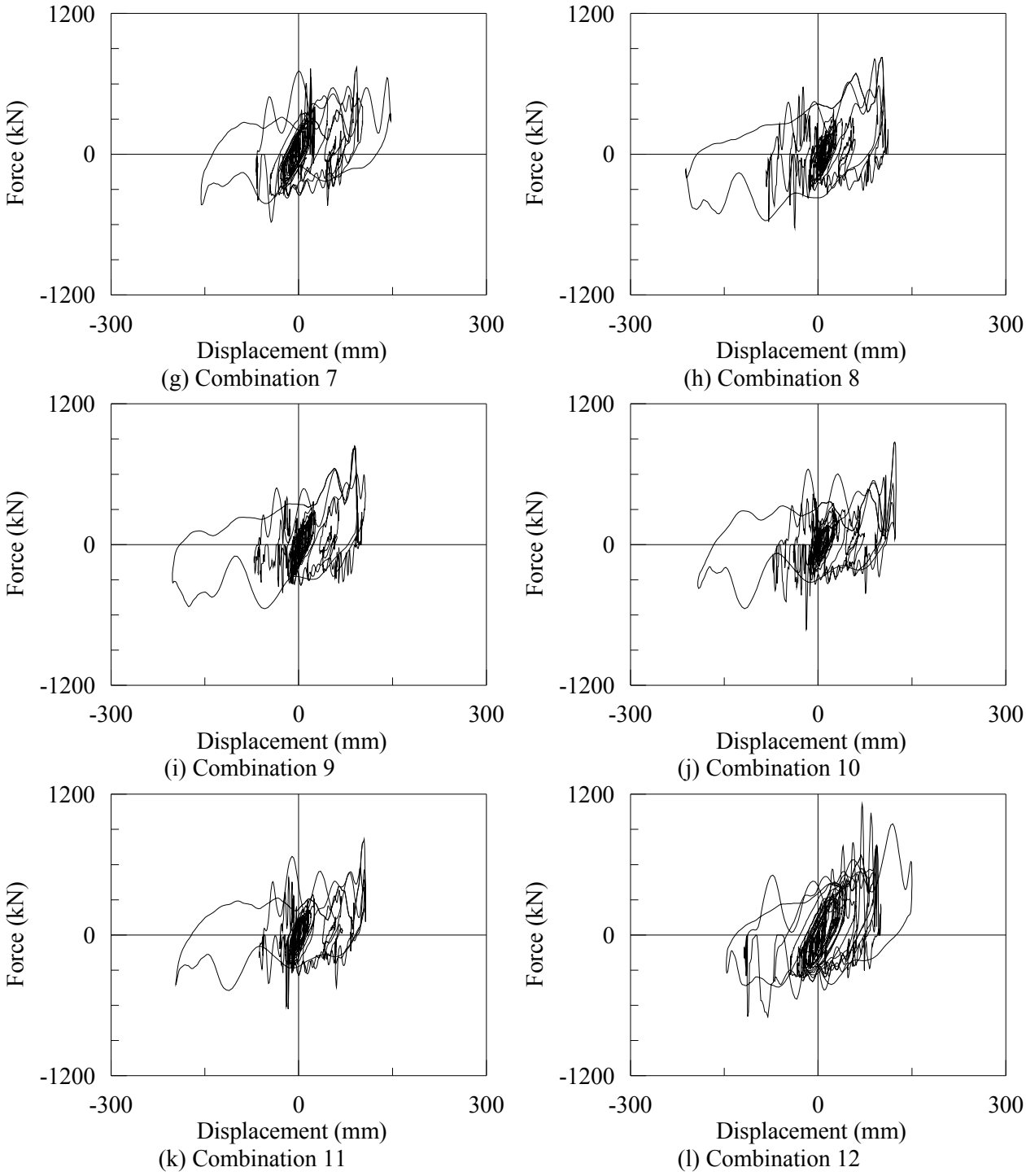

Figure 8-11: Hysteresis along the *y* direction of the isolator at Corner A of the base-isolated building, input scale factor = 4.5 (cont.)

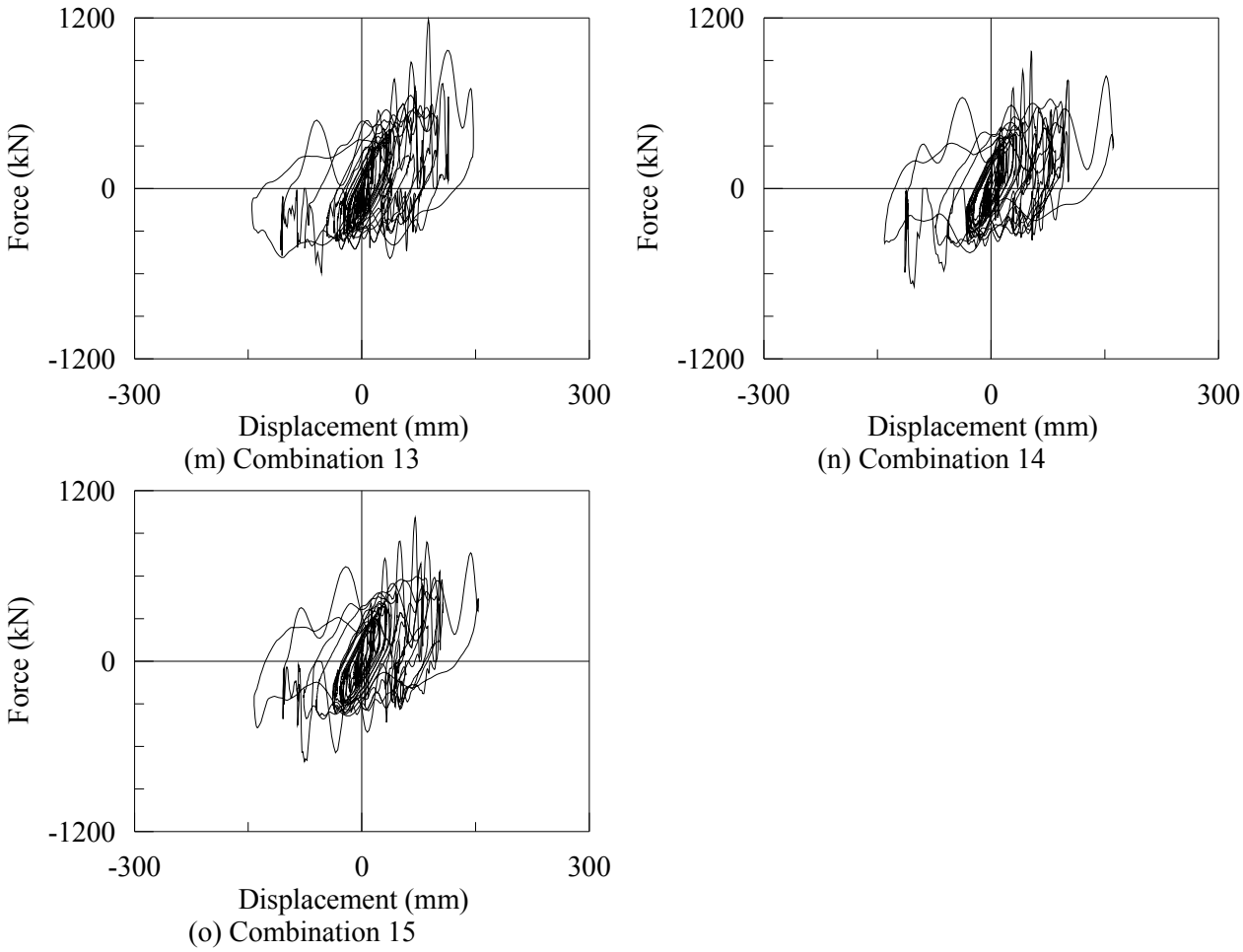

Figure 8-11: Hysteresis along the *y* direction of the isolator at Corner A of the base-isolated building, input scale factor = 4.5

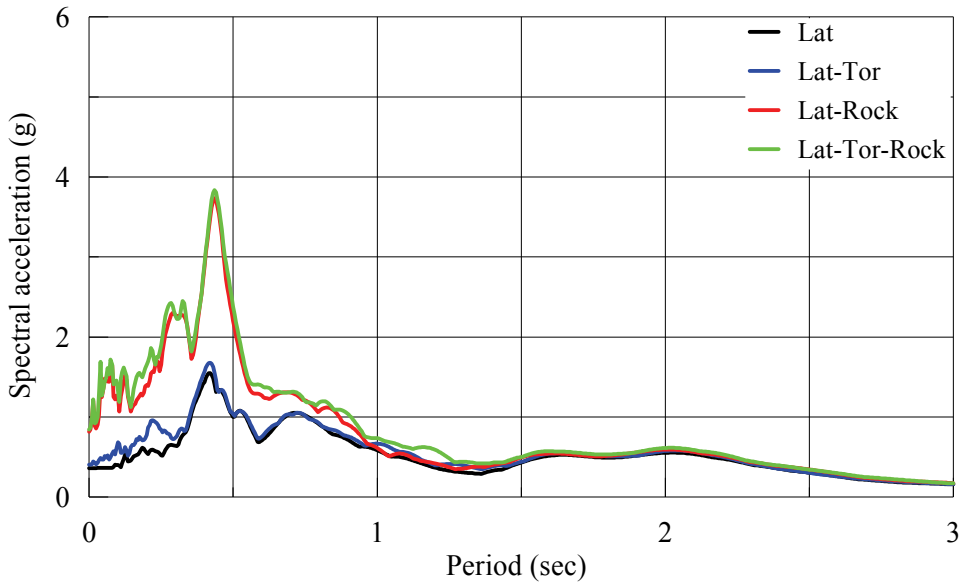

Figure 8-12: Floor acceleration spectra along the *x* direction at roof level, Corner A of the base-isolated building, input scale factor = 4.5

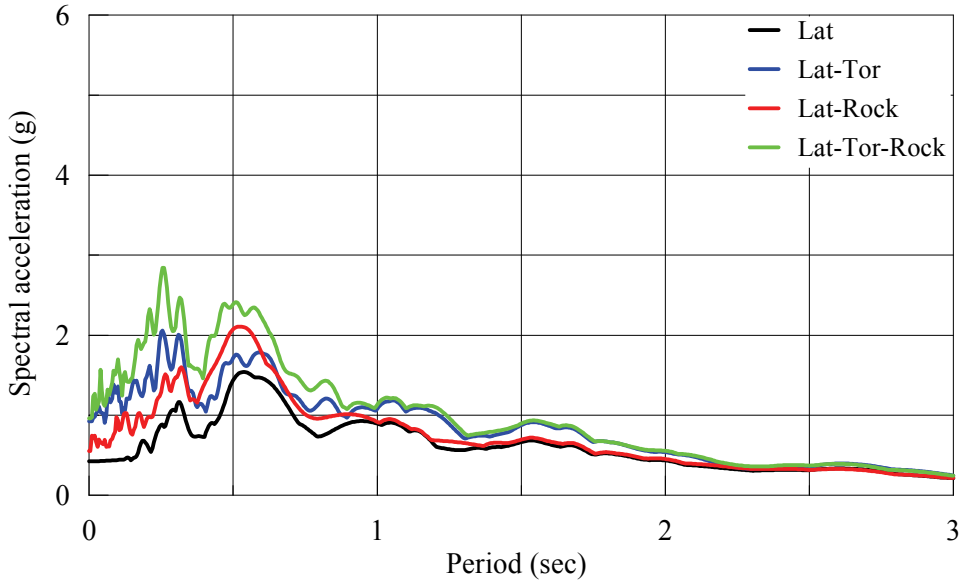

Figure 8-13: Floor acceleration spectra along the *y* direction at roof level, Corner A of the base-isolated building, input scale factor = 4.5

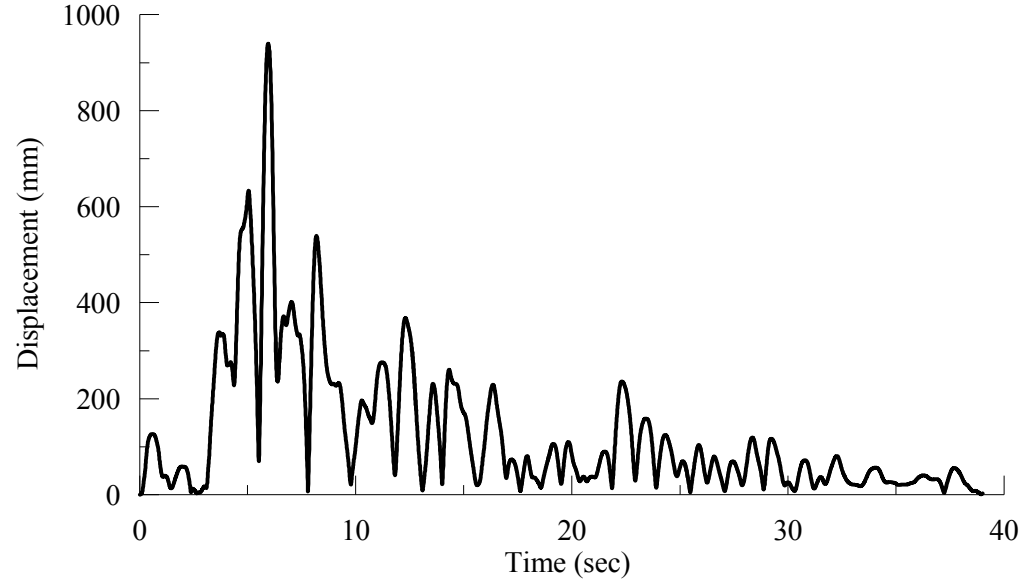

(a) Resultant displacement of the isolator at Corner A

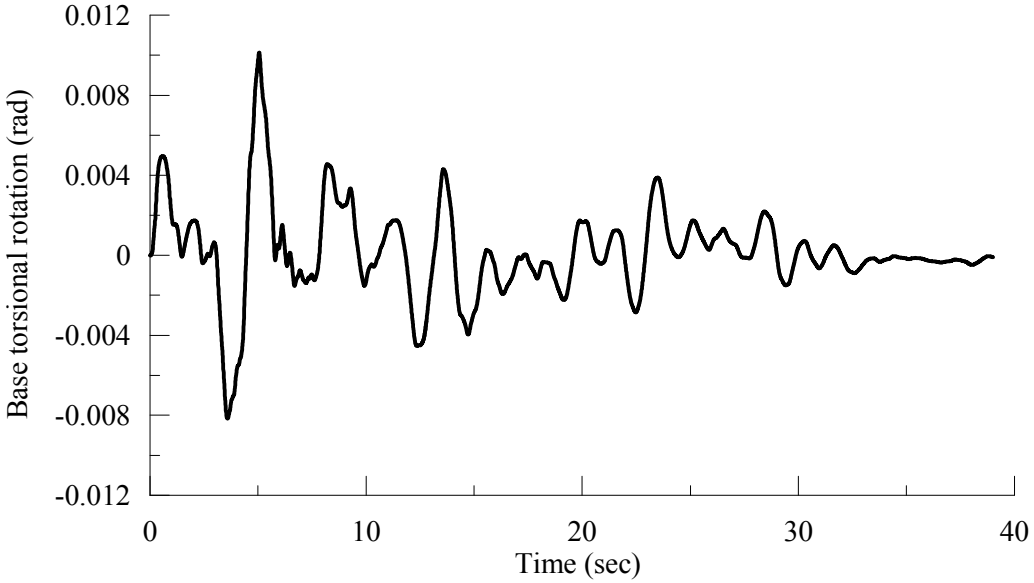

(b) Torsional rotation at the base

Figure 8-14: Response histories of the base-isolated building, input scale factor = 12

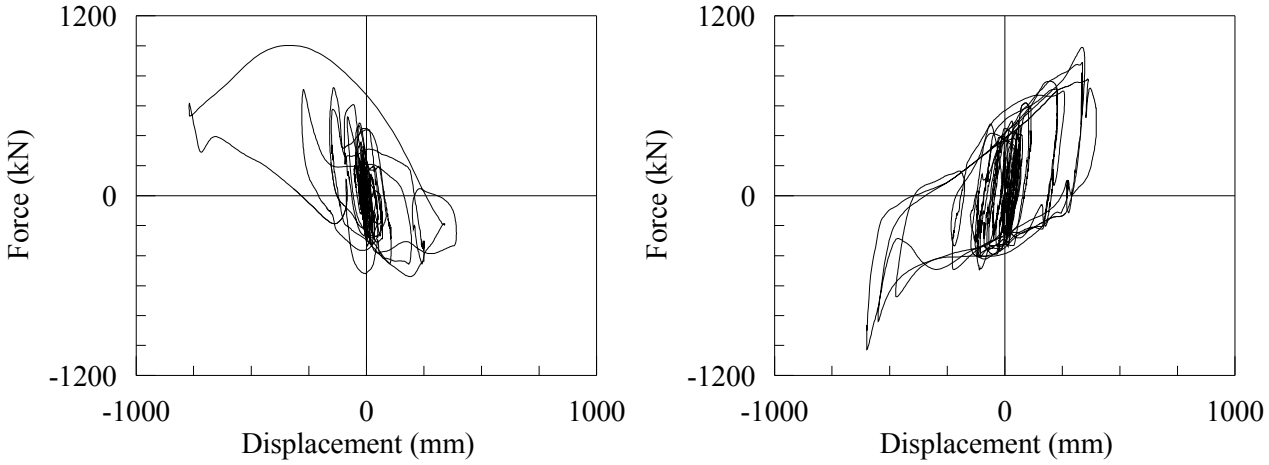

(a) *x* direction, lateral-torsional excitation

(b) *y* direction, lateral-torsional excitation

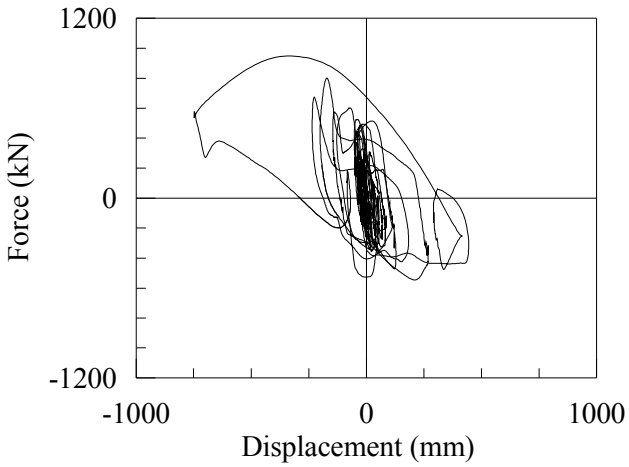

(c) *x* direction, lateral excitation only

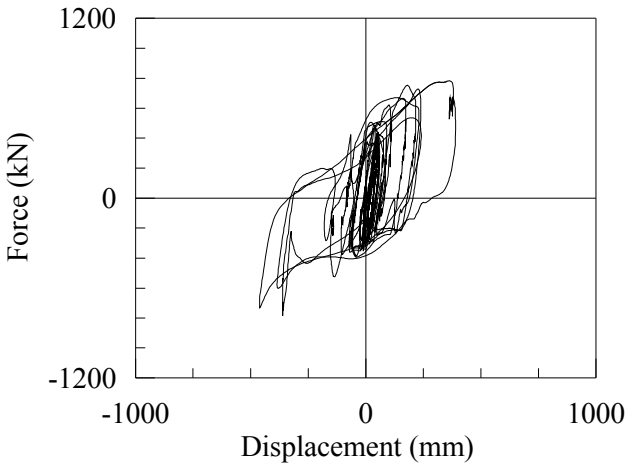

(d) *y* direction, lateral excitation only

Figure 8-15: Hysteresis of the isolator at Corner A, input scale factor = 12

Table 8-10: Maximum displacement at the roof level (fixed-base building)

	Displacement along x direction				Displacement along y direction			
	Corner A	Corner B	Corner C	Corner D	Corner A	Corner B	Corner C	Corner D
Combination	(mm)	(mm)	(mm)	(mm)	(mm)	(mm)	(mm)	(mm)
1	119	119	119	119	167	167	167	167
2	119	119	119	119	149	149	185	185
3	119	119	119	119	185	185	149	149
4	121	121	121	121	167	167	167	167
5	121	121	121	121	166	166	166	166
6	118	118	118	118	167	167	167	167
7	118	118	118	118	166	166	166	166
8	121	122	122	121	150	150	185	185
9	121	122	122	121	148	148	184	184
10	118	118	118	118	150	150	185	185
11	118	118	118	118	148	148	184	184
12	122	121	121	122	185	185	150	150
13	122	121	121	122	184	184	148	148
14	118	118	118	118	185	185	150	150
15	118	118	118	118	184	184	148	148
Lat	119	119	119	119	167	167	167	167
Lat-Tor	119	119	119	119	185	185	185	185
Lat-Rock	121	121	121	121	167	167	167	167
Lat-Tor-Rock	122	122	122	122	185	185	185	185
Increase (%)								
Torsional only	0	0	0	0	11	11	11	11
Rocking only	2	2	2	2	0	0	0	0
Torsional and Rocking	2	2	2	2	11	11	11	11

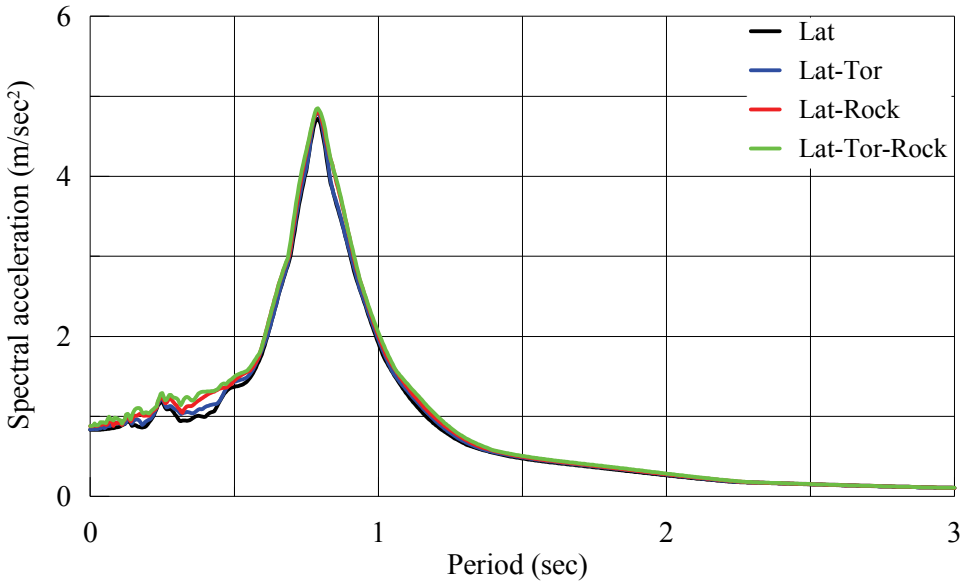

Figure 8-16: Floor acceleration spectra along the *x* direction at roof level, Corner A of the fixed-base building, input scale factor = 1.0

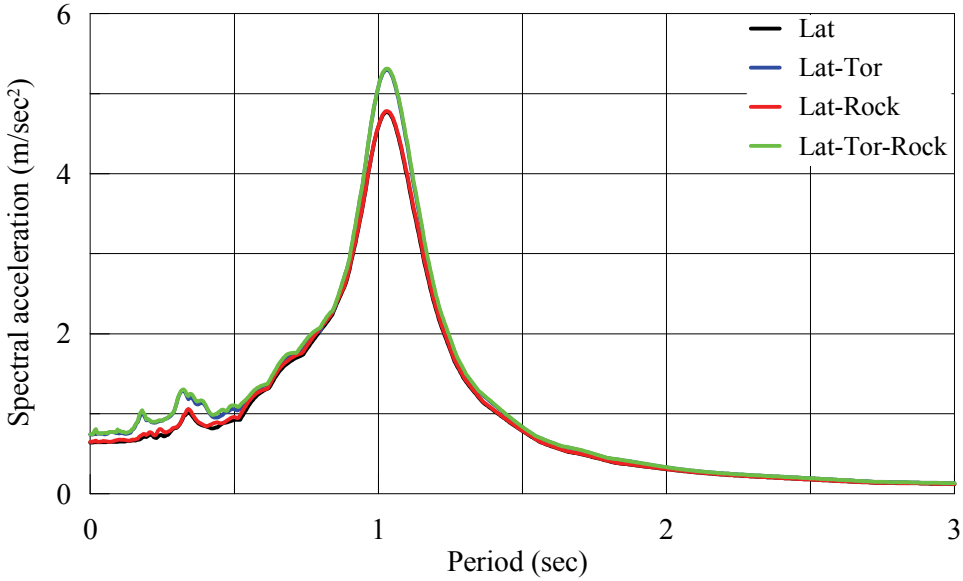

Figure 8-17: Floor acceleration spectra along the *y* direction at roof level, Corner A of the fixed-base building, input scale factor = 1.0

CHAPTER 9

SUMMARY, CONCLUSIONS AND RECOMMENDATIONS

9.1. Summary

Seismic analysis and design of buildings and safety-related nuclear structures is traditionally based on translational components of earthquake ground motion. Rotational components of ground motion, torsion about the vertical axis and rocking about orthogonal horizontal axes, are not routinely considered because such components have not been recorded and their effects on the response of structures are unknown. Rotational recordings are unavailable because instruments are by-and-large unavailable.

The characterization of rotational components of ground motion is a focus of this report. Because recordings of rotational components are unavailable, procedures are derived to extract rotational components of ground motion from recorded translational data. Two categories of procedures are proposed: Single Station Procedure (SSP) and Multiple Station Procedure (MSP).

Single station procedures employ translational data recorded at a single station. They approximate the free-field displacement surface around the recording station. The rotational components are computed from the surface using the associated spatial derivatives. A number of assumptions must be made for the calculation, including plane wave propagation, existence of a principal plane, and material properties such as wave velocity. Multiple station procedures employ three-component translational acceleration time series recorded in an array of closely spaced but spatially distributed accelerographs. These MSPs calculate a best-fit plane surface across the array at every instant of time. The rotational components are estimated using the slope of the best-fit surface. The MSPs do not assume plane wave propagation and the existence of a principal plane. The Geodetic Method (GM) of Spudich et al. (1995) considers stations at and below the ground surface, which requires the specification of soil properties and constraint equations to account for the presence of a free (ground) surface.

One SSP is developed in this report to estimate rotational acceleration histories of ground motion from three translational acceleration histories recorded at a single station. The procedure assumes the existence of a principal plane (the vertical plane containing the recording station and the epicenter) and the propagation of P and S waves along this principal plane. The rocking acceleration is computed from the decomposed P and SV wave components of the vertical acceleration. The torsional acceleration is computed from the SH component of the horizontal acceleration, which is obtained by taking the resultant of the components of the measured accelerations along the direction normal to the principal plane. This problem is indeterminate to the first degree. The required additional condition is derived from the assumption of an equal angle of incidence of P and SV waves for low frequency harmonics and a power compatibility criterion for high frequency harmonics. The derivation initially assumed a point source for earthquake shaking, which was then relaxed to accommodate a finite length of fault rupture and an arbitrary location for the epicenter along the fault.

Multiple MSPs are developed in this report. All use three-component translational acceleration time series recorded in an array of seismic accelerographs. First, the GM procedure of Spudich et al. is restricted to the use of surface stations and the procedure is shown to be independent of soil properties; the constraint equations are identically satisfied, which leads to an uncoupling of the calculations along the orthogonal directions. Whereas a linear best-fit distribution surface is employed in the GM, the actual surface is expected to be wavy. To obtain free-field rotational components and enable a comparison with the estimates of rotational components using the SSP, the curvature of the distribution surface must be computed. A second-order Taylor expansion of the displacement field about the reference station is performed for this purpose. The procedure is termed the Acceleration Gradient Method (AGM). The shortcomings of AGM are identified and substantially eliminated in the Surface Distribution Method (SDM). The SDM assumes the recorded translational data are due to the propagation of two waves of the same type propagating orthogonal to each other at the same apparent velocity. The best-fit surface, which

characteristically varies with the harmonics of the propagating plane wave, is computed in the frequency domain.

The newly developed MSPs enable the development of a design procedure for dense seismic arrays, whose primary purpose is to extract rotational ground motions. A study is performed to determine how the choice of stations in a dense array affects the computed rotational components. Design criteria are proposed to determine the length of the array, the number of recording stations and their spatial distribution, all based on the use of the SDM. Implementation of these criteria requires calculation of site-specific characteristics of the expected ground motion, namely, the apparent seismic wave velocity, its frequency content, and the frequency of the modal harmonic.

Accidental eccentricity is used in seismic codes and standards for the analysis and design of structures to account for uncertainties in the mass and mechanical properties of the framing, and the effects of torsional ground motion. The method implemented in codes and standards to address accidental eccentricity involves shifting the center of mass at each floor by a fraction of the building dimension. This method is shown not to produce the desired result, which is an increase in torsional response with an increase in accidental eccentricity. An improved definition of accidental eccentricity is proposed and studied for a wide range of one-story elastic systems, and nonlinear isolation systems

A preliminary investigation of the effect of rotational ground motions on the response of structures is performed. The rotational excitations are calculated using the SDM. The sample structures are a tower subjected to horizontal and rocking ground motions, and four-story, base-isolated and fixed-based buildings subjected to horizontal, torsional and rocking ground motions.

9.2. Conclusions

The key conclusions of the research described in this report are:

1. Analysis of translational time series data at a station using the SSP identified the location of the epicenter on a fault of finite rupture length as a factor in the calculation of rocking spectra

but not torsional spectra. A comparison of rotational spectra computed using the SSP and a point earthquake source and using the GM showed the spectra are similar at periods greater than 1 second. Spectral ordinates at shorter periods computed using the GM are significantly less than those computed using the SSP, which is attributed to the underlying assumption in the GM of a plane surface for the recorded data at any time instant.

2. The Geodetic Method can be considered as a calculation of rotational components induced in a rigid foundation whose geometry is defined by the spatial distribution of the recording stations. Rotational components computed using the GM are not free-field components of motion.
3. The second order Acceleration Gradient Method (AGM2) captures higher frequency content that is averaged out by the GM. The rotational components computed using the AGM2 at exterior stations in an array are less accurate than those computed at the interior stations because 1) of the increased distance between the subject station as the reference station and the most distant station (separation distance), and 2) the associated error is proportional to the square of the separation distance. The AGM2 cannot capture high frequency content beyond a limit, which decreases in value as the dimension of the seismic array increases.
4. Third and higher order variants of the AGM are not recommended because the associated numerical errors will significantly affect the computations.
5. The SDM can capture most of the high frequency content if the rotational components are primarily due to one type of body or surface wave. The required condition is nearly satisfied when computing the torsional motion from both near-fault and far-field records and rocking motion from far-field records. However, if computing the rocking motion from near-fault records, the required condition is not strictly satisfied if the contributions from the P and SV waves to the recorded vertical motion are comparable in value over a wide range of frequency.

6. The definition of material properties and site/event specific data is not required for the use of the AGM2. The uncertainty involved in the computation of the rotational components is therefore smaller than that of the SDM because the latter uses uncertain parameters such as apparent wave velocity and the orientation of the principal plane. Both the SDM and the AGM2 can be used to compute rotational ground motion at interior stations of a seismic array.
7. The results of analysis using the GM are not affected by the choice of recording stations in an array if the dimension of the array is greater than a minimum requirement, which is as small as 25 m for the recorded data considered in this report. The results of analysis using the AGM2 and SDM can be affected by array dimension. The greater the length of the array, the smaller the effect.
8. The AGM2 is expected to provide reliable results when the recorded translational time series are narrow banded and the array dimension is close to a half wavelength of the modal harmonic.
9. The current approach in seismic codes and standards of accounting for the effects of accidental torsion by shifting the center of mass at each floor level should not be used for response-history analysis because the modal properties of the structure change when the centers of mass are moved. The alternative definition of accidental eccentricity proposed here predicts the torsional amplification correctly, namely, increasing torsional response with increasing accidental eccentricity. The proposed definition of the accidental eccentricity can also be used to quantify sources of accidental torsion other than torsional ground motion.
10. a) The response of a fixed-base chimney can be significantly increased by the inclusion of rocking ground motion. The amplification of response changes as the height of the chimney increases. b) The response of a four-story, base-isolated building, including displacements in the isolators and floor spectral demands, can be amplified by the inclusion of the torsional component of ground motion. Rocking will affect the floor spectral demand, story drift and

may lead to uplift at some isolator locations. c) The response of a four-story, fixed-base building was not affected significantly by the rotational components of ground motion. d) The above conclusions are specific to the structures studied and ground motions used for analysis. Further studies are required to generalize the conclusions.

9.3. Recommendations

Instrumental recordings of rotational motions should be used to validate the Single Station Procedure and the Multiple Station Procedures developed here after their deployment in the free field.

Rotational ground motions (rocking and torsional) should be addressed in the seismic analysis and design of buildings and safety-related nuclear structures. The impact of these components of motion, in terms of percentage increase in response, will vary by structure type, geometry and seismic input. Rocking input will be particularly important for tall and slender structures such as chimneys. Torsional input may be important for low-rise fixed-base buildings. Both rocking and torsional inputs should be considered in seismically isolated buildings.

Rotational ground motions can be computed using either a Single Station Procedures (SSP) or a Multiple Station Procedure (MSPs). The SSP may be more useful because the MSPs require data recorded in dense arrays and those arrays are few in number around the world. The SSP can be employed wherever translational data are recorded provided site-specific geologic data and information on the rupture process are available. Analysis of data using the SSP could result in the development of ground motion prediction equations, seismic hazard curves and uniform hazard spectra for rotational components of ground motion.

The Surface Distribution Method (SDM) is the preferred MSP. The parameters required for the SDM computations, which include apparent wave velocity in the array, can be computed by statistical analysis of SSP-processed data recorded at individual stations in the array. The SDM should be used to aid in the design of dense arrays that are deployed to characterize rotational components of ground motion.

The contribution of torsional ground motion to accidental eccentricity should be reevaluated using the definition proposed here. Torsional components of ground motion extracted from a large number of translational ground motions recorded on different sites should be used to analyze a family of archetype buildings to calibrate the required accidental eccentricity. This value of eccentricity can then be augmented to account for the other sources of accidental torsion.

CHAPTER 10

REFERENCES

Large Scale Seismic Testing Array. LLSST. Lotung, Taiwan.

Achenbach, J. D. (1973). Wave Propagation in Elastic Solids, North-Holland.

Aki, K. and Richards, P. G. (2002). Quantitative Seismology, Second Ed., Sausalito, California, University Science Books.

Aki, K. and Richards, P. G. (1980). Quantitative Seismology, First Ed., New York, W. H. Freeman.

Aki, K. and Tsujiura, M. (1959). "Correlation study of near earthquake waves." Bulletin of Earthquake Research Institute, University of Tokyo, 37: 207-231.

ASCE (2010). Minimum Design Loads for Buildings and Other Structures, Standard ASCE/SEI 7-10, American Society of Civil Engineers, Reston, VA.

ASCE (2000). Seismic Analysis of Safety-Related Nuclear Structures and Commentary, Standard ASCE 4-98, American Society of Civil Engineers, Reston, VA.

Basu, D. and Jain, S. K. (2007). "Alternative method to locate centre of rigidity in asymmetric buildings." Earthquake Engineering and Structural Dynamics, 36 (7): 965-973.

Bendat, J. S. and Piersol, A. G. (1986). Random Data: Analysis and Measurement Procedures, John Wiley & Sons.

Bodin, P., Gomberg, J., Singh, S. K. and Santoyo, M. (1997). "Dynamic deformations of shallow sediments in the valley of Mexico, Part I: three-dimensional strains and rotations recorded on a seismic array." Bulletin of Seismological Society of America, 87 (3): 528-539.

Bolt, B. A. (1988). Earthquakes. New York, W.H. Freeman.

Bouchon, M. (1980). "The motion of the ground during an earthquake. Part 1: the case of a strike-slip fault." Journal of Geophysical Research, 85: 356-366.

Bouchon, M. (1980). "The motion of the ground during an earthquake. Part 2: the case of a dip-slip fault." Journal of Geophysical Research, 85: 367-375.

Bouchon, M. (1979). "Discrete wavenumber representation of elastic wave fields in three-space dimensions." Journal of Geophysical Research, 84: 3609-3614.

Bouchon, M. and Aki, K. (1982). "Strain, tilt and rotation associated with strong ground motion in the vicinity of earthquake faults." Bulletin of Seismological Society of America, 72: 1717-1738.

Bouchon, M. and Aki, K. (1977). "Discrete wave number representation of seismic-source wave fields." Bulletin of Seismological Society of America, 67: 259-277.

Bycroft, G. N. (1980). "Soil-foundation interaction and differential ground motions." Earthquake Engineering and Structural Dynamics, 8: 397-404.

Castellani, A. and Boffi, G. (1989). "On the rotational components of seismic motion." Earthquake Engineering and Structural Dynamics, 18: 785-797.

Castellani, A. and Boffi, G. (1986). "Rotational components of the surface ground motion during and earthquake." Earthquake Engineering and Structural Dynamics, 14: 751-767.

Castellani, A. and Zembaty, Z. (1996). "Comparison between earthquake rotation spectra obtained by different experimental sources." Engineering Structures, 18 (8): 597-603.

Chen, C. H., Mok, C. M., Power, M. S., Tank, Y. K., Tank, H. T. and Stepp, J. C. (1990). "Equivalent linear versus nonlinear ground response analyses at Lotung seismic experiment site." *Fourth U.S. National Conference on Earthquake Engineering*, Palm Springs, California: 327-336.

Chiang, S. C. (1976). "A seismic refraction prospecting of the Ilan plain." Mining Technology, 14: 215-221.

Chung, J. K. (2007). "Estimation of ground strain using accelerograms recorded by two dense seismic arrays at Lotung, Taiwan." Terrestrial Atmospheric and Oceanic Sciences, 18 (4): 715-737.

Cochard, A., Igel, H., Schuberth, B., Suryanto, W., Velikoseltsev, A., Schreiber, K. U., Wasserman, J., Scherbaum, F. and Volmer, D. (2006). Rotational motions in seismology: theory, observation, simulation. Earthquake Source Asymmetry, Structural Media and Rotation Effects. R. Teisseyre, M. Takeo and E. M. (Editors). New York, Springer. Chapter 30.

Constantinou, M. C., Whittaker, A. S., Kalpakidis, Y., Fenz, D. M. and Warn, G. P. (2007). "Performance of Seismic Isolation Hardware Under Service and Seismic Loading." *MCEER-07-0012*, Multidisciplinary Center for Earthquake Engineering Research, SUNY,Buffalo, NY.

Corotis, R. B., Vanmarcke, E. H. and Cornell, C. A. (1972). "First passage of nonstationary random process." Journal of Engineering Mechanics, ASCE, 98: 401-414.

Cowsik, R. (2007). "An instrument for direct observations of seismic and normal-mode rotational oscillations of the earth." *Proceedings of the National Academy of Sciences, USA*: 6893-6898

CSI (2009). "SAP 2000: Static and Dynamic Finite Element Analysis of Structures." *Computers and Structures, Inc*., Berkeley, California.

De-La-Llera, J. C. and Almazan, J. L. (2003). "An experimental study of nominally symmetric and asymmetric structures isolated with the FPS." Earthquake Engineering and Structural Dynamics, 32: 891-918.

De-La-Llera, J. C. and Chopra, A. K. (1997). "Evaluation of seismic code provisions using strong-motion building records from the 1994 Northridge earthquake." *UCB/EERC-97/16*, Earthquake Engineering Research Center, University of California, Berkeley.

De-La-Llera, J. C. and Chopra, A. K. (1995). "Estimation of accidental torsion effects for seismic design of buildings." Journal of Structural Engineering, ASCE, 121 (1): 102-114.

De-La-Llera, J. C. and Chopra, A. K. (1994a). "Evaluation of code accidental-torsion provisions from building records." Journal of Structural Engineering, ASCE, 120 (2): 597-615.

De-La-Llera, J. C. and Chopra, A. K. (1994b). "Accidental eccentricity in buildings due to stiffness uncertainty." Earthquake Engineering and Structural Dynamics, 23: 117-136.

De-La-Llera, J. C. and Chopra, A. K. (1994c). "Accidental torsion in buildings due to base rotational excitation." Earthquake Engineering and Structural Dynamics, 23: 1003-1021.

De-La-Llera, J. C. and Chopra, A. K. (1994d). "Using accidental eccentricity in code specified static and dynamic analyses of buildings." Earthquake Engineering and Structural Dynamics, 23: 947-967.

De-La-Llera, J. C. and Chopra, A. K. (1994e). "Accidental and natural torsion in earthquake response and design of buildings." *Report No. UCB/EERC-94/07*, Earthquake Engineering Research Center, University of California, Berkeley.

Galperin, E. I. (1985). Vertical Seismic Profiling and Its Exploration Potential. Dordrecht, Reidel Publishing.

Gazetas, G. (1982). "Analysis of machine foundation vibrations: state of the art." Soil Dynamics and Earthquake Engineering, 2 (1): 1-42.

Ghayamghamian, M. R. and Nouri, G. R. (2007). "On the characteristics of ground motion rotational components using Chiba dense array data." Earthquake Engineering and Structural Dynamics, 36: 1407-1429.

Goel, R. K. and Chopra, A. K. (1993). "Seismic code analysis of buildings without locating centers of rigidity." Journal of Structural Engineering, ASCE, 119 (10): 3039-3055.

Goldstein, P. and Archuleta, R. J. (1987). "Array analysis of seismic signals." Geophysical Research Letters, 14 (1): 13-16.

Gomberg, J. (1997). "Dynamic deformations and M 6.7, Northridge, California earthquake." Soil Dynamics and Earthquake Engineering, 16: 471-494.

Gomberg, J. and Bodin, P. (1994). "Triggering of Ms = 5.4 Little Skull Mountain, Nevada, earthquake with dynamic strains." Bulletin of Seismological Society of America, 84 (3): 844-853.

Graizer, V. M. (2010). "Strong motion recordings and residual displacements: what are we actually recording in strong motion seismology?" Seismological Research Letters, 81 (4): 635-639.

Graizer, V. M. (2009a). "The response to complex ground motions of seismometers with Galperin sensor configuration. " Bulletin of Seismological Society of America, 99 (2B): 1366-1377.

Graizer, V. M. (2009b). "Tutorial on measuring rotations using multipendulum systems." Bulletin of Seismological Society of America, 99 (2B): 1064-1072.

Graizer, V. M. (2006). "Tilts in strong ground motion." Bulletin of Seismological Society of America, 96 (6): 2090-2102.

Graizer, V. M. (2005). "Effect of tilt on strong motion data processing." Soil Dynamics and Earthquake Engineering, 25: 197-204.

Graizer, V. M. (1989). "On intertial seismometry." Izvestiya, Earth Physics, 25 (1): 26-29.

Graizer, V. M. and Kalkan, E. (2008). "Response of pendulums to complex input ground motion." Soil Dynamics and Earthquake Engineering, 28: 621-631.

Hart, G., DiJulio, M. and Lew, M. (1975). "Torsional response of high-rise buildings." Journal of Structural Division, ASCE, 101: 397-414.

Haskell, N. A. (1953). "The dispersion of surface waves in multilayered media." Bulletin of Seismological Society of America, 43: 17-34.

Hejal, R. and Chopra, A. K. (1987). "Earthquake response of torsionally-coupled buildings." *UCB/EERC-87/20*, Earthquake Engineering Research Center, University of California, Berkeley.

Hernandez, J. J. and Lopez, O. A. (2004). "Dependence of accidental torsion on structural system properties." *13th World Conference on Earthquake Engineering*, Vancouver, B. C., Canada, Paper No. 1165.

Igel, H., Cochard, A., Wassermann, J., Flaws, A., Schreiber, K. U., Velikoseltsev, A. and Dinh, N. P. (2007). "Broad-band observations of earthquake-induced rotational ground motions." Geophysical Journal International, 168: 182-196.

Igel, H., Lee, H. K. and Todorovska, M. I. (2006). "Inauguration of the International Working Group on Rotational Seismology (IWGoRS)." *AGU, Fall Meeting, Rotational Seismology Sessions: S22A, S23B*.

Igel, H., Schreiber, K. U., Schuberth, B., Flaws, A., Velikoseltsev, A. and Cochard, A. (2005). "Observation and modelling of rotational motions induced by distant large earthquakes: the M 8.1 Tokachi-oki earhquake September 25, 2003." Geophysical Research Letters, 32: L08309.

Kalkan, E. and Graizer, V. M. (2007). "Coupled tilt and translational ground motion response spectra." Journal of Structural Engineering, ASCE 133 (5): 609-619.

Kameda, H. (1975). "Evolutionary spectra of seismogram by multifilter." Journal of Engineering Mechanics, ASCE, 101: 787-801.

Kerekes, A. K. (2001). "Seismic array design by spatial convolution." Geophysics, 66 (4): 1195–1207.

Laouami, N. and Labbe, P. (2002). "Experimental analysis of seismic torsional ground motion recorded by the LSST-Lotung array." Earthquake Engineering and Structural Dynamics, 31: 2141-2148.

Lee, H. K., Celebi, M., Todorovska, M. I. and Diggles, M. (2007). "Rotational seismology and engineering." *First International Workshop*, US Geological Survey, Open file Report No. 2007-1144, version 2.0.

Lee, V. W. and Trifunac, M. D. (1987). "Rocking strong earthquake accelerations." Soil Dynamics and Earthquake Engineering, 6: 75-89.

Lee, V. W. and Trifunac, M. D. (1985). "Torsional accelerograms." Soil Dynamics and Earthquake Engineering, 4: 132-139.

Li, H.-N., Sun, L.-Y. and Wang, S.-Y. (2004). "Improved approach for obtaining rotational components of seismic motion." Nuclear Engineering and Design, 232: 131-137.

Li, H.-N., Sun, L.-Y. and Wang, S.-Y. (2002). "Frequency dispersion characteristics of phase velocities in surface wave for rotational components of seismic motion." Journal of Sound and Vibration, 258 (5): 815-827.

Lin, W. H., Chopra, A. K. and De-La-Llera, J. C. (2001). "Accidental torsion in buildings: Analysis versus earthquake motions." Journal of Structural Engineering, ASCE, 127 (5): 475-481.

LLSST http://www.earth.sinica.edu.tw/~smdmc/llsst/llsst.htm.

Lomnitz, C. (1997). "Frequency response of a strainmeter." Bulletin of Seismological Society of America, 87 (4): 1078-1080.

McLeod, D. P., Stedman, G. E., Webb, T. H. and Schreiber, K. U. (1998). "Comparison of standard and ring laser rotational seismograms." Bulletin of Seismological Society of America, 88: 1495-1503.

Menke, W. (1984). Geophysical Data Analysis: Discrete Inverse Theory. International Geophysics Series, Academic Press, Inc. 45.

Moh and Associated-Consulting-Engineers (1986). "Report on the installation of settlement monitoring instruments for Lotung seismic experiment station." Taipei, Taiwan.

Nagarajaiah, S., Reinhorn, A. M. and Constantinou, M. C. (1989). "Nonlinear dynamic analysis of three-dimensional base isolated structures (3D-BASIS) " *MCEER-89-0018*, Multidisciplinary Center for Earthquake Engineering Research, SUNY,Buffalo, NY.

Newmark, N. M. (1969). "Torsion in symmetrical buildings." *Proc. Fourth World Conference on Earthquake Engineering*, Santiago, Chile: 19-32.

Niazi, M. (1986). "Inferred displacements, velocities and rotations of a long rigid foundation located at El Centro differential array site during the 1979 Imperial Valley, California, earthquake." Earthquake Engineering and Structural Dynamics, 14: 531-542.

Nigbor, R. L. (1994). "Six degree-of-freedom ground-motion measurement." Bulletin of Seismological Society of America, 84 (5): 1665-1669.

Nigbor, R. L., Evans, J. R. and Hutt, C. R. (2009). "Laboratory and field testing of commercial rotational seismometers." Bulletin of Seismological Society of America, 99 (2B): 1215-1227.

Pancha, A., Webb, T. H., Stedman, G. E., McLeod, D. P. and Schreiber, K. U. (2000). "Ring laser detection of rotations from teleseismic waves." Geophysical Research Letter, 27: 3553-3556.

Park, Y. J., Wen, Y. K. and Ang, A. H. S. (1985). "Random vibration of hysteretic systems under bi-directional ground motions." Earthquake Engineering and Structural Dynamics, 14 (4): 543–557.

Penzien, J. and Watabe, M. (1975). "Characteristics of 3-dimensional earthquake ground motion." Earthquake Engineering and Structural Dynamics, 3: 365-373.

Politopoulos, I. (2010). "Response of seismically isolated structures to rocking-type excitations." Earthquake Engineering and Structural Dynamics, 39: 325-342.

Roy, R. (1987). "ESPRIT: Estimation of signal parameters via rotational invariance techniques," PhD Dissertation, Department of Electrical Engineering, Stanford University, Stanford, CA.

Sarlis, A. A. S. and Constantinou, M. C. (2010). "Modeling triple friction pendulum isolators in program SAP2000." *Personal communication*, University at Buffalo, State University of New York

Schmidt, R. (1981). "A signal subspace approach to multiple emitter location and spectral estimation," PhD Dissertation, Department of Electrical Engineering, Stanford University, Stanford CA.

Schreiber, K. U., Hautmann, J. N., Velikoseltsev, A., Wassermann, J., Igel, H., Otero, J., Vernon, F. and Wells, J.-P. R. (2009). "Ring laser measurements of ground rotations for seismology." Bulletin of Seismological Society of America, 99 (2B): 1190-1198.

Schreiber, K. U., Stedman, G. E., Igel, H. and Flaws, A. (2006). Ring laser gyroscopes as rotation sensors for seismic wave studies. Earthquake Source Asymmetry, Structural Media and Rotation Effects. R. Teisseyre, M. Takeo and E. M. (Editors). New York, Springer. Chapter 29.

Shakib, H. and Tohidi, R. Z. (2002). "Evaluation of accidental eccentricity in buildings due to rotational component of earthquake." Journal of Earthquake Engineering, 6 (4): 431-445.

Singh, S. K., Santoyo, M., Bodin, P. and Gomberg, J. (1997). "Dynamic deformations of shallow sediments in the valley of Mexico, Part II: single-station estimates." Bulletin of Seismological Society of America, 87 (3): 540-550.

Soong, T. T. (2004). Fundamentals of Probability and Statistics for Engineers, John Wiley & Sons, Ltd.

Spudich, P., Steck, L. K., Hellweg, M., Fletcher, J. B. and Baker, L. (1995). "Transient stress at Parkfield, California, produced by the M 7.4 Landers earthquake of June 28, 1992: Observations from the UPSAR dense seismograph array." Journal of Geophysical Research, 100: 675-690.

Stedman, G. E., Li, Z. and Bilger, H. R. (1995). "Sideband analysis and seismic detection in a large ring laser." Applied Optics, 34: 5375-5385.

Sugito, M., Goto, H. and Aikawa, F. (1984). "Simplified separation technique of body and surface waves in strong motion accelerograms." *Structural Engineering/Earthquake Engineering, Proc. Japan Society of Civil Engineers*: 71-76.

Takamori, A., Araya, A., Otake, Y., Ishidoshiro, K. and Ando, M. (2009). "Research and development status of a new rotational seismometer based on the flux pinning effect of a superconductor." Bulletin of Seismological Society of America, 99 (2B): 1174-1180.

Takeo, M. (1998). "Ground rotational motions recorded in near-source region of earthquakes." Geophysical Research Letter: 25 (789-792).

Trifunac, M. D. (1982). "A note on rotational components of earthquake motions for incident body waves." Soil Dynamics and Earthquake Engineering, 1: 11-19.

Tso, W. K. (1990). "Static Eccentricity Concept for Torsional Moment Estimation." Journal of Structural Engineering, ASCE, 116 (5): 1199-1212.

Tuncer, T. E. and Friedlander, B., Eds. (2009). Classical and Modern Direction-of-Arrival Estimation, Elsevier.

Wells, D. L. and Coppersmith, K. J. (1994). "New empirical relationships among magnitude, rupture length, rupture width, rupture area, and surface displacement." Bulletin of Seismological Society of America, 84 (4): 974-1002.

Wen, K. L. and Yeh, Y. T. (1984). "Seismic velocity structure beneath the SMART-1 array." Bulletin of Institute of Earth Science, Academia Sinica, 4: 51-72.

Wen, Y. K. (1976). "Method for random vibration of hysteretic systems." Journal of Engineering Mechanics, ASCE, 102 (2): 249–263.

Wolf, J. P., Obernhueber, P. and Weber, B. (1983). "Response of a nuclear plant on aseismic bearings to horizontally propagating waves." Earthquake Engineering and Structural Dynamics, 11: 483-499.

Wong, H. L. and Trifunac, M. D. (1979). "Generation of artificial strong motion accelerograms." Earthquake Engineering and Structural Dynamics, 7: 509-527.

Zembaty, Z. (2009a). "Tutorial on surface rotation from wave passage effects: Stochastic spectral approach." Bulletin of Seismological Society of America, 99 (2B): 1040-1049.

Zembaty, Z. (2009b). "Rotational seismic code definition in Eurocode 8, Part 6, for slender tower-shaped structures." Bulletin of Seismological Society of America, 99 (2B): 1483-1485.

Zembaty, Z. and Boffi, G. (1994). "Effect of rotational seismic ground motion on dynamic response of slender towers." European Earthquake Engineering, 8: 3-11.

Zwartjes, P. M. and Sacchi, M. D. (2007). "Fourier reconstruction of nonuniformly sampled, aliased seismic data." Geophysics, 72 (1): V21-V32.

MCEER Technical Reports

MCEER publishes technical reports on a variety of subjects written by authors funded through MCEER. These reports are available from both MCEER Publications and the National Technical Information Service (NTIS). Requests for reports should be directed to MCEER Publications, MCEER, University at Buffalo, State University of New York, 133A Ketter Hall, Buffalo, New York 14260. Reports can also be requested through NTIS, P.O. Box 1425, Springfield, Virginia 22151. NTIS accession numbers are shown in parenthesis, if available.

NCEER-87-0001 "First-Year Program in Research, Education and Technology Transfer," 3/5/87, (PB88-134275, A04, MF-A01).

NCEER-87-0002 "Experimental Evaluation of Instantaneous Optimal Algorithms for Structural Control," by R.C. Lin, T.T. Soong and A.M. Reinhorn, 4/20/87, (PB88-134341, A04, MF-A01).

NCEER-87-0003 "Experimentation Using the Earthquake Simulation Facilities at University at Buffalo," by A.M. Reinhorn and R.L. Ketter, to be published.

NCEER-87-0004 "The System Characteristics and Performance of a Shaking Table," by J.S. Hwang, K.C. Chang and G.C. Lee, 6/1/87, (PB88-134259, A03, MF-A01). This report is available only through NTIS (see address given above).

NCEER-87-0005 "A Finite Element Formulation for Nonlinear Viscoplastic Material Using a Q Model," by O. Gyebi and G. Dasgupta, 11/2/87, (PB88-213764, A08, MF-A01).

NCEER-87-0006 "Symbolic Manipulation Program (SMP) - Algebraic Codes for Two and Three Dimensional Finite Element Formulations," by X. Lee and G. Dasgupta, 11/9/87, (PB88-218522, A05, MF-A01).

NCEER-87-0007 "Instantaneous Optimal Control Laws for Tall Buildings Under Seismic Excitations," by J.N. Yang, A. Akbarpour and P. Ghaemmaghami, 6/10/87, (PB88-134333, A06, MF-A01). This report is only available through NTIS (see address given above).

NCEER-87-0008 "IDARC: Inelastic Damage Analysis of Reinforced Concrete Frame - Shear-Wall Structures," by Y.J. Park, A.M. Reinhorn and S.K. Kunnath, 7/20/87, (PB88-134325, A09, MF-A01). This report is only available through NTIS (see address given above).

NCEER-87-0009 "Liquefaction Potential for New York State: A Preliminary Report on Sites in Manhattan and Buffalo," by M. Budhu, V. Vijayakumar, R.F. Giese and L. Baumgras, 8/31/87, (PB88-163704, A03, MF-A01). This report is available only through NTIS (see address given above).

NCEER-87-0010 "Vertical and Torsional Vibration of Foundations in Inhomogeneous Media," by A.S. Veletsos and K.W. Dotson, 6/1/87, (PB88-134291, A03, MF-A01). This report is only available through NTIS (see address given above).

NCEER-87-0011 "Seismic Probabilistic Risk Assessment and Seismic Margins Studies for Nuclear Power Plants," by Howard H.M. Hwang, 6/15/87, (PB88-134267, A03, MF-A01). This report is only available through NTIS (see address given above).

NCEER-87-0012 "Parametric Studies of Frequency Response of Secondary Systems Under Ground-Acceleration Excitations," by Y. Yong and Y.K. Lin, 6/10/87, (PB88-134309, A03, MF-A01). This report is only available through NTIS (see address given above).

NCEER-87-0013 "Frequency Response of Secondary Systems Under Seismic Excitation," by J.A. HoLung, J. Cai and Y.K. Lin, 7/31/87, (PB88-134317, A05, MF-A01). This report is only available through NTIS (see address given above).

NCEER-87-0014 "Modelling Earthquake Ground Motions in Seismically Active Regions Using Parametric Time Series Methods," by G.W. Ellis and A.S. Cakmak, 8/25/87, (PB88-134283, A08, MF-A01). This report is only available through NTIS (see address given above).

NCEER-87-0015 "Detection and Assessment of Seismic Structural Damage," by E. DiPasquale and A.S. Cakmak, 8/25/87, (PB88-163712, A05, MF-A01). This report is only available through NTIS (see address given above).

NCEER-87-0016 "Pipeline Experiment at Parkfield, California," by J. Isenberg and E. Richardson, 9/15/87, (PB88-163720, A03, MF-A01). This report is available only through NTIS (see address given above).

NCEER-87-0017 "Digital Simulation of Seismic Ground Motion," by M. Shinozuka, G. Deodatis and T. Harada, 8/31/87, (PB88-155197, A04, MF-A01). This report is available only through NTIS (see address given above).

NCEER-87-0018 "Practical Considerations for Structural Control: System Uncertainty, System Time Delay and Truncation of Small Control Forces," J.N. Yang and A. Akbarpour, 8/10/87, (PB88-163738, A08, MF-A01). This report is only available through NTIS (see address given above).

NCEER-87-0019 "Modal Analysis of Nonclassically Damped Structural Systems Using Canonical Transformation," by J.N. Yang, S. Sarkani and F.X. Long, 9/27/87, (PB88-187851, A04, MF-A01).

NCEER-87-0020 "A Nonstationary Solution in Random Vibration Theory," by J.R. Red-Horse and P.D. Spanos, 11/3/87, (PB88-163746, A03, MF-A01).

NCEER-87-0021 "Horizontal Impedances for Radially Inhomogeneous Viscoelastic Soil Layers," by A.S. Veletsos and K.W. Dotson, 10/15/87, (PB88-150859, A04, MF-A01).

NCEER-87-0022 "Seismic Damage Assessment of Reinforced Concrete Members," by Y.S. Chung, C. Meyer and M. Shinozuka, 10/9/87, (PB88-150867, A05, MF-A01). This report is available only through NTIS (see address given above).

NCEER-87-0023 "Active Structural Control in Civil Engineering," by T.T. Soong, 11/11/87, (PB88-187778, A03, MF-A01).

NCEER-87-0024 "Vertical and Torsional Impedances for Radially Inhomogeneous Viscoelastic Soil Layers," by K.W. Dotson and A.S. Veletsos, 12/87, (PB88-187786, A03, MF-A01).

NCEER-87-0025 "Proceedings from the Symposium on Seismic Hazards, Ground Motions, Soil-Liquefaction and Engineering Practice in Eastern North America," October 20-22, 1987, edited by K.H. Jacob, 12/87, (PB88-188115, A23, MF-A01). This report is available only through NTIS (see address given above).

NCEER-87-0026 "Report on the Whittier-Narrows, California, Earthquake of October 1, 1987," by J. Pantelic and A. Reinhorn, 11/87, (PB88-187752, A03, MF-A01). This report is available only through NTIS (see address given above).

NCEER-87-0027 "Design of a Modular Program for Transient Nonlinear Analysis of Large 3-D Building Structures," by S. Srivastav and J.F. Abel, 12/30/87, (PB88-187950, A05, MF-A01). This report is only available through NTIS (see address given above).

NCEER-87-0028 "Second-Year Program in Research, Education and Technology Transfer," 3/8/88, (PB88-219480, A04, MF-A01).

NCEER-88-0001 "Workshop on Seismic Computer Analysis and Design of Buildings With Interactive Graphics," by W. McGuire, J.F. Abel and C.H. Conley, 1/18/88, (PB88-187760, A03, MF-A01). This report is only available through NTIS (see address given above).

NCEER-88-0002 "Optimal Control of Nonlinear Flexible Structures," by J.N. Yang, F.X. Long and D. Wong, 1/22/88, (PB88-213772, A06, MF-A01).

NCEER-88-0003 "Substructuring Techniques in the Time Domain for Primary-Secondary Structural Systems," by G.D. Manolis and G. Juhn, 2/10/88, (PB88-213780, A04, MF-A01).

NCEER-88-0004 "Iterative Seismic Analysis of Primary-Secondary Systems," by A. Singhal, L.D. Lutes and P.D. Spanos, 2/23/88, (PB88-213798, A04, MF-A01).

NCEER-88-0005 "Stochastic Finite Element Expansion for Random Media," by P.D. Spanos and R. Ghanem, 3/14/88, (PB88-213806, A03, MF-A01).

NCEER-88-0006 "Combining Structural Optimization and Structural Control," by F.Y. Cheng and C.P. Pantelides, 1/10/88, (PB88-213814, A05, MF-A01).

NCEER-88-0007 "Seismic Performance Assessment of Code-Designed Structures," by H.H-M. Hwang, J-W. Jaw and H-J. Shau, 3/20/88, (PB88-219423, A04, MF-A01). This report is only available through NTIS (see address given above).

NCEER-88-0008 "Reliability Analysis of Code-Designed Structures Under Natural Hazards," by H.H-M. Hwang, H. Ushiba and M. Shinozuka, 2/29/88, (PB88-229471, A07, MF-A01). This report is only available through NTIS (see address given above).

NCEER-88-0009 "Seismic Fragility Analysis of Shear Wall Structures," by J-W Jaw and H.H-M. Hwang, 4/30/88, (PB89-102867, A04, MF-A01).

NCEER-88-0010 "Base Isolation of a Multi-Story Building Under a Harmonic Ground Motion - A Comparison of Performances of Various Systems," by F-G Fan, G. Ahmadi and I.G. Tadjbakhsh, 5/18/88, (PB89-122238, A06, MF-A01). This report is only available through NTIS (see address given above).

NCEER-88-0011 "Seismic Floor Response Spectra for a Combined System by Green's Functions," by F.M. Lavelle, L.A. Bergman and P.D. Spanos, 5/1/88, (PB89-102875, A03, MF-A01).

NCEER-88-0012 "A New Solution Technique for Randomly Excited Hysteretic Structures," by G.Q. Cai and Y.K. Lin, 5/16/88, (PB89-102883, A03, MF-A01).

NCEER-88-0013 "A Study of Radiation Damping and Soil-Structure Interaction Effects in the Centrifuge," by K. Weissman, supervised by J.H. Prevost, 5/24/88, (PB89-144703, A06, MF-A01).

NCEER-88-0014 "Parameter Identification and Implementation of a Kinematic Plasticity Model for Frictional Soils," by J.H. Prevost and D.V. Griffiths, to be published.

NCEER-88-0015 "Two- and Three- Dimensional Dynamic Finite Element Analyses of the Long Valley Dam," by D.V. Griffiths and J.H. Prevost, 6/17/88, (PB89-144711, A04, MF-A01).

NCEER-88-0016 "Damage Assessment of Reinforced Concrete Structures in Eastern United States," by A.M. Reinhorn, M.J. Seidel, S.K. Kunnath and Y.J. Park, 6/15/88, (PB89-122220, A04, MF-A01). This report is only available through NTIS (see address given above).

NCEER-88-0017 "Dynamic Compliance of Vertically Loaded Strip Foundations in Multilayered Viscoelastic Soils," by S. Ahmad and A.S.M. Israil, 6/17/88, (PB89-102891, A04, MF-A01).

NCEER-88-0018 "An Experimental Study of Seismic Structural Response With Added Viscoelastic Dampers," by R.C. Lin, Z. Liang, T.T. Soong and R.H. Zhang, 6/30/88, (PB89-122212, A05, MF-A01). This report is available only through NTIS (see address given above).

NCEER-88-0019 "Experimental Investigation of Primary - Secondary System Interaction," by G.D. Manolis, G. Juhn and A.M. Reinhorn, 5/27/88, (PB89-122204, A04, MF-A01).

NCEER-88-0020 "A Response Spectrum Approach For Analysis of Nonclassically Damped Structures," by J.N. Yang, S. Sarkani and F.X. Long, 4/22/88, (PB89-102909, A04, MF-A01).

NCEER-88-0021 "Seismic Interaction of Structures and Soils: Stochastic Approach," by A.S. Veletsos and A.M. Prasad, 7/21/88, (PB89-122196, A04, MF-A01). This report is only available through NTIS (see address given above).

NCEER-88-0022 "Identification of the Serviceability Limit State and Detection of Seismic Structural Damage," by E. DiPasquale and A.S. Cakmak, 6/15/88, (PB89-122188, A05, MF-A01). This report is available only through NTIS (see address given above).

NCEER-88-0023 "Multi-Hazard Risk Analysis: Case of a Simple Offshore Structure," by B.K. Bhartia and E.H. Vanmarcke, 7/21/88, (PB89-145213, A05, MF-A01).

NCEER-88-0024 "Automated Seismic Design of Reinforced Concrete Buildings," by Y.S. Chung, C. Meyer and M. Shinozuka, 7/5/88, (PB89-122170, A06, MF-A01). This report is available only through NTIS (see address given above).

NCEER-88-0025 "Experimental Study of Active Control of MDOF Structures Under Seismic Excitations," by L.L. Chung, R.C. Lin, T.T. Soong and A.M. Reinhorn, 7/10/88, (PB89-122600, A04, MF-A01).

NCEER-88-0026 "Earthquake Simulation Tests of a Low-Rise Metal Structure," by J.S. Hwang, K.C. Chang, G.C. Lee and R.L. Ketter, 8/1/88, (PB89-102917, A04, MF-A01).

NCEER-88-0027 "Systems Study of Urban Response and Reconstruction Due to Catastrophic Earthquakes," by F. Kozin and H.K. Zhou, 9/22/88, (PB90-162348, A04, MF-A01).

NCEER-88-0028 "Seismic Fragility Analysis of Plane Frame Structures," by H.H-M. Hwang and Y.K. Low, 7/31/88, (PB89-131445, A06, MF-A01).

NCEER-88-0029 "Response Analysis of Stochastic Structures," by A. Kardara, C. Bucher and M. Shinozuka, 9/22/88, (PB89-174429, A04, MF-A01).

NCEER-88-0030 "Nonnormal Accelerations Due to Yielding in a Primary Structure," by D.C.K. Chen and L.D. Lutes, 9/19/88, (PB89-131437, A04, MF-A01).

NCEER-88-0031 "Design Approaches for Soil-Structure Interaction," by A.S. Veletsos, A.M. Prasad and Y. Tang, 12/30/88, (PB89-174437, A03, MF-A01). This report is available only through NTIS (see address given above).

NCEER-88-0032 "A Re-evaluation of Design Spectra for Seismic Damage Control," by C.J. Turkstra and A.G. Tallin, 11/7/88, (PB89-145221, A05, MF-A01).

NCEER-88-0033 "The Behavior and Design of Noncontact Lap Splices Subjected to Repeated Inelastic Tensile Loading," by V.E. Sagan, P. Gergely and R.N. White, 12/8/88, (PB89-163737, A08, MF-A01).

NCEER-88-0034 "Seismic Response of Pile Foundations," by S.M. Mamoon, P.K. Banerjee and S. Ahmad, 11/1/88, (PB89-145239, A04, MF-A01).

NCEER-88-0035 "Modeling of R/C Building Structures With Flexible Floor Diaphragms (IDARC2)," by A.M. Reinhorn, S.K. Kunnath and N. Panahshahi, 9/7/88, (PB89-207153, A07, MF-A01).

NCEER-88-0036 "Solution of the Dam-Reservoir Interaction Problem Using a Combination of FEM, BEM with Particular Integrals, Modal Analysis, and Substructuring," by C-S. Tsai, G.C. Lee and R.L. Ketter, 12/31/88, (PB89-207146, A04, MF-A01).

NCEER-88-0037 "Optimal Placement of Actuators for Structural Control," by F.Y. Cheng and C.P. Pantelides, 8/15/88, (PB89-162846, A05, MF-A01).

NCEER-88-0038 "Teflon Bearings in Aseismic Base Isolation: Experimental Studies and Mathematical Modeling," by A. Mokha, M.C. Constantinou and A.M. Reinhorn, 12/5/88, (PB89-218457, A10, MF-A01). This report is available only through NTIS (see address given above).

NCEER-88-0039 "Seismic Behavior of Flat Slab High-Rise Buildings in the New York City Area," by P. Weidlinger and M. Ettouney, 10/15/88, (PB90-145681, A04, MF-A01).

NCEER-88-0040 "Evaluation of the Earthquake Resistance of Existing Buildings in New York City," by P. Weidlinger and M. Ettouney, 10/15/88, to be published.

NCEER-88-0041 "Small-Scale Modeling Techniques for Reinforced Concrete Structures Subjected to Seismic Loads," by W. Kim, A. El-Attar and R.N. White, 11/22/88, (PB89-189625, A05, MF-A01).

NCEER-88-0042 "Modeling Strong Ground Motion from Multiple Event Earthquakes," by G.W. Ellis and A.S. Cakmak, 10/15/88, (PB89-174445, A03, MF-A01).

NCEER-88-0043 "Nonstationary Models of Seismic Ground Acceleration," by M. Grigoriu, S.E. Ruiz and E. Rosenblueth, 7/15/88, (PB89-189617, A04, MF-A01).

NCEER-88-0044 "SARCF User's Guide: Seismic Analysis of Reinforced Concrete Frames," by Y.S. Chung, C. Meyer and M. Shinozuka, 11/9/88, (PB89-174452, A08, MF-A01).

NCEER-88-0045 "First Expert Panel Meeting on Disaster Research and Planning," edited by J. Pantelic and J. Stoyle, 9/15/88, (PB89-174460, A05, MF-A01).

NCEER-88-0046 "Preliminary Studies of the Effect of Degrading Infill Walls on the Nonlinear Seismic Response of Steel Frames," by C.Z. Chrysostomou, P. Gergely and J.F. Abel, 12/19/88, (PB89-208383, A05, MF-A01).

NCEER-88-0047 "Reinforced Concrete Frame Component Testing Facility - Design, Construction, Instrumentation and Operation," by S.P. Pessiki, C. Conley, T. Bond, P. Gergely and R.N. White, 12/16/88, (PB89-174478, A04, MF-A01).

NCEER-89-0001 "Effects of Protective Cushion and Soil Compliancy on the Response of Equipment Within a Seismically Excited Building," by J.A. HoLung, 2/16/89, (PB89-207179, A04, MF-A01).

NCEER-89-0002 "Statistical Evaluation of Response Modification Factors for Reinforced Concrete Structures," by H.H-M. Hwang and J-W. Jaw, 2/17/89, (PB89-207187, A05, MF-A01).

NCEER-89-0003 "Hysteretic Columns Under Random Excitation," by G-Q. Cai and Y.K. Lin, 1/9/89, (PB89-196513, A03, MF-A01).

NCEER-89-0004 "Experimental Study of `Elephant Foot Bulge' Instability of Thin-Walled Metal Tanks," by Z-H. Jia and R.L. Ketter, 2/22/89, (PB89-207195, A03, MF-A01).

NCEER-89-0005 "Experiment on Performance of Buried Pipelines Across San Andreas Fault," by J. Isenberg, E. Richardson and T.D. O'Rourke, 3/10/89, (PB89-218440, A04, MF-A01). This report is available only through NTIS (see address given above).

NCEER-89-0006 "A Knowledge-Based Approach to Structural Design of Earthquake-Resistant Buildings," by M. Subramani, P. Gergely, C.H. Conley, J.F. Abel and A.H. Zaghw, 1/15/89, (PB89-218465, A06, MF-A01).

NCEER-89-0007 "Liquefaction Hazards and Their Effects on Buried Pipelines," by T.D. O'Rourke and P.A. Lane, 2/1/89, (PB89-218481, A09, MF-A01).

NCEER-89-0008 "Fundamentals of System Identification in Structural Dynamics," by H. Imai, C-B. Yun, O. Maruyama and M. Shinozuka, 1/26/89, (PB89-207211, A04, MF-A01).

NCEER-89-0009 "Effects of the 1985 Michoacan Earthquake on Water Systems and Other Buried Lifelines in Mexico," by A.G. Ayala and M.J. O'Rourke, 3/8/89, (PB89-207229, A06, MF-A01).

NCEER-89-R010 "NCEER Bibliography of Earthquake Education Materials," by K.E.K. Ross, Second Revision, 9/1/89, (PB90-125352, A05, MF-A01). This report is replaced by NCEER-92-0018.

NCEER-89-0011 "Inelastic Three-Dimensional Response Analysis of Reinforced Concrete Building Structures (IDARC-3D), Part I - Modeling," by S.K. Kunnath and A.M. Reinhorn, 4/17/89, (PB90-114612, A07, MF-A01). This report is available only through NTIS (see address given above).

NCEER-89-0012 "Recommended Modifications to ATC-14," by C.D. Poland and J.O. Malley, 4/12/89, (PB90-108648, A15, MF-A01).

NCEER-89-0013 "Repair and Strengthening of Beam-to-Column Connections Subjected to Earthquake Loading," by M. Corazao and A.J. Durrani, 2/28/89, (PB90-109885, A06, MF-A01).

NCEER-89-0014 "Program EXKAL2 for Identification of Structural Dynamic Systems," by O. Maruyama, C-B. Yun, M. Hoshiya and M. Shinozuka, 5/19/89, (PB90-109877, A09, MF-A01).

NCEER-89-0015 "Response of Frames With Bolted Semi-Rigid Connections, Part I - Experimental Study and Analytical Predictions," by P.J. DiCorso, A.M. Reinhorn, J.R. Dickerson, J.B. Radziminski and W.L. Harper, 6/1/89, to be published.

NCEER-89-0016 "ARMA Monte Carlo Simulation in Probabilistic Structural Analysis," by P.D. Spanos and M.P. Mignolet, 7/10/89, (PB90-109893, A03, MF-A01).

NCEER-89-P017 "Preliminary Proceedings from the Conference on Disaster Preparedness - The Place of Earthquake Education in Our Schools," Edited by K.E.K. Ross, 6/23/89, (PB90-108606, A03, MF-A01).

NCEER-89-0017 "Proceedings from the Conference on Disaster Preparedness - The Place of Earthquake Education in Our Schools," Edited by K.E.K. Ross, 12/31/89, (PB90-207895, A012, MF-A02). This report is available only through NTIS (see address given above).

NCEER-89-0018 "Multidimensional Models of Hysteretic Material Behavior for Vibration Analysis of Shape Memory Energy Absorbing Devices, by E.J. Graesser and F.A. Cozzarelli, 6/7/89, (PB90-164146, A04, MF-A01).

NCEER-89-0019 "Nonlinear Dynamic Analysis of Three-Dimensional Base Isolated Structures (3D-BASIS)," by S. Nagarajaiah, A.M. Reinhorn and M.C. Constantinou, 8/3/89, (PB90-161936, A06, MF-A01). This report has been replaced by NCEER-93-0011.

NCEER-89-0020 "Structural Control Considering Time-Rate of Control Forces and Control Rate Constraints," by F.Y. Cheng and C.P. Pantelides, 8/3/89, (PB90-120445, A04, MF-A01).

NCEER-89-0021 "Subsurface Conditions of Memphis and Shelby County," by K.W. Ng, T-S. Chang and H-H.M. Hwang, 7/26/89, (PB90-120437, A03, MF-A01).

NCEER-89-0022 "Seismic Wave Propagation Effects on Straight Jointed Buried Pipelines," by K. Elhmadi and M.J. O'Rourke, 8/24/89, (PB90-162322, A10, MF-A02).

NCEER-89-0023 "Workshop on Serviceability Analysis of Water Delivery Systems," edited by M. Grigoriu, 3/6/89, (PB90-127424, A03, MF-A01).

NCEER-89-0024 "Shaking Table Study of a 1/5 Scale Steel Frame Composed of Tapered Members," by K.C. Chang, J.S. Hwang and G.C. Lee, 9/18/89, (PB90-160169, A04, MF-A01).

NCEER-89-0025 "DYNA1D: A Computer Program for Nonlinear Seismic Site Response Analysis - Technical Documentation," by Jean H. Prevost, 9/14/89, (PB90-161944, A07, MF-A01). This report is available only through NTIS (see address given above).

NCEER-89-0026 "1:4 Scale Model Studies of Active Tendon Systems and Active Mass Dampers for Aseismic Protection," by A.M. Reinhorn, T.T. Soong, R.C. Lin, Y.P. Yang, Y. Fukao, H. Abe and M. Nakai, 9/15/89, (PB90-173246, A10, MF-A02). This report is available only through NTIS (see address given above).

NCEER-89-0027 "Scattering of Waves by Inclusions in a Nonhomogeneous Elastic Half Space Solved by Boundary Element Methods," by P.K. Hadley, A. Askar and A.S. Cakmak, 6/15/89, (PB90-145699, A07, MF-A01).

NCEER-89-0028 "Statistical Evaluation of Deflection Amplification Factors for Reinforced Concrete Structures," by H.H.M. Hwang, J-W. Jaw and A.L. Ch'ng, 8/31/89, (PB90-164633, A05, MF-A01).

NCEER-89-0029 "Bedrock Accelerations in Memphis Area Due to Large New Madrid Earthquakes," by H.H.M. Hwang, C.H.S. Chen and G. Yu, 11/7/89, (PB90-162330, A04, MF-A01).

NCEER-89-0030 "Seismic Behavior and Response Sensitivity of Secondary Structural Systems," by Y.Q. Chen and T.T. Soong, 10/23/89, (PB90-164658, A08, MF-A01).

NCEER-89-0031 "Random Vibration and Reliability Analysis of Primary-Secondary Structural Systems," by Y. Ibrahim, M. Grigoriu and T.T. Soong, 11/10/89, (PB90-161951, A04, MF-A01).

NCEER-89-0032 "Proceedings from the Second U.S. - Japan Workshop on Liquefaction, Large Ground Deformation and Their Effects on Lifelines, September 26-29, 1989," Edited by T.D. O'Rourke and M. Hamada, 12/1/89, (PB90-209388, A22, MF-A03).

NCEER-89-0033 "Deterministic Model for Seismic Damage Evaluation of Reinforced Concrete Structures," by J.M. Bracci, A.M. Reinhorn, J.B. Mander and S.K. Kunnath, 9/27/89, (PB91-108803, A06, MF-A01).

NCEER-89-0034 "On the Relation Between Local and Global Damage Indices," by E. DiPasquale and A.S. Cakmak, 8/15/89, (PB90-173865, A05, MF-A01).

NCEER-89-0035 "Cyclic Undrained Behavior of Nonplastic and Low Plasticity Silts," by A.J. Walker and H.E. Stewart, 7/26/89, (PB90-183518, A10, MF-A01).

NCEER-89-0036 "Liquefaction Potential of Surficial Deposits in the City of Buffalo, New York," by M. Budhu, R. Giese and L. Baumgrass, 1/17/89, (PB90-208455, A04, MF-A01).

NCEER-89-0037 "A Deterministic Assessment of Effects of Ground Motion Incoherence," by A.S. Veletsos and Y. Tang, 7/15/89, (PB90-164294, A03, MF-A01).

NCEER-89-0038 "Workshop on Ground Motion Parameters for Seismic Hazard Mapping," July 17-18, 1989, edited by R.V. Whitman, 12/1/89, (PB90-173923, A04, MF-A01).

NCEER-89-0039 "Seismic Effects on Elevated Transit Lines of the New York City Transit Authority," by C.J. Costantino, C.A. Miller and E. Heymsfield, 12/26/89, (PB90-207887, A06, MF-A01).

NCEER-89-0040 "Centrifugal Modeling of Dynamic Soil-Structure Interaction," by K. Weissman, Supervised by J.H. Prevost, 5/10/89, (PB90-207879, A07, MF-A01).

NCEER-89-0041 "Linearized Identification of Buildings With Cores for Seismic Vulnerability Assessment," by I-K. Ho and A.E. Aktan, 11/1/89, (PB90-251943, A07, MF-A01).

NCEER-90-0001 "Geotechnical and Lifeline Aspects of the October 17, 1989 Loma Prieta Earthquake in San Francisco," by T.D. O'Rourke, H.E. Stewart, F.T. Blackburn and T.S. Dickerman, 1/90, (PB90-208596, A05, MF-A01).

NCEER-90-0002 "Nonnormal Secondary Response Due to Yielding in a Primary Structure," by D.C.K. Chen and L.D. Lutes, 2/28/90, (PB90-251976, A07, MF-A01).

NCEER-90-0003 "Earthquake Education Materials for Grades K-12," by K.E.K. Ross, 4/16/90, (PB91-251984, A05, MF-A05). This report has been replaced by NCEER-92-0018.

NCEER-90-0004 "Catalog of Strong Motion Stations in Eastern North America," by R.W. Busby, 4/3/90, (PB90-251984, A05, MF-A01).

NCEER-90-0005 "NCEER Strong-Motion Data Base: A User Manual for the GeoBase Release (Version 1.0 for the Sun3)," by P. Friberg and K. Jacob, 3/31/90 (PB90-258062, A04, MF-A01).

NCEER-90-0006 "Seismic Hazard Along a Crude Oil Pipeline in the Event of an 1811-1812 Type New Madrid Earthquake," by H.H.M. Hwang and C-H.S. Chen, 4/16/90, (PB90-258054, A04, MF-A01).

NCEER-90-0007 "Site-Specific Response Spectra for Memphis Sheahan Pumping Station," by H.H.M. Hwang and C.S. Lee, 5/15/90, (PB91-108811, A05, MF-A01).

NCEER-90-0008 "Pilot Study on Seismic Vulnerability of Crude Oil Transmission Systems," by T. Ariman, R. Dobry, M. Grigoriu, F. Kozin, M. O'Rourke, T. O'Rourke and M. Shinozuka, 5/25/90, (PB91-108837, A06, MF-A01).

NCEER-90-0009 "A Program to Generate Site Dependent Time Histories: EQGEN," by G.W. Ellis, M. Srinivasan and A.S. Cakmak, 1/30/90, (PB91-108829, A04, MF-A01).

NCEER-90-0010 "Active Isolation for Seismic Protection of Operating Rooms," by M.E. Talbott, Supervised by M. Shinozuka, 6/8/9, (PB91-110205, A05, MF-A01).

NCEER-90-0011 "Program LINEARID for Identification of Linear Structural Dynamic Systems," by C-B. Yun and M. Shinozuka, 6/25/90, (PB91-110312, A08, MF-A01).

NCEER-90-0012 "Two-Dimensional Two-Phase Elasto-Plastic Seismic Response of Earth Dams," by A.N. Yiagos, Supervised by J.H. Prevost, 6/20/90, (PB91-110197, A13, MF-A02).

NCEER-90-0013 "Secondary Systems in Base-Isolated Structures: Experimental Investigation, Stochastic Response and Stochastic Sensitivity," by G.D. Manolis, G. Juhn, M.C. Constantinou and A.M. Reinhorn, 7/1/90, (PB91-110320, A08, MF-A01).

NCEER-90-0014 "Seismic Behavior of Lightly-Reinforced Concrete Column and Beam-Column Joint Details," by S.P. Pessiki, C.H. Conley, P. Gergely and R.N. White, 8/22/90, (PB91-108795, A11, MF-A02).

NCEER-90-0015 "Two Hybrid Control Systems for Building Structures Under Strong Earthquakes," by J.N. Yang and A. Danielians, 6/29/90, (PB91-125393, A04, MF-A01).

NCEER-90-0016 "Instantaneous Optimal Control with Acceleration and Velocity Feedback," by J.N. Yang and Z. Li, 6/29/90, (PB91-125401, A03, MF-A01).

NCEER-90-0017 "Reconnaissance Report on the Northern Iran Earthquake of June 21, 1990," by M. Mehrain, 10/4/90, (PB91-125377, A03, MF-A01).

NCEER-90-0018 "Evaluation of Liquefaction Potential in Memphis and Shelby County," by T.S. Chang, P.S. Tang, C.S. Lee and H. Hwang, 8/10/90, (PB91-125427, A09, MF-A01).

NCEER-90-0019 "Experimental and Analytical Study of a Combined Sliding Disc Bearing and Helical Steel Spring Isolation System," by M.C. Constantinou, A.S. Mokha and A.M. Reinhorn, 10/4/90, (PB91-125385, A06, MF-A01). This report is available only through NTIS (see address given above).

NCEER-90-0020 "Experimental Study and Analytical Prediction of Earthquake Response of a Sliding Isolation System with a Spherical Surface," by A.S. Mokha, M.C. Constantinou and A.M. Reinhorn, 10/11/90, (PB91-125419, A05, MF-A01).

NCEER-90-0021 "Dynamic Interaction Factors for Floating Pile Groups," by G. Gazetas, K. Fan, A. Kaynia and E. Kausel, 9/10/90, (PB91-170381, A05, MF-A01).

NCEER-90-0022 "Evaluation of Seismic Damage Indices for Reinforced Concrete Structures," by S. Rodriguez-Gomez and A.S. Cakmak, 9/30/90, PB91-171322, A06, MF-A01).

NCEER-90-0023 "Study of Site Response at a Selected Memphis Site," by H. Desai, S. Ahmad, E.S. Gazetas and M.R. Oh, 10/11/90, (PB91-196857, A03, MF-A01).

NCEER-90-0024 "A User's Guide to Strongmo: Version 1.0 of NCEER's Strong-Motion Data Access Tool for PCs and Terminals," by P.A. Friberg and C.A.T. Susch, 11/15/90, (PB91-171272, A03, MF-A01).

NCEER-90-0025 "A Three-Dimensional Analytical Study of Spatial Variability of Seismic Ground Motions," by L-L. Hong and A.H.-S. Ang, 10/30/90, (PB91-170399, A09, MF-A01).

NCEER-90-0026 "MUMOID User's Guide - A Program for the Identification of Modal Parameters," by S. Rodriguez-Gomez and E. DiPasquale, 9/30/90, (PB91-171298, A04, MF-A01).

NCEER-90-0027 "SARCF-II User's Guide - Seismic Analysis of Reinforced Concrete Frames," by S. Rodriguez-Gomez, Y.S. Chung and C. Meyer, 9/30/90, (PB91-171280, A05, MF-A01).

NCEER-90-0028 "Viscous Dampers: Testing, Modeling and Application in Vibration and Seismic Isolation," by N. Makris and M.C. Constantinou, 12/20/90 (PB91-190561, A06, MF-A01).

NCEER-90-0029 "Soil Effects on Earthquake Ground Motions in the Memphis Area," by H. Hwang, C.S. Lee, K.W. Ng and T.S. Chang, 8/2/90, (PB91-190751, A05, MF-A01).

NCEER-91-0001 "Proceedings from the Third Japan-U.S. Workshop on Earthquake Resistant Design of Lifeline Facilities and Countermeasures for Soil Liquefaction, December 17-19, 1990," edited by T.D. O'Rourke and M. Hamada, 2/1/91, (PB91-179259, A99, MF-A04).

NCEER-91-0002 "Physical Space Solutions of Non-Proportionally Damped Systems," by M. Tong, Z. Liang and G.C. Lee, 1/15/91, (PB91-179242, A04, MF-A01).

NCEER-91-0003 "Seismic Response of Single Piles and Pile Groups," by K. Fan and G. Gazetas, 1/10/91, (PB92-174994, A04, MF-A01).

NCEER-91-0004 "Damping of Structures: Part 1 - Theory of Complex Damping," by Z. Liang and G. Lee, 10/10/91, (PB92-197235, A12, MF-A03).

NCEER-91-0005 "3D-BASIS - Nonlinear Dynamic Analysis of Three Dimensional Base Isolated Structures: Part II," by S. Nagarajaiah, A.M. Reinhorn and M.C. Constantinou, 2/28/91, (PB91-190553, A07, MF-A01). This report has been replaced by NCEER-93-0011.

NCEER-91-0006 "A Multidimensional Hysteretic Model for Plasticity Deforming Metals in Energy Absorbing Devices," by E.J. Graesser and F.A. Cozzarelli, 4/9/91, (PB92-108364, A04, MF-A01).

NCEER-91-0007 "A Framework for Customizable Knowledge-Based Expert Systems with an Application to a KBES for Evaluating the Seismic Resistance of Existing Buildings," by E.G. Ibarra-Anaya and S.J. Fenves, 4/9/91, (PB91-210930, A08, MF-A01).

NCEER-91-0008 "Nonlinear Analysis of Steel Frames with Semi-Rigid Connections Using the Capacity Spectrum Method," by G.G. Deierlein, S-H. Hsieh, Y-J. Shen and J.F. Abel, 7/2/91, (PB92-113828, A05, MF-A01).

NCEER-91-0009 "Earthquake Education Materials for Grades K-12," by K.E.K. Ross, 4/30/91, (PB91-212142, A06, MF-A01). This report has been replaced by NCEER-92-0018.

NCEER-91-0010 "Phase Wave Velocities and Displacement Phase Differences in a Harmonically Oscillating Pile," by N. Makris and G. Gazetas, 7/8/91, (PB92-108356, A04, MF-A01).

NCEER-91-0011 "Dynamic Characteristics of a Full-Size Five-Story Steel Structure and a 2/5 Scale Model," by K.C. Chang, G.C. Yao, G.C. Lee, D.S. Hao and Y.C. Yeh," 7/2/91, (PB93-116648, A06, MF-A02).

NCEER-91-0012 "Seismic Response of a 2/5 Scale Steel Structure with Added Viscoelastic Dampers," by K.C. Chang, T.T. Soong, S-T. Oh and M.L. Lai, 5/17/91, (PB92-110816, A05, MF-A01).

NCEER-91-0013 "Earthquake Response of Retaining Walls; Full-Scale Testing and Computational Modeling," by S. Alampalli and A-W.M. Elgamal, 6/20/91, to be published.

NCEER-91-0014 "3D-BASIS-M: Nonlinear Dynamic Analysis of Multiple Building Base Isolated Structures," by P.C. Tsopelas, S. Nagarajaiah, M.C. Constantinou and A.M. Reinhorn, 5/28/91, (PB92-113885, A09, MF-A02).

NCEER-91-0015 "Evaluation of SEAOC Design Requirements for Sliding Isolated Structures," by D. Theodossiou and M.C. Constantinou, 6/10/91, (PB92-114602, A11, MF-A03).

NCEER-91-0016 "Closed-Loop Modal Testing of a 27-Story Reinforced Concrete Flat Plate-Core Building," by H.R. Somaprasad, T. Toksoy, H. Yoshiyuki and A.E. Aktan, 7/15/91, (PB92-129980, A07, MF-A02).

NCEER-91-0017 "Shake Table Test of a 1/6 Scale Two-Story Lightly Reinforced Concrete Building," by A.G. El-Attar, R.N. White and P. Gergely, 2/28/91, (PB92-222447, A06, MF-A02).

NCEER-91-0018 "Shake Table Test of a 1/8 Scale Three-Story Lightly Reinforced Concrete Building," by A.G. El-Attar, R.N. White and P. Gergely, 2/28/91, (PB93-116630, A08, MF-A02).

NCEER-91-0019 "Transfer Functions for Rigid Rectangular Foundations," by A.S. Veletsos, A.M. Prasad and W.H. Wu, 7/31/91, to be published.

NCEER-91-0020 "Hybrid Control of Seismic-Excited Nonlinear and Inelastic Structural Systems," by J.N. Yang, Z. Li and A. Danielians, 8/1/91, (PB92-143171, A06, MF-A02).

NCEER-91-0021 "The NCEER-91 Earthquake Catalog: Improved Intensity-Based Magnitudes and Recurrence Relations for U.S. Earthquakes East of New Madrid," by L. Seeber and J.G. Armbruster, 8/28/91, (PB92-176742, A06, MF-A02).

NCEER-91-0022 "Proceedings from the Implementation of Earthquake Planning and Education in Schools: The Need for Change - The Roles of the Changemakers," by K.E.K. Ross and F. Winslow, 7/23/91, (PB92-129998, A12, MF-A03).

NCEER-91-0023 "A Study of Reliability-Based Criteria for Seismic Design of Reinforced Concrete Frame Buildings," by H.H.M. Hwang and H-M. Hsu, 8/10/91, (PB92-140235, A09, MF-A02).

NCEER-91-0024 "Experimental Verification of a Number of Structural System Identification Algorithms," by R.G. Ghanem, H. Gavin and M. Shinozuka, 9/18/91, (PB92-176577, A18, MF-A04).

NCEER-91-0025 "Probabilistic Evaluation of Liquefaction Potential," by H.H.M. Hwang and C.S. Lee," 11/25/91, (PB92-143429, A05, MF-A01).

NCEER-91-0026 "Instantaneous Optimal Control for Linear, Nonlinear and Hysteretic Structures - Stable Controllers," by J.N. Yang and Z. Li, 11/15/91, (PB92-163807, A04, MF-A01).

NCEER-91-0027 "Experimental and Theoretical Study of a Sliding Isolation System for Bridges," by M.C. Constantinou, A. Kartoum, A.M. Reinhorn and P. Bradford, 11/15/91, (PB92-176973, A10, MF-A03).

NCEER-92-0001 "Case Studies of Liquefaction and Lifeline Performance During Past Earthquakes, Volume 1: Japanese Case Studies," Edited by M. Hamada and T. O'Rourke, 2/17/92, (PB92-197243, A18, MF-A04).

NCEER-92-0002 "Case Studies of Liquefaction and Lifeline Performance During Past Earthquakes, Volume 2: United States Case Studies," Edited by T. O'Rourke and M. Hamada, 2/17/92, (PB92-197250, A20, MF-A04).

NCEER-92-0003 "Issues in Earthquake Education," Edited by K. Ross, 2/3/92, (PB92-222389, A07, MF-A02).

NCEER-92-0004 "Proceedings from the First U.S. - Japan Workshop on Earthquake Protective Systems for Bridges," Edited by I.G. Buckle, 2/4/92, (PB94-142239, A99, MF-A06).

NCEER-92-0005 "Seismic Ground Motion from a Haskell-Type Source in a Multiple-Layered Half-Space," A.P. Theoharis, G. Deodatis and M. Shinozuka, 1/2/92, to be published.

NCEER-92-0006 "Proceedings from the Site Effects Workshop," Edited by R. Whitman, 2/29/92, (PB92-197201, A04, MF-A01).

NCEER-92-0007 "Engineering Evaluation of Permanent Ground Deformations Due to Seismically-Induced Liquefaction," by M.H. Baziar, R. Dobry and A-W.M. Elgamal, 3/24/92, (PB92-222421, A13, MF-A03).

NCEER-92-0008 "A Procedure for the Seismic Evaluation of Buildings in the Central and Eastern United States," by C.D. Poland and J.O. Malley, 4/2/92, (PB92-222439, A20, MF-A04).

NCEER-92-0009 "Experimental and Analytical Study of a Hybrid Isolation System Using Friction Controllable Sliding Bearings," by M.Q. Feng, S. Fujii and M. Shinozuka, 5/15/92, (PB93-150282, A06, MF-A02).

NCEER-92-0010 "Seismic Resistance of Slab-Column Connections in Existing Non-Ductile Flat-Plate Buildings," by A.J. Durrani and Y. Du, 5/18/92, (PB93-116812, A06, MF-A02).

NCEER-92-0011 "The Hysteretic and Dynamic Behavior of Brick Masonry Walls Upgraded by Ferrocement Coatings Under Cyclic Loading and Strong Simulated Ground Motion," by H. Lee and S.P. Prawel, 5/11/92, to be published.

NCEER-92-0012 "Study of Wire Rope Systems for Seismic Protection of Equipment in Buildings," by G.F. Demetriades, M.C. Constantinou and A.M. Reinhorn, 5/20/92, (PB93-116655, A08, MF-A02).

NCEER-92-0013 "Shape Memory Structural Dampers: Material Properties, Design and Seismic Testing," by P.R. Witting and F.A. Cozzarelli, 5/26/92, (PB93-116663, A05, MF-A01).

NCEER-92-0014 "Longitudinal Permanent Ground Deformation Effects on Buried Continuous Pipelines," by M.J. O'Rourke, and C. Nordberg, 6/15/92, (PB93-116671, A08, MF-A02).

NCEER-92-0015 "A Simulation Method for Stationary Gaussian Random Functions Based on the Sampling Theorem," by M. Grigoriu and S. Balopoulou, 6/11/92, (PB93-127496, A05, MF-A01).

NCEER-92-0016 "Gravity-Load-Designed Reinforced Concrete Buildings: Seismic Evaluation of Existing Construction and Detailing Strategies for Improved Seismic Resistance," by G.W. Hoffmann, S.K. Kunnath, A.M. Reinhorn and J.B. Mander, 7/15/92, (PB94-142007, A08, MF-A02).

NCEER-92-0017 "Observations on Water System and Pipeline Performance in the Limón Area of Costa Rica Due to the April 22, 1991 Earthquake," by M. O'Rourke and D. Ballantyne, 6/30/92, (PB93-126811, A06, MF-A02).

NCEER-92-0018 "Fourth Edition of Earthquake Education Materials for Grades K-12," Edited by K.E.K. Ross, 8/10/92, (PB93-114023, A07, MF-A02).

NCEER-92-0019 "Proceedings from the Fourth Japan-U.S. Workshop on Earthquake Resistant Design of Lifeline Facilities and Countermeasures for Soil Liquefaction," Edited by M. Hamada and T.D. O'Rourke, 8/12/92, (PB93-163939, A99, MF-E11).

NCEER-92-0020 "Active Bracing System: A Full Scale Implementation of Active Control," by A.M. Reinhorn, T.T. Soong, R.C. Lin, M.A. Riley, Y.P. Wang, S. Aizawa and M. Higashino, 8/14/92, (PB93-127512, A06, MF-A02).

NCEER-92-0021 "Empirical Analysis of Horizontal Ground Displacement Generated by Liquefaction-Induced Lateral Spreads," by S.F. Bartlett and T.L. Youd, 8/17/92, (PB93-188241, A06, MF-A02).

NCEER-92-0022 "IDARC Version 3.0: Inelastic Damage Analysis of Reinforced Concrete Structures," by S.K. Kunnath, A.M. Reinhorn and R.F. Lobo, 8/31/92, (PB93-227502, A07, MF-A02).

NCEER-92-0023 "A Semi-Empirical Analysis of Strong-Motion Peaks in Terms of Seismic Source, Propagation Path and Local Site Conditions, by M. Kamiyama, M.J. O'Rourke and R. Flores-Berrones, 9/9/92, (PB93-150266, A08, MF-A02).

NCEER-92-0024 "Seismic Behavior of Reinforced Concrete Frame Structures with Nonductile Details, Part I: Summary of Experimental Findings of Full Scale Beam-Column Joint Tests," by A. Beres, R.N. White and P. Gergely, 9/30/92, (PB93-227783, A05, MF-A01).

NCEER-92-0025 "Experimental Results of Repaired and Retrofitted Beam-Column Joint Tests in Lightly Reinforced Concrete Frame Buildings," by A. Beres, S. El-Borgi, R.N. White and P. Gergely, 10/29/92, (PB93-227791, A05, MF-A01).

NCEER-92-0026 "A Generalization of Optimal Control Theory: Linear and Nonlinear Structures," by J.N. Yang, Z. Li and S. Vongchavalitkul, 11/2/92, (PB93-188621, A05, MF-A01).

NCEER-92-0027 "Seismic Resistance of Reinforced Concrete Frame Structures Designed Only for Gravity Loads: Part I - Design and Properties of a One-Third Scale Model Structure," by J.M. Bracci, A.M. Reinhorn and J.B. Mander, 12/1/92, (PB94-104502, A08, MF-A02).

NCEER-92-0028 "Seismic Resistance of Reinforced Concrete Frame Structures Designed Only for Gravity Loads: Part II - Experimental Performance of Subassemblages," by L.E. Aycardi, J.B. Mander and A.M. Reinhorn, 12/1/92, (PB94-104510, A08, MF-A02).

NCEER-92-0029 "Seismic Resistance of Reinforced Concrete Frame Structures Designed Only for Gravity Loads: Part III - Experimental Performance and Analytical Study of a Structural Model," by J.M. Bracci, A.M. Reinhorn and J.B. Mander, 12/1/92, (PB93-227528, A09, MF-A01).

NCEER-92-0030 "Evaluation of Seismic Retrofit of Reinforced Concrete Frame Structures: Part I - Experimental Performance of Retrofitted Subassemblages," by D. Choudhuri, J.B. Mander and A.M. Reinhorn, 12/8/92, (PB93-198307, A07, MF-A02).

NCEER-92-0031 "Evaluation of Seismic Retrofit of Reinforced Concrete Frame Structures: Part II - Experimental Performance and Analytical Study of a Retrofitted Structural Model," by J.M. Bracci, A.M. Reinhorn and J.B. Mander, 12/8/92, (PB93-198315, A09, MF-A03).

NCEER-92-0032 "Experimental and Analytical Investigation of Seismic Response of Structures with Supplemental Fluid Viscous Dampers," by M.C. Constantinou and M.D. Symans, 12/21/92, (PB93-191435, A10, MF-A03). This report is available only through NTIS (see address given above).

NCEER-92-0033 "Reconnaissance Report on the Cairo, Egypt Earthquake of October 12, 1992," by M. Khater, 12/23/92, (PB93-188621, A03, MF-A01).

NCEER-92-0034 "Low-Level Dynamic Characteristics of Four Tall Flat-Plate Buildings in New York City," by H. Gavin, S. Yuan, J. Grossman, E. Pekelis and K. Jacob, 12/28/92, (PB93-188217, A07, MF-A02).

NCEER-93-0001 "An Experimental Study on the Seismic Performance of Brick-Infilled Steel Frames With and Without Retrofit," by J.B. Mander, B. Nair, K. Wojtkowski and J. Ma, 1/29/93, (PB93-227510, A07, MF-A02).

NCEER-93-0002 "Social Accounting for Disaster Preparedness and Recovery Planning," by S. Cole, E. Pantoja and V. Razak, 2/22/93, (PB94-142114, A12, MF-A03).

NCEER-93-0003 "Assessment of 1991 NEHRP Provisions for Nonstructural Components and Recommended Revisions," by T.T. Soong, G. Chen, Z. Wu, R-H. Zhang and M. Grigoriu, 3/1/93, (PB93-188639, A06, MF-A02).

NCEER-93-0004 "Evaluation of Static and Response Spectrum Analysis Procedures of SEAOC/UBC for Seismic Isolated Structures," by C.W. Winters and M.C. Constantinou, 3/23/93, (PB93-198299, A10, MF-A03).

NCEER-93-0005 "Earthquakes in the Northeast - Are We Ignoring the Hazard? A Workshop on Earthquake Science and Safety for Educators," edited by K.E.K. Ross, 4/2/93, (PB94-103066, A09, MF-A02).

NCEER-93-0006 "Inelastic Response of Reinforced Concrete Structures with Viscoelastic Braces," by R.F. Lobo, J.M. Bracci, K.L. Shen, A.M. Reinhorn and T.T. Soong, 4/5/93, (PB93-227486, A05, MF-A02).

NCEER-93-0007 "Seismic Testing of Installation Methods for Computers and Data Processing Equipment," by K. Kosar, T.T. Soong, K.L. Shen, J.A. HoLung and Y.K. Lin, 4/12/93, (PB93-198299, A07, MF-A02).

NCEER-93-0008 "Retrofit of Reinforced Concrete Frames Using Added Dampers," by A. Reinhorn, M. Constantinou and C. Li, to be published.

NCEER-93-0009 "Seismic Behavior and Design Guidelines for Steel Frame Structures with Added Viscoelastic Dampers," by K.C. Chang, M.L. Lai, T.T. Soong, D.S. Hao and Y.C. Yeh, 5/1/93, (PB94-141959, A07, MF-A02).

NCEER-93-0010 "Seismic Performance of Shear-Critical Reinforced Concrete Bridge Piers," by J.B. Mander, S.M. Waheed, M.T.A. Chaudhary and S.S. Chen, 5/12/93, (PB93-227494, A08, MF-A02).

NCEER-93-0011 "3D-BASIS-TABS: Computer Program for Nonlinear Dynamic Analysis of Three Dimensional Base Isolated Structures," by S. Nagarajaiah, C. Li, A.M. Reinhorn and M.C. Constantinou, 8/2/93, (PB94-141819, A09, MF-A02).

NCEER-93-0012 "Effects of Hydrocarbon Spills from an Oil Pipeline Break on Ground Water," by O.J. Helweg and H.H.M. Hwang, 8/3/93, (PB94-141942, A06, MF-A02).

NCEER-93-0013 "Simplified Procedures for Seismic Design of Nonstructural Components and Assessment of Current Code Provisions," by M.P. Singh, L.E. Suarez, E.E. Matheu and G.O. Maldonado, 8/4/93, (PB94-141827, A09, MF-A02).

NCEER-93-0014 "An Energy Approach to Seismic Analysis and Design of Secondary Systems," by G. Chen and T.T. Soong, 8/6/93, (PB94-142767, A11, MF-A03).

NCEER-93-0015 "Proceedings from School Sites: Becoming Prepared for Earthquakes - Commemorating the Third Anniversary of the Loma Prieta Earthquake," Edited by F.E. Winslow and K.E.K. Ross, 8/16/93, (PB94-154275, A16, MF-A02).

NCEER-93-0016 "Reconnaissance Report of Damage to Historic Monuments in Cairo, Egypt Following the October 12, 1992 Dahshur Earthquake," by D. Sykora, D. Look, G. Croci, E. Karaesmen and E. Karaesmen, 8/19/93, (PB94-142221, A08, MF-A02).

NCEER-93-0017 "The Island of Guam Earthquake of August 8, 1993," by S.W. Swan and S.K. Harris, 9/30/93, (PB94-141843, A04, MF-A01).

NCEER-93-0018 "Engineering Aspects of the October 12, 1992 Egyptian Earthquake," by A.W. Elgamal, M. Amer, K. Adalier and A. Abul-Fadl, 10/7/93, (PB94-141983, A05, MF-A01).

NCEER-93-0019 "Development of an Earthquake Motion Simulator and its Application in Dynamic Centrifuge Testing," by I. Krstelj, Supervised by J.H. Prevost, 10/23/93, (PB94-181773, A-10, MF-A03).

NCEER-93-0020 "NCEER-Taisei Corporation Research Program on Sliding Seismic Isolation Systems for Bridges: Experimental and Analytical Study of a Friction Pendulum System (FPS)," by M.C. Constantinou, P. Tsopelas, Y-S. Kim and S. Okamoto, 11/1/93, (PB94-142775, A08, MF-A02).

NCEER-93-0021 "Finite Element Modeling of Elastomeric Seismic Isolation Bearings," by L.J. Billings, Supervised by R. Shepherd, 11/8/93, to be published.

NCEER-93-0022 "Seismic Vulnerability of Equipment in Critical Facilities: Life-Safety and Operational Consequences," by K. Porter, G.S. Johnson, M.M. Zadeh, C. Scawthorn and S. Eder, 11/24/93, (PB94-181765, A16, MF-A03).

NCEER-93-0023 "Hokkaido Nansei-oki, Japan Earthquake of July 12, 1993, by P.I. Yanev and C.R. Scawthorn, 12/23/93, (PB94-181500, A07, MF-A01).

NCEER-94-0001 "An Evaluation of Seismic Serviceability of Water Supply Networks with Application to the San Francisco Auxiliary Water Supply System," by I. Markov, Supervised by M. Grigoriu and T. O'Rourke, 1/21/94, (PB94-204013, A07, MF-A02).

NCEER-94-0002 "NCEER-Taisei Corporation Research Program on Sliding Seismic Isolation Systems for Bridges: Experimental and Analytical Study of Systems Consisting of Sliding Bearings, Rubber Restoring Force Devices and Fluid Dampers," Volumes I and II, by P. Tsopelas, S. Okamoto, M.C. Constantinou, D. Ozaki and S. Fujii, 2/4/94, (PB94-181740, A09, MF-A02 and PB94-181757, A12, MF-A03).

NCEER-94-0003 "A Markov Model for Local and Global Damage Indices in Seismic Analysis," by S. Rahman and M. Grigoriu, 2/18/94, (PB94-206000, A12, MF-A03).

NCEER-94-0004 "Proceedings from the NCEER Workshop on Seismic Response of Masonry Infills," edited by D.P. Abrams, 3/1/94, (PB94-180783, A07, MF-A02).

NCEER-94-0005 "The Northridge, California Earthquake of January 17, 1994: General Reconnaissance Report," edited by J.D. Goltz, 3/11/94, (PB94-193943, A10, MF-A03).

NCEER-94-0006 "Seismic Energy Based Fatigue Damage Analysis of Bridge Columns: Part I - Evaluation of Seismic Capacity," by G.A. Chang and J.B. Mander, 3/14/94, (PB94-219185, A11, MF-A03).

NCEER-94-0007 "Seismic Isolation of Multi-Story Frame Structures Using Spherical Sliding Isolation Systems," by T.M. Al-Hussaini, V.A. Zayas and M.C. Constantinou, 3/17/94, (PB94-193745, A09, MF-A02).

NCEER-94-0008 "The Northridge, California Earthquake of January 17, 1994: Performance of Highway Bridges," edited by I.G. Buckle, 3/24/94, (PB94-193851, A06, MF-A02).

NCEER-94-0009 "Proceedings of the Third U.S.-Japan Workshop on Earthquake Protective Systems for Bridges," edited by I.G. Buckle and I. Friedland, 3/31/94, (PB94-195815, A99, MF-A06).

NCEER-94-0010 "3D-BASIS-ME: Computer Program for Nonlinear Dynamic Analysis of Seismically Isolated Single and Multiple Structures and Liquid Storage Tanks," by P.C. Tsopelas, M.C. Constantinou and A.M. Reinhorn, 4/12/94, (PB94-204922, A09, MF-A02).

NCEER-94-0011 "The Northridge, California Earthquake of January 17, 1994: Performance of Gas Transmission Pipelines," by T.D. O'Rourke and M.C. Palmer, 5/16/94, (PB94-204989, A05, MF-A01).

NCEER-94-0012 "Feasibility Study of Replacement Procedures and Earthquake Performance Related to Gas Transmission Pipelines," by T.D. O'Rourke and M.C. Palmer, 5/25/94, (PB94-206638, A09, MF-A02).

NCEER-94-0013 "Seismic Energy Based Fatigue Damage Analysis of Bridge Columns: Part II - Evaluation of Seismic Demand," by G.A. Chang and J.B. Mander, 6/1/94, (PB95-18106, A08, MF-A02).

NCEER-94-0014 "NCEER-Taisei Corporation Research Program on Sliding Seismic Isolation Systems for Bridges: Experimental and Analytical Study of a System Consisting of Sliding Bearings and Fluid Restoring Force/Damping Devices," by P. Tsopelas and M.C. Constantinou, 6/13/94, (PB94-219144, A10, MF-A03).

NCEER-94-0015 "Generation of Hazard-Consistent Fragility Curves for Seismic Loss Estimation Studies," by H. Hwang and J-R. Huo, 6/14/94, (PB95-181996, A09, MF-A02).

NCEER-94-0016 "Seismic Study of Building Frames with Added Energy-Absorbing Devices," by W.S. Pong, C.S. Tsai and G.C. Lee, 6/20/94, (PB94-219136, A10, A03).

NCEER-94-0017 "Sliding Mode Control for Seismic-Excited Linear and Nonlinear Civil Engineering Structures," by J. Yang, J. Wu, A. Agrawal and Z. Li, 6/21/94, (PB95-138483, A06, MF-A02).

NCEER-94-0018 "3D-BASIS-TABS Version 2.0: Computer Program for Nonlinear Dynamic Analysis of Three Dimensional Base Isolated Structures," by A.M. Reinhorn, S. Nagarajaiah, M.C. Constantinou, P. Tsopelas and R. Li, 6/22/94, (PB95-182176, A08, MF-A02).

NCEER-94-0019 "Proceedings of the International Workshop on Civil Infrastructure Systems: Application of Intelligent Systems and Advanced Materials on Bridge Systems," Edited by G.C. Lee and K.C. Chang, 7/18/94, (PB95-252474, A20, MF-A04).

NCEER-94-0020 "Study of Seismic Isolation Systems for Computer Floors," by V. Lambrou and M.C. Constantinou, 7/19/94, (PB95-138533, A10, MF-A03).

NCEER-94-0021 "Proceedings of the U.S.-Italian Workshop on Guidelines for Seismic Evaluation and Rehabilitation of Unreinforced Masonry Buildings," Edited by D.P. Abrams and G.M. Calvi, 7/20/94, (PB95-138749, A13, MF-A03).

NCEER-94-0022 "NCEER-Taisei Corporation Research Program on Sliding Seismic Isolation Systems for Bridges: Experimental and Analytical Study of a System Consisting of Lubricated PTFE Sliding Bearings and Mild Steel Dampers," by P. Tsopelas and M.C. Constantinou, 7/22/94, (PB95-182184, A08, MF-A02).

NCEER-94-0023 “Development of Reliability-Based Design Criteria for Buildings Under Seismic Load,” by Y.K. Wen, H. Hwang and M. Shinozuka, 8/1/94, (PB95-211934, A08, MF-A02).

NCEER-94-0024 “Experimental Verification of Acceleration Feedback Control Strategies for an Active Tendon System,” by S.J. Dyke, B.F. Spencer, Jr., P. Quast, M.K. Sain, D.C. Kaspari, Jr. and T.T. Soong, 8/29/94, (PB95-212320, A05, MF-A01).

NCEER-94-0025 “Seismic Retrofitting Manual for Highway Bridges,” Edited by I.G. Buckle and I.F. Friedland, published by the Federal Highway Administration (PB95-212676, A15, MF-A03).

NCEER-94-0026 “Proceedings from the Fifth U.S.-Japan Workshop on Earthquake Resistant Design of Lifeline Facilities and Countermeasures Against Soil Liquefaction,” Edited by T.D. O’Rourke and M. Hamada, 11/7/94, (PB95-220802, A99, MF-E08).

NCEER-95-0001 "Experimental and Analytical Investigation of Seismic Retrofit of Structures with Supplemental Damping: Part 1 - Fluid Viscous Damping Devices," by A.M. Reinhorn, C. Li and M.C. Constantinou, 1/3/95, (PB95-266599, A09, MF-A02).

NCEER-95-0002 "Experimental and Analytical Study of Low-Cycle Fatigue Behavior of Semi-Rigid Top-And-Seat Angle Connections," by G. Pekcan, J.B. Mander and S.S. Chen, 1/5/95, (PB95-220042, A07, MF-A02).

NCEER-95-0003 "NCEER-ATC Joint Study on Fragility of Buildings," by T. Anagnos, C. Rojahn and A.S. Kiremidjian, 1/20/95, (PB95-220026, A06, MF-A02).

NCEER-95-0004 "Nonlinear Control Algorithms for Peak Response Reduction," by Z. Wu, T.T. Soong, V. Gattulli and R.C. Lin, 2/16/95, (PB95-220349, A05, MF-A01).

NCEER-95-0005 "Pipeline Replacement Feasibility Study: A Methodology for Minimizing Seismic and Corrosion Risks to Underground Natural Gas Pipelines," by R.T. Eguchi, H.A. Seligson and D.G. Honegger, 3/2/95, (PB95-252326, A06, MF-A02).

NCEER-95-0006 "Evaluation of Seismic Performance of an 11-Story Frame Building During the 1994 Northridge Earthquake," by F. Naeim, R. DiSulio, K. Benuska, A. Reinhorn and C. Li, to be published.

NCEER-95-0007 "Prioritization of Bridges for Seismic Retrofitting," by N. Basöz and A.S. Kiremidjian, 4/24/95, (PB95-252300, A08, MF-A02).

NCEER-95-0008 "Method for Developing Motion Damage Relationships for Reinforced Concrete Frames," by A. Singhal and A.S. Kiremidjian, 5/11/95, (PB95-266607, A06, MF-A02).

NCEER-95-0009 "Experimental and Analytical Investigation of Seismic Retrofit of Structures with Supplemental Damping: Part II - Friction Devices," by C. Li and A.M. Reinhorn, 7/6/95, (PB96-128087, A11, MF-A03).

NCEER-95-0010 "Experimental Performance and Analytical Study of a Non-Ductile Reinforced Concrete Frame Structure Retrofitted with Elastomeric Spring Dampers," by G. Pekcan, J.B. Mander and S.S. Chen, 7/14/95, (PB96-137161, A08, MF-A02).

NCEER-95-0011 "Development and Experimental Study of Semi-Active Fluid Damping Devices for Seismic Protection of Structures," by M.D. Symans and M.C. Constantinou, 8/3/95, (PB96-136940, A23, MF-A04).

NCEER-95-0012 "Real-Time Structural Parameter Modification (RSPM): Development of Innervated Structures," by Z. Liang, M. Tong and G.C. Lee, 4/11/95, (PB96-137153, A06, MF-A01).

NCEER-95-0013 "Experimental and Analytical Investigation of Seismic Retrofit of Structures with Supplemental Damping: Part III - Viscous Damping Walls," by A.M. Reinhorn and C. Li, 10/1/95, (PB96-176409, A11, MF-A03).

NCEER-95-0014 "Seismic Fragility Analysis of Equipment and Structures in a Memphis Electric Substation," by J-R. Huo and H.H.M. Hwang, 8/10/95, (PB96-128087, A09, MF-A02).

NCEER-95-0015 "The Hanshin-Awaji Earthquake of January 17, 1995: Performance of Lifelines," Edited by M. Shinozuka, 11/3/95, (PB96-176383, A15, MF-A03).

NCEER-95-0016 "Highway Culvert Performance During Earthquakes," by T.L. Youd and C.J. Beckman, available as NCEER-96-0015.

NCEER-95-0017 "The Hanshin-Awaji Earthquake of January 17, 1995: Performance of Highway Bridges," Edited by I.G. Buckle, 12/1/95, to be published.

NCEER-95-0018 "Modeling of Masonry Infill Panels for Structural Analysis," by A.M. Reinhorn, A. Madan, R.E. Valles, Y. Reichmann and J.B. Mander, 12/8/95, (PB97-110886, MF-A01, A06).

NCEER-95-0019 "Optimal Polynomial Control for Linear and Nonlinear Structures," by A.K. Agrawal and J.N. Yang, 12/11/95, (PB96-168737, A07, MF-A02).

NCEER-95-0020 "Retrofit of Non-Ductile Reinforced Concrete Frames Using Friction Dampers," by R.S. Rao, P. Gergely and R.N. White, 12/22/95, (PB97-133508, A10, MF-A02).

NCEER-95-0021 "Parametric Results for Seismic Response of Pile-Supported Bridge Bents," by G. Mylonakis, A. Nikolaou and G. Gazetas, 12/22/95, (PB97-100242, A12, MF-A03).

NCEER-95-0022 "Kinematic Bending Moments in Seismically Stressed Piles," by A. Nikolaou, G. Mylonakis and G. Gazetas, 12/23/95, (PB97-113914, MF-A03, A13).

NCEER-96-0001 "Dynamic Response of Unreinforced Masonry Buildings with Flexible Diaphragms," by A.C. Costley and D.P. Abrams," 10/10/96, (PB97-133573, MF-A03, A15).

NCEER-96-0002 "State of the Art Review: Foundations and Retaining Structures," by I. Po Lam, to be published.

NCEER-96-0003 "Ductility of Rectangular Reinforced Concrete Bridge Columns with Moderate Confinement," by N. Wehbe, M. Saiidi, D. Sanders and B. Douglas, 11/7/96, (PB97-133557, A06, MF-A02).

NCEER-96-0004 "Proceedings of the Long-Span Bridge Seismic Research Workshop," edited by I.G. Buckle and I.M. Friedland, to be published.

NCEER-96-0005 "Establish Representative Pier Types for Comprehensive Study: Eastern United States," by J. Kulicki and Z. Prucz, 5/28/96, (PB98-119217, A07, MF-A02).

NCEER-96-0006 "Establish Representative Pier Types for Comprehensive Study: Western United States," by R. Imbsen, R.A. Schamber and T.A. Osterkamp, 5/28/96, (PB98-118607, A07, MF-A02).

NCEER-96-0007 "Nonlinear Control Techniques for Dynamical Systems with Uncertain Parameters," by R.G. Ghanem and M.I. Bujakov, 5/27/96, (PB97-100259, A17, MF-A03).

NCEER-96-0008 "Seismic Evaluation of a 30-Year Old Non-Ductile Highway Bridge Pier and Its Retrofit," by J.B. Mander, B. Mahmoodzadegan, S. Bhadra and S.S. Chen, 5/31/96, (PB97-110902, MF-A03, A10).

NCEER-96-0009 "Seismic Performance of a Model Reinforced Concrete Bridge Pier Before and After Retrofit," by J.B. Mander, J.H. Kim and C.A. Ligozio, 5/31/96, (PB97-110910, MF-A02, A10).

NCEER-96-0010 "IDARC2D Version 4.0: A Computer Program for the Inelastic Damage Analysis of Buildings," by R.E. Valles, A.M. Reinhorn, S.K. Kunnath, C. Li and A. Madan, 6/3/96, (PB97-100234, A17, MF-A03).

NCEER-96-0011 "Estimation of the Economic Impact of Multiple Lifeline Disruption: Memphis Light, Gas and Water Division Case Study," by S.E. Chang, H.A. Seligson and R.T. Eguchi, 8/16/96, (PB97-133490, A11, MF-A03).

NCEER-96-0012 "Proceedings from the Sixth Japan-U.S. Workshop on Earthquake Resistant Design of Lifeline Facilities and Countermeasures Against Soil Liquefaction, Edited by M. Hamada and T. O'Rourke, 9/11/96, (PB97-133581, A99, MF-A06).

NCEER-96-0013 "Chemical Hazards, Mitigation and Preparedness in Areas of High Seismic Risk: A Methodology for Estimating the Risk of Post-Earthquake Hazardous Materials Release," by H.A. Seligson, R.T. Eguchi, K.J. Tierney and K. Richmond, 11/7/96, (PB97-133565, MF-A02, A08).

NCEER-96-0014 "Response of Steel Bridge Bearings to Reversed Cyclic Loading," by J.B. Mander, D-K. Kim, S.S. Chen and G.J. Premus, 11/13/96, (PB97-140735, A12, MF-A03).

NCEER-96-0015 "Highway Culvert Performance During Past Earthquakes," by T.L. Youd and C.J. Beckman, 11/25/96, (PB97-133532, A06, MF-A01).

NCEER-97-0001 "Evaluation, Prevention and Mitigation of Pounding Effects in Building Structures," by R.E. Valles and A.M. Reinhorn, 2/20/97, (PB97-159552, A14, MF-A03).

NCEER-97-0002 "Seismic Design Criteria for Bridges and Other Highway Structures," by C. Rojahn, R. Mayes, D.G. Anderson, J. Clark, J.H. Hom, R.V. Nutt and M.J. O'Rourke, 4/30/97, (PB97-194658, A06, MF-A03).

NCEER-97-0003 “Proceedings of the U.S.-Italian Workshop on Seismic Evaluation and Retrofit,” Edited by D.P. Abrams and G.M. Calvi, 3/19/97, (PB97-194666, A13, MF-A03).

NCEER-97-0004 "Investigation of Seismic Response of Buildings with Linear and Nonlinear Fluid Viscous Dampers," by A.A. Seleemah and M.C. Constantinou, 5/21/97, (PB98-109002, A15, MF-A03).

NCEER-97-0005 "Proceedings of the Workshop on Earthquake Engineering Frontiers in Transportation Facilities," edited by G.C. Lee and I.M. Friedland, 8/29/97, (PB98-128911, A25, MR-A04).

NCEER-97-0006 "Cumulative Seismic Damage of Reinforced Concrete Bridge Piers," by S.K. Kunnath, A. El-Bahy, A. Taylor and W. Stone, 9/2/97, (PB98-108814, A11, MF-A03).

NCEER-97-0007 "Structural Details to Accommodate Seismic Movements of Highway Bridges and Retaining Walls," by R.A. Imbsen, R.A. Schamber, E. Thorkildsen, A. Kartoum, B.T. Martin, T.N. Rosser and J.M. Kulicki, 9/3/97, (PB98-108996, A09, MF-A02).

NCEER-97-0008 "A Method for Earthquake Motion-Damage Relationships with Application to Reinforced Concrete Frames," by A. Singhal and A.S. Kiremidjian, 9/10/97, (PB98-108988, A13, MF-A03).

NCEER-97-0009 "Seismic Analysis and Design of Bridge Abutments Considering Sliding and Rotation," by K. Fishman and R. Richards, Jr., 9/15/97, (PB98-108897, A06, MF-A02).

NCEER-97-0010 "Proceedings of the FHWA/NCEER Workshop on the National Representation of Seismic Ground Motion for New and Existing Highway Facilities," edited by I.M. Friedland, M.S. Power and R.L. Mayes, 9/22/97, (PB98-128903, A21, MF-A04).

NCEER-97-0011 "Seismic Analysis for Design or Retrofit of Gravity Bridge Abutments," by K.L. Fishman, R. Richards, Jr. and R.C. Divito, 10/2/97, (PB98-128937, A08, MF-A02).

NCEER-97-0012 "Evaluation of Simplified Methods of Analysis for Yielding Structures," by P. Tsopelas, M.C. Constantinou, C.A. Kircher and A.S. Whittaker, 10/31/97, (PB98-128929, A10, MF-A03).

NCEER-97-0013 "Seismic Design of Bridge Columns Based on Control and Repairability of Damage," by C-T. Cheng and J.B. Mander, 12/8/97, (PB98-144249, A11, MF-A03).

NCEER-97-0014 "Seismic Resistance of Bridge Piers Based on Damage Avoidance Design," by J.B. Mander and C-T. Cheng, 12/10/97, (PB98-144223, A09, MF-A02).

NCEER-97-0015 “Seismic Response of Nominally Symmetric Systems with Strength Uncertainty,” by S. Balopoulou and M. Grigoriu, 12/23/97, (PB98-153422, A11, MF-A03).

NCEER-97-0016 “Evaluation of Seismic Retrofit Methods for Reinforced Concrete Bridge Columns,” by T.J. Wipf, F.W. Klaiber and F.M. Russo, 12/28/97, (PB98-144215, A12, MF-A03).

NCEER-97-0017 “Seismic Fragility of Existing Conventional Reinforced Concrete Highway Bridges,” by C.L. Mullen and A.S. Cakmak, 12/30/97, (PB98-153406, A08, MF-A02).

NCEER-97-0018 “Loss Asssessment of Memphis Buildings,” edited by D.P. Abrams and M. Shinozuka, 12/31/97, (PB98-144231, A13, MF-A03).

NCEER-97-0019 “Seismic Evaluation of Frames with Infill Walls Using Quasi-static Experiments,” by K.M. Mosalam, R.N. White and P. Gergely, 12/31/97, (PB98-153455, A07, MF-A02).

NCEER-97-0020 “Seismic Evaluation of Frames with Infill Walls Using Pseudo-dynamic Experiments,” by K.M. Mosalam, R.N. White and P. Gergely, 12/31/97, (PB98-153430, A07, MF-A02).

NCEER-97-0021 “Computational Strategies for Frames with Infill Walls: Discrete and Smeared Crack Analyses and Seismic Fragility,” by K.M. Mosalam, R.N. White and P. Gergely, 12/31/97, (PB98-153414, A10, MF-A02).

NCEER-97-0022 "Proceedings of the NCEER Workshop on Evaluation of Liquefaction Resistance of Soils," edited by T.L. Youd and I.M. Idriss, 12/31/97, (PB98-155617, A15, MF-A03).

MCEER-98-0001 "Extraction of Nonlinear Hysteretic Properties of Seismically Isolated Bridges from Quick-Release Field Tests," by Q. Chen, B.M. Douglas, E.M. Maragakis and I.G. Buckle, 5/26/98, (PB99-118838, A06, MF-A01).

MCEER-98-0002 "Methodologies for Evaluating the Importance of Highway Bridges," by A. Thomas, S. Eshenaur and J. Kulicki, 5/29/98, (PB99-118846, A10, MF-A02).

MCEER-98-0003 "Capacity Design of Bridge Piers and the Analysis of Overstrength," by J.B. Mander, A. Dutta and P. Goel, 6/1/98, (PB99-118853, A09, MF-A02).

MCEER-98-0004 "Evaluation of Bridge Damage Data from the Loma Prieta and Northridge, California Earthquakes," by N. Basoz and A. Kiremidjian, 6/2/98, (PB99-118861, A15, MF-A03).

MCEER-98-0005 "Screening Guide for Rapid Assessment of Liquefaction Hazard at Highway Bridge Sites," by T. L. Youd, 6/16/98, (PB99-118879, A06, not available on microfiche).

MCEER-98-0006 "Structural Steel and Steel/Concrete Interface Details for Bridges," by P. Ritchie, N. Kauhl and J. Kulicki, 7/13/98, (PB99-118945, A06, MF-A01).

MCEER-98-0007 "Capacity Design and Fatigue Analysis of Confined Concrete Columns," by A. Dutta and J.B. Mander, 7/14/98, (PB99-118960, A14, MF-A03).

MCEER-98-0008 "Proceedings of the Workshop on Performance Criteria for Telecommunication Services Under Earthquake Conditions," edited by A.J. Schiff, 7/15/98, (PB99-118952, A08, MF-A02).

MCEER-98-0009 "Fatigue Analysis of Unconfined Concrete Columns," by J.B. Mander, A. Dutta and J.H. Kim, 9/12/98, (PB99-123655, A10, MF-A02).

MCEER-98-0010 "Centrifuge Modeling of Cyclic Lateral Response of Pile-Cap Systems and Seat-Type Abutments in Dry Sands," by A.D. Gadre and R. Dobry, 10/2/98, (PB99-123606, A13, MF-A03).

MCEER-98-0011 "IDARC-BRIDGE: A Computational Platform for Seismic Damage Assessment of Bridge Structures," by A.M. Reinhorn, V. Simeonov, G. Mylonakis and Y. Reichman, 10/2/98, (PB99-162919, A15, MF-A03).

MCEER-98-0012 "Experimental Investigation of the Dynamic Response of Two Bridges Before and After Retrofitting with Elastomeric Bearings," by D.A. Wendichansky, S.S. Chen and J.B. Mander, 10/2/98, (PB99-162927, A15, MF-A03).

MCEER-98-0013 "Design Procedures for Hinge Restrainers and Hinge Sear Width for Multiple-Frame Bridges," by R. Des Roches and G.L. Fenves, 11/3/98, (PB99-140477, A13, MF-A03).

MCEER-98-0014 "Response Modification Factors for Seismically Isolated Bridges," by M.C. Constantinou and J.K. Quarshie, 11/3/98, (PB99-140485, A14, MF-A03).

MCEER-98-0015 "Proceedings of the U.S.-Italy Workshop on Seismic Protective Systems for Bridges," edited by I.M. Friedland and M.C. Constantinou, 11/3/98, (PB2000-101711, A22, MF-A04).

MCEER-98-0016 "Appropriate Seismic Reliability for Critical Equipment Systems: Recommendations Based on Regional Analysis of Financial and Life Loss," by K. Porter, C. Scawthorn, C. Taylor and N. Blais, 11/10/98, (PB99-157265, A08, MF-A02).

MCEER-98-0017 "Proceedings of the U.S. Japan Joint Seminar on Civil Infrastructure Systems Research," edited by M. Shinozuka and A. Rose, 11/12/98, (PB99-156713, A16, MF-A03).

MCEER-98-0018 "Modeling of Pile Footings and Drilled Shafts for Seismic Design," by I. PoLam, M. Kapuskar and D. Chaudhuri, 12/21/98, (PB99-157257, A09, MF-A02).

MCEER-99-0001 "Seismic Evaluation of a Masonry Infilled Reinforced Concrete Frame by Pseudodynamic Testing," by S.G. Buonopane and R.N. White, 2/16/99, (PB99-162851, A09, MF-A02).

MCEER-99-0002 "Response History Analysis of Structures with Seismic Isolation and Energy Dissipation Systems: Verification Examples for Program SAP2000," by J. Scheller and M.C. Constantinou, 2/22/99, (PB99-162869, A08, MF-A02).

MCEER-99-0003 "Experimental Study on the Seismic Design and Retrofit of Bridge Columns Including Axial Load Effects," by A. Dutta, T. Kokorina and J.B. Mander, 2/22/99, (PB99-162877, A09, MF-A02).

MCEER-99-0004 "Experimental Study of Bridge Elastomeric and Other Isolation and Energy Dissipation Systems with Emphasis on Uplift Prevention and High Velocity Near-source Seismic Excitation," by A. Kasalanati and M. C. Constantinou, 2/26/99, (PB99-162885, A12, MF-A03).

MCEER-99-0005 "Truss Modeling of Reinforced Concrete Shear-flexure Behavior," by J.H. Kim and J.B. Mander, 3/8/99, (PB99-163693, A12, MF-A03).

MCEER-99-0006 "Experimental Investigation and Computational Modeling of Seismic Response of a 1:4 Scale Model Steel Structure with a Load Balancing Supplemental Damping System," by G. Pekcan, J.B. Mander and S.S. Chen, 4/2/99, (PB99-162893, A11, MF-A03).

MCEER-99-0007 "Effect of Vertical Ground Motions on the Structural Response of Highway Bridges," by M.R. Button, C.J. Cronin and R.L. Mayes, 4/10/99, (PB2000-101411, A10, MF-A03).

MCEER-99-0008 "Seismic Reliability Assessment of Critical Facilities: A Handbook, Supporting Documentation, and Model Code Provisions," by G.S. Johnson, R.E. Sheppard, M.D. Quilici, S.J. Eder and C.R. Scawthorn, 4/12/99, (PB2000-101701, A18, MF-A04).

MCEER-99-0009 "Impact Assessment of Selected MCEER Highway Project Research on the Seismic Design of Highway Structures," by C. Rojahn, R. Mayes, D.G. Anderson, J.H. Clark, D'Appolonia Engineering, S. Gloyd and R.V. Nutt, 4/14/99, (PB99-162901, A10, MF-A02).

MCEER-99-0010 "Site Factors and Site Categories in Seismic Codes," by R. Dobry, R. Ramos and M.S. Power, 7/19/99, (PB2000-101705, A08, MF-A02).

MCEER-99-0011 "Restrainer Design Procedures for Multi-Span Simply-Supported Bridges," by M.J. Randall, M. Saiidi, E. Maragakis and T. Isakovic, 7/20/99, (PB2000-101702, A10, MF-A02).

MCEER-99-0012 "Property Modification Factors for Seismic Isolation Bearings," by M.C. Constantinou, P. Tsopelas, A. Kasalanati and E. Wolff, 7/20/99, (PB2000-103387, A11, MF-A03).

MCEER-99-0013 "Critical Seismic Issues for Existing Steel Bridges," by P. Ritchie, N. Kauhl and J. Kulicki, 7/20/99, (PB2000-101697, A09, MF-A02).

MCEER-99-0014 "Nonstructural Damage Database," by A. Kao, T.T. Soong and A. Vender, 7/24/99, (PB2000-101407, A06, MF-A01).

MCEER-99-0015 "Guide to Remedial Measures for Liquefaction Mitigation at Existing Highway Bridge Sites," by H.G. Cooke and J. K. Mitchell, 7/26/99, (PB2000-101703, A11, MF-A03).

MCEER-99-0016 "Proceedings of the MCEER Workshop on Ground Motion Methodologies for the Eastern United States," edited by N. Abrahamson and A. Becker, 8/11/99, (PB2000-103385, A07, MF-A02).

MCEER-99-0017 "Quindío, Colombia Earthquake of January 25, 1999: Reconnaissance Report," by A.P. Asfura and P.J. Flores, 10/4/99, (PB2000-106893, A06, MF-A01).

MCEER-99-0018 "Hysteretic Models for Cyclic Behavior of Deteriorating Inelastic Structures," by M.V. Sivaselvan and A.M. Reinhorn, 11/5/99, (PB2000-103386, A08, MF-A02).

MCEER-99-0019 "Proceedings of the 7th U.S.- Japan Workshop on Earthquake Resistant Design of Lifeline Facilities and Countermeasures Against Soil Liquefaction," edited by T.D. O'Rourke, J.P. Bardet and M. Hamada, 11/19/99, (PB2000-103354, A99, MF-A06).

MCEER-99-0020 "Development of Measurement Capability for Micro-Vibration Evaluations with Application to Chip Fabrication Facilities," by G.C. Lee, Z. Liang, J.W. Song, J.D. Shen and W.C. Liu, 12/1/99, (PB2000-105993, A08, MF-A02).

MCEER-99-0021 "Design and Retrofit Methodology for Building Structures with Supplemental Energy Dissipating Systems," by G. Pekcan, J.B. Mander and S.S. Chen, 12/31/99, (PB2000-105994, A11, MF-A03).

MCEER-00-0001 "The Marmara, Turkey Earthquake of August 17, 1999: Reconnaissance Report," edited by C. Scawthorn; with major contributions by M. Bruneau, R. Eguchi, T. Holzer, G. Johnson, J. Mander, J. Mitchell, W. Mitchell, A. Papageorgiou, C. Scaethorn, and G. Webb, 3/23/00, (PB2000-106200, A11, MF-A03).

MCEER-00-0002 "Proceedings of the MCEER Workshop for Seismic Hazard Mitigation of Health Care Facilities," edited by G.C. Lee, M. Ettouney, M. Grigoriu, J. Hauer and J. Nigg, 3/29/00, (PB2000-106892, A08, MF-A02).

MCEER-00-0003 "The Chi-Chi, Taiwan Earthquake of September 21, 1999: Reconnaissance Report," edited by G.C. Lee and C.H. Loh, with major contributions by G.C. Lee, M. Bruneau, I.G. Buckle, S.E. Chang, P.J. Flores, T.D. O'Rourke, M. Shinozuka, T.T. Soong, C-H. Loh, K-C. Chang, Z-J. Chen, J-S. Hwang, M-L. Lin, G-Y. Liu, K-C. Tsai, G.C. Yao and C-L. Yen, 4/30/00, (PB2001-100980, A10, MF-A02).

MCEER-00-0004 "Seismic Retrofit of End-Sway Frames of Steel Deck-Truss Bridges with a Supplemental Tendon System: Experimental and Analytical Investigation," by G. Pekcan, J.B. Mander and S.S. Chen, 7/1/00, (PB2001-100982, A10, MF-A02).

MCEER-00-0005 "Sliding Fragility of Unrestrained Equipment in Critical Facilities," by W.H. Chong and T.T. Soong, 7/5/00, (PB2001-100983, A08, MF-A02).

MCEER-00-0006 "Seismic Response of Reinforced Concrete Bridge Pier Walls in the Weak Direction," by N. Abo-Shadi, M. Saiidi and D. Sanders, 7/17/00, (PB2001-100981, A17, MF-A03).

MCEER-00-0007 "Low-Cycle Fatigue Behavior of Longitudinal Reinforcement in Reinforced Concrete Bridge Columns," by J. Brown and S.K. Kunnath, 7/23/00, (PB2001-104392, A08, MF-A02).

MCEER-00-0008 "Soil Structure Interaction of Bridges for Seismic Analysis," I. PoLam and H. Law, 9/25/00, (PB2001-105397, A08, MF-A02).

MCEER-00-0009 "Proceedings of the First MCEER Workshop on Mitigation of Earthquake Disaster by Advanced Technologies (MEDAT-1), edited by M. Shinozuka, D.J. Inman and T.D. O'Rourke, 11/10/00, (PB2001-105399, A14, MF-A03).

MCEER-00-0010 "Development and Evaluation of Simplified Procedures for Analysis and Design of Buildings with Passive Energy Dissipation Systems, Revision 01," by O.M. Ramirez, M.C. Constantinou, C.A. Kircher, A.S. Whittaker, M.W. Johnson, J.D. Gomez and C. Chrysostomou, 11/16/01, (PB2001-105523, A23, MF-A04).

MCEER-00-0011 "Dynamic Soil-Foundation-Structure Interaction Analyses of Large Caissons," by C-Y. Chang, C-M. Mok, Z-L. Wang, R. Settgast, F. Waggoner, M.A. Ketchum, H.M. Gonnermann and C-C. Chin, 12/30/00, (PB2001-104373, A07, MF-A02).

MCEER-00-0012 "Experimental Evaluation of Seismic Performance of Bridge Restrainers," by A.G. Vlassis, E.M. Maragakis and M. Saiid Saiidi, 12/30/00, (PB2001-104354, A09, MF-A02).

MCEER-00-0013 "Effect of Spatial Variation of Ground Motion on Highway Structures," by M. Shinozuka, V. Saxena and G. Deodatis, 12/31/00, (PB2001-108755, A13, MF-A03).

MCEER-00-0014 "A Risk-Based Methodology for Assessing the Seismic Performance of Highway Systems," by S.D. Werner, C.E. Taylor, J.E. Moore, II, J.S. Walton and S. Cho, 12/31/00, (PB2001-108756, A14, MF-A03).

MCEER-01-0001 "Experimental Investigation of P-Delta Effects to Collapse During Earthquakes," by D. Vian and M. Bruneau, 6/25/01, (PB2002-100534, A17, MF-A03).

MCEER-01-0002 "Proceedings of the Second MCEER Workshop on Mitigation of Earthquake Disaster by Advanced Technologies (MEDAT-2)," edited by M. Bruneau and D.J. Inman, 7/23/01, (PB2002-100434, A16, MF-A03).

MCEER-01-0003 "Sensitivity Analysis of Dynamic Systems Subjected to Seismic Loads," by C. Roth and M. Grigoriu, 9/18/01, (PB2003-100884, A12, MF-A03).

MCEER-01-0004 "Overcoming Obstacles to Implementing Earthquake Hazard Mitigation Policies: Stage 1 Report," by D.J. Alesch and W.J. Petak, 12/17/01, (PB2002-107949, A07, MF-A02).

MCEER-01-0005 "Updating Real-Time Earthquake Loss Estimates: Methods, Problems and Insights," by C.E. Taylor, S.E. Chang and R.T. Eguchi, 12/17/01, (PB2002-107948, A05, MF-A01).

MCEER-01-0006 "Experimental Investigation and Retrofit of Steel Pile Foundations and Pile Bents Under Cyclic Lateral Loadings," by A. Shama, J. Mander, B. Blabac and S. Chen, 12/31/01, (PB2002-107950, A13, MF-A03).

MCEER-02-0001 "Assessment of Performance of Bolu Viaduct in the 1999 Duzce Earthquake in Turkey" by P.C. Roussis, M.C. Constantinou, M. Erdik, E. Durukal and M. Dicleli, 5/8/02, (PB2003-100883, A08, MF-A02).

MCEER-02-0002 "Seismic Behavior of Rail Counterweight Systems of Elevators in Buildings," by M.P. Singh, Rildova and L.E. Suarez, 5/27/02. (PB2003-100882, A11, MF-A03).

MCEER-02-0003 "Development of Analysis and Design Procedures for Spread Footings," by G. Mylonakis, G. Gazetas, S. Nikolaou and A. Chauncey, 10/02/02, (PB2004-101636, A13, MF-A03, CD-A13).

MCEER-02-0004 "Bare-Earth Algorithms for Use with SAR and LIDAR Digital Elevation Models," by C.K. Huyck, R.T. Eguchi and B. Houshmand, 10/16/02, (PB2004-101637, A07, CD-A07).

MCEER-02-0005 "Review of Energy Dissipation of Compression Members in Concentrically Braced Frames," by K.Lee and M. Bruneau, 10/18/02, (PB2004-101638, A10, CD-A10).

MCEER-03-0001 "Experimental Investigation of Light-Gauge Steel Plate Shear Walls for the Seismic Retrofit of Buildings" by J. Berman and M. Bruneau, 5/2/03, (PB2004-101622, A10, MF-A03, CD-A10).

MCEER-03-0002 "Statistical Analysis of Fragility Curves," by M. Shinozuka, M.Q. Feng, H. Kim, T. Uzawa and T. Ueda, 6/16/03, (PB2004-101849, A09, CD-A09).

MCEER-03-0003 "Proceedings of the Eighth U.S.-Japan Workshop on Earthquake Resistant Design f Lifeline Facilities and Countermeasures Against Liquefaction," edited by M. Hamada, J.P. Bardet and T.D. O'Rourke, 6/30/03, (PB2004-104386, A99, CD-A99).

MCEER-03-0004 "Proceedings of the PRC-US Workshop on Seismic Analysis and Design of Special Bridges," edited by L.C. Fan and G.C. Lee, 7/15/03, (PB2004-104387, A14, CD-A14).

MCEER-03-0005 "Urban Disaster Recovery: A Framework and Simulation Model," by S.B. Miles and S.E. Chang, 7/25/03, (PB2004-104388, A07, CD-A07).

MCEER-03-0006 "Behavior of Underground Piping Joints Due to Static and Dynamic Loading," by R.D. Meis, M. Maragakis and R. Siddharthan, 11/17/03, (PB2005-102194, A13, MF-A03, CD-A00).

MCEER-04-0001 "Experimental Study of Seismic Isolation Systems with Emphasis on Secondary System Response and Verification of Accuracy of Dynamic Response History Analysis Methods," by E. Wolff and M. Constantinou, 1/16/04 (PB2005-102195, A99, MF-E08, CD-A00).

MCEER-04-0002 "Tension, Compression and Cyclic Testing of Engineered Cementitious Composite Materials," by K. Kesner and S.L. Billington, 3/1/04, (PB2005-102196, A08, CD-A08).

MCEER-04-0003 "Cyclic Testing of Braces Laterally Restrained by Steel Studs to Enhance Performance During Earthquakes," by O.C. Celik, J.W. Berman and M. Bruneau, 3/16/04, (PB2005-102197, A13, MF-A03, CD-A00).

MCEER-04-0004 "Methodologies for Post Earthquake Building Damage Detection Using SAR and Optical Remote Sensing: Application to the August 17, 1999 Marmara, Turkey Earthquake," by C.K. Huyck, B.J. Adams, S. Cho, R.T. Eguchi, B. Mansouri and B. Houshmand, 6/15/04, (PB2005-104888, A10, CD-A00).

MCEER-04-0005 "Nonlinear Structural Analysis Towards Collapse Simulation: A Dynamical Systems Approach," by M.V. Sivaselvan and A.M. Reinhorn, 6/16/04, (PB2005-104889, A11, MF-A03, CD-A00).

MCEER-04-0006 "Proceedings of the Second PRC-US Workshop on Seismic Analysis and Design of Special Bridges," edited by G.C. Lee and L.C. Fan, 6/25/04, (PB2005-104890, A16, CD-A00).

MCEER-04-0007 "Seismic Vulnerability Evaluation of Axially Loaded Steel Built-up Laced Members," by K. Lee and M. Bruneau, 6/30/04, (PB2005-104891, A16, CD-A00).

MCEER-04-0008 "Evaluation of Accuracy of Simplified Methods of Analysis and Design of Buildings with Damping Systems for Near-Fault and for Soft-Soil Seismic Motions," by E.A. Pavlou and M.C. Constantinou, 8/16/04, (PB2005-104892, A08, MF-A02, CD-A00).

MCEER-04-0009 "Assessment of Geotechnical Issues in Acute Care Facilities in California," by M. Lew, T.D. O'Rourke, R. Dobry and M. Koch, 9/15/04, (PB2005-104893, A08, CD-A00).

MCEER-04-0010 "Scissor-Jack-Damper Energy Dissipation System," by A.N. Sigaher-Boyle and M.C. Constantinou, 12/1/04 (PB2005-108221).

MCEER-04-0011 "Seismic Retrofit of Bridge Steel Truss Piers Using a Controlled Rocking Approach," by M. Pollino and M. Bruneau, 12/20/04 (PB2006-105795).

MCEER-05-0001 "Experimental and Analytical Studies of Structures Seismically Isolated with an Uplift-Restraint Isolation System," by P.C. Roussis and M.C. Constantinou, 1/10/05 (PB2005-108222).

MCEER-05-0002 "A Versatile Experimentation Model for Study of Structures Near Collapse Applied to Seismic Evaluation of Irregular Structures," by D. Kusumastuti, A.M. Reinhorn and A. Rutenberg, 3/31/05 (PB2006-101523).

MCEER-05-0003 "Proceedings of the Third PRC-US Workshop on Seismic Analysis and Design of Special Bridges," edited by L.C. Fan and G.C. Lee, 4/20/05, (PB2006-105796).

MCEER-05-0004 "Approaches for the Seismic Retrofit of Braced Steel Bridge Piers and Proof-of-Concept Testing of an Eccentrically Braced Frame with Tubular Link," by J.W. Berman and M. Bruneau, 4/21/05 (PB2006-101524).

MCEER-05-0005 "Simulation of Strong Ground Motions for Seismic Fragility Evaluation of Nonstructural Components in Hospitals," by A. Wanitkorkul and A. Filiatrault, 5/26/05 (PB2006-500027).

MCEER-05-0006 "Seismic Safety in California Hospitals: Assessing an Attempt to Accelerate the Replacement or Seismic Retrofit of Older Hospital Facilities," by D.J. Alesch, L.A. Arendt and W.J. Petak, 6/6/05 (PB2006-105794).

MCEER-05-0007 "Development of Seismic Strengthening and Retrofit Strategies for Critical Facilities Using Engineered Cementitious Composite Materials," by K. Kesner and S.L. Billington, 8/29/05 (PB2006-111701).

MCEER-05-0008 "Experimental and Analytical Studies of Base Isolation Systems for Seismic Protection of Power Transformers," by N. Murota, M.Q. Feng and G-Y. Liu, 9/30/05 (PB2006-111702).

MCEER-05-0009 "3D-BASIS-ME-MB: Computer Program for Nonlinear Dynamic Analysis of Seismically Isolated Structures," by P.C. Tsopelas, P.C. Roussis, M.C. Constantinou, R. Buchanan and A.M. Reinhorn, 10/3/05 (PB2006-111703).

MCEER-05-0010 "Steel Plate Shear Walls for Seismic Design and Retrofit of Building Structures," by D. Vian and M. Bruneau, 12/15/05 (PB2006-111704).

MCEER-05-0011 "The Performance-Based Design Paradigm," by M.J. Astrella and A. Whittaker, 12/15/05 (PB2006-111705).

MCEER-06-0001 "Seismic Fragility of Suspended Ceiling Systems," H. Badillo-Almaraz, A.S. Whittaker, A.M. Reinhorn and G.P. Cimellaro, 2/4/06 (PB2006-111706).

MCEER-06-0002 "Multi-Dimensional Fragility of Structures," by G.P. Cimellaro, A.M. Reinhorn and M. Bruneau, 3/1/06 (PB2007-106974, A09, MF-A02, CD A00).

MCEER-06-0003 "Built-Up Shear Links as Energy Dissipators for Seismic Protection of Bridges," by P. Dusicka, A.M. Itani and I.G. Buckle, 3/15/06 (PB2006-111708).

MCEER-06-0004 "Analytical Investigation of the Structural Fuse Concept," by R.E. Vargas and M. Bruneau, 3/16/06 (PB2006-111709).

MCEER-06-0005 "Experimental Investigation of the Structural Fuse Concept," by R.E. Vargas and M. Bruneau, 3/17/06 (PB2006-111710).

MCEER-06-0006 "Further Development of Tubular Eccentrically Braced Frame Links for the Seismic Retrofit of Braced Steel Truss Bridge Piers," by J.W. Berman and M. Bruneau, 3/27/06 (PB2007-105147).

MCEER-06-0007 "REDARS Validation Report," by S. Cho, C.K. Huyck, S. Ghosh and R.T. Eguchi, 8/8/06 (PB2007-106983).

MCEER-06-0008 "Review of Current NDE Technologies for Post-Earthquake Assessment of Retrofitted Bridge Columns," by J.W. Song, Z. Liang and G.C. Lee, 8/21/06 (PB2007-106984).

MCEER-06-0009 "Liquefaction Remediation in Silty Soils Using Dynamic Compaction and Stone Columns," by S. Thevanayagam, G.R. Martin, R. Nashed, T. Shenthan, T. Kanagalingam and N. Ecemis, 8/28/06 (PB2007-106985).

MCEER-06-0010 "Conceptual Design and Experimental Investigation of Polymer Matrix Composite Infill Panels for Seismic Retrofitting," by W. Jung, M. Chiewanichakorn and A.J. Aref, 9/21/06 (PB2007-106986).

MCEER-06-0011 "A Study of the Coupled Horizontal-Vertical Behavior of Elastomeric and Lead-Rubber Seismic Isolation Bearings," by G.P. Warn and A.S. Whittaker, 9/22/06 (PB2007-108679).

MCEER-06-0012 "Proceedings of the Fourth PRC-US Workshop on Seismic Analysis and Design of Special Bridges: Advancing Bridge Technologies in Research, Design, Construction and Preservation," Edited by L.C. Fan, G.C. Lee and L. Ziang, 10/12/06 (PB2007-109042).

MCEER-06-0013 "Cyclic Response and Low Cycle Fatigue Characteristics of Plate Steels," by P. Dusicka, A.M. Itani and I.G. Buckle, 11/1/06 06 (PB2007-106987).

MCEER-06-0014 "Proceedings of the Second US-Taiwan Bridge Engineering Workshop," edited by W.P. Yen, J. Shen, J-Y. Chen and M. Wang, 11/15/06 (PB2008-500041).

MCEER-06-0015 "User Manual and Technical Documentation for the REDARS^{TM} Import Wizard," by S. Cho, S. Ghosh, C.K. Huyck and S.D. Werner, 11/30/06 (PB2007-114766).

MCEER-06-0016 "Hazard Mitigation Strategy and Monitoring Technologies for Urban and Infrastructure Public Buildings: Proceedings of the China-US Workshops," edited by X.Y. Zhou, A.L. Zhang, G.C. Lee and M. Tong, 12/12/06 (PB2008-500018).

MCEER-07-0001 "Static and Kinetic Coefficients of Friction for Rigid Blocks," by C. Kafali, S. Fathali, M. Grigoriu and A.S. Whittaker, 3/20/07 (PB2007-114767).

MCEER-07-0002 "Hazard Mitigation Investment Decision Making: Organizational Response to Legislative Mandate," by L.A. Arendt, D.J. Alesch and W.J. Petak, 4/9/07 (PB2007-114768).

MCEER-07-0003 "Seismic Behavior of Bidirectional-Resistant Ductile End Diaphragms with Unbonded Braces in Straight or Skewed Steel Bridges," by O. Celik and M. Bruneau, 4/11/07 (PB2008-105141).

MCEER-07-0004 "Modeling Pile Behavior in Large Pile Groups Under Lateral Loading," by A.M. Dodds and G.R. Martin, 4/16/07(PB2008-105142).

MCEER-07-0005 "Experimental Investigation of Blast Performance of Seismically Resistant Concrete-Filled Steel Tube Bridge Piers," by S. Fujikura, M. Bruneau and D. Lopez-Garcia, 4/20/07 (PB2008-105143).

MCEER-07-0006 "Seismic Analysis of Conventional and Isolated Liquefied Natural Gas Tanks Using Mechanical Analogs," by I.P. Christovasilis and A.S. Whittaker, 5/1/07.

MCEER-07-0007 "Experimental Seismic Performance Evaluation of Isolation/Restraint Systems for Mechanical Equipment – Part 1: Heavy Equipment Study," by S. Fathali and A. Filiatrault, 6/6/07 (PB2008-105144).

MCEER-07-0008 "Seismic Vulnerability of Timber Bridges and Timber Substructures," by A.A. Sharma, J.B. Mander, I.M. Friedland and D.R. Allicock, 6/7/07 (PB2008-105145).

MCEER-07-0009 "Experimental and Analytical Study of the XY-Friction Pendulum (XY-FP) Bearing for Bridge Applications," by C.C. Marin-Artieda, A.S. Whittaker and M.C. Constantinou, 6/7/07 (PB2008-105191).

MCEER-07-0010 "Proceedings of the PRC-US Earthquake Engineering Forum for Young Researchers," Edited by G.C. Lee and X.Z. Qi, 6/8/07 (PB2008-500058).

MCEER-07-0011 "Design Recommendations for Perforated Steel Plate Shear Walls," by R. Purba and M. Bruneau, 6/18/07, (PB2008-105192).

MCEER-07-0012 "Performance of Seismic Isolation Hardware Under Service and Seismic Loading," by M.C. Constantinou, A.S. Whittaker, Y. Kalpakidis, D.M. Fenz and G.P. Warn, 8/27/07, (PB2008-105193).

MCEER-07-0013 "Experimental Evaluation of the Seismic Performance of Hospital Piping Subassemblies," by E.R. Goodwin, E. Maragakis and A.M. Itani, 9/4/07, (PB2008-105194).

MCEER-07-0014 "A Simulation Model of Urban Disaster Recovery and Resilience: Implementation for the 1994 Northridge Earthquake," by S. Miles and S.E. Chang, 9/7/07, (PB2008-106426).

MCEER-07-0015 "Statistical and Mechanistic Fragility Analysis of Concrete Bridges," by M. Shinozuka, S. Banerjee and S-H. Kim, 9/10/07, (PB2008-106427).

MCEER-07-0016 "Three-Dimensional Modeling of Inelastic Buckling in Frame Structures," by M. Schachter and AM. Reinhorn, 9/13/07, (PB2008-108125).

MCEER-07-0017 "Modeling of Seismic Wave Scattering on Pile Groups and Caissons," by I. Po Lam, H. Law and C.T. Yang, 9/17/07 (PB2008-108150).

MCEER-07-0018 "Bridge Foundations: Modeling Large Pile Groups and Caissons for Seismic Design," by I. Po Lam, H. Law and G.R. Martin (Coordinating Author), 12/1/07 (PB2008-111190).

MCEER-07-0019 "Principles and Performance of Roller Seismic Isolation Bearings for Highway Bridges," by G.C. Lee, Y.C. Ou, Z. Liang, T.C. Niu and J. Song, 12/10/07 (PB2009-110466).

MCEER-07-0020 "Centrifuge Modeling of Permeability and Pinning Reinforcement Effects on Pile Response to Lateral Spreading," by L.L Gonzalez-Lagos, T. Abdoun and R. Dobry, 12/10/07 (PB2008-111191).

MCEER-07-0021 "Damage to the Highway System from the Pisco, Perú Earthquake of August 15, 2007," by J.S. O'Connor, L. Mesa and M. Nykamp, 12/10/07, (PB2008-108126).

MCEER-07-0022 "Experimental Seismic Performance Evaluation of Isolation/Restraint Systems for Mechanical Equipment – Part 2: Light Equipment Study," by S. Fathali and A. Filiatrault, 12/13/07 (PB2008-111192).

MCEER-07-0023 "Fragility Considerations in Highway Bridge Design," by M. Shinozuka, S. Banerjee and S.H. Kim, 12/14/07 (PB2008-111193).

MCEER-07-0024 "Performance Estimates for Seismically Isolated Bridges," by G.P. Warn and A.S. Whittaker, 12/30/07 (PB2008-112230).

MCEER-08-0001 "Seismic Performance of Steel Girder Bridge Superstructures with Conventional Cross Frames," by L.P. Carden, A.M. Itani and I.G. Buckle, 1/7/08, (PB2008-112231).

MCEER-08-0002 "Seismic Performance of Steel Girder Bridge Superstructures with Ductile End Cross Frames with Seismic Isolators," by L.P. Carden, A.M. Itani and I.G. Buckle, 1/7/08 (PB2008-112232).

MCEER-08-0003 "Analytical and Experimental Investigation of a Controlled Rocking Approach for Seismic Protection of Bridge Steel Truss Piers," by M. Pollino and M. Bruneau, 1/21/08 (PB2008-112233).

MCEER-08-0004 "Linking Lifeline Infrastructure Performance and Community Disaster Resilience: Models and Multi-Stakeholder Processes," by S.E. Chang, C. Pasion, K. Tatebe and R. Ahmad, 3/3/08 (PB2008-112234).

MCEER-08-0005 "Modal Analysis of Generally Damped Linear Structures Subjected to Seismic Excitations," by J. Song, Y-L. Chu, Z. Liang and G.C. Lee, 3/4/08 (PB2009-102311).

MCEER-08-0006 "System Performance Under Multi-Hazard Environments," by C. Kafali and M. Grigoriu, 3/4/08 (PB2008-112235).

MCEER-08-0007 "Mechanical Behavior of Multi-Spherical Sliding Bearings," by D.M. Fenz and M.C. Constantinou, 3/6/08 (PB2008-112236).

MCEER-08-0008 "Post-Earthquake Restoration of the Los Angeles Water Supply System," by T.H.P. Tabucchi and R.A. Davidson, 3/7/08 (PB2008-112237).

MCEER-08-0009 "Fragility Analysis of Water Supply Systems," by A. Jacobson and M. Grigoriu, 3/10/08 (PB2009-105545).

MCEER-08-0010 "Experimental Investigation of Full-Scale Two-Story Steel Plate Shear Walls with Reduced Beam Section Connections," by B. Qu, M. Bruneau, C-H. Lin and K-C. Tsai, 3/17/08 (PB2009-106368).

MCEER-08-0011 "Seismic Evaluation and Rehabilitation of Critical Components of Electrical Power Systems," S. Ersoy, B. Feizi, A. Ashrafi and M. Ala Saadeghvaziri, 3/17/08 (PB2009-105546).

MCEER-08-0012 "Seismic Behavior and Design of Boundary Frame Members of Steel Plate Shear Walls," by B. Qu and M. Bruneau, 4/26/08 . (PB2009-106744).

MCEER-08-0013 "Development and Appraisal of a Numerical Cyclic Loading Protocol for Quantifying Building System Performance," by A. Filiatrault, A. Wanitkorkul and M. Constantinou, 4/27/08 (PB2009-107906).

MCEER-08-0014 "Structural and Nonstructural Earthquake Design: The Challenge of Integrating Specialty Areas in Designing Complex, Critical Facilities," by W.J. Petak and D.J. Alesch, 4/30/08 (PB2009-107907).

MCEER-08-0015 "Seismic Performance Evaluation of Water Systems," by Y. Wang and T.D. O'Rourke, 5/5/08 (PB2009-107908).

MCEER-08-0016 "Seismic Response Modeling of Water Supply Systems," by P. Shi and T.D. O'Rourke, 5/5/08 (PB2009-107910).

MCEER-08-0017 "Numerical and Experimental Studies of Self-Centering Post-Tensioned Steel Frames," by D. Wang and A. Filiatrault, 5/12/08 (PB2009-110479).

MCEER-08-0018 "Development, Implementation and Verification of Dynamic Analysis Models for Multi-Spherical Sliding Bearings," by D.M. Fenz and M.C. Constantinou, 8/15/08 (PB2009-107911).

MCEER-08-0019 "Performance Assessment of Conventional and Base Isolated Nuclear Power Plants for Earthquake Blast Loadings," by Y.N. Huang, A.S. Whittaker and N. Luco, 10/28/08 (PB2009-107912).

MCEER-08-0020 "Remote Sensing for Resilient Multi-Hazard Disaster Response – Volume I: Introduction to Damage Assessment Methodologies," by B.J. Adams and R.T. Eguchi, 11/17/08 (PB2010-102695).

MCEER-08-0021 "Remote Sensing for Resilient Multi-Hazard Disaster Response – Volume II: Counting the Number of Collapsed Buildings Using an Object-Oriented Analysis: Case Study of the 2003 Bam Earthquake," by L. Gusella, C.K. Huyck and B.J. Adams, 11/17/08 (PB2010-100925).

MCEER-08-0022 "Remote Sensing for Resilient Multi-Hazard Disaster Response – Volume III: Multi-Sensor Image Fusion Techniques for Robust Neighborhood-Scale Urban Damage Assessment," by B.J. Adams and A. McMillan, 11/17/08 (PB2010-100926).

MCEER-08-0023 "Remote Sensing for Resilient Multi-Hazard Disaster Response – Volume IV: A Study of Multi-Temporal and Multi-Resolution SAR Imagery for Post-Katrina Flood Monitoring in New Orleans," by A. McMillan, J.G. Morley, B.J. Adams and S. Chesworth, 11/17/08 (PB2010-100927).

MCEER-08-0024 "Remote Sensing for Resilient Multi-Hazard Disaster Response – Volume V: Integration of Remote Sensing Imagery and VIEWS^{TM} Field Data for Post-Hurricane Charley Building Damage Assessment," by J.A. Womble, K. Mehta and B.J. Adams, 11/17/08 (PB2009-115532).

MCEER-08-0025 "Building Inventory Compilation for Disaster Management: Application of Remote Sensing and Statistical Modeling," by P. Sarabandi, A.S. Kiremidjian, R.T. Eguchi and B. J. Adams, 11/20/08 (PB2009-110484).

MCEER-08-0026 "New Experimental Capabilities and Loading Protocols for Seismic Qualification and Fragility Assessment of Nonstructural Systems," by R. Retamales, G. Mosqueda, A. Filiatrault and A. Reinhorn, 11/24/08 (PB2009-110485).

MCEER-08-0027 "Effects of Heating and Load History on the Behavior of Lead-Rubber Bearings," by I.V. Kalpakidis and M.C. Constantinou, 12/1/08 (PB2009-115533).

MCEER-08-0028 "Experimental and Analytical Investigation of Blast Performance of Seismically Resistant Bridge Piers," by S.Fujikura and M. Bruneau, 12/8/08 (PB2009-115534).

MCEER-08-0029 "Evolutionary Methodology for Aseismic Decision Support," by Y. Hu and G. Dargush, 12/15/08.

MCEER-08-0030 "Development of a Steel Plate Shear Wall Bridge Pier System Conceived from a Multi-Hazard Perspective," by D. Keller and M. Bruneau, 12/19/08 (PB2010-102696).

MCEER-09-0001 "Modal Analysis of Arbitrarily Damped Three-Dimensional Linear Structures Subjected to Seismic Excitations," by Y.L. Chu, J. Song and G.C. Lee, 1/31/09 (PB2010-100922).

MCEER-09-0002 "Air-Blast Effects on Structural Shapes," by G. Ballantyne, A.S. Whittaker, A.J. Aref and G.F. Dargush, 2/2/09 (PB2010-102697).

MCEER-09-0003 "Water Supply Performance During Earthquakes and Extreme Events," by A.L. Bonneau and T.D. O'Rourke, 2/16/09 (PB2010-100923).

MCEER-09-0004 "Generalized Linear (Mixed) Models of Post-Earthquake Ignitions," by R.A. Davidson, 7/20/09 (PB2010-102698).

MCEER-09-0005 "Seismic Testing of a Full-Scale Two-Story Light-Frame Wood Building: NEESWood Benchmark Test," by I.P. Christovasilis, A. Filiatrault and A. Wanitkorkul, 7/22/09 (PB2012-102401).

MCEER-09-0006 "IDARC2D Version 7.0: A Program for the Inelastic Damage Analysis of Structures," by A.M. Reinhorn, H. Roh, M. Sivaselvan, S.K. Kunnath, R.E. Valles, A. Madan, C. Li, R. Lobo and Y.J. Park, 7/28/09 (PB2010-103199).

MCEER-09-0007 "Enhancements to Hospital Resiliency: Improving Emergency Planning for and Response to Hurricanes," by D.B. Hess and L.A. Arendt, 7/30/09 (PB2010-100924).

MCEER-09-0008 "Assessment of Base-Isolated Nuclear Structures for Design and Beyond-Design Basis Earthquake Shaking," by Y.N. Huang, A.S. Whittaker, R.P. Kennedy and R.L. Mayes, 8/20/09 (PB2010-102699).

MCEER-09-0009 "Quantification of Disaster Resilience of Health Care Facilities," by G.P. Cimellaro, C. Fumo, A.M Reinhorn and M. Bruneau, 9/14/09 (PB2010-105384).

MCEER-09-0010 "Performance-Based Assessment and Design of Squat Reinforced Concrete Shear Walls," by C.K. Gulec and A.S. Whittaker, 9/15/09 (PB2010-102700).

MCEER-09-0011 "Proceedings of the Fourth US-Taiwan Bridge Engineering Workshop," edited by W.P. Yen, J.J. Shen, T.M. Lee and R.B. Zheng, 10/27/09 (PB2010-500009).

MCEER-09-0012 "Proceedings of the Special International Workshop on Seismic Connection Details for Segmental Bridge Construction," edited by W. Phillip Yen and George C. Lee, 12/21/09 (PB2012-102402).

MCEER-10-0001 "Direct Displacement Procedure for Performance-Based Seismic Design of Multistory Woodframe Structures," by W. Pang and D. Rosowsky, 4/26/10 (PB2012-102403).

MCEER-10-0002 "Simplified Direct Displacement Design of Six-Story NEESWood Capstone Building and Pre-Test Seismic Performance Assessment," by W. Pang, D. Rosowsky, J. van de Lindt and S. Pei, 5/28/10 (PB2012-102404).

MCEER-10-0003 "Integration of Seismic Protection Systems in Performance-Based Seismic Design of Woodframed Structures," by J.K. Shinde and M.D. Symans, 6/18/10 (PB2012-102405).

MCEER-10-0004 "Modeling and Seismic Evaluation of Nonstructural Components: Testing Frame for Experimental Evaluation of Suspended Ceiling Systems," by A.M. Reinhorn, K.P. Ryu and G. Maddaloni, 6/30/10 (PB2012-102406).

MCEER-10-0005 "Analytical Development and Experimental Validation of a Structural-Fuse Bridge Pier Concept," by S. El-Bahey and M. Bruneau, 10/1/10 (PB2012-102407).

MCEER-10-0006 "A Framework for Defining and Measuring Resilience at the Community Scale: The PEOPLES Resilience Framework," by C.S. Renschler, A.E. Frazier, L.A. Arendt, G.P. Cimellaro, A.M. Reinhorn and M. Bruneau, 10/8/10 (PB2012-102408).

MCEER-10-0007 "Impact of Horizontal Boundary Elements Design on Seismic Behavior of Steel Plate Shear Walls," by R. Purba and M. Bruneau, 11/14/10 (PB2012-102409).

MCEER-10-0008 "Seismic Testing of a Full-Scale Mid-Rise Building: The NEESWood Capstone Test," by S. Pei, J.W. van de Lindt, S.E. Pryor, H. Shimizu, H. Isoda and D.R. Rammer, 12/1/10 (PB2012-102410).

MCEER-10-0009 "Modeling the Effects of Detonations of High Explosives to Inform Blast-Resistant Design," by P. Sherkar, A.S. Whittaker and A.J. Aref, 12/1/10 (PB2012-102411).

MCEER-10-0010 "L'Aquila Earthquake of April 6, 2009 in Italy: Rebuilding a Resilient City to Withstand Multiple Hazards," by G.P. Cimellaro, I.P. Christovasilis, A.M. Reinhorn, A. De Stefano and T. Kirova, 12/29/10.

MCEER-11-0001 "Numerical and Experimental Investigation of the Seismic Response of Light-Frame Wood Structures," by I.P. Christovasilis and A. Filiatrault, 8/8/11 (PB2012-102412).

MCEER-11-0002 "Seismic Design and Analysis of a Precast Segmental Concrete Bridge Model," by M. Anagnostopoulou, A. Filiatrault and A. Aref, 9/15/11.

MCEER-11-0003 'Proceedings of the Workshop on Improving Earthquake Response of Substation Equipment," Edited by A.M. Reinhorn, 9/19/11 (PB2012-102413).

MCEER-11-0004 "LRFD-Based Analysis and Design Procedures for Bridge Bearings and Seismic Isolators," by M.C. Constantinou, I. Kalpakidis, A. Filiatrault and R.A. Ecker Lay, 9/26/11.

MCEER-11-0005 "Experimental Seismic Evaluation, Model Parameterization, and Effects of Cold-Formed Steel-Framed Gypsum Partition Walls on the Seismic Performance of an Essential Facility," by R. Davies, R. Retamales, G. Mosqueda and A. Filiatrault, 10/12/11.

MCEER-11-0006 "Modeling and Seismic Performance Evaluation of High Voltage Transformers and Bushings," by A.M. Reinhorn, K. Oikonomou, H. Roh, A. Schiff and L. Kempner, Jr., 10/3/11.

MCEER-11-0007 "Extreme Load Combinations: A Survey of State Bridge Engineers," by G.C. Lee, Z. Liang, J.J. Shen and J.S. O'Connor, 10/14/11.

MCEER-12-0001 "Simplified Analysis Procedures in Support of Performance Based Seismic Design," by Y.N. Huang and A.S. Whittaker.

MCEER-12-0002 "Seismic Protection of Electrical Transformer Bushing Systems by Stiffening Techniques," by M. Koliou, A. Filiatrault, A.M. Reinhorn and N. Oliveto, 6/1/12.

MCEER-12-0003 "Post-Earthquake Bridge Inspection Guidelines," by J.S. O'Connor and S. Alampalli, 6/8/12.

MCEER-12-0004 "Integrated Design Methodology for Isolated Floor Systems in Single-Degree-of-Freedom Structural Fuse Systems," by S. Cui, M. Bruneau and M.C. Constantinou, 6/13/12.

MCEER-12-0005 "Characterizing the Rotational Components of Earthquake Ground Motion," by D. Basu, A.S. Whittaker and M.C. Constantinou, 6/15/12.

APPENDIX A

AGM2 AND HIGH FREQUENCY ERRORS

The AGM2 procedure of Chapter 4 cannot address contributions from frequencies higher than $c/2L$ (c = apparent wave velocity and L = array length), defined here as the *threshold frequency*, in the recorded acceleration data because the higher modes introduce at least one change of sign in the curvature of the surface within the length of the array. However, because the assumed best fit surface is second order, it cannot capture this change of sign in the curvature and effectively averages the contributions from the higher frequencies in the recorded data. The threshold frequency is constant regardless of the phase of the instantaneous wave train. This loss of high frequency content does not become significant until the number of changes of sign in the curvature of the surface within the length of the array exceeds two. In this case, the accumulated error also depends on the phase of the instantaneous wave train. The rotational acceleration computed using AGM2 may underestimate contributions from frequencies higher than the threshold frequency, but the error will remain small if the recorded translational acceleration data has little frequency content beyond twice the threshold frequency, equal to c/L.

To support these statements, consider a linear array of length L with 21 uniformly spaced stations (at $0.05L$). For simplicity, first assume the recorded motion is comprised of a single frequency with an amplitude five units; the associated wavelength is λ. Considering the central station as the reference station, the value recorded at the reference station is subtracted from those recorded at the remaining stations and the resulting distribution surface is plotted. Note the distribution surface includes 20 data points (not 21). A quadratic best-fit surface is then computed and the goodness-of-fit is measured by the parameter R^2 (Soong, 2004): the closer the value to unity the better is the fit. Several cases are now illustrated assuming the phase of the recorded motion is 0, $\pi/8$, $\pi/4$, $3\pi/8$ and $\pi/2$. Figure A-1 illustrates the cases for $\lambda = L/2$ and $\lambda = L$. Similarly, the cases for $\lambda = 3L/2$ and $\lambda = 2L$ are shown

in Figure A-2. Figure A-3 presents the cases for $\lambda = 5L/2$ and $\lambda = 3L$. Figure A-3 and panels f through j of Figure A-2 indicate that regardless of the phase of the wave train, the goodness-of-fit is excellent ($R^2 > 0.98$) when $\lambda \geq 2L$. Panels a through e of Figure A-2 indicate a reasonable level of goodness of fit ($R^2 > 0.90$) for $\lambda \geq 1.5L$. For $\lambda = L$, panels f through j of Figure A-1 show $R^2 \geq 0.51$ depending upon the phase of the wave train. Finally, for $\lambda = L/2$, panels a through e of Figures A1 indicate R^2 as low as 0.12, depending upon the phase of the wave train. This comparison clearly indicates that the high frequency errors will be negligible if $\lambda \geq 2L$ and will remain small unless $\lambda \leq L$.

This example assumes the recorded motion is composed of one frequency. Actual recorded motion includes many frequencies with varying amplitudes and phases. In the absence of known data, and for the purpose of illustration, consider now a motion comprising three frequencies with the same amplitude and phase. The amplitude is five units as before. Figures A4 through A8 present the goodness-of-quadratic fit when $\lambda = 2L,\ 3L$ and $4L$, and the phase is varied from 0 to $\pi/2$ in increments of $\pi/8$. In these figures, RQ^2 represents R^2 for the quadratic fit. The goodness-of-fit is excellent ($RQ^2 > 0.99$) for frequency content such that $\lambda \geq 2L$, namely, f_{max} (Hz) is $c/2L$. Next, the three wavelengths are assumed to be $\lambda = L,\ 2L$ and $3L$. Results are presented in Figures A9 through A13. A reasonable level of fit is noted with $RQ^2 > 0.9$ in all cases because the frequency content of the motion indicate $\lambda \geq L$, or f_{max} (Hz) is c/L. The last triplet of wavelengths is $\lambda = L/2,\ L$ and $2L$. The resulting goodness-of-fit is presented in Figures A14 through A18. The fit is poor and RQ^2 is as low as 0.4, depending upon the phase of the wave train, because the frequency content of the recorded motion show f_{max} (Hz) $> c/L$.

Similar results are expected for any arbitrary set of frequency contents in recorded data. However, it must be noted that the quadratic fit used here is slightly different than the AGM2, because the weight matrix considered here is the identity matrix. Accordingly, the results of the quadratic fit described here is not independent of the selection of the reference station. Despite this difference, the above presentation

illustrates the concept of a threshold frequency. Figures A4 through A18 also include the linear-fit, which may be considered as the product of the Geodetic Method (see Chapter 2) except for the weight matrix. In these figures, RL^2 represents R^2 for the linear-fit. A comparison of the goodness of the quadratic and linear fits indicates the recovery of higher frequencies using the AGM2.

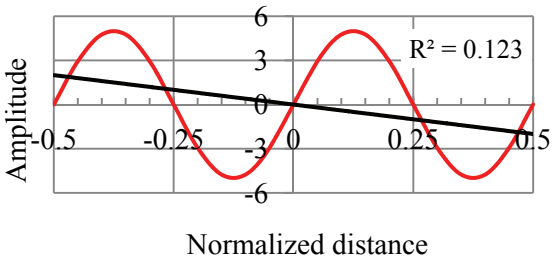

(a) $\lambda = L/2,\ \phi = 0$

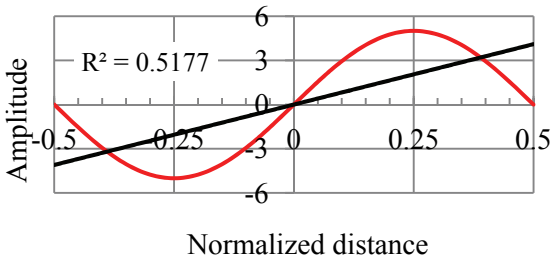

(f) $\lambda = L,\ \phi = 0$

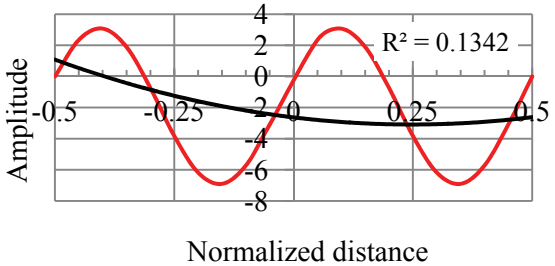

(b) $\lambda = L/2,\ \phi = \pi/8$

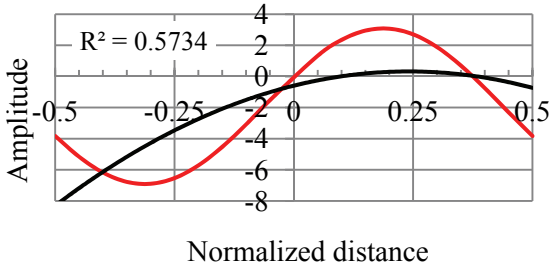

(g) $\lambda = L,\ \phi = \pi/8$

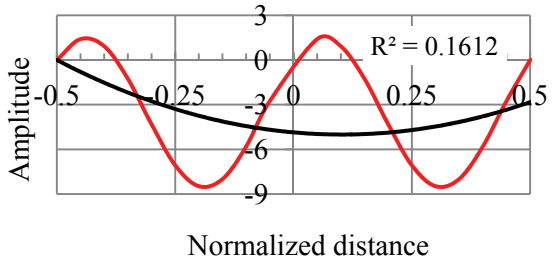

(c) $\lambda = L/2,\ \phi = \pi/4$

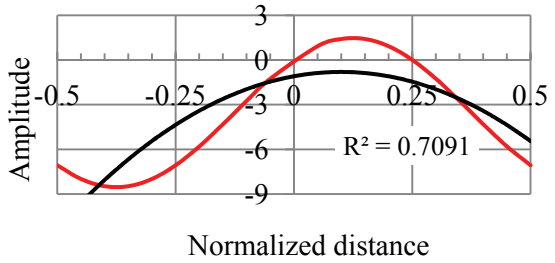

(h) $\lambda = L,\ \phi = \pi/4$

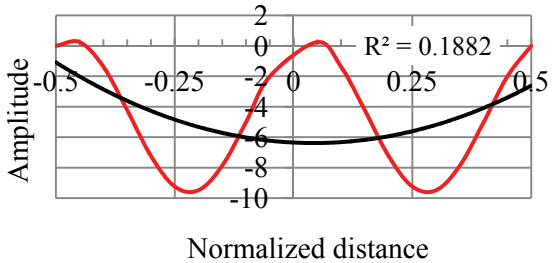

(d) $\lambda = L/2,\ \phi = 3\pi/8$

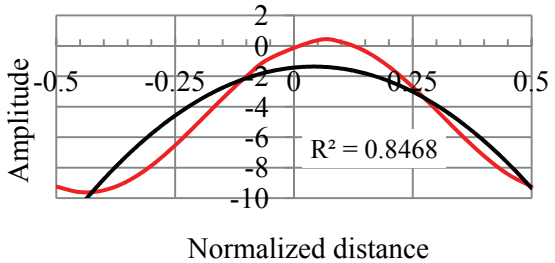

(i) $\lambda = L,\ \phi = 3\pi/8$

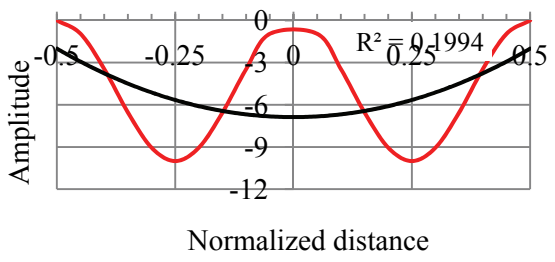

(e) $\lambda = L/2,\ \phi = \pi/2$

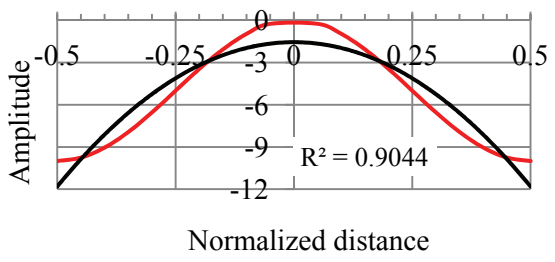

(j) $\lambda = L,\ \phi = \pi/2$

Figure A-1: Best-fit using AGM2 for $\lambda = L/2$ and $\lambda = L$

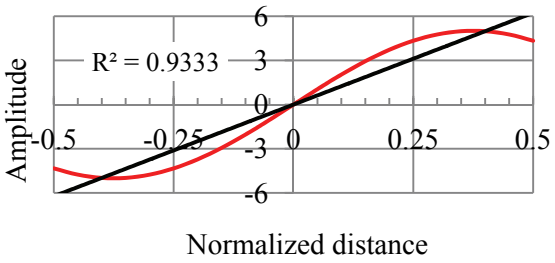

(a) $\lambda = 3L/2,\ \phi = 0$

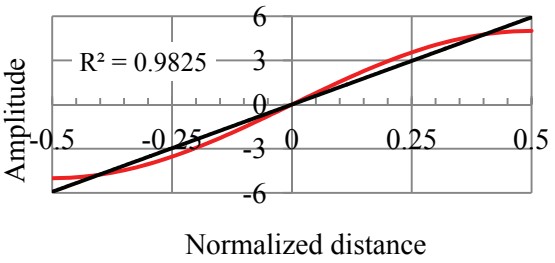

(f) $\lambda = 2L,\ \phi = 0$

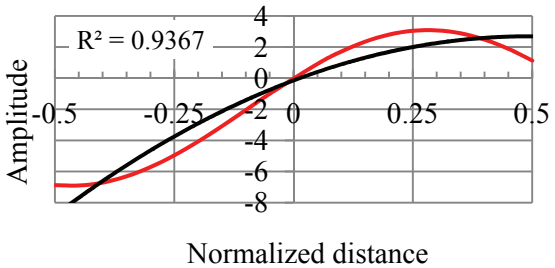

(b) $\lambda = 3L/2,\ \phi = \pi/8$

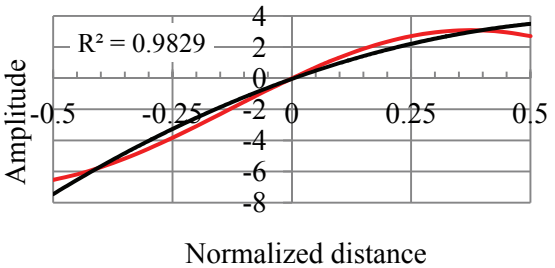

(g) $\lambda = 2L,\ \phi = \pi/8$

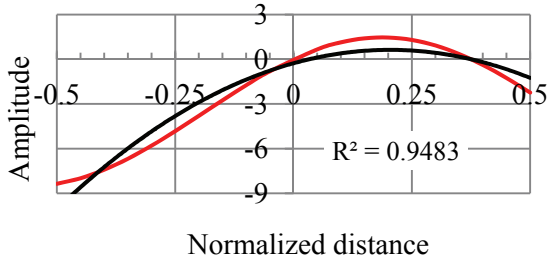

(c) $\lambda = 3L/2,\ \phi = \pi/4$

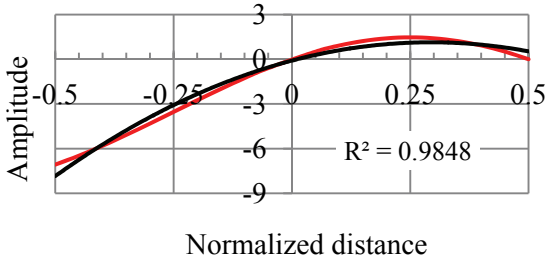

(h) $\lambda = 2L,\ \phi = \pi/4$

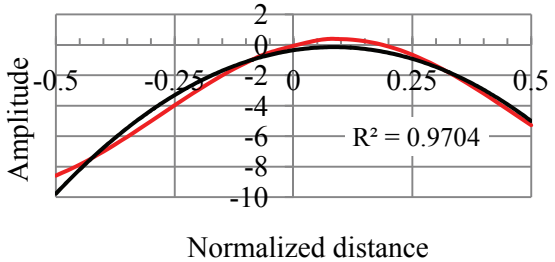

(d) $\lambda = 3L/2,\ \phi = 3\pi/8$

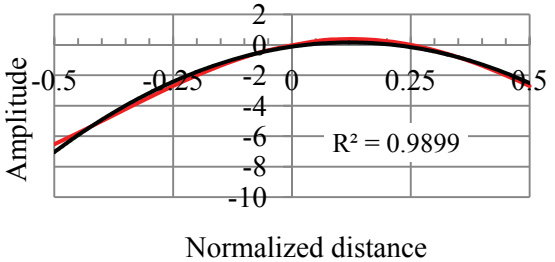

(i) $\lambda = 2L,\ \phi = 3\pi/8$

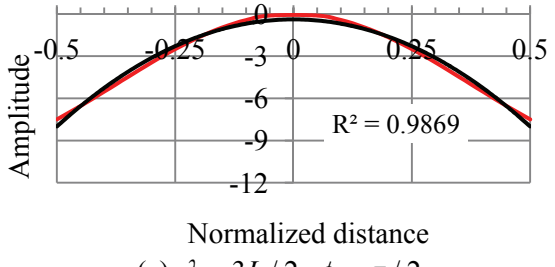

(e) $\lambda = 3L/2,\ \phi = \pi/2$

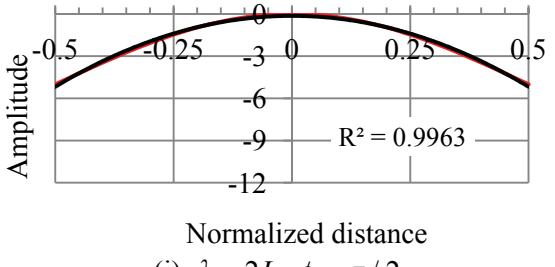

(j) $\lambda = 2L,\ \phi = \pi/2$

Figure A-2: Best-fit using AGM2 for $\lambda = 3L/2$ and $\lambda = 2L$

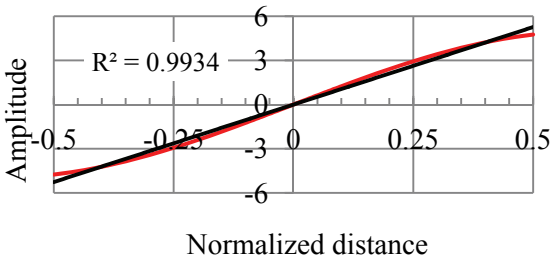

(a) $\lambda = 5L/2,\ \phi = 0$

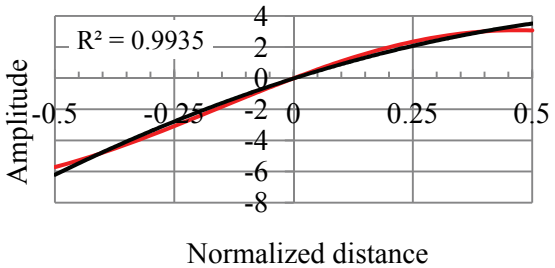

(b) $\lambda = 5L/2,\ \phi = \pi/8$

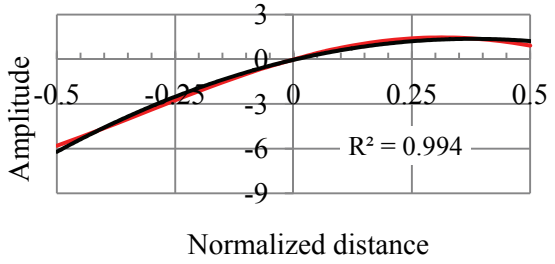

(c) $\lambda = 5L/2,\ \phi = \pi/4$

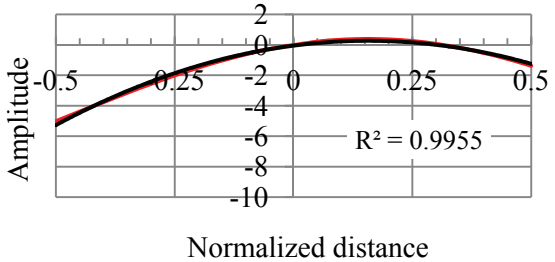

(d) $\lambda = 5L/2,\ \phi = 3\pi/8$

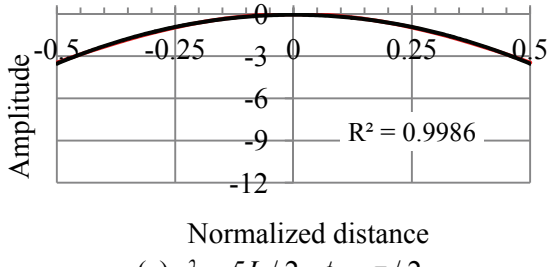

(e) $\lambda = 5L/2,\ \phi = \pi/2$

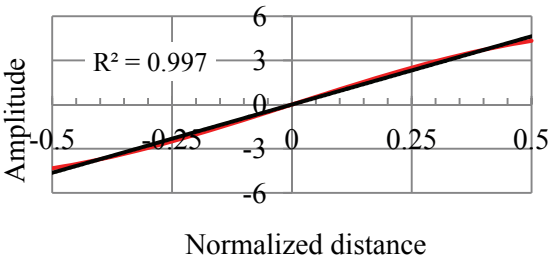

(f) $\lambda = 3L,\ \phi = 0$

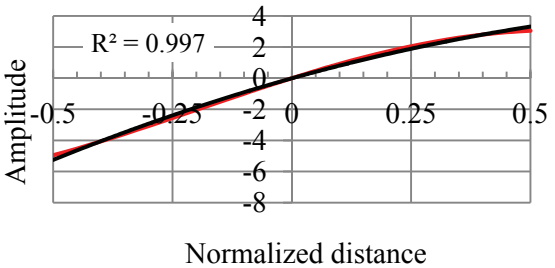

(g) $\lambda = 3L,\ \phi = \pi/8$

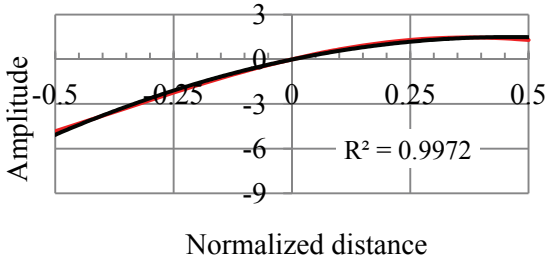

(h) $\lambda = 3L,\ \phi = \pi/4$

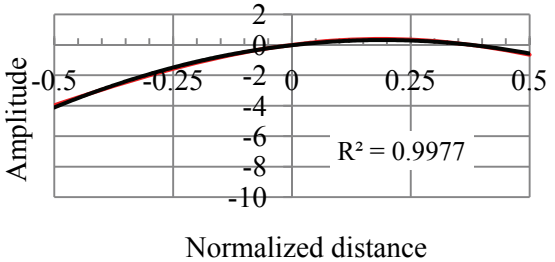

(i) $\lambda = 3L,\ \phi = 3\pi/8$

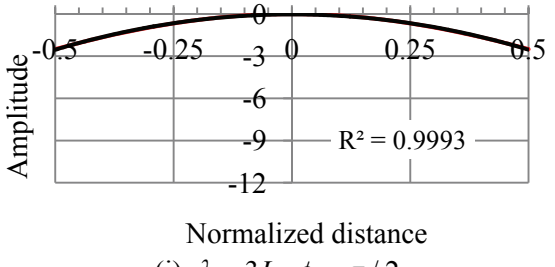

(j) $\lambda = 3L,\ \phi = \pi/2$

Figure A-3: Best-fit using AGM2 for $\lambda = 5L/2$ and $\lambda = 3L$

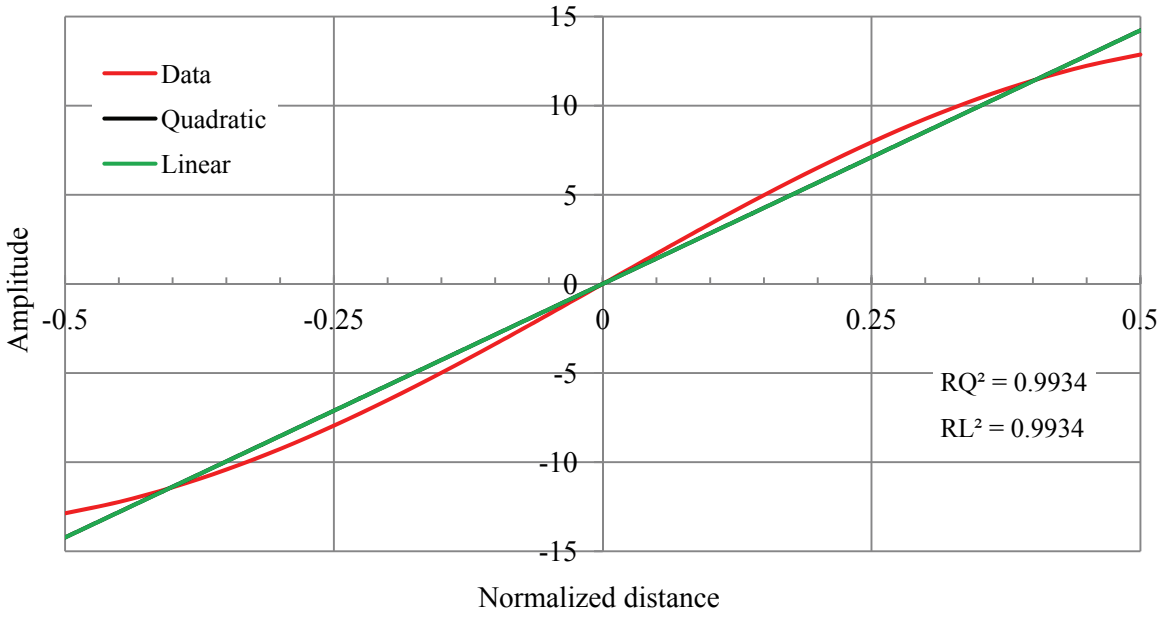

Figure A-4: Quadratic and linear fit for $\lambda = 2L,\ 3L,\ 4L$, and $\phi = 0$

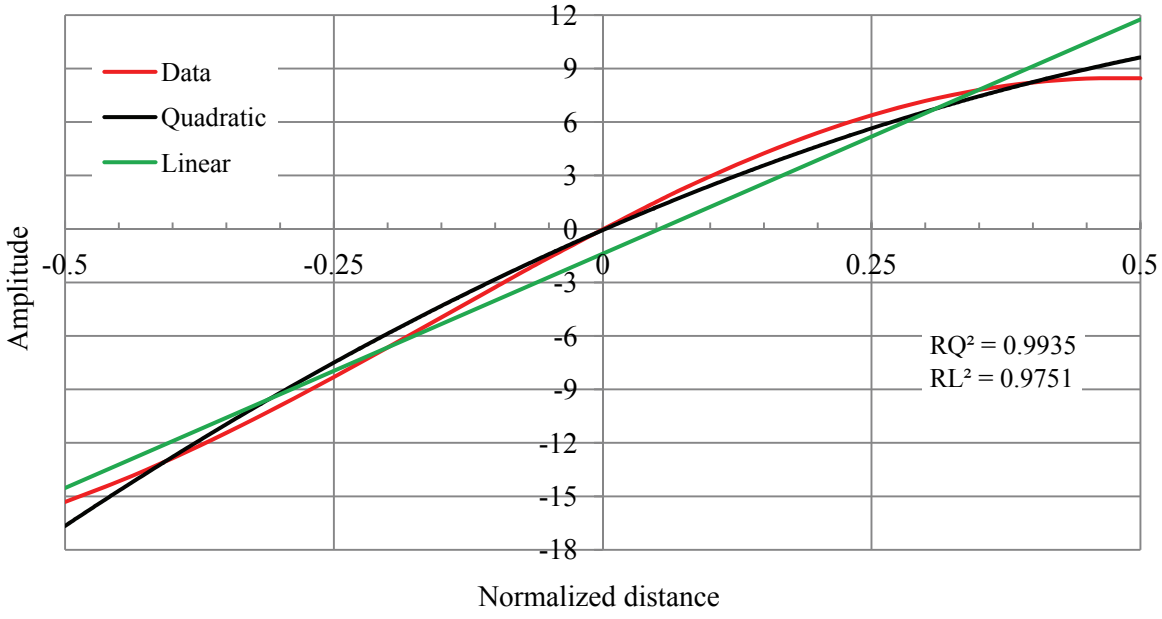

Figure A-5: Quadratic and linear fit for $\lambda = 2L,\ 3L,\ 4L$, and $\phi = \pi / 8$

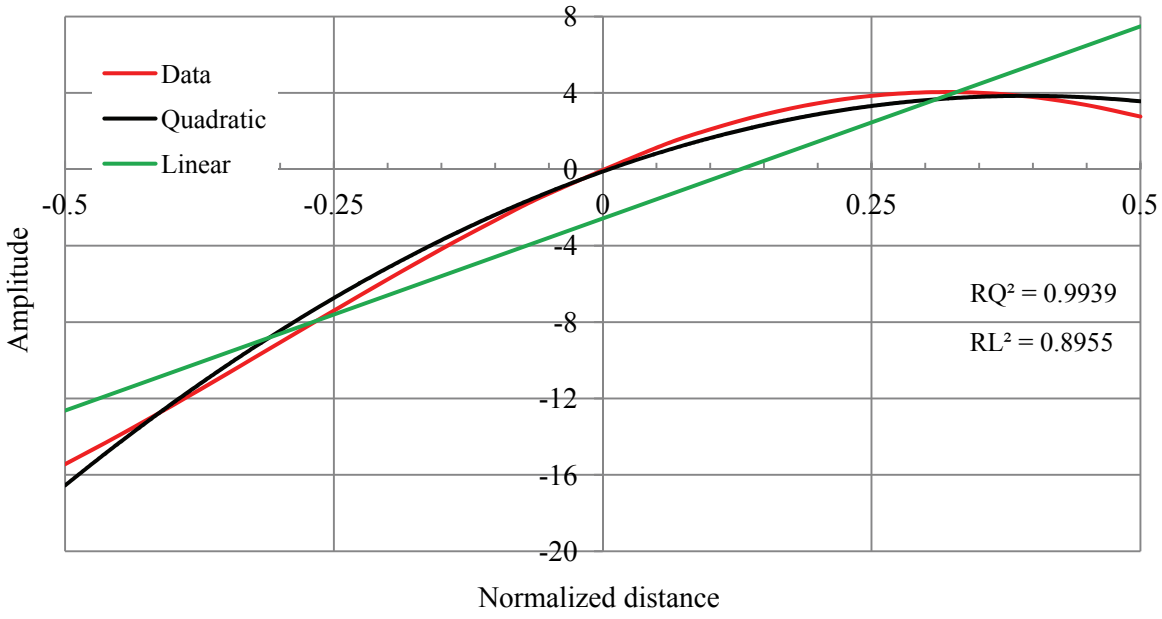

Figure A-6: Quadratic and linear fit for $\lambda = 2L,\ 3L,\ 4L$ and $\phi = \pi / 4$

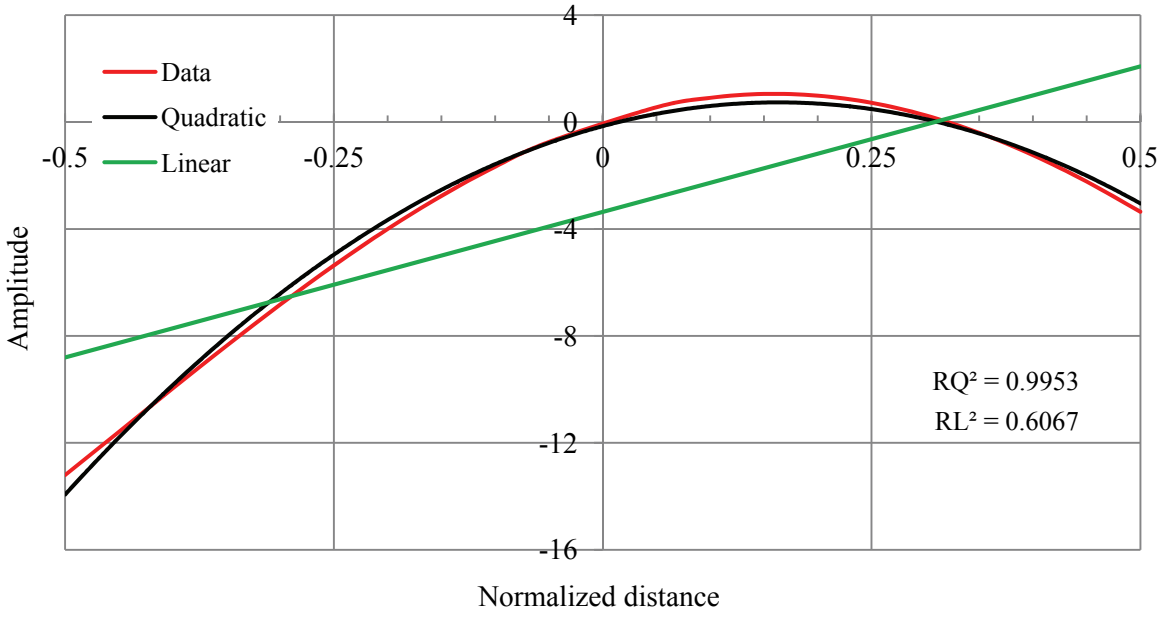

Figure A-7: Quadratic and linear fit for $\lambda = 2L,\ 3L,\ 4L$, and $\phi = 3\pi / 8$

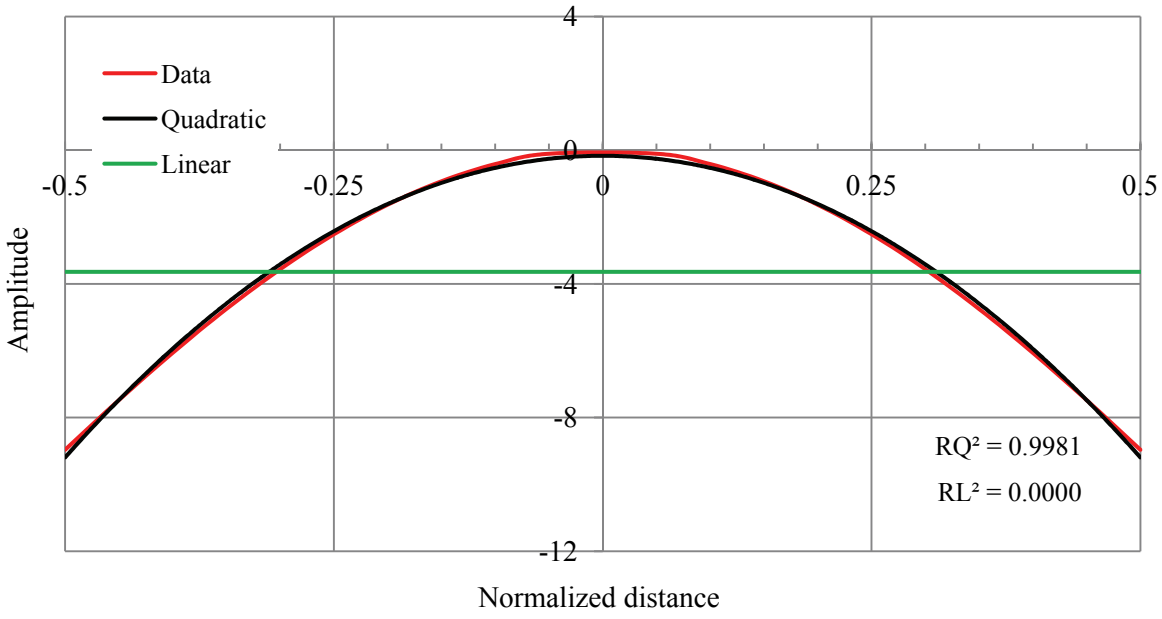

Figure A-8: Quadratic and linear fit for $\lambda = 2L,\ 3L,\ 4L$, and $\phi = \pi / 2$

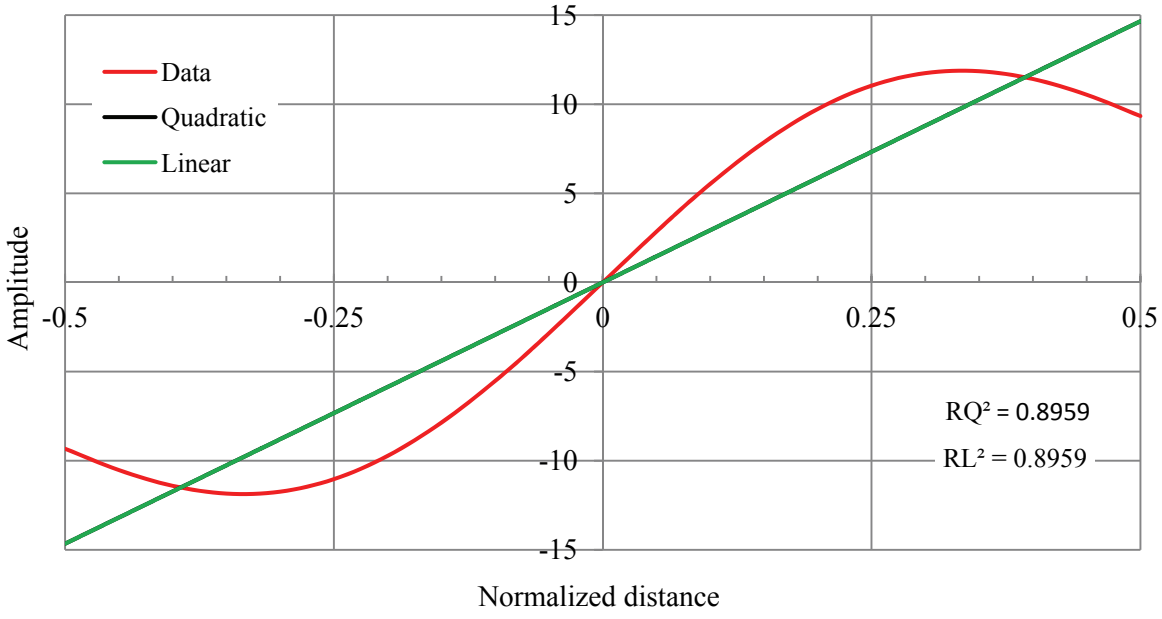

Figure A-9: Quadratic and linear fit for $\lambda = L,\ 2L,\ 3L$, and $\phi = 0$

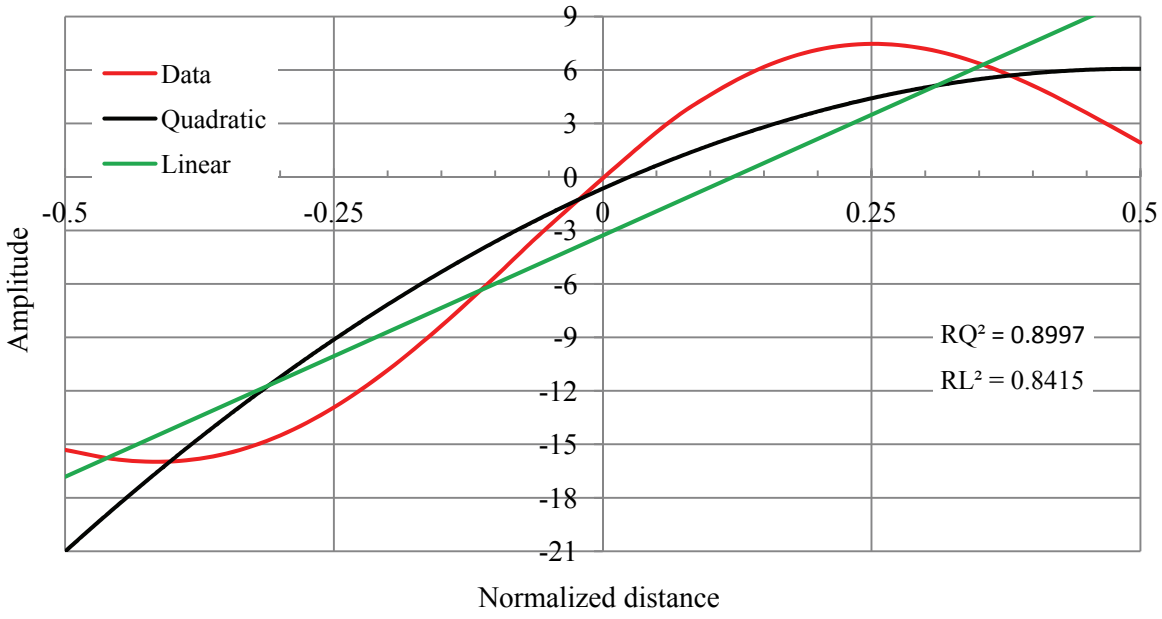

Figure A-10: Quadratic and linear fit for $\lambda = L,\ 2L,\ 3L$, and $\phi = \pi / 8$

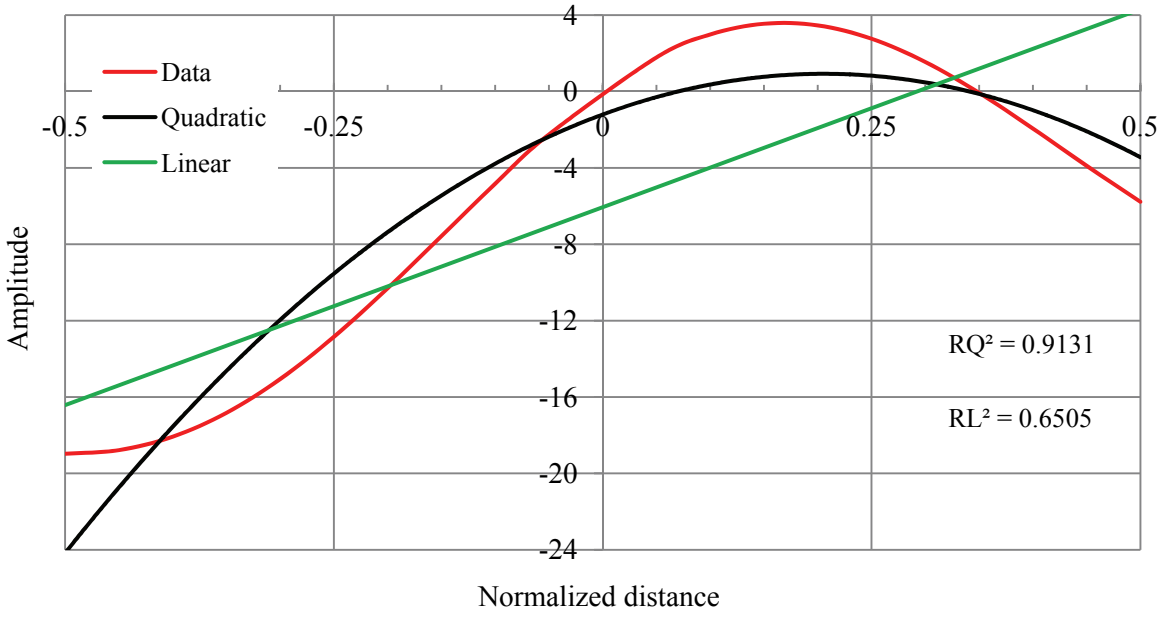

Figure A-11: Quadratic and linear fit for $\lambda = L,\ 2L,\ 3L$, and $\phi = \pi / 4$

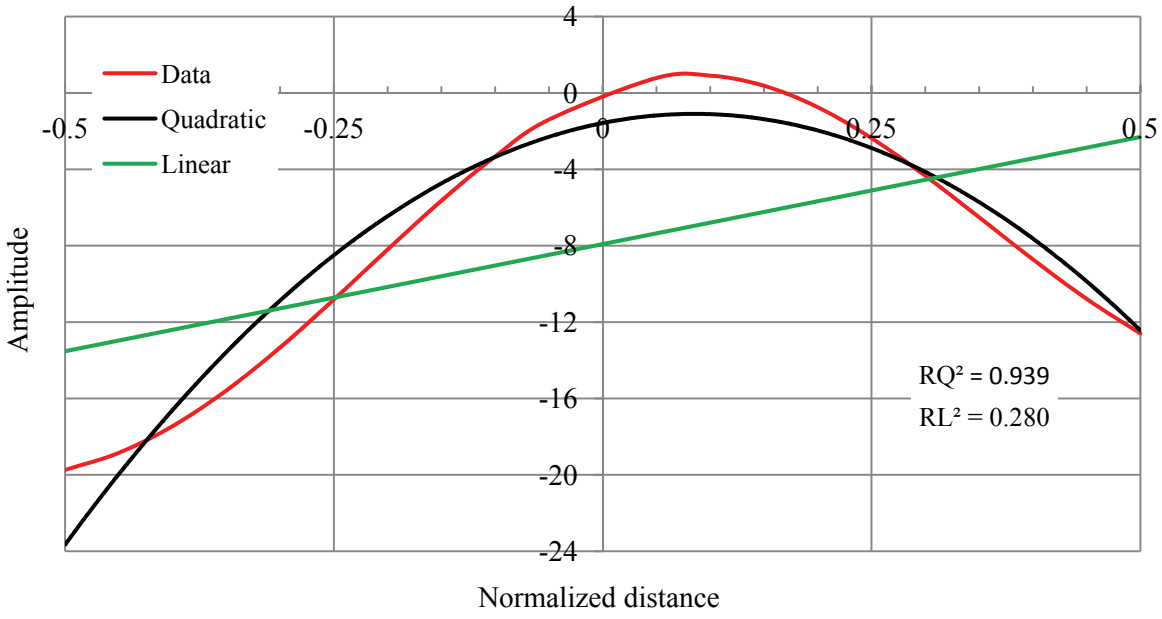

Figure A-12: Quadratic and linear fit for $\lambda = L,\ 2L,\ 3L$, and $\phi = 3\pi/8$

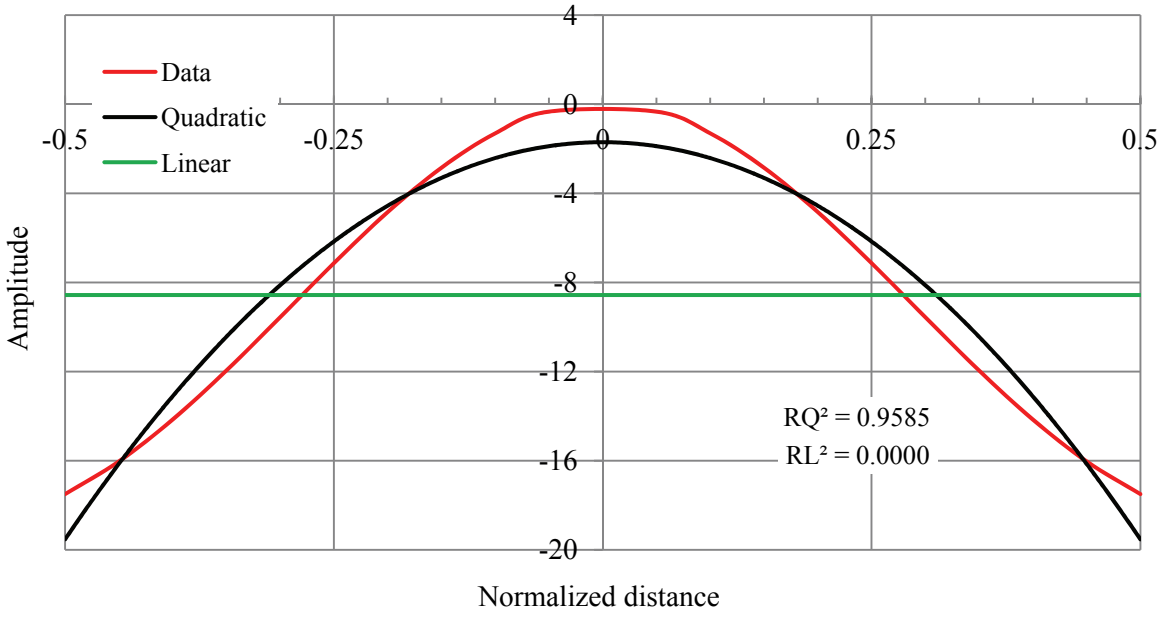

Figure A-13: Quadratic and linear fit for $\lambda = L,\ 2L,\ 3L$, and $\phi = \pi/2$

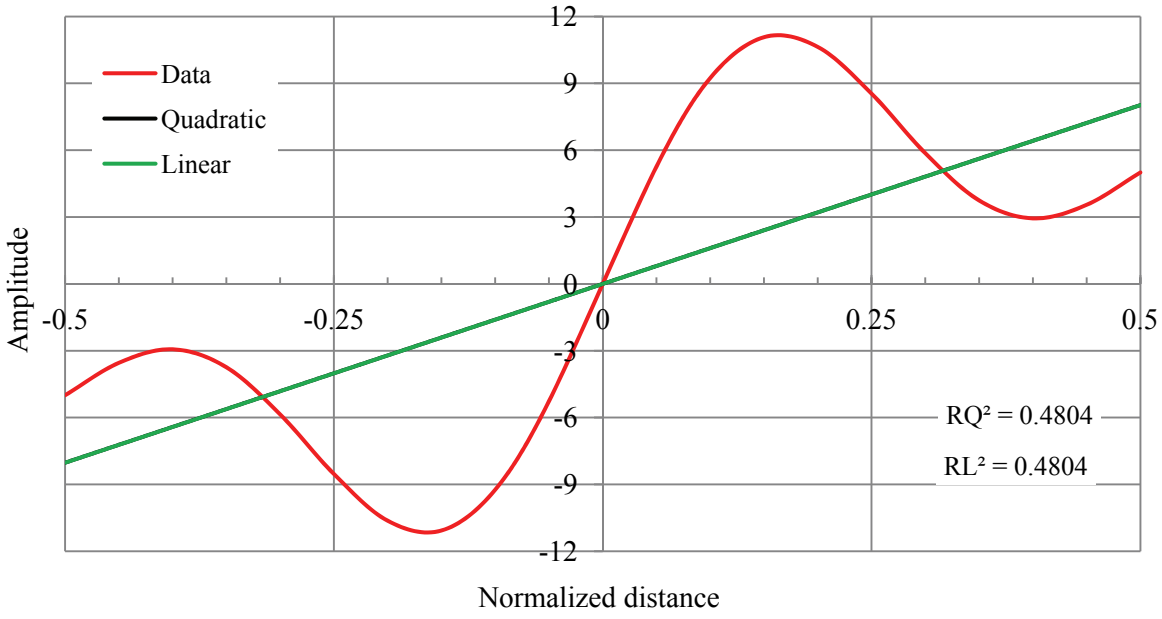

Figure A-14: Quadratic and linear fit for $\lambda = L/2,\ L,\ 2L$, and $\phi = 0$

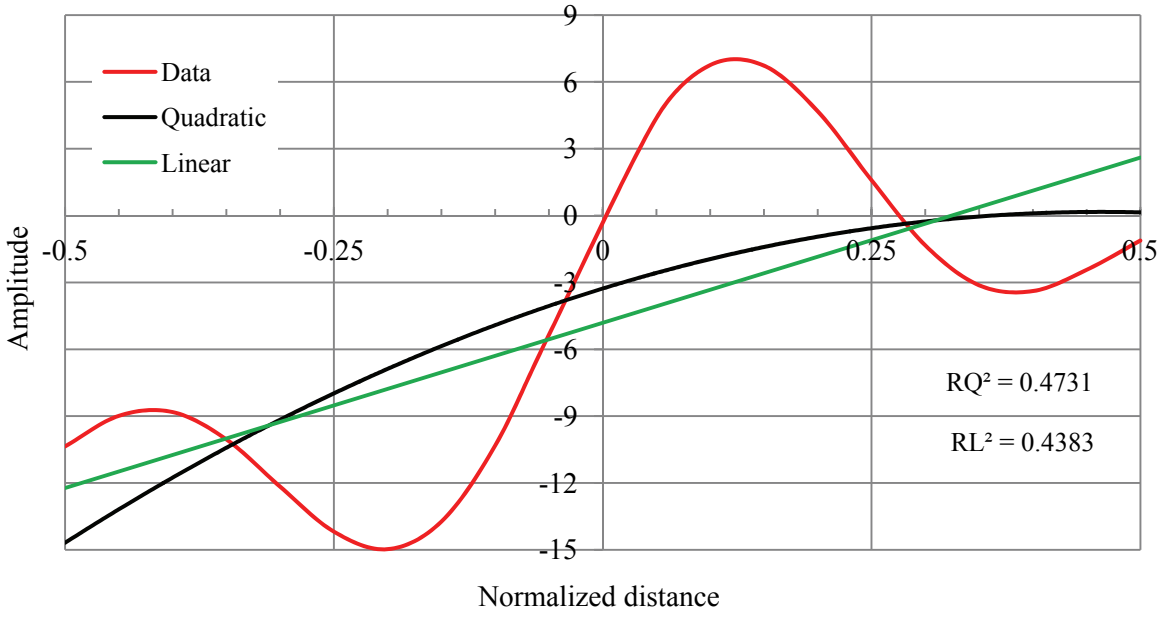

Figure A-15: Quadratic and linear fit for $\lambda = L/2,\ L,\ 2L$, and $\phi = \pi/8$

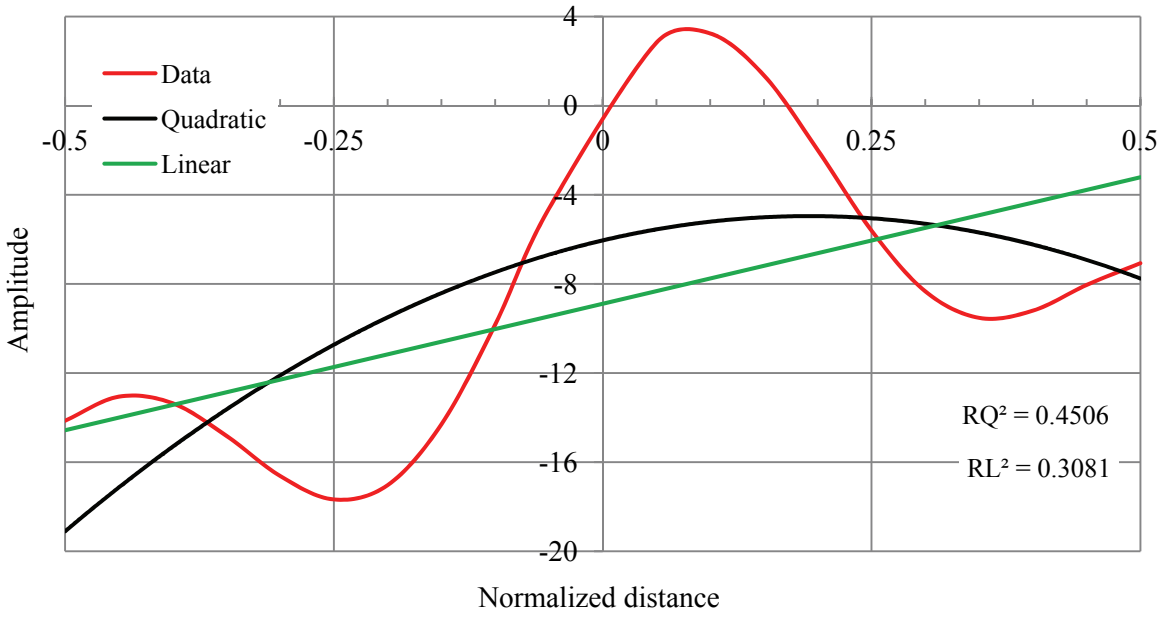

Figure A-16: Quadratic and linear fit for $\lambda = L/2,\ L,\ 2L$, and $\phi = \pi/4$

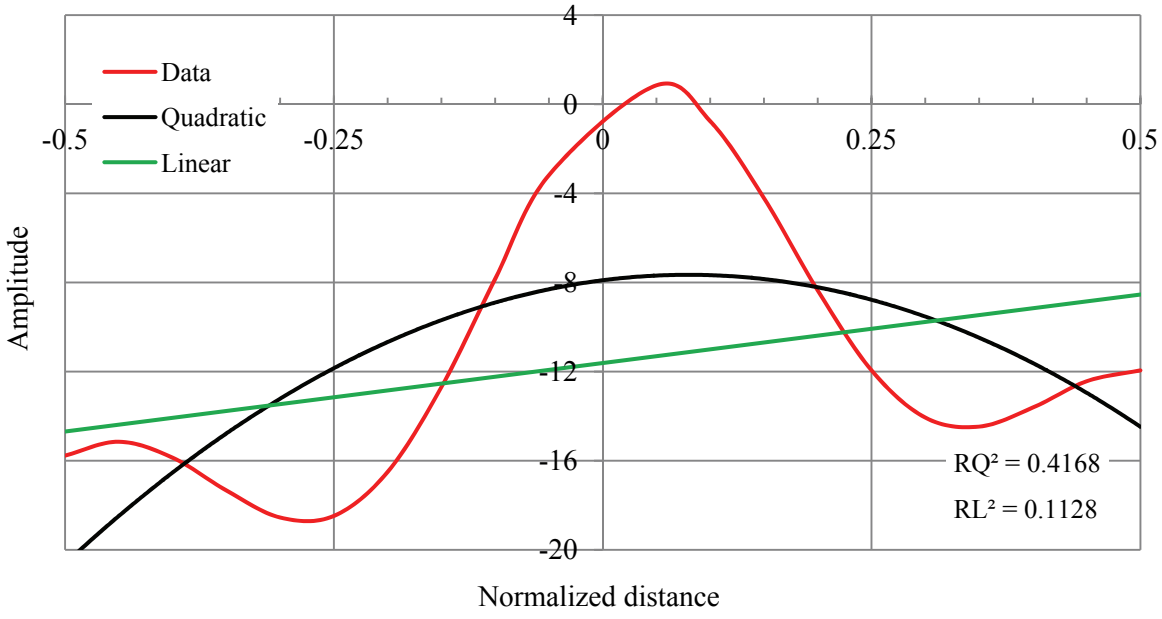

Figure A-17: Quadratic and linear fit for $\lambda = L/2,\ L,\ 2L$, and $\phi = 3\pi/8$

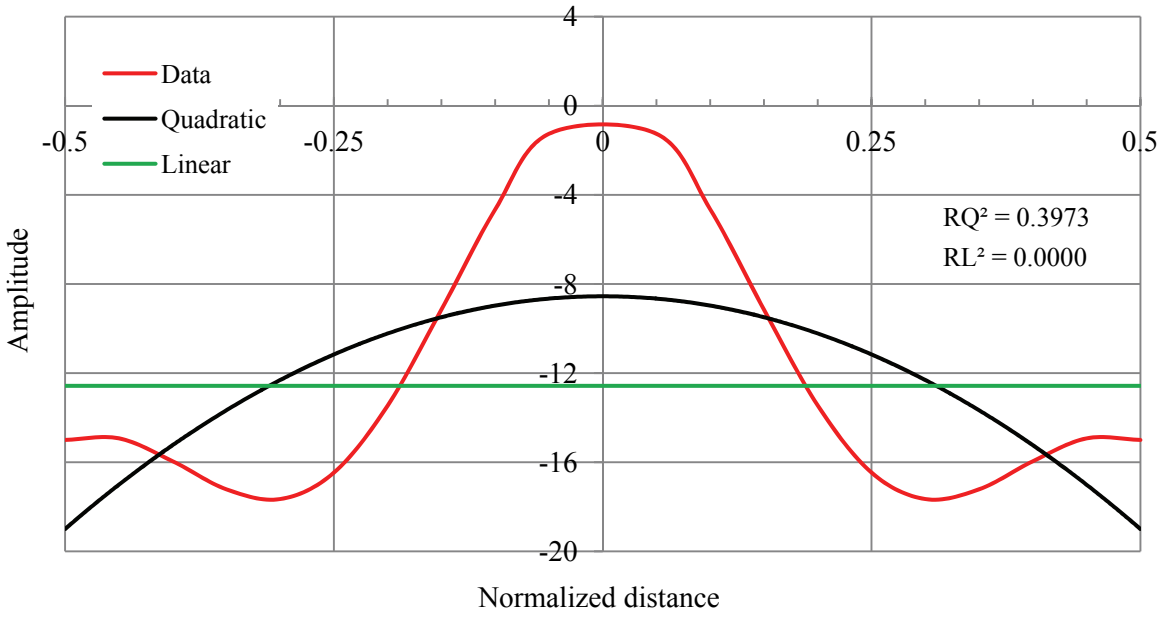

Figure A-18: Quadratic and linear fit for $\lambda = L/2,\ L,\ 2L$, and $\phi = \pi/2$

APPENDIX B
UTILITY OF THE ACCELERATION GRADIENT METHOD

B.1. Introduction

The Acceleration Gradient Method (AGM) of Chapter 4 can capture the high frequency components in the rotational motion better than the Geodetic Method (GM) of Chapter 2. However, it cannot capture frequency content beyond a threshold frequency of $c/2L$, where c and L are the apparent wave velocity and array dimension, respectively. This limitation, described here as a high frequency error (HFE), is not significant unless the recorded ground motion has significant frequency content at a frequency greater than twice the threshold frequency; see Appendix A for details. Therefore, the smaller the dimension of the dense array used for the calculation of rotational motion, the higher the threshold frequency and the smaller the HFE in the computed rotational motion. However, the rotational spectrum computed using the Surface Distribution Method (SDM) (see Chapter 5) does not lead to a stabilized (i.e., *actual*) spectrum until the array length exceeds a minimum length, which is equal to the greater of (see Chapter 6): 1) a half wavelength of the modal harmonic (MH), and 2) a quarter wavelength of the contributive lowest harmonic (CLH). The difference between the computed spectrum using a given array length and the *actual* spectrum is defined as the sensitivity error. Hence, the longer the array length, the smaller the associated sensitivity error. Rotational spectra calculated using the AGM are also subject to sensitivity error.

The SDM does not contain HFEs and increasing the array dimension leads to a better estimation of the rotational motion. This is not the case with the AGM since the sensitivity error decreases but HFE increases as the array dimension increases. Consequently, the following two questions arise: 1) How reliable is the rotational motion computed using the AGM? and 2) Under what circumstances does the AGM generate reliable results? These two questions are addressed in this appendix. Section B.2 presents

the procedure to identify the MH, CLH and CHH from a given earthquake record. Section B.3 presents the theoretical background, which is supported by a frequency domain interpretation of the AGM in Section B.4. Further, a method based on the modal harmonic (MH) is designed in Section B.5 for the purpose of numerical illustration, which is presented in Section B.6.

B.2. Calculation of MH, CLH and CHH

Two ways to calculate the frequencies associated with the MH, CLH and CHH are discussed in Chapter 6: 1) Fourier amplitude spectrum, and b) 5% damped response spectrum. The jaggedness present in the Fourier spectrum makes the calculation difficult and the use of the response spectrum is preferred. This is explained below and the data used for this purpose are the translation motions recorded at the station FA1_1 of the Large Scale Seismic Testing (LSST) array, Lotung, Taiwan during the M6.1 event of 1986. Figure B-1 presents the Fourier amplitude spectra for the recorded EW, NS and the vertical accelerations. The calculations of the frequencies associated with the MH, CLH and CHH are illustrated in Figure B-2: i) the frequency at which the peak amplitude occurs is the MH, and ii) the lowest and highest frequencies at an amplitude of 10% of the peak amplitude identify the CLH and CHH, respectively. Similar data are presented in Figures B-3 and B-4 for the NS and vertical accelerations, respectively. In each case, the frequency (= 0.02 Hz) associated the CLH is unrealistically low. Further, the vertical motion is characterized by two nearly equal (peak) amplitudes, at 2.03 Hz and 7.84 Hz (Figure B-4) making the calculations questionable.

Similar calculation using the response spectra are shown in Figures B-5 and B-6 for the horizontal and vertical accelerations, respectively. The reciprocal of the periods indicated in these figures give the required frequencies. Note the CHH cannot be computed using the response-spectrum approach, but the frequencies of the MH and CLH are more realistic than those obtained using the Fourier amplitude spectra.

The frequency associated with the CHH is usually not required for analysis. The design of the dense array presented in Chapter 6 is based on the assumption that the CHH frequency is twice that of the MH. The response-spectrum approach should be used to compute the frequencies for the MH and CLH. The Fourier amplitude spectra may be used to identify the CHH, if required.

B.3. Reliability of AGM Rotational Spectra

Rotational spectra computed using the AGM will be acceptable if the associated sensitivity error and HFE, as described in Section B.1, are small for all practical purposes. For the sensitivity error to be small, the array length should satisfy

$$L \geq \max\left[\frac{\lambda_{MH}}{2} \quad \frac{\lambda_{CLH}}{4}\right] \tag{B-1}$$

Even though Eq (B-1) was proposed for use with the SDM, it is used here with the AGM. Denoting c as the apparent wave velocity, the threshold frequency f can be expressed using Eq (B-1) as

$$\begin{aligned} f = \frac{c}{2L} &\leq \frac{c}{2\max\left[\frac{\lambda_{MH}}{2} \quad \frac{\lambda_{CLH}}{4}\right]} \\ &\leq \min\left[f_{MH} \quad 2f_{CLH}\right] \end{aligned} \tag{B-2}$$

Here f_{MH} and f_{CLH} are the frequency of the MH and CLH, respectively. Eq (B-2) should be satisfied to minimize the sensitivity error. The HFE increases if the upper limit of the frequency content exceeds twice the threshold frequency as shown in Appendix A. Denoting f_{CHH} as the frequency of the contributing highest harmonic (CHH), it is required that

$$f_{CHH} < 2f \tag{B-3}$$

Combining Eq (B-2) and Eq (B-3), a condition of acceptability for the AGM may be expressed as

$$f_{CHH} < 2f \leq 2\min\left[f_{MH} \quad 2f_{CLH}\right] \tag{B-4}$$

Eq (B-4) implies a narrow banded process if $2f_{CLH} > f_{MH}$. An example of a narrow banded acceleration history is

$$f_{MH} \approx f, \;\; 2f_{CLH} > f_{MH}, \; f_{CHH} < 2f_{MH} \tag{B-5}$$

The conditions $2f_{CLH} > f_{MH}$ and $f_{CHH} < 2f_{MH}$ define the frequency bounds for a narrow banded process. The AGM is expected to produce acceptable results if the array length and the recorded acceleration histories approximately satisfy Eq (B-4). The torsional spectra will be acceptable if both horizontal acceleration histories satisfy Eq (B-4). The rocking spectra will be acceptable if the vertical motion satisfies Eq (B-4).

The M 6.1 event recorded by the Large Scale Seismic Testing (LSST) array in Lotung, Taiwan in 1986, is considered here for analysis. Based on the translational data recorded at the station FA1_1, f_{MH} for the EW and NS directions are calculated per Section B.2 as 1.32 Hz and 1.59 Hz, respectively; $f_{MH} =$ 1.32 Hz is used in Eq (B-2). Similarly, f_{CLH} for the EW and NS directions are computed as 0.38 Hz and 0.52 Hz, respectively; $f_{CLH} =$ 0.38 Hz is used in Eq (B-2). The array length is $L = 75$ m (see Chapter 6) and the apparent SH wave velocity is $c_{sh} = 249$ m/sec (see Chapter 5). The threshold frequency associated with the estimation of the torsional motion may be calculated as $f = c_{sh}/2L = 1.66$ Hz. The value of $f/\min[f_{MH} \;\; 2f_{CLH}]$ is 2.18 and significantly greater than 1. The array length is therefore not adequate per Eq (B-2) to minimize the sensitivity error. The Fourier amplitude spectrum of the SH wave contribution to recorded motion shown in Figure 5-9 indicates that f_{CHH} is not significantly greater than $2f =$ 3.32 Hz. This is also seen in Figures B-2 and B-3 for the recorded EW and NS components, respectively. Accordingly, the horizontal motions are not narrow banded.

The presence of a sensitivity error overestimates the ordinates of the rotational spectra at all periods as evident in Chapter 6. Accordingly, the torsional spectra computed in Chapter 4 using the AGM should overestimate the actual spectral demands. If the array length was such that it satisfied Eq (B-2), which was the case with $L > 164$ m, the torsional spectra computed using AGM would be free of the sensitivity error. However, the threshold frequency would be reduced to $f < 0.76$ Hz and the spectral ordinates would be underestimated at periods of less than 0.66 sec $(1/(2 \times 0.76))$. Such a spectrum may not be

particularly useful for torsional analysis of most structures. The AGM will not produce useful torsional spectra for this seismic event even with an increased array dimension.

A similar calculation for the vertical spectrum shows that $f_{MH} =$ 7.4 Hz and $f_{CLH} =$ 0.92 Hz (see Section B.2). The array length is $L = 75$ m and the apparent P wave velocity is $c_p =$ 951 m/sec (see Chapter 5), the threshold frequency is $f = c_p / 2L =$ 6.34 Hz. The value of $f / \min[f_{MH} \quad 2f_{CLH}]$ is 3.45, which is significantly greater than 1. The array length is not adequate to minimize the sensitivity error. The Fourier amplitude spectrum of the vertical acceleration shows significant frequency content at frequencies greater than $2f =$ 12.38 Hz. Accordingly, the vertical motion is not narrow banded. To minimize the sensitivity error, the required array length is $L > 259$ m but the threshold frequency would then be reduced to $f <$ 1.84 Hz, leading to a significant underestimation of the spectral ordinates at periods of less than 0.27 sec ($1/(2 \times 1.86)$). Again, such a spectrum may not be particularly useful for rocking analysis of most structures. The use of the AGM will not produce useful rocking spectra for this seismic event.

The following steps should be taken to assess whether the AGM can be used to extract rotational components from translational data recorded in a dense array: 1) use the SSP as described in Chapter 3 to compute the apparent SH and P wave velocities; 2) compute the frequencies associated with MH, CLH and CHH for the horizontal and vertical motions recorded at the reference station; 3) check if $2f_{CLH} > f_{MH}$ and $f_{CHH} < 2f_{MH}$ are approximately satisfied; 4) if the checks are not satisfied by both the recorded horizontal motions the AGM should not be used to compute the torsional spectra; else, use the AGM with array length such that $f_{MH} \approx f$, that is, an array length equal to the half wavelength (SH wave) of the MH; and 5) The AGM cannot be used to compute the rocking spectra if the checks are not satisfied by the recorded vertical motion; else, use the AGM with array length equal to a half wavelength (P wave) of the MH.

Note the AGM requires a specified array length to be used, even if the array spans over a relatively large area. Following the rectangular definition presented in Chapter 6, this specific dimension may be obtained by selecting a few of the stations located around the reference station.

B.4. A Frequency Domain Interpretation of the AGM

The overdetermined problem solved in Chapters 2 and 4 is of the form

$$[A]\{p\} = \{\Delta\ddot{u}\} = [D]\{\ddot{u}\} \tag{B-6}$$

where $[A]$ is the data kernel that only depends on the layout of the stations and not on the recorded data; $\{p\}$ is the vector of gradient parameters to be evaluated; $\{\ddot{u}\}$ is the recorded ground motion along one of the orthogonal directions and $[D]$ is a difference matrix. Denoting the Fourier transform by a superscript '*', Eq (B-6) can be expressed in the frequency domain as

$$[A]\{p^*(\omega_r)\} = \{\Delta\ddot{u}^*(\omega_r)\} = [D]\{\ddot{u}^*(\omega_r)\} \tag{B-7}$$

Assuming the weight matrix $W_e = \left[DD^T\right]^{-1}$ as defined in Chapter 2, the solution of the overdetermined problem (Eq (B-7)) associated with the r^{th} discrete frequency (ω_r) can be expressed as

$$\{\bar{p}^*(\omega_r)\} = \left[A^T W_e A\right]^{-1}\left[A^T W_e\right][D]\{\ddot{u}^*(\omega_r)\} \tag{B-8}$$

After calculating the solution vector $\{\bar{p}^*(\omega_r)\}$ at each discrete frequency and then taking the inverse FFT, it may be shown that

$$\{\bar{p}\} = \left[A^T W_e A\right]^{-1}\left[A^T W_e\right][D]\{\ddot{u}\} \tag{B-9}$$

which is the solution of Eq (B-6), as obtained in Chapter 4. Therefore, Eq (B-8) represents the same solution as Eq (B-9), except in the frequency domain. Similarly, Eq (B-7) represents the same problem as Eq (B-6), except in the frequency domain.

The overdetermined problem given by Eq (B-7) is now compared with the problem solved in the SDM using Eq (5-10). Unlike in the AGM, the kernel $[A]$ in the SDM is frequency dependent. Similarly, the solution vector Eq (B-8) is compared with that obtained in the SDM using Eq (5-11). Aside from the frequency dependency of the kernel $[A]$ in the SDM, it is also noted that: a) the weight matrices W and W_e are different, b) the number of rows of the kernel $[A]$ in the AGM is one less than that in the SDM, and c) the matrix $[D]$ is not present in the SDM. This is because the best-fit surface associated with any discrete frequency is computed in the SDM through the Fourier coefficients of the recorded acceleration data. However, the frequency domain representation of the AGM presented here first computes the difference in the acceleration histories at any station with respect to that recorded at the reference station, and then computes the best-fit surface through the Fourier coefficients associated with any discrete frequency of these derived acceleration histories. This justifies the difference in the number of rows in the kernel and the role of the matrix $[D]$ in the AGM, which is not used in the SDM. Further, the difference in weight matrices between the AGM and the SDM is due to their theoretical backgrounds.

It is now evident that the AGM of Chapter 4 is a form of the SDM, albeit with a few exceptions. The most important exception is the frequency independent kernel, which characterizes the target distribution surface in the SDM. The target distribution surface in the frequency domain interpretation of the AGM is always quadratic over the array length, regardless of the wavelength of the considered harmonic. This proves the SDM is better at capturing higher frequencies than the AGM.

B.5. Dominant Frequency Method (DFM)—Formulation and Illustration

It has been shown in Section B.3 that the use of the AGM may lead to reliable rotational spectra if the associated recorded acceleration history is fairly narrow banded as identified in Eq (B-5) with a dominant contribution from the MH. In this case, the actual distribution surface at any time instant is expected to take the form of a wave with wavelength approximately equal to λ_{MH}. Eq (5-8) and Eq (5-9) are now rewritten for the distribution surface of the Fourier coefficient associated with the r^{th} discrete frequency in the SDM as follows:

$$\begin{Bmatrix} a(x,y) & b(x,y) \end{Bmatrix} = \begin{Bmatrix} G_1 & G_2 & G_3 & G_4 \end{Bmatrix} \begin{bmatrix} P_{ar} & P_{br} \\ Q_{ar} & Q_{br} \\ R_{ar} & R_{br} \\ S_{ar} & S_{br} \end{bmatrix} \tag{B-10}$$

where the elements of $\{G\}$ are given by

$$\begin{aligned} &G_1 = \cos(xk_r \cos\eta + yk_r \sin\eta);\ G_2 = \sin(xk_r \cos\eta + yk_r \sin\eta) \\ &G_3 = \cos(-xk_r \sin\eta + yk_r \cos\eta);\ G_4 = \sin(-xk_r \sin\eta + yk_r \cos\eta) \end{aligned} \tag{B-11}$$

All the variables in this equation were defined in Chapter 5 and are not repeated here. Taking the inverse FFT of Eq (B-10), the acceleration history contributed from the r^{th} harmonic is given by

$$\ddot{W}_r(t) = \begin{Bmatrix} G_1 & G_2 & G_3 & G_4 \end{Bmatrix} \begin{Bmatrix} P_r(t) \\ Q_r(t) \\ R_r(t) \\ S_r(t) \end{Bmatrix} \tag{B-12}$$

where the column vector on the right is given by

$$\begin{aligned} &P_r(t) = 2P_{ar}\cos\omega_r t + 2P_{br}\sin\omega_r t,\ Q_r(t) = 2Q_{ar}\cos\omega_r t + 2Q_{br}\sin\omega_r t \\ &R_r(t) = 2R_{ar}\cos\omega_r t + 2R_{br}\sin\omega_r t,\ S_r(t) = 2S_{ar}\cos\omega_r t + 2S_{br}\sin\omega_r t \end{aligned} \tag{B-13}$$

For a narrow banded acceleration history, the distribution surface at any time instant will be predominantly governed by the contribution from the MH. Accordingly, the row vector on the right side

of Eq (B-12) may be considered frequency independent and equal to that in the MH. Summing the contributions from all the harmonics,

$$\ddot{W}(t)=\sum_{r=1}^{N}\ddot{W}_r(t)=\{G_1 \quad G_2 \quad G_3 \quad G_4\}_{MCH}\left\{\sum_{r=1}^{N}P_r(t) \quad \sum_{r=1}^{N}Q_r(t) \quad \sum_{r=1}^{N}R_r(t) \quad \sum_{r=1}^{N}S_r(t)\right\}^T \quad \text{(B-14)}$$

At any time instant, Eq (B-14) can be evaluated by considering each station, including the reference station, one by one. The resulting equations can then be assembled in a matrix form, which lead to an overdetermined problem. The solution of the overdetermined problem is obtained using a least-squares method. The weight matrix used in this least-squares method is a diagonal matrix where the weight assigned to the reference station that is much greater (e.g., 1000) than at any other stations (e.g., 1). Physically, this constrains the distribution surface to pass through the recorded data at the reference station. After the distribution surface is obtained, a spatial derivative of the acceleration is then calculated from Eq (B-14) by replacing the row vector on the right side by its appropriate spatial derivative computed from Eq (B-11). The time series of the spatial derivatives of the acceleration can be calculated by repeating the procedure at each time instant.

Use of the ground motion data in the DFM is similar to that in the SDM. For example, the recorded horizontal motions are first rotated normal to the principal plane and the SH wave contribution is identified. The components of this acceleration history along the recording directions are used to define the horizontal acceleration field. The apparent SH wave velocity is used to compute λ_{MH} for the horizontal motions and the apparent P wave velocity is used for the vertical motion.

The SDM procedure described in Chapter 5 is superior to the DFM because the target distribution surface used in SDM accounts for the variation of wavelengths in each harmonic. However, the DFM is addressed here primarily to gain insight into the high frequency error (HFE) and sensitivity error involved in the AGM. The DFM is appropriate for a narrow banded acceleration history with significant contributions from the MH. If the DFM is used to analyze an earthquake record that is not narrow banded, the computed rotational motions will be contaminated by the HFE and SE. Because of the similarity

(frequency independent) in the target distribution surfaces in DFM and AGM, both methods are expected to generate similar rotational components. This is true for any earthquake record. Further, the DFM (and AGM) are expected to produce rotational spectra similar to those obtained using the SDM if Eq (B-5) is satisfied. Eq (B-5) represents a subclass of the narrow banded acceleration histories given by Eq (B-4), when $\lambda_{MH} > \lambda_{CLH}/2$. In this case, the array length required to minimize the SE is $\lambda_{MH}/2$.

B.6. Comparison of Rotational Spectra

Rotational spectra computed using the DFM and AGM (Chapter 4) are compared here. The comparison also includes the spectra calculated using the GM (Chapter 2) and SDM (Chapter 5). Since the earthquake records analyzed here are not narrow banded, it is expected that the spectra computed using the AGM and DFM will be similar but will differ from the SDM. The torsional spectra presented in Figure B-7 conform to this expectation at the interior stations with one exception: the SDM spectra are also very similar to those computed using the DFM or AGM. This may be attributed to the earlier observation in Section B.3 that the recorded horizontal motions are narrow banded on the high frequency side but not on the low frequency side. Since the AGM spectra at the exterior stations are subjected to numerical error as noted in Chapter 4, the torsional spectra at the exterior stations do not conform to the expectation. A comparison of the rocking spectra on the *xz* and *yz* planes is enabled by Figures B-8 and B-9. These spectra approximately satisfy the expectation at the interior station. If the SRSS *xz*-*yz* spectra are considered as a unified measure of rocking motion, the comparison presented in Figure B-10 better conforms to the expectation at the interior stations. In all three cases, as shown in Figure B-8 through B-10, the comparison at exterior stations does not conform due to the numerical error involved in the AGM. In all the comparisons presented above, spectra computed using the GM are also included to enable an evaluation of the high frequency components that are lost using the GM.

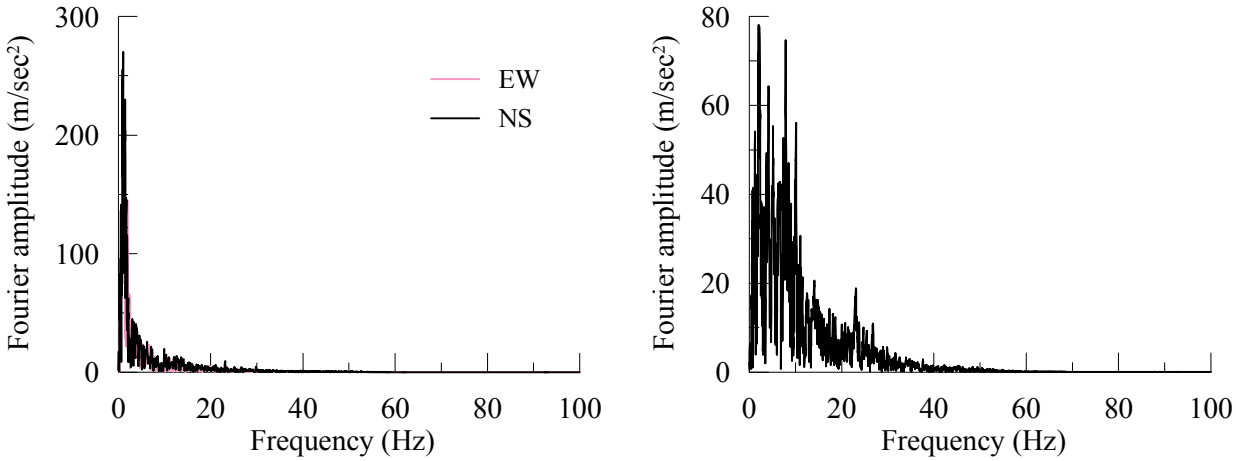

(a) Frequency range 0-100Hz (EW and NS) (b) Frequency range 0-100Hz (Vertical)

Figure B-1: Fourier amplitude spectra of the recorded horizontal and vertical accelerations

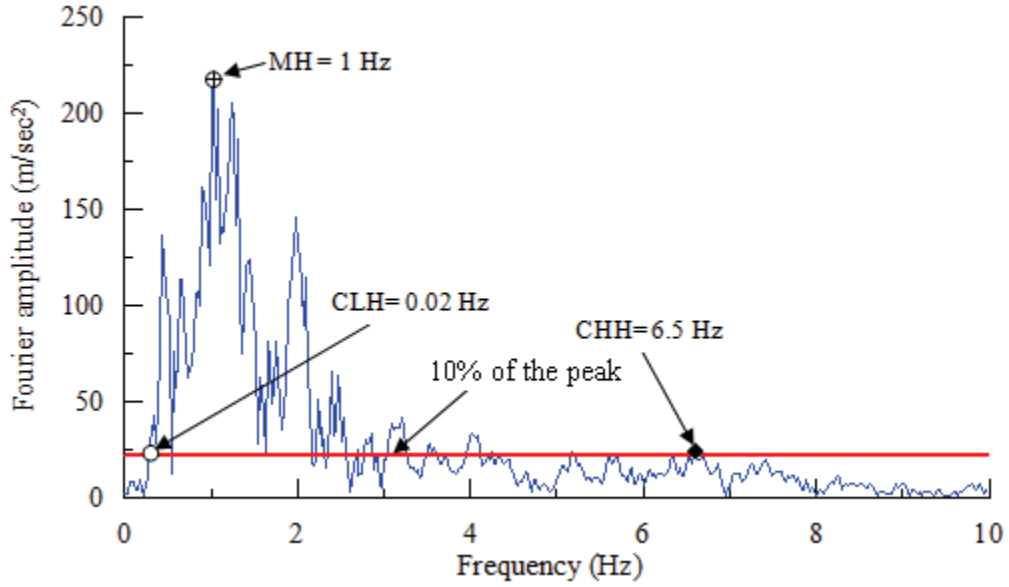

Figure B-2: MH, CLH and CHH for the EW acceleration using Fourier amplitude spectrum

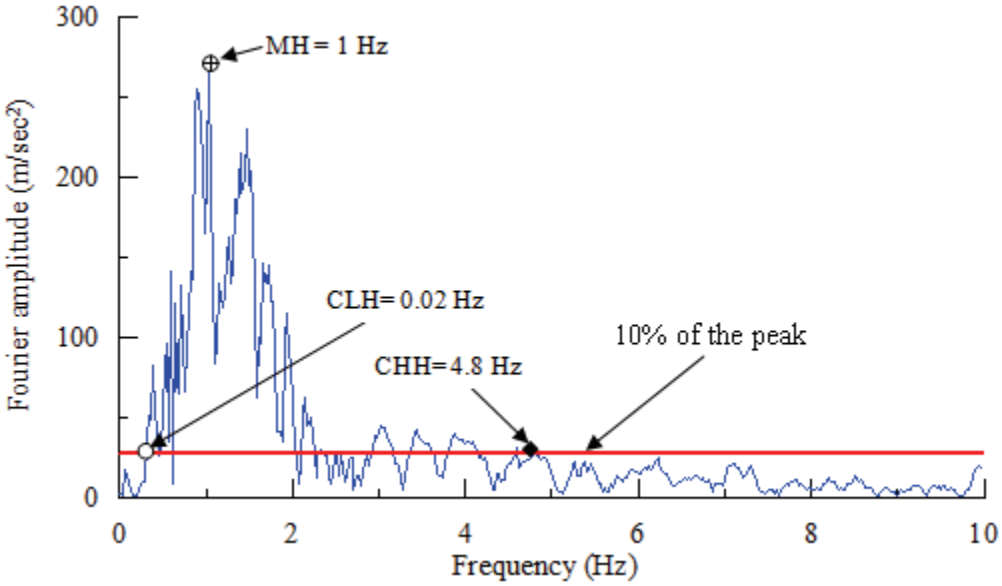

Figure B-3: MH, CLH and CHH for the NS acceleration using Fourier amplitude spectrum

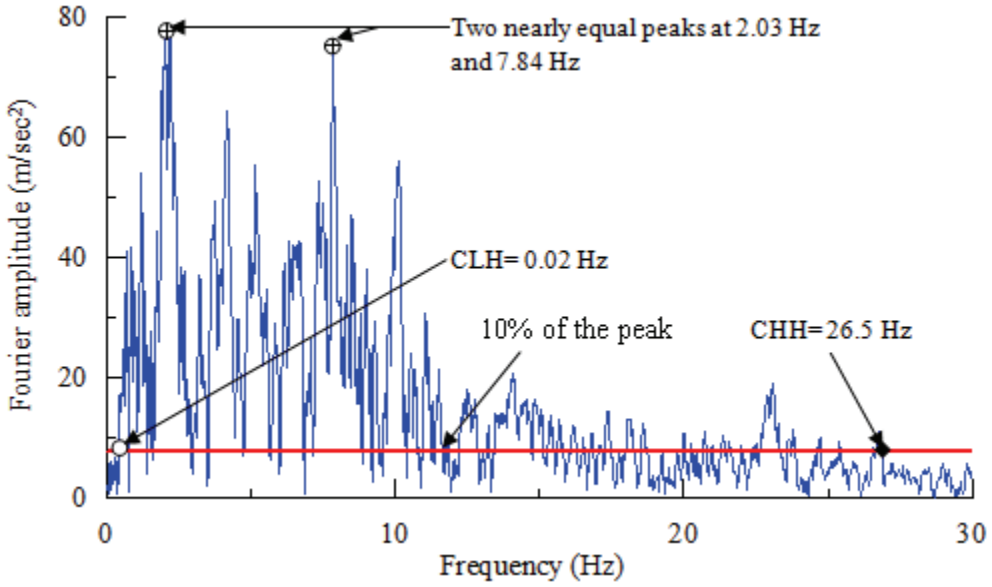

Figure B-4: MH, CLH and CHH for the vertical acceleration using Fourier amplitude spectrum

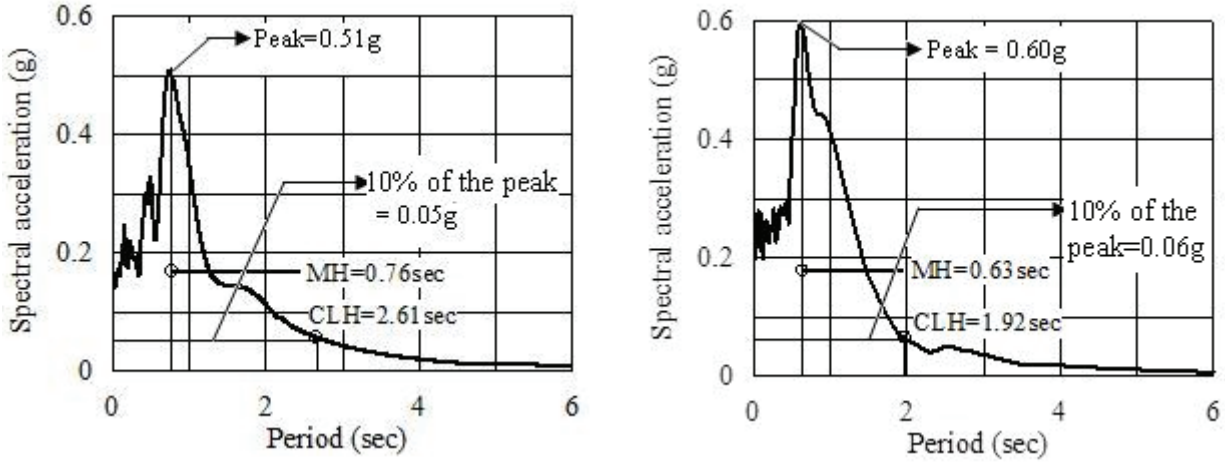

(a) EW direction

(b) NS direction

Figure B-5: Identifying MH and CLH for the horizontal motion using response spectra

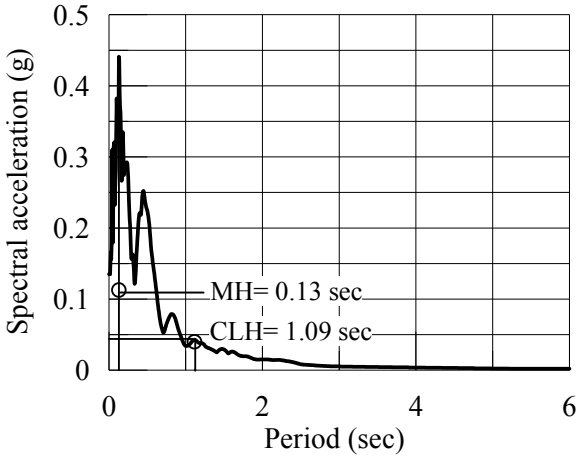

Figure B-6: Identifying MH and CLH for the vertical motion using response spectra

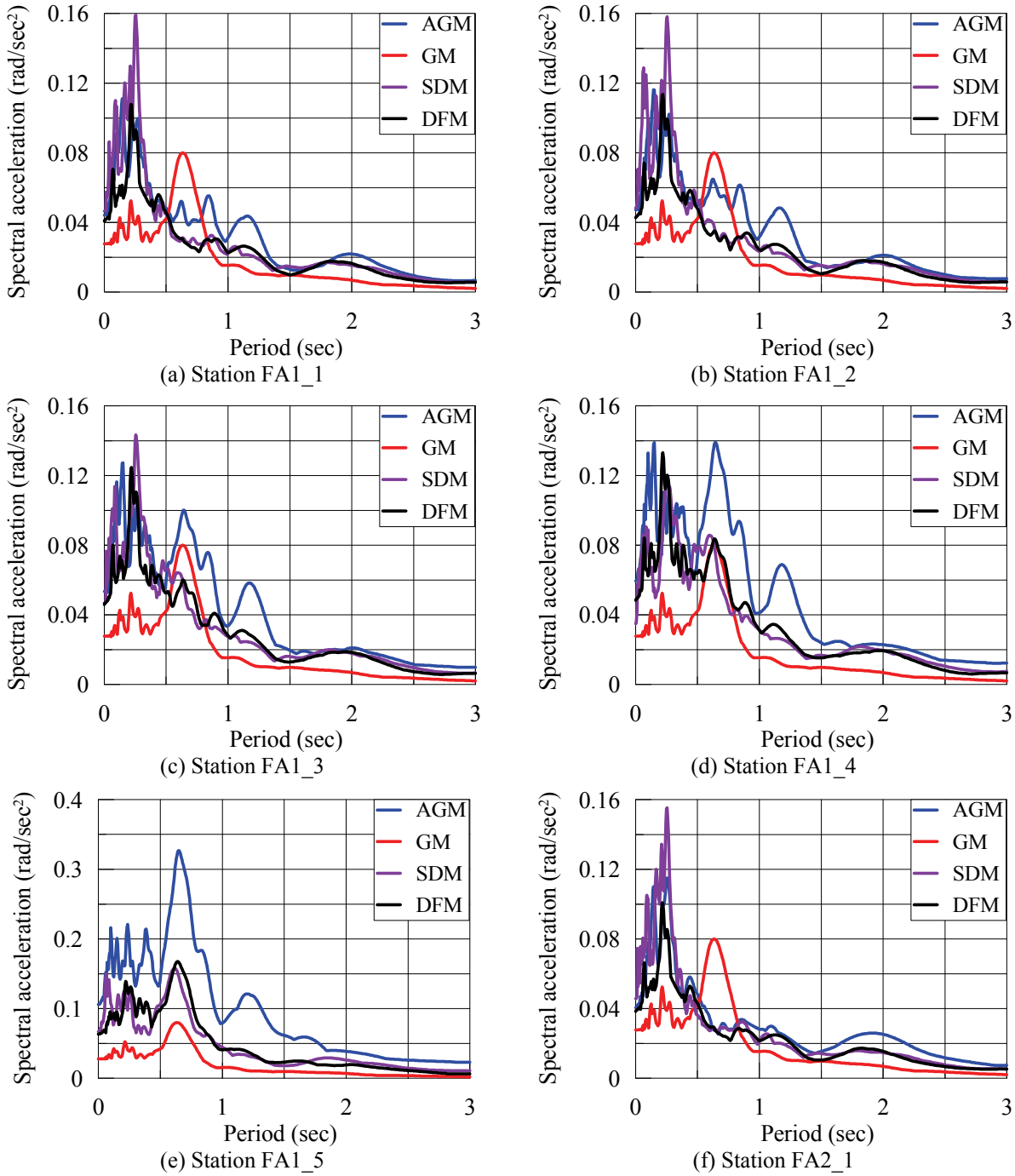

Figure B-7: Torsional spectra computed using four different methods

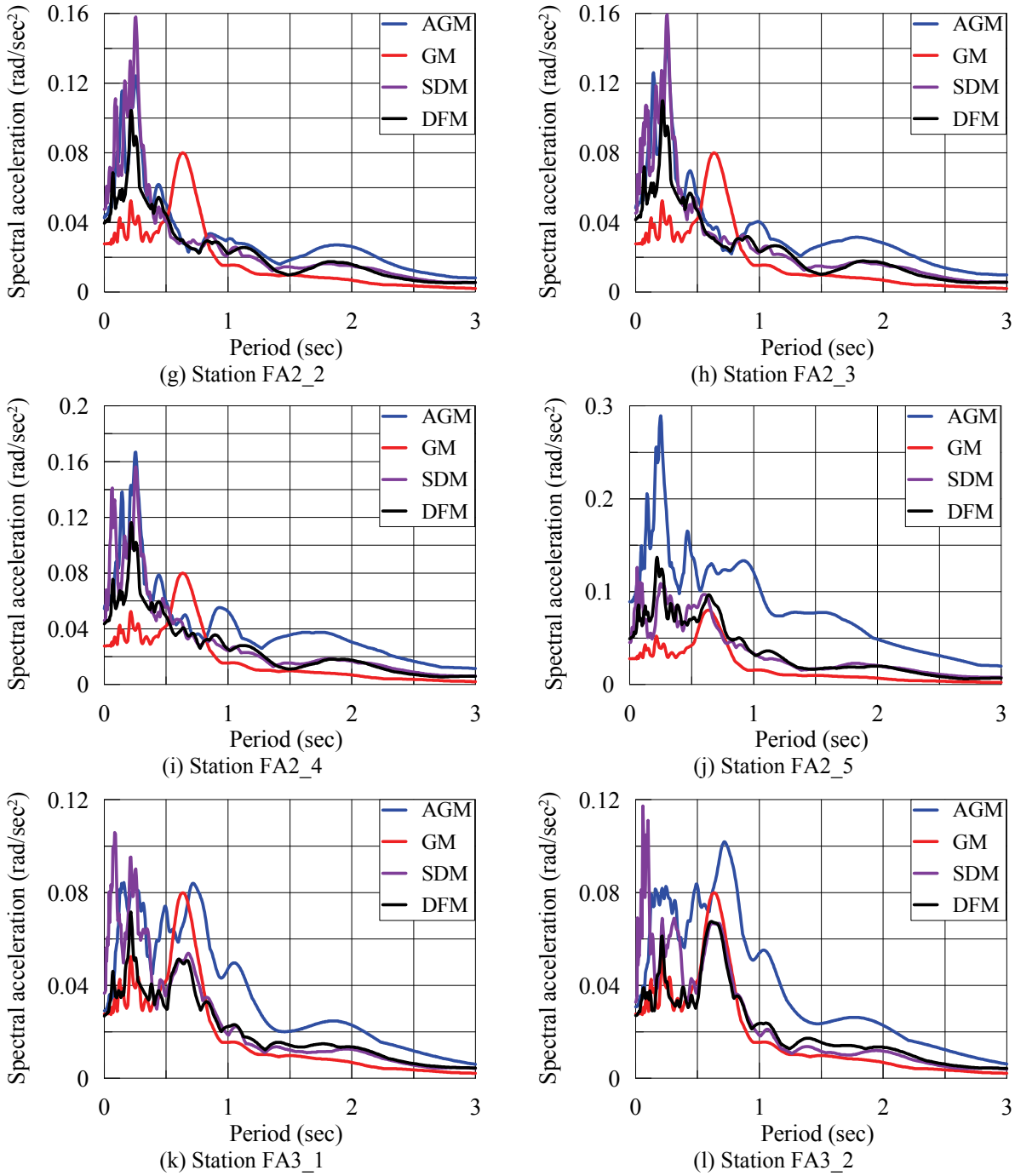

Figure B-7: Torsional spectra computed using four different methods (cont.)

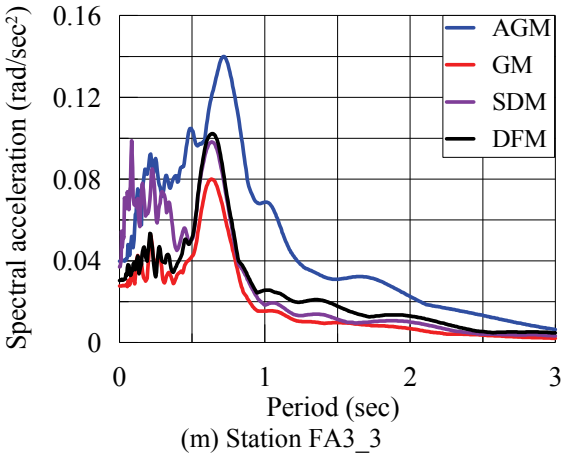

(m) Station FA3_3

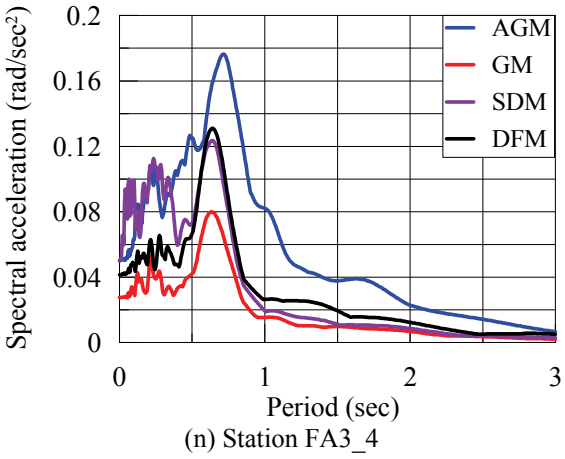

(n) Station FA3_4

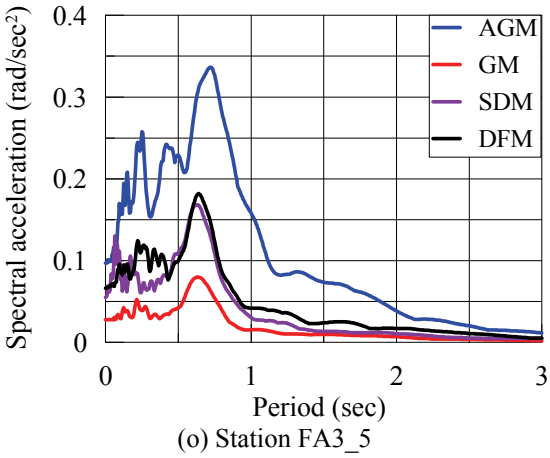

(o) Station FA3_5

Figure B-7: Torsional spectra computed using four different methods (cont.)

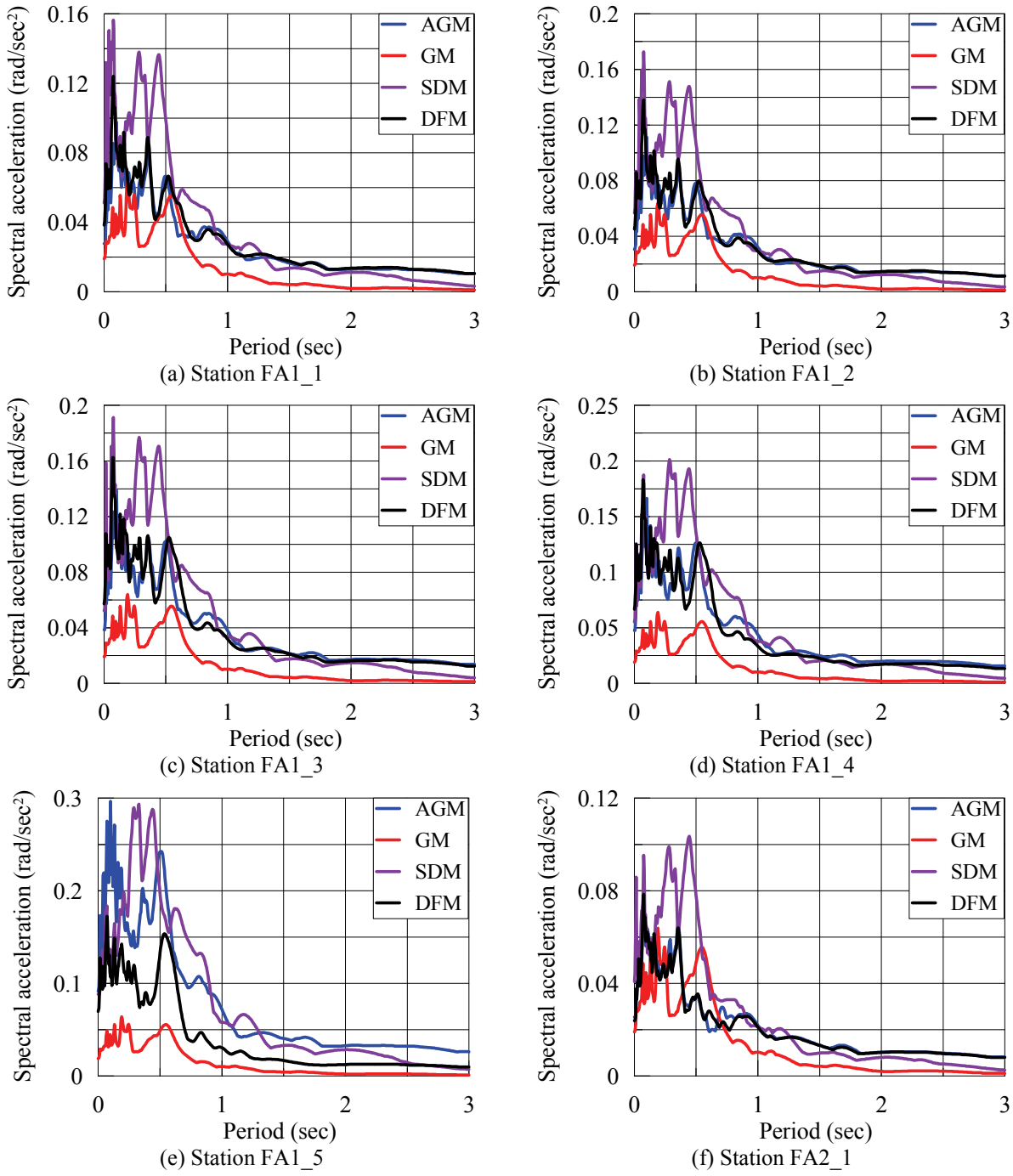

Figure B-8: Rocking (*xz* plane) spectra computed using four different methods

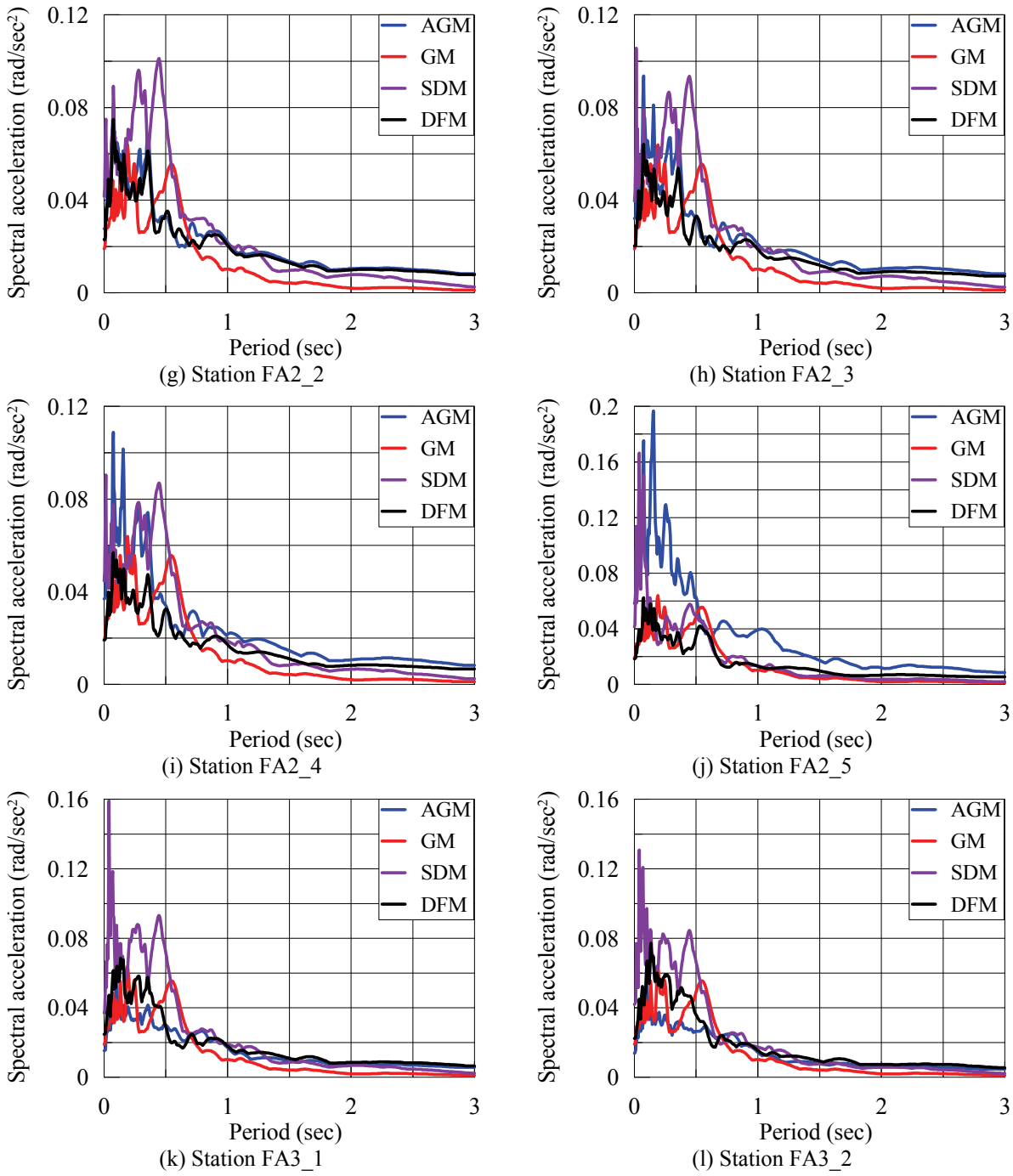

Figure B-8: Rocking (*xz* plane) spectra computed using four different methods (cont.)

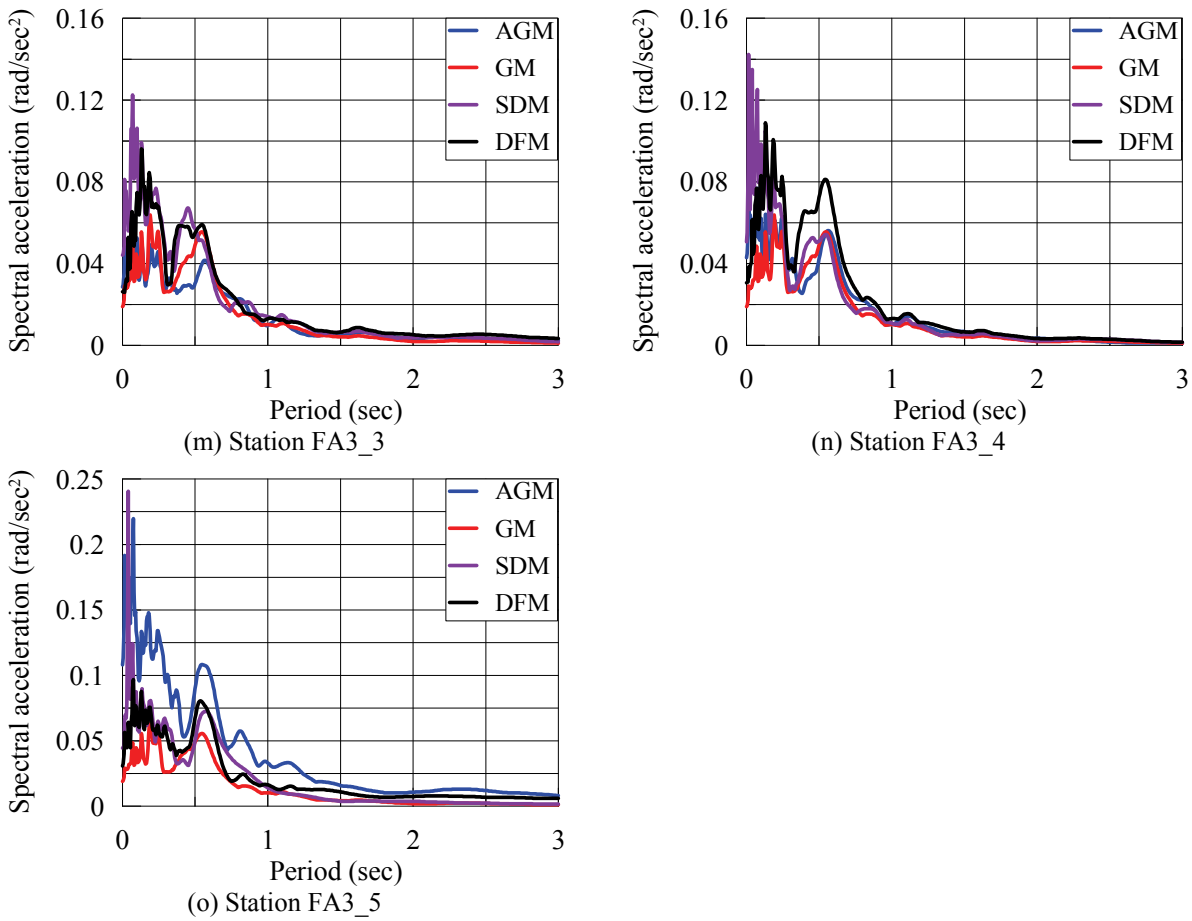

Figure B-8: Rocking (*xz* plane) spectra computed using four different methods (cont.)

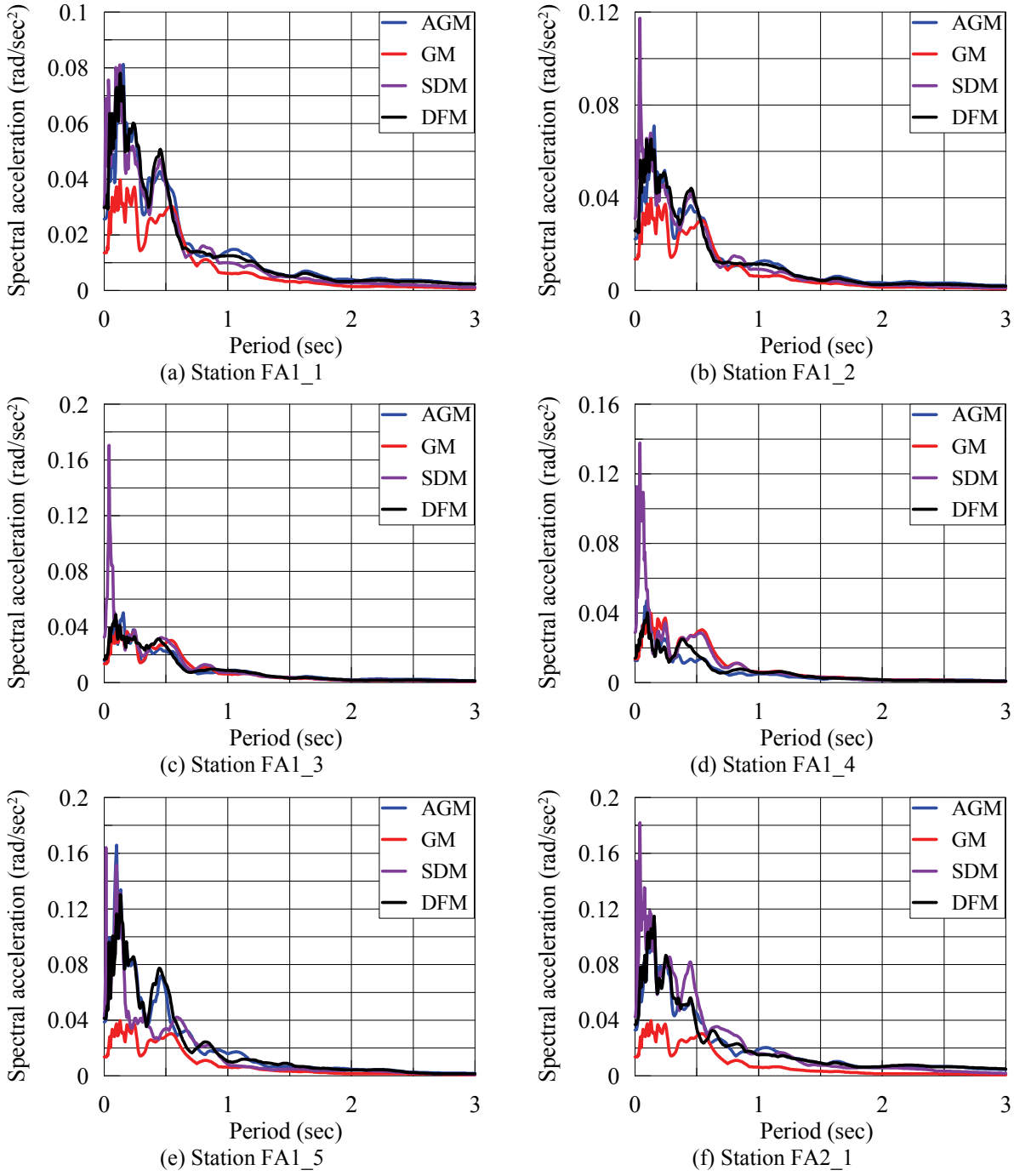

Figure B-9: Rocking (*yz* plane) spectra computed using four different methods

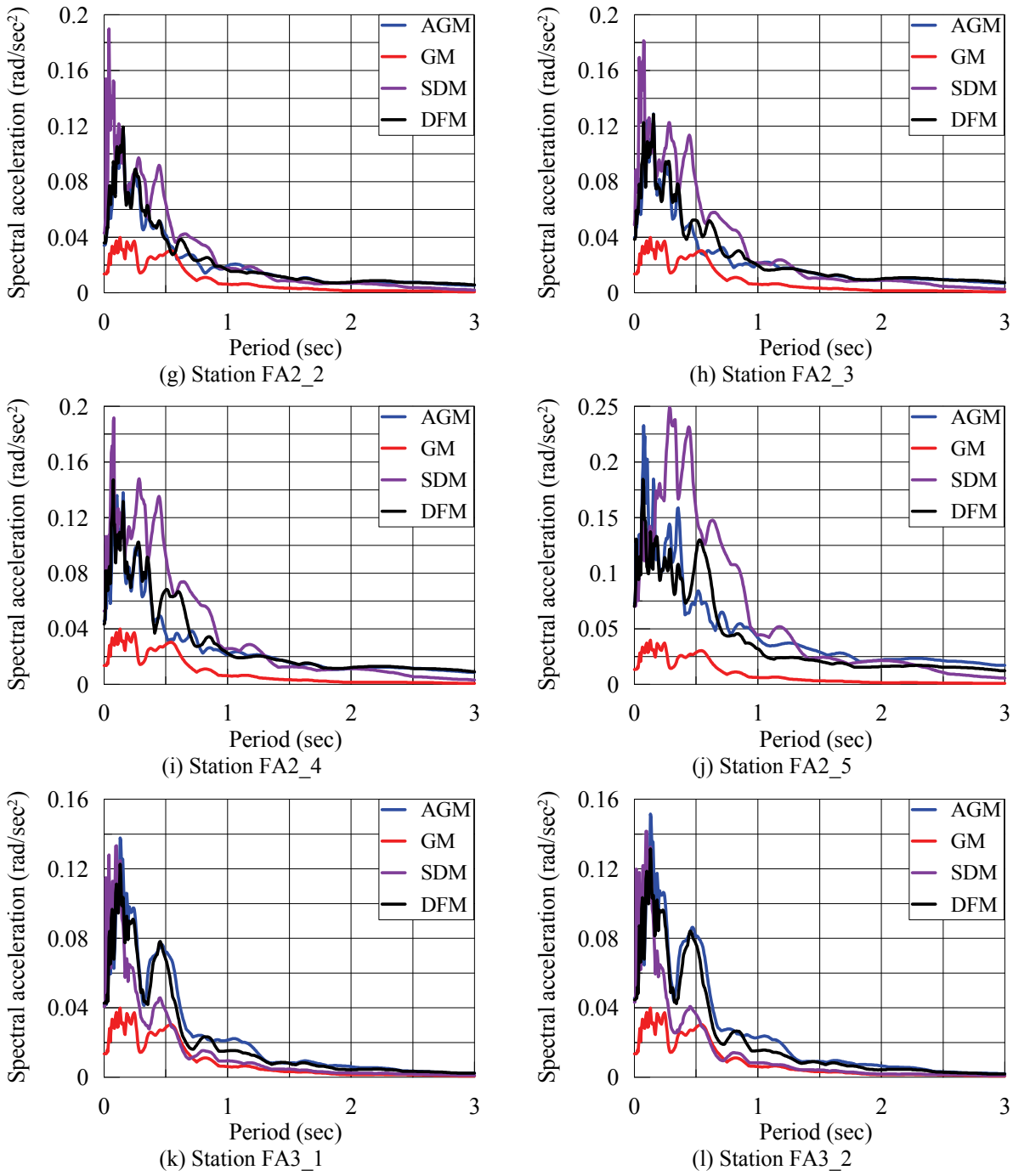

Figure B-9: Rocking (*yz* plane) spectra computed using four different methods (cont.)

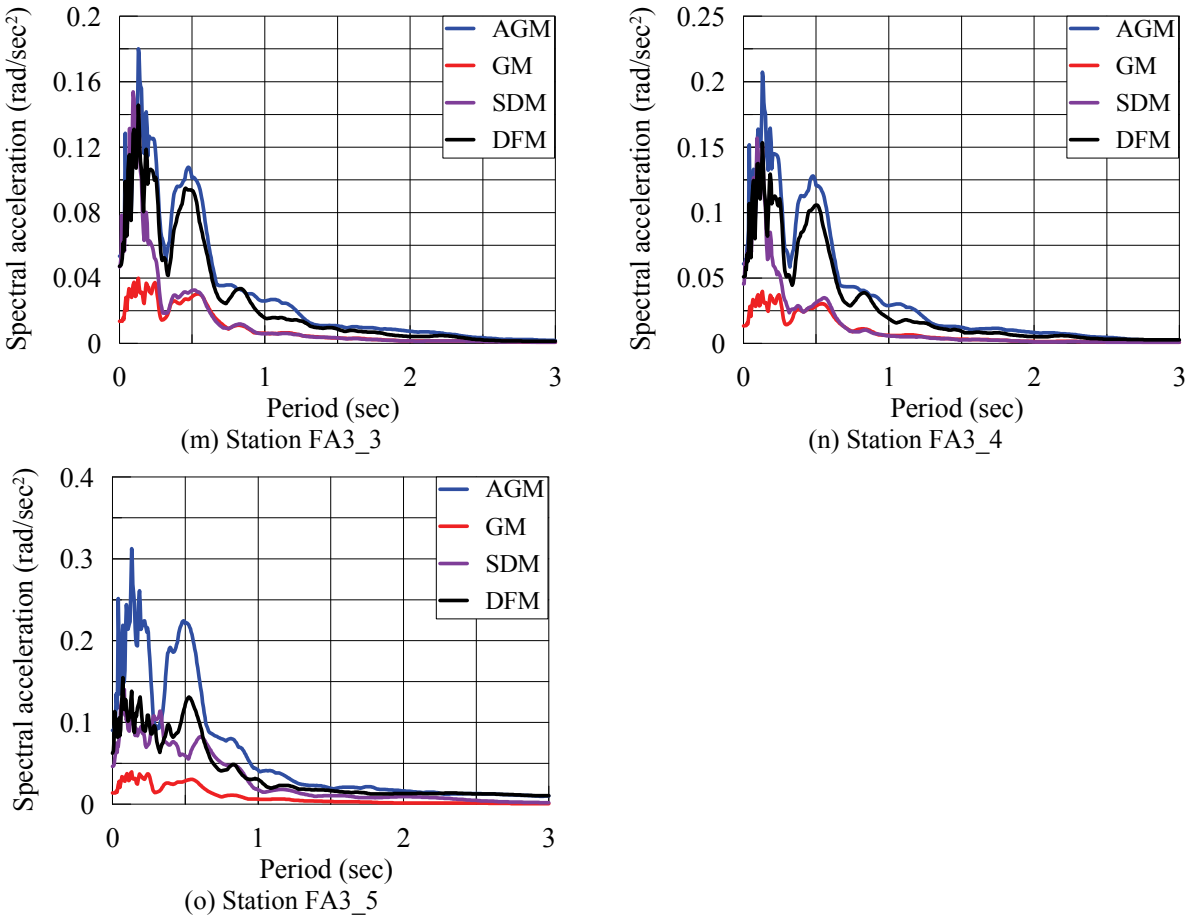

Figure B-9: Rocking (*yz* plane) spectra computed using four different methods (cont.)

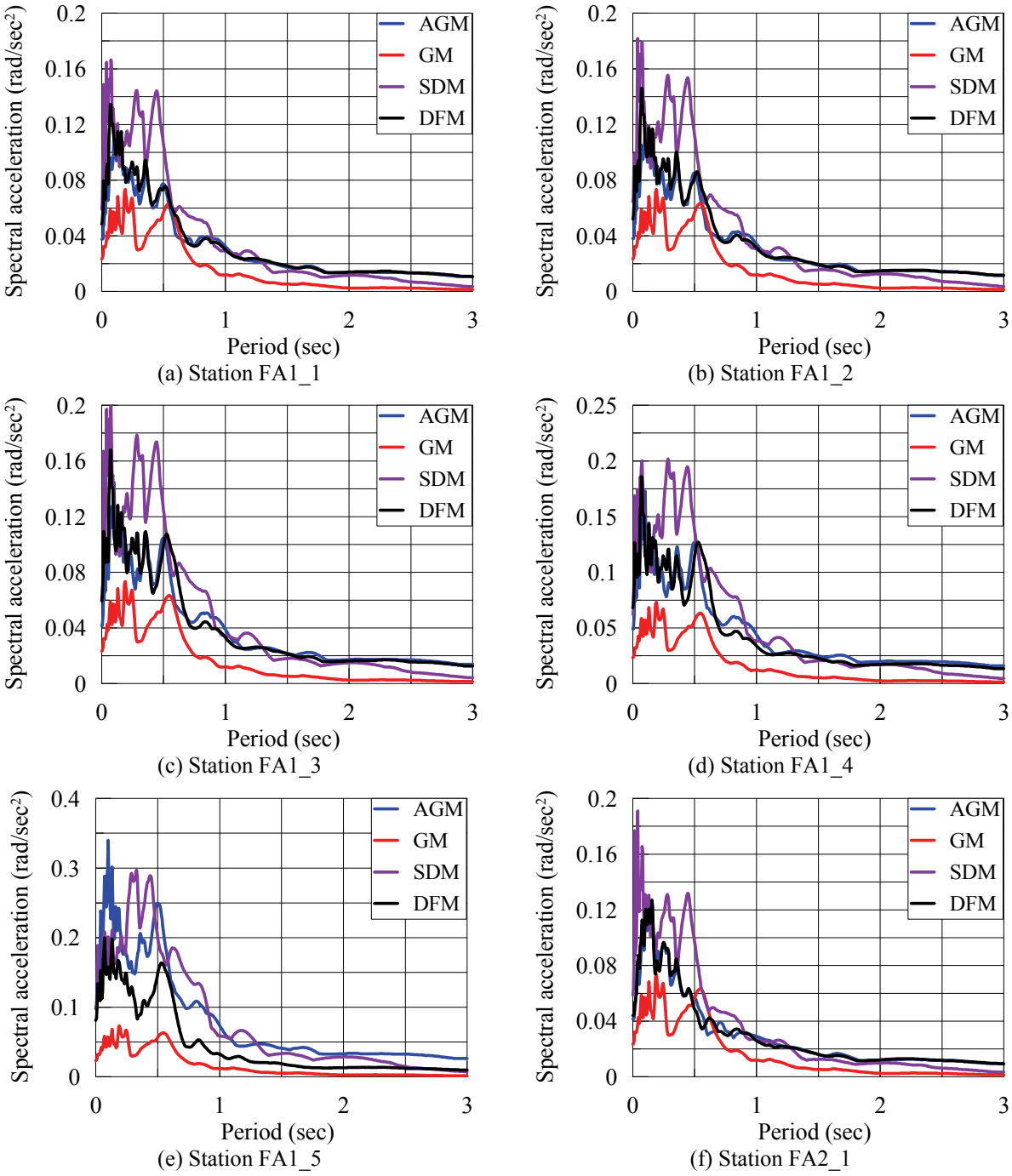

Figure B-10: Rocking (SRSS) spectra computed using four different methods

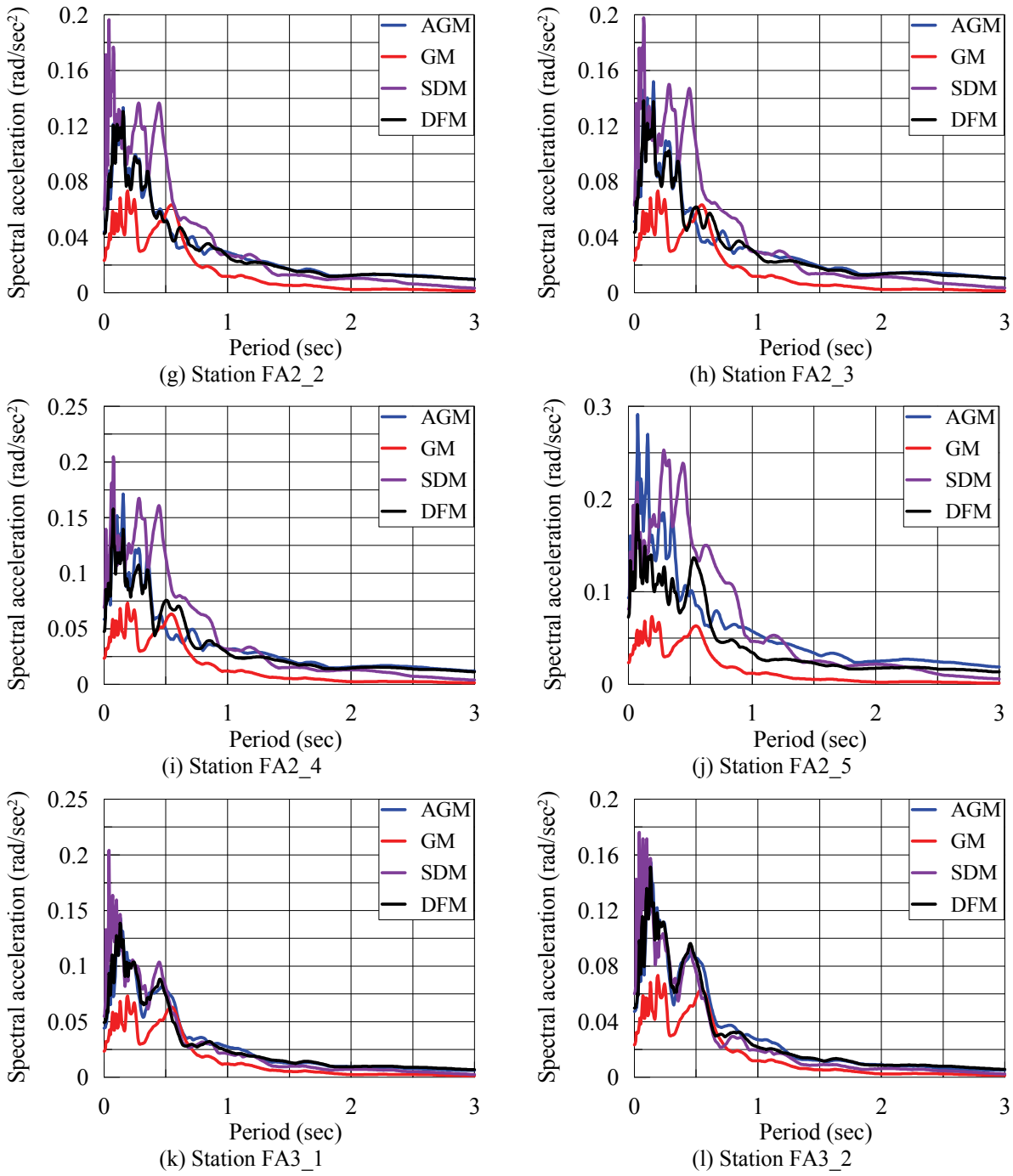

Figure B-10: Rocking (SRSS) spectra computed using four different method (cont.)

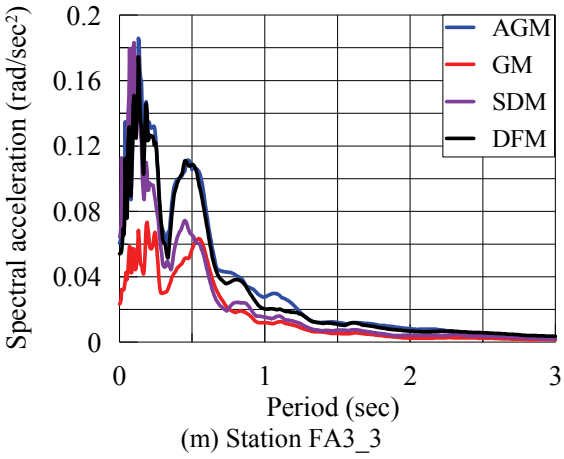

(m) Station FA3_3

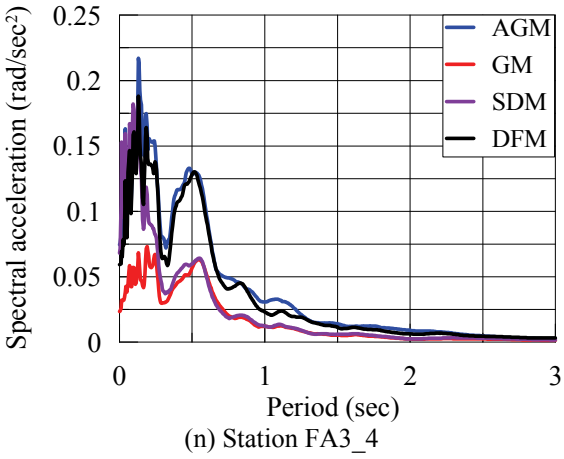

(n) Station FA3_4

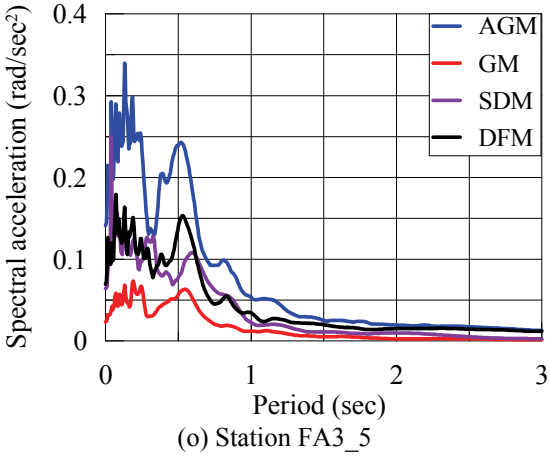

(o) Station FA3_5

Figure B-10: Rocking (SRSS) spectra computed using four different methods (cont.)

APPENDIX C

DYNAMIC ANALYSIS OF A ONE-STORY TORSIONALLY COUPLED BUILDING

C.1. Building Model Description and Equation of Motion

The one story torsionally coupled building shown in Figure C-1 is subjected to translational excitation in the *x* and *y* directions (a_{gx} and a_{gy}) and a torsional excitation ($a_{g\theta}$). The building is symmetric about the *x* axis. The center of mass (CM) of the building is initially located at the geometric center of the deck. The actual eccentricity of the building is the distance between the CM and center of rigidity (CR) and is denoted here as e. To account for the accidental torsion in the elements on Side A (Figure C-1), the CM is shifted away from the CR by an offset equal to the accidental eccentricity (e_a). The total static eccentricity is $e_s = e + e_a$.

Defining the degrees of freedom $U = \{u_x \quad u_y \quad u_\theta\}^T$ at the CM, the equation of motion of the building at the initial elastic state is

$$\begin{aligned} &m\begin{bmatrix}1 & & \\ & 1 & \\ & & r^2\end{bmatrix}\begin{Bmatrix}\ddot{u}_x \\ \ddot{u}_y \\ \ddot{u}_\theta\end{Bmatrix}+\begin{bmatrix}C_x & 0 & 0 \\ 0 & C_y & C_{y\theta} \\ 0 & C_{y\theta} & C_\theta\end{bmatrix}\begin{Bmatrix}\dot{u}_x \\ \dot{u}_y \\ \dot{u}_\theta\end{Bmatrix}+\begin{bmatrix}K_x & 0 & 0 \\ 0 & K_y & e_sK_y \\ 0 & e_sK_y & K_\theta\end{bmatrix}\begin{Bmatrix}u_x \\ u_y \\ u_\theta\end{Bmatrix} \\ &=-m\begin{bmatrix}1 & & \\ & 1 & \\ & & r^2\end{bmatrix}\left\{\begin{Bmatrix}1 \\ 0 \\ 0\end{Bmatrix}a_{gx}(t)+\begin{Bmatrix}0 \\ 1 \\ 0\end{Bmatrix}a_{gy}(t)+\begin{Bmatrix}0 \\ 0 \\ 1\end{Bmatrix}a_{g\theta}(t)\right\}\end{aligned} \tag{C-1}$$

where m is the mass and r is the radius of gyration about the vertical axis passing through the CM. The stiffness matrix is the elastic stiffness matrix in which K_x and K_y are the total stiffness along the *x* and *y*

directions, respectively, and K_θ is the torsional stiffness about the CM. The Rayleigh damping (inherent) matrix is assumed and is constant throughout.

To account for inelastic response in the model, the contribution of the stiffness matrix in Eq (C-1) is expressed as follows:

$$F_{sx} = \sum_{i=1}^{N_x} f_{sxi}, F_{sy} = \sum_{j=1}^{N_y} f_{syj}, F_{s\theta} = -\sum_{i=1}^{N_x} y_i f_{sxi} + \sum_{j=1}^{N_y} x_j f_{syj} \tag{C-2}$$

where f_{sxi} and f_{syj} are the resistance provided by the i^{th} x direction element and the j^{th} y-direction element, located at a distance y_i and x_j, respectively, from the CM; and N_x and N_y are the number of stiffness-contributing elements along x and y directions, respectively. The displacements along the x and y directions are related to those at the CM are:

$$\begin{aligned} u_{xi}^e &= u_x - y_i u_\theta \\ u_{yj}^e &= u_y + x_j u_\theta \end{aligned} \tag{C-3}$$

The equations of motion are:

$$\begin{aligned} \ddot{u}_x &= -\frac{1}{m} F_{sx} - \frac{C_x}{m} \dot{u}_x - a_{gx}(t) \\ \ddot{u}_y &= -\frac{1}{m} F_{sy} - \frac{C_y}{m} \dot{u}_y - \frac{C_{y\theta}}{m} \dot{u}_\theta - a_{gy}(t) \\ \ddot{u}_\theta &= -\frac{1}{mr^2} F_{s\theta} - \frac{C_{\theta y}}{mr^2} \dot{u}_y - \frac{C_\theta}{mr^2} \dot{u}_\theta - a_{g\theta}(t) \end{aligned} \tag{C-4}$$

C.2. Force-Displacement Model

The force-displacement relationship for the i^{th} x direction element and the j^{th} y direction element may be expressed as

$$
\begin{aligned}
f_{sxi} &= \alpha_{xi}\frac{f_{yxi}}{Y_{xi}}u_{xi}^{e} + \left(1-\alpha_{xi}\right)f_{yxi}Z_{xi} \\
\dot{Z}_{xi} &= \frac{1}{Y_{xi}}\left[\dot{u}_{xi}^{e} - 0.5\left|\dot{u}_{xi}^{e}\right|Z_{xi}\left|Z_{xi}\right|^{\eta-1} - 0.5\dot{u}_{xi}^{e}\left|Z_{xi}\right|^{\eta}\right]
\end{aligned}
\tag{C-5}
$$

$$
\begin{aligned}
f_{syj} &= \alpha_{yj}\frac{f_{yyj}}{Y_{yj}}u_{yj}^{e} + \left(1-\alpha_{yj}\right)f_{yyj}Z_{yj} \\
\dot{Z}_{yj} &= \frac{1}{Y_{yj}}\left[\dot{u}_{yj}^{e} - 0.5\left|\dot{u}_{yj}^{e}\right|Z_{yj}\left|Z_{yj}\right|^{\eta-1} - 0.5\dot{u}_{yj}^{e}\left|Z_{yj}\right|^{\eta}\right]
\end{aligned}
\tag{C-6}
$$

where α is the post-elastic stiffness ratio, Y is the yield displacement, Z is a hysteretic variable and η is an exponent that controls the smoothness of transition from the elastic to post-elastic regime.

.

Utilizing Eq (C-3) into Eq (C-5) and Eq (C-6),

$$
\begin{aligned}
f_{sxi} &= \alpha_{xi}\frac{f_{yxi}}{Y_{xi}}\left(u_x - y_i u_\theta\right) + \left(1-\alpha_{xi}\right)f_{yxi}Z_{xi} \\
\dot{Z}_{xi} &= \frac{1}{Y_{xi}}\left[\left(\dot{u}_x - y_i\dot{u}_\theta\right) - 0.5\left|\dot{u}_x - y_i\dot{u}_\theta\right|Z_{xi}\left|Z_{xi}\right|^{\eta-1} - 0.5\left(\dot{u}_x - y_i\dot{u}_\theta\right)\left|Z_{xi}\right|^{\eta}\right]
\end{aligned}
\tag{C-7}
$$

$$
\begin{aligned}
f_{syj} &= \alpha_{yj}\frac{f_{yyj}}{Y_{yj}}\left(u_y + x_j u_\theta\right) + \left(1-\alpha_{yj}\right)f_{yyj}Z_{yj} \\
\dot{Z}_{yj} &= \frac{1}{Y_{yj}}\left[\left(\dot{u}_y + x_j\dot{u}_\theta\right) - 0.5\left|\dot{u}_y + x_j\dot{u}_\theta\right|Z_{yj}\left|Z_{yj}\right|^{\eta-1} - 0.5\left(\dot{u}_y + x_j\dot{u}_\theta\right)\left|Z_{yj}\right|^{\eta}\right]
\end{aligned}
\tag{C-8}
$$

Substituting Eq (C-2), Eq (C-7) and Eq (C-8) into Eq (C-4), the equations of motion for the nonlinear system are

$$
\begin{aligned}
\ddot{u}_x &= -\frac{1}{m}\sum_{i=1}^{N_x}\left[\alpha_{xi}\frac{f_{yxi}}{Y_{xi}}\left(u_x - y_i u_\theta\right) + \left(1-\alpha_{xi}\right) f_{yxi} Z_{xi}\right] - \frac{C_x}{m}\dot{u}_x - a_{gx}(t) \\
\ddot{u}_y &= -\frac{1}{m}\sum_{j=1}^{N_y}\left[\alpha_{yj}\frac{f_{yyj}}{Y_{yj}}\left(u_y + x_j u_\theta\right) + \left(1-\alpha_{yj}\right) f_{yyj} Z_{yj}\right] - \frac{C_y}{m}\dot{u}_y - \frac{C_{y\theta}}{m}\dot{u}_\theta - a_{gy}(t) \\
\ddot{u}_\theta &= \frac{1}{mr^2}\sum_{i=1}^{N_x}\left[y_i\alpha_{xi}\frac{f_{yxi}}{Y_{xi}}\left(u_x - y_i u_\theta\right) + y_i\left(1-\alpha_{xi}\right) f_{yxi} Z_{xi}\right] \\
&\quad -\frac{1}{mr^2}\sum_{j=1}^{N_y}\left[x_j\alpha_{yj}\frac{f_{yyj}}{Y_{yj}}\left(u_y + x_j u_\theta\right) + x_j\left(1-\alpha_{yj}\right) f_{yyj} Z_{yj}\right] - \frac{C_{\theta y}}{mr^2}\dot{u}_y - \frac{C_\theta}{mr^2}\dot{u}_\theta - a_{g\theta}(t)
\end{aligned}
\tag{C-9}
$$

A complete description of the equations of motion includes the second part of Eq (C-7) for $i = 1,...,N_x$ and the second part of Eq (C-8) for $j = 1,...,N_y$. These $\left(N_x + N_y\right)$ equations control the hysteretic behavior.

C.3. State-Space Form of the Equations of Motion

Three auxiliary equations of the form $\dot{u}_x = \dot{u}_x$, $\dot{u}_y = \dot{u}_y$ and $\dot{u}_\theta = \dot{u}_\theta$ are introduced to obtain a total of $\left(N_x + N_y + 6\right)$ equations: i) three equilibrium equations, ii) $\left(N_x + N_y\right)$ equations controlling the element hysteretic behavior, and three auxiliary equations. These equations may be expressed in a state-space form as follows:

$$\dot{V} = \phi(V)$$

$$V = \left\{ u_x \quad u_y \quad u_\theta \quad \dot{u}_x \quad \dot{u}_y \quad \dot{u}_\theta \quad Z_{xi}\left(i = 1, N_x\right) \quad Z_{yj}\left(j = 1, N_y\right) \right\}^T$$

$$\phi_1(V) = V_4$$

$$\phi_2(V) = V_5$$

$$\phi_3(V) = V_6$$

$$\phi_4(V) = -\frac{1}{m}\sum_{i=1}^{N_x}\left[\alpha_{xi}\frac{f_{yxi}}{Y_{xi}}\left(V_1 - y_i V_3\right) + \left(1-\alpha_{xi}\right) f_{yxi} V_{i+6}\right] - \frac{C_x}{m}V_4 - a_{gx}(t)$$

$$\phi_5(V) = -\frac{1}{m}\sum_{j=1}^{N_y}\left[\alpha_{yj}\frac{f_{yyj}}{Y_{yj}}\left(V_2 + x_j V_3\right) + \left(1-\alpha_{yj}\right) f_{yyj} V_{j+N_x+6}\right] - \frac{C_y}{m}V_5 - \frac{C_{y\theta}}{m}V_6 - a_{gy}(t)$$

$$\begin{aligned}\phi_6(V) = {} & \frac{1}{mr^2}\sum_{i=1}^{N_x}\left[y_i\alpha_{xi}\frac{f_{yxi}}{Y_{xi}}\left(V_1 - y_i V_3\right) + y_i\left(1-\alpha_{xi}\right) f_{yxi} V_{i+6}\right] \\ & - \frac{1}{mr^2}\sum_{j=1}^{N_y}\left[x_j\alpha_{yj}\frac{f_{yyj}}{Y_{yj}}\left(V_2 + x_j V_3\right) + x_j\left(1-\alpha_{yj}\right) f_{yyj} V_{j+N_x+6}\right] - \frac{C_{\theta y}}{mr^2}V_5 - \frac{C_\theta}{mr^2}V_6 - a_{g\theta}(t)\end{aligned}$$

$$\phi_{i+6}(V) = \frac{1}{Y_{xi}}\left[\left(V_4 - y_i V_6\right) - 0.5\left|V_4 - y_i V_6\right| V_{i+6}\left|V_{i+6}\right|^{\eta-1} - 0.5\left(V_4 - y_i V_6\right)\left|V_{i+6}\right|^{\eta}\right] \quad i = 1,\ 2, \ldots N_x \qquad \text{(C-10)}$$

$$\phi_{j+N_x+6}(V) = \frac{1}{Y_{yj}}\begin{bmatrix}\left(V_5 + x_j V_6\right) - 0.5\left|\left(V_5 + x_j V_6\right)\right| V_{j+N_x+6}\left|V_{j+N_x+6}\right|^{\eta-1} \\ -0.5\left(V_5 + x_j V_6\right)\left|V_{j+N_x+6}\right|^{\eta}\end{bmatrix} \quad j = 1, 2, \ldots N_y$$

where all the terms have been defined previously. For an elastic system, the state-space equations from [Eq (C-10)] are reduced to

$$\begin{aligned}&\dot{V} = \phi(V);\ V = \left\{ u_x \quad u_y \quad u_\theta \quad \dot{u}_x \quad \dot{u}_y \quad \dot{u}_\theta \right\}^T \\ &\phi_1(V) = V_4;\ \phi_2(V) = V_5;\ \phi_3(V) = V_6;\ \phi_4(V) = -\frac{K_x}{m}V_1 - \frac{C_x}{m}V_4 - a_{gx}(t); \\ &\phi_5(V) = -\frac{K_y}{m}V_2 - \frac{K_{y\theta}}{m}V_3 - \frac{C_y}{m}V_5 - \frac{C_{y\theta}}{m}V_6 - a_{gy}(t) \\ &\phi_6(V) = -\frac{K_{\theta y}}{mr^2}V_2 - \frac{K_\theta}{mr^2}V_3 - \frac{C_{\theta y}}{mr^2}V_5 - \frac{C_\theta}{mr^2}V_6 - a_{g\theta}(t)\end{aligned} \qquad \text{(C-11)}$$

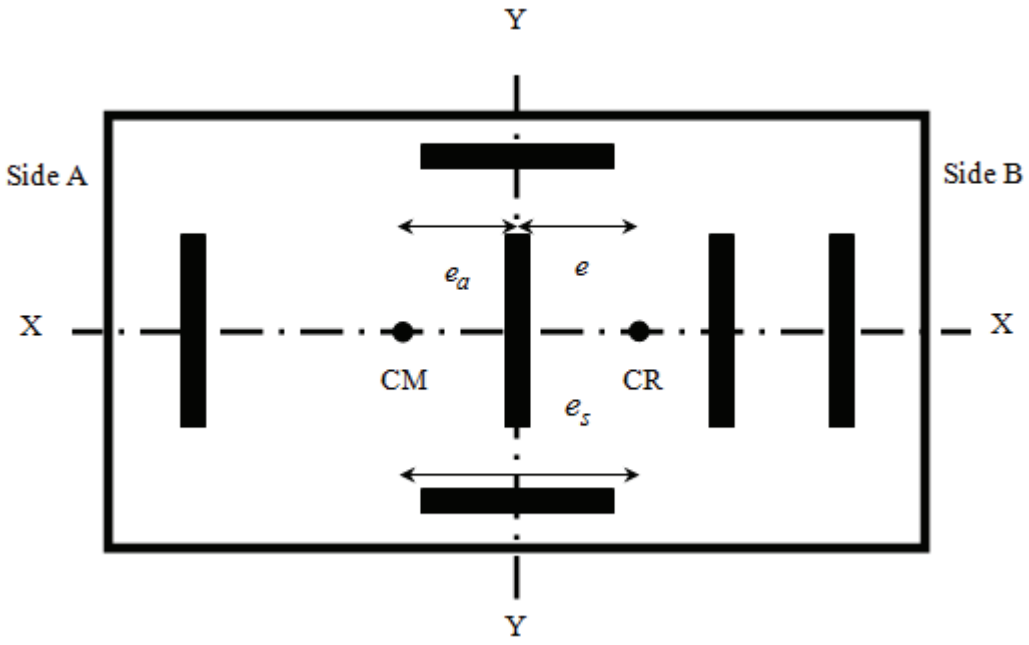

Figure C-1: One story, singly symmetric torsionally coupled building

APPENDIX D

SEISMIC ANALYSIS OF A CHIMNEY SUBJECTED TO TRANSLATIONAL AND ROCKING GROUND MOTIONS

D.1. Introduction

A computer program is developed to analyze a two dimensional continuum model of a cantilever-type structure for translational and rocking ground motion with the following features and/or assumptions:

1. The mass and stiffness distribution can be arbitrary but must be continuous or piecewise continuous; concentrated/lumped spring/masses are not allowed.
2. Shear deformations are negligible.
3. $P-\Delta$ effects are accounted for.
4. The foundation can be fixed or the soil beneath the foundation can be modeled with frequency-independent horizontal and rotational springs and dampers.
5. The foundation can be modeled adequately with its mass and mass moment of inertia.
6. Structural damping is assumed as mass proportional and the damping coefficient is computed based on the fixed-base, undamped first mode.
7. The numerical solution is performed using direct time integration. An explicit finite-difference procedure is used. The order of the analysis is two. Second-order central difference expressions are usually used for the temporal and spatial derivatives. However, the single-sided second order difference expressions are also used whenever required.
8. Discretizations in time and space are related using a stability criterion derived here.

This appendix presents a brief description of the program and its verification using SAP2000 (CSI, 2009).

D.2. Program Description-General Case with Flexible Foundation

The program considers the discretization along the height of the chimney in a non-dimensional form. The governing differential equation Eq (10.1) is rewritten as

$$m\left(h^*\right)\frac{\partial^2 u\left(h^*,t\right)}{\partial t^2}+c\left(h^*\right)\frac{\partial u\left(h^*,t\right)}{\partial t}+\frac{1}{H^4}\frac{\partial^2}{\partial h^{*2}}\left[EI\left(h^*\right)\frac{\partial^2 u\left(h^*,t\right)}{\partial h^{*2}}\right]+\frac{1}{H^2}\frac{\partial}{\partial h^*}\left[F_A\left(h^*,t\right)\frac{\partial u\left(h^*,t\right)}{\partial h^*}\right]=P_{eff}\left(h^*,t\right)$$

$$P_{eff}\left(h^*,t\right)=-m\left(h^*\right)\frac{\partial^2 u_g\left(t\right)}{\partial t^2}+Hh^*m\left(h^*\right)\frac{\partial^2\theta_g\left(t\right)}{\partial t^2}+\frac{1}{H}\frac{\partial F_A\left(h^*,t\right)}{\partial h^*}\theta_g\left(t\right) \tag{D-1}$$

The associated boundary conditions, Eq (10.2) through Eq (10.5) are modified to

$$m_f\frac{\partial^2 u\left(0,t\right)}{\partial t^2}+C_f\frac{\partial u\left(0,t\right)}{\partial t}+K_f u\left(0,t\right)+\frac{1}{H}F_A\left(0,t\right)\frac{\partial u\left(0,t\right)}{\partial h^*}+\frac{1}{H^3}\frac{\partial}{\partial h^*}\left[EI\left(0\right)\frac{\partial^2 u\left(0,t\right)}{\partial h^{*2}}\right]=G\left(t\right)$$

$$G\left(t\right)=-m_f\frac{\partial^2 u_g\left(t\right)}{\partial t^2}+F_A\left(0,t\right)\theta_g\left(t\right) \tag{D-2}$$

$$\frac{I_f}{H}\frac{\partial^3 u\left(0,t\right)}{\partial h^*\partial t^2}+\frac{C_{fr}}{H}\frac{\partial^2 u\left(0,t\right)}{\partial h^*\partial t}+\frac{K_{fr}}{H}\frac{\partial u\left(0,t\right)}{\partial h^*}-\frac{1}{H^2}EI\left(0\right)\frac{\partial^2 u\left(0,t\right)}{\partial h^{*2}}=R\left(t\right)$$

$$R\left(t\right)=I_f\frac{\partial^2 u_g\left(t\right)}{\partial t^2} \tag{D-3}$$

$$\frac{1}{H^3}\frac{\partial}{\partial h^*}\left[EI\left(1\right)\frac{\partial^2 u\left(1,t\right)}{\partial h^{*2}}\right]+\frac{1}{H}F_A\left(1,t\right)\frac{\partial u\left(1,t\right)}{\partial h^*}=F_A\left(1,t\right)\theta_g\left(t\right) \tag{D-4}$$

$$\frac{\partial^2 u\left(1,t\right)}{\partial h^{*2}}=0 \tag{D-5}$$

The explicit finite difference method is employed, which first computes a variety of coefficients (e.g., Q,R,B and E) and then assembles these coefficients into a set of matrices (e.g., $[\gamma],[\alpha],[\delta]$ and $\{\Omega\}$). The solution at each time instant is the computed using these matrices. A summary of the coefficients Q,R,B and E (Section D.2.1 through D.2.4, respectively), the matrices *GAMA*, *ALPHA* and *DELTA*

(Section D.2.5 through D2.7, respectively), the vector *OMEGA* (Section D.2.8), and the governing equation to calculate the solution vector (Section D.2.9) is presented below.

D.2.1. Coefficient Q

At h_j^* $j = 0, n$

$$Q_1\left(h_j^*\right) = \frac{m\left(h_j^*\right)}{\left(\Delta t\right)^2} + \frac{c\left(h_j^*\right)}{2\Delta t} \tag{D-6}$$

$$Q_2\left(h_j^*\right) = \frac{m\left(h_j^*\right)}{\left(\Delta t\right)^2} - \frac{c\left(h_j^*\right)}{2\Delta t} \tag{D-7}$$

$$Q_3\left(h_j^*\right) = -\frac{2m\left(h_j^*\right)}{\left(\Delta t\right)^2} - \frac{2EI''\left(h_j^*\right)}{H^4\left(\Delta h^*\right)^2} + \frac{6EI\left(h_j^*\right)}{H^4\left(\Delta h^*\right)^4} - \frac{2F_A\left(h_j^*\right)}{H^2\left(\Delta h^*\right)^2} \tag{D-8}$$

$$Q_4\left(h_j^*\right) = \frac{EI''\left(h_j^*\right)}{H^4\left(\Delta h^*\right)^2} - \frac{2EI'\left(h_j^*\right)}{H^4\left(\Delta h^*\right)^3} - \frac{4EI\left(h_j^*\right)}{H^4\left(\Delta h^*\right)^4} + \frac{F_A'\left(h_j^*\right)}{H^2\left(2\Delta h^*\right)} + \frac{F_A\left(h_j^*\right)}{H^2\left(\Delta h^*\right)^2} \tag{D-9}$$

$$Q_5\left(h_j^*\right) = \frac{EI''\left(h_j^*\right)}{H^4\left(\Delta h^*\right)^2} + \frac{2EI'\left(h_j^*\right)}{H^4\left(\Delta h^*\right)^3} - \frac{4EI\left(h_j^*\right)}{H^4\left(\Delta h^*\right)^4} - \frac{F_A'\left(h_j^*\right)}{H^2\left(2\Delta h^*\right)} + \frac{F_A\left(h_j^*\right)}{H^2\left(\Delta h^*\right)^2} \tag{D-10}$$

$$Q_6\left(h_j^*\right) = \frac{EI\left(h_j^*\right)}{H^4\left(\Delta h^*\right)^4} + \frac{EI'\left(h_j^*\right)}{H^4\left(\Delta h^*\right)^3} \tag{D-11}$$

$$Q_7\left(h_j^*\right) = \frac{EI\left(h_j^*\right)}{H^4\left(\Delta h^*\right)^4} - \frac{EI'\left(h_j^*\right)}{H^4\left(\Delta h^*\right)^3} \tag{D-12}$$

D.2.2. Coefficient R

These coefficients are defined only at h_j^*, $j = 0$.

$$R_1 = \frac{m_f}{\left(\Delta t\right)^2} + \frac{C_f}{2\Delta t} \tag{D-13}$$

$$R_2 = \frac{m_f}{\left(\Delta t\right)^2} - \frac{C_f}{2\Delta t} \tag{D-14}$$

$$R_3 = -\frac{2m_f}{\left(\Delta t\right)^2} + K_f - \frac{2EI'\left(h_0^*\right)}{H^3\left(\Delta h^*\right)^2} \tag{D-15}$$

$$R_4 = \frac{1}{H}\frac{F_A\left(h_0^*\right)}{2\Delta h^*} + \frac{EI'\left(h_0^*\right)}{H^3\left(\Delta h^*\right)^2} - \frac{EI\left(h_0^*\right)}{H^3\left(\Delta h^*\right)^3} \tag{D-16}$$

$$R_5 = -\frac{1}{H}\frac{F_A\left(h_0^*\right)}{2\Delta h^*} + \frac{EI'\left(h_0^*\right)}{H^3\left(\Delta h^*\right)^2} + \frac{EI\left(h_0^*\right)}{H^3\left(\Delta h^*\right)^3} \tag{D-17}$$

$$R_6 = \frac{EI\left(h_0^*\right)}{2H^3\left(\Delta h^*\right)^3} \tag{D-18}$$

$$R_7 = -\frac{EI\left(h_0^*\right)}{2H^3\left(\Delta h^*\right)^3} \tag{D-19}$$

D.2.3. Coefficient B

These coefficients are defined only at h_j^*, $j = 0$.

$$B_1 = \frac{I_f}{H\Delta h^*\left(\Delta t\right)^2} + \frac{C_{fr}}{2H\Delta h^*\Delta t} \tag{D-20}$$

$$B_2 = \frac{I_f}{H\Delta h^*\left(\Delta t\right)^2} - \frac{C_{fr}}{2H\Delta h^*\Delta t} \tag{D-21}$$

$$B_3 = \frac{3I_f}{H\Delta h^*\left(\Delta t\right)^2} + \frac{2EI\left(h_0^*\right)}{H^2\left(\Delta h^*\right)^2} \tag{D-22}$$

$$B_4 = -\frac{4I_f}{H\Delta h^*\left(\Delta t\right)^2} + \frac{K_{fr}}{2H\Delta h^*} - \frac{EI\left(h_0^*\right)}{H^2\left(\Delta h^*\right)^2} \tag{D-23}$$

$$B_5 = \frac{I_f}{H\Delta h^*\left(\Delta t\right)^2} \tag{D-24}$$

$$B_6 = -\frac{K_{fr}}{2H\Delta h^*} - \frac{EI\left(h_0^*\right)}{H^2\left(\Delta h^*\right)^2} \tag{D-25}$$

D.2.4. Coefficient E

These coefficients are defined only at h_j^*, $j = n$.

$$E_1 = -\frac{EI\left(h_n^*\right)}{2H^3\left(\Delta h^*\right)^3} \tag{D-26}$$

$$E_2 = \frac{EI'\left(h_n^*\right)}{H^3\left(\Delta h^*\right)^2} + \frac{EI\left(h_n^*\right)}{H^3\left(\Delta h^*\right)^3} - \frac{F_A\left(h_n^*\right)}{2H\Delta h^*} \tag{D-27}$$

$$E_3 = -\frac{2EI'\left(h_n^*\right)}{H^3\left(\Delta h^*\right)^2} \tag{D-28}$$

$$E_4 = \frac{EI'\left(h_n^*\right)}{H^3\left(\Delta h^*\right)^2} - \frac{EI\left(h_n^*\right)}{H^3\left(\Delta h^*\right)^3} + \frac{F_A\left(h_n^*\right)}{2H\Delta h^*} \tag{D-29}$$

$$E_5 = \frac{EI\left(h_n^*\right)}{2H^3\left(\Delta h^*\right)^3} \tag{D-30}$$

D.2.5. Matrix GAMA

For row1 ($h^* = 0$, i.e., h_0^*),

$$\gamma_{11} = Q_1 + \frac{3}{2}\left(\frac{B_1}{B_6}\right)\left(Q_5 - Q_7\frac{R_5}{R_7}\right) - Q_7\frac{R_1}{R_7} \tag{D-31}$$

$$\gamma_{12} = -2\left(\frac{B_1}{B_6}\right)\left(Q_5 - Q_7\frac{R_5}{R_7}\right) \tag{D-32}$$

$$\gamma_{13} = \frac{1}{2}\left(\frac{B_1}{B_6}\right)\left(Q_5 - Q_7\frac{R_5}{R_7}\right) \tag{D-33}$$

For row 2 ($h^* = \Delta h^*$, i.e., h_1^*),

$$\gamma_{21} = \frac{3}{2}Q_7\left(\frac{B_1}{B_6}\right) \tag{D-34}$$

$$\gamma_{22} = Q_1 - 2\left(\frac{B_1}{B_6}\right)Q_7 \tag{D-35}$$

$$\gamma_{23} = \frac{1}{2}Q_7\left(\frac{B_1}{B_6}\right) \tag{D-36}$$

For row 3 to $n+1$ ($\bar{k} = 3, n+1$, i.e., $h_2^*, h_3^*, ..., h_n^*$),

$$\gamma_{\bar{k}\,\bar{k}} = Q_1 \tag{D-37}$$

D.2.6. Matrix ALPHA

For row1 ($h^* = 0$, i.e., h_0^*),

$$\alpha_{11} = Q_2 + \frac{3}{2}\left(\frac{B_2}{B_6}\right)\left(Q_5 - Q_7\frac{R_5}{R_7}\right) - Q_7\frac{R_2}{R_7} \tag{D-38}$$

$$\alpha_{12} = -2\left(\frac{B_2}{B_6}\right)\left(Q_5 - Q_7\frac{R_5}{R_7}\right) \tag{D-39}$$

$$\alpha_{13} = \frac{1}{2}\left(\frac{B_2}{B_6}\right)\left(Q_5 - Q_7\frac{R_5}{R_7}\right) \tag{D-40}$$

For row 2 ($h^* = \Delta h^*$, i.e., h_1^*),

$$\alpha_{21} = \frac{3}{2}Q_7\left(\frac{B_2}{B_6}\right) \tag{D-41}$$

$$\alpha_{22} = Q_2 - 2Q_7\left(\frac{B_2}{B_6}\right) \tag{D-42}$$

$$\alpha_{23} = \frac{1}{2}Q_7\left(\frac{B_2}{B_6}\right) \tag{D-43}$$

For row 3 to $n+1$ ($\bar{k} = 3, n+1$, i.e., $h_2^*, h_3^*, ..., h_n^*$),

$$\alpha_{\bar{k}\,\bar{k}} = Q_2 \tag{D-44}$$

D.2.7. Matrix DELTA

For row1 ($h^* = 0$, i.e., h_0^*),

$$\delta_{11} = Q_3 - \left(\frac{B_3}{B_6}\right)\left(Q_5 - Q_7\frac{R_5}{R_7}\right) - Q_7\frac{R_3}{R_7} \tag{D-45}$$

$$\delta_{12} = Q_4 - \left(\frac{B_4}{B_6}\right)\left(Q_5 - Q_7\frac{R_5}{R_7}\right) - Q_7\frac{R_4}{R_7} \tag{D-46}$$

$$\delta_{13} = Q_6 - \left(\frac{B_5}{B_6}\right)\left(Q_5 - Q_7\frac{R_5}{R_7}\right) - Q_7\frac{R_6}{R_7} \tag{D-47}$$

For row 2 ($h^* = \Delta h^*$, i.e., h_1^*),

$$\delta_{21} = Q_5 - Q_7\left(\frac{B_3}{B_6}\right) \tag{D-48}$$

$$\delta_{22} = Q_3 - Q_7\left(\frac{B_4}{B_6}\right) \tag{D-49}$$

$$\delta_{23} = Q_4 - Q_7\left(\frac{B_5}{B_6}\right) \tag{D-50}$$

$$\delta_{24} = Q_6 \tag{D-51}$$

For row 3 to $n-1$ ($\bar{k} = 3, n-1$, i.e., $h_2^*, h_3^*, ..., h_{n-2}^*$),

$$\delta_{\bar{k}\,\bar{k}-2} = Q_7;\ \delta_{\bar{k}\,\bar{k}-1} = Q_5;\ \delta_{\bar{k}\,\bar{k}} = Q_3;\ \delta_{\bar{k}\,\bar{k}+1} = Q_4;\ \delta_{\bar{k}\,\bar{k}+2} = Q_6; \tag{D-52}$$

For row n ($\bar{k} = n$, i.e., h_{n-1}^*),

$$\delta_{\bar{k}\,\bar{k}-2} = Q_7;\ \delta_{\bar{k}\,\bar{k}-1} = Q_5;\ \delta_{\bar{k}\,\bar{k}} = Q_3 - Q_6;\ \delta_{\bar{k}\,\bar{k}+1} = Q_4 + 2Q_6; \tag{D-53}$$

For row $n+1$ ($\bar{k} = n+1$, i.e., h_n^*),

$$\delta_{\bar{k}\,\bar{k}-2} = Q_7 - Q_6\frac{E_1}{E_5};\ \delta_{\bar{k}\,\bar{k}-1} = Q_5 - Q_4 + Q_6\left(-\frac{E_2}{E_5} + \frac{E_4}{E_5}\right);\ \delta_{\bar{k}\,\bar{k}} = Q_3 + 2Q_4 + Q_6\left(-\frac{E_3}{E_5} - \frac{2E_4}{E_5}\right); \tag{D-54}$$

D.2.8. Vector OMEGA

For row1 ($h^* = 0$, i.e., h_0^*),

$$\Omega_1(t_k) = P_{eff}\left(h_0^*, t_k\right) - \frac{Q_7}{R_7} G(t_k) - \left(Q_5 - Q_7 \frac{R_5}{R_7}\right) \frac{R(t_k)}{B_6} \tag{D-55}$$

For row 2 ($h^* = \Delta h^*$, i.e., h_1^*),

$$\Omega_2(t_k) = P_{eff}\left(h_1^*, t_k\right) - \frac{Q_7}{B_6} R(t_k) \tag{D-56}$$

For row 3 to $n-1$ ($\bar{k} = 3, n-1$, i.e., $h_2^*, h_3^*, ..., h_{n-2}^*$),

$$\Omega_{\bar{k}}(t_k) = P_{eff}\left(h_{\bar{k}-1}^*, t_k\right) \tag{D-57}$$

For row n ($\bar{k} = n$, i.e., h_{n-1}^*),

$$\Omega_{\bar{k}}(t_k) = P_{eff}\left(h_{\bar{k}-1}^*, t_k\right) \tag{D-58}$$

For row $n+1$ ($\bar{k} = n+1$, i.e., h_n^*),

$$\Omega_{\bar{k}}(t_k) = P_{eff}\left(h_{\bar{k}-1}^*, t_k\right) - \frac{Q_6}{E_5} F_A\left(h_{\bar{k}-1}^*\right) \theta_g(t_k) \tag{D-59}$$

In the above equations,

$$P_{eff}\left(h_j^*, t_k\right) = -m\left(h_j^*\right) \ddot{u}_g(t_k) + H h_j^* m\left(h_j^*\right) \ddot{\theta}_g(t_k) + \frac{1}{H} F_A'\left(h_j^*\right) \theta_g(t_k) \tag{D-60}$$

$$G(t_k) = -m_f \ddot{u}_g(t_k) + F_A\left(h_0^*\right) \theta_g(t_k) \tag{D-61}$$

$$R(t_k) = I_f \ddot{\theta}_g(t_k) \tag{D-62}$$

D.2.9. Solution Vector

At time $t = t_1$

$$\left\{u\left(h^*,t_1\right)\right\}=[\gamma]^{-1}\left[-[\alpha+\delta]\left\{u\left(h^*,t_0\right)\right\}+\Delta t[\alpha]\left\{V_0\left(h^*\right)\right\}-\frac{\left(\Delta t\right)^2}{2}[\alpha]\left\{a_0\left(h^*\right)\right\}+\left\{\Omega\left(t_0\right)\right\}\right] \tag{D-63}$$

and subsequently,

$$\left\{u\left(h^*,t_{k+1}\right)\right\}=[\gamma]^{-1}\left[-[\alpha]\left\{u\left(h^*,t_{k-1}\right)\right\}-[\delta]\left\{u\left(h^*,t_k\right)\right\}+\left\{\Omega\left(t_k\right)\right\}\right] \tag{D-64}$$

Here $\left\{u\left(h^*,t_0\right)\right\}$ and $\left\{V_0\left(h^*\right)\right\}$ are the initial displacement and velocity profiles and are known from the specified initial conditions. Vector $\left\{a_0\left(h^*\right)\right\}$ is the acceleration distribution at time $t=0$, which is known from the equilibrium equation at the same time instant.

D.3. Fixed-Base Case

The fixed base can be treated using the general case by assuming high values for the foundation stiffness and damping. However, to avoid the numerical instability associated with such values, the case is formulated separately. The necessary modifications for the fixed base case are as follows. Matrices $[\gamma]$ and $[\alpha]$ are diagonal with element Q_1 and Q_2, respectively. Matrix $[\delta]$ is modified such that for the first row, $j=1$,

$$\delta_{11}=Q_3+Q_7;\ \delta_{12}=Q_4;\ \delta_{13}=Q_6; \tag{D-65}$$

For $j=2$,

$$\delta_{21}=Q_5;\ \delta_{22}=Q_3;\ \delta_{23}=Q_4;\ \delta_{24}=Q_6; \tag{D-66}$$

For $j=3,n-2$,

$$\delta_{j\,j-2}=Q_7;\ \delta_{j\,j-1}=Q_5;\ \delta_{j\,j}=Q_3;\ \delta_{j\,j+1}=Q_4;\ \delta_{j\,j+2}=Q_6; \tag{D-67}$$

For $j = n-1$,

$$\delta_{j\,j-2} = Q_7;\ \delta_{j\,j-1} = Q_5;\ \delta_{j\,j} = Q_3 - Q_6;\ \delta_{j\,j+1} = Q_4 + 2Q_6; \tag{D-68}$$

For $j = n$,

$$\delta_{j\,j-2} = Q_7 - Q_6\frac{E_1}{E_5};\ \delta_{j\,j-1} = Q_5 - Q_4 + Q_6\left(-\frac{E_2}{E_5} + \frac{E_4}{E_5}\right);\ \delta_{j\,j} = Q_3 + 2Q_4 + Q_6\left(-\frac{E_3}{E_5} - \frac{2E_4}{E_5}\right); \tag{D-69}$$

The vector $\{\Omega\}$ is modified such that for any element except the last,

$$\Omega_j(t_k) = P_{eff}\left(h_j^*, t_k\right) \tag{D-70}$$

and for the last element $j = n$,

$$\Omega_j(t_k) = P_{eff}\left(h_j^*, t_k\right) - \frac{Q_6}{E_5}F_A\left(h_j^*\right)\theta_g\left(t_k\right) \tag{D-71}$$

The remainder of the derivation is identical to the general case. Note the size of the problem for the fixed-base case is n but is $n+1$ in the general case.

D.4. Base Shear and Base Moment

The solution vector computed above gives the displacement profile. Expression for the shear $\left(V_B\right)$ and moment $\left(M_B\right)$ at the end (base) of the element are given as follows:

General case

$$V_B(t) = K_f u\left(h_0^*,t\right) + \frac{F_A\left(h_0^*\right)}{H\Delta h^*}\left[-1.5u\left(h_0^*,t\right) + 2u\left(h_1^*,t\right) - 0.5u\left(h_2^*,t\right)\right]$$
$$+\frac{2EI'\left(h_0^*\right)}{H^3\left(\Delta h^*\right)^2}\left[u\left(h_0^*,t\right) - 2.5u\left(h_1^*,t\right) + 2u\left(h_2^*,t\right) - 0.5u\left(h_3^*,t\right)\right] \tag{D-72}$$
$$+\frac{6EI\left(h_0^*\right)}{H^3\left(\Delta h^*\right)^3}\left[-\frac{1}{2.4}u\left(h_0^*,t\right) + 1.5u\left(h_1^*,t\right) - 2u\left(h_2^*,t\right) + \frac{1}{0.8571}u\left(h_3^*,t\right) - 0.25u\left(h_4^*,t\right)\right]$$

$$M_B(t) = \frac{K_{fr}}{H\Delta h^*}\left[-1.5u\left(h_0^*,t\right) + 2u\left(h_1^*,t\right) - 0.5u\left(h_2^*,t\right)\right]$$
$$-\frac{2EI\left(h_0^*\right)}{H^2\left(\Delta h^*\right)^2}\left[u\left(h_0^*,t\right) - 2.5u\left(h_1^*,t\right) + 2u\left(h_2^*,t\right) - 0.5u\left(h_3^*,t\right)\right] \tag{D-73}$$

Fixed-Base case

$$V_B(t) = \frac{2EI'\left(h_0^*\right)}{H^3\left(\Delta h^*\right)^2}u\left(h_1^*,t\right)$$
$$+\frac{6EI\left(h_0^*\right)}{H^3\left(\Delta h^*\right)^3}\left[1.5u\left(h_1^*,t\right) - 2u\left(h_2^*,t\right) + \frac{1}{0.8571}u\left(h_3^*,t\right) - 0.25u\left(h_4^*,t\right)\right] \tag{D-74}$$

$$M_B(t) = -\frac{2EI\left(h_0^*\right)}{H^2\left(\Delta h^*\right)^2}u\left(h_1^*,t\right) \tag{D-75}$$

D.5. Stability Criterion

At any time instant, the solution vector will be stable per Eq (D-64) if $[\gamma]^{-1}[\alpha]$ and $[\gamma]^{-1}[\delta]$ are bounded. Matrix $[\gamma]^{-1}$ is diagonal with elements $1/Q_1$ except for the first 3×3 sub-matrix. For the solution at any point in the model, except for the lowest three nodes in the chimney, $[\gamma]^{-1}$ can be replaced by $1/Q_1$. Now, investigating the elements in $[\alpha]$ and $[\delta]$, the stability criterion may be shown to be

$$\frac{6EI_{\max}}{H^4\left(\Delta h^*\right)^4}\frac{1}{Q_1}<1 \tag{D-76}$$

For a tapering chimney and assuming the cross-section is largest at the base, Eq (D-76) can be reduced to

$$n<\left(\frac{\rho A_b}{6EI_b}\right)^{\frac{1}{4}}\frac{H}{\sqrt{\Delta t}} \tag{D-77}$$

where n is the number of elements used to define the chimney; A_b and EI_b are the cross-sectional area and area moment of inertia at the base; ρ is the material density; H is the height of the chimney; and Δt is the time step used in the analysis.

D.6. Program Verification

The performance of the program is evaluated by comparing results with those obtained from the analysis of an associated stick model in SAP2000 (CSI, 2009). For this purpose, a straight circular RC chimney of 35 m height with outer and inner diameters equal to 5 and 4.8 m, respectively, is considered. The foundation diameter is 10 m and its depth is 2 m. The ground motions are the same as described in Section 8.3.2. The material properties are those presented in Section 8.3.4.

The validation of the fixed base case is considered first followed by an example that includes foundation flexibility. For the validation, an analysis time step 0.001 sec is used. The recorded data is reported at the interval of 0.005 sec. Cubic interpolation is employed for any intermediate time. According to the stability criteria and analysis time step, the required number of line elements required to define the chimney is 9.

D.6.1. Validation for the Fixed-Base Case

The tip-displacement, base shear and base moment are selected for the purpose of comparison. Figures D-1 through D-3 enables the comparison when only horizontal excitation is considered. Figures

D-4 through D-6 presents data from analysis with horizontal and rocking motions. Finally, Figures D-7 through D-9 presents the results when all three excitations, namely, horizontal, rocking and vertical are considered. The vertical excitation does not noticeably influence the response, which is likely due to the relatively low axial load. The results of analysis using SAP2000 and the code described herein are virtually identical.

D.6.2. Validation for the Flexible Base Case

The Young's modulus and Poisson's ratio for the soil are set equal to 2419 kN/m^2 and 0.33, respectively. The properties of the spring and damper are calculated using the formulae presented by Gazetus (1983). These values are reported in Table D-1. The following response parameters are selected for the purpose of comparison: i) tip displacement, ii) base displacement, iii) horizontal force and moment at the foundation springs, and iv) base shear and base moment at the member end just above the base. Figures D-10 through D-15 enables the comparison when only horizontal excitation is considered. Figures D-16 through D-21 presents data from analysis with horizontal and rocking motions. Finally, Figures D-22 through D-27 presents the results when all three excitations, namely, horizontal, rocking and vertical are considered. The results of analysis using SAP2000 and the code described herein are virtually identical. Again, the vertical excitation does not have a significant effect on the responses.

Table D-1: Foundation modeling parameters

m_f (ton)	c_f (kN-sec/m)	k_f (kN/m)	I_f (ton-m^2)	c_{fr} (kN-m-sec/rad)	k_f (kN-m/rad)
393	14730	430867	2454	146680	8949613

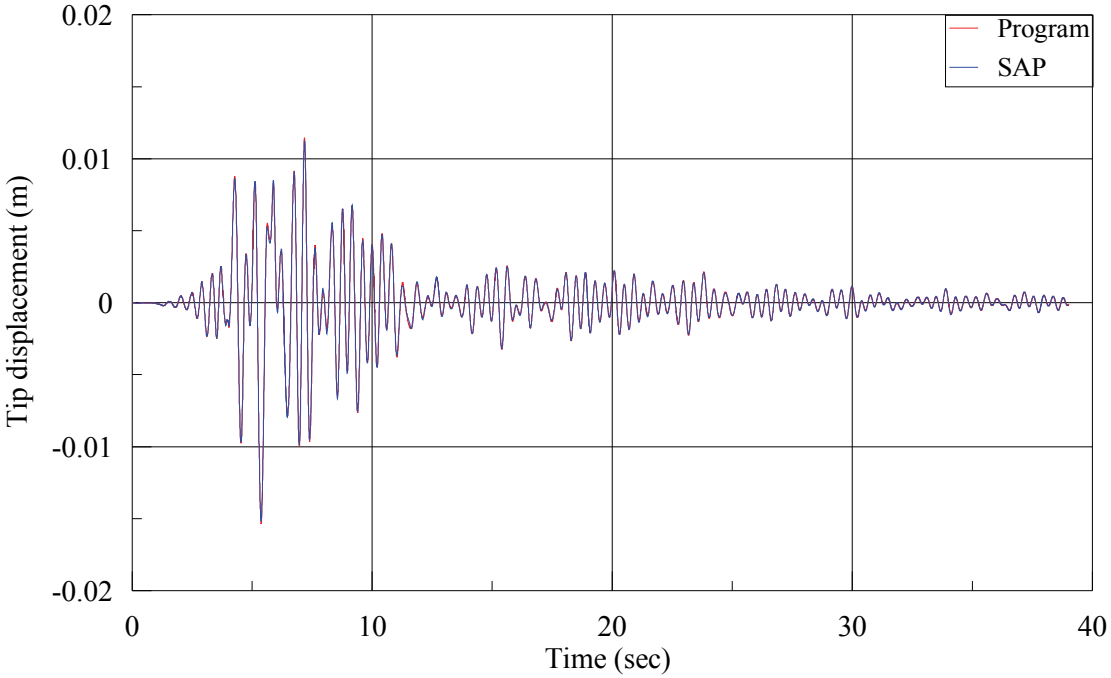

Figure D-1: Tip displacement under horizontal excitation, fixed base

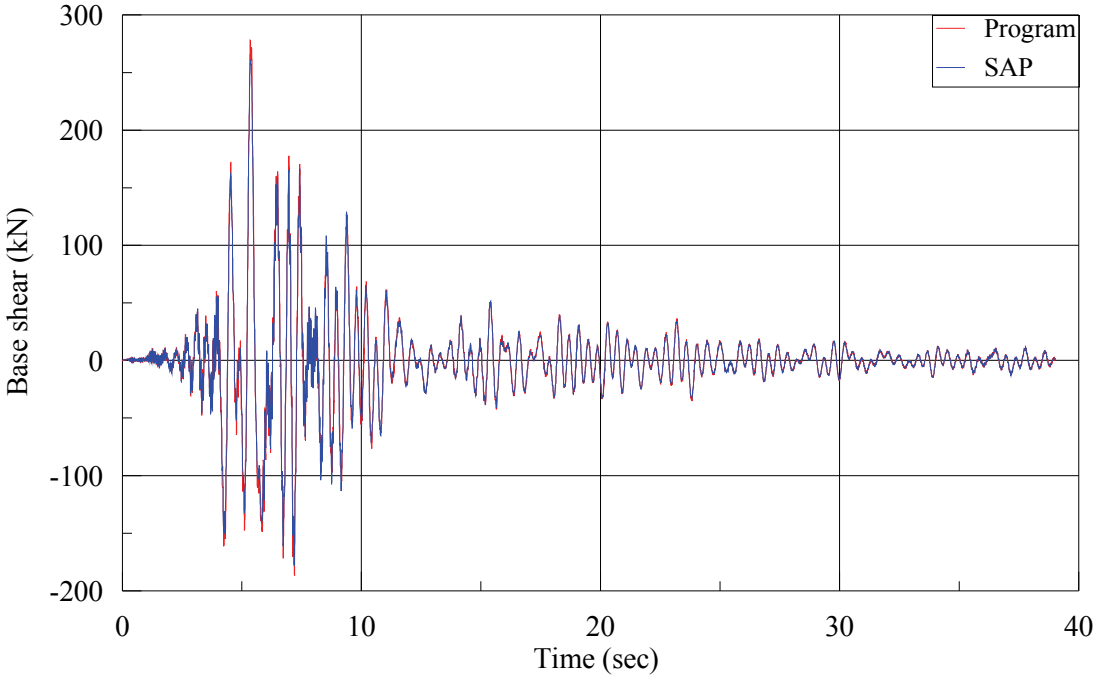

Figure D-2: Base shear under horizontal excitation, fixed base

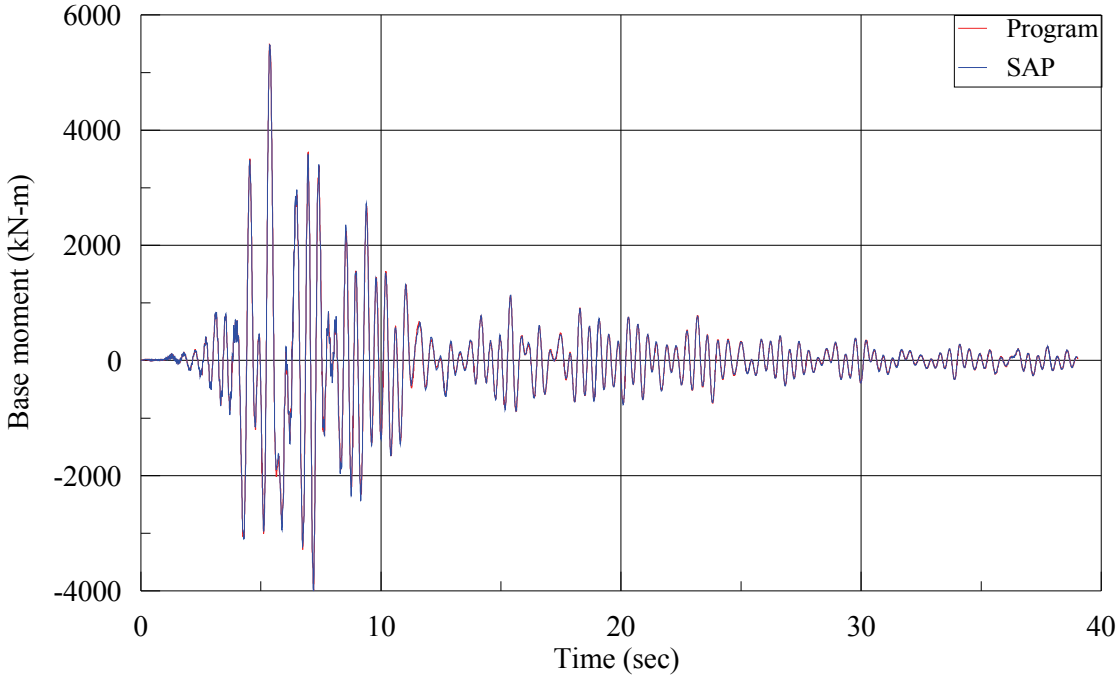

Figure D-3: Base moment under horizontal excitation, fixed base

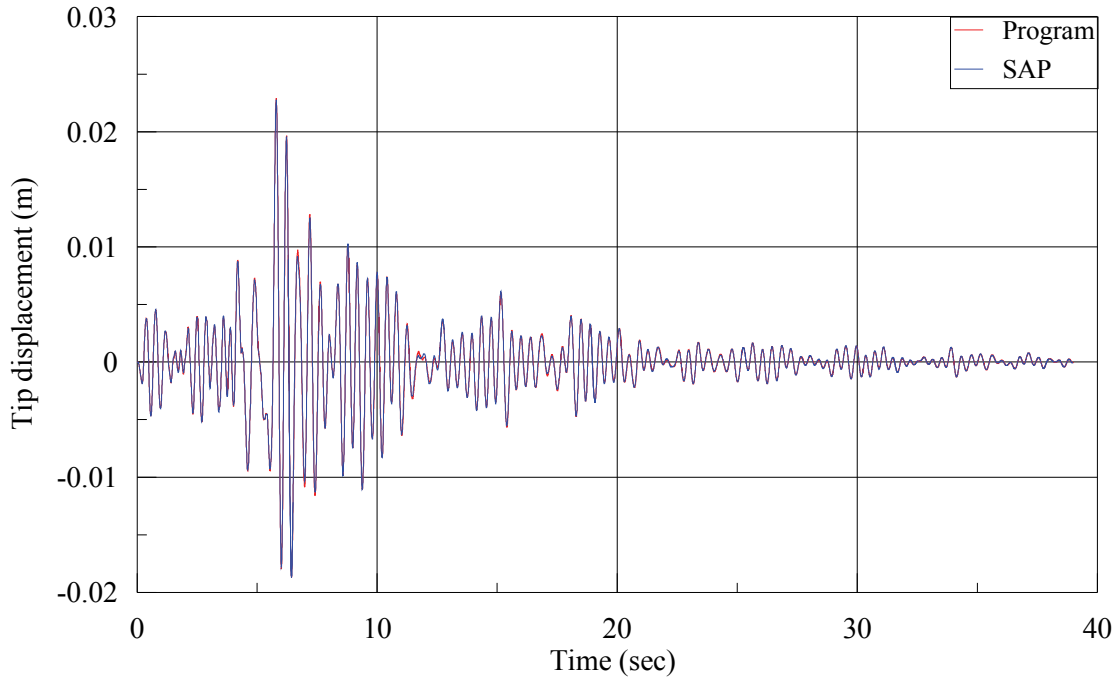

Figure D-4: Tip displacement under horizontal and rocking excitations, fixed base

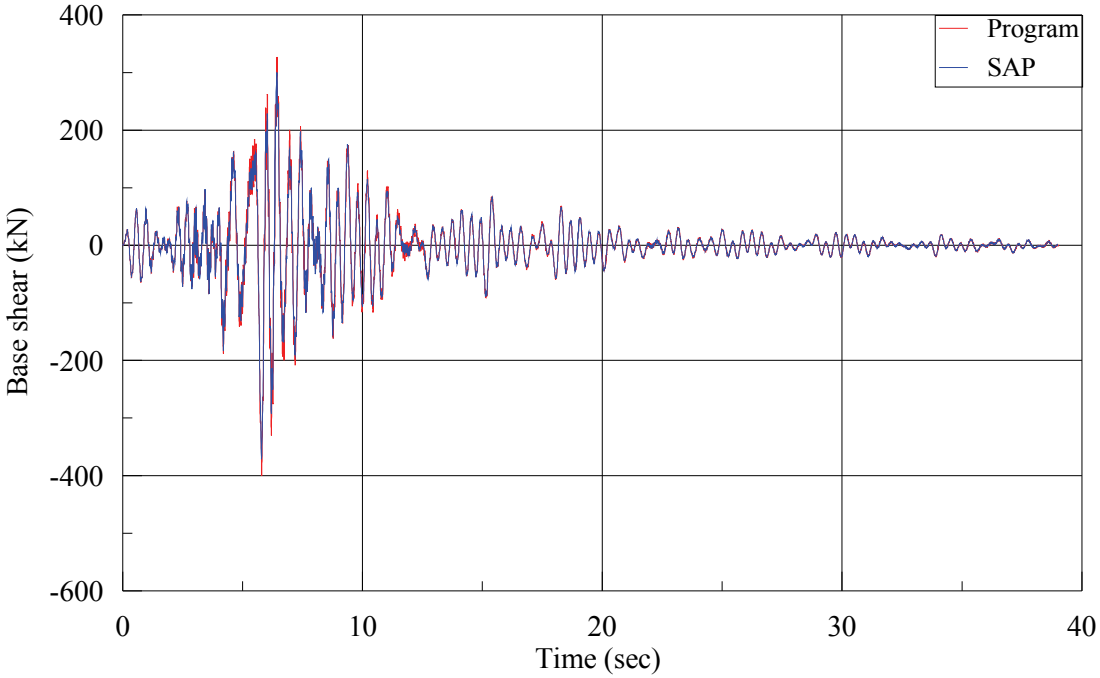

Figure D-5: Base shear under horizontal and rocking excitations, fixed base

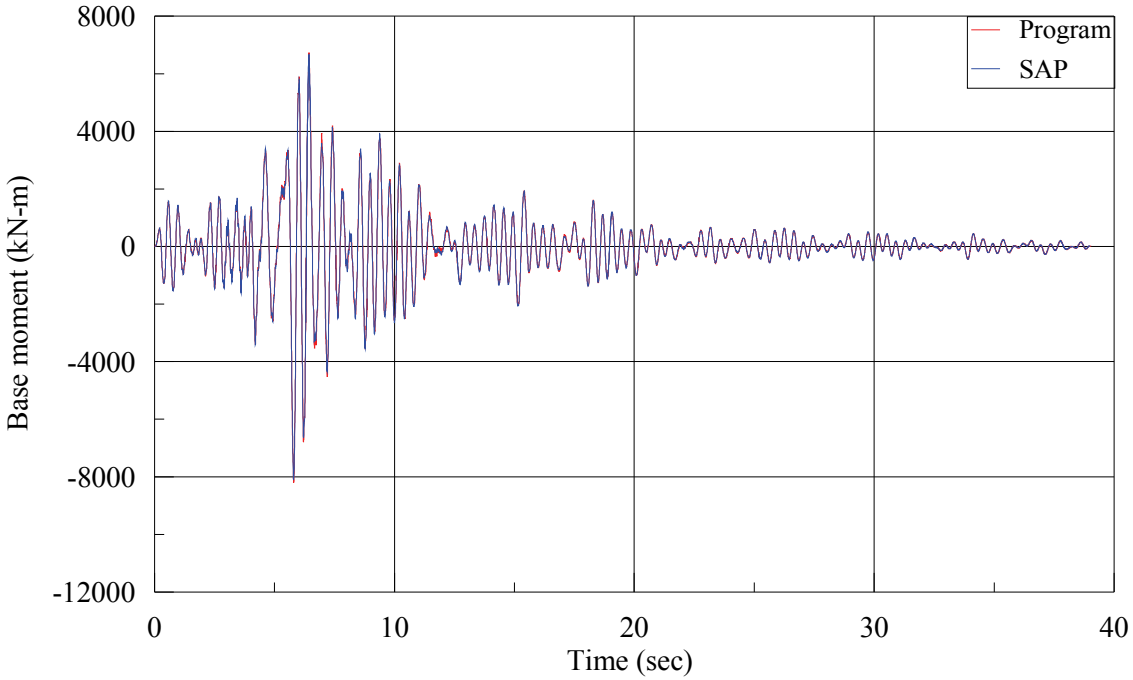

Figure D-6: Base moment under horizontal and rocking excitations, fixed base

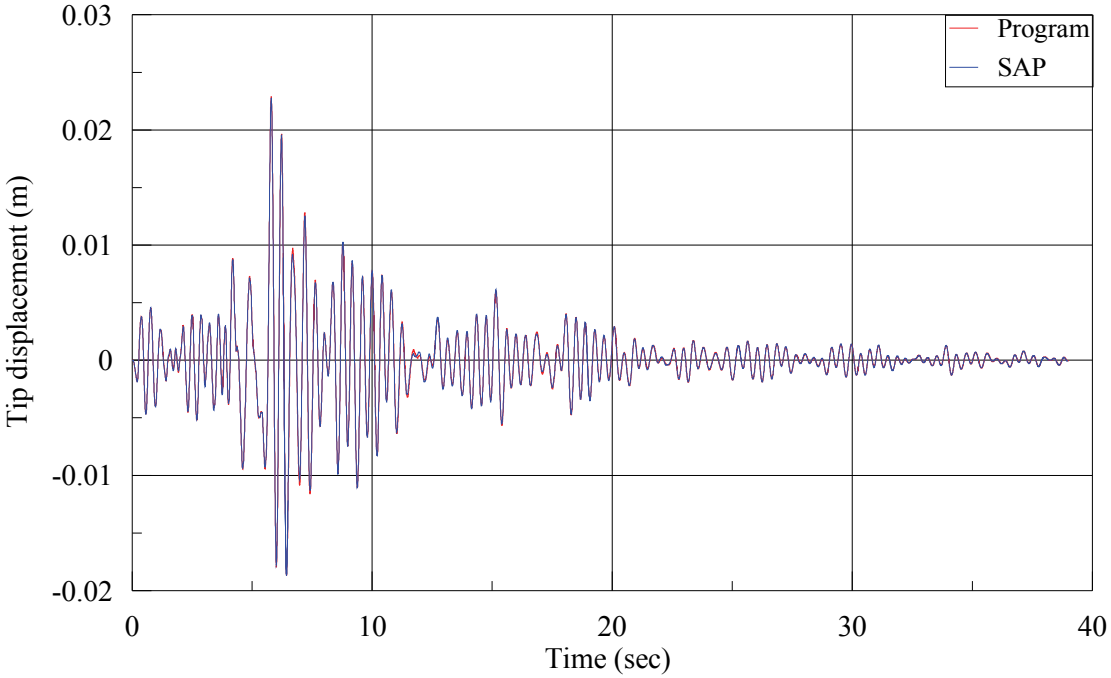

Figure D-7: Tip displacement under horizontal, rocking and vertical excitations, fixed base

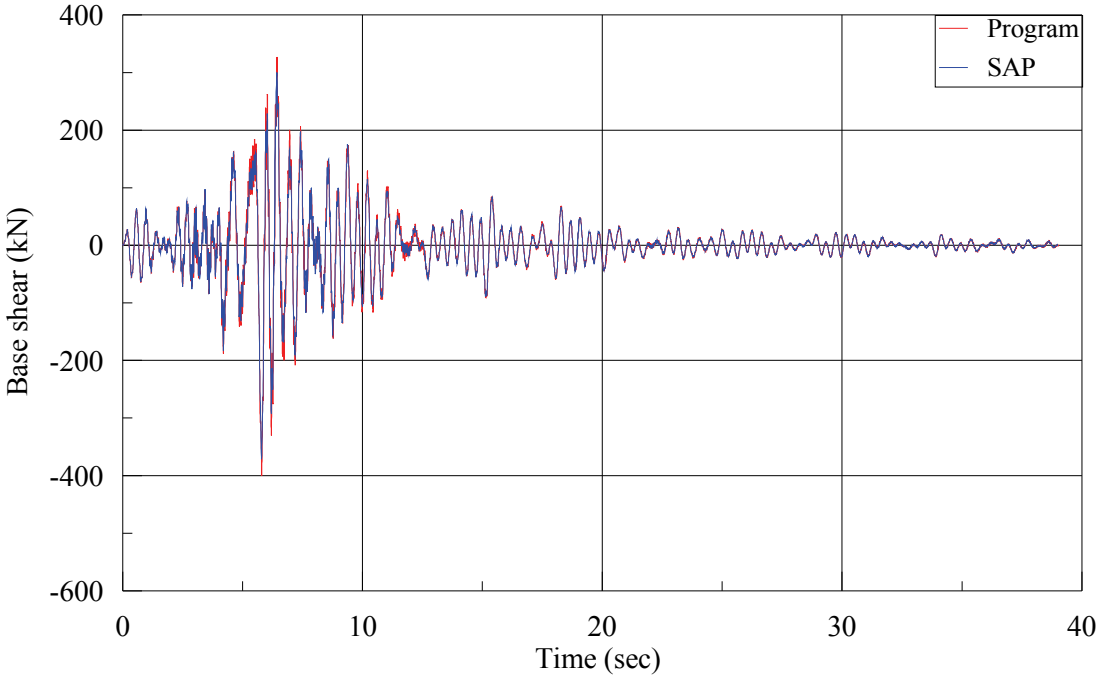

Figure D-8: Base shear under horizontal, rocking and vertical excitations, fixed base

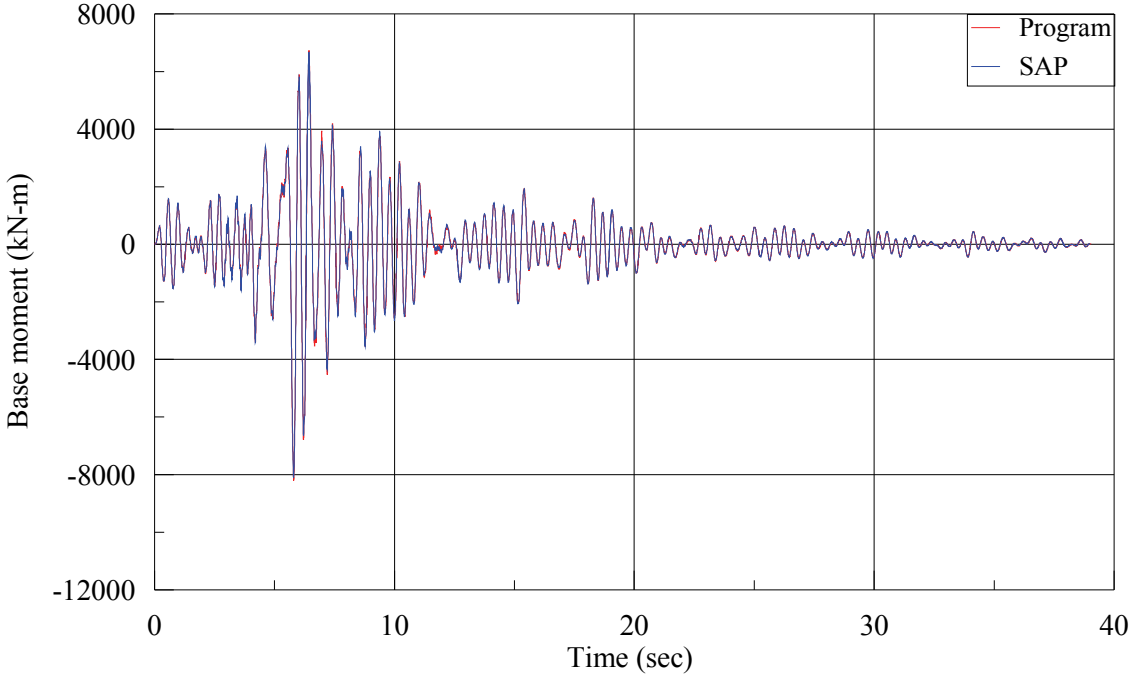

Figure D-9: Base moment under horizontal, rocking and vertical excitations, fixed base

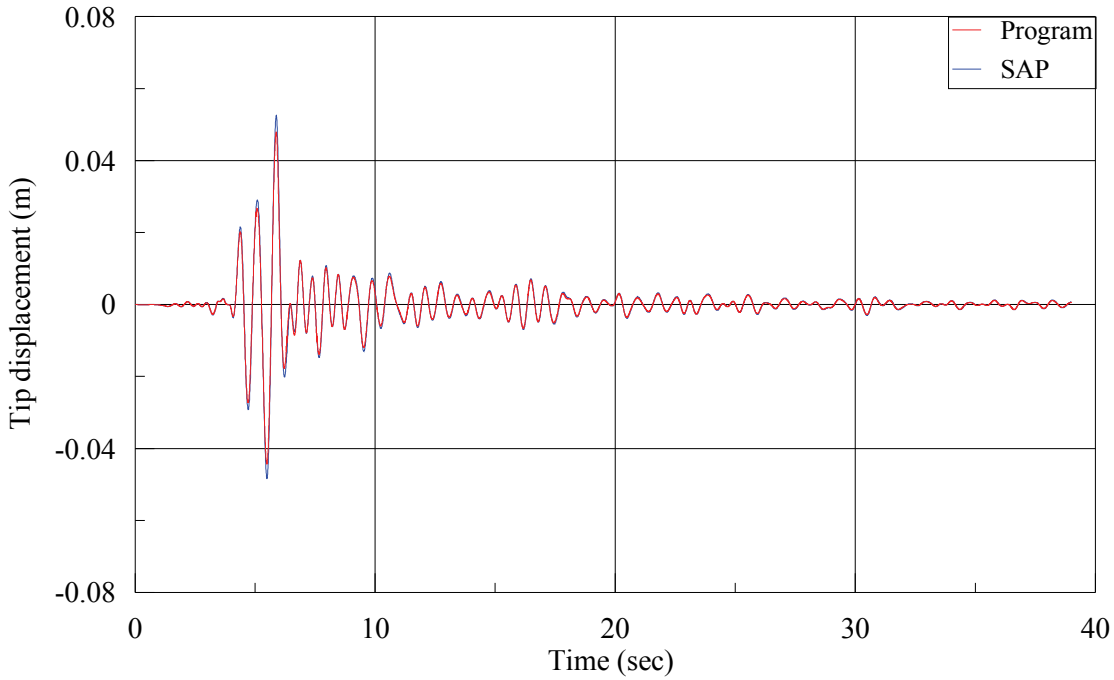

Figure D-10: Tip displacement under horizontal excitation, flexible base

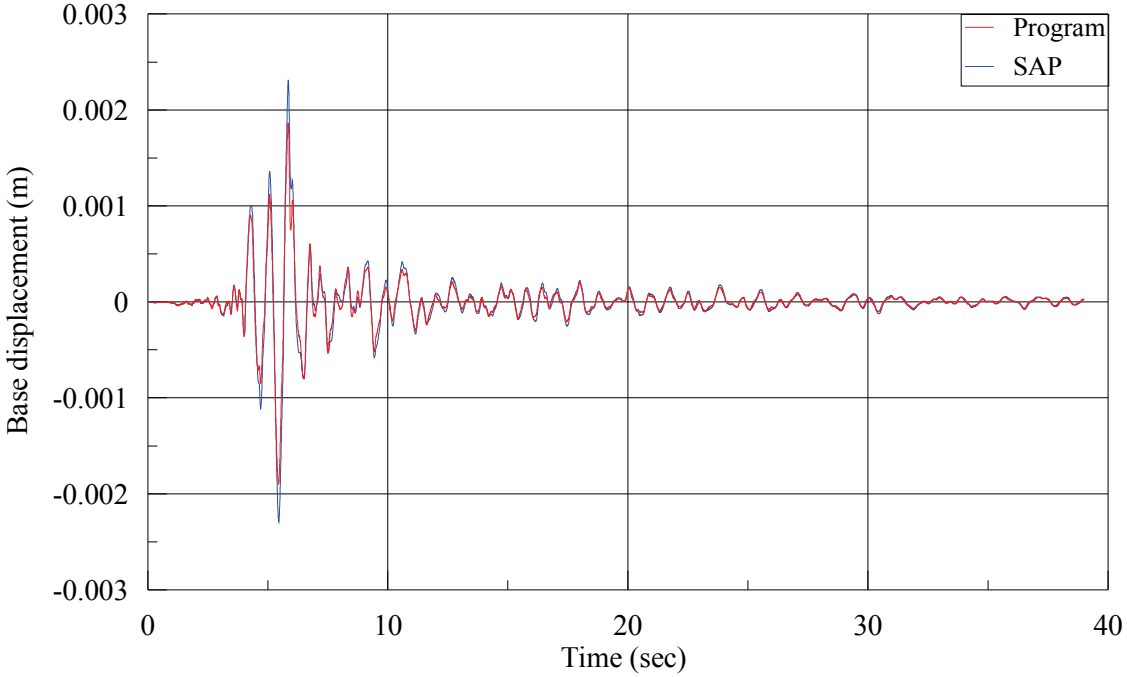

Figure D-11: Base displacement under horizontal excitation, flexible base

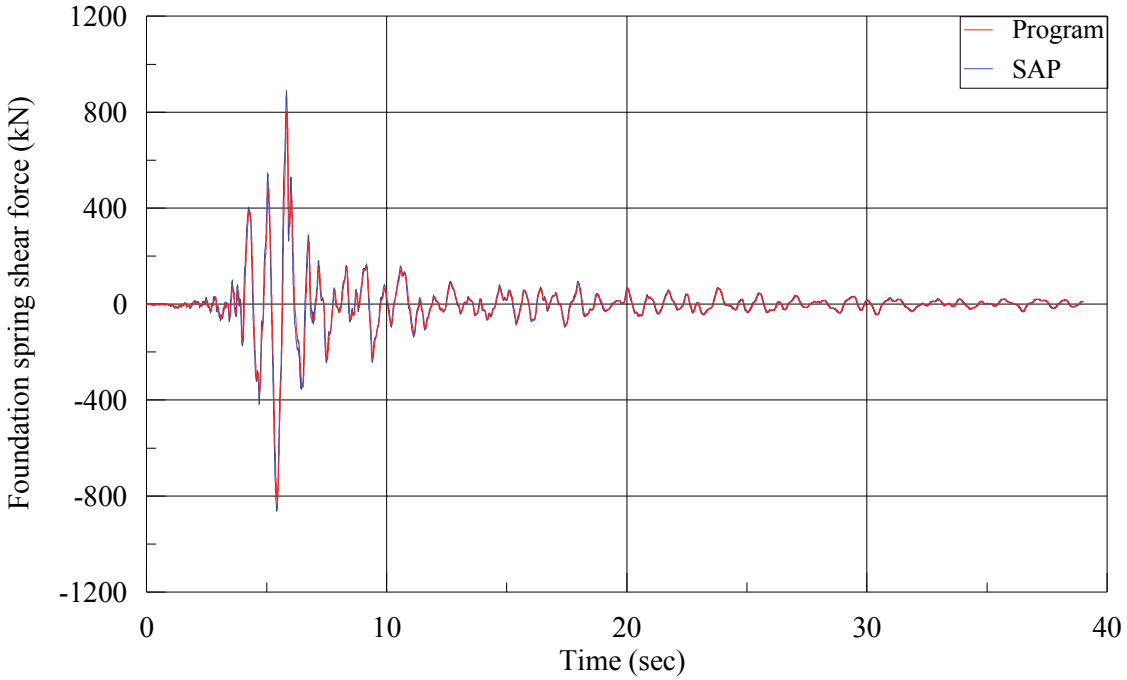

Figure D-12: Foundation spring shear force under horizontal excitation, flexible base

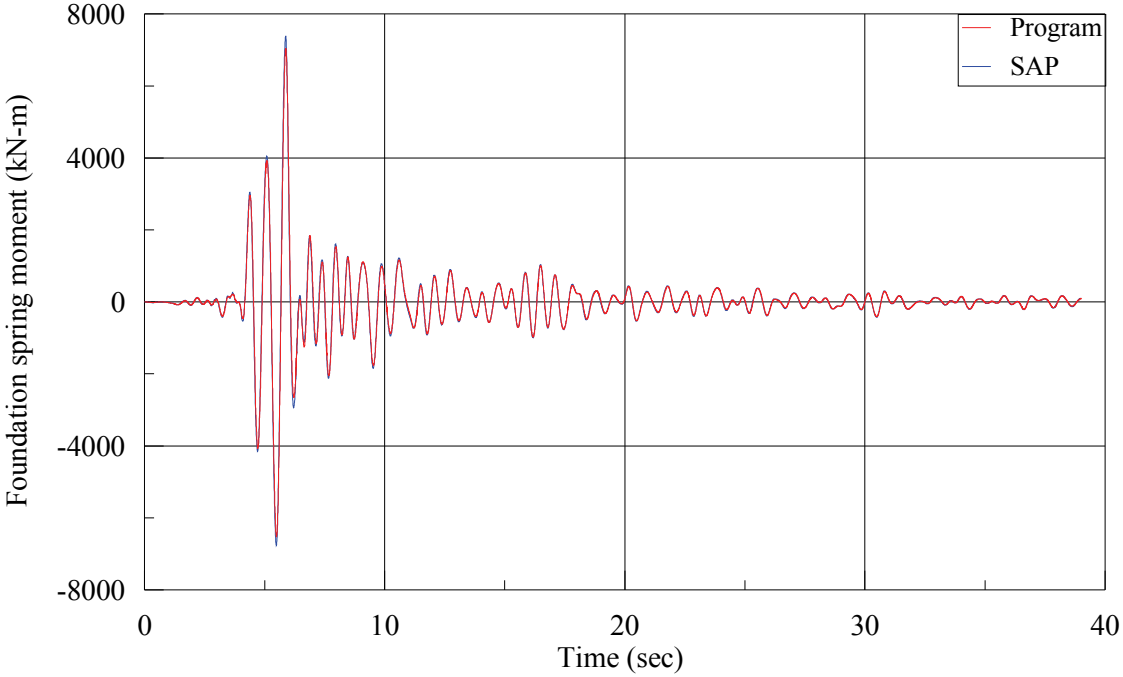

Figure D-13: Foundation spring moment under horizontal excitation, flexible base

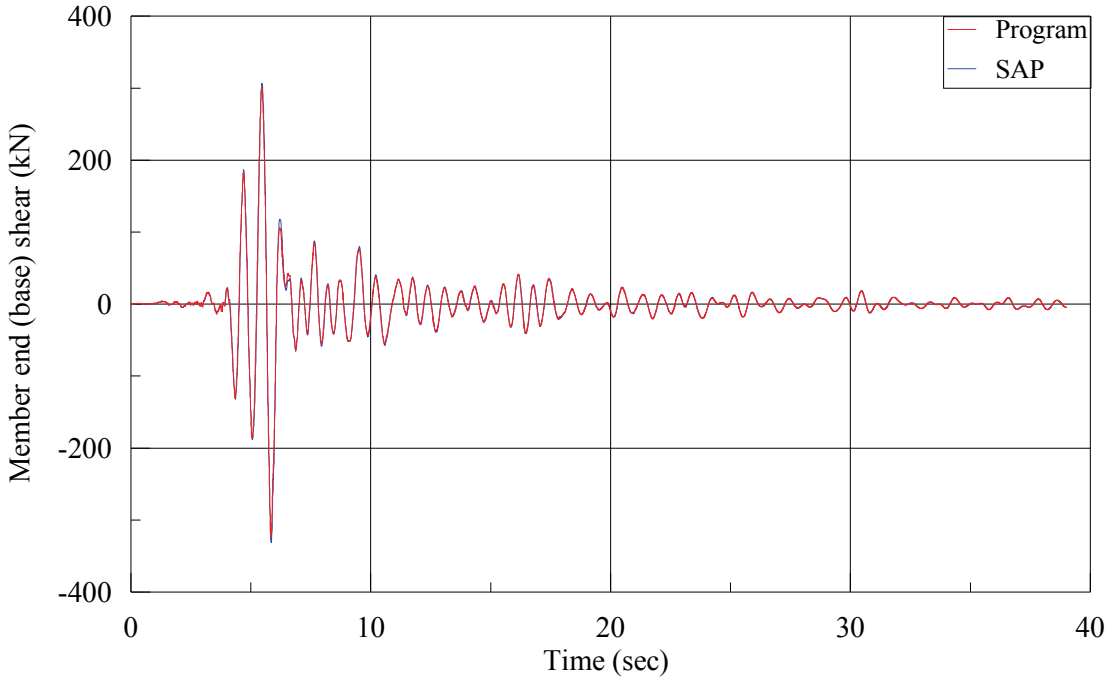

Figure D-14: Member end (base) shear under horizontal excitation, flexible base

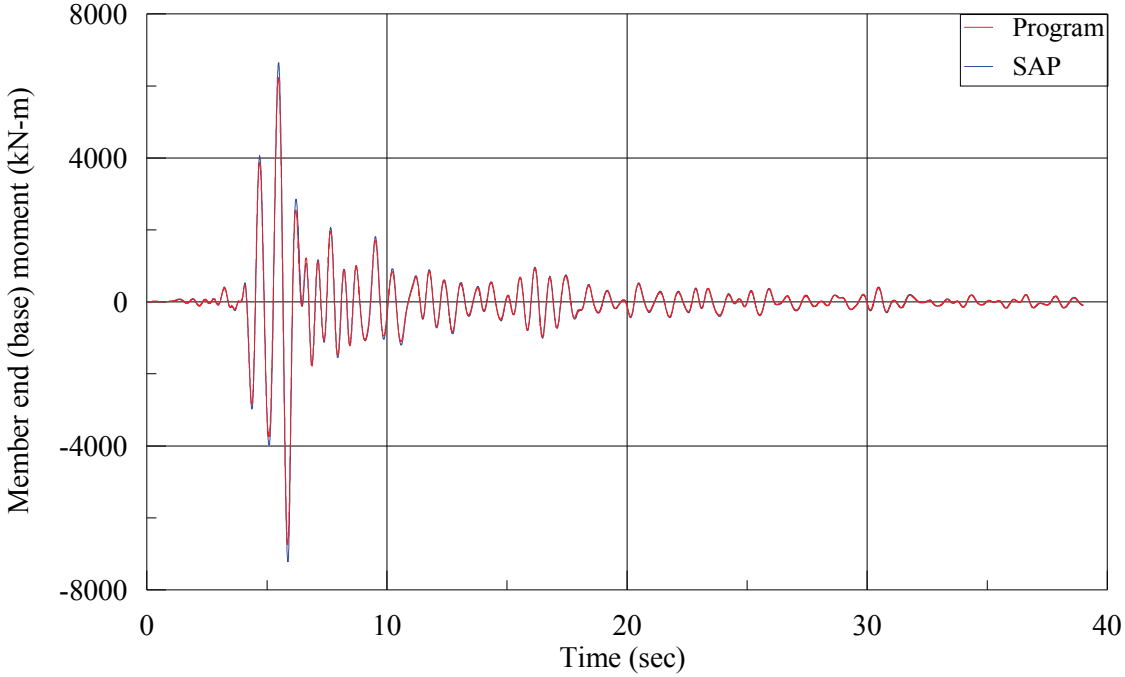

Figure D-15: Member end (base) moment under horizontal excitation, flexible base

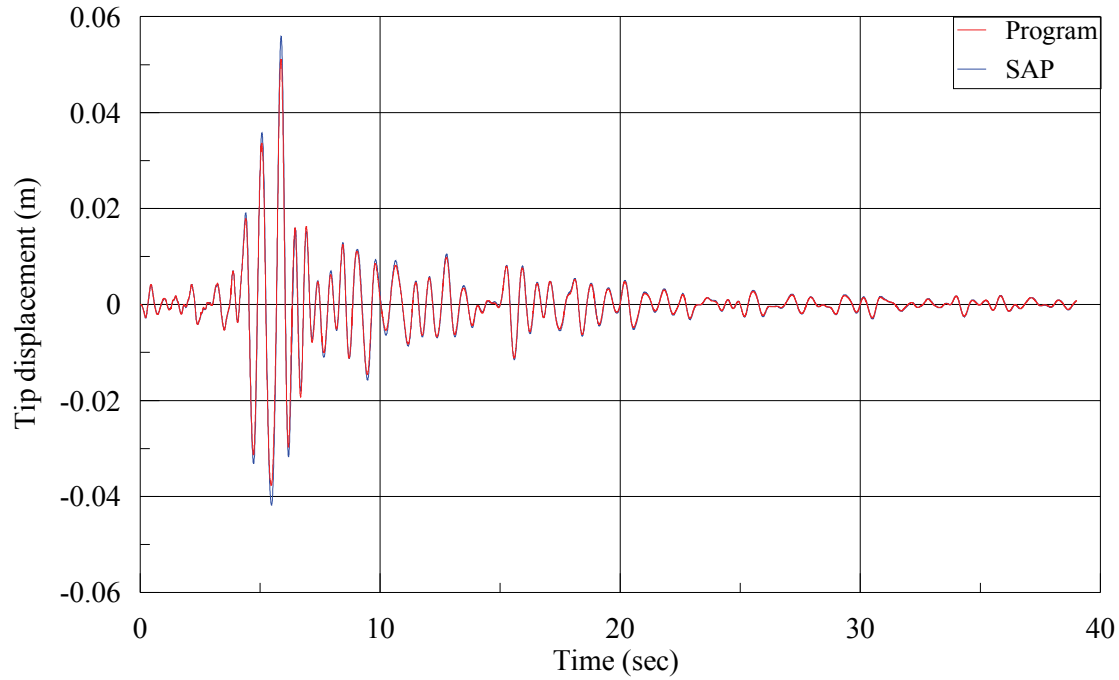

Figure D-16: Tip displacement under horizontal and rocking excitations, flexible base

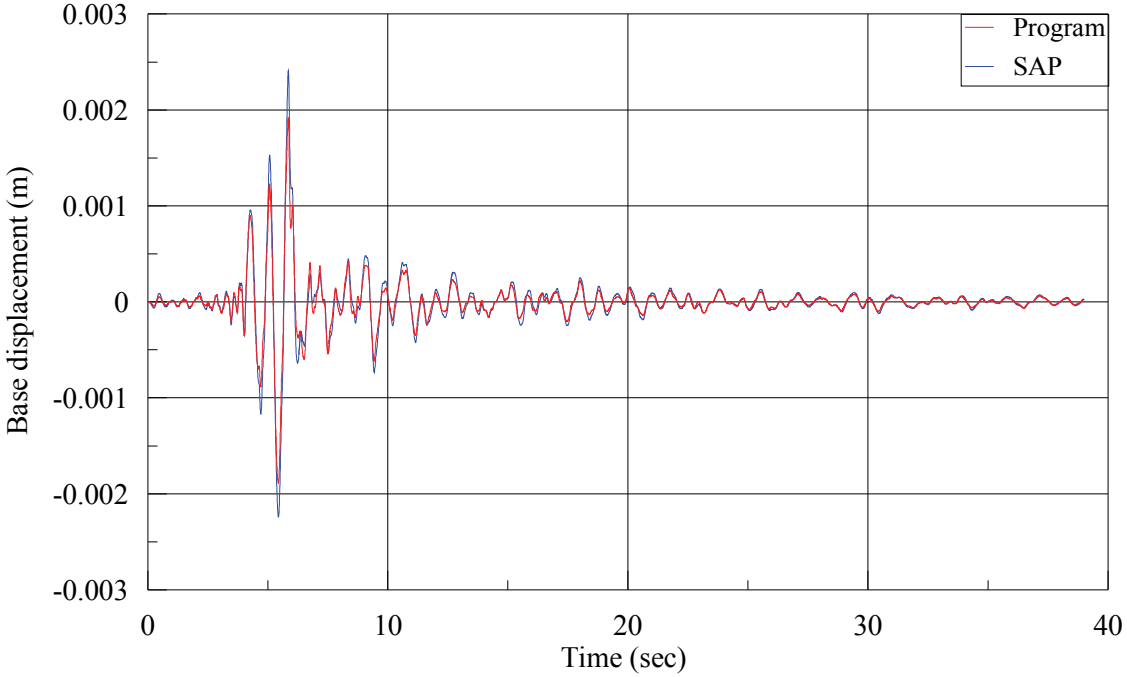

Figure D-17: Base displacement under horizontal and rocking excitations, flexible base

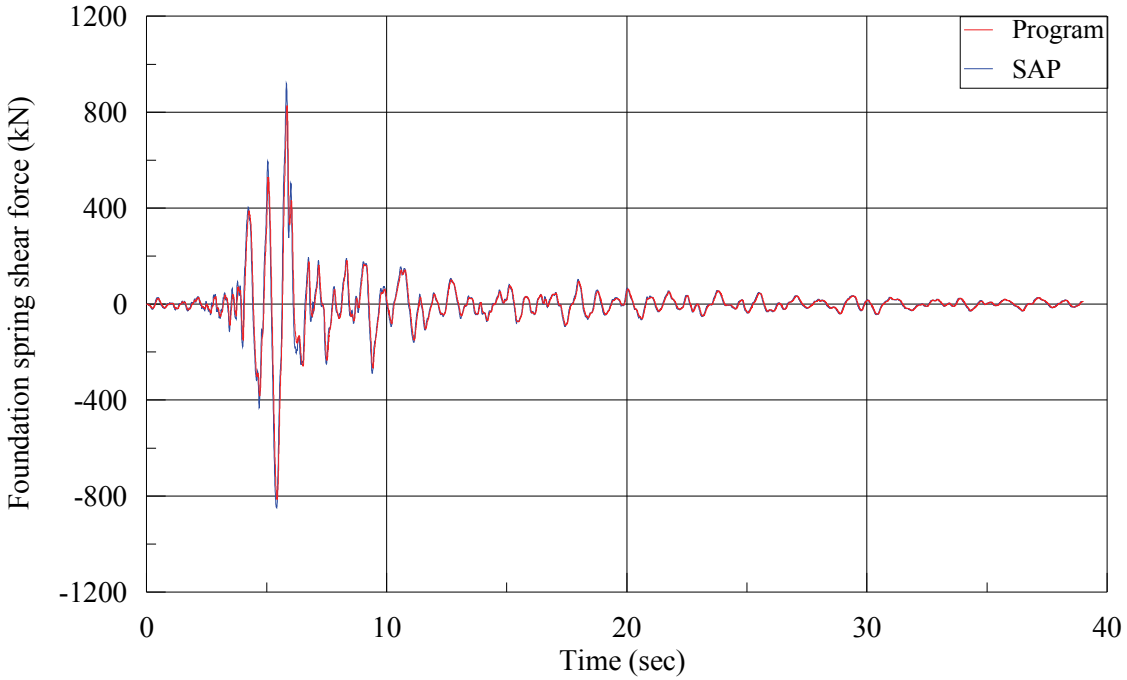

Figure D-18: Foundation spring shear force under horizontal and rocking excitations, flexible base

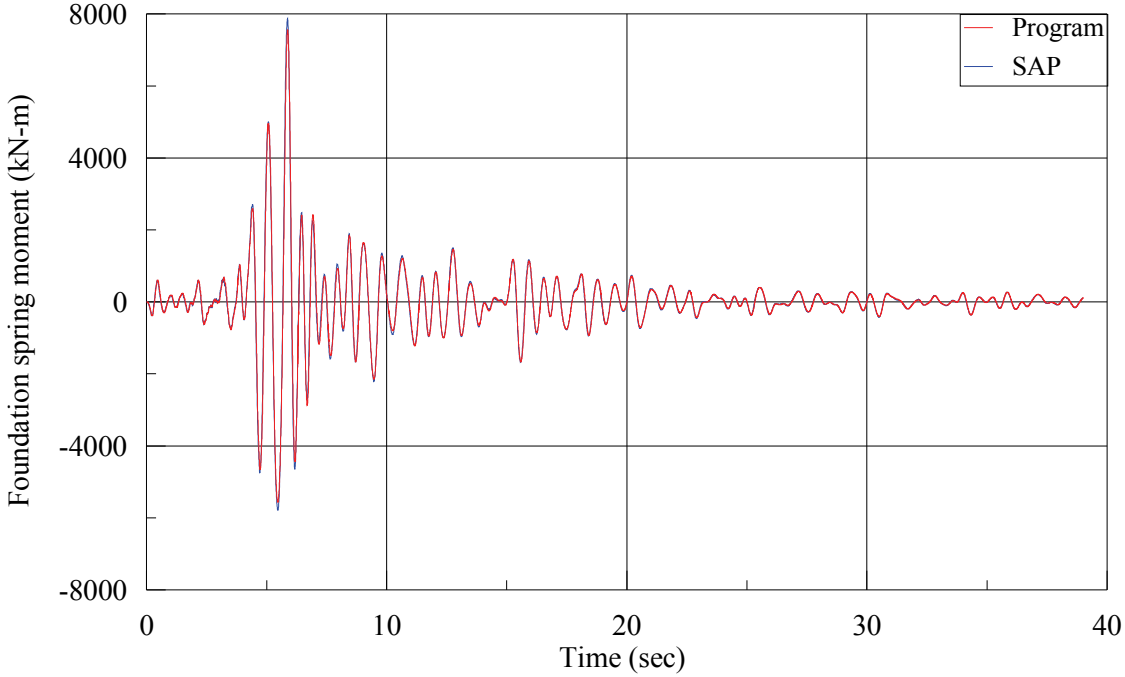

Figure D-19: Foundation spring moment under horizontal and rocking excitations, flexible base

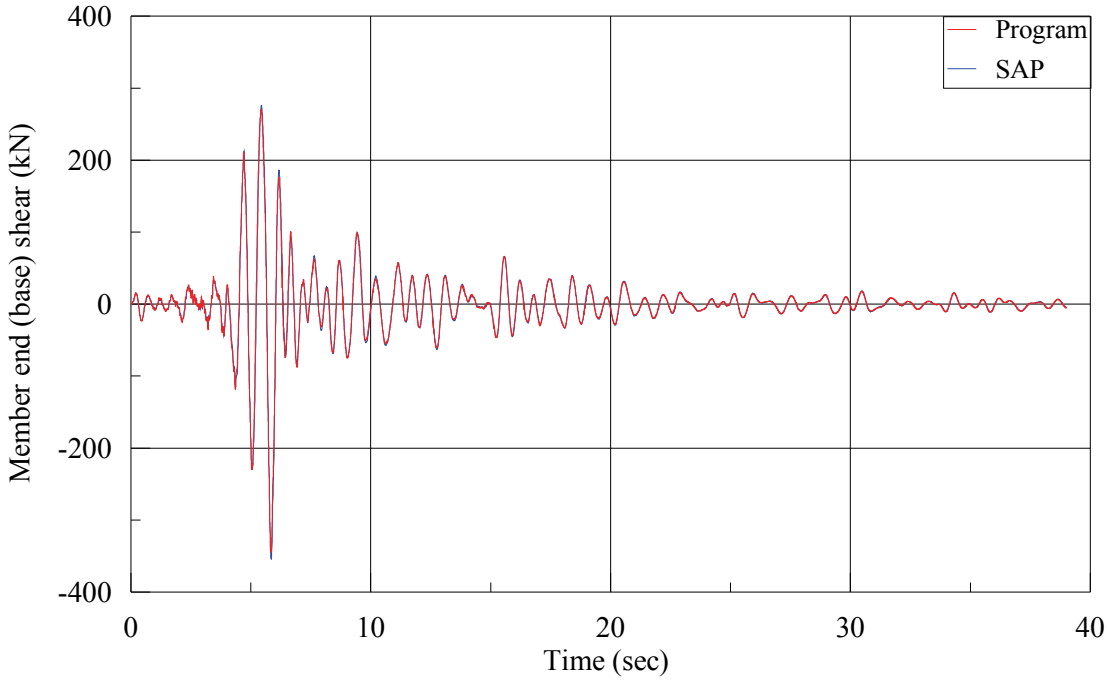

Figure D-20: Member end (base) shear under horizontal and rocking excitations, flexible base

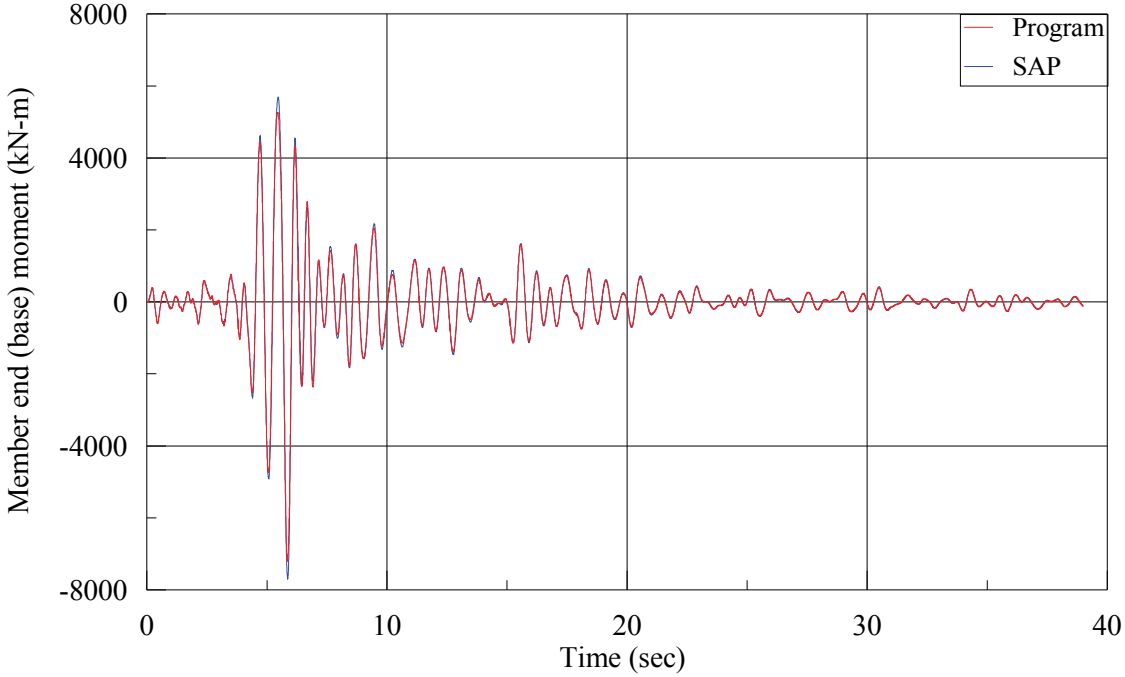

Figure D-21: Member end (base) moment under horizontal and rocking excitations, flexible base

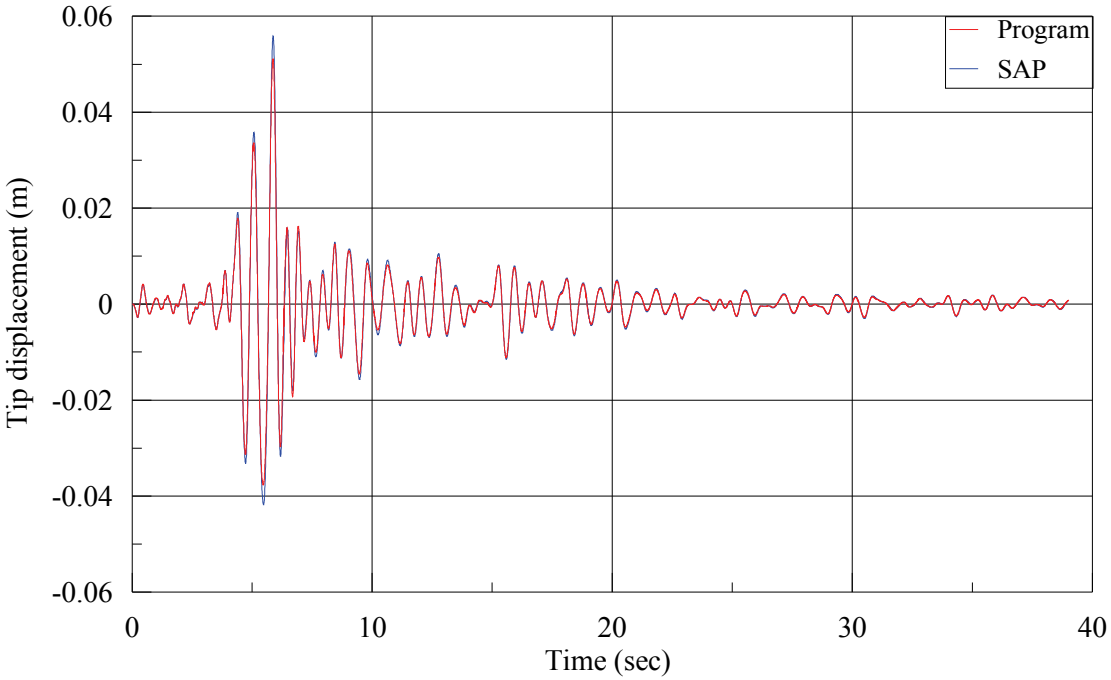

Figure D-22: Tip displacement under horizontal, rocking and vertical excitation, flexible base

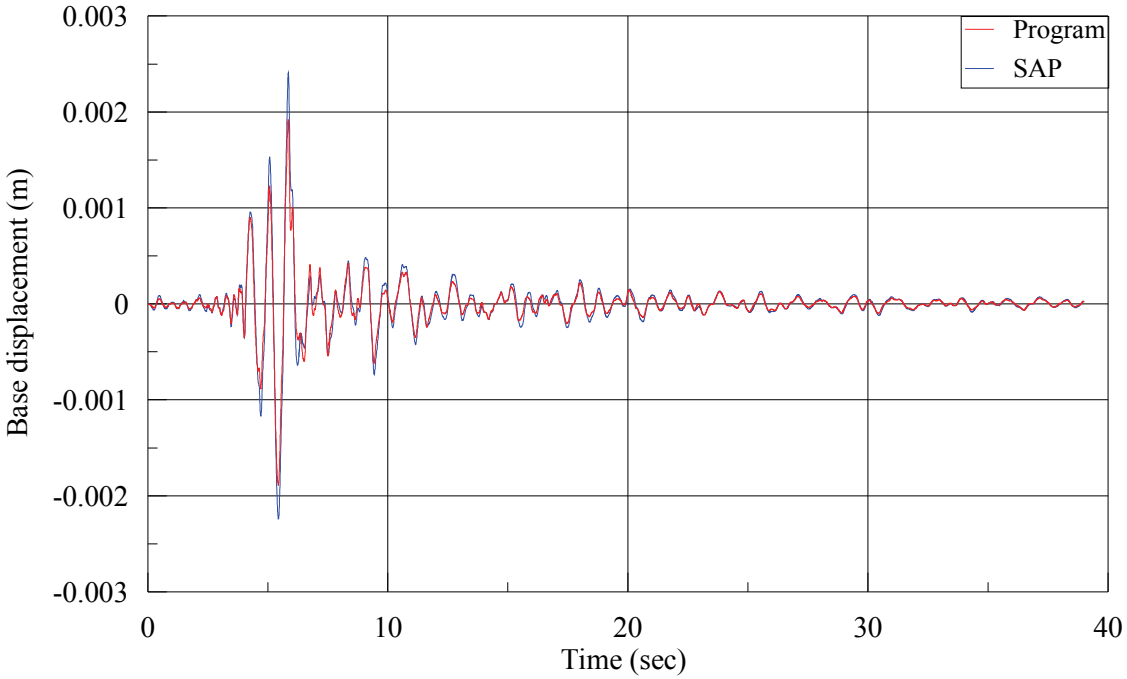

Figure D-23: Base displacement under horizontal, rocking and vertical excitation, flexible base

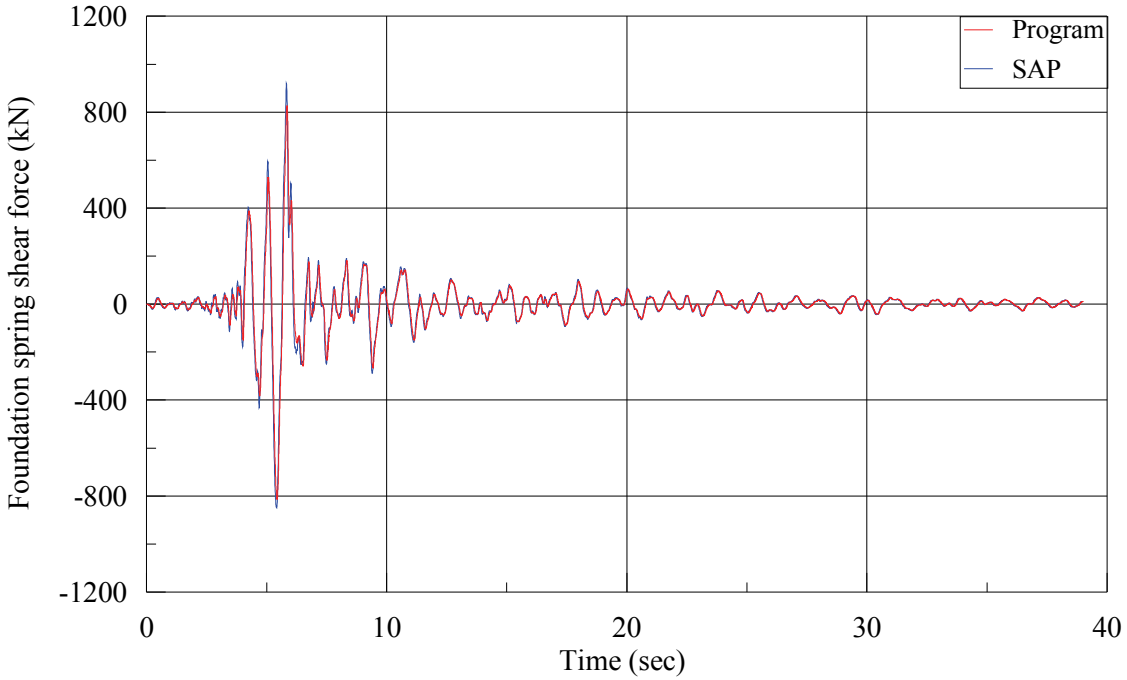

Figure D-24: Foundation spring shear force under horizontal, rocking and vertical excitation, flexible base

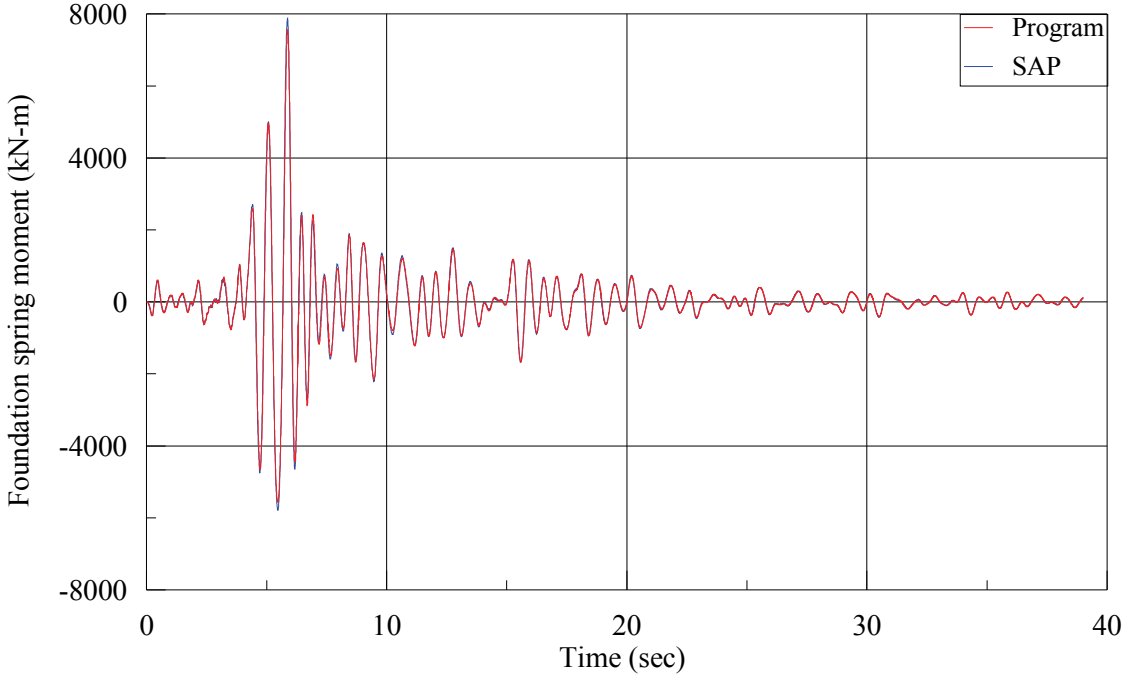

Figure D-25: Foundation spring moment under horizontal, rocking and vertical excitation, flexible base

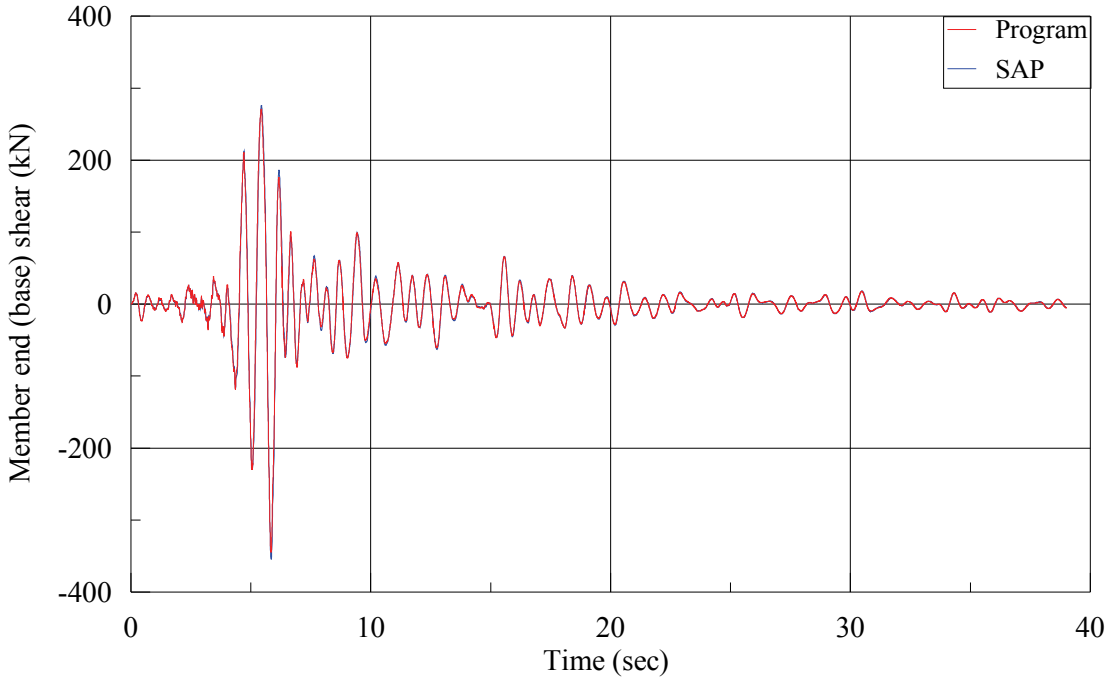

Figure D-26: Member end (base) shear under horizontal, rocking and vertical excitation, flexible base

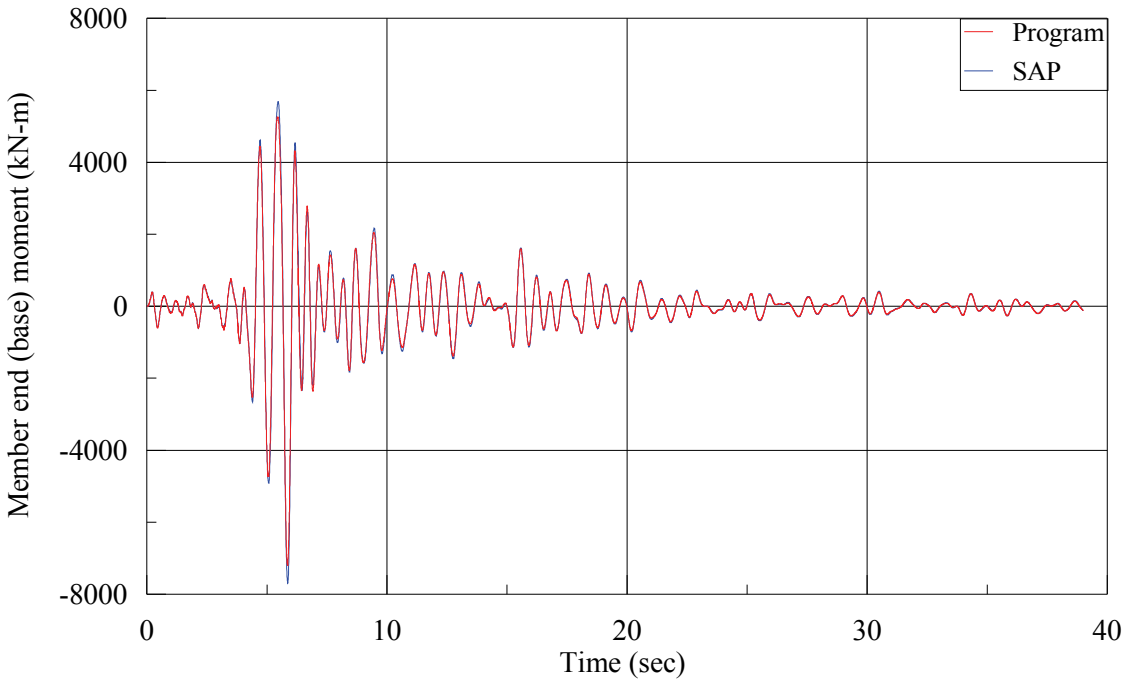

Figure D-27: Member end (base) moment under horizontal, rocking and vertical excitation, flexible base

ISSN 1520-295X